

Founded by Richard von Mises in 1921

Edited in cooperation with Universität Potsdam
and Gesellschaft für Angewandte Mathematik und Mechanik e. V. (GAMM)
Editors-in-Chief: E. Kreuzer, R. Mennicken, H. Schwetlick

DISTRIBUTION STATEMENT A
Approved for Public Release
Distribution Unlimited

GAMM 2000

Annual Meeting

Short Communications in Mathematics and Mechanics
Section 9–25

University of Göttingen, Germany
April 2–7, 2000

Edited by Gerd E. A. Meier, DLR Göttingen

 **WILEY-VCH**

Volume 81 · 2001
Supplement 3

20010927 023

To our Authors

ZAMM publishes original papers (main articles and short communications), the lectures presented at the annual GAMM conferences, and survey articles (requested by the Editorial Office of ZAMM). Papers in English (preferably) to be submitted for publication should be sent to the address at the bottom of this page (master and one copy), in the case of original papers together with an explicit assurance that they have not been published previously in, or are submitted to, another public journal. Authors are held fully responsible for all information included in their paper and should have one copy available for correction purposes. They get two sets of page proofs, one of them has to be returned within one week. Authors may be charged for extensive corrections in the text; corrections in the figures are not possible.

Manuscripts may be submitted in typewritten form or on disk together with a printout that is identical with the text on the disk. Manuscripts should be one-sided, double-spaced with wide margins at both sides, each sheet numbered, beginning with authors' names and the title of the paper. Extra types (like bold-faced letters etc.) should be marked or printed. Please, distinguish 1, l, e; v, v, w, w; o, O, 0 (zero); k, K, x; i; i; x, x (cross), z etc. **Formulas** must be typed clearly legible (never use pencil). Formulas used in the text have to be numbered at the right margin. Use abbreviations for long terms, "exp" instead of "e" for extensive exponents, bold-faced letters for vectors etc. instead of arrows; avoid hierarchies of indices and exponents if possible. The end of a proof should be marked.

When preparing your ZAMM article with LATEX, please use the special class file **zamm.cls** (for LATEX 2e) or style file **zamm.sty** (for LATEX 2.09), respectively. Please, download these files from the internet site <http://www.wiley-vch.de/berlin/journals/zamm> (or contact the editorial office).

Figures should be submitted on separate sheets, drawn with Indian ink and numbered consecutively. Figure captions, tables, and footnotes (if not avoidable) should be inserted in the final place in the text.

References should be numbered in brackets throughout the text and collected according to these numbers in the appended bibliography (References). Each reference should contain Author(s), title, and complete bibliographical coordinates following the subsequent examples.

Books (Reports, Preprints etc.):

IRONS, B. M.; SHRIVE, N. G.: Numerical methods in engineering and applied science – Numbers are fun. Ellis Horwood Series in Mathematics and Its Applications. Ellis Horwood Ltd., Chichester 1987.

Articles in periodicals:

KASSEM, S. E.: Wave source potentials for two superposed fluids, each of finite depth. *Indian J. Pure Appl. Math.* **18** (1987) 2, 186–193.

Articles in Proceedings etc.:

LABISCH, F. K.: Some remarks on the morphology of nonunique solutions in nonlinear elastostatics. In: KÜPPER, T.; SEYDEL, R.; TROGER, H. (eds.): Bifurcation: Analysis, algorithms, applications. Proc. Conf. at the Univ. of Dortmund, August 18–22, 1988. Internat. Ser. of Numer. Mathematics, Vol. 79, Birkhäuser Verlag, Basel–Boston–Stuttgart 1987, pp. 177–184.

To each original paper and review article, a **summary** of 5 to 10 lines in English (for manuscripts of more than 10 pages also in German) and a short list of key-words and corresponding AMS (MOS) classification numbers are needed.

The precise address of each author with full name, academic title etc. is to be added. Information on address changes is appreciated.

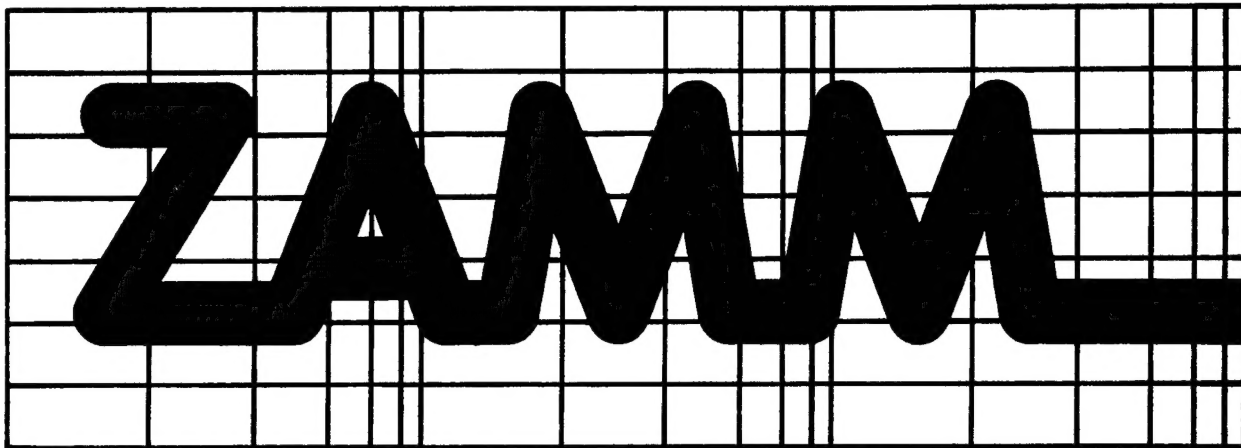
Assignment of Rights for Journal Contributions

With the acceptance of the manuscript for publication in ZAMM – Zeitschrift für Angewandte Mathematik und Mechanik, WILEY-VCH Verlag GmbH acquires exclusively for three years from the date on which the article is published and thereafter for the full term of copyright, including any future extensions, on a nonexclusive basis all publishing rights including those of pre-publication, reprinting, translating, other forms of reproduction e.g. by photocopy, microform, or other means including machine-readable forms like CD-ROM, CD-I, DVD, diskettes, electronic storage and publishing via Local Area Networks, Intranet and Internet, and other data networks and other forms of distribution e.g. by Document Delivery-Services of this article world-wide. This includes the right of WILEY-VCH Verlag GmbH to transfer to third parties the partial or full rights. Moreover, the provisions of laws of the Federal Republic of Germany apply.

Editorial Office „ZAMM“
University of Potsdam
Institute of Mathematics
POB 60 15 53
D-14415 Potsdam
Germany

REPORT DOCUMENTATION PAGE			Form Approved OMB No. 0704-0188	
Public reporting burden for this collection of information is estimated to average 1 hour per response, including the time for reviewing instructions, searching existing data sources, gathering and maintaining the data needed, and completing and reviewing the collection of information. Send comments regarding this burden estimate or any other aspect of this collection of information, including suggestions for reducing this burden to Washington Headquarters Services, Directorate for Information Operations and Reports, 1215 Jefferson Davis Highway, Suite 1204, Arlington, VA 22202-4302, and to the Office of Management and Budget, Paperwork Reduction Project (0704-0188), Washington, DC 20503.				
1. AGENCY USE ONLY (Leave blank)		2. REPORT DATE		3. REPORT TYPE AND DATES COVERED
		April 2000		Conference Proceedings
4. TITLE AND SUBTITLE			5. FUNDING NUMBERS	
GAMM 2000 Annual Meeting, Minisymposia, University of Gottingen, Germany, April 2-7, 2000 – Supplement 3			F61775-00-WF017	
6. AUTHOR(S)				
Conference Committee				
7. PERFORMING ORGANIZATION NAME(S) AND ADDRESS(ES)			8. Performing Organization Report Number	
Deutsches Zentrum für Luft- und Raumfahrt Bunsenstr. 10 Gottingen D-37073 Germany			N/A	
9. SPONSORING/MONITORING AGENCY NAME(S) AND ADDRESS(ES)			10. SPONSORING/MONITORING AGENCY REPORT NUMBER	
EOARD PSC 802 Box 14 FPO 09499-0200			CSP 00-5017	
11. SUPPLEMENTARY NOTES				
Conference Proceedings in three volumes. Journal of Applied Mathematics and Mechanics (ZAMM), Volume 81 – 2001, Supplement 1, 2 and 3, ISSN 0946-8463				
12a. DISTRIBUTION/AVAILABILITY STATEMENT			12b. DISTRIBUTION CODE	
Approved for public release; distribution is unlimited.			A	
ABSTRACT (Maximum 200 words)				
The Final Proceedings for GAMM 2000, 2-7 April 2000. This is an interdisciplinary conference in Fluid Mechanics and Numerics in general and include topics such as Aspects of Vortex Dynamics; Controlling Chaos; Multi-scale Theory; Flow Control and optimization; Gas Dynamic; Aerothermodynamic; Turbulence; and others.				
14. SUBJECT TERMS			15. NUMBER OF PAGES	
EOARD, Fluid mechanics, Boundary layer			3 Volumes	
			16. PRICE CODE	
17. SECURITY CLASSIFICATION OF REPORT	18. SECURITY CLASSIFICATION OF THIS PAGE	19. SECURITY CLASSIFICATION OF ABSTRACT	20. LIMITATION OF ABSTRACT	
UNCLASSIFIED	UNCLASSIFIED	UNCLASSIFIED	UL	

Journal of Applied Mathematics and Mechanics



Zeitschrift für Angewandte Mathematik und Mechanik

Founded by Richard von Mises in 1921

Edited in cooperation with Universität Potsdam
and Gesellschaft für Angewandte Mathematik und Mechanik e. V. (GAMM)

Editors-in-Chief: E. Kreuzer, R. Mennicken, H. Schwetlick

GAMM 2000

Annual Meeting

Short Communications in Mathematics and Mechanics
Section 9–29

University of Göttingen, Germany
April 2–7, 2000

Edited by Gerd E. A. Meier, DLR Göttingen

 **WILEY-VCH**

Volume 81 · 2001
Supplement 3

AQ F01-12-2613

The aim and scope of ZAMM is, in agreement with the intentions of its founder Richard von Mises, one of the outstanding scientists of our century in both Mathematics and Mechanics: to publish new results and survey articles, the proceedings of the annual GAMM conferences, book reviews and information on applied mathematics (mainly on numerical mathematics and various parts and applications of analysis, in particular numerical aspects of differential and integral equations), on the whole field of theoretical and applied mechanics (mechanics of particles and systems, solid mechanics, fluid mechanics, thermodynamics) and on mathematical physics.

The journal is of interest for persons working in applied mathematics and mechanics as well as on mathematical or mechanical questions in other sciences, for instance mechanical and civil engineering, electrotechniques, and chemistry.

In Übereinstimmung mit den Zielstellungen des Begründers der ZAMM, Richard von Mises, eines der bedeutendsten Wissenschaftler unseres Jahrhunderts auf dem Gebiet der Mathematik und Mechanik, publiziert die Zeitschrift neue Ergebnisse und Übersichtsartikel, die Vorträge auf den jährlichen GAMM-Tagungen, Buchbesprechungen und Informationen über Angewandte Mathematik (hauptsächlich über numerische Mathematik und verschiedene Teile sowie Anwendungen der Analysis, insbesondere numerische Aspekte bei Differential- und Integralgleichungen), über das gesamte Gebiet der theoretischen und angewandten Mechanik (Mechanik von Mehrkörpersystemen, Festkörpermechanik, Strömungsmechanik, Thermodynamik) und über mathematische Physik.

Die Zeitschrift wendet sich an Vertreter der angewandten Mathematik und Mechanik wie auch an Wissenschaftler und Ingenieure, die sich mit mathematischen oder theoretisch-mechanischen Fragen auf anderen Gebieten, z. B. Maschinenbau und Technik, Elektrotechnik und Chemie, befassen.

Where to order

Please place your order with

WILEY-VCH, P.O. Box 10 11 61, D-69451 Weinheim, telephone: (0 62 01) 60 61 46, telefax: (0 62 01) 60 61 72, telex: 467 155 vchwh d, e-mail: subservice@wiley-vch.de.

Bezugsmöglichkeiten

Bitte richten Sie Ihre Bestellungen an

WILEY-VCH, Postfach 10 11 61, D-69451 Weinheim, Telefon: (0 62 01) 60 61 46, Telefax: (0 62 01) 60 61 72, Telex: 467 155 vchwh d, e-mail: subservice@wiley-vch.de.

For our American customers:

Zeitschrift für Angewandte Mathematik und Mechanik (ISSN 0044-2267) is published twelve times a year (January–December) with three additional issues (ISSN 0946-8463), – 15 issues –, by WILEY-VCH Verlag Berlin GmbH, Böhningstr. 10, D-13086 Berlin, Germany and distributed by John Wiley & Sons, Inc., Distribution Centre, 1 Wiley Drive, Somerset, New Jersey 08 875-1272; telephone: (908) 469-4400; fax: (908) 302-2300; telex: 833 434. Annual subscription price 2000 US\$ 2048.00 including postage and handling; personal rate US\$ 258.00. Periodicals postage paid at Jamaica, NY 11431. Air freight and mailing in the USA by Publications Expediting Services Inc., 200 Meacham Ave., Elmont NY 11003; Send address changes to: ZAMM – Zeitschrift für Angewandte Mathematik und Mechanik, c/o Publications Expediting Inc., 200 Meacham Ave., Elmont NY 11003.

Zeitschrift für Angewandte Mathematik und Mechanik

Edited in cooperation with Universität Potsdam, Institut für Mathematik and Gesellschaft für Angewandte Mathematik und Mechanik e.V. (GAMM) by Prof. Dr.-Ing. Edwin Kreuzer, TU Hamburg-Harburg, AB Meerestechnik II, Eißendorfer Str. 42, D-21073 Hamburg, Prof. Dr. Reinhard Mennicken, NWF I-Mathematik, Universität Regensburg, Universitätsstr. 31, D-93053 Regensburg, and Prof. Dr. Hubert Schwetlick, TU Dresden, Institut für Numerische Mathematik, D-01062 Dresden (Editors-in-Chief). Editorial Office: Redaktion ZAMM, Universität Potsdam, Institut für Mathematik, Postfach 60 15 53, D-14415 Potsdam; telephone: (03 31) 9 77 44 62, fax: (03 31) 9 77 44 06, e-mail: zamm@rz.uni-potsdam.de.

Publishers: WILEY-VCH Verlag Berlin GmbH, Böhningstr. 10, D-13086 Berlin; telephone: (0 30) 47 03 13 25, 47 03 13 27 or 47 03 13 50; telefax: (0 30) 47 03 13 99; URL: <http://www.wiley-vch.de/berlin>; Bank account: Dresdner Bank Weinheim, account no. 754 624 500; BLZ 670 800 50.

Managing director: Dr. Manfred Antoni.

Advertisement: telephone (0 30) 47 03 13 25, 47 03 13 50.

Production at: Druckhaus „Thomas Müntzer“ GmbH, D-99947 Bad Langensalza.

In 2001 the journal is published in one volume per year consisting of fifteen numbers. The subscription price 2001 in Europe is € 1628,-; in the rest of the world \$ 2048.00; personal rate € 208,-; \$ 268.00. Single copy € 125,-; \$ 157.00 incl. postage and handling. Special prices of supplements for members of GAMM and SIAM.

The publisher must be notified of a cancellation of a subscription not later than three months before the end of the calendar year. After that date the subscription is automatically prolonged for another year.

Authorization to photocopy items for internal or personal use, or the internal or personal use of specific clients, is granted by WILEY-VCH Verlag Berlin GmbH, provided that the base fee of US\$ 17.50 per copy, plus US\$.50 per page is paid directly to Copyright Clearance Center, 27 Congress Street, SALEM, MA 01970, USA. For those organizations that have been granted a photocopy license by CCC, a separate system of payment has been arranged. The fee code for users of the Transactional Reporting Service is: 0044-2267/2000 US\$ 17.50 + .50.

All rights reserved (including those of translations into foreign languages). No part of this issue may be reproduced in any form, by photoprint, microfilm, or any other means, nor transmitted into a machine language, without written permission from the publishers.

© 2001 by WILEY-VCH Verlag Berlin GmbH. Printed in the Federal Republic of Germany.

Printed on chlorine- and acid-free paper.

Preface

The annual scientific conference of the Society for Applied Mathematics and Mechanics (GAMM) was held at the University of Göttingen, Germany, April 2–7, 2000. These meetings provide a forum for the exchange of ideas between the different mechanical engineering disciplines and mathematics.

In total 949 scientists from 33 countries attended the conference. There were 16 plenary lectures, 95 papers were presented in minisymposia and 624 contributions were presented in a large number of parallel sessions divided into 25 sections. The themes of the minisymposia and sections can be found in the tables of contents of each volume. More detailed information about the meeting is given in the GAMM Letter Nr. 2, 2000.

The following list gives the titles of the plenary lectures. These are not contained in the present proceedings, but are expected to be published in the regular volumes of ZAMM.

- R. J. Adrian, University of Illinois: Velocity Field Measurement
- L. D. Brown, University of Pennsylvania: Asymptotic Equivalence for Infinite Dimensional Statistical Problems
- R. E. Caflisch, University of California: Prandtl's Boundary Layer Equation
- U. Christensen, University of Göttingen: Fluidmechanik des Erdinneren
- D. L. Colton, University of Delaware: Inverse Scattering Techniques for Detecting Burned Objects
- P. Deuflhard, Konrad-Zuse-Center Berlin: From Molecular Dynamics to Conformational Dynamics in Drug Design
- U. Helmke, University of Würzburg: Computation and Control: A Dynamical Systems Perspective
- A. Hübner, University of Illinois: Controlling Chaos
- W. Jüptner, BIAS Bremen: Theoretische Grundlagen interferometrischer Meßverfahren zur Auswertung interferometrischer Medaten in der experimentellen Festkörpermechanik
- M. Karpel, Technion Haifa: Procedures and Models for Aeroservoelastic Analysis and Design
- R. V. Kohn, New York University: Energy Minimization, Microstructure, and Pattern Formation in Grain Boundaries and Ferromagnets
- C. Miehe, University of Stuttgart: Computational Plasticity at Finite Strains
- H. Pottmann, TU Wien: Computational Geometry
- A. Quarteroni, EPFL Lausanne: Multimodels in Fluid Dynamics
- W. Schneider, TU Wien: Continuous Solidification Processes
- P. D. Spanos, Rice University Houston: Stochastic Processes in Mechanics

Ludwig Prandtl Laudatio

- J. Zierep, Technical University of Karlsruhe:

Ludwig Prandtl Memorial Lecture

- P. Saffman, F.R.S., California Institute of Technology, Pasadena: Aspects of Vortex Dynamics

Public Lecture

- W. Send, DLR Göttingen: Vom Vogelflug zum Düsenklipper

The three volumes of the proceedings comprise most of the contributions to the minisymposia and sections. The manuscripts were submitted in camera-ready form, were reviewed by two external referees and examined by a member of the Editorial Team. The contributions to the minisymposia and the invited contributions to the sections were restricted to four pages and the short communications to two pages. A manuscript which was judged not to be acceptable in its present form (although it may contain publishable material) had to be rejected since time constraints did not allow for a revision process. We take this opportunity to express our appreciation to all the authors who submitted their manuscripts.

The proceedings are organized as follows:

Volume I contains the papers presented in the minisymposia.

Volume II contains the contributions to Sections 1–8.

Volume III contains the contributions to Sections 9–25.

The conference was supported by grants of the

- Deutsche Forschungsgemeinschaft
- Niedersächsisches Ministerium für Wissenschaft und Kultur
- Deutsches Zentrum für Luft- und Raumfahrt

and

- European Office of Aerospace Research & Development (EOARD)
- DaimlerChrysler Aerospace Airbus GmbH
- EAM Göttingen
- Sparkasse Göttingen
- Druckerei Kinzel, Göttingen
- Walter de Gruyter & Co.
- B.G. Teubner GmbH Stuttgart
- Wiley-VCH Verlag
- Springer Verlag
- Editions Elsevier

We greatly appreciate the generous support given by these institutions.

A conference of this size is the result of a collaborative effort. We would like to thank the plenary speakers, the organizers of the minisymposia and sections, the local organizers and all the authors for their contributions to the annual meeting and to these proceedings. We also thank the GAMM presidency and Mr. Trinkl from WILEY-VCH for their cooperation in the editorial process.

Special thanks are due to the external referees without whose help and expert advice a fair evaluation of the submitted manuscripts would not have been possible.

Finally we thank Elisabeth Winkels for her continuous assistance in preparing the three volumes of these proceedings.

Göttingen, March 2001

The Editor
Prof. Dr. Gerd E. A. Meier

Table of Contents

Preface	S437
Section 9 Inviscid Flows, Gas Dynamics	
Chaired by: A. Dillmann, H. Sobieczky	
Chernigovski, S., Glatzel, W., Fricke, K. J.	
Strange-Mode Instabilities in Luminous Stars	S447
Dillmann, A.	
Can Linear Potential Theory Predict Supersonic Jets?	S449
Dobes, J., Fort, J., Fürst, J., Halama, J., Kozel, K.	
Comparison of Several Numerical Methods for Internal Transonic Flow Problems	S451
Fokin, D., Wagner, S.	
A Field-Panel Method for Subsonic and Transonic 3D Wing Calculation	S453
Hirschler, T.	
Collapsing Cylindrical Shock waves in Gases with Low Absorptivities	S455
van Keuk, J., Ballmann, J.	
Numerical Simulation of Inviscid Shock Interactions on Double-Wedges	S457
Section 10 Viscous Flows, Turbulence	
Chaired by: W. Nitsche, H. Thiele	
Böhme, G., Wünsch, O.	
Über Symmetrien schleichender Strömungsvorgänge in verfahrenstechnischen Apparaten	S459
Breuer, M.	
Towards Technical Application of Large Eddy Simulation	S461
Exner, A., Kluwick, A.	
The Interaction Problem for the Locally Cooled Free Convection Boundary Layer	S463
Farge, M., Pellegrino, G., Schneider, K.	
Wavelet filtering of Three-Dimensional Turbulence	S465
Franke, J., Frank, W.	
Temporal Commutation Errors in Large-Eddy Simulation	S467
Heiken, S., Demuth, R., Laurien, E.	
Dependency of the Bypass-Transition on the Initiating Disturbance	S469
Heinz, S.	
Advanced Methods to Compute Multiphase Turbulent Reacting Flows	S471
Kluwick, A., Gittler, P.	
Transonic Laminar Interacting Boundary Layers in Narrow Channels	S473
Kluwick, A., Kronberger, R.	
On the Interaction of a 2-dimensional Transonic Turbulent Boundary Layer with a Localized 3-dimensional Disturbance	S475
Krumbein, A.	
Laminar-turbulente Transitionsvorgabe im DLR Navier-Stokes-Löser FLOWer	S477
Mang, J., Ungarisch, M., Schaflinger, U.	
Numerical Investigation of the Spin-Up of a Two-Layer Fluid	S479
Rung, T., Lübecke, H., Thiele, F.	
Universal Wall-Boundary Conditions for Turbulence-Transport Models	S481
Sadiki, A., Maltsev, A., Janicka, J.	
Performance of Turbulence Models of Second Order in Predicting Turbulent Mixing in Jet Exhaust behind Aircraft Engines	S483
Schneider, K., Farge, M.	
Coherent Vortex Simulation (CVS) of Two-Dimensional Turbulence	S485
Scholle, M., Wierschem, A., Aksel, N.	
Creeping Newtonian Film Flow Down an Inclined Wavy Plane. Part I	S487
Tuliszka-Sznitko, E., Soong, C. Y.	
Linear Stability Theory of Non-Isothermal Flow between Two Rotating Disks	S489
Wagner, C.	
An Eddy Viscosity Scaled Dynamic Scale Similarity Model	S491

Wierschem, A., Scholle, M., Aksel, N. Creeping Newtonian Film Flow Down an Inclined Wavy Plane. Part II	S493
Zlatanovski, T. Settling Velocity of Porous Particles Using the Particle-in-Cell Model	S495

Section 11 Heat and Mass Transfer, Convective Flows

Chaired by: H. Herwig, D. Mewes

Henselowsky, C., Kuhlmann, H. C., Rath, H. J. Heat Transfer from Hot Wires at Small Forced-Flow Velocities	S497
Hozejowski, L., Hozejowska, S., Sokala, M. Stability of Solutions for Some Inverse Heat Conduction Problems by Heat Functions Method	S499
Hribersek, M. Inexact Newton-Krylow Methods for Nonlinear Forced Heat Convection Problems by BEM.	S501
Lee, Y.-S., Kuhlmann, H. C., Rath, H. J., Chun, Ch.-H. Stability of Thermocapillary Flow in Cylindrical Liquid Bridges: Rotation of the Hot Disk	S503
Marcic, M., Zgonik, M., Avsec, J. Combustion of the Diesel Fuel Spray	S505
Mocikat, H., Prazak, J., Göppert, St., Herwig, H. Konvektiver Wärmeübergang bei instationärer Anströmung	S507
Nienhäuser, Ch., Kuhlmann, H. C., Rath, H. J. Instability of Buoyant-Thermocapillary Flows in Non-Cylindrical Liquid Bridges	S509
Severin, J., Beckert, K., Herwig, H. Plane Channel Flow with Heat Transfer: Stability Analysis with a Commercial CFD-Code	S511
Steinrück, H. Upstream Travelling Waves in the Boundary Layer of a Horizontal Mixed Convection Flow	S513

Section 12 Multiphase Flows, Flows of Reactive Fluids

Chaired by: B. Rogg, G. H. Schnerr

Avsec, J., Marcic, M. The Calculation of Velocity of Sound near the Liquid-Gas Transition	S515
Baumbach, V., Dreyer, M., Rath, H. J. Coating by Capillary Transport through Porous Media	S517
Bielert, U., Kotchourko, A., Burgeth, B., Breitung, W. Numerical Simulation of Large Scale Hydrogen Explosions in Complex Geometries	S519
Diebels, S., Ehlers, W., Markert, B. Neglect of the Fluid Extra Stresses in Volumetrically Coupled Solid-Fluid Problems	S521
Ehlers, W., Blome, P. A Multi-Phase Soil Model Including a Soil-Foundation Interface	S523
Favier, V., Vervisch, L. Partial Premixing in Diffusion Flame Quenching	S525
Geiß, S., Sadiki, A., Maltsev, A., Dreizler, A., Janicka, J. Investigations of Turbulence Modulation in Turbulent Particle Laden Flows	S527
Gerlinger, W., Schneider, K., Bockhorn, H. Direct Numerical Simulation of Three-dimensional Flame Instabilities	S529
Gerlinger, W., Schneider, K., Bockhorn, H. Mixing in Two-dimensional Turbulent Reactive Flows	S531
Gutheil, E. Structure and Extinction of Laminar Ethanol/Air Spray Flames	S533
Huld, T., Wilkening, H. 3D Simulations of Turbulent Deflagrations Using Dynamic Grid Adaptation	S537
Indenbirken, M., Strauß, K. Zur Modellierung komplexer partikelbeladener Strömungen mit der kinetischen Theorie granularer Medien	S539
Kempf, A., Forkel, H., Chen, J.-Y., Sadiki, A., Janicka, J. Large Eddy Simulation of a Counterflow Configuration	S541
Lange, M., Warnatz, J. Parallel DNS of Turbulent Non-Premixed Flames with Adaptive Chemistry	S543

Luo, K.	
Some Recent Findings on Turbulent Diffusion Flames from DNS	S545
Machu, G., Meile, W., Nitsche, L., Schaflinger, U.	
The Motion of a Swarm of Particles Travelling through a Quiescent, Viscous Fluid	S547
Meile, W., Machu, G., Schaflinger, U.	
Experimental Investigation of Viscous Drop Formation from a Needle	S549
Meinköhn, D.	
Liquid-Fuelled Rocket Propulsion: The Role of Atomization Processes in Combustion chamber Instabilities	S551
Meironke, H., Szymczyk, J. A.	
Experimentelle Untersuchungen der Deformation einer Phasengrenze einer aufsteigenden Gasblase	S553
Niemann, J., Laurien, E.	
Computing Virtual Mass by Direct Numerical Simulation	S555
Rumberg, O., Rogg, B.	
A Three Variable Formalism for Turbulent Reactive Sprays	S557
Saptoadi, D., Laurien, E.	
Simplified Two-Fluid Model for the Simulation of Two Phase Bubbly Flows	S559
Sauer, J., Schnerr, G. H.	
Development of a New Cavitation Model based on Bubble Dynamics	S561
Steiner, H., Bushe, W. K.	
Large Eddy Simulation of a Turbulent Reacting Jet-Flame	S563
Teppner, R., Schaflinger, U.	
Bubble Formation on Inclined Surfaces	S565
Thevenin, D., Gicquel, O., Darabiha, N.	
Computations of NOx Emissions of Domestic Boilers	S567
van Dongen, M. E. H., Lamanna, G., Prast, B.	
Condensing Nozzle Flows: Ludwig Tube Experiments and Numerical/Theoretical Modelling	S569
Vortmann, C., Schnerr, G. H.	
A New Law of State Model for Cavitation at Non-Equilibrium	S573
Winkler, G., Heiler, M., Schnerr, G. H.	
Simulation of Condensation Processes in Turbines Including Impurity Effects	S575
Wölk, G., Dreyer, M., Rath, H. J.	
Gas/Liquid Two-Phase Flow under Low Gravity Conditions	S577
Wursthorn, S., Schnerr, G. H.	
Numerical Investigation of Performance Losses in a Centrifugal Pump due to Cavitation	S579
Yuan, W., Schnerr, G. H.	
Numerical Simulation of Cavitating Flow in Injector Nozzles	S581

Section 13 Waves, Acoustics
Chaired by: A. Kluwick, H. Körner

Delfs, J., Grogger, H., Lauke, Th., Lummer, M., Yin, J.	
Numerical Description of Acoustic Sources in Airframe Noise	S583
Dziecielak, R.	
Lamb's Problem for a Fluid-Saturated Porous Medium with a Structure	S585
Konicek, P., Bednarik, M., Cervenka, M.	
Nonlinear Effects in the Sound Field of the Circular Piston	S587
Langer, S., Antes, H.	
Schalltransmission durch Isolierfenster	S589
Schanz, M., Cheng, A. H.-D.	
Wave Propagation in a One-dimensional Poroelastic Column	S591
Ziegler, F.	
The 3-D Dynamic Green Functions Expanded in Plane Waves	S593

Section 14 Applied Analysis
Chaired by: H.-H. Alber, P. Hähner

Chelminski, K.	
On Noncoercive Models in the Theory of Inelastic Deformations with Internal Variables	S595
Gasser, I.	
The Small Debye Length Limit in a Hydrodynamic Model for Charged Fluids	S597

Gwiazda, P.	
On the Model Chan-Bodner-Lindholm in the Theory of Inelastic Deformation.....	S599
Knobloch, S.	
Zur Behandlung des Elastizitätsproblems in Gebieten mit Ecken	S601
Kunze, M.	
On the Period of Periodic Motions of a Particle in a Scalar Wave Field	S603
Neff, P.	
A Model Describing Small Elastic Deformations and Korn's Inequality with Nonconstant Coefficients	S607
Raguz, A.	
Compensated Compactness for Higher Order Differential Relations	S609

Section 15 Mathematical Methods of the Natural and Engineering Sciences

Chaired by: G. Dziuk, P. Maaß

Berger, A.	
Regular and Chaotic Motion of a Kicked Pendulum: A Markovian Approach	S611
Callies, M., Callies, R.	
Hochgenaue Konturliniengenerierung	S613
Kohout, M., Schreiber, I., Kubicek, M.	
Numerical Continuation of Homo/Heteroclinic Orbits with an Oscillatory Approach to Stationary Point ...	S615
Kucaba-Pietal, A.	
Squeeze Film of Micropolar Fluid – Theory and Application	S617
Langemann, D.	
Numerical Analysis of the Polygonalization of Railway Wheels	S619
Rieder, A.	
How to Scale Reconstruction filters in 2D-computerized Tomography	S621
Schagerl, M., Berger, A.	
On the Appropriate Treatment of Singularly Perturbed Wave Equations.....	S623
Vrdoljak, M., Jankovic, S.	
Aircraft Performance Obtained from Modified Point Mass Model.	S625

Section 16 Computer Algebra and Computer Analysis

Chaired by: G.-M. Greuel, S. M. Rump

Lunter, G.	
A Generalization of Gröbner Bases Helps to Compute Singularity Theory Transformations	S627
Seiler, W. M.	
Index Concepts for General Systems of Partial Differential Equations.....	S629
Wichmann, T.	
Computer Aided Generation of Approximate DAE Systems for Symbolic Analog Circuit Design.....	S633
Zerz, E.	
Some Applications of Gröbner Bases in Multidimensional Systems Theory.....	S635

Section 17 Applied Stochastics, Operations Research

Chaired by: E. Brunner, M. Denker

Kolesnik, A. D.	
On Diffusion at Finite Speed in a Plane.....	S637
Mazur-Sniady, K., Sniady, P.	
Reliability of the Beam with Variable Cross-Section under Stochastic Excitation	S639
Richter, M., vom Scheidt, J., Starkloff, H.-J.	
Moment Functions for Solutions of Random Boundary Value Problems	S641
Sieniawska, R., Wysocka, A., Zukowski, S.	
Reliability of Elastic-Plastic Bar Systems Loaded Dynamically	S643
Sniady, P., Sieniawska, R., Zukowski, S.	
Random Response of a System due to Periodic Excitation with Gaussian and Non-Gaussian Disturbances	S645
Socha, L.	
Statistical Linearization of the Duffing Oscillator under non-Gaussian Excitations with Criteria in Probability Density Function Space	S647

Starkloff, H.-J., vom Scheidt, J., Wunderlich, R. RandomVibration Systems with Weakly Correlated Random Excitation.....	S649
Wunderlich, R., vom Scheidt, J., Starkloff, H.-J. Low-Dimensional Approximations of Random Vibration Systems.....	S651
Section 18 Optimization	
Chaired by: H. A. Eschenauer, J. Werner	
Aurnhammer, A., Marti, K. Adaptive Optimal Stochastic Trajectory Planning in Real-Time Using Neural Network Approximations....	S653
Bittner, L. Shortest Curves for Vehicles on Surfaces of Celestial Bodies	S655
Blachut, J. Optimal Design of Steel Barrelled Shells	S657
Burgmair, R., Pfeiffer, F. Prozeßspezifische Roboteroptimierung	S659
Ciglaric, I., Krasna, S., Prebil, I. Optimal Path Synthesis of the Four-bar Mechanism	S661
Engels, H., Becker, W. Optimization of Patch Reinforcement around Circular Holes in Isotropic and Anisotropic Plates.....	S663
Glocker, C. Spatial Friction as Standard NLCP	S665
Hansel, W., Becker, W. Weight-Minimal Laminate Structures under Stress Constraints	S667
Hörnlein, H. R. E. M. Effiziente semi-analytische Gradientenberechnung in der Strukturoptimierung.....	S669
Istratie, V. Optimal Rendezvous with Constraints on Circular and Elliptical Orbits	S671
Kegl, M. An Efficient Shape Parameterization Concept for Structural Optimization.....	S673
Kiriazov, P. On Optimal Control of Mobile Robots.....	S675
Konickova, J. Sufficient Condition of Basis Stability of an Interval Linear Programming Problem	S677
Krajin, A., Beg, D. A Priori Constraint Elimination	S679
Kutylowski, R. The ε -Relaxed approach in Topology Optimization for Various ε -Functions.....	S681
Lindemann, J., Becker, W. Optimization of Composite Laminates under Uniaxial Tension with Respect to the Free-Edge Effect	S683
Marti, K. Robust Optimal Control of Robots by means of Stochastic Optimization	S685
Meckbach, S., Ehrenstein, G. W. Erweitertes Optimierungsverfahren für den Spritzgießprozess	S687
Mikulski, L. Querschnittsoptimierung unter mehrfacher Belastung	S689
Rijpkema, J. J. M., Schoofs, A. J. G., Etman, L. F. P. RSM Based Design Optimization	S691
Rottler A., Eschenauer, H. A. Optimal Layouts of Structural Components Considering Fatigue Strength.....	S693
Schwarz, St., Kemmler, R., Ramm, E. Structural Optimization in Nonlinear Mechanics	S695
Stöckl, G. Topology Optimization of Trusses under Stochastic Uncertainty	S697
Ververne, K., de Boer, H., van Keulen, F. Accuracy and Implementation of Refined Second Order Semi-Analytical Design Sensitivities	S699
Vietor, Th. Optimal Design in Automotive Engineering with Scattering Design Variables	S701
Vondrak, V., Dostal, Z., Rasmussen, J. Duality Based Contact Shape Optimization	S703

Section 19 Numerical Analysis
Chaired by: R. Kornhuber, W. Mackens

Bastian, M., Schmidt, J. W.	
Nonnegative Interpolation with Clough-Tocher Splines of Cubic Precision	S705
Benner, P.	
On a Numerical Method for the Regularization of Descriptor Systems	S707
Boese, F. G.	
On the Distribution of the Zeros of Polynomials Related to the Daubechies Wavelets	S709
Detmers, F., Herzberger, J.	
Enge Schranken für den Effektivzinssatz nach der PAngV bei einem Annuitätenproblem	S711
Dyllong, E., Luther, W.	
Flatness Criteria for Subdivision of Rotational Bézier Curves and Surfaces	S713
Ehrhardt, K., Borchardt, J., Grund, F., Horn, D.	
Distributed Dynamic Process Simulation	S715
Faßbender, H., Benner, P.	
Computing Roots of Matrix Products	S717
Flajs, R., Saje, M., Zakrajsek, E.	
Global Convergence of Newton's Method to the Solution of Equations of Reissner's Elastica	S719
Hofferek, B., Voss, H.	
Eigenvalue Reanalysis and Condensation with General Masters	S721
Korelc, J.	
Multi-language Approach in Automatic Generation of Numerical Procedures	S723
Müller, L., Lube, G.	
A Nonoverlapping DDM for the Nonstationary Navier-Stokes Problem	S725
Pelzer, A., Hofferek, B., Voss, H.	
Implementing Global Masters into Parallel Condensation	S727
Schinnerl, M., Langer, U., Lerch, R.	
Multigrid Simulation of Electromagnetic Actuators	S729
Schwetlick, H., Schnabel, U.	
An Inverse Subspace Iteration for Computing q Smallest Singular Values of a Matrix	S731
Wieners, C.	
The Application of Multigrid Methods to Plasticity at Finite Strains	S733

Section 20 Numerical Treatment of Ordinary and Algebro-Differential Equations
Chaired by: G. Lube, R. Weiner

Arnold, M.	
Constraint Partitioning in Dynamic Iteration Methods	S735
Bartel, A., Günther, M.	
Developments in Multirating for Coupled Systems	S739
Callies, R.	
Multidimensional Stepsize Control	S743
Linß, T.	
Uniform Pointwise Convergence of Finite Difference Schemes for Quasilinear Convection-Diffusion Problems	S745
Neher, M.	
Berechenbare Schranken von Taylorkoeffizienten analytischer Funktionen	S747
Schmitt, B. A., Weiner, R., Podhaisky, H.	
Parallel Two-Step W -Methods	S749

Section 21 Numerical Treatment of Partial Differential Equations
Chaired by: L. Angermann, G. Lube

Adolph, T., Schönauer, W.	
The Generation of High Quality Difference and Error Formulae of Arbitrary Order on 3-D Unstructured Grids	S753
Angermann, L., Wang, S.	
A Conforming Exponentially Fitted Finite Element Scheme for the Semiconductor Continuity Equations in 3D	S755
Chapko, R.	
On the Numerical Solution of the Hyperbolic Evolution Problem on Closed Curve	S757

Fischer, B., Ludwig, M., Meister, A. A Finite Volume Method to Compute the Steady State Temperature Distribution in Premature or Newborn Infants	S759
Fröhner, A., Linß, T., Roos, H.-G. The ε -Uniform Convergence of a Defect-Correction Method on a Shishkin Mesh	S761
Haschke, H., Heinrichs, W. Splitting Techniques for the Navier-Stokes Equations	S763
Heinrichs, W., Loch, B. Spectral Schemes on Triangular Elements	S765
Knopp, T., Lube, G., Rapin, G. Stabilized FEM with Shock-capturing for Advection-diffusion Problems	S767

Section 22 Space Transport Systems, Aerothermodynamics

Chaired by: W. Kordulla, G. Koppenwallner

Callies, R., Wimmer, G. Stabilisierte Hyperschallflugbahnen	S769
Dinkelmann, M., Wächter, M., Sachs, G. Flugbahn-Optimalsteuerung für ein Hyperschall-Flugsystem zur Verringerung des instationären Wärmetransfers	S771
Fedorova, N. N., Fedorchenko, I. A., Schüle, E. Experimental and Numerical Investigation of the Oblique Shock Wave/Turbulent Boundary Layer Interaction at $M = 5$	S773
Sachs, G., Mayrhofer, M. Reichweitensteigerung bei Hyperschall-Notflugbahnen durch Optimalsteuerung des Treibstoff-Ablaufvorgangs	S775
Ting, C.-C. Visualization of Supersonic Flow past EOS	S777

Section 23 Formation of Structures in Nonlinear Systems

Chaired by: F. H. Busse

Albensoeder, S., Kuhlmann, H. C., Rath, H. J. The Lid-Driven Cavity Revisited: Stability of Two-Dimensional Flow	S779
Blohm, C., Albensoeder, S., Kuhlmann, H. C., Broda, M., Rath, H. J. The Two-Sided Lid-Driven Cavity: Aspect-Ratio Dependence of the Flow Stability	S781
Class, A. G. Rotating Polyhedral Flames	S783
Leyboldt, J., Kuhlmann, H. C., Rath, H. J. Stability of Hydrothermal-Wave States	S785

Section 24 Aerodynamics and Experimental Technics since Prandtl

Chaired by: E. H. Hirschel, H.-U. Meier

Lutz, Th. Airfoil Design and Optimization	S787
Schulte-Werning, B., Heine, C., Matschke, G. Slipstream Development and Wake Flow Characteristics of Modern High-Speed Trains	S789

Section 25 Invited Session: Flow Control and Optimization

Chaired by: M. Gunzburger, G. E. A. Meier

Hinze, M. A Remark on Second Order Methods in Control of Fluid Flow	S791
Slawig, T. Domain Optimization for the Navier-Stokes Equations by an Embedding Domain Technique	S793

Author Index	S795
---------------------------	------

CHERNIGOVSKI, S., GLATZEL, W., FRICKE, K.J.

Strange - Mode Instabilities in Luminous Stars

If radiation pressure contributes significantly to the total pressure in models for the envelopes of hot and luminous stars, such as massive objects and Wolf - Rayet stars, strange - mode instabilities with growth rates in the dynamical range do occur. The properties of these mechanical instabilities are reviewed and an intuitive model of the underlying instability mechanism is discussed. Adopting spherical geometry the evolution of the instabilities has been followed into the nonlinear regime by numerical simulation. Multiple shocks are formed and velocity amplitudes above 10^2 km/sec are reached which can imply direct mass loss of the objects.

1. Introduction

Strange - mode instabilities are a common phenomenon in models for the envelopes of luminous stars with luminosity to mass ratios in excess of $\approx 10^3$ (in solar units), where the most violent examples have been discovered in models for Wolf - Rayet stars (see [5] and [8]). The phenomenon can be identified by performing a *standard* linear, non-adiabatic stability analysis of *standard* stellar models for the objects mentioned and is then found to be present both within the radial (see [3] and [7]) and nonradial (see [6]) spectrum of eigenfrequencies. There is no common precise definition of the term "strange modes". In a loose sense they are additional modes neither fitting in nor following the dependence on stellar parameters of the "ordinary" spectrum. In general they are connected with instabilities having growth rates in the dynamical range.

2. The mechanism of strange - mode instabilities

A useful tool to classify modes and to identify the mechanism of an instability is the NAR approximation, where "NAR" stands for non - adiabatic - reversible (see [1]). It consists of neglecting the time derivative of the entropy in the energy conservation equation for the perturbation. Physically, this can be realized either by adiabatic changes of state or by vanishing heat capacity which is equivalent to very large or very small ratios of thermal and dynamical timescales respectively. The second case is considered in the NAR approximation. Consequently, it is justified, if matter cannot store heat efficiently, the thermal timescale in the stellar envelope is short, as a consequence of low densities heat capacities are small, and large deviations from adiabatic behaviour prevail. Such conditions are in fact met in the envelopes of the luminous stars considered here. As a consequence of the first law of thermodynamics the luminosity perturbation vanishes in the NAR approximation. Moreover, zero heat capacity implies disregarding the thermodynamics of the system: in the NAR approximation it is reduced to its mechanical aspects. Thus thermal modes and any instability mechanism relying on a thermal, Carnot - type process, are excluded. Neglecting the time derivative of the entropy implies time reversibility with the consequence that eigenfrequencies come in complex conjugate pairs. Thus the NAR approximation may be used to distinguish between thermal and mechanical origin of both modes and instability mechanisms. As the thermodynamics of the system is essentially disregarded in the NAR approximation one would expect it to be rather unrealistic. However, surprisingly, for Wolf - Rayet stars it provides even quantitatively correct results. In particular, strange - mode instabilities still exist in the NAR approximation. As a consequence, the instability can be described in terms of mechanical quantities only and the luminosity perturbation is not essential for its mechanism. Apart from large deviations from adiabatic behaviour the high luminosity to mass ratios of the envelopes considered also imply the ratio β of gas pressure and total pressure to be negligible. Therefore the model presented here (see also [2]) is based on the NAR approximation and the limit $\beta \rightarrow 0$. With these assumptions the mechanical equations (mass and momentum conservation) may be condensed into an acoustic wave equation for pressure (\tilde{p}) and density ($\tilde{\rho}$) perturbation:

$$\frac{\partial^2 \tilde{\rho}}{\partial t^2} - \frac{\partial^2 \tilde{p}}{\partial r^2} = 0$$

It has to be closed by a linear relation between \tilde{p} and $\tilde{\rho}$ which is provided here by the diffusion equation for energy

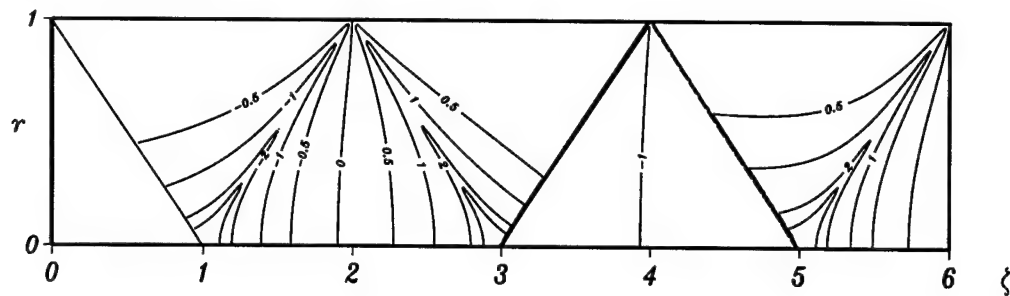


Figure 1: Dimensionless density perturbation (1) for $\frac{1}{\kappa p_0} \Delta p = 1$.

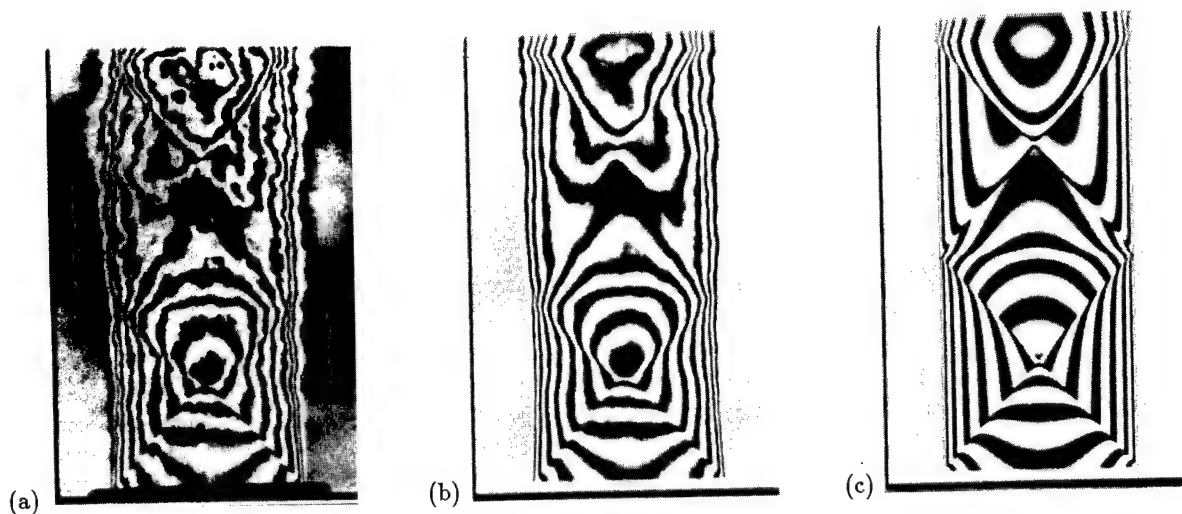


Figure 2: Mach-Zehnder interferograms for an overexpanded supersonic jet with $M_0 = 1.48$, $\frac{1}{\kappa p_0} \Delta p = -0.092$ and $\frac{\rho}{\rho_\infty} = 1.370$ (flow direction from bottom to top). (a) experimental snapshot image; (b) time-averaged interferogram computed from eight subsequent snapshots; (c) theoretical interferogram computed from Pack's solution.

fluctuations in the jet's free shear layer, only the portions close to the nozzle orifice are clearly visible. In order to eliminate these perturbations, the time-averaged interferogram (b) was produced by extracting the phase shift of eight subsequent snapshots via inversion of (3), calculating the pixel-wise arithmetic mean and then resubstituting the averaged phase shift into (3) to obtain the intensity of the time-averaged image. Thus, the turbulent fluctuations are almost completely eliminated and the steady potential core of the jet appears with surprising clarity. Photograph (c) shows the corresponding theoretical interferogram as computed from (1), (2) and (3). The remarkable agreement between theory and experiment demonstrates that linear potential theory is indeed able to describe the essential features of supersonic free jets correctly, except some minor deviations in the free shear layer and in the focussing regions $\zeta = 1, 3, \dots$ where the theoretical solution predicts infinite density values. A more extensive comparison between theory and experiment based on the basis of Mach-Zehnder interferometry and computerized tomography has been reported in a recent paper [4].

4. References

- 1 PACK, D.C.: A note on Prandtl's formula for the wave-length of a supersonic gas jet, *Quart. J. Mech. and App. Math.* **3** (1950), 173–181.
- 2 DILLMANN, A.: Linear potential theory of steady internal supersonic flow with quasi-cylindrical geometry, *J. Fluid Mech.*

J. DOBEŠ, J. FOŘT, J. FÜRST, J. HALAMA, K. KOZEL

Comparison of Several Numerical Methods for Internal Transonic Flow Problems

This contribution summarizes results of several numerical methods developed at our department. Presented methods are based on central TVD schemes, upwind TVD schemes with or without Riemann solver, ENO schemes and Lax-Wendroff type schemes. The results of 2D methods, computed on either structured quadrilateral grids or unstructured grids composed of triangles and quadrilaterals, are compared on 2D axial and radial turbine cascade and 2D axial compressor cascade. A comparison of results, obtained on structured hexahedral grids, is shown for 3D axial turbine cascade of Škoda Pilsen enterprise.

1. Numerical methods

A transonic flow field in all presented cases is modeled by the system of Euler equations (1). The non-zero right hand side term Q is taken into account only for 3D case of rotor flow, when the system is written in relative frame of reference rotating around axis x with angular velocity Ω .

$$W_t + F_x + G_y + H_z = Q \quad (1)$$

Following finite volume methods have been involved:

1. methods for structured H-type grids (quadrilateral in 2D and hexahedral in 3D)
 - (a) 2nd order method based on Ni's cell-vertex scheme with 2nd order artificial dissipation
 - (b) 2nd order method based on full TVD MacCormack cell-centered scheme
2. 2D methods for unstructured triangular grids
 - (a) 1st order upwind method based on approximate Roe's Riemann solver with entropy correction (Harten, Hyman 1983) and explicit Euler integration in time
 - (b) 2nd order implicit upwind method based on approximate Osher's Riemann solver (1st order treated implicitly and higher order explicitly), linear system is solved by restarted GMRES with ILU preconditioner, piecewise linear reconstruction is done by weighted ENO method

2. Numerical results

Numerical results for axial turbine cascade SE 1050 shows weak points of structured H-type grid in the vicinity of leading and trailing edges. The worse geometrical description of the leading edge for H-type grid compared to unstructured grid produce certain amount of entropy which affects the flow field near profile and streamwise the trailing edge, see fig.1.a. Calculation on adapted unstructured grid (fig.1.c) captures very good the shock wave structure, disadvantages of structured grid are suppressed by O-H multiblock grid (fig.1.b).



(a) 'TVD MacCormack' (H-type grid) (b) 'Ni' (struct. multiblock grid) (c) 'Osher' (adapted unstruct. grid)

Fig.1: a transonic flow through axial turbine cascade SE 1050

Results in fig.2 (isolines of Mach number) shows good agreement of results for a not too common technical application - a transonic flow through a radial turbine cascade.

Results in fig.3 show the influence of AVDR (axial velocity density ratio) for compresor cascade MAN GSH-1 at off-design conditions $i = -7deg$.

Results in fig.4 (isolines of Mach number) show the computed 3D flow field through axial turbine cascade.

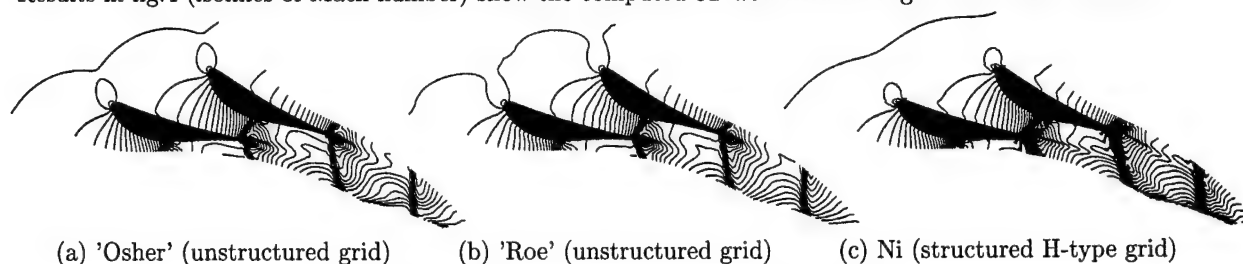


Fig.2: a transonic flow through a radial cascade



Fig.3: 2D transonic flow through axial compressor MAN GSH-1, $AVDR = 1.0$ left, $AVDR = 1.1$ right

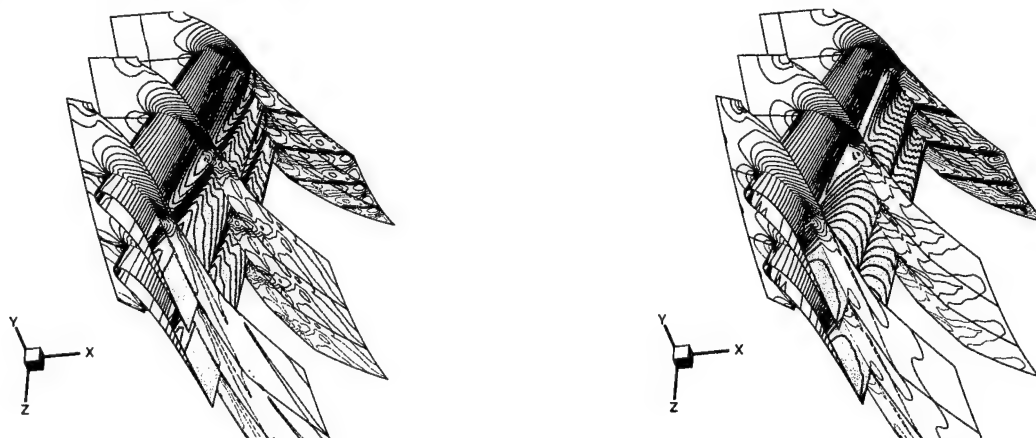


Fig.4: 3D transonic flow through axial cascade, TVD MacCormack scheme left, Ni's scheme right

Acknowledgements

This work is supported by the grants No. 101/98/1229 and 201/98/0528 of Grant Agency of Czech Republic and by the Research Project No. J04/98/212200009 of MSM CR.

3. References

- 1 ANGOT P., FÜRST J., KOZEL K.: TVD and ENO Schemes for Multidimensional Steady and Unsteady Flows - A Comparative Analysis, Proc. Finite Volumes for Complex Applications - Problems and Perspectives, editors: Benkhaldoun F., Vilsmeier R., Rouen 1996, Hermes, pp 283-290
- 2 FOT J., FÜRST J., HALAMA J., KOZEL K.: Numerical Solution of 2D and 3D Transonic Flow Through a Cascade, Proceedings of '4th International Symposium on Experimental and Computational Aerothermodynamics of Internal Flows' Vol.I, Dresden, 1999, ISBN 3-86005-209-8, pp 231-240

Addresses: J. DOBEŠ, J. FOŘT, J. FÜRST, J. HALAMA, K. KOZEL, Dept. of Technical Mathematics, Fac. of Mech. Eng. CTU Prague, Karlovo nám. 13, Prague 2, CZ-121 35

FOKIN, D.; WAGNER, S.

A Field-Panel Method For Subsonic And Transonic 3D Wing Calculation

The development of fast numerical methods for calculating sub- and transonic flow over 3D configurations is important for numerical optimization purposes. One efficient approach, namely field panel method, is based on the boundary-element methods solving the full potential equation (see e.g. [1]). The algorithm incorporates panel methods for calculating the basic incompressible flow and compressible field iterations. The purpose of the present work is to develop a mathematically well based and efficient numerical field-panel method for the analysis of transonic flow over 3D wings, that could be further used for design and optimisation of transonic wings in a given range of free stream Mach numbers.

1. Formulation of the problem and method of solution

Consider a steady potential flow over a wing with symmetric profile at zero angle of attack Fig. 1. The unity flow vector at infinity \vec{v}_∞ is directed along x axis. All velocities are related to the velocity at infinity, all lengths are related to the chord length of the wing root section. The value of the free stream Mach number is given as $M_\infty < 1$. The wing is symmetrical with reference to the xy -plane. The shape of the wing surface S is given in the form $z = f(x, y)$ with $x, y \in S_1$ where S_1 is the shape of the wing planform in xy plane. We denote the flow region outside the wing as D . It is required to determine the distribution of the flow parameters in D . Namely, the distribution of the Mach number in the flow field and the distribution of the pressure coefficient on the wing surface.

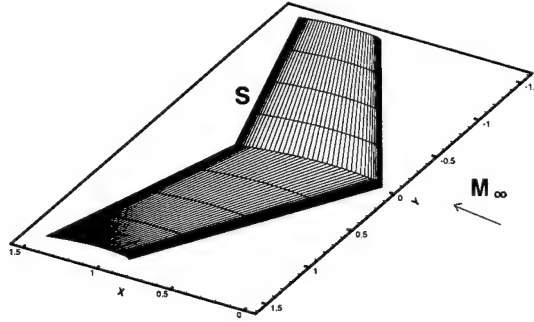


Figure 1: Formulation of the problem

Assume that the flow over the wing is isentropic and satisfies the full potential equation. This assumption is valid if the intensity of transonic shocks is such that we can neglect the entropy changes across the shock. This type of flow is described by a disturbance potential function $\varphi(x, y, z)$ satisfying the full potential equation

$$\Delta\varphi = \sigma \quad (1)$$

where

$$\sigma = \frac{v_x^2}{a^2} \frac{\partial^2 \varphi}{\partial x^2} + \frac{v_y^2}{a^2} \frac{\partial^2 \varphi}{\partial y^2} + \frac{v_z^2}{a^2} \frac{\partial^2 \varphi}{\partial z^2} + \frac{2v_x v_y}{a^2} \frac{\partial^2 \varphi}{\partial x \partial y} + \frac{2v_y v_z}{a^2} \frac{\partial^2 \varphi}{\partial y \partial z} + \frac{2v_z v_x}{a^2} \frac{\partial^2 \varphi}{\partial z \partial x}. \quad (2)$$

Here v_x, v_y, v_z are the velocity vector components, a is the velocity of sound. The flow impermeability condition on the wing is $\vec{n} \cdot \nabla \varphi = -\vec{n} \cdot \vec{v}_\infty$, where \vec{n} is the vector normal to the wing surface. The solution of the problem is sought in the following integral form

$$\varphi(\vec{p}_0) = -\frac{1}{4\pi} \int_{\vec{p} \in S_1} \frac{\tau(\vec{p}) dS_1}{|\vec{p} - \vec{p}_0|} - \frac{1}{4\pi} \int_{\vec{p} \in R^3} \frac{\sigma(\vec{p}) d\xi d\eta d\zeta}{|\vec{p} - \vec{p}_0|} \quad (3)$$

where $\vec{p} = (\xi, \eta, \zeta)$ is an integration variable point, \vec{p}_0 is the reference point. The function φ from (3) satisfies to (1) if σ is of the form (2). Then the impermeability condition of the wing can be rewritten as

$$\frac{\vec{n}}{4\pi} \int_{\vec{p} \in S_1} \frac{\tau(\vec{p})(\vec{p} - \vec{p}_0) dS_1}{|\vec{p} - \vec{p}_0|^{3/2}} + \frac{\vec{n}}{4\pi} \int_{\vec{p} \in R^3} \frac{\sigma(\vec{p})(\vec{p} - \vec{p}_0) d\xi d\eta d\zeta}{|\vec{p} - \vec{p}_0|^{3/2}} = -\vec{n} \cdot \vec{v}_\infty, \quad p_0 \in S \quad (4)$$

Relationships (4), (2) with the account of (3) give a system of integro - differential equations for finding the function τ on the planform surface and σ in the flow. To solve the system the planform surface S_1 is presented as a collection of quadrilateral panels with piecewise constant distribution of τ and the impermeability condition is satisfied in

prescribed collocation points on the wing surface. The values of σ are also assumed to be constant in every cell of some equidistant volume mesh, containing the wing. Suppose that some initial approximation for σ is given (say $\sigma = 0$). The relationship (4) is reduced to a system of linear equations for finding τ on the planform panels. Then the distribution of the disturbance potential is found from (3) in the cell centers of the equidistant volume mesh. The new values of σ are calculated from (2) through the central finite difference scheme in subsonic regions. For supersonic regions an additional artificial viscosity term is added to σ in order to stabilize the iteration process. The iterations are continued until a convergence criterion is fulfilled.

2. Calculation examples

Consider the case of a swept ONERA wing for $M = 0.9$ (Fig. 1). The thickness of the wing root section is 8%, the wing span is $L = 3$. The planform surface consists of 49×15 rectilinear panels. The wing collocation points are located just above the centers of the planform panels. The equidistant volume mesh contains all the wing collocation points inside. The calculations are performed for the three meshes with different number of cell divisions, namely, $29 \times 15 \times 29$, $49 \times 15 \times 49$, $69 \times 15 \times 69$. The resulting pressure coefficient distributions are presented by dashed lines, dashed and dotted lines and solid lines correspondingly in Fig. 2 for section $y = 0.75$ and in Fig. 3 for section $y = 0.25$.

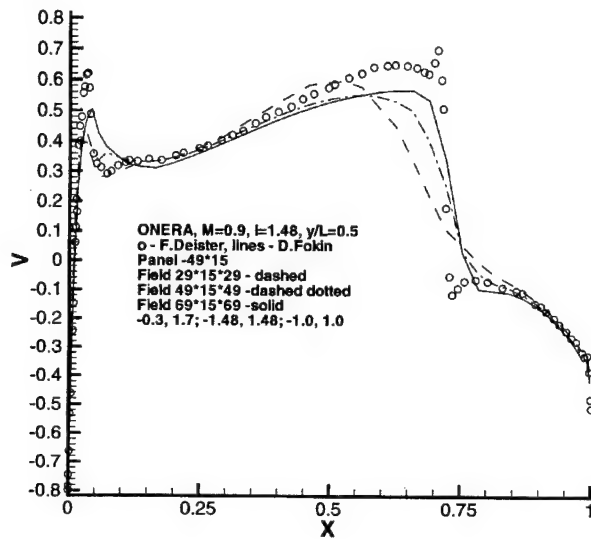


Figure 2: Pressure distributions at section $y/L = 0.5$

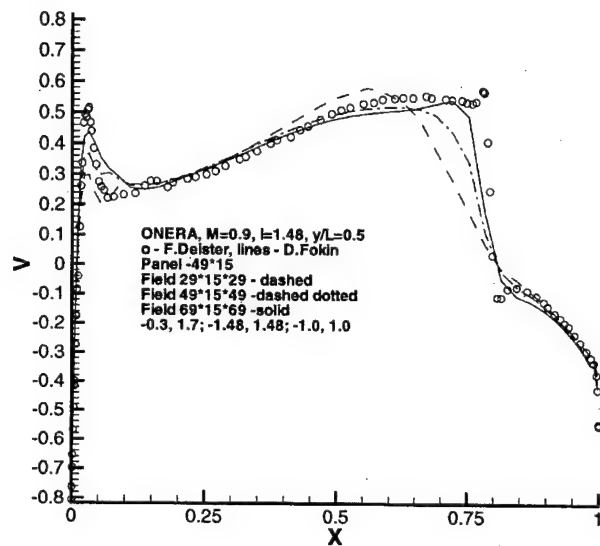


Figure 3: Pressure distributions at section $y/L = 0.75$

For comparison also calculation results of calculation, obtained by means of a finite volume Euler code [2] are presented (circles). For the coarse mesh (dashed lines) the pressure coefficient curves as resulting with the present field panel method are too smooth in the shock region. As the mesh becomes finer (dashed and dotted and solid lines) the shock strength increases and its position moves to the position obtained with the Euler solver [2]. We can also mention a well exposed suction peak near the leading edge of the wing captured by the proposed method.

Acknowledgements

The research is supported by Alexander von Humbolt foundation. The first author would also like to thank for the support of the Russian foundation for basic researches projects 99-01-00365, 99-01-00173, 99-0104029.

3. References

- 1 ROETTGERMANN, A.: Eine Methode zur Beruecksichtigung kompressibler und transsonischer Effekte in Randlelementverfahren. Ph.D. Thesis, University of Stuttgart, 1994, 175 p.
- 2 DEISTER, F.; HIRSCH, E.: Adaptive Cartesian/Prism Grid Generation and Solutions for Arbitrary Geometries. Proc. 37th AIAA Aerospace Science Meeting and Exhibit, Jan 11-14, 1999, Reno. AIAA 99-0782, 19 p.

Addresses: DMITRI FOKIN, IAG, University of Stuttgart, D-70550 Stuttgart, Germany

HIRSCHLER, T.

Collapsing cylindrical shock waves in gases with low absorptivities

In the self-similar formulation of the collapse of a cylindrical shock wave in radiating gas the temperature gradient at the shock front is an undetermined quantity. Together with the absorptivity an arbitrary choice of these two variables is the basis of a parametric study. The parametric study focuses upon gases with low absorptivities and is extended up to the isothermal limit where the absorptivity is equal to zero. In this context it is shown that the heat flux at the shock front is almost negligible. For gases with low absorptivities the assumption of an adiabatic shock front is therefore a sufficient accurate approximation.

1. Basic Equations

The flow field behind a collapsing cylindrical shock wave depends on the radius r and the time t . The domain of validity of the similarity solution is the immediate vicinity of the axis of symmetry. The domain of validity shall be bounded by a reference point given by R_0 and t_0 . The reference point lies on the shock path $R(t)$. At this point the self-similar solution fits together with an outer solution. Similarity requires that the logarithmic derivation of the shock front velocity $W(t)$ with respect to $R(t)$ is a constant, i.e. $d \ln W(t) / d \ln R(t) = -\lambda/2$ or $R(t) = R_0(t/t_0)^{2/(2+\lambda)}$. The more the shock front is accelerated the higher λ is. Provided that the velocity, pressure, density, heat flux and speed of sound are of the form $u(r, t) = f(x)W(t)$, $p(r, t) = \rho_a g(x)W(t)^2$, $\rho(r, t) = \rho_a h(x)$, $q(r, t) = \rho_a Q(x)W(t)^3$ and $a^2(r, t) = \Theta(x)W(t)^2$, respectively, where $x(r, t) = r/R(t)$ is the similarity variable and ρ_a the density of the ambient medium, the diffusion approximation for the radiative heat transfer equation and the conservation equations for a nonadiabatic flow of an ideal, inviscous gas, with a constant ratio of specific heats γ , can be reduced to five ordinary differential equations for the temperature, velocity, pressure, density and heat flux coefficient Θ , f , g , h and Q , respectively, given as [1]

$$\frac{d\Theta}{dx} = \frac{-Q}{\Gamma \Theta^{(1/2-1/\lambda)}}, \quad \frac{df}{dx} = \frac{\left(\frac{f-x}{\gamma}\right) \left(\frac{d\Theta}{dx}\right) + \left(\frac{\lambda}{2}\right) f(f-x) + \left(\frac{gf}{h}\right) \left(\frac{1}{x}\right)}{(f-x)^2 - \left(\frac{g}{h}\right)}, \quad (1a, b)$$

$$\frac{dg}{dx} = h \left[\left(\frac{\lambda}{2}\right) f - (f-x) \left(\frac{df}{dx}\right) \right], \quad \frac{dh}{dx} = -\frac{h}{(f-x)} \left[\left(\frac{f}{x}\right) + \left(\frac{df}{dx}\right) \right], \quad (1c, d)$$

$$\frac{dQ}{dx} = -\frac{Q}{x} + \left(\frac{1}{\gamma-1}\right) \left[g\lambda - \gamma g f \left(\frac{1}{x}\right) - (f-x) \left(\frac{\lambda}{2}\right) f h + h \left[(f-x)^2 - \Theta \right] \left(\frac{df}{dx}\right) \right]. \quad (1e)$$

λ is the eigenvalue of (1). It must be determined such that in the zero of the denominator of (1b) the numerator in (1b) also vanishes. The heat transfer parameter Γ is a parameter of the solution. In the adiabatic case the gas has an infinite absorptivity. Although $d\Theta/dx \neq 0$ no heat flows and $Q = 0$. Thus, according to (1a), $\Gamma = 0$. If the gas has no absorptivity, the heat flux will cause a sudden temperature equalisation $d\Theta/dx = 0$ and the flow field will become isothermal. With $Q \neq 0$, according to (1a), $\Gamma \rightarrow \infty$. At the shock front the coefficients must fulfil the conditions

$$h_n = \frac{1}{1-f_n}, \quad g_n = f_n, \quad \Theta_n = \gamma f_n (1-f_n), \quad (2a, b, c)$$

$$Q_n = f_n \left(\frac{\gamma+1}{2(\gamma-1)} \right) \left[\left(\frac{2}{\gamma+1} \right) - f_n \right], \quad Q_n = -\Gamma \Theta_n^{1/2-1/\lambda} \left(\frac{d\Theta}{dx} \right) \Big|_n. \quad (2d, e)$$

These are five equations for the six unknowns f_n , g_n , h_n , Θ_n , Q_n and the temperature coefficient gradient at the shock front $(d\Theta/dx)|_n$. The latter directly corresponds to the temperature gradient at the shock front. In the flow field of a collapsing shock wave the highest temperature occurs at the shock front and hence $(d\Theta/dx)|_n \leq 0$ and, according to (2e), $Q_n \geq 0$. At an adiabatic shock front $(d\Theta/dx)|_n = 0$. In the framework of similarity $(d\Theta/dx)|_n$ can be taken as parameter [2]. Together with Γ it is the basis of the following parametric study. In the first part of the parametric study the shock front is assumed to be adiabatic and Γ is varied. In the second part a gas with a low absorptivity $\Gamma = 50$ is assumed and $(d\Theta/dx)|_n \neq 0$. In the following γ is assumed to be 7/5.

2. Parametric Study

Assuming an adiabatic shock front, all solutions pass through the same shock point $P_n = (F_n, Z_n)$ and the origin in the $F = f/x, Z = \Theta/x^2$ -plane, as shown in figure 1. The origin corresponds to the moment of collapse, where $R = 0$ and $x \rightarrow \infty$. A nonadiabatic solution $\Gamma \neq 0$ becomes singular in the point of intersection with $Z = \gamma(1 - F)^2$, which corresponds to a denominator equal to zero in (1b). The solutions for gases with low absorptivities ($\Gamma \gg 1$) hardly deviate from each other. Thus, the singular points of these solutions almost coincide in figure 1. The equation system in the adiabatic case $\Gamma = 0$ can be deduced from (1e) with $(1/x)d(Qx)/dx = 0$. The singular point lies then on $Z = (1 - F)^2$. According to figure 2, the acceleration of the shock front increases with an increase of radiation.

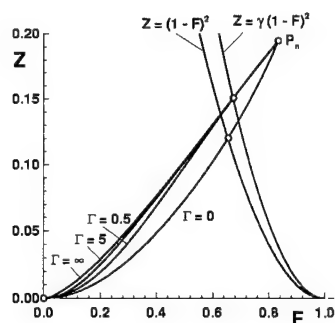


Figure 1. Solutions with an adiabatic shock front

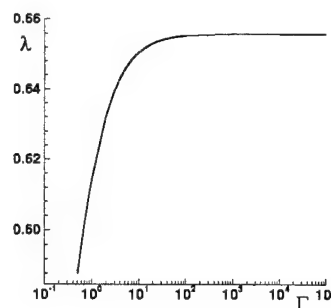


Figure 2. Distribution of the eigenvalue λ over the heat transfer parameter Γ

Assuming for all solutions in figure 1 the same shock front velocity W_0 at the reference point, R_0 becomes smaller for an increasing Γ . In a smaller domain of validity of the similarity solution, however, the converging geometry accelerates the shock front more as radiation retards it. The variation of $(d\Theta/dx)|_n$ for $\Gamma = 50$ is shown in figure 3. The relation between $(d\Theta/dx)|_n$ and the shock point co-ordinate is given in figure 4. Solutions are physically possible

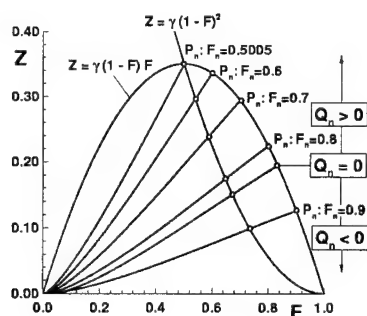


Figure 3. Solutions with a nonadiabatic shock front

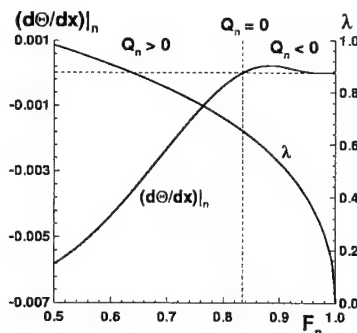


Figure 4. Distributions of the eigenvalue λ and the temperature coefficient gradient $(d\Theta/dx)|_n$ over the shock point co-ordinate F_n .

for $Q_n \geq 0$. A decrease of $(d\Theta/dx)|_n$ means an increase of the energy withdrawal from the shock front. As shown in figure 4, λ increases then. This can again be explained by the placement of R_0 . According to figure 4, for a gas with a low absorptivity $(d\Theta/dx)|_n \approx 0$ and hence $Q_n \approx 0$. According to figure 1, solutions for gases with low absorptivities are closely related to each other. Thus, for such gases the shock front can be assumed to be adiabatic.

3. References

- 1 A. F. GHONIEM, M. M. KAMEL, S. A. BERGER, AND A. K. OPPENHEIM: "Effects of internal heat transfer on the structure of self-similar blast waves," J. Fluid Mech. **117** (1982), 473-491
- 2 J. R. NICAstro: "Similarity analysis of radiative gasdynamics with spherical symmetry." Phys. Fluids **13** (1970), 2000-2006

Address: DR. THOMAS HIRSCHLER, Institute of Fluid Mechanics and Heat Transfer, Technical University Graz, Inffeldgasse 25, A-8010 Graz, Austria.

VAN KEUK, J.; BALLMANN, J.

Numerical Simulation of Inviscid Shock Interactions on Double-Wedges

In supersonic and hypersonic flight double wedge geometries can cause very complex interaction phenomena between different wave types. These interactions can sometimes lead to anomalously high pressure and heat loads on the contour of aerospace planes like the ELAC1 configuration developed in the Collaborative Research Center (SFB 253) in Aachen. For the numerical simulation of such flows one has to use a method that should be both robust and accurate. The algorithm used here is based on the DLR FLOWer-Code extended by several Upwind-Splitting Methods for the physically correct description of the inviscid flux vector. Numerical solutions of 2D inviscid shock interactions on double-wedge geometries are presented and compared with corresponding results of other authors.

1. Physical Model / Numerical Method

The two-dimensional Euler equations for perfect gas flow are solved with a finite volume method, which is based on the well-known DLR FLOWer-Code [1]. This code is formulated as a cell vertex centered finite volume scheme in a block structure, and it has been extended by different Upwind-Discretization Techniques (e.g. van Leer / Hänel, AUSM, AUSM+, AUSMD/V, LDS, HLLE, Roe (Harten/Yee)) to better capture the directed propagation of information inherent in the inviscid part of the equations [5]. The scheme used in this work is the AUSMD/V Flux-Vector Splitting of Wada and Liou [6], a successful update of the well-known original AUSM proposed by Liou and Steffen [3]. Formally second order accuracy in space is achieved by means of MUSCL-Extrapolation, and the limiter functions for the TVD-property are those of Roe ("minmod", "superbee") and van Leer. Time integration for asymptotically steady state solutions is performed by an explicit 5-Stage Runge-Kutta scheme in connection with several optional convergence acceleration techniques such as local time stepping, implicit residual smoothing or the FMG-FAS multigrid method. An implicit formulation based on Jameson's Dual Time Stepping Technique is used in order to be able to apply the convergence acceleration techniques also to unsteady flows.

2. Results

According to the work of Olejniczak, Wright and Candler [4] two-dimensional inviscid shock interactions on double-wedge geometries are simulated, that are similar to those studied by Edney for blunt body flows with an incident shock [2]. Such investigations are thoroughly of practical relevance, since situations like these can appear as detail problems on hypersonic aerospace planes at control flaps, fins and, in particular, in the intake region. Values of $M_\infty = 9.0$ and $\kappa = 1.4$ are chosen for the free stream Mach number and the ratio of specific heats at a fixed first wedge angle of $\Theta_1 = 15.0^\circ$. A computational grid consisting of 800×400 points has been used in every case. The second wedge angle is varied from $\Theta_2 = 45.0^\circ$ via $\Theta_2 = 50.0^\circ$ up to $\Theta_2 = 60.0^\circ$ and within this region the structure of the solution is completely changing as it is shown in Fig. 1 and 2. The calculated Mach number distributions are displayed and subsonic regions are shaded. For $\Theta_2 = 45.0^\circ$ the very complex so-called Type V interaction appears, that consists of seven shocks and three contact surfaces. If the second wedge angle is changed to $\Theta_2 = 50.0^\circ$ the deflection of the flow via the second ramp can no longer be realized by an attached oblique shock, so the well-known Type IV interaction is formed. Here the interaction is characterized by five shocks and two contact surfaces enclosing a supersonic jet. Finally, if the second wedge angle is further increased, the interaction point moves more upstream and an interaction appears, that Olejniczak, Wright and Candler call Type IVr interaction and that consists of four shocks and one contact surface. Although not displayed it is worth mentioning that the maximum wall pressures for these cases vary between 400 and 700 times the free stream value! In Fig. 1, 2 the computed Mach number distributions are compared with those of Olejniczak, Wright and Candler showing a good agreement. All the flow phenomena like the shock positions and angles, the contact surfaces and the supersonic jets are resolved in a similar way.

Subject of future work will be an extension of the FLOWer-Code for the simulation of flows in chemical and thermal non-equilibrium in order to simulate the real flight case, where the gas will not behave as thermally and calorically perfect.

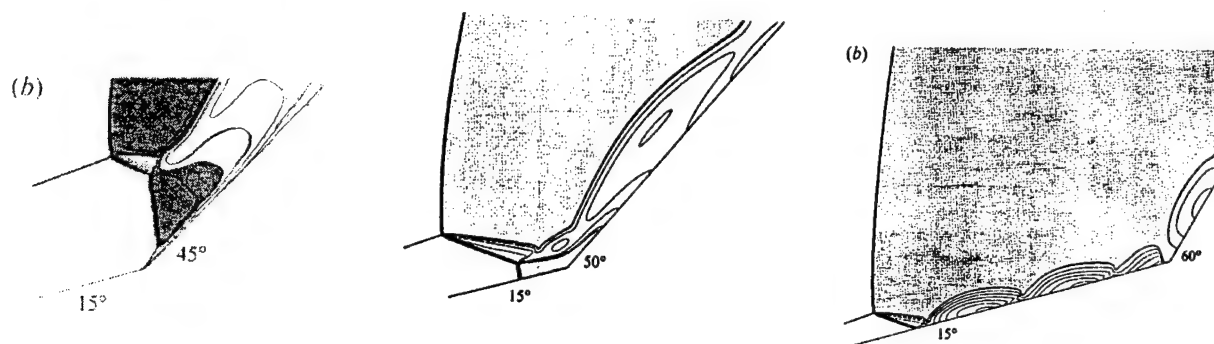


Figure 1: Type V-IV-IVr Transition (Olejniczak, Wright, Candler)

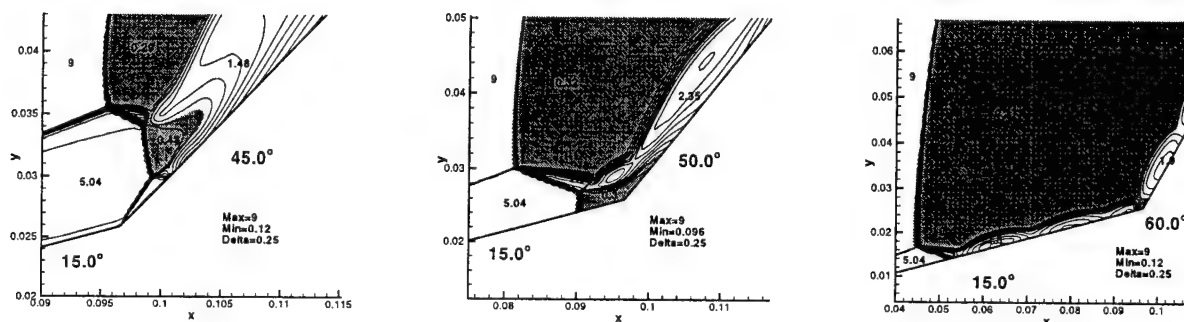


Figure 2: Type V-IV-IVr Transition (van Keuk, Ballmann)

Acknowledgements

This paper has been prepared within the scope of a PhD project of the Collaborative Research Center (SFB 253) "Fundamentals of Design of Aerospace Planes" at the RWTH Aachen, Germany, which is supported by the Deutsche Forschungsgemeinschaft (DFG).

3. References

- 1 DEUTSCHES ZENTRUM FÜR LUFT- UND RAUMFAHRT E. V.: FLOWer Version 114.1, Installation and User Handbook. Projekt MEGAFLOW (1997).
- 2 EDNEY, B.: Anomalous Heat Transfer and Pressure Distributions on Blunt Bodies at Hypersonic Speeds in the Presence of an Impinging Shock. Report 115, Flygtekniska Forsöksanstalten (The Aeronautical Research Institute of Sweden), Stockholm (1968).
- 3 LIOU, M. S., STEFFEN, C. J.: A New Flux Splitting Scheme. J. Comp. Phys. **107** (1993), 23-39.
- 4 OLEJNICZAK, J., WRIGHT, M. J., CANDLER, G. V.: Numerical Study of Inviscid Shock Interactions on Double-Wedge Geometries. J. Fluid Mech. **352** (1997), 1-25.
- 5 VAN KEUK, J., BALLMANN, J.: Two-Dimensional Riemann Problems: Assessment Tests for Upwind Methods for Multi-Dimensional Supersonic Flow Problems. Proceedings of the Finite Volumes for Complex Applications - Problems and Perspectives II Symposium, Duisburg (1999), 671-682.
- 6 WADA, Y., LIOU, M. S.: A Flux Splitting Scheme with High-Resolution and Robustness for Discontinuities. AIAA-Paper 94-0083 (1994).

Addresses: DIPL.-ING. JÖRN VAN KEUK, PROF. DR.-ING. JOSEF BALLMANN, Lehr- und Forschungsgebiet für Mechanik der RWTH Aachen, Templergraben 64, D-52062 Aachen

BÖHME, G., WÜNSCH, O.

Über Symmetrien schleichender Strömungsvorgänge in verfahrenstechnischen Apparaten

1. Theoretische Grundlagen

Die in der Kunststoffaufbereitung und in der Lebensmittelindustrie zu verarbeitenden fluiden Stoffe sind oft sehr zäh, so daß die Strömungsprozesse durch kleine Reynolds-Zahlen gekennzeichnet sind. Die Analyse solcher Strömungsvorgänge erfolgt dann sinnvollerweise auf der Basis der Bewegungs- und Kontinuitätsgleichungen für schleichende inkompressible Strömungen

$$-\text{grad } p(\mathbf{r}, t) + \text{div } \mathbf{T}(\mathbf{r}, t) - \frac{\Delta p_L}{L} \mathbf{e}_z = 0, \quad \text{div } \mathbf{v}(\mathbf{r}, t) = 0 \quad (1)$$

in Verbindung mit den Stoffgleichungen für nichtlinear viskose Flüssigkeiten

$$\mathbf{T}(\mathbf{r}, t) = 2\eta(\dot{\gamma}^2) \mathbf{D}(\mathbf{r}, t), \quad \dot{\gamma}^2 := 2 \text{sp } \mathbf{D}^2(\mathbf{r}, t). \quad (2)$$

Dabei bezeichnet \mathbf{v} den Geschwindigkeitsvektor, \mathbf{T} den Reibungsspannungstensor, \mathbf{D} den Verzerrungsgeschwindigkeitstensor, $\Delta p_L/L$ den mittleren axialen Druckgradienten und p die "Feinstruktur" des Druckfelds über dem in z -Richtung linear anwachsenden Druckanteil. Da Zeitableitungen fehlen, degeneriert die Zeit t zu einem Parameter. Jede instationäre schleichende Strömung kann deshalb als Folge voneinander unabhängiger, quasistationärer "Momentaufnahmen" aufgefaßt werden. Die Feldgleichungen sind außerdem invariant gegenüber der Transformation $\Delta p_L \rightarrow -\Delta p_L$, $\mathbf{v} \rightarrow -\mathbf{v}$, $p \rightarrow \text{const} - p$. Bei einem Vorzeichenwechsel des aufgeprägten Druckgradienten und der kinematischen Randbedingungen ändert sich deshalb überall in der Flüssigkeit lediglich das Vorzeichen des Geschwindigkeitsvektors, d.h. die Strömung läuft wie ein Film beim Rückspulen zeitlich invers ab (kinematische Reversibilität). In Verbindung mit geometrischen Invarianzen des Strömungsraums resultieren daraus bemerkenswerte Eigenschaften der dreidimensionalen Strömungs-, Deformations- und Spannungsfelder.

2. Symmetrien in statischen Mischern und Doppelschnecken

Der in Abb. 1 skizzierte statische Mischer besteht aus einem Gerüst schmaler Stege, die bezüglich der z -Richtung abwechselnd um $\pm 45^\circ$ geneigt sind. Benachbarte Segmente sind jeweils um 90° gegeneinander versetzt. Der geometrisch komplexe Strömungsraum ist invariant gegenüber einer 180° -Drehung um die y -Achse. Deshalb erkennt man in der inversen Bewegung die ursprüngliche Strömung wieder. Das führt zu folgenden Symmetrien für die kartesischen Komponenten des Eulerschen Geschwindigkeitsfelds [1]:

$$u(-x, y, -z) = u(x, y, z), \quad v(-x, y, -z) = -v(x, y, z), \quad w(-x, y, -z) = w(x, y, z). \quad (3)$$

Experimentelle Fakten stützen diese theoretischen Prognosen in überzeugender Weise (Abb. 2). Die Symmetrien schlagen auf die Bahnen materieller Punkte durch, die durch Integration des Differentialgleichungssystems

$$\frac{dx}{dt} = u(x, y, z), \quad \frac{dy}{dt} = v(x, y, z), \quad \frac{dz}{dt} = w(x, y, z) \quad (4)$$

bei Vorgabe der Anfangspositionen (x_0, y_0, z_0) zur Zeit t_0 zu berechnen sind. Die in Abb. 1 enthaltenen Bahnen A und A' verlaufen invers zueinander: Jede Position (x, y, z) längs A kehrt – mit einem Vorzeichenwechsel der Koordinaten x und z – auf der korrespondierenden Bahn A' wieder, wenn man diese rückwärts durchläuft. Demzufolge besitzt auch ein Poincaré-Schnitt des dynamischen Systems (4) mehr Symmetrien als die geometrische Konfiguration (Abb. 3). Die Symmetrien (3) spiegeln sich auch im Deformationszustand und nach Gl. (2) dann auch im Spannungszustand wider. Abb. 4 zeigt eine Häufigkeitsverteilung der kinematischen Feldgröße $\alpha := \det \mathbf{D} / (0.5 \text{sp } \mathbf{D}^2)^{3/2}$, die den Anteil der Dehnung an der Gesamtdeformation der Fluidelemente beschreibt. Mit jedem Fluidelement, das mit $\alpha > 0$ gedehnt wird, korrespondiert ein räumlich entferntes Element, das mit $-\alpha$ gestaucht wird.

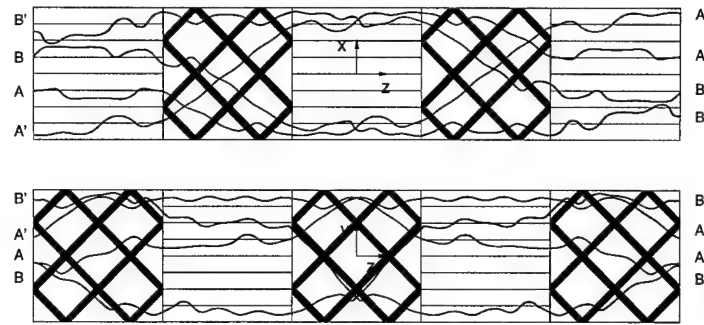


Abbildung 1: Statistischer Mischer vom Typ SMX mit 4 Bahnlinien bei Betrachtung von oben und von der Seite [1]

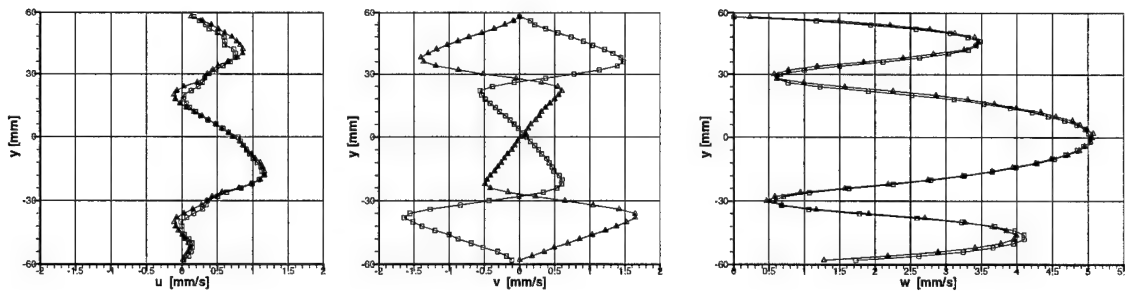


Abbildung 2: Experimentell ermittelte Geschwindigkeitsprofile an korrespondierenden Positionen; Quadrate: 5 mm vor dem ersten Segment, $x = 29$ mm; Dreiecke: 5 mm hinter dem letzten Segment, $x = -29$ mm [2]

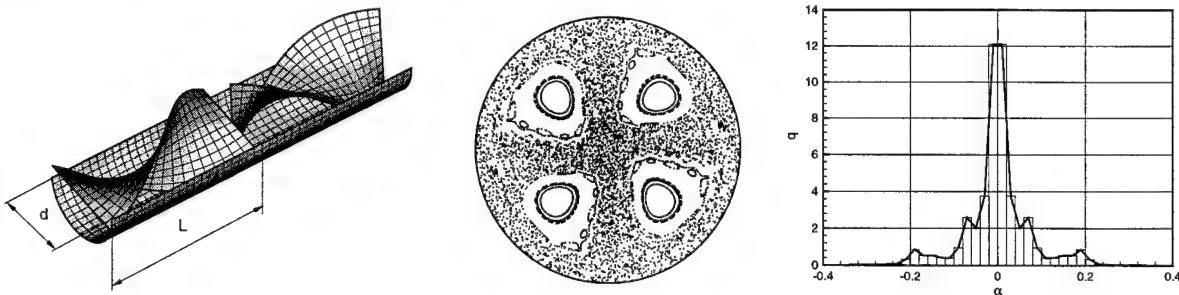


Abbildung 3: Zwei Segmente eines statischen Mixers vom Typ Kenics mit zweizähliger Geometrie und zugehöriger Poincaré-Schnitt für $L/d = 0.98$ mit vierzähliger Symmetrie aufgrund der kinematischen Reversibilität [3]

Abbildung 4: Dehnungsanteil an der Gesamtdeformation in einer Gleichdralldoppelschnecke: relative Häufigkeitsdichte $q(\alpha)$ [3]

Diese Symmetrien können einerseits ausgenutzt werden, um bei der numerischen Simulation der Strömung das Berechnungsgebiet drastisch zu reduzieren. Sie führen andererseits zu der Erkenntnis, daß periodisch aufgebaute Apparate nicht ideal mischen.

3. Literatur

- 1 WÜNSCH, O.; BÖHME, G.: Numerical simulation of 3d viscous fluid flow and convective mixing in a static mixer. Arch. Appl. Mech. (2000), 91–102.
- 2 LEITNER, M.: Dreidimensionale Laser-Doppler-Velocimetrie zur Analyse der Strömung in statischen Mischelementen. Dissertation, Univ. d. Bundeswehr Hamburg 2001.
- 3 WÜNSCH, O.: Strömungsmechanik des laminaren Mischens. Habilitationsschrift, Univ. d. Bundeswehr Hamburg 1999.

Adresse: PROF. DR. G. BÖHME, PRIV.-DOZ. DR.-ING. O. WÜNSCH, Universität der Bundeswehr Hamburg, Institut für Strömungslehre und Strömungsmaschinen, D-22039 Hamburg

BREUER, M.

Towards Technical Application of Large Eddy Simulation

The paper is concerned with the computation of high Reynolds number circular cylinder flow ($Re = 3900/140,000$) based on the large eddy simulation (LES) technique. Because this flow involves a variety of complex flow features encountered in technical applications, successful simulations for this test case, especially at high Reynolds numbers, can be considered as the first step to real world applications of LES. Based on an efficient finite-volume LES code, a detailed study on different aspects influencing the quality of LES results was carried out. In the present paper, some of the results are presented and compared with experimental measurements available.

1. Introduction

During the last decades the performance of the fastest supercomputers in the world has been increasing about one order of magnitude every five years and despite occasionally contrary prophecies, this trend is still continuing. The hardware development and concurrent progress in numerical methods have strongly influenced the simulation approaches for turbulent flows enabling the application of advanced techniques such as Large Eddy Simulation. LES is not new. However, in the past the application was mainly restricted to flows involving simple geometries and low Reynolds numbers. The long-term objective of the present work is to promote LES for high- Re flows of practical relevance. This requires the validation of the applied physical models and numerical methods by detailed investigations based on well-documented test cases. Because the flow past circular cylinders involves remarkably complex flow features such as thin separating shear layers, transition and large-scale vortex motion, it can be considered as the *paradigm* of complex flows and as an ideal test case for LES. Based on this flow, a series of investigations on different numerical and modeling aspects has been carried out [1-3]. In this short contribution, some results of the high- Re case ($Re = 140,000$) are presented and compared with experimental data by Cantwell and Coles [4].

2. Computational Basics

The LES approach can be defined as the '*golden mean*' between direct numerical simulation (DNS) and classical turbulence modeling based on the Reynolds-averaged Navier-Stokes equations (RANS) combined with statistical turbulence models. For DNS the entire spectrum of turbulent eddies down to the smallest length scale (Kolmogorov length) has to be resolved by a numerical method, whereas in the RANS approach an appropriate turbulence model has to take into account the effect of all length scales. Contrary to DNS and RANS, in LES the spectrum of turbulent motions is split into the large energy-carrying vortices which can be resolved by the numerical method applied and all non-resolvable small-scale vortices called subgrid scales (SGS). Its influence on the large-scale motion has to be modeled. However, such SGS models have, in many situations, a much simpler task than RANS models because only that part of the spectrum has to be taken into account which is easier to model. With respect to CPU-time, LES has also to be classified between DNS and RANS, because it generally requires considerably larger resources than RANS due to the three-dimensional and time-dependent approach, but less CPU-time than DNS owing to reduced resolution requirements.

The LES code *LESOC* used for the solution of the filtered Navier-Stokes equations, is based on a 3-D finite-volume method for arbitrary non-orthogonal, block-structured grids [1-3]. The spatial discretization of all fluxes is based on central differences of second-order accuracy. A low-storage multi-stage Runge-Kutta method (second-order accurate) is applied for time-marching. In order to ensure the coupling of pressure and velocity fields on non-staggered grids, the momentum interpolation technique is used. For modeling the non-resolvable subgrid scales, two different models are implemented, namely the well-known Smagorinsky model with Van Driest damping near solid walls and the dynamic approach with a Smagorinsky base model. Moreover, computations were performed without any subgrid scale model in order to investigate the influence of the model on the resolved scales. *LESOC* is highly vectorized and additionally parallelized by domain decomposition with explicit message-passing based on MPI allowing efficient computations on vector-parallel machines. For more details, we refer to [1-3].

3. Results for the Circular Cylinder Flow

For sub-critical Reynolds numbers ($200 \lesssim Re \lesssim 5 \cdot 10^5$) the boundary layer at the cylinder is laminar up to the separation point and transition to turbulence takes place in the free shear layer. In the wake, the well-known von Kármán vortex street with periodic vortex shedding is observed, which was visualized by streaklines (see [3]). The predicted Strouhal number of the vortex shedding frequency varies around 0.2 based on the different grids and SGS models applied. This value is in good agreement with generally accepted experimental data for $Re = 140,000$. Fig. 1 shows a qualitative comparison of the computed LES results and the experimental data by Cantwell and Coles [4]. The streamlines and vector fields were obtained by averaging the instantaneous flow field in time and in the spanwise direction. Unfortunately, no measurements were taken for the front part of the cylinder and in the direct vicinity of the rear. However, in accordance with the experimental data, the LES computation predicts an attached recirculation region behind the cylinder which is much shorter than for $Re = 3900$ (see Fig. 1(c)). In contrast to $Re = 3900$, no small counter-rotating vortices attached to the backward side of the cylinder can be observed for the high- Re case. The primary separation angle is at about $\Theta_{Sep} \approx 91^\circ$, which means that the separation point is still behind the apex of the cylinder. An immediate transition to turbulence close to the cylinder is observed in the free shear layers. Compared with the low- Re case, transition to turbulence moves farther upstream. A more detailed investigation of the predicted results based on velocity profiles (see [2–3]) shows that the LES results are in satisfactory agreement with the experimental data, especially in the near wake. Owing to the coarse resolution in the far wake, larger deviations were observed here. Additionally to the mean flow field, higher order statistics have been analyzed. In Fig. 2 the total resolved streamwise Reynolds stress $\overline{u'u'}$, the cross-stream component $\overline{v'v'}$, and the shear stress $\overline{u'v'}$ are depicted. These distributions are in reasonable agreement with the measured values of Cantwell and Coles [4]. In conclusion, the LES results agree satisfactorily with experimental data. The present work has demonstrated that LES of practically relevant high- Re flows should become feasible in the near future, particularly for flows involving large-scale vortex motion.

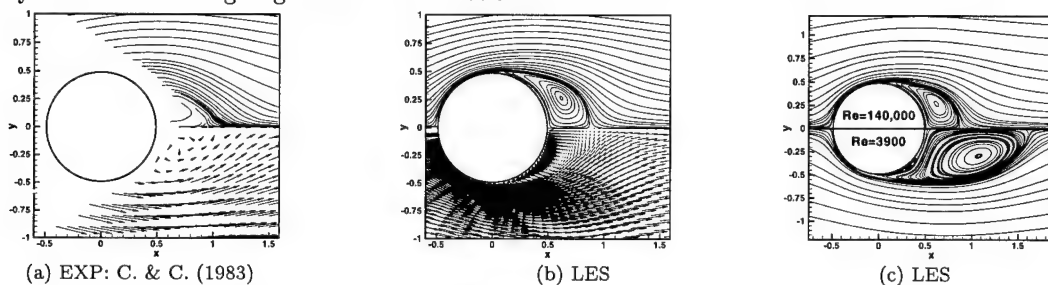


Figure 1: Time-averaged flow past a cylinder: (a) measurements by Cantwell and Coles [4] at $Re = 140,000$, (b) LES at $Re = 140,000$, (c) comparison of LES results for two Re , upper part: $Re = 140,000$, lower part: $Re = 3900$.

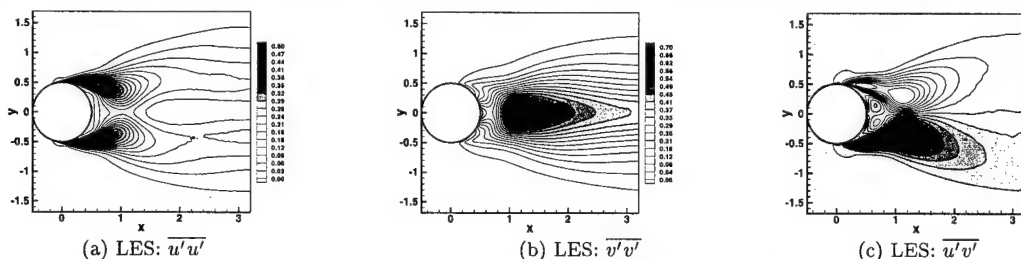


Figure 2: Time-averaged flow field of the sub-critical flow past a cylinder at $Re = 140,000$, total resolved stress components: (a) streamwise Reynolds stress $\overline{u'u'}$, (b) cross-streamwise Reynolds stress $\overline{v'v'}$, (c) shear stress $\overline{u'v'}$.

4. References

- 1 BREUER, M.: *Large Eddy Simulation of the Sub-Critical Flow Past a Circular Cylinder: Numerical and Modeling Aspects*, Int. J. Num. Methods Fluids, vol. 28, pp. 1281–1302, John Wiley & Sons Limited, Chichester, (1998).
- 2 BREUER, M.: *Large Eddy Simulation of High Reynolds Number Circular Cylinder Flow*, Proc. Workshop on Indust. & Environ. Appl. of DNS & LES, Aug. 5–7, 1998, Istanbul, Lecture Notes in Physics, vol. 529, pp. 176–189, Springer, (1999).
- 3 BREUER, M.: *A Challenging Test Case for Large Eddy Simulation: High Reynolds Number Circular Cylinder Flow*, Int. J. Heat Fluid Flow, vol. 21, no. 5, pp. 648–654, Elsevier Science B.V., Amsterdam, (2000).
- 4 CANTWELL, B., COLES, D.: *An Experimental Study on Entrainment and Transport in the Turbulent Near Wake of a Circular Cylinder*, J. Fluid Mechanics, vol. 136, pp. 321–374, (1983).

Address: MICHAEL BREUER, Institute of Fluid Mechanics (LSTM), University of Erlangen-Nürnberg, Cauerstr. 4, D-91058 Erlangen, Germany, breuer@lstm.uni-erlangen.de

A. EXNER AND A. KLUWICK

The interaction problem for the locally cooled free convection boundary layer

The free convection boundary layer which forms on a heated vertical flat plate of constant temperature is investigated in the vicinity of a localized disturbance of the wall temperature. In a small region the wall is cooled in a prescribed manner. The short strong disturbance results in an interaction problem which is solved numerically. If the disturbances are sufficiently weak, the interaction equations can be linearised allowing for analytical solutions. For strong disturbances, a numerical calculation of the non-linear interaction problem is performed.

1. Problem formulation

The wall temperature of a constantly heated vertical flat plate is disturbed at some distance \tilde{L} from the leading edge in a region of streamwise extent $\sigma\tilde{L}$ with the non-dimensional parameter $\sigma \ll 1$. The flow is investigated in the limit $Gr = \frac{\tilde{L}^3 \tilde{g}(\tilde{T}_0 - \tilde{T}_\infty)}{\tilde{\nu}_\infty^2 \tilde{T}_\infty} \rightarrow \infty$ and for $Pr = \frac{\tilde{\alpha}_\infty}{\tilde{\nu}_\infty} = O(1)$ with \tilde{g} , \tilde{T}_0 , \tilde{T}_∞ , $\tilde{\nu}_\infty$ and $\tilde{\alpha}_\infty$ denoting gravitational acceleration, undisturbed wall temperature, ambient temperature, kinematic viscosity and specific heat conductivity, respectively. The temperature disturbance $\vartheta_w(x)$ is taken to be a continuous function of the non-dimensional wall coordinate $x = (\tilde{x}/\tilde{L} - 1)/\sigma$. We assume steady laminar two-dimensional flow. Dissipation shall be negligible and the Boussinesq approximation is adopted. Inspection of the momentum equation shows that a temperature disturbance of amplitude $\sim (\tilde{T}_\infty - \tilde{T}_0)\sigma^{-1/3}$ is necessary to provoke separation. Two different flow regimes have to be distinguished depending on the magnitude of σ . For $1 \gg \sigma \gg Gr^{-3/14}$ marginal separation occurs (EXNER AND KLUWICK 1999). On the other hand viscous-inviscid interaction comes into play when $\sigma = O(Gr^{-3/14})$. This case will be investigated in the following.

A double-deck structure of streamwise extent $Gr^{-3/14}$ is appropriate to describe the flow in the vicinity of the disturbance with an outer predominantly inviscid layer (main deck MD) of thickness $Gr^{-1/4}$ and a thin sublayer adjacent to the wall (lower deck LD) of thickness $Gr^{-9/28}$ where viscous effects dominate. The flow in the LD is retarded by the disturbance which leads to a thickening of this layer, thereby causing a displacement of the MD flow. The disturbance of the temperature field is confined to the LD. In the MD, the flow, in leading order, is determined by the similarity profile $U_0(y_{MD})$ of the unperturbed flow, which is shifted away from the wall by a distance $a(x)$ denoting the displacement thickness. Similar to the problem studied by SMITH AND DUCK (1977), the pressure induced in the MD by the flow displacement is given by

$$p(x, y_{MD}) = a''(x) \int_{y_{MD}}^{\infty} dy U_0(y)^2. \quad (1)$$

In the LD, the pressure is a function of the wall coordinate x only. Applying the pressure law (1), the LD problem is described by the system of equations

$$\frac{\partial \Psi}{\partial y} \frac{\partial^2 \Psi}{\partial x \partial y} - \frac{\partial \Psi}{\partial x} \frac{\partial^2 \Psi}{\partial y^2} = \vartheta - \frac{d^3 a}{dx^3} + \frac{\partial^3 \Psi}{\partial y^3}, \quad (2)$$

$$\frac{\partial \Psi}{\partial y} \frac{\partial \vartheta}{\partial x} - \frac{\partial \Psi}{\partial x} \frac{\partial \vartheta}{\partial y} = \frac{1}{Pr} \frac{\partial^2 \vartheta}{\partial y^2}, \quad (3)$$

$$\begin{aligned} y = 0: \quad \Psi = \frac{\partial \Psi}{\partial y} = 0, \quad \vartheta = \vartheta_w(x); \quad y \rightarrow \infty: \quad \frac{\partial \Psi}{\partial y} = y - a(x), \quad \vartheta = 0; \\ x \rightarrow -\infty: \quad \frac{\partial \Psi}{\partial y} = y, \quad \vartheta = 0, \quad a = 0 \end{aligned}$$

where Ψ and $\vartheta = Gr^{-1/14}(\tilde{T} - \tilde{T}_\infty)/(\tilde{T}_0 - \tilde{T}_\infty)$ denote the stream function and the temperature disturbance, respectively.

2. Results

For small but finite disturbances $\vartheta_w(x) = \epsilon g_w(x)$, $\epsilon \ll 1$, the flow quantities can be expanded into series of the perturbation parameter ϵ , leading to a linear system for the disturbances which can be solved by Fourier transform methods. Solutions of a simple form are obtained for $Pr = 1$ which show pronounced upstream influence of the disturbance as it is typical for interaction problems. For the specific choice $g_w(x) = \exp(-4x^2)$, the solutions for the disturbances of the skin friction $(\tau_w(x) - 1)/\epsilon$ and the displacement thickness $a(x)/\epsilon$ are given by

$$\begin{aligned} \frac{(\tau_w(x) - 1)}{\epsilon} &= \frac{1}{4\sqrt{\pi}} \int_0^\infty d\omega \frac{[\theta(\omega^{14/3} + \phi) \cos(\omega x - \frac{\pi}{3}) + (\theta^2 \cos(\omega x) + \phi \cos(\omega x - \frac{\pi}{3})) \omega^{7/3}] \omega^{7/3}}{\omega^{1/3} [\omega^{14/3} + \sqrt{3}\theta \omega^{7/3} + \theta^2]} e^{-\frac{\omega^2}{16}} \\ \frac{a(x)}{\epsilon} &= -\frac{(\phi - \theta^2)}{\phi \sqrt{16\pi}} \int_0^\infty d\omega \frac{[\sin(\omega x) \omega^{7/3} + \theta \cos(\omega x - \pi/3)]}{\omega^{2/3} [\omega^{14/3} + \sqrt{3}\theta \omega^{7/3} + \theta^2]} e^{-\frac{\omega^2}{16}} \end{aligned} \quad (4)$$

with $\theta = -3\text{Ai}'(0)$ and $\phi = 3\text{Ai}(0)$. For values of the perturbation parameter ϵ up to ~ 0.1 , the linearised results are found to be in good agreement with numerical solutions of the non-linear problem.

For stronger disturbances, i. e. when the perturbation analysis is not applicable, the non-linear system (2-3) has to be solved numerically. To this end, a marching procedure using a Newton-Raphson solver and a Crank-Nicholson discretisation scheme was applied starting from an unperturbed state of the flow sufficiently far upstream of the disturbance. To account for effects of free interaction, a small positive pressure disturbance was imposed at the starting point of the calculation. Its value was adjusted by a shooting method. Representative results for $Pr = 0.7$, $\vartheta_w(x) = -2.4 \exp(-4x^2)$ are given in Figs. 1-3.

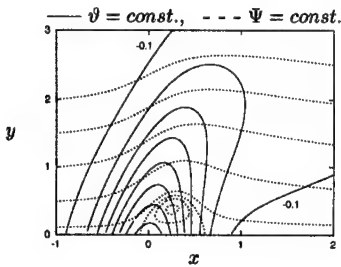


Fig. 1

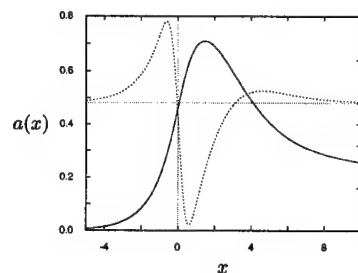


Fig. 2

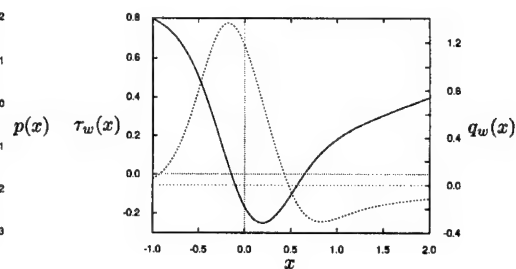


Fig. 3

In Fig. 1, isotherms with constant spacing $\Delta\vartheta = 0.3$ between subsequent lines with values ranging from -0.1 to -2.2 (solid curves) and streamlines (dashed curves) are displayed. A separation bubble is formed at the wall close to $x = 0$ and flow displacement is apparent in its vicinity. The temperature field shows a large region of cooled medium distorted in downstream direction by convection, and the disturbance rapidly decays as the wall distance increases. Fig. 2 shows the displacement thickness $a(x)$ and the induced pressure $p(x) = a''(x)$. Both quantities begin to differ from 0 already some distance upstream of the region where a significant deviation of the wall temperature from its unperturbed value occurs which is clearly an effect of interaction. Wall heat flux $q_w(x)$ and skin friction $\tau_w(x)$ are plotted in Fig. 3. Note the section of negative values of skin friction corresponding to the region of separated flow in Fig. 1. It is found that separation is retarded by interaction compared to the case of non-interacting flow.

Finally it has to be mentioned that the above analysis as well as the problem treated by EXNER AND KLUWICK 1999 can easily be generalised to wall jets in the limit $Re \rightarrow \infty$ since temperature disturbances are confined within the thin viscous sublayer and the solutions do not depend on the temperature profile of the oncoming undisturbed boundary layer. A characteristic temperature difference for the wall jet problem to define the strength of the disturbance can be extracted from the Reynolds number.

3. References

- EXNER, A. AND KLUWICK, A.: Locally cooled free-convection boundary layer on the verge of separation. ZAMM 79, Suppl. 3 (1999), 711-712.
- SMITH, F.T. AND DUCK, P.W.: Separation of jets or thermal boundary layers from the wall. Q. Jl. Mech. appl. Math. 30, 2 (1977), 143-156.

Addresses: DIPL.-ING. ALFRED EXNER, PROF. DR. ALFRED KLUWICK, Technische Universität Wien, Institut für Strömungslehre und Wärmeübertragung, Wiedner Hptstr. 7, A-1040 Wien, Austria.

MARIE FARGE, GIULIO PELLEGRINO AND KAI SCHNEIDER

Wavelet filtering of three-dimensional turbulence

We present a new vortex tube extraction method for three-dimensional turbulent flows. The method is based on an orthogonal wavelet decomposition of the vorticity vector field. The coherent part of the flow is reconstructed from the strongest wavelet coefficients using an universal threshold criterion. As example we present the vortex tube extraction of three-dimensional homogeneous isotropic turbulence.

The importance and the role of coherent structures (coherent vorticity tubes) in 3D turbulence have been established largely by high resolution numerical simulations, see e.g. [1]. In the past we have developed a wavelet method to extract coherent vortices in 2D turbulent flows [2,3], at which the remaining background flow exhibits Gaussian statistics.

In this paper, we propose a new wavelet based method to separate three-dimensional flows into an organized part, corresponding to the coherent vorticity tubes, and a random part, corresponding to the incoherent background flow. As an example, we consider DNS data of statistically stationary 3D homogeneous and isotropic turbulence. The flow has been computed by Meneguzzi & Vincent [1] using a pseudo-spectral scheme with resolution $N = 240^3$ corresponding to a microscale Reynolds number of 150. We project each component of the vorticity vector field $\vec{\omega}$ onto a three-dimensional orthogonal wavelet basis. Then we reconstruct the coherent vorticity field ($\vec{\omega}_>$) from those wavelet coefficients for which the modulus of the wavelet coefficient vector is larger than $(4/3Z \log_{10} N)^{1/2}$ (where Z denotes the total enstrophy and N the number of grid points), while the incoherent background flow ($\vec{\omega}_<$) is reconstructed from the weak coefficients. We find that only 2.8% of the coefficients represent the coherent vorticity tubes (cf. Fig. 1, left) and retain 74.7% of total enstrophy. The remaining 97.2% of the coefficients represent the unorganized background flow (cf. Fig. 1, right) containing 25.3% of the total enstrophy. The energy spectra (Fig. 2, left) show that both components ($\vec{\omega}_>$ and $\vec{\omega}_<$) are multiscale, although the coherent part only differs at high wavenumbers from the original field ($\vec{\omega}$), which confirms the fact that vorticity tubes are multiscale. The pdf of vorticity (Fig. 2) for the coherent part is very similar to the original pdf, which confirms the fact that most of the statistical information is preserved by the wavelet filtering. The pdf of the background field is not exactly Gaussian as in the 2D case, however its variance is strongly reduced. For further details we refer the reader to [4].

The motivation for the above approach is the development of a new semi-deterministic turbulence model, called Coherent Vortex Simulation (CVS) [2,5] for simulating high Reynolds number flows. Therein, the evolution of the coherent vorticity tubes is calculated in an adaptive wavelet basis, which dynamically adjusts to the flow evolution, while the influence of the incoherent background flow is statistically modelled.

Acknowledgements

We acknowledge support from the French-German Procope program (contract N. F 01220ZE/D 9822768) and the European TMR program (contract N. FMRX-CT 98-0184). We thank Maurice Meneguzzi for providing us with the DNS data.

1. References

- 1 A. VINCENT, M. MENEGUZZI. The spatial structure and statistical properties of homogeneous turbulence. *J. Fluid Mech.*, Vol. 225, pp. 1-20, 1991.
- 2 M. FARGE, K. SCHNEIDER AND N. KEVLAHAN. Non-Gaussianity and Coherent Vortex Simulation for two-dimensional turbulence using an adaptive orthonormal wavelet basis. *Phys. Fluids*, **11**(8), 2187-2201, 1999.
- 3 K. SCHNEIDER AND M. FARGE. Wavelet approach for modelling and computing turbulence. *Lecture Series 1998-05 Advances in turbulence modelling*, von Karman Institute for Fluid Dynamics, Bruxelles, 132 pages, 1998.
- 4 M. FARGE, G. PELLEGRINO AND K. SCHNEIDER. Coherent Vortex Extraction in 3D Turbulent Flows using orthogonal wavelets. *Phys. Rev. Lett.* submitted.
- 5 M. FARGE AND K. SCHNEIDER. Coherent Vortex Simulation (CVS), a semi-deterministic turbulence model using wavelets. *Flow, Turbulence and Combustion*, submitted.

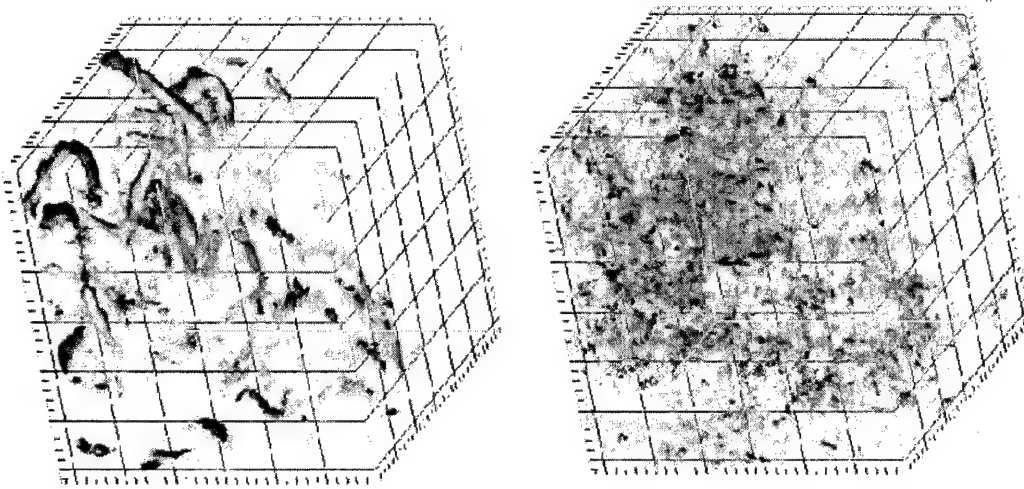


Figure 1: Isosurfaces of vorticity. Left: coherent vorticity field $\vec{\omega}_>$ reconstructed from 3% of the wavelet coefficients. Right: background vorticity $\vec{\omega}_<$ reconstructed from 97% of the wavelet coefficients. Note that the coherent vorticity is similar to the original field $\vec{\omega}$ (not shown here).

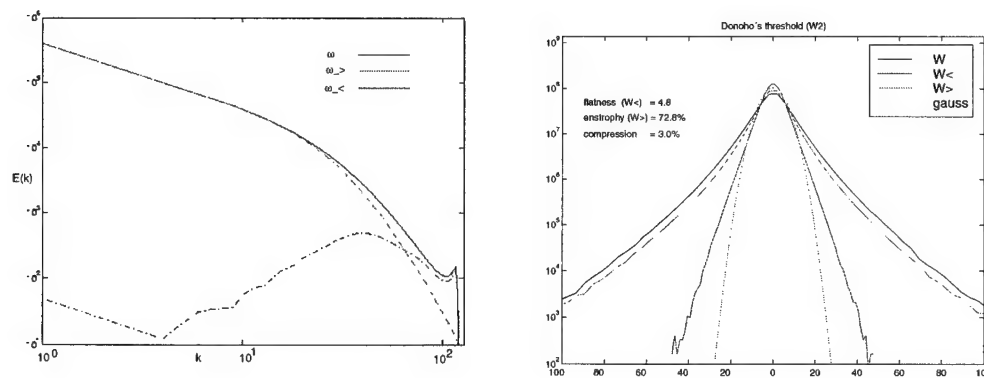


Figure 2: Energy spectra (left) and pdf of vorticity (right) of the total field $\vec{\omega}$, the coherent field $\vec{\omega}_>$ and the background field $\vec{\omega}_<$.

Address: MARIE FARGE, LMD-CNRS, Ecole Normale Supérieure, 24 rue Lhomond, 75231 Paris Cedex 05, France
 GIULIO PELLEGRINO, ICT, Universität Karlsruhe (TH), Kaiserstr. 12, 76128 Karlsruhe Germany
 KAI SCHNEIDER, CMI, Université de Provence, 39 rue F. Joliot-Curie, 13453 Marseille Cedex 13, France

FRANKE, J., FRANK, W.

Temporal Commutation Errors in Large-Eddy Simulation

The spatial filtering applied in large eddy simulations leads to additional closure problems if the filter width varies in space and time. While the spatial commutation error has been examined, the temporal commutation error has not been studied, despite its relevance for in-cylinder flow simulations [1]. Here some theoretical results for the temporal commutation error are presented. It is shown that a temporally varying domain leads to an additional constraint on the filter function. The results are illustrated for a simple scalar problem.

1. Introduction

In large eddy simulation (LES) a spatially filtered flowfield is computed. The evolution equations for the filtered flow variables are derived by applying a spatial filter to the Navier-Stokes-equations. If the filter is homogeneous in each coordinate direction, only the non-linear terms lead to a closure problem that can be expressed as generalized central moments. The equation system for the resolved flow variables has to be closed by a subgrid scale (SGS) model. But if the filter is non-homogeneous in any coordinate direction spatial filtering and partial derivation do not commute, leading to an additional closure problem. This commutation error has been analysed for non-homogeneous filters in space [2,3]. These arise if non-equidistant grids are used in the computation of the resolved field, because the grid-width determines explicitly or implicitly the filter-width. For a temporal variation of the filter-width, corresponding to a temporally varying grid, the resulting commutation error has not been discussed explicitly [3]. Therefore we present the temporal commutation error for the one-dimensional case and discuss its implications for the basic equations of LES with temporally varying grids.

2. Definitions and simple example

In the following we restrict ourselves to the one-dimensional case in space, as the three dimensional case is generally recovered by multiplication of the three one-dimensional filter functions $G(x-y; \Delta)$, which depend on the filter width Δ . Furthermore we will only allow a continuous temporally varying filter width $\Delta(t)$, which is constant in space. Then the filtered value $\bar{u}(x, t)$ of any scalar flow variable $u(x, t)$ in the domain $x \in [a(t), b(t)]$ is defined by the moving average

$$\bar{u}(x, t) = \int_{a(t)}^{b(t)} G(x-y; \Delta(t)) u(y, t) dy \quad , \quad \int_{a(t)}^{b(t)} G(x-y; \Delta(t)) dy = 1 \quad . \quad (1)$$

The second equality restricts the filter function to those that are mean-preserving. For a temporally varying filter width, this leads to an additional constraint pertaining to the time derivative

$$\int_{a(t)}^{b(t)} \frac{\partial G}{\partial \Delta} \frac{d\Delta(t)}{dt} dy = - \left[G(x-b(t), t) \frac{db(t)}{dt} - G(x-a(t), t) \frac{da(t)}{dt} \right] \quad . \quad (2)$$

Eqn.(2) might be called the FILTER CONSERVATION LAW as it corresponds to the GEOMETRIC CONSERVATION LAW in FV- or FE-computations with temporally varying grids (e.g. [4]). It should be noted, that eqn.(2) is obtained by applying the moving average of eqn.(1) before any discretization issue is addressed.

If this average is applied to the linear wave equation, $\partial u / \partial t + \partial u / \partial x = 0$, two additional terms appear in the differential equation for the filtered variable \bar{u}

$$\frac{\partial \bar{u}(x, t)}{\partial t} + \frac{\partial \bar{u}(x, t)}{\partial x} + C_t[u](x, t) + C_x[u](x, t) = 0 \quad .$$

Due to the spatially constant filter width the spatial commutation error C_x only consists of a surface term [2, 3]

$$C_x = \frac{\partial \bar{u}}{\partial x} - \frac{\partial \bar{u}}{\partial x} = [G(x-y; \Delta(t)) u(y, t)]_{y=a(t)}^{y=b(t)} \quad .$$

The temporal commutation error C_t shows an additional local closure problem, because the knowledge of the unfiltered quantity u is necessary in the entire domain,

$$C_t = \frac{\partial \bar{u}}{\partial t} - \frac{\partial \bar{u}}{\partial t} = \left[G(x-y; \Delta(t)) u(y, t) \frac{dy}{dt} \right]_{y=a(t)}^{y=b(t)} - \int_{a(t)}^{b(t)} u(y, t) \frac{\partial G}{\partial \Delta} \frac{d\Delta(t)}{dt} dy \quad .$$

The influence of C_t on the resolved \bar{u} will be demonstrated by a simple example displayed in figure 1a. Applying a temporally varying box filter, $G_B(|x-y|) = 1/\Delta(t)$ for $|x-y| \leq \Delta(t)/2$ and $G_B(|x-y|) = 0$ elsewhere, to the steady function $u(x) = 5(\cos(5x) + \cos(100x))$, a time dependent filtered function $\bar{u}(x, t) = 2(\cos(5x) \sin(2.5\Delta(t)) + \cos(100x) \sin(50\Delta(t)))/\Delta(t)$ emerges.

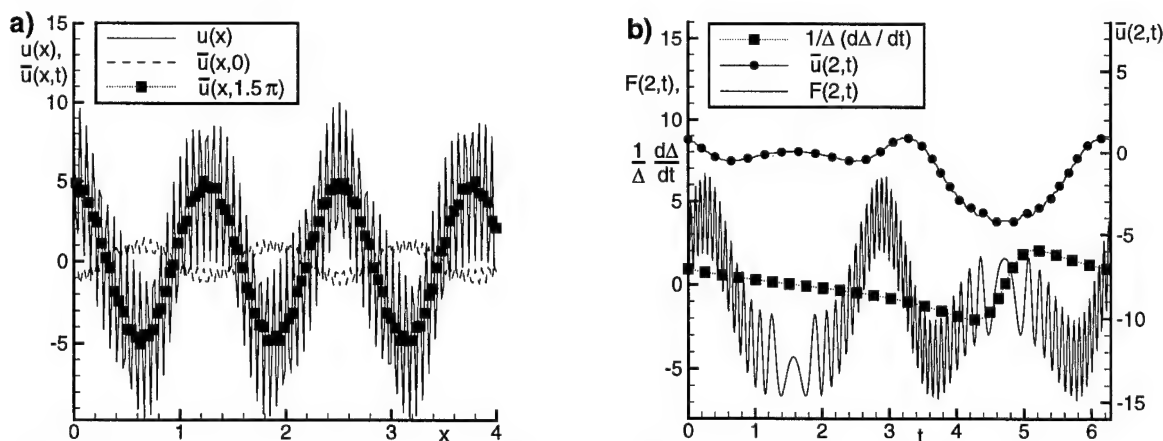


Figure 1: a) $u(x)$, $\bar{u}(x, 0)$ and $\bar{u}(x, 3/2\pi)$ for $\Delta(t) = 2 + 1.8 \sin(t)$; b) $\bar{u}(2, t)$ and RHS of eqn.(3) for $x = 2$

If the boundary terms are neglected, the temporal evolution of \bar{u} is given by the local temporal commutation error,

$$\frac{\partial \bar{u}}{\partial t} = -C_t = -\frac{1}{\Delta(t)} \frac{d\Delta(t)}{dt} \left[\bar{u}(x, t) - \frac{u(x + \Delta(t)/2) + u(x - \Delta(t)/2)}{2} \right] = -\frac{1}{\Delta(t)} \frac{d\Delta(t)}{dt} F(x, t) \quad (3)$$

Generally, a decrease in the resolved quantity would be expected, if the filter width is increasing, leading to a deterioration of the resolution quality. However, as can be seen from figure 1b, where \bar{u} and the terms on the RHS of eqn.(3) are plotted for $x = 2$ over time, there can be an increase in \bar{u} if the filter width is increasing and vice versa. This is due to the magnitude of the transport of unfiltered u over the filter's boundary appearing in the square brackets in eqn.(3).

3. Conclusions

In this short communication we have shown that the application of a filter function with temporally varying filter width leads to an additional constraint, the FILTER CONSERVATION LAW, and an additional closure problem, the temporal commutation error. This term appears in the basic equations of LES for computations with moving grids prior to discretization and has to be modelled. Another possibility is the application of filtering to the equations in general curvilinear coordinates, extending the work of Jordan [5] to time. Then no commutation error will result.

4. References

- 1 HAWORTH, D. C.: Large-Eddy Simulation of In-Cylinder Flows. *Oil & Gas Science and Technology* **54** (1999), 175–185
- 2 GHOSAL, S.: Mathematical and Physical Constraints on Large-Eddy Simulation of Turbulence. *AIAA Journal* **37** (1999), 425–433
- 3 FUREBY, C., TABOR, G.: Mathematical and Physical Constraints on Large-Eddy Simulations. *Theoret. Comput. Fluid Dynamics* **9** (1997), 85–102
- 4 THOMAS, P.D., LOMBARD, C.K.: Geometric Conservation Law and its Application to Flow Computations on Moving Grids. *AIAA Journal* **17** (1979), 1030–1037
- 5 JORDAN, S. A.: A Large-Eddy Simulation Methodology in Generalized Curvilinear Coordinates. *J. Computational Physics* **148** (1999), 322–340

Addresses: DR.-ING. J. FRANKE, PROF. DR.-ING. W. FRANK, University of Siegen, Institute of Fluid- und Thermodynamik, Paul-Bonatz-Strasse 9-11, D-57076 Siegen, Germany

S. HEIKEN, R. DEMUTH, E. LAURIEN

Dependency of the Bypass-Transition on the Initiating Disturbance

Numerical Simulations are made by integration of the three-dimensional Navier-Stokes equations for the early stages of the turbulent spot development in accelerated flat plate boundary layers. Several initial finite amplitude disturbances are stretched and develop a steep velocity gradient in the spanwise direction. The structure, visualized by tracer particles, becomes more complex and looks similar to a turbulent spot, shown in experiments by Elder.

1. Introduction

It is essential to understand the laminar-turbulent transition initiated by local finite amplitude disturbances in compressible boundary layers for the development of improved transition prediction methods, e.g. for boundary layers on turbomachine blades, where bypass-transition is dominant [1]. The early stages of the turbulent spot development are simulated numerically in the present research. To investigate the dependency of the spot development on the initiating disturbances, various disturbances are compared.

2. Integration Domain and Numerical Method

To integrate the compressible, three-dimensional Navier-Stokes equations within a cartesian box, a finite-difference spectral method [2] with periodic boundary conditions in the horizontal, streamwise (x_1) and spanwise (x_2) directions, is used. At the wall, no slip and isothermal boundary conditions are imposed. Disturbance and base flow are superposed at the beginning of the simulation. To prevent the disturbance from reaching the horizontal boundaries, the integration domain is chosen large enough.

In the present work, a vortex pair and a torus vortex, Fig.1, both also investigated by Henningson et al. [3], are used. Owing to observations of Perry et al. [4], further disturbances like a hairpin vortex and a disturbance formed by six small Λ vortices, Fig.1 are tested. They are placed near the upstream boundary of the integration domain at the beginning of the simulation. The investigated base flow has no variation in the horizontal directions and is chosen according to an experiment by Hoheisel et al. [5]. The parameters for this case are $Re_\delta = 10700$ (based on the boundary layer thickness δ) and (the Mach number) $Ma = 0.6$. The numerical resolution is 32×64 modes \times 76 points (streamwise, $x \times$ spanwise, $y \times$ wall normal, z -direction), aliasing-free up to cubic products. A time step width of $\Delta t = 0.01$ is used.

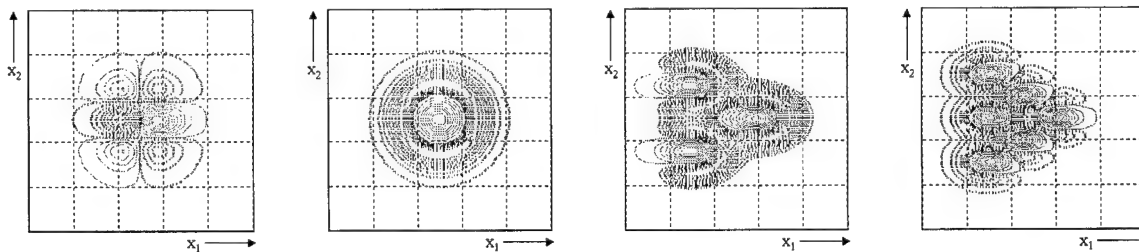


Figure 1: Isolines of the wall normal velocity (solid = positive, dotted = negative) for the initial disturbances, vortex pair, torus vortex, hairpin and six small Λ vortices (left to right)

3. Results

The initial disturbances are stretched as they move downstream. In all cases, a steep gradient in the spanwise direction develops and the flow structure becomes more compact. This mechanism is dominant in all cases. Owing to the regions with upwards velocity, apart from the wall, marker-particles are lifted up into regions with higher downstream velocity and accelerate. So, due to the velocity field, there are accumulations of particles and regions

with fewer particles, [6]. There are overlaps of the upwards and downwards parts of the disturbances in all cases as already described for the vortex pair in [7]. In the later stages, $t > 10$, the vortex centres of the disturbances start to form a helix in space. The differences between these cases are the structures at the end of the simulations, Figs. 2 and 3. These structures depend on the initial disturbance.

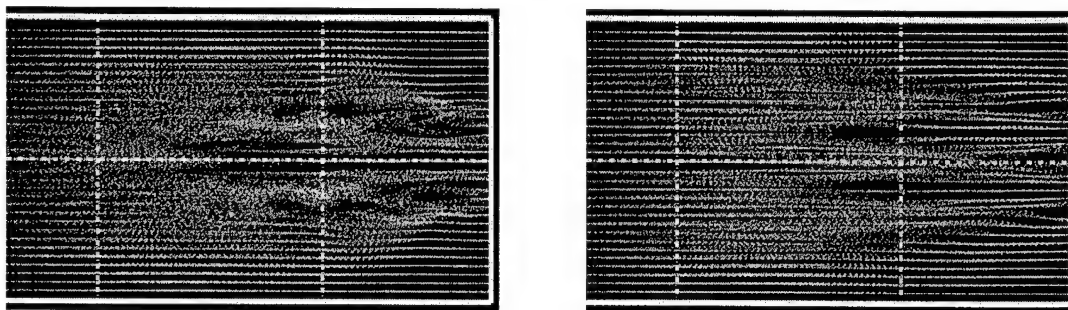


Figure 2: Particle Plot for the dimensionless time $t = 2$ (left) and $t = 6$ (right)

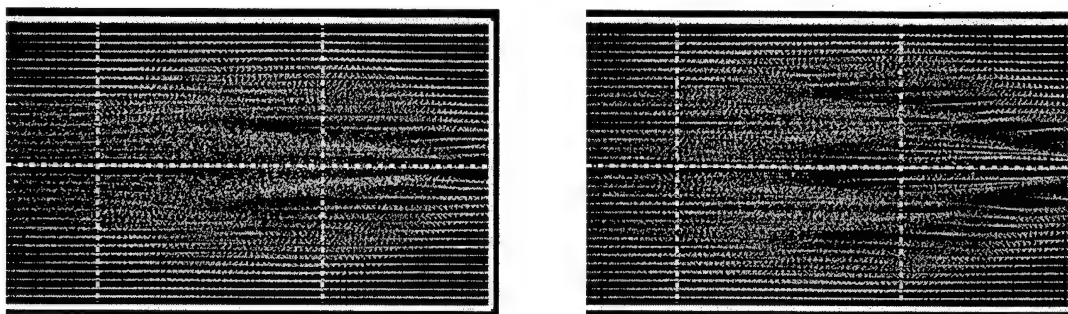


Figure 3: Particle Plot for the dimensionless time $t = 10$ (left) and $t = 14$ (right)

4. Conclusions

All disturbances show the same dominant mechanisms as describe above. The structures they lead to are different and depend on the initial disturbance.

Acknowledgements

The present work is supported by the DFG La 553/8.

5. References

- 1 MAYLE, R.E. : The Role of Laminar-Turbulent Transition in Gas Turbine Engines, *Journal of Turbomachinery* **113** (1991), 509-537.
- 2 DELFS, J. : Numerische Simulation der transitionellen schallnahen Plattengrenzschichtströmung, Dissertation, Technische Universität Braunschweig, ZLR Forschungsbericht (1994) 94-105.
- 3 HENNINGSON, D.S., LUNDBLADH, A. AND JOHANSSON, A.V. : A mechanism for bypass transition from localized disturbances in wall-bounded shear flows, *J. Fluid Mech* **250** (1993), 169-207.
- 4 PERRY, A.E. LIM, T.T. AND TEH, E.W. : A visual study of turbulent spots, *JFM* **104** (1981), 387-405.
- 5 HOHEISEL, H. AND SEYB, N.J. : The Boundary-Layer Behaviour of Highly Loaded Compressor Cascades at Transonic Flow Conditions, AGARD CP **401** (1995), 4-1 – 4-17
- 6 HEIKEN, S., DEMUTH, R. AND LAURIEN, E. : Visualisation of Bypass-Transition Simulations using Tracer Particles, *ZAMM* (1999)
- 7 LAURIEN, E., DEMUTH, R. AND HEIKEN, S. : Numerische Simulation der räumlichen und zeitlichen Entwicklung lokaler Störungen in Grenzschichten, *ZAMM* (1998).

Addresses: DIPL.-ING. S. HEIKEN, DIPL.-ING. R. DEMUTH, PROF. DR.-ING. E. LAURIEN University of Stuttgart, IKE, Pfaffenwaldring 31, 70550 Stuttgart,

Heinz, S.

Advanced Methods to Compute Multiphase Turbulent Reacting Flows

PDF and FDF methods do not require approximations for chemical reactions, which makes them extremely valuable for reacting flow calculations. The performance of these methods depends significantly on the accuracy of simulating small-scale mixing processes. It is illustrated, in which way models may be developed that simulate mixing for various phases as a multi-scale process in dependence on different factors. Further developments towards a system of very accurate and (less expensive) simplified methodologies for reacting flow calculations are pointed out.

1. Computation of turbulent reacting flows

Mainly due to the required computational costs, technologically-relevant multiphase turbulent reacting flows cannot be calculated in general by solving the basic equations of thermo- and fluid dynamics directly, i.e., through adopting direct numerical simulation (DNS) [1]. Basic methodologies for simulating such flows are shown in Table 1.

Equations for averaged fields	Hybrid methods	Equations for instantaneous fields
LES methods	Velocity field: LES methods Scalar fields: FDF methods	FDF methods
RANS methods	Velocity field: RANS methods Scalar fields: PDF methods	PDF methods

Table 1. Basic techniques for high-Reynolds number turbulent reacting flow simulations: large-eddy simulation (LES), Reynolds-averaged Navier Stokes (RANS), filter density function (FDF) and probability density function (PDF) methods.

RANS and LES methodologies, which solve equations for averaged (filtered) velocities and scalars, are well-known standard techniques for the calculation of high-Reynolds number turbulent flows. The simulation of technologically-relevant turbulent flows by means of RANS techniques is very attractive due to their relative simplicity and computational costs, but usually applied models are known to perform poorly in the prediction of even basic turbulent flows that are far from equilibrium [2-3]. Apart from the simulation of near-wall regions, that problem may be overcome through adopting LES methods, but both RANS and LES methods can be applied successfully to reacting flow simulations only if the chemistry is very fast or slow compared to turbulent flow changes [4].

PDF and FDF methods enable a much more comprehensive description of turbulence than do RANS and LES techniques: they provide the full (one-point) statistics. The essential advantage of applying PDF or FDF methods to reacting flow calculations is given by the fact that arbitrary complicated chemistry can be treated without any need for adopting approximations [1, 5-6]. In that way, the modelling of the complex turbulence-chemistry interaction can be reduced significantly. However, accurate simulations of turbulent mixing are still a challenge [7].

2. Advanced methods

The complexity of mixing processes and the differences between mixing in gases ($Sc \approx 1$) and liquids ($Sc \gg 1$) are illustrated in Figure 1. The scalar spectrum has for Schmidt numbers $Sc > 1$ in addition to the inertial-convective a viscous-convective subrange. The Kolmogorov-scale (k_K) and Batchelor-scale (k_B) wavenumbers are separated through the Schmidt number Sc , $k_B = Sc^{1/2} k_K$. Thus, the characteristic mixing times in liquids are much larger than in gases, which may result in significant effects on the efficiency of chemical conversions. The mixing may be also remarkably

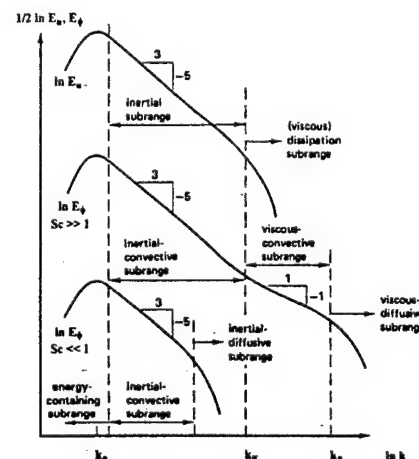


Figure 1. Idealized velocity (E_v) and scalar (E_ϕ) spectral density functions in fully developed homogeneous, isotropic turbulence.

influenced by other effects, as Reynolds number variations, the influence of the scalar-production-to-dissipation ratio, and correlations with the velocity field.

To simulate real conditions, mixing has to be calculated for a high number of chemical substances, which react according to complex schemes. Thus, simply-structured mixing models have to be preferred, where all the variations of the mixing processes are reflected through changes of a scalar quantity: the mixing frequency.

A way to extend the 'interaction by exchange with the mean' (IEM) mixing model, which is applied in most of the simulations of real flows, has been developed recently by Heinz and Roekaerts [8, 9]. A typical example for the variations of the mixing rate R_α is shown (for a scalar production-to-dissipation ratio $p_\alpha = 1$) in Figure 2: For growing turbulent Reynolds numbers Re_1 , R_α approaches C_ϕ (the constant standard value for the mixing rate which applies the IEM model) asymptotically. The effect of the Schmidt number Sc is consistent with Figure 1: higher Sc -values increase the characteristic mixing time R_α^{-1} . The new multi-scale IEM (MSIEM) model was shown to work well in simulations of parallel chemical reactions in a tubular reactor [8, 9].

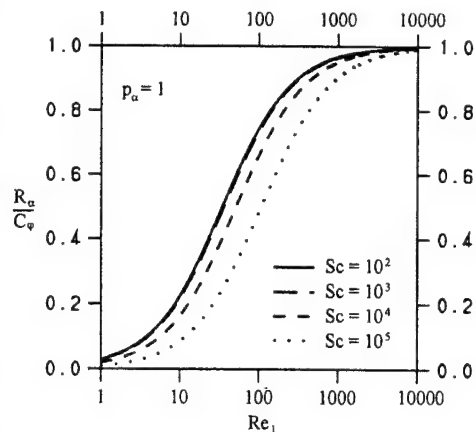


Figure 2. The turbulent Reynolds number (Re_1) dependence of the normalized mixing rate R_α / C_ϕ for different Schmidt number Sc and a scalar production-to-dissipation ratio $p_\alpha = 1$.

3. Summary

Within the frame of hybrid methods (see Table 1), the application of advanced models for small-scale mixing is a simple way to improve the accuracy of reacting flow computations significantly. Full PDF or FDF methods have to be applied under conditions, where the coupling between flow and chemistry is relevant. Such full PDF [10] and FDF [11] methodologies are currently under development.

4. References

- 1 Pope, S. B.: Turbulent Flows; Cambridge University Press (2000).
- 2 Speziale, C. G. and Xu, X.: Towards the Development of Second-Order Closure Models for Nonequilibrium Turbulent Flows; *Int. J. Heat and Fluid Flow* 17 (1996), 238-244.
- 3 Kassinos, S., Langer, C. A., and Reynolds, W. C.: Structure Based Turbulence Modelling for Wall-Bounded Flows; *Turbulence and Shear Flow-1* (1999), edited by S. Banerjee and J. K. Keaton, Begell House, Inc. New York, Wallingford, 233-238.
- 4 Fox, R. O.: Computational Methods for Turbulent Reacting Flows in the Chemical Process Industry; *Revue de l'Institut Francais du Petrole* 51 (1996), 215-243.
- 5 Colucci, P. J., Jaber, F. A., Givi, P. and Pope, S. B.: Filtered Density Function for Large Eddy Simulations of Turbulent Reactive Flows; *Phys. Fluids* 10 (1998), 499-515.
- 6 Jaber, F. A., Colucci, P. J., James, S., Givi, P. and Pope, S. B.: Filtered Mass Density Function for Large-Eddy Simulation of Turbulent Reacting Flows; *J. Fluid Mech.* 401 (1999), 85-121.
- 7 Baldyga, J. and Bourne, J. R.: Turbulent Mixing and Chemical Reactions; John Wiley & Sons, Chichester | New York | Weinheim | Brisbane | Singapore | Toronto (1999).
- 8 Heinz, S. and Roekaerts, D.: PDF Modelling of Turbulent Reacting Flows: Reynolds and Damköhler Number Effects; *Turbulence and Shear Flow-1* (1999), edited by Banerjee, S. and Eaton, J. K., Begell House, Inc., New York, Wallingford, 339-344.
- 9 Heinz, S. and Roekaerts, D.: Reynolds Number Effects on Mixing and Reaction in a Turbulent Pipe Flow; under consideration for publication in *Chem. Eng. Sci.* (2000).
- 10 Muradoglu, M., Jenny, P., Pope, S. B. and Caughey, D. A.: A Consistent Hybrid Finite-Volume/Particle Method for the PDF Equations of Turbulent Reacting Flows; *J. Comput. Phys.* 154 (1999), 342-371.
- 11 Heinz, S.: Unified Equations for Turbulent Reacting Flows; under consideration for publication in *Phys. Fluids* (2000).

Address: Dr. Stefan Heinz, Technische Universität München, Lehrstuhl für Fluidmechanik, Boltzmannstr. 15, 85747 D-Garching, Germany, Email: heinz@flm.mw.tum.de

A. KLUWICK, PH. GITTNER

Transonic laminar interacting boundary layers in narrow channels

The investigation of transonic viscous-inviscid interactions is hampered by the fact that the nonlinear small disturbance equation which governs the external flow has to be solved simultaneously with the nonlinear boundary layer equations. This poses an extremely difficult numerical problem which has been treated so far with limited success only. However, if the medium is confined in a sufficiently narrow channel, the flow outside the viscous wall layers is one-dimensional in the leading order approximation which in turn allows the derivation of a solution in closed form. This significantly simplifies the construction of numerical solutions which nevertheless display essential features of transonic flows associated with the transition from subsonic to supersonic conditions or/and vice versa.

The present paper is concerned with viscous-inviscid interactions of steady transonic flows in narrow channels which are triggered, for example, by a shallow deformation of the channel walls, Fig. 1. Asymptotic analysis for large Reynolds number $Re = \bar{U}_\infty \bar{L} / \bar{\nu} \gg 1$ then shows that a consistent interaction theory in which the flow inside the inviscid core region is almost one-dimensional can be formulated if the heights \bar{H} and \bar{h} of the channel and the surface mounted obstacle are of the orders $Re^{-1/4} \bar{L}$ and $Re^{-7/2} \bar{L}$ and if the length $\bar{\Delta}$ of the obstacle and \bar{H} are of comparable size. Here \bar{u}_∞ , \bar{L} and $\bar{\nu}$ denote the flow velocity in the core region just upstream of the local interaction region, a characteristic length associated with the unperturbed boundary layers adjacent to the channel walls and a reference value of the kinematic viscosity.

Similar to the case of external transonic flows the local interaction region exhibits a triple deck structure. As there, the role of the main deck is to transfer the displacement effects exerted by the lower deck unchanged to the upper deck (which comprises the inviscid core region) and to transfer the resulting pressure disturbances unchanged to the lower deck. Here, the fluid motion is governed by the boundary layer equations in incompressible form

$$\frac{\partial U}{\partial X} + \frac{\partial V}{\partial Y} = 0, \quad U \frac{\partial U}{\partial X} + V \frac{\partial U}{\partial Y} = -\frac{dP}{dX} + \frac{\partial^2 U}{\partial Y^2} \quad (1)$$

where (X, Y) , (U, V) and P denote Cartesian coordinates parallel and normal to the freestream direction, the corresponding velocity components and the pressure. All quantities are suitably scaled, see e.g. [3]. The boundary conditions include the no slip condition on the channel walls and the requirement that the unperturbed velocity profile is recovered in the limit $X \rightarrow -\infty$

$$Y = F(X) : \quad U = 0 = 0, \quad X \rightarrow -\infty : \quad U = Y. \quad (2)$$

Let $-A(X)$ denote the perturbation of the displacement thickness caused by the interaction process, the appropriate behaviour of U at large distances Y from the wall can be written as

$$Y \rightarrow \infty : \quad U = Y + A(X). \quad (3)$$

Inside the upper deck region we have a weakly perturbed quasi one-dimensional flow. As a result, pressure disturbances resulting from the boundary layer displacement can be calculated from elementary properties of the massflux velocity relationship and the well known leading order approximation between the pressure and velocity disturbances.

Taylor series expansion for $|M_\infty - 1| \ll 1$ up to second order and substitution of the scaled quantities used in equation (1) to (3) then yields

$$P = -\operatorname{sgn}(1 - M_\infty) \left(1 \pm \sqrt{1 + \Lambda A(X)} \right) \quad (4)$$

where $\Lambda = 2|1 - M_\infty^2|^{-3/2} Re^{-1/4} (\bar{\rho}_w / \bar{\rho}_\infty) \lambda = O(1)$ represents a transonic similarity parameter which depends on Re , the Mach number M_∞ in the unperturbed core region as well as the wall density nondimensionalized with the freestream density and the nondimensional wall shear λ of the unperturbed flow.

One remarkable property of interacting external supersonic flows is the phenomenon of upstream influence. The associated mechanism was clarified first by OSWATITSCH AND WIEGHARDT 1941, [2] and formulated mathematically

by Lighthill 1953, [1]. Nonlinear effects were later studied by Stewartson and Williams 1969, [3], who showed that the possibility of upstream influence manifests itself in the existence of nonlinear eigensolutions of the lower deck problem, now commonly termed compressive/expansive free interaction solution.

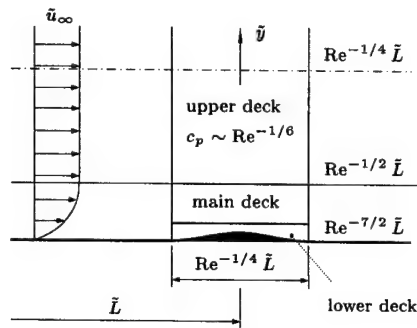


Fig. 1

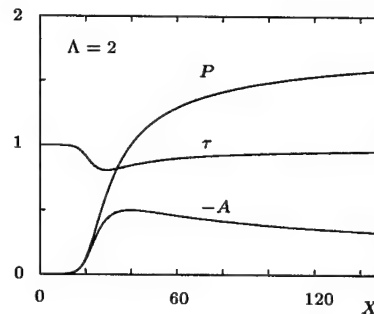


Fig. 2

As a first application of the interaction equation (1)-(4) let us investigate the upstream influence of weak disturbances in transonic internal flows. To this end U, V and P are expressed in the form

$$U \sim Y - a_1 e^{\kappa X} f_1'(Y), \quad V \sim a_1 \kappa e^{\kappa X} f_1(Y), \quad P \sim a_1 e^{\kappa X} \quad (5)$$

where $a_1 \ll 1$ characterises the amplitude of the perturbations. Linearization of the governing equations with respect to a_1 and introduction of the stretched coordinate $z = \kappa^{1/3} Y$ then shows that $f_1'' = d^2 f_1 / dz^2$ satisfies the Airy equation $z f_1'' = f_1'''$. Furthermore, κ is found to be given by the relationship $\kappa = (\text{sgn}(M_\infty^2 - 1)/\Lambda)^3$ which implies that upstream influence is possible in supersonic flow $M_\infty > 1$ only and becomes more pronounced as $\Lambda \rightarrow \infty$, e.g. as $M_\infty \rightarrow 1$ with Re held fixed. In order to extend the flow behaviour described by equations (5) into the nonlinear regime it is necessary to solve the interaction equations numerically. Representative results for a compressive free interaction are depicted in Fig. 2. In agreement with the predictions of linear theory the pressure disturbances initially increase exponentially with X . As expected, the pressure increase causes the displacement thickness to increase too while the wall shear drops. Critical flow conditions are reached for $P = 1$ where $-A$ exhibits a local maximum. The displacement thickness thus forms a viscous throat which in turn allows for a continuous transition from supersonic to subsonic flow conditions in the inviscid core region of the channel. Also note that $-A \rightarrow 0$ as $X \rightarrow \infty$ so that the total pressure increase agrees with the amplitude of a weak normal shock wave.

We therefore, conclude that (i) compressive interaction solutions of the lower deck problem (1)-(4) represent acceptable global solutions which (ii) have an obvious physical meaning. They describe normal shock waves which - in narrow channels - cannot exist as discontinuities but are smeared out through the action of viscous forces. It should be noted, however, that the mechanism responsible for the shock structure shown in Fig. 2 is completely different from the one causing the celebrated Taylor profile of weak shocks in unconfined flows. In the latter case viscous normal stresses and heat conduction are the dominating dissipative effects. Both contributions are negligible small to the order considered in the present study where the dissolution of the shock discontinuity into a continuous compression wave results from presence of viscous shear stresses which generate boundary layers in which disturbances can propagate upstream. The compressive free interaction solution discussed so far describes the transition from supersonic to subsonic flow conditions which takes place in a channel of constant cross section. A material constriction in the form of a Laval nozzle, however, is required to accelerate a flow from subsonic to supersonic conditions. Corresponding solutions of the interaction equations will be presented in a separate publication.

References

- 1 Lighthill, M. J.: On boundary layers and upstream influence II. supersonic flows without separation., Proc. R. Soc. A 217 (1953) 478-507.
- 2 OSWATITSCH, K. AND WIEGHARDT, K.: Theoretische Untersuchungen über stationäre Potentialströmungen und Grenzschichten, Tech. rep., Lilienthal-Gesellschaft für Luftfahrtforschung, (1941).
- 3 STEWARTSON, K. AND WILLIAMS, P. G.: Self-induced separation, Proc. Roy. Soc. A 312 (1969) 181-206.

Addresses: PROF. DR. ALFRED KLUWICK, Technical University of Vienna, Department of Fluid Dynamics and Heat Transfer, Wiedner Hauptstraße 7, A-1040 Vienna, Austria.

PROF. DR. PHILIPP GITTNER, Institut für Mechanik und Maschinenlehre, Abteilung für Strömungslehre und Wärmeübertragung, Johannes Kepler Universität Linz, Altenbergerstraße 69, A-4040 Linz.

A. KLUWICK AND R. KRONBERGER

On the interaction of a 2-dimensional transonic turbulent boundary layer with a localized 3-dimensional disturbance

If a weak normal shock wave impinges on a fully attached transonic turbulent boundary layer, a three layer structure develops. In the outer defect region the solution of the interaction problem may be described as an irrotational perturbation to the oncoming stream. Hence a potential Φ can be introduced, which is governed by a generalized transonic small-disturbance equation. In the present study it is shown that, for a suitable scaled problem, the interaction of the incoming boundary layer with a small 3-dimensional obstacle can be described by an equation of similar type. Numerical studies are carried out focusing on the formation of the local supersonic region within the defect region of the boundary layer.

1. Introduction

Due to its practical importance, especially in the field of turbomachinery and aircraft design, the transonic shock - boundary layer interaction problem has been the object of extensive investigations in the last decades. In our study we will closely follow the work of MELNIK AND GROSSMAN (1974). Therefore, as a starting point we consider a weak normal shock wave impinging on a turbulent boundary layer on a flat plate and restrict ourself to the limit of large Reynolds numbers i.e. almost vanishing boundary layer thickness and infinitesimally weak shocks, that is the double limit

$$M_\infty^2 - 1 \ll 1, \quad \epsilon = \sqrt{C_f/2} \ll 1 \quad \text{with} \quad \chi_t = \frac{M_\infty^2 - 1}{\epsilon} = O(1). \quad (1)$$

Here the skin friction coefficient C_f defines a small parameter ϵ which can be shown to be of the Order $O(1/\log Re)$ and M_∞ denotes the local Mach number at the edge of the boundary layer. Furthermore, we assume that the ratio χ_t has a fixed value of order $O(1)$. In this limit, the velocity jump across the shock wave is of the same order as the velocity defect in the approaching boundary layer. The pertinent length scales that describe the asymptotic structure of the flow field can then be expressed in terms of ϵ . The vertical extent of the interaction region is fixed by the upstream flow to be of the order of a boundary layer thickness, i.e. $O(\epsilon)$, whereas the streamwise length scale follows from transonic considerations about the slope of the characteristics to $O(\epsilon^{3/2})$. This length scale describes the outer or defect part of the interaction region, in which turbulent and viscous stresses associated with the interaction process are negligible in a first approximation. In addition two inner regions are required, namely a conventional compressible wall layer to satisfy the no-slip condition at the wall and a so-called blending layer to smooth the discontinuity between the shear stress in the outer and the wall layer and in which turbulent stresses and inertia terms play the dominant role. Since displacement effects of the two inner layers turn out to be negligibly small to second order, appropriate boundary conditions can be formulated in the defect layer for the calculation of the first order pressure correction which, as can be shown, is directly proportional to the first order skin friction correction. In the following, we will, therefore, focus on the solution in the defect layer.

2. Formulation of the Problem

Specifically, we investigate the interaction problem of an incoming turbulent boundary layer with a small 3-dimensional obstacle. In agreement with the results summarized in section 1, its streamwise extent is assumed to be of order $O(\epsilon^{3/2})$. The external flow is taken to be subsonic, $M_\infty < 1$. The basic set of equations describing the problem consists of the time-averaged Navier-Stokes equations. Inspection of the momentum equations leads to the appropriate length scale in the z -direction which turns out to be of order $O(\epsilon)$. Wider humps can be dealt with by superposition of 2D-solutions. Accordingly, coordinates are made dimensionless with an appropriate length L^* and scaled as follows:

$$\bar{x} = \epsilon^{3/2} x, \quad \bar{y} = \epsilon y, \quad \bar{z} = \epsilon z. \quad (2)$$

Here the bar denotes unscaled dimensionless coordinates. Velocities, density and pressure are made non-dimensional with respect to the undisturbed velocity u_∞^* , undisturbed density ρ_∞^* and $\rho_\infty^* u_\infty^{*2}$. Expansion of the various field

quantities leads to $u = 1 + \varepsilon u^{(1)} + \dots$, $v = \varepsilon^{3/2} v^{(1)} + \dots$, $w = \varepsilon^{3/2} w^{(1)} + \dots$, $\rho = 1 + \varepsilon \rho^{(1)} + \dots$ and $p = p_\infty + \varepsilon p^{(1)} + \dots$. The energy equation is simplified using the Crocco-Busemann integral and takes the inviscid form $\frac{1}{\gamma-1} c^2 + \frac{1}{2} u^2 = \text{const.}$ The basic equations then reduce to $[\chi_t + (\gamma+1)u^{(1)}] \partial_x u^{(1)} - \partial_y v^{(1)} - \partial_z w^{(1)} = 0$ in first order. Introduction of a potential $\Phi^{(1)}$ according to $u^{(1)} = u_{in} + \Phi^{(1)}_{,x}$, $v^{(1)} = \Phi^{(1)}_{,y}$ and $w^{(1)} = \Phi^{(1)}_{,z}$ leads to the final form

$$(\gamma+1)[\lambda(y) - \Phi^{(1)}_{,x}] \Phi^{(1)}_{,xx} + \Phi^{(1)}_{,yy} + \Phi^{(1)}_{,zz} = 0 \quad (3)$$

with $\lambda = -[\chi_t/(\gamma+1) + u_{in}]$ and the known distribution from the oncoming boundary layer $u_{in} = \frac{1}{\kappa}[\log y + \tilde{\pi}(1 + \cos \pi y)]$. Since the flow is subsonic, vanishing perturbations are imposed at the edges of the calculation domain. At the wall, linearized boundary conditions can be imposed which describe the flow past an obstacle with thickness of the order $O(\varepsilon^3)$ and require

$$v^{(1)} = \Phi^{(1)}_{,y} = h'(x). \quad (4)$$

3. Results

Typical results for a special form of the obstacle profile given by $h = \tau x(1-x)z(1-z)$ with $\tau = O(1)$ are shown in Figs. 1 and 2. The similarity parameter is fixed to $\chi_t = -7.5$. In Fig. 1 pressure corrections at the wall for $\tau = 1.0, 3.0, 5.0, 6.0, 7.0$ and 9.0 are plotted. For increasing obstacle height τ , a local supersonic region develops which can extend beyond the defect layer as is shown in Fig. 2. Here, the edge of the boundary layer corresponds to $y = 1$. Note that in Fig. 2 the x -extent of the obstacle was stretched in order to obtain a better resolution of the supersonic domain. With increasing values of the similarity parameter χ_t , e.g. decreasing values of the boundary layer thickness, the wall pressure distribution slowly approaches the inviscid case. However, the discontinuity remains smeared out at the wall and no Oswatitsch-Zierp singularity develops as in the case of inviscid flows.

Following MURMAN AND COLE (1971) type depending differencing combined with a line relaxation method was used to solve equation (3) of mixed elliptic-hyperbolic type. Grid refinement was applied with respect to the second derivative of $\Phi^{(1)}$. Typically 10^6 gridpoints were necessary for 3-dimensional calculations.

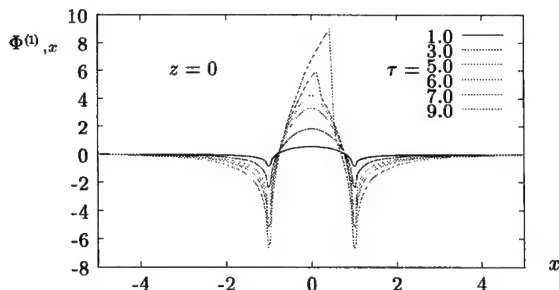


Fig. 1: Wall Pressure Distribution

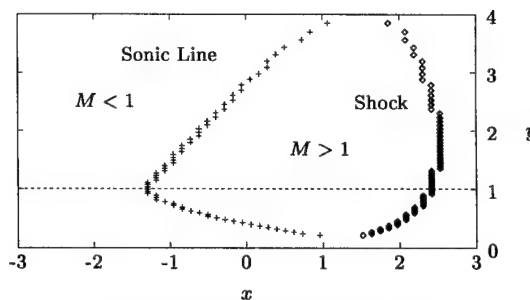


Fig. 2: Local Supersonic Region

4. Conclusion

In this study, we present a method for the calculation of the interaction of a 2-dimensional transonic turbulent boundary layer with localized 3-dimensional disturbances. It turns out that, within the given assumptions, the first order skin friction is proportional to the defect layer wall pressure correction and can be calculated without any turbulence closure. Typical applications are the calculation of turbulent boundary layer flows past valves or rivets. We also want to mention that the extension to 3-dimensional boundary layers is straightforward and results in an additional term in $\lambda(y)$ entering equ. (3) only.

5. References

- 1 R. E. MELNIK AND B. GROSSMAN: Analysis of the interaction of a weak normal shock wave with a turbulent boundary layer, AIAA Paper, 74-598 (1974).
- 2 E. MURMAN AND J. COLE: Calculation of plane steady transonic flows, AIAA Journal, (1971).

Addresses: A. Kluwick and R. Kronberger, Vienna University of Technology,
Institute of Fluid Dynamics and Heat Transfer, Wiedner Hauptstraße 7,
A-1040 Vienna, Austria

KRUMBEIN, A.

Laminar-turbulente Transitionsvorgabe im DLR Navier-Stokes-Löser FLOWer

Die Modellierung der laminar-turbulenten Transition in Navier-Stokes-Lösern ist eine notwendige Anforderung für die Berechnung von Strömungskonfigurationen in der Luftfahrtindustrie. Häufig werden quantitativ oder sogar qualitativ richtige Ergebnisse nur unter Berücksichtigung der Transition erzielt. Eine Technik zur Transitionsvorgabe zerteilt das Berechnungsgebiet in laminare und turbulente Bereiche, die durch Transitionslinien auf der Konfigurationsoberfläche festgelegt sind. Die Transitionslinien werden ins Oberflächennetz abgebildet, womit eine Einteilung in laminare und turbulente Stücke vorliegt. In direkter Nachbarschaft zu laminaren Wandsegmenten werden laminare Raumgebiete erzeugt, deren Ausdehnung in Wandnormalenrichtung variabel ist. Turbulenzgrößen (z.B. μ_t) werden in geeigneter Weise numerisch behandelt. Vorgestellt werden Ergebnisse an mehrkomponentigen, 2- und 3-dimensionalen Konfigurationen (3-Element-Profil, Hubschrauber, Flügel-Rumpf-TW-Pylon).

1. Transitionsetzen auf Oberflächen

Die Einteilung des Berechnungsgebiets in laminare und turbulente Bereiche wird zunächst auf der Oberfläche der Konfiguration durch Abbildung einer vorgegebenen Transitionslinie in Form eines orientierten Polygonzugs in das Oberflächennetz vorgenommen. Die Abbildung erfolgt über den Vergleich der Longitudinalrichtungsordinate x eines Oberflächenpunkts P_S mit derjenigen eines P_S zugeordneten Punkts der Transitionslinie P_T , der mittels Projektion von P_S und der Transitionslinie in die auf der x -Richtung senkrecht stehenden $y-z$ -Ebene durch

$$\begin{aligned} y(P_T) &= [y(P_S)\Delta y^2 + y(P_{T,i})\Delta z^2 + [z(P_S) - z(P_{T,i})]\Delta y\Delta z]/(\Delta y^2 + \Delta z^2), \\ z(P_T) &= \Delta z/\Delta y[y(P_T) - y(P_{T,i})] + z(P_{T,i}) \end{aligned} \quad (1)$$

und $x(P_T)$, bestimmt mit z.B. linearer Interpolation in Transitionslinienrichtung, gegeben ist, Abb. 1.

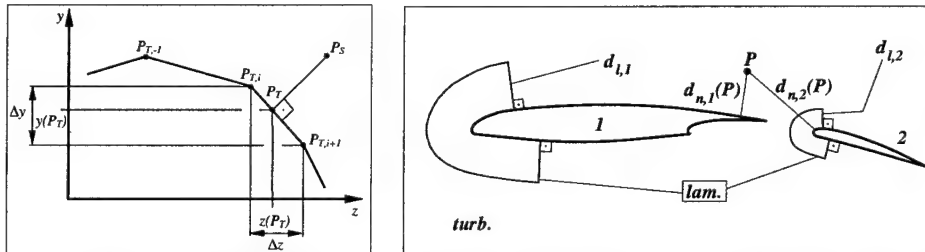


Abb. 1: Projektion der Transitionslinie in $y-z$ -Ebene und Laminarzonen an 2-Komponenten-Konfiguration

Durch Zuordnung eines laminar-turbulenten Status $ltflag(P_S)$ per

$$\begin{aligned} x(P_S) &\geq x(P_T) \Rightarrow ltflag(P_S) = 1 \Leftrightarrow turbulent, \\ x(P_S) &< x(P_T) \Rightarrow ltflag(P_S) = 0 \Leftrightarrow laminar \end{aligned} \quad (2)$$

werden laminare und turbulente Oberflächenpunkte identifiziert. Jede Konfigurationskomponente mit Transitionslinie wird in dieser Weise behandelt.

2. Transitionsetzen im Raum

In direkter Nachbarschaft der laminaren Oberflächenstücke wird die laminare Grenzschicht approximiert durch Laminarzonen, erzeugt durch Projektion der Oberflächenkontour ins Strömungsfeld. Die wandnormale Ausdehnung der Zonen ist steuerbar durch einen begrenzenden Abstand d_l zwischen der Oberfläche und dem Aussenrand der Zone. Zur Erzeugung der Zonen wird bei Existenz von n_C Transitionslinien mit den begrenzenden Abständen $d_{l,i}$, $i = 1, \dots, n_C$ für jeden Feldpunkt P folgender Algorithmus durchlaufen:

- 1) Berechnung des Wandabstands $d_{n,i}(P)$, $i = 1, \dots, n_C$ zu jeder Oberfläche mit Transitionslinie.
- 2) Bestimmung des P nächst gelegenen Oberflächenpunkts $P_{S,i}^n$ auf jeder Oberfläche mit Transitionslinie.
- 3) Anwendung folgender Bedingung für alle Konfigurationskomponenten mit Transitionslinie, Abb. 1:

$$d_{n,i}(P) < d_{l,i} \Rightarrow ltflag(P) = ltflag(P_{S,i}^n), i = 1, \dots, n_C \quad (3)$$

Der Algorithmus wird nach einer "voll turbulenten" Initialisierung des Strömungsfelds angewendet, was zu einer "Laminarisierung" bestimmter Turbulenzgrößen führt. Seine Anwendung ist auf strukturierten und unstrukturierten Rechennetzen möglich und ist im Fall strukturierter Netze topologieunabhängig.

3. Laminar-turbulenter Status

Während der Erzeugung der Strömungslösung mit FLOWer wird der laminar-turbulente Status $ltflag(P)$ bei Einsatz algebraischer Wirbelviskositätsmodelle zur Laminarisierung der Wirbelviskosität μ_t verwendet,

$$\mu_t^{code}(P) = ltflag(P)\mu_t(P), \quad (4)$$

bei Transportgleichungsmodellen wird zusätzlich der Produktionsterm P_t manipuliert,

$$P_t^{code}(P) = \min[P_t(P), D_t(P)C_t^{ltflag(P)}], \quad (5)$$

mit dem Destruktionsterm D_t und einem Limiter $C_t > 0$.

4. Ergebnisse

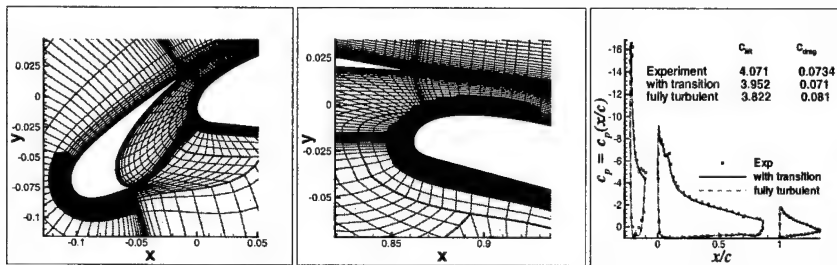


Abb. 2: Laminarzonen an Vorfliigel und Hauptelement (links) und an der Klappe (rechts) eines 3-Element-Profiles und c_p -Verteilungen

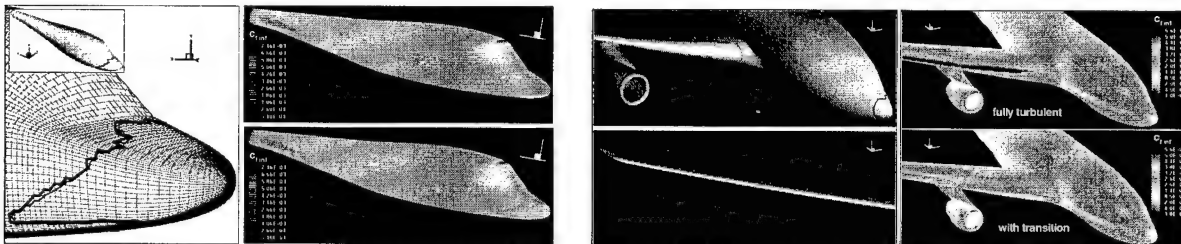


Abb. 3 (links): Vorgegebene (dünn) und abgebildete (dick) Transitionslinie an Hubschrauberrumpf und c_f -Verteilungen für voll turbulente Rechnung (oben) und Rechnung mit Transition (unten)

Abb. 4 (rechts): Rumpf-Flügel-Triebwerk-Pylon-Konfiguration mit Transitionslinien an Rumpf, Triebwerk und Pylon und c_f -Verteilungen für voll turbulente Rechnung und mit Transition

5. References

- 1 AUMANN, P.; BARTELHEIMER, W.; BLEECKE, H.; EISFELD, B.; LIESER, J.; HEINRICH, R.; KROLL, N.; KUNTZ, M.; MONSEN, E.; RADDATZ, J.; REISCH, U.; ROLL, B.: FLOWer Installation and User Handbook, Release 115, Doc.Nr. MEGAFLow-1001, Institut für Entwurfsaerodynamik, Deutsches Zentrum für Luft- und Raumfahrt e.V., 1998
- 2 KRUMBEIN, A.: AVTAC Advanced Viscous Flow Simulation Tools for Complete Civil Aircraft Design - Transition Prescription and Prediction, Deliverable Task 3.2, AVTAC/DEL/DLR/D3.2C5, July 1999

Address: DR. ANDREAS KRUMBEIN, Deutsches Zentrum für Luft- und Raumfahrt e.V. - DLR,
Institut für Entwurfsaerodynamik, Lilienthalplatz 7, D-38108 Braunschweig

MANG, J.; UNGARISH, M.; SCHAFLINGER[†], U.

Numerical investigation of the spin-up of a two-layer fluid

The spin-up of a two-layer fluid with a free surface in a cylindrical container rotating about a vertical axis is investigated numerically, using axisymmetric finite differences. As Linden & van Heijst (1984) have shown, the flow inside the viscous boundary layer at the bottom leads to the accumulation of the heavier lower-layer fluid near the side wall. Thereby, a bare spot in which the light fluid is in direct contact with the bottom is formed around the axis. The present simulation gives new insight into the internal structures and interaction of the two fluids. Preliminary results indicate strong mixing inside the region of heavy fluid.

1. Introduction and description of the problem

An initially stationary cylindrical container open to the atmosphere is filled with two fluids of different densities ρ_u^* and ρ_l^* but equal kinematic viscosities ν^* . (Dimensional variables are marked by an upper asterisk.) The height of the free surface is denoted by H and the initial height of the interface Σ is denoted by h_0 with $h_0 \ll H$. At the time $t = 0^+$ the container is abruptly set into rapid rotation Ω^* about its vertical axis. The transient motion during which the initially stationary fluids acquire a state of solid body rotation with the angular velocity of the container is termed spin-up. The flow is expected to be driven by a secondary convective motion, sustained by the quasi-steady thin viscous Ekman layer above the bottom boundary. The present work investigates the influence the density jump at Σ exerts on the spin-up dynamics. The spin-up of two-layer liquid systems is of relevance to the design of centrifuges used in chemical and biological engineering applications (Lim et al. 1993) as well as geophysical problems (Linden & van Heijst 1984).

2. Direct Numerical Simulations

The governing equations are formulated in a cylindrical coordinate system co-rotating with the container. With the scaling

$$[\mathbf{r}^*, \mathbf{v}^*, t^*, \mathbf{P}^*] = [\mathbf{R}^* \mathbf{r}, \mathbf{R}^* \Omega^* \mathbf{v}, \Omega^{*-1} t, \rho_u^* (\Omega^* \mathbf{R}^*)^2 \mathbf{P}] \quad (1)$$

the continuity equation and momentum balance become

$$\nabla \cdot \mathbf{v} = 0 \quad \text{and} \quad \frac{d\mathbf{v}}{dt} + 2\hat{\mathbf{z}} \times \mathbf{v} = \frac{1}{1 + \gamma\phi} [-\nabla p + \phi \mathbf{f} + Ek \nabla^2 \mathbf{v}], \quad (2)$$

with the reduced pressure and the body-force acceleration \mathbf{f} given by

$$p = P + \left(-\frac{r^2}{2} + \frac{g^*}{\Omega^{*2} R^*} z\right) \quad \text{and} \quad \mathbf{f} = \gamma \mathbf{r} \hat{\mathbf{r}} - \frac{1}{Fr^2} \hat{\mathbf{z}}. \quad (3)$$

A density function $0 \leq \phi(\mathbf{r}, t) \leq 1$ subject to a transport equation is defined to capture the deformation of the moving interface Σ . Pure upper-layer fluid is represented by $\phi = 0$ and pure lower-layer fluid by $\phi = 1$.

$$\rho^*(\mathbf{r}, t) = \rho_u^* [1 + \gamma \phi(\mathbf{r}, t)] \quad \text{where} \quad \gamma = (\rho_l^* - \rho_u^*) / \rho_u^* ; \quad \frac{d\phi}{dt} = \nabla \cdot D \nabla \phi \quad (4)$$

The dimensionless parameters governing the problem are the Ekman number, and the global Froude number

$$Ek = \nu^* / \Omega^* R^{*2} \quad \text{and} \quad Fr^2 = \Omega^{*2} R^* / g^*, \quad \text{where} \quad g^* = \gamma g^*. \quad (5)$$

The initial conditions are $\mathbf{v} = -r\hat{\theta}$, $\phi = 1$ ($z \leq h_0$), and $\phi = 0$ elsewhere at $t = 0$. At solid boundaries, no-slip and no-penetration are prescribed. At the free surface, w and the tangential stress vanish. These conditions neglect the deformation of the free surface caused by the centrifugal force which is justified for small values of $\Omega^{*2} R^{*2} / 4g^* H^*$ and γ . The governing equations are discretised on a staggered grid using forward finite difference approximations in time and centred finite difference approximations in space. The numerical procedure is to solve a Poisson equation for p , next to compute the velocity field at the new time step and finally, the density function.

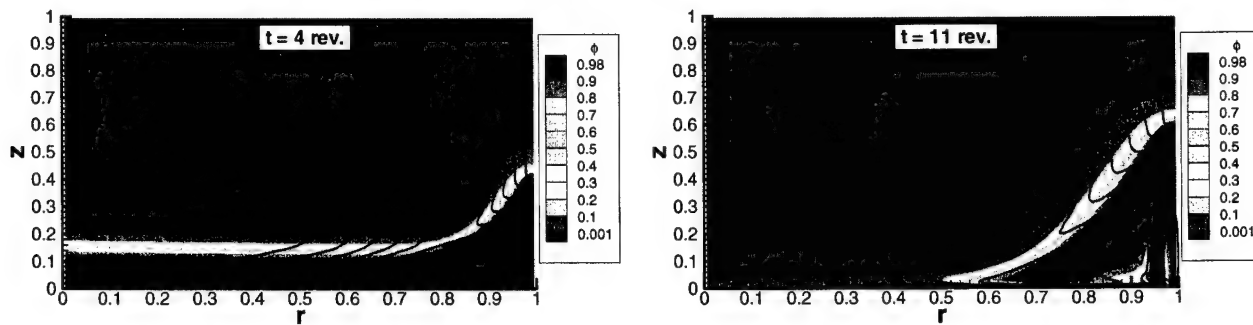


Figure 1: Density function $\phi(r, z)$ and stream lines: $\gamma = 5.1 \cdot 10^{-3}$, $Fr^2 = 8$, $Ek = 5 \cdot 10^{-5}$, $H = 1$, $h_0 = 0.2$

Figure 1 shows the ϕ -field and the stream lines in an r, z -plane after 4 and 11 revolutions of the system. The z -axis coincides with the axis of the container. Light grey corresponds to $\phi = 0$, and dark grey corresponds to $\phi = 1$. The density jump at the interface is smeared by diffusion. Within the first revolution, a quasi-steady thin Ekman layer develops, as indicated by the close packing of stream lines near the horizontal bottom-boundary. The Ekman layer transports fluid from the centre to the periphery. In the non-rotating region it sucks fluid from the core and thereby causes Σ to descend. In the partially spun-up region it expels fluid and h increases. The heavy lower-layer fluid cannot overcome the density jump at Σ , the stream lines are deflected and the fluid circulates back to the centre. Σ is horizontal in the region where the dense layer is still at rest. The inclined part of Σ corresponds to the region where the lower layer is already partly spun-up. It coincides with a free Ekman-like shear layer which is indicated by the bending of the stream lines. The free shear layer smoothes out the difference in ω between the lower and the upper layer. It supports the spin-up of the upper layer and counteracts the spin-up of the dense layer.

Figure 1 corresponds to a case of weak stratification where the secondary convective flow faces only little resistance from gravity. The interface descends rapidly. Eventually, it intersects the bottom of the container. The circular region in which the upper-layer fluid is in direct contact with the bottom boundary is termed "bare spot". The formation of "bare spots" is relevant to oceanographic flows because it provides a mechanism for the removal of sediments into fluid layers which are typically not in contact with the sea bottom. The spin-up of the upper layer will be significantly accelerated because at this stage also the upper-layer fluid is directly affected by an Ekman layer at the bottom boundary. Figure 1, moreover, indicates a possible mixing between the two fluids as the Ekman layer pumps upper-layer fluid into the dense layer. Such an intrusion was reported by Smeed (1987) in an experimental investigation of a related problem.

3. Conclusions

The spin-up of a two-layer fluid is driven by the Ekman layer at the bottom of the container. However, the transient flow is more complicated and the spin-up takes significantly longer than in the single-fluid case. The spin-up of the upper layer is carried out by a secondary convective flow sustained by an Ekman-like shear layer which smoothes out the difference in angular velocities along the deforming interface. In weakly stratified configurations the deformation of Σ is stronger and may culminate in the formation of a "bare spot" where the upper layer comes into direct contact with the horizontal bottom boundary. In such events, upper-layer fluid may intrude into the dense-fluid region via the Ekman-layer. The flow variables ω , u , and p are z -independent in the initial phase of the flow which suggests a simplified analytical formulation based on the classical Wedemeyer single-phase spin-up model.

4. References

- 1 LINDEN, P. F., VAN HEIJST, G. J. F.: Two-layer spin-up and frontogenesis. *J. Fluid Mech.* **143** (1984), 69–94.
- 2 SMEED, D. A.: A laboratory model of benthic fronts. *Deep Sea Res.* **34** (1987), 1431–1459.
- 3 LIM, T. G., CHOI, S., HYUN, J. M.: Transient interface shape of a two-layer liquid in an abruptly rotating cylinder. *Trans. ASME* **115** (1993), 324–329.

Addresses: DI JOHANNES MANG, PROF. DR. UWE SCHAFLINGER[†], Graz University of Technology, Department of Mechanical Engineering, Austria.

PROF. MARIUS UNGARISH, PHD, Israel Institute of Technology, Department of Computer Science, Haifa.

RUNG, T.; LÜBCKE, H.; THIELE, F.

Universal wall-boundary conditions for turbulence-transport models

In the industrial design process of fluids engineering devices, the use of numerical simulation is of ever increasing importance. The predictive quality of such simulations is often governed by the representation of turbulence. Virtually all industrial simulations mimic the influence of turbulence by a closure model based on transport equations for statistical turbulence properties. Besides the derivation of such transport-equation models, the adequate formulation of wall-boundary conditions has come into the focus of attention. Conventional boundary conditions rely on the validity of specific flow conditions pertaining to the wall-shear stress and the resolution properties of the computational grid in the wall-adjacent region. Since the shear stress is part of the simulation result, this approach – strictly speaking – requires the anticipation of the solution. Moreover, it significantly affects the efficiency and flexibility of the simulation due to the associated mesh constraints. The principal aim of this research is the development of a universal boundary condition. Examples included show encouraging results for attached and separated flows.

1. Introduction

Traditional approaches towards the formulation of wall-boundary conditions for RANS are either based on *high-Re* number or *low-Re* number assumptions. The former technique avoids the resolution of the near-wall region, which in contrast has to be appropriately resolved by the latter. Due to the lower computational cost, high-Re number (*law-of-the-wall*) boundary conditions, which assume that all quantities scale with the friction velocity, are usually preferred in industrial flow simulations. The simultaneous presence of pressure gradient and shear in the near-wall region of most industrial flows leads to a complex, anisotropic turbulence structure, where the flow is no longer universally controlled by the wall-shear stress. Recent proposals based on generalized wall functions [1] are advantageous for the stability and the efficiency of the algorithm. This is, however, at the expense of a poor validity in complex near-wall flows and might deteriorate the predictive capabilities particularly in adverse pressure gradient flows. The paper aims to advocate a universal boundary condition which does not require specific grid-resolution properties in the near-wall regime. The approach provides conditions for mean momentum and turbulence properties located in the wall-adjacent node and adapts itself to the solution. It contributes to the flexibility and therefore simplifies the grid-generation process. The latter is particularly important for the simulation of complex industrial flows, where a fair and continuous resolution of the viscous sublayer is neither desirable nor feasible. The approach is expected to improve the multi-grid performance of the algorithm.

2. Universal wall boundary condition

The present universal wall-boundary condition is based on a *low-Re* modification of the traditional law-of-the-wall boundary condition. The key features of the approach are series expansions for mean-momentum and turbulence properties, which provide an asymptotic matching of the log-layer and the viscous sublayer. The starting point is an approximation of the non-dimensional wall distance Y^+ in the entire wall region

$$Y^+ = U^+ \frac{1}{\kappa} \ln \left[e^{(\kappa U^+)} - \{1 - \kappa U^+ + 0.5(\kappa U^+)^2 - \dots\} \right], \quad \kappa = 0.41, \quad E = 8.43. \quad (1)$$

Equation (1) is used to update the friction velocity U_τ and the wall-shear stress in an iterative procedure, viz.

$$\tau_w = (1 - \phi)\tau_{w,low} + \phi\tau_{w,high}, \quad \text{with} \quad \phi = (1 - e^{-0.09 Y^+})^2. \quad (2)$$

The low-Re wall-shear stress is determined by the viscous stress, $\tau_{w,high}$ follows from the log-law ($|\tau_{w,high}| = \rho \kappa U_\tau / (E Y^+)$). Neumann conditions are imposed for the turbulent-kinetic energy k which holds for both, low and high-Re regimes. Additionally, the production of k is manipulated in the wall-adjacent node according to $P_k = |\tau_w| \sqrt{k} c_\mu^{0.25} / (\kappa n)$, where n is the wall-normal distance and $c_\mu = 0.09$ the anisotropy parameter. The wall-adjacent turbulent-length scale is evaluated from a modified log-law constraint, e.g.

$$\varepsilon = k^{3/2} / L_\varepsilon, \quad L_\varepsilon = \kappa c_\mu^{-0.75} n (1 - e^{-\gamma_\varepsilon Re_k}) \quad \text{or} \quad \omega = k^{1/2} / (c_\mu L_\omega), \quad L_\omega = \kappa c_\mu^{-0.75} n (1 - e^{-\gamma_\omega Re_k}). \quad (3)$$

The remaining parameters of eq. (3) are determined from an asymptotic matching of the linear Taylor-series expansion of the length scales to the near-wall turbulence ($\gamma_\varepsilon = 0.2$ and $\gamma_\omega = 0.057$).

3. Validation

The first validation example is a fully-developed channel flow. Results are reported for various Reynolds numbers employing the same numerical grid. The grid accurately resolves the viscous sublayer for the lowest Reynolds number investigated ($Re_\tau = 197$), the remaining Reynolds numbers feature a continuous transition from low-Re to high-Re conditions. Figure 1 indicates, that the logarithmic behaviour of the mean velocity profile is accurately predicted for all Reynolds numbers investigated. Details of the near-wall regime are captured depending on the resolution quality of the grid. An important advantage of the universal-boundary condition is the grid-adaptive character of

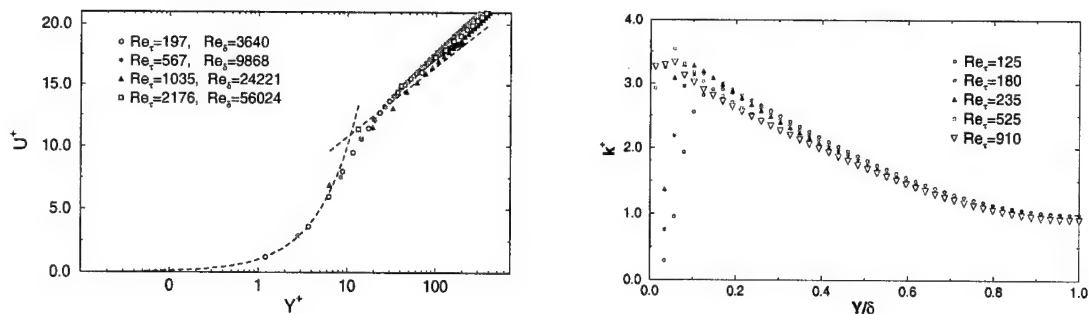


Figure 1: Performance of the universal wall-boundary condition in a channel at various Re numbers (Wilcox $k-\omega$ model [2]); Mean velocity (left) and turbulent-kinetic energy (right). Symbols correspond to the grid-point locations.

the formulation. The second example investigates the flow over a backward-facing step at $Re = 37\,500$ [3]. The focal point of this exercise is the recirculation regime along the step site. Hence, the grid accurately resolves the near-wall phenomena of the bottom-wall boundary layer ($Y^+ \approx 0.5$), but provides only a coarse resolution ($Y^+ \approx 40$) of the upper-wall boundary layer. The simultaneous application of conventional high- and low-Re boundary conditions is usually considered to be unfeasible for coding reasons. The use of low-Re boundary conditions, however, might be fatal in this case, as indicated by the pressure distribution displayed in figure 2. In contrast to this, the present universal boundary condition can adapt to the coarse grid of the upper wall and is not afflicted with a deterioration of the over-all-solution quality.

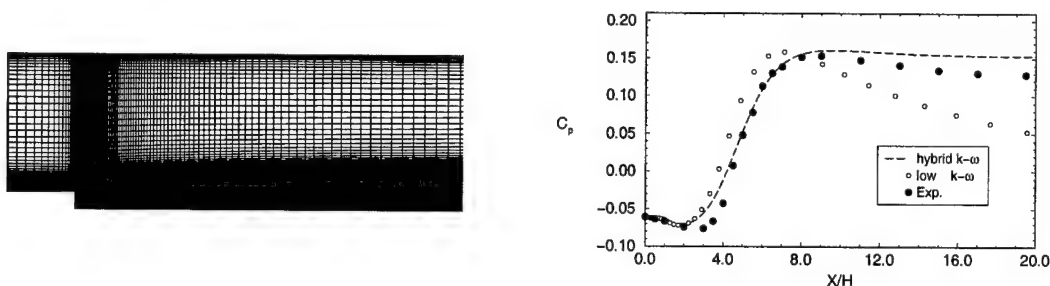


Figure 2: Numerical grid and step side distribution of the pressure coefficient for a backward-facing step flow

4. References

- 1 GROTJANS, H., MENTER, F.R.: Wall Functions for General Application CFD Codes. Proc. 4th European CFD Conference, Athens, Greece, Sept. 1998, Vol.1, pp. 1112-1117
- 2 WILCOX, D.C.: Reassessment of the scale determining equation for advanced turbulence models. AIAA Journal **26**, pp. 1299-1310, 1988
- 3 DRIVER, D.M., SEEGMILLER, H.J.: Features of a reattaching turbulent shear layer in a divergent channel flow. AIAA Journal **23**, pp. 163-171, 1985

Addresses: T. RUNG, H. LÜBCKE, F. THIELE Technische Universität Berlin, Hermann-Föttinger-Institut für Strömungsmechanik, Müller-Brelau-Strasse 8, D-10623, Berlin, Germany

A. SADIKI, A. MALTSEV, J. JANICKA

Performance of Turbulence Models of Second Order in Predicting Turbulent Mixing in Jet Exhaust behind Aircraft Engines

The modeling of near-field jet from aircraft engines is considered as an important task for a subsequent study on chemistry and micro-physics in far-away spatial regions of the aircraft wake. The main goal of this study is to investigate the performance of transport equation turbulence and mixing models for the prediction of near-field jet exhaust plumes. Turbulence is modelled with three different models (two different linear second order moment closures (Reynolds stress transport models) and $k-\epsilon$ model). Scalar fluxes are modeled by corresponding transport equation models. Finite-rate chemistry is considered. Results, obtained with and without chemical reactions, show that turbulence and mixing modeling effects on the chemistry and flow field are significant and should be taken into account in modeling of near-field exhaust plumes.

1. Introduction

The interaction between the aircraft engine exhaust plume and the surrounding air mass appears these last days to be a focal research point in many investigations into the influence of engine emissions on global climate changes. Kärcher et al. (1994, 1996) [4] [5] founded their studies on an empirical turbulence model for modeling the microphysics and chemistry during plume expansion. Wang and Chen (1997) [9] studied the microscale turbulence and chemistry interaction in near-field to manifest the importance of microscale mixing processes occurring at different scales and developed a reduced chemical reaction mechanism. Anderson et al. (1996) [1] used in the initial plume the two-equations model up to the first 100 meters in calculations of the flow field and chemical kinetics from the engine combustor out to a distance of about 20.2 km. It occurs, that one area that lacks fundamental understanding is to gain insight into the turbulence modeling effect on the predicted jet exhaust transport and mixing fields. Focussing on chemistry, in particular on turbulence-chemistry interaction, it is well known that the chemical or combustion process is strongly dependent on the mixing of the fuel (here exhaust gas) and oxidant streams (here surrounding air mass), so that it is necessary to capture the major features of the flow and mixing fields before further detailed investigations can be performed. In the framework of statistical moment closures, second-moment closures represent an optimum simple choice for a reasonably detailed representation of the turbulence and mixing. The turbulence is modelled with three different models (two different linear second order moment closures [7], [3] and a standard two-equations model). Various scalar fluxes are modeled by corresponding transport equations models [3].

2. Numerical method, initial and boundary conditions

For the simulation of the flow field the well-known Patankar-Spalding [1967] [8] finite-difference procedure was used. The main advantage of this procedure lies in special choice of grid which adjusts its width so as to conform to the thickness of the layer in which significant property gradients are present. The flow field is assumed to be steady state, axisymmetric, isobaric (at an ambient air pressure) and diffusive terms are assumed to be significant only in radial direction (parabolic approximation). The numerical integration is carried out by marching in axial direction x . The scheme has a first order of accuracy in marching direction and second order of accuracy in radial direction. Two types of initial and boundary conditions were considered. First case is the only heat transfer problem without consideration of chemical reactions. Model input was taken from the work of Kärcher and Fabian [1994] [4]. The second case in which chemistry effects are simulated represents the same type of engine, but with some differences in geometrical and dynamical parameters. Such initial and boundary conditions can be found in works by Kärcher et al. [1996] [4] and Wang & Chen [1997] [9].

3. Chemical reaction mechanism

Chemical data were taken from Chen and Wang [9]. Following this mechanism the calculation of the chemical source term in enthalpy and mole fractions transport equations was carried out using Chemkin package [Kee et al., 1989] [6]. This package includes the Gas-Phase Subroutine Library that returns information on elements, species, reactions, equation of state, thermodynamic properties, and chemical reaction rates. The gas inside each computational cell was assumed to be perfectly mixed, so that no microscale mixing consideration is necessary.

4. Results and discussions

As mentioned above, the first simulation case includes only heat transfer problem. Results for the first case are presented in Fig. 1 and Fig. 2. Comparison is performed with results of BOAT RANS code (Dash and Pergament, 1978) [2] which is the only existing reference for this kind of initial and boundary conditions. Fig.1 shows the decay of the centerline temperature and velocity during jet expansion. In Fig.2 one can see the jet diameter evolution taken as double radius in which axial velocity component is 30 time less than the central value. With second order models, in particular with Jones and Musonge [3], important properties of the flow reveal overall acceptable agreement. The correct prediction of these fields must be emphasized here in comparison to the results in previous work [4]. Secondly, simulations were carried out for the second type of model input. Fig. 3 shows the main nitrogen species centerline evolution. Results are in good qualitative agreement with results obtained by previous authors [5], [9], [10] (not shown here because of the lack of space), but there is some quantitative difference, especially for results obtained with the Jones Musonge turbulence model.

As shown in these results, the turbulence and mixing modeling effect on the flow and the chemistry is significant and should be carefully taken into account in modeling of jet exhaust behind aircraft engines.

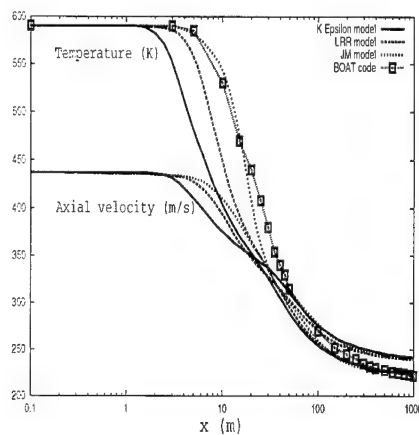


Fig. 1: Centerline temperature and axial velocity evolution

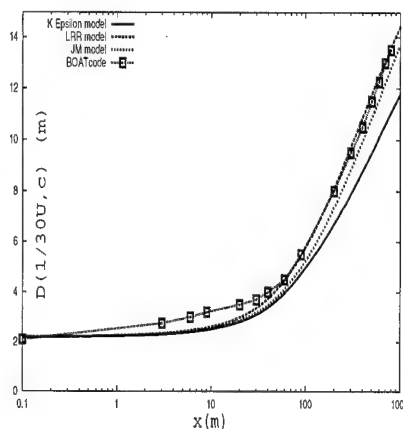


Fig. 2: Jet diameter $1/30U_c$ evolution

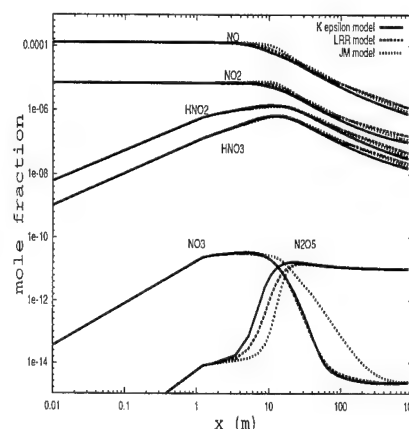


Fig. 3: Centerline major nitrogen species evolution

Acknowledgements

This work has been supported by "Fritz und Margot Faudi-Stiftung". The authors are indebted to Prof. J.Y. Chen of Berkeley University (USA) and Dr. Ing. A.Hinz (TU Darmstadt) for helpful comments and discussion.

References

- 1 ANDERSON M.R. MIAKE-LYE R.C. BROWN R.C. KOLB C.E. Calculation of exhaust plume structure and emissions of the ER 2 aircraft in the stratosphere. J. Geophys. Res., vol. 101, pp 4025-4032, 1996
- 2 DASH S.M. PERGAMENT H.S. A Computational Model for the Prediction of Jet Entrainment in the Vicinity of Nozzle Boattails (The BOAT Code), Contractor Report 3075, NASA, 1978
- 3 JONES W.P. MUSONGE P. Closure of the Reynolds stress and scalar flux equations. Phys. Fluids 31, pp. 3589-3604, 1991
- 4 KÄRCHER B. FABIAN P. Dynamics of aircraft exhaust plumes in the jet-regime. Ann. Geophysicae 12, pp 911-919, 1994
- 5 KÄRCHER B. HIRSCHBERG M.M. FABIAN P. Small-scale chemical evolution of aircraft exhaust species at cruising altitudes. J. of Geophys. Res., vol. 101, pp 15,169-15,190, 1996
- 6 KEE R.J. RUPLEY F.M. MILLER J.A. Chemkin-II: A FORTRAN chemical kinetics package for the analysis of gas-phase chemical kinetics, Rep. SAND 89-8009, Sandia Natl. Lab., 1989
- 7 LAUNDER B.E. REECE G.J. RODI W. Progress in development of a Reynolds-stress turbulence closure. J. Fluid Mech. 68, pp 537-566, 1975
- 8 PATANKAR S. V. SPALDING D.B. 1967 A finite-difference procedure for solving the equations of the two-dimensional boundary layer. Int. J. Heat Mass Transfer 10, pp 1389-1411, 1967
- 9 WANG Z. CHEN J.-Y. Modeling of microscale turbulence and chemistry interaction in near-field aircraft plumes. J. Geophys. Res., vol. 102, pp 12,871-12,883, 1997
- 10 WANG Z. Numerical Modeling of Chemistry, Turbulent Mixing and Aerosol Dynamics in Near-Field Aircraft Plumes. PhD thesis, Univ. of Calif. at Berkeley, 1998

Addresses: A. SADIKI, A. MALTSEV, J. JANICKA Technische Universität Darmstadt, FG Energie- und Kraftwerkstechnik, Petersenstr. 30, 64287 Darmstadt, Germany

KAI SCHNEIDER AND MARIE FARGE

Coherent Vortex Simulation (CVS) of two-dimensional turbulence

We present a new turbulence model to compute fully developed turbulent flows. The method is based on the solution of the wavelet filtered Navier-Stokes equations in vorticity-velocity formulation using an adaptive wavelet discretization. As application we present a Coherent Vortex Simulation (CVS) of a two-dimensional mixing layer and compare the results with those obtained with Direct Numerical Simulation (DNS).

In this paper we propose a new turbulence model, called Coherent Vortex Simulation (CVS) [1,4] for computing fully developed turbulent flows. This new approach for CFD is based on the observation that turbulent flows contain both an organized part (the coherent vortices) and a random part (the incoherent background flow). In classically used LES-methods the Navier-Stokes equations are low-pass filtered and only the evolution of the large scales of the flow is computed, while the effect of the small scales onto the large scales is modelled. Hence, the intermittent behaviour of the flow is only partially taken into account due to the lack of small scales. CVS is based on the multi-scale computation of the coherent part of the vorticity (characterized by a non-Gaussian multiscale behaviour and responsible for the intermittency), while the influence of the incoherent background flow is statistically modelled (characterized by Gaussian statistics and likewise multiscale).

We filter the two-dimensional Navier-Stokes equations using a nonlinear orthogonal wavelet filter and obtain an evolution equation for the coherent vorticity $\omega_>$:

$$\begin{aligned} \partial_t \omega_> + \nabla \cdot (\omega_> \vec{V}_>) - \nu \nabla^2 \omega_> &= \nabla \times \vec{F}_> - \nabla \cdot \tau \\ \nabla \cdot \vec{V}_> &= 0, \end{aligned} \quad (1)$$

which includes an unknown term, $\tau = (\omega \vec{V})_> - \omega_> \vec{V}_>$, to be modelled. This incoherent stress term describes the effect of the discarded incoherent terms onto the resolved coherent terms. We compensate the loss of enstrophy of the wavelet filtering by a conditional forcing term acting in the region of strong nonlinear activity [2]. In contrast to LES, where the underlying computational grid is static, the CVS method employs regridding which dynamically adjusts to the flow by refining in regions of strong gradients.

As example we compute a temporally growing two-dimensional mixing layer using the CVS method (cf. Fig. 1). To validate the approach we compare the results with DNS data obtained using a classical spectral method. We observe that in the CVS approach all scales of the flow are well resolved, however with a reduced number of degrees of freedom (cf. Fig. 2).

Acknowledgements

We acknowledge support from the French-German Procope program (contract N. F 01220ZE/D 9822768) and the European TMR program (contract N. FMRX-CT 98-0184).

1. References

- 1 M. FARGE, K. SCHNEIDER AND N. KEVLAHAN. Non-Gaussianity and Coherent Vortex Simulation for two-dimensional turbulence using an adaptive orthonormal wavelet basis. *Phys. Fluids*, **11**(8), 2187-2201, 1999.
- 2 K. SCHNEIDER AND M. FARGE. Wavelet forcing for numerical simulation of two-dimensional turbulence. *C. R. Acad. Sci. Paris Série II* **325**, 263-270, 1997.
- 3 K. SCHNEIDER AND M. FARGE. Numerical simulation of a mixing layer in an adaptive wavelet basis. *C. R. Acad. Sci. Paris Série II*, to appear.
- 4 M. FARGE AND K. SCHNEIDER. Coherent Vortex Simulation (CVS), a semi-deterministic turbulence model using wavelets. *Flow, Turbulence and Combustion*, submitted.

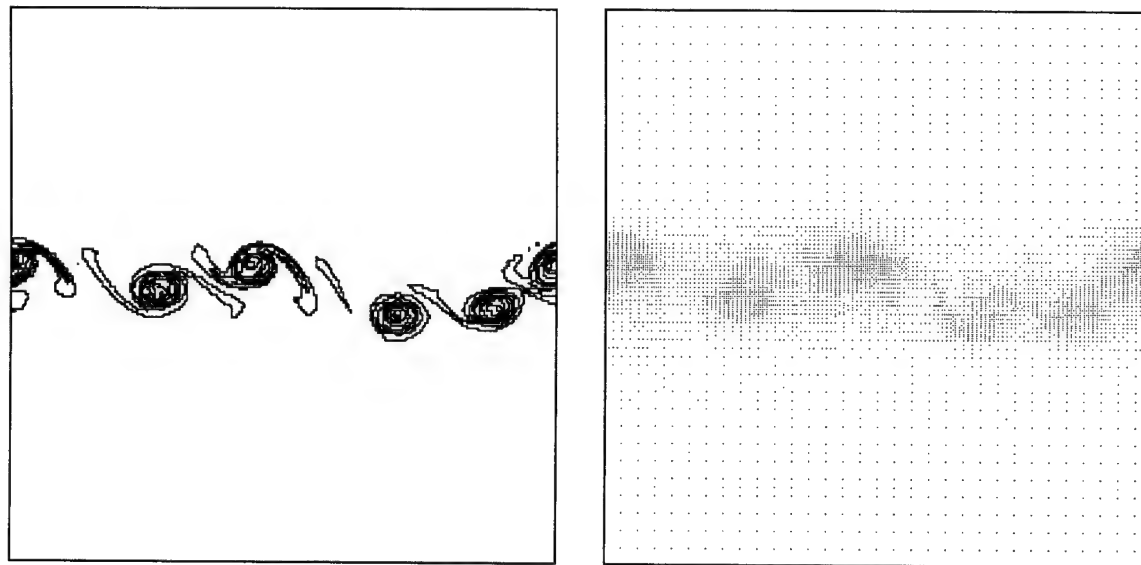


Figure 1: CVS computation of a two-dimensional mixing layer. Left: isolines of vorticity ($\omega = 0.1, 0.4, 0.7, 1.0, 1.3, 1.6$) at $t = 37.5$ s. Right: corresponding adaptive grid in physical space. Note that the grid dynamically adapts to the flow evolution both in scale and space.

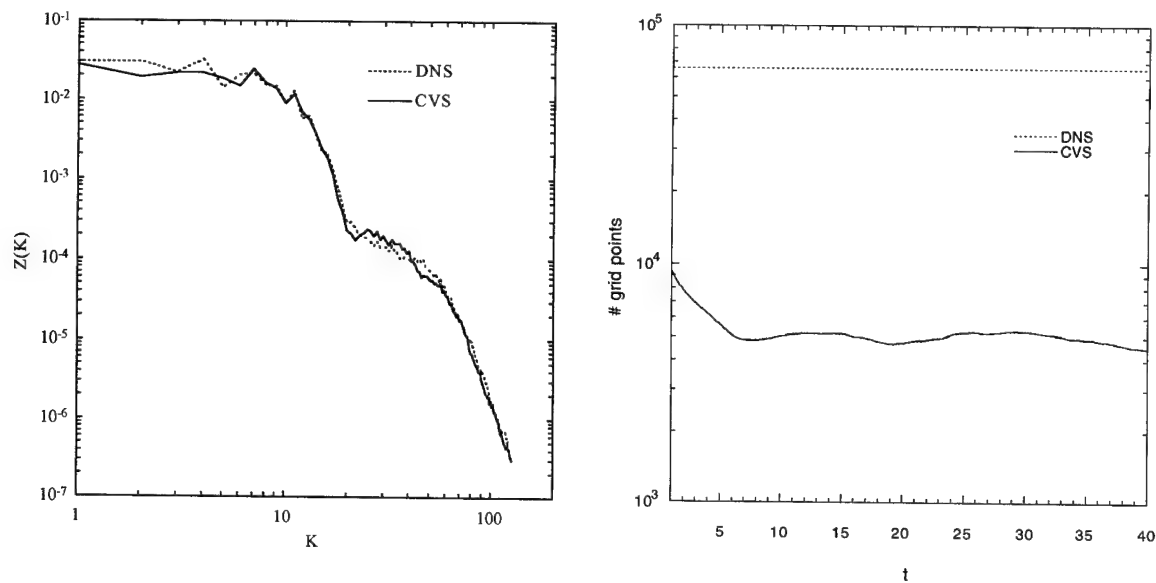


Figure 2: Left: comparison of corresponding enstrophy spectrum with a DNS calculation. Right: time evolution of the number of grid points. Note that at $t = 37.5$ s only 4700 grid points are used in CVS method, while DNS uses 65538.

Address: KAI SCHNEIDER, ICT, Universität Karlsruhe (TH), Kaiserstr. 12, 76128 Karlsruhe Germany
MARIE FARGE, LMD-CNRS, Ecole Normale Supérieure, 24 rue Lhomond, 75231 Paris Cedex 05, France

M. SCHOLLE, A. WIERSCHEM, N. AKSEL

Creeping Newtonian Film Flow Down an Inclined Wavy Plane. Part I

Theoretical investigations are made on the influence of a sinusoidal bottom topography on a gravity driven, Newtonian film flow. Neglecting inertia effects the surface shape is obtained for small amplitudes of the bottom profile using perturbation theory. For thick films and large bottom amplitudes an exact analytical approach is developed.

1. Formulation of the problem

Various methodical approaches are available for an analytical treatment of film flows which differ with respect to coordinates, scalings and perturbation parameters. One method developed by Wang is based on a local coordinate system [1]. In this formulation the boundary conditions at the bottom can be fulfilled exactly. Especially if the film is thin compared to the bottom profile amplitude this approach provides good results [2]. If the film height is large compared to the bottom profile amplitude, however, the use of globally defined Cartesian coordinates is more adequate because the equations of motions can be fulfilled exactly. This case is discussed in the following.

Let the X - and the Z -axis be orientated parallel and perpendicular to the mean inclination α of the plane. We introduce a representation in terms of dimensionless, complex coordinates ξ and $\bar{\xi}$ by the transformation

$$\xi := \frac{\pi}{\lambda} (Z + iX), \quad \bar{\xi} := \frac{\pi}{\lambda} (Z - iX) \quad (1)$$

with the wavelength λ of the bottom profile as scaling factor. Note that ξ and $\bar{\xi}$ are the two independent characteristics of the Laplace equation. Furthermore, we join the vector components U and W of the velocity field together to a dimensionless, complex velocity field

$$v := \frac{1}{U_0} (U + iW), \quad \text{with } U_0 := \frac{\rho g \sin \alpha}{2\eta} H_0^2. \quad (2)$$

The scaling factor U_0 is the surface velocity of a fully developed, plane film flow depending on mass density ρ and viscosity η of the fluid, the gravity acceleration g , the inclination angle α and on the film height H_0 of a flat bottom shape. Neglecting inertia effects ($Re \rightarrow 0$) Navier-Stokes equations and continuity equation read

$$-2\pi i \frac{\partial P}{\partial \xi} + (2\pi h)^2 \frac{\partial^2 v}{\partial \xi \partial \bar{\xi}} + 2[1 - i \cot \alpha] = 0 \quad \text{and} \quad \text{Im} \left(\frac{\partial v}{\partial \bar{\xi}} \right) = 0 \quad (3)$$

with the real-valued pressure P scaled by $\eta U_0 \lambda H_0^{-2}$ and with the scaled film thickness $h := H_0/\lambda$. Integration of the second equation with respect to ξ , followed by an integration with respect to $\bar{\xi}$ provides

$$v = v_1 \frac{\xi + \bar{\xi}}{2\pi h} - \frac{[\xi + \bar{\xi}]^2}{[2\pi h]^2} + \overline{Q(\xi)} + R(\xi) + [\xi + \bar{\xi}] Q'(\xi) \quad (4)$$

$$P = P_0 - \frac{\cot \alpha}{\pi} [\xi + \bar{\xi}] - 2\pi i h^2 [Q'(\xi) - \overline{Q'(\xi)}] \quad (5)$$

as general solution of (3). The prime denotes the first order derivative. The two periodic, yet open functions $Q(\xi)$ and $R(\xi)$ are due to the two integration steps. Let $\zeta := A/\lambda$ be the aspect ratio 'amplitude per wavelength' and $Ca := \eta U_0/\sigma$ be the capillary number. Then, Q and R have to be determined from the no-slip condition $v \equiv 0$ at the bottom $\xi = \beta(x) := -\pi \zeta \cos(x) + ix/2$ and from the kinematic and dynamic boundary conditions at the free surface $\xi = \varphi(x) := [f(x) + ix]/2$:

$$\{v\varphi'(x) + \bar{v}\bar{\varphi}'(x)\}_{\xi=\varphi(x)} = 0 \quad (6)$$

$$\left\{ \left[2\pi(P - P_{air}) + \frac{(2\pi h)^2}{Ca} [1 + f'(x)^2]^{-3/2} f''(x) \right] \bar{\varphi}'(x) - i(2\pi h)^2 \frac{\partial v}{\partial \xi} \varphi'(x) \right\}_{\xi=\varphi(x)} = 0 \quad (7)$$

2. Results for small wave amplitudes

If the amplitude of the bottom profile is small compared to its periodic length, i.e. if $\zeta \ll 1$, regular perturbation methods can be applied: Writing the boundary conditions in a Taylor series with respect to the perturbation parameter ζ the first order approximation delivers a harmonic form of Q , R and the surface shape $f(x)$,

$$Q(\xi) = \sum_{n=\pm 1} Q_n \exp(2n\xi), \quad R(\xi) = \sum_{n=\pm 1} R_n \exp(2n\xi), \quad f(x) = 2\pi h - r2\pi\zeta \cos(x + \Delta), \quad (8)$$

with the four complex-valued coefficients $Q_{\pm 1}$, $R_{\pm 1}$, the real-valued damping factor r and the real-valued phase shift Δ depending only on the film thickness h and on the combined parameter

$$\mu := \frac{1}{2Ca} + \frac{\cot \alpha}{(2\pi h)^2} \quad (9)$$

as the two concise parameters. Thus, in leading order the inclination angle α and the capillary number Ca are included via μ . Figure 1 shows phase shift and damping factor versus film height for three different inclination angles neglecting the capillarity. Independent of the inclination angle the phase shift reaches a maximum at $h \approx 0.177$

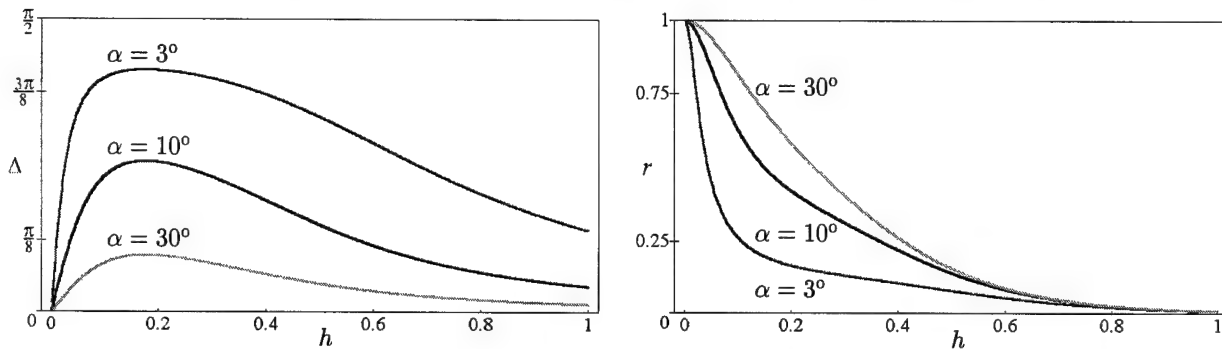


Figure 1: Phase shift Δ and damping factor r of the surface shape versus film thickness.

whereas the damping factor decreases monotonously. For $h \rightarrow 0$ the surface shape fits to the bottom shape and for $h \rightarrow \infty$ the film surface becomes flat.

3. Large wave amplitudes — roughness

For large aspect ratios $\zeta = A/\lambda$ the perturbation approach is not straightforward. However, if the bottom profile amplitude is much smaller than the film height ($A \ll H_0$) a flat film surface can be assumed. After re-scaling $\tilde{v} := 2\pi h v$ and applying the limit $h \rightarrow \infty$ the velocity field reads in Fourier representation:

$$\tilde{v} = \tilde{v}_0 + 2[\xi + \bar{\xi}] + \sum_{n=1}^{\infty} [\bar{q}_n \exp(-2n\bar{\xi}) + (r_n - 2n[\xi + \bar{\xi}]q_n) \exp(-2n\xi)] \quad (10)$$

Hence, the problem is reduced to the determination of the coefficients q_n and r_n by fulfilling the no-slip condition $\tilde{v} = 0$ at the bottom $\xi = \beta(x)$ which results in a linear algebraic system of equations,

$$\sum_{n=1}^{\infty} [F_{k,n}^+ q_n + E_{k,n}^+ r_n] = 2\zeta \delta_{k1}, \quad \sum_{n=1}^{\infty} [F_{k,n}^- q_n + E_{k,n}^- r_n] = 0, \quad (11)$$

where the matrix elements are given by $E_{k,n}^{\pm} := I_{k-n}(n\zeta) \pm I_{k+n}(n\zeta)$ and $F_{k,n}^{\pm} := E_{k,n}^{\pm} + na[E_{k-1,n}^{\pm} + E_{k+1,n}^{\pm}]$ with the modified Bessel functions I_n . By solving this infinite system of equations for a finite order N the velocity field \tilde{v} is obtained with sufficient accuracy.

4. References

- 1 WANG, C. Y.: Thin film flowing down a curved surface. ZAMP 35 (1984), 532-544
- 2 WIERSCHEM, A.; SCHOLLE, M.; AKSEL, N.: Creeping Newtonian Film Flow Down an Inclined Wavy Plane. Part II

Address: M. SCHOLLE, A. WIERSCHEM, N. AKSEL, Universität Bayreuth, Lehrstuhl für Technische Mechanik und Strömungsmechanik, Universitätsstraße 30, D-95440 Bayreuth, Germany.

EWA TULISZKA-SZNITKO AND CHYI-YEOU SOONG

Linear Stability Theory of Non-Isothermal Flow Between Two Rotating Disks

The objective of the present study is to investigate the flow stability of mixed convection in non-isothermal rotating fluids between a rotating disk and a stationary one. The buoyancy effects stemmed from the rotational forces, including centrifugal and Coriolis, are taken into account. A similarity model of thermal flow with the assumption of Boussinesq fluids is formulated for generating axially symmetric solutions of the basic state. Disturbance equations are derived by using the concept of small perturbation of normal mode expressions, and then solved by the Chebyshev collocation spectral method. The influences of the rotation-induced buoyancy effects and the rotational conditions on the flow stability characteristics of the two-disk rotating fluid motion are explored. The present results disclose the mechanisms and the significance of the rotation-induced buoyancy on flow stability characteristics of the non-isothermal fluids in the rotor-stator disk systems.

1. Introduction

The rotating-disk flows, especially the one between two co-axial disks, are highly complicated in nature. The complexities reflected in multiplicity of the flow states and bifurcation phenomena are stemmed from the non-linearity of the rotating fluids. In the course of the increasing rotating rate or in dimensionless form, the rotational Reynolds number $Re = \sqrt{S^2 \Omega_1 / \nu}$ (S is a distance between disks), the steady laminar flow may turn to the asymmetric, time-dependent or oscillatory state, and then to the chaotic state, that means a turbulent flow. A profound stability study may provide more evidence of the instability evolution and the transition processes. To reach this end, the linear stability analysis is a good starting point for the study of the loss of stability.

In the past decades, numerous works have been conducted to explore the flow structure and the instabilities associated with the rotating-disk flows. According to the experimental results of the earlier single-disk studies summarized in the book of Greenspan [1], two types of instability waves, classes I and II, appeared over the disk in order. The waves of each of these families form a series of horizontal rolling vortices. Relatively a few works were devoted to the flow between the two rotating disks. One of them is Itoh [2] who analyzed the hydrodynamic nature of the flow between two rotating disks. Once the non-isothermal flow condition is considered, thermal effects and the rotational-induced buoyancy become important and influential in stability characteristics and the critical conditions. Basically, the flow mechanisms are closely related to the non-linearity. Before performing the nonlinear stability analysis, the classical linear stability analysis is a good starting point. We can conduct the linear stability analysis to find the critical condition for the loss of symmetry or steadiness (only). In the present work we analyze the neutral conditions under the influences of the rotation-induced buoyancy effects.

2. Formulation of the problem

Fig. 1 shows schematically a physical model of the mixed convection heat transfer between two disks rotating at rates Ω_1 and Ω_2 , respectively. A cylindrical co-ordinate system (R, Z, φ) is fixed on and rotating with the disk 1. In the present study, the value of $\Omega_2 = 0$ represents a rotor/stator disk system. The flow field is assumed to be laminar, steady and axisymmetric and is described by Navier-Stokes equations, continuity equation and energy equation. To take into account the buoyancy effects induced by the involved body forces, the Boussinesq approximation is invoked, i.e. the density associated with the terms of gravity, the centrifugal and the Coriolis forces due to the disk rotation, and the curvilinear motion of the fluids are all considered as variable. The Boussinesq linear density-temperature relation can be written in the following form $\rho = \rho_r [1 - \bar{\beta}(T - T_r)]$ where r denotes a reference state and $\bar{\beta} = -1/\rho_r (\partial \rho / \partial T)_p$ is the thermal-expansion coefficient. The disturbance equations are derived by expressing the velocity, pressure and temperature fields as a superposition of the basic state and the perturbed flow. A similarity model of the thermal flow with the assumption of Boussinesq is formulated for generating basic solutions of the axially symmetric flows. The similarity equations with the appropriate boundary conditions create a nonlinear two-point boundary value problem, which can be solved by a shooting method with modified Newton's method to update the guessed values. Solutions can be easily obtained for lower Re_s by using the conventional shooting method. However, due to the stiffness of the system, the convergent solution is getting hard to bring about as Re_s increases.

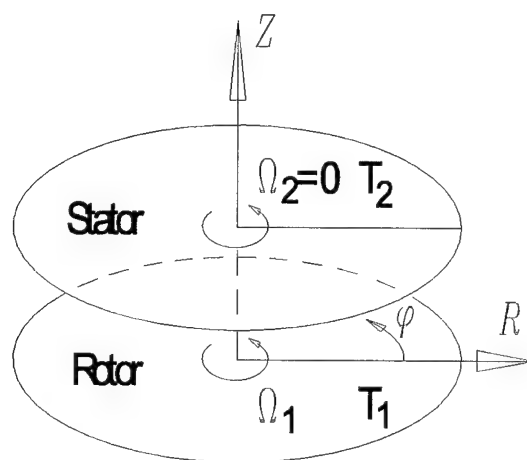


Figure 1: Schematic picture of the rotating disks system.

To improve the accuracy and the convergence characteristics, non-uniform grid, under-relaxation third-order discrete continuation techniques are applied (Soong [2]). The linear stability equations (temporal approach) are solved by the spectral collocation method based on the Chebyshev polynomials.

The fluid flow between the two disks may have two different patterns. One is the so-called Batchelor-type flow, and the other is of Stewartson-type. Since the flow between a rotating disks system at high rotating rate behaves as a Batchelor-type flow the present study concentrates on the flow of this type. In the present paper we analyze the influence of two governing parameters, Re_s and B on instability characteristics and critical parameters. The parameter $B = \beta(T_2 - T_1)$ is the so-called thermal Rossby number. For validity of Boussinesq approximation, the values of B has to be limited to a small range, e.g. $|B| \leq 0.1$ in this study. For all of the boundary layers studied here on disk 1 and disk 2, two different types of instability i.e. type I and type II were obtained. Type II occurs at the lower local Reynolds number $Re = \sqrt{R^2 \Omega_1 / \nu}$; for the higher Re type I instability is dominant. We have found that, $B > 0$ or $T_2 > T_1$ stabilizes type II instability and destabilizes type I instability on disk 1. Simultaneously $B < 0$ or $T_1 > T_2$ stabilizes both type I and II on disk 2. For all analyzed examples the boundary layer of disk 2 (stator) turned out to be more unstable than that on the rotating disk 1 for any considered values of B . To verify the present computations, we have compared our instability results with the previous data of hydrodynamic instability, without thermal effect, i.e. $B = 0$ presented in Itoh's paper [2]. The present predictions are of a little deviation from Itoh's (less than 1%).

Acknowledgements

Ewa Tuliszka-Sznitko is grateful to Prof. W. Riess from the University of Hannover for his help and cooperation. The study was supported by the Polish State Committee for Scientific Research in the frame of Grant No. 7T07A00317 and the National Science Council of the Republic of China in the frame of Grant No. NSC-89-2212-E-014-006. The computations were partly performed on the Cray J916 at the Poznan Computer Center (Poland).

3. References

- 1 GREENSPAN, H.P.: The Theory of Rotating Fluids, Cambridge University Press, UK (1968).
- 2 ITOH, M.: On the Instability of the Flow between Coaxial Rotating Disks, in Boundary Layer Stability and Transition to Turbulence, ASME FED 114 (1991), 83–89.
- 3 SOONG, C.Y., CHYUAN, C.H.: Investigation of Buoyancy Effects in Non- Isothermal Rotating Flows by Scaling Analysis and a Novel Similarity Model. Chinese Journal of Mechanics, 14 (4) (1998), 193–207.

Addresses: EWA TULISZKA-SZNITKO, Institute of Thermal Engineering, Technical University of Poznan, 60-965 Poznan, Poland, e-mail: sznitko@sol.put.poznan.pl

CHYI-YEOW SOONG, Department of Aeronautical Engineering, Chung Cheng Institute of Technology, Tahsi, Taoyuan, Taiwan 33509, Republic of China, e-mail: cysoong@ccit.edu.tw

WAGNER, C.

An eddy viscosity scaled dynamic scale similarity model

A new subgrid scale model for Large Eddy Simulations (LES) of wall-bounded turbulent flows, which is based on scale similarity between resolved stresses and subgrid scale stresses, is proposed. Testing this model a posteriori, the fully developed turbulent channel flow was simulated for a low Reynolds number (based on the channel height H and friction velocity u_τ) of $Re = 360$. Additionally a coarse direct numerical simulation (DNS) without model and a LES with a dynamic Smagorinsky model were performed. Excellent agreement is obtained applying the new model in comparison with Kim et al.'s [2] DNS data base.

1. Foundations

The dimensionless top-hat filtered incompressible Navier-Stokes equations read:

$$\partial \bar{u}_i / \partial x_i = 0 \quad , \quad \partial \bar{u}_i / \partial t + \partial (\bar{u}_i \bar{u}_j) / \partial x_j + \partial \tau_{ij} / \partial x_j = -\partial \bar{p} / \partial x_i + 1/Re \partial (2S_{ij}) / \partial x_j \quad (1)$$

The velocity vector $\bar{u}_i = (\bar{u}_x, \bar{u}_y, \bar{u}_z)$ and the pressure field \bar{p} in eq. (1) represent top-hat filtered values, which have been integrated over the discrete volume $\bar{\Delta} = \Delta x \Delta y \Delta z$ as described in Wagner [7]. Re denotes the Reynolds number, $\tau_{ij} = \bar{u}_i \bar{u}_j - \bar{u}_i \bar{u}_j$ the subgrid scale stress tensor and $\bar{S}_{ij} = 1/2(\partial \bar{u}_i / \partial x_j + \partial \bar{u}_j / \partial x_i)$ the strain rate tensor.

Assuming isotropic turbulence and a Kolmogorov spectrum with $-5/3$ decay in the inertial subrange the unknown subgrid scale stress tensor τ_{ij} can be modeled in terms of a constant C , an eddy-viscosity ν_t and the strain rate tensor, i.e. $\tau_{ij} \approx C \bar{\nu}_t \bar{S}_{ij}$. There are many variants of these so-called eddy-viscosity models. Smagorinsky [6] originally proposed the eddy-viscosity $\nu_{t,S}$ as shown in eq. (2, left). The model by Métails and Lesieur [5] uses a structure function based eddy-viscosity, which can be rephrased in terms of the velocity gradient tensor $\bar{A}_{ij} = \partial \bar{u}_i / \partial x_j$ for further use in Germano's dynamic process [1]. The resulting eddy-viscosity $\bar{\nu}_{t,A}$ is presented in eq. (2, right).

$$\bar{\nu}_{t,S} = -\bar{\Delta}^{2/3} (2\bar{S}_{ij}\bar{S}_{ij})^{1/2} \quad \text{or} \quad \bar{\nu}_{t,A} = -\bar{\Delta}^{2/3} (\bar{A}_{ij}\bar{A}_{ij})^{1/2} \quad (2)$$

The trace of the strain rate tensor vanishes in incompressible flow due to the continuity eq. (1, left). Consequently in anisotropic wall-bounded flows only the deviatoric part of subgrid scale stress tensor $t_{ij} = \tau_{ij} - \tau_{kk}\delta_{ij}$ (δ_{ij} denotes the Kronecker symbol), can be modeled using an eddy-viscosity ansatz. In order to determine the constant C in wall-bounded flows the additional filtering operation (\cdot) , which represents the average over the discrete volume $\bar{\Delta} = 2\Delta x 2\Delta y \Delta z$, is introduced to access scale invariance through Germano's dynamic process [1]. The according eddy-viscosity relations for the two filter levels read:

$$t_{ij} \approx C \bar{\nu}_t \bar{S}_{ij} \quad \text{and} \quad T_{ij} = \widetilde{\bar{u}_i \bar{u}_j} - \widetilde{\bar{u}_i} \widetilde{\bar{u}_j} - (\widetilde{\bar{u}_k \bar{u}_k} - \widetilde{\bar{u}_k} \widetilde{\bar{u}_k}) \delta_{ij} \approx C \bar{\nu}_t \bar{S}_{ij} \quad (3)$$

Subtracting the filtered subgrid scale stress tensor \bar{t}_{ij} from T_{ij} leads to the resolved stress tensor L_{ij} and, in consequence of eq. (3), to an equation for the unknown constant C . Applying the least-square formula, which was introduced by Lilly [3], the constant can be approximated. Additional statistical averaging (denoted by $\langle \cdot \rangle$) minimizes the error and ensures C to be positive definite.

$$L_{ij} - L_{kk}\delta_{ij} = T_{ij} - \bar{t}_{ij} \approx C(\bar{\nu}_t \bar{S}_{ij} - \widetilde{\bar{\nu}_t \bar{S}_{ij}}) = C M_{ij} \quad \Rightarrow \quad C = -\frac{1}{2} \frac{\langle L_{ij} M_{ij} \rangle}{\langle M_{ij} M_{ij} \rangle} \quad (4)$$

2. Scale similarity model

It is well-known that the strain rate tensor S_{ij} and the subgrid scale stress tensor τ_{ij} correlate very poorly. On the other hand, correlation between τ_{ij} and L_{ij} is very high, if top-hat filtering is applied. This led Liu et al. [4] to propose the scale similarity relation eq. (5), which leaves C_L unknown.

$$\tau_{ij} = C_L L_{ij} \quad \text{or} \quad t_{ij} = C_L (L_{ij} - L_{kk}\delta_{ij}) \quad (5)$$

In order to determine C_L , it is proposed to substitute eq. (3, left) and (4, left) into eq. (5, right) to obtain eq. (6, left), which can be solved for C_L with $\nu_t = \nu_{t,S}$ or $\nu_t = \nu_{t,A}$ (eq. (2)) applying the least square formula. Additional statistical averaging forces C_L to be smooth in homogeneous directions, which is necessary to ensure scale similarity of the statistically averaged tensors of resolved stresses $\langle L_{ij} \rangle$ and subgrid scale stresses $\langle \tau_{ij} \rangle$, i.e. $\langle \tau_{ij} \rangle = C_L \langle L_{ij} \rangle$.

$$\bar{\nu}_t \bar{S}_{ij} = C_L M_{ij} \quad \Rightarrow \quad C_L = \frac{\langle \bar{\nu}_t \bar{S}_{ij} M_{ij} \rangle}{\langle M_{ij} M_{ij} \rangle} \quad \Rightarrow \quad \tau_{ij} = \frac{\langle \bar{\nu}_t \bar{S}_{ij} M_{ij} \rangle}{\langle M_{ij} M_{ij} \rangle} L_{ij} \quad (6)$$

3. Results

The performance of the new model has been tested by a Large Eddy Simulation of turbulent channel flow solving eq. (1) with a finite-volume method of second-order accuracy in staggered cartesian grids. 64×64 points in (x,y)-directions and 95 points, which are refined in wall normal z-direction using a tangent hyperbolic law, resolve the computational domain extending $2\pi \times \pi \times 1$ in $x \times y \times z$ -directions. The flow is driven by a constant pressure gradient $dp/dx = 2$ and the Reynolds number equals $Re = (u_\tau H)/\nu = 360$ (ν represents the dynamic viscosity).

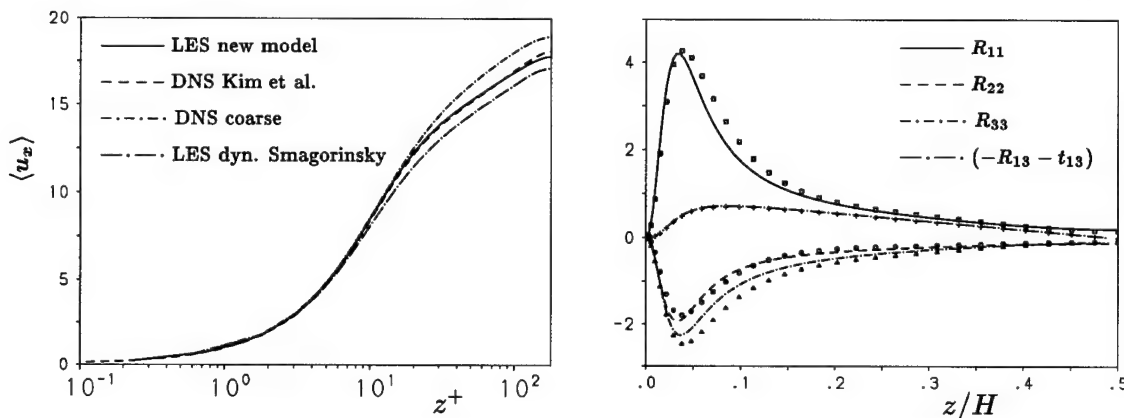


Figure 1: Mean velocity profiles (left) predicted in different LES and DNS. Profiles of the deviatoric part of the Reynolds stress tensor (right) calculated in LES with the new model (lines) and in DNS by Kim et al. (symbols).

In fig. 1 (left) the mean streamwise velocity profiles computed in a coarse direct numerical simulation (DNS) (LES without model), a LES using the dynamic Smagorinsky model and a LES with the new scale similarity model are plotted over the logarithmically scaled wall distance in wall units $z^+ = zRe$. While the coarse DNS leads to overprediction of wall shear stress, the LES with the dynamic Smagorinsky model produces the opposite. The mean velocity profile obtained with the new model utilizing $\nu_t = \nu_{t,A}$ in eq. (6), agrees remarkably well with results reported by Kim et al. [2]. It must be noted that employing $\nu_{t,S}$ instead of $\nu_{t,A}$ leads to almost identical results (not presented). Fig. 1 (right) contains profiles of the deviatoric part of the Reynolds stress tensor $R_{ij} = \langle u_i u_j \rangle - \langle u_i \rangle \langle u_j \rangle - (\langle u_k u_k \rangle - \langle u_k \rangle \langle u_k \rangle) \delta_{ij}$. The comparison with Kim et al.'s data [2] also demonstrates that the new scale similarity model produces reliable forecasts in turbulent channel flows.

4. References

- 1 GERMANO, M.: Turbulence: the filtering approach; J. Fluid Mech. A 5:1282-84 (1992).
- 2 KIM, J., MOIN, P., MOSER, R.: Turbulence statistics in fully developed channel flow at low Reynolds number; J. Fluid Mech. A 177:133-166, (1987).
- 3 LILLY, DK.: A proposed modification of the Germano subgrid scale closure method; Phys. Fluids A 4:633-35 (1992).
- 4 LIU, S., MENEVEAU, D., KATZ, J.: On the properties of similarity subgrid-scale models as deduced from measurements in a turbulent jet; J. Fluid Mech. 275:83-119, (1994).
- 5 MÉTAIS, O., LESIEUR, M.: Spectral large-eddy simulation of isotropic and stably stratified turbulence; J. Fluid Mech. 239:157-94, (1992).
- 6 SMAGORINSKY, J.: General circulation experiments with the primitive equations. I. The basic experiment; Mon. Weather Rev. 91:99, (1963).
- 7 WAGNER, C.: Direkte Numerische Simulationen turbulenter Strömungen in einer Rohrerweiterung; Dissertation, Fortschr.-Ber. VDI Reihe 7, Nr. 283, VDI Verlag, Düsseldorf, (1996).

Address: DR.-ING CLAUS WAGNER, Institut für Strömungsmechanik, DLR Göttingen, D-37073 Göttingen
Germany

WIERSCHEM, A.; SCHOLLE, M.; AKSEL, N.

Creeping Newtonian Film Flow Down an Inclined Wavy Plane. Part II

We consider the creeping film flow down an inclined wavy plane. For large wavelengths and thin films we consider two different approaches depending on the order of the amplitude of the wavy bottom profile and compare them to experimental results.

1. Introduction

The flow down an inclined plane is a well studied problem in classical hydrodynamics. However, little is known about the effects of bottom profile variations on the flow of a liquid film. Films flowing down curved surfaces have been studied theoretically by Wang [1] and numerically by Pozrikidis [2]. However, we are not aware of any experimental results concerning this subject. Additional to the study by Wang we take here another approach for small wavy perturbations. Together with a further theoretical method described in this volume [3], the different approaches are compared to first experimental findings.

2. Theoretical Approach

The film flow down a sinusoidal wavy plane has three geometrical lengths: the wavelength of the bottom profile λ , its amplitude A , and the film thickness H . Here we are interested in the case where the film is rather thin. For thick films see [3]. The wavelength is assumed to be always larger than the other two scales. Thus we may distinguish between two remaining cases: One with small amplitudes and one where the amplitude is much larger than the film thickness. In the first case we may use the ratio between amplitude and wavelength as the perturbation parameter.

$$A \approx H \ll \lambda; \quad \varepsilon = \frac{A}{\lambda} \quad H \ll A < \lambda; \quad \delta = \frac{H}{\lambda} \quad (1)$$

Both cases are treated conveniently in local coordinates. For easier comparison with experimental data, we give here the leading order results in dimensional form. In line with Wang [1] we obtain at leading order in δ the creeping film flow corresponding to the local inclination angle:

$$\begin{aligned} U &= \frac{g}{2\nu} \left[2H_0 \left(\frac{\sin \alpha}{\sin(\alpha - \theta)} \right)^{\frac{1}{3}} - Z \right] Z \sin(\alpha - \theta) \\ W &= \frac{1}{3} \frac{g}{2\nu} \left[2H_0 \left(\frac{\sin \alpha}{\sin(\alpha - \theta)} \right)^{\frac{1}{3}} - Z \right] Z^2 \cos(\alpha - \theta) \frac{\partial \theta}{\partial X} \\ H &= H_0 \left(\frac{\sin \alpha}{\sin(\alpha - \theta)} \right)^{\frac{1}{3}} \\ P &= P_{Air} + \rho g \cos(\alpha - \theta) \left[H_0 \left(\frac{\sin \alpha}{\sin(\alpha - \theta)} \right)^{\frac{1}{3}} - Z \right] - \sigma \frac{\partial^2 H}{\partial X^2} \end{aligned} \quad (2)$$

Here U , W , X , and Z are the velocity components and the coordinates parallel and orthogonal to the bottom profile, respectively. The film thickness is denoted with H and the pressure with P , whereas g , ν , α , θ , σ and H_0 are the gravitational acceleration, kinematic viscosity, mean inclination angle, inclination angle relative to the mean, surface tension and film thickness at mean inclination angle, respectively. For small amplitudes in linear order ε we obtain:

$$\begin{aligned} U &= \frac{g}{2\nu} (2H_0 - Z) Z \sin \alpha - \frac{g}{2\nu} \frac{\partial B}{\partial X} \left(\frac{4}{3} H_0 - Z \right) Z \cos \alpha \\ W &= \frac{1}{3} \frac{g}{2\nu} \frac{\partial^2 B}{\partial X^2} (2H_0 - Z) Z^2 \cos \alpha \\ H &= H_0 \left(1 + \frac{1}{3} \frac{\partial B}{\partial X} \cot \alpha \right) \\ P &= P_{Air} + \rho g (H_0 - Z) \cos \alpha - \rho g \frac{\partial B}{\partial X} \left(\frac{1}{3} H_0 \cot 2\alpha \cos \alpha + Z \sin \alpha \right) \end{aligned} \quad (3)$$

where B is the bottom profile. It gives the first correction to the solution of the creeping flow over a flat bottom.

3. Experimental System and Results

We studied the film flow of silicon oil with a dynamic viscosity of 970 mPas over a ramp with three consecutive waves of 300 mm length and 15 mm amplitude after a flat part of 1000 mm length. The latter serves to compare the flow over the wavy profile to that over a flat bottom. The film thickness has been measured from the side with a CCD-camera mounted with a microscope objective. The camera is fixed to an XYZ-transverse unit and scans the bottom and the free liquid surface.

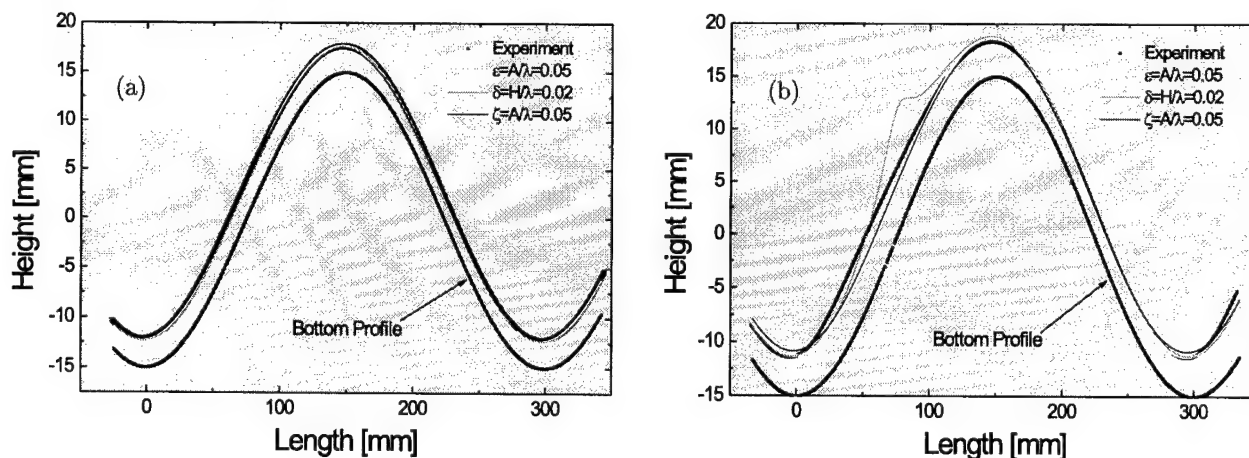


Figure 1: Comparison of experimental and theoretical film thickness for different inclination angles. (a) Reynolds number $Re = 0.04$, mean inclination angle $\alpha = 28^\circ$, (b) $Re = 0.056$, $\alpha = 18^\circ$.

Besides the two theoretical approaches with exact boundary conditions mentioned above, we compare the experimental data to the results obtained in [3]. This method consists in solving the exact volume equations and perturbing the boundary conditions for small bottom-profile amplitudes $A \ll \lambda$; $\zeta = A/\lambda$. The comparison is shown in Figure 1. All approaches match reasonably well to the experimental curve for a mean inclination angle of 28° , as seen in Figure 1(a). At leading order as considered here, Wang's result fits best the measured film thickness, yet it has the lowest expansion parameter for the experimental setup. However, at lower inclination angle the situation changes. For the ramp used, the lowest local slope becomes zero at a mean inclination of 17.4° and reaches negative values at lower tilt. Despite the fact that the bottom profile is monotonously falling at 18° mean inclination, the theoretical approaches do not describe the experiment properly as shown in Figure 1(b). They all show considerable deviations at the flat side of the profile. Neither of these approaches describes the damming up at the beginning of the flat side of the slope. Wang's approach diverges the most from the experimental curve. This is due to the base approximation of his approach. The assumption that the creeping film flow corresponds to the local inclination angle leads to extremely thick films at the flattest part of the bottom slope, which is not encountered in experiment.

Acknowledgements

The authors thank Mrs. Lepski for collaborating in carrying out the experiments.

4. References

- 1 WANG, C. Y.: Thin film flowing down a curved surface. ZAMP **35** (1984), 532–544
- 2 POZRIKIDIS, C.: The flow of a liquid film along a periodic wall. J. Fluid Mech. **188** (1988), 275–300
- 3 SCHOLLE, M.; WIERSCHEM, A.; AKSEL, N.: Creeping Newtonian Film Flow Down an Inclined Wavy Plane. Part I

Address: DR. A. WIERSCHEM, DR. M. SCHOLLE, PROF. DR. N. AKSEL, Universität Bayreuth, Lehrstuhl für Technische Mechanik und Strömungsmechanik, Universitätsstraße 30, D-95440 Bayreuth, Germany.

ZLATANOVSKI T.

Settling velocity of porous particles using the particle-in-cell model

We extend the particle-in-cell model to the case of settling porous particles. The particle swarm is assumed to consist of identical unit cells each containing a porous particle surrounded by a fluid shell. The steady axisymmetric creeping flow in this multifield unit cell model is assumed to be governed by the Stokes equation in the fluid shell and the Brinkman equation in the porous particle. Analytical solutions for the case of porous-sphere-in-cell and porous-spheroid-in-cell model are obtained.

1. Introduction

Settling operations with porous particles are encountered in many engineering applications. We apply the concept of the particle-in-cell model to computationally predict settling velocity of an assemblage of porous particles moving together in bulk through a fluid, as in sedimentation. The boundary value problem is reduced to consideration of a single particle, region (2), and its bounding fluid envelope, region (1). The volume of the fluid cell is chosen so that the porous particle volume fraction in the cell, $\gamma = V_p/V_{cell}$, equals the porous particle volume fraction of the swarm. Under the same assumptions as in the case of the rigid-particle-in-cell model [1], the non-dimensional governing equations for the porous-particle-in-cell model are

$$\Delta \mathbf{v}^{(1)} = Eu \text{Regrad} p^{(1)} \quad - \text{Stokes' equation in (1)} \quad (1)$$

$$\Delta \mathbf{v}^{(2)} - K^2 \mathbf{v}^{(2)} = Eu \text{Regrad} p^{(2)} \quad - \text{Brinkman's equation in (2)} \quad (2)$$

$$\text{div} \mathbf{v}^{(i)} = 0 \quad i = 1, 2 \quad (3)$$

where $K^2 = L^2/k$; k denotes the permeability of the porous particle, and L is an appropriate length-scale.

The boundary conditions to be satisfied on the shell-particle interface are continuity of velocity, pressure and tangential stress. On the outer fluid cell surface we apply Happel's boundary conditions, i.e., uniform velocity in the direction of main axis and vanishing tangential stress component, which are physically more realistic than Kuwabara's assumption of vanishing vorticity instead of vanishing tangential stress. Using the stream function formulation for axisymmetric creeping flow, the problem reduces to the following equations for the stream function

$$E^4 \Psi^{(1)} = 0 \quad - \text{Stokes} \quad (4)$$

$$E^4 \Psi^{(2)} - K^2 E^2 \Psi^{(2)} = 0 \quad - \text{Brinkman}, \quad (5)$$

and the equations $\Delta p^{(i)} = 0$, $i = 1, 2$ for the pressure in the two flow regions, which are all to be solved using the above specified boundary conditions, and where E^2 is the Stokes differential operator in the specified coordinate system.

2. The case of a porous-sphere-in-cell

For this case we have obtained a closed form solution of the problem. The settling velocity of a swarm of porous spherical particles, U , relative to the settling velocity of a single particle of the swarm alone, U_0 , is given by

$$\frac{U}{U_0} = \frac{3 \left(1 - \frac{\tanh K}{K}\right) A - B \tanh K}{2K^2 + 3 \left(1 - \frac{\tanh K}{K}\right) C - D \tanh K} \quad (6)$$

where $A = 90s^5 K + (3 + 42s^5 - 30s^6) K^3 + (2 - 3s + 3s^5 - 2s^6) K^5$, $C = 3K^2 + 2K(15 + K^2)s^5$, $B = 90s^5 + (3 + 72s^5 - 30s^6) K^2 - (3s - 15s^5 + 12s^6) K^4$, $D = 3K^2 + 6(5 + 2K^2)s^5$, and $K = b/\sqrt{k}$, $s = \sqrt[3]{\gamma}$, $\gamma = (b/a)^3$, b = particle diameter, a = diameter of the fluid shell outer surface. In the limiting case as $k \rightarrow 0$ we obtain the

expression for the relative settling velocity of a swarm of rigid spherical particles as given in [1]. Figure 1 shows the computed streamline pattern of a porous-sphere-in-cell structure.

3. The case of a porous-spheroid-in-cell

The case of settling elongated axisymmetric porous particles can be best modeled by the porous-prolate-spheroid-in-cell approach. However, this problem is more complicated than the former one, and there is no closed form solution of this problem, even for the rigid-spheroid-in-cell model. The rigid-spheroid-in-cell model was treated in [2]. The problem of Stokes/Brinkman flow past and through a single porous spheroid in uniform far-field flow was solved in [3]. To solve the present problem we have derived and used appropriate general solutions of the Brinkman, Stokes and the Laplace equations in spheroidal coordinates. From our numerical calculations to this problem we give here (Figure 2) the streamline pattern for a porous prolate spheroidal particle in confocal fluid shell.

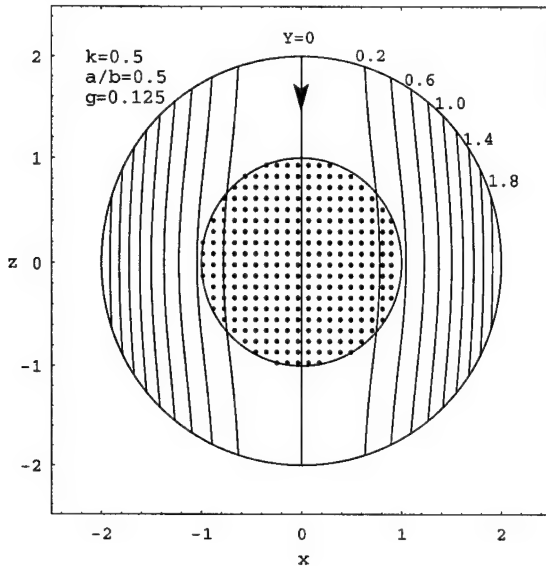


Figure 1: Streamline pattern of a porous-sphere-in-cell

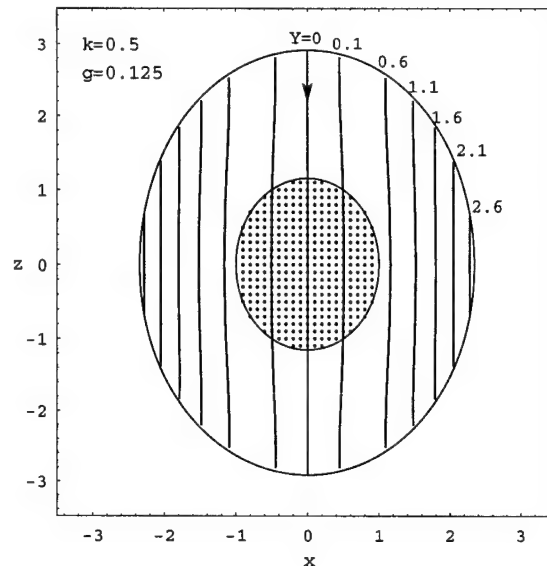


Figure 2: Streamline pattern of a porous-spheroid-in-cell (semi focal distance $c = \sqrt{3}$)

4. Conclusions

Unit cell models have proven to be a very useful approach in the analytical treatment of complex flows involving a great number of particles. In the most cases, such models consider only impermeable spherical particles. Here we have employed the concept of particle-in-cell model to the case of sedimenting swarm of porous particles, using the widely accepted Brinkman equation for the flow through the porous medium of the particles. We have solved the boundary value problem arising in this type of particle-in-cell model both for the case of porous spherical and spheroidal particles.

In order to find to which extent the analytical solutions here obtained agree with the real situation, measurements of settling time and terminal velocity of sedimenting porous particles have to be performed.

5. References

- 1 HAPPEL, J., BRENNER, H.: Low Reynolds Number Hydrodynamics; Prentice-Hall, Englewood Cliffs 1965.
- 2 DASSIOS, G., HADJINICOLAOU, M., COUTELIERS, F. A., PAYATAKES, A. C.: Stokes flow in spheroidal particle-in-cell models with Happel and Kuwabara boundary conditions; *Int. J. Eng. Sci.* **33** (1995), 1465–1490.
- 3 ZLATANOVSKI, T.: Axisymmetric creeping flow past a porous prolate spheroidal particle using the Brinkman model; *Q. Jl. Mech. appl. Math.* **52** (1999), 111–126.

Address: PROF. DR. TOMISLAV ZLATANOVSKI, Faculty of Mechanical Engineering,
Saints Cyril and Methodius University, 91000 Skopje, Republic of Macedonia

HENSELOWSKY, C.; KUHLMANN, H. C.; RATH, H. J.

Heat transfer from hot wires at small forced-flow velocities

At very low velocities ($v \leq 0.1$ m/s), hot-wire measurements are significantly influenced by free convection. To assess the contribution of free-convection heat transfer to the heat balance of hot-wire probes, measurements under gravitational and under microgravity conditions are compared in a velocity range $0 \leq v \leq 0.3$ m/s corresponding to a Reynolds number range $Re \leq 0.1$. The measurements were made with horizontal hot-wire probes in cross flow in air at 21.8°C . For creeping flow three distinct regions can be observed in which different factors dominate the heat transport. While free convection prevails at $Re = 0$, forced convection dominates for $Re > Gr^{1/3}$. At intermediate Reynolds numbers both transport mechanisms must be considered.

1. Introduction

The heat transfer from hot wires in low-velocity forced flows can be significantly influenced by buoyancy effects. In order to quantify this buoyant contribution to the total heat transfer, experiments under weightlessness were compared with laboratory measurements. The microgravity (μg) measurements have been carried in the *Drop Tower Bremen* which provides a reduced gravity level of $10^{-5}g$ during a period of 4.7 s. In this work two wires with different aspect ratios $\Gamma = l/d$, where l and d are the wire length and the wire diameter, respectively, were investigated at different wire temperatures. Measurements have been made with horizontal hot wires placed normal to a horizontal air stream. The experimental setup is described in [3].

2. Dimensionless numbers and probe dimensions

All fluid properties like the kinematic viscosity ν , thermal expansion coefficient β , thermal conductivity λ , and thermal diffusivity κ to determine the dimensionless Reynolds number $Re = U \cdot d/\nu$, Nusselt number $Nu = \alpha \cdot d/\lambda$, Grashof number $Gr = g \cdot d^3 \cdot \beta \cdot (T_w - T_a)/\nu^2$, and Prandtl number $Pr = \nu/\kappa$ have been evaluated at the film temperature T_f which is defined as the arithmetic mean of the wire temperature T_w and the fluid temperature T_∞ . The diameters of the hot wires used were so small that the molecular nature of air had to be taken into account. Therefore, the Nusselt number was recalculated to a continuum Nusselt number $Nu_c = Nu/(1 - 2 \cdot Kn \cdot Nu)$, where Kn is the Knudsen number; see [2]. The probe properties are specified in Table 1.

Probe	Material	Wire ends	Length [mm]	Diameter [μm]	Aspect ratio Γ
1. TSI 1210-T1.5	W/Pt	coated	1.27	3.8	334
2. HFI	W/Pt	uncoated	4.0	5.0	800

Table 1: Probe properties

3. Results

Figure 1 shows the calibration curves for $1g$ and μg measurements for different wire temperatures. Below a certain threshold Reynolds number Re_* , both curves differ, while they coincide for $Re > Re_*$, where Re_* was found graphically from the figures below. For $Re > Re_*$ the both Nusselt-number curves follow the modified King law $Nu_c = A + BRe^n$ [4] with different calibration constants (A,B,n). For $Re < Re_*$ the Nusselt numbers measured under μg conditions are well described by a linear dependence $Nu_c = a + bRe$.

Collis and Williams [2] found experimentally that the influence of free convection can be neglect when $Re > Gr^{1/3}$. Table 2 shows a comparison of this criterion [2] with the experimentally determined range of transition Reynolds numbers Re_* for different overheat ratios. For the short TSI-hot-wire probe the transition-Reynolds-number values are in good agreement with the classical criterion. For the wire with high aspect ratio (HFI) the measured transitional Reynolds numbers are slightly larger than predicted by [2].

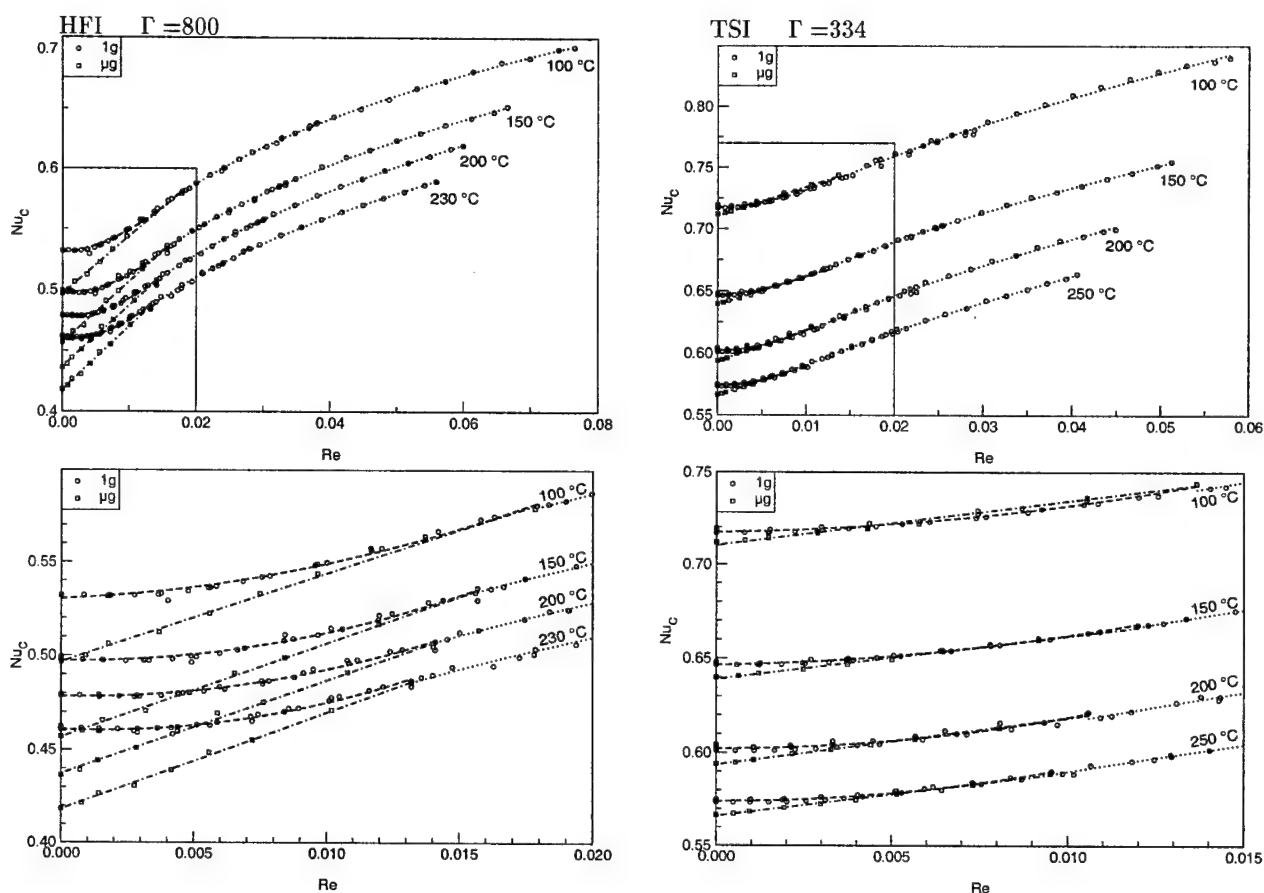


Figure 1: Heat-transfer Nusselt numbers for 1g and μ g conditions. The lower figures show magnifications of the regions boxed in the upper figures

	HFI	TSI
$Re > Gr^{1/3}$	0.009 – 0.0098	0.0070 – 0.0074
Re_* found here	0.013 – 0.0180	0.0067 – 0.0087

Table 2: Comparison of the measured transition-Reynolds-number range with the classical criterion by [2]. The range is determined by the different overhear ratios.

Acknowledgements

This work has been supported by DFG and DLR e.V. We are very grateful to the Hermann-Föttinger-Institut for custom manufacturing of the high-aspect-ratio probe (HFI).

4. References

- 1 BRUUN, H.H.: Hot-Wire Anemometry - Principles and signal analyses. Oxford University Press (1995).
- 2 COLLIS, D.C. AND WILLIAMS, M.J.: Two-dimensional convection from heated wires at low Reynolds numbers. J. Fluid Mech. 6 (1959), 357–384.
- 3 HENSELOWSKY, C. AND KUHLMANN, H.C. AND RATH, H.J.: Experimental Setup for Low Reynolds Number Calibration of Thermal Anemometers. ZAMM 80/3 (2000), 685–686.
- 4 KING, L.V.: On the Convection of Heat from Small Cylinders in a Stream of Fluid: Determination of the Convection Constants of Small Platinum Wires with Applications to Hot-Wire Anemometry. Phil. Trans. Roy. Soc. A214 (1914), 373–432.

Addresses: HENSELOWSKY, C.; PRIV. DOZ. KUHLMANN, H.C.; PROF. DR. RATH, H.J., ZARM – University of Bremen, Am Fallturm, D-28359 Bremen, Germany, e-mail: marvin@zarm.uni-bremen.de.

HOŻEJOWSKI L., HOŻEJOWSKA S., SOKAŁA M.

Stability of solutions for some inverse heat conduction problems by heat functions method

1. Heat functions for transient problems of heat conduction in (r, t) -coordinates

The heat functions of the first and second kind, $g_n(r, t)$ and $u_n(r, t)$, are defined as the coefficients of p^{2n} in the power series expansion of the generating functions, respectively

$$U(r, t, p) = I_0(pr)e^{p^2 t},$$

$$W(r, t, p) = K_0(pr)e^{p^2 t} + (\gamma + \ln \frac{p}{2})I_0(pr)e^{p^2 t},$$

where γ is Euler's constant. Both $g_n(r, t)$ and $u_n(r, t)$ are clearly solutions of the heat equation

$$\frac{\partial^2 T}{\partial r^2} + \frac{1}{r} \frac{\partial T}{\partial r} = \frac{\partial T}{\partial t}, \quad t \geq 0, a \leq r \leq b,$$

and therefore show good applicability for problems governed by this equation. A more detailed investigation of their properties can be found in [1].

2. Solution of some inverse problems by heat functions method

The solution of a boundary value problem in a long (possibly hollow) cylinder Ω can be approximated with a linear combination of the heat functions

$$T(r, t) \approx \theta^{(k)}(r, t) = \sum_{n=0}^N c_n^{(k)} g_n(r, t) + \sum_{m=0}^M d_m^{(k)} u_m(r, t), \quad r \in \Omega, k\Delta t \leq t \leq (k+1)\Delta t, k = 0, 1, 2, \dots$$

The coefficients $c_n^{(k)}$ and $d_m^{(k)}$ are chosen to minimize the functional whose terms represent the residuals at the boundaries. The approximate formula for $T(r, t)$ can be extended beyond the region of the direct problem to be used for solution of an inverse problem.

3. Stability of the computational algorithm

Suppose the boundary temperature of a long solid cylinder is to be inferred from the initial temperature distribution and the temperature histories at a certain inner location. Measurements of temperature contain errors: $\delta T^{(k)}$ in the current time interval and $\delta T^{(k-1)}$ in the previous time interval. They cause error of the solution, $\delta \theta^{(k)}$, and the relationship between these quantities is given in the form

$$\delta \theta^{(k)} = A \delta T^{(k-1)} + B \delta T^{(k)}$$

in which A and B are certain matrices.

If we demand that the error should not propagate with time, the condition $\|A\|_S < 1$ must be satisfied. ($\|A\|_S$ is largest of the eigenvalues of the matrix AA^T).

4. Numerical examples

Example 1. A long solid cylinder (radius $R = 0.02\text{m}$, $\alpha = 14.4 \times 10^{-6}\text{m}^2/\text{s}$ is initially at 0°C . The measurements of temperature at $r = 0.0198\text{m}$ are taken with the time step $t_{step} = 0.14\text{s}$. The unknown to solve for is the temperature at $r = R$. The graph shows how stability condition is satisfied when Δt grows from 0.28s to 2.8s and $M = 0$ and $N = 4, 6, 9$.

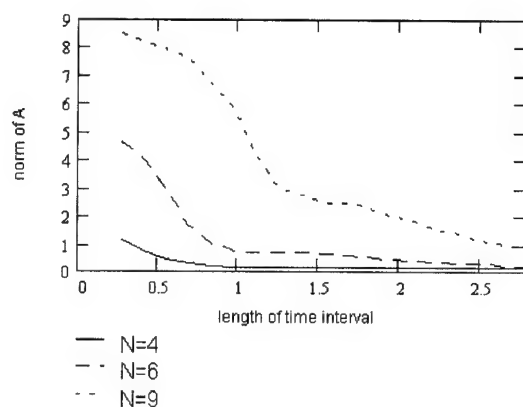


Fig. 1 Values of $\|A\|_S$ for various lengths of the time interval Δt

Example 2. A long hollow cylinder of radius $a \leq r \leq b$, ($a = 0.01\text{m}$, $b = 0.05\text{m}$, $\alpha = 6.76 \times 10^{-6}\text{m}^2/\text{s}$) is initially at 60°C . For times $t > 0$ heat is dissipated by convection from the boundary surface at $r = a$ into a surrounding at 24°C ($h = 2 \times 10^4\text{W}/\text{m}^2\text{K}$). Measurements of the temperature at $r = 0.48\text{m}$ are taken with the time step t_{step} a) 0.7s , b) 1.8s . The results are presented for $M = N = 2$ and $M = N = 3$. The graph shows $\|A\|_S$ when Δt changes from a) 0.7s to 19s , b) 1.8s to 19s

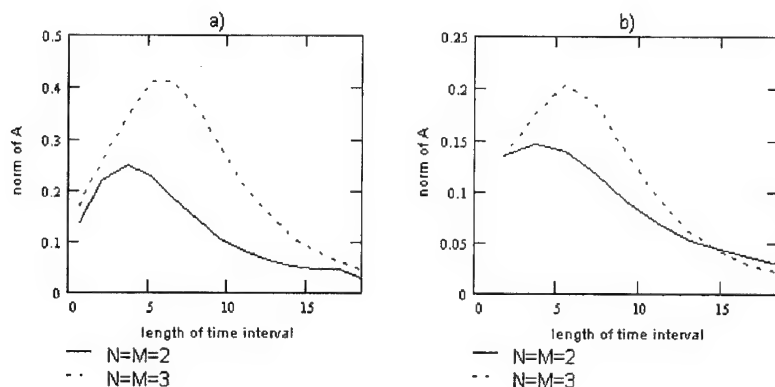


Fig. 2 Values of $\|A\|_S$ when both kinds of the heat functions are used

The obtained results show that propagation of the measurement errors is smaller when t_{step} increases and when fewer heat functions of either kind are used in the solution. When M , N and t_{step} are fixed, it is possible to find such a length of the time interval Δt for which the condition $\|A\|_S < 1$ is satisfied.

5. References

- 1 FUTAKIEWICZ S.: Heat functions method for solving direct and inverse heat conduction problems, (in Polish), Politechnika Poznańska, Ph.D. Thesis, 1999

Addresses: LESZEK HOŻEJOWSKI, SYLWIA HOŻEJOWSKA, MAŁGORZATA SOKAŁA,
Kielce University of Technology Al. 1000-lecia PP 7, 25-314 Kielce, Poland
e-mail: hozej@tu.kielce.pl, ztspst@tu.kielce.pl, sokala@tu.kielce.pl

HRIBERŠEK, M.

Inexact Newton-Krylov Methods for Nonlinear Forced Heat Convection Problems by BEM

A preconditioned inexact Newton-Krylov nonlinear iterative method is constructed for computation of nonlinear heat transfer problems by Boundary Element Methods. The performance of the iterative method is tested on conjugate heat transfer problem in a thick wall channel.

1. Problem definition

Applying an approximation method for a solution of conjugate heat transfer problem inevitably leads to nonlinear systems of equations, which have to be solved in order to obtain a numerical solution to a selected problem. This is also the case with Boundary-Domain Integral Method (BDIM) [1], a version of Boundary Element Method for fluid flow and heat transfer problems.

As a frame for the solution the diffusion-convective heat transport equation was chosen,

$$\frac{DT}{Dt} = \kappa \frac{\partial^2 T}{\partial x_j \partial x_j}, \quad (1)$$

which is in BDIM transformed into an algebraic equivalent [1]:

$$[H_t]\{T\} = \frac{1}{\kappa}[G_t]\left\{\kappa \frac{\partial T}{\partial n} - T v_n\right\} + \frac{1}{\kappa}[D_{ti}][\hat{v}_i]\{T\} + [B_t]\{T\}_{F-1}, \quad (2)$$

with κ being the thermal diffusivity. With known velocity vector field and given boundary and initial conditions the task of the solution algorithm is to compute the corresponding temperature and its derivatives field in the fluid and solid part of the computational domain. The equation (2) is a nonlinear one and can be written in general form as N nonlinear equations with variables $x_i, i = 1, 2, \dots, N$:

$$\mathbf{F}(\mathbf{x}) = 0, \quad F_i(x_1, x_2, \dots, x_N) = 0, \quad i = 1, 2, \dots, N. \quad (3)$$

In case of equation (2) we can construct the $\mathbf{F}(\mathbf{x}) = 0$ as follows. After applying boundary and initial conditions to the selected heat transfer problem the following nonlinear equations set is obtained:

$$\mathbf{A}\mathbf{x} = \mathbf{b}(\mathbf{x}), \quad \mathbf{b}(\mathbf{x}) = \mathbf{b}_{BC} + \mathbf{b}_v(\mathbf{x}), \quad (4)$$

where \mathbf{b}_{BC} is the right hand side (RHS) vector due to boundary and initial conditions and $\mathbf{b}_v(\mathbf{x})$ is on \mathbf{x} dependent RHS vector due to variable velocity field. Unknowns \mathbf{x} are T and $\frac{\partial T}{\partial n}$. Hence,

$$\mathbf{A}\mathbf{x} - \mathbf{b}_v(\mathbf{x}) - \mathbf{b}_{BC} = 0 \quad \rightarrow \quad \mathbf{F}(\mathbf{x}) = \mathbf{A}\mathbf{x} - \mathbf{b}_v(\mathbf{x}) - \mathbf{b}_{BC}. \quad (5)$$

2. Nonlinear solution algorithm

For the solution of equation (3) the inexact Newton-Krylov method [2] was selected. It's main advantage over the standard Newton's method is a global convergency for almost any initial guess. In the general Newton's algorithm,

$$\mathbf{J}\delta\mathbf{x} = -\mathbf{F}^n(\mathbf{x}), \quad \rightarrow \quad \mathbf{x}^{n+1} = \mathbf{x}^n + \delta\mathbf{x}, \quad (6)$$

the Jacobian \mathbf{J} of the system \mathbf{F} is now computed approximately using the finite difference formula:

$$\mathbf{J} = \begin{bmatrix} \frac{\partial F_1}{\partial x_1} & \frac{\partial F_1}{\partial x_2} & \dots & \frac{\partial F_1}{\partial x_N} \\ \vdots & \vdots & \dots & \vdots \\ \frac{\partial F_N}{\partial x_1} & \frac{\partial F_N}{\partial x_2} & \dots & \frac{\partial F_N}{\partial x_N} \end{bmatrix}, \quad \frac{\partial F_i}{\partial x_j} = \frac{F_i(\mathbf{x} + h_j \mathbf{e}_j) - F_i(\mathbf{x})}{h_j}, \quad (7)$$

with $h_j = \sqrt{\eta} \text{MAX}\{|x_j|, \text{typ } x_j\} \text{sign}(x_j)$ the stepsize, η = the relative error in computing $F_i(\mathbf{x})$ (machine epsilon) and $\text{typ } x_j > 0$ the typical size of x_j . Evaluation of Jacobian \mathbf{J} in BDIM is computationally favourable, as the use

of macro element with Subdomain technique allows local (element-wise) evaluation of \mathbf{J} and as a result the \mathbf{J} has the same sparsity pattern a system matrix \mathbf{A} , saving computer memory. Another important and decisive feature of Inexact Newton's method is only approximate computation of the Newton's step $\delta\mathbf{x}$.

In the process of searching of the solution to (3) the method has to decide whether the new step $\delta\mathbf{x}$ leads to convergence. Among different strategies for adopting $\delta\mathbf{x}$ the linesearch backtracking technique [2] was applied, where the check whether \mathbf{F} is being minimized by the new step is performed as

$$\|\mathbf{J}(\mathbf{x}^n)\delta\mathbf{x} + \mathbf{F}(\mathbf{x}^n)\| < \eta\|\mathbf{F}(\mathbf{x}^n)\|, \quad (8)$$

with forcing term $\eta \in [0, 1]$. If (8) holds, $\delta\mathbf{x}$ is accepted, otherwise backtracking search is performed along the descent direction for $f = \frac{1}{2}\mathbf{F}\mathbf{F}$ to find a new $\delta\mathbf{x}$. To ensure low number of backtracks in the early stages of nonlinear loop and to increase the convergency in the vicinity of the solution, a dynamic setting of $\eta = (0.5)^n$ (n =nonlinear loop) was applied.

It is important to realize that the norm of \mathbf{F} in (8) appears also as a norm to minimize when a Krylov method is applied for the solution of the step $\delta\mathbf{x}$ in (6). Therefore, choosing a monotonically converging Krylov method, like GMRES [2], ensures a fast solution to the linear problems together with a decrease of the norm of the nonlinear function \mathbf{F} , hence leading to a fast and reliable nonlinear solution. The nonlinear iterative method is therefore based on Newton-Krylov iterations. In order to increase convergence of GMRES and to avoid problems with rising memory demands of GMRES as linear iterations increase, preconditioning from the right has to be applied, i.e.

$$\mathbf{J}\delta\mathbf{x} = -\mathbf{F} \rightarrow \mathbf{J}\mathbf{Q}^{-1}\mathbf{Q}\delta\mathbf{x} = -\mathbf{F}. \quad (9)$$

Due to changing value of the stopping criterion η during nonlinear iterations a flexible preconditioning was applied, resulting in the use of the diagonal preconditioning in the early stages and the level based fill-in (ILU(1)) incomplete lower upper factorization [1] in the rest of nonlinear iterations. For large value of η low value of l was selected (ILU(0)), and for small value of η a higher value of l (ILU(1)-ILU(4)) was selected.

3. Results and conclusions

Conjugate forced heat convection in a thick wall channel with constant outside wall temperature, Fig.1 (left), was computed with the use of different nonlinear iteration schemes. Computational mesh consisted of 480 cells. The Peclet number value, based on the channel height, was 100. As can be observed, Fig.1 (right), the underrelaxation scheme is very sensitive to the choice of underrelaxation parameter Θ and converges only for smaller values, whereas Inexact Newton-GMRES method converges almost quadratically. Hence, the inexact Newton-Krylov method presents a strong alternative to commonly used nonlinear iteration schemes in BEM.

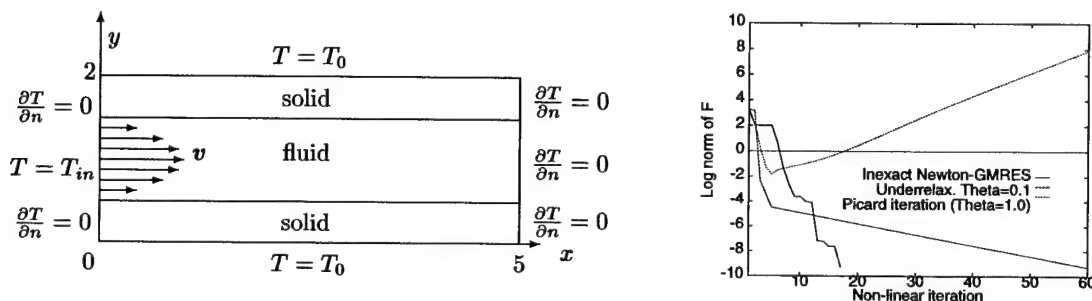


Figure 1: Computational domain and boundary conditions (left), convergence of nonlinear iterative methods (right)

4. References

- 1 HRIBERŠEK, M., ŠKERGET, L.: Fast Boundary-Domain Integral Algorithm for Computation of Incompressible Fluid Flow Problems; Int. J. Num. Meth. Fluids 31, (1999), 891-907.
- 2 BROWN, P.N., SAAD, Y.: Hybrid Krylov methods for nonlinear systems of equations; SIAM J. Sci. Statist. Comput., 11 (1990), 450-481.

Addresses: DR. MATJAZ HRIBERŠEK Faculty of Mechanical Engineering, Smetanova 17, 2000 Maribor, Slovenia.

LEE, Y.-S.; KUHLMANN, H. C.; RATH, H. J.; CHUN, CH.-H.

Stability of thermocapillary flow in cylindrical liquid bridges: Rotation of the hot disk

The thermocapillary flow in a differentially heated cylindrical liquid bridge under steady rotation of the hot disk is considered in the limit of zero capillary number. Steady flow states and their three-dimensional stability are calculated numerically. It is shown that the vortex breakdown caused by the rotation is strongly affected by the thermocapillary flow. A linear stability analysis reveals that the most dangerous perturbations are oscillatory with azimuthal wavenumber $m = 1$ or $m = 2$ depending on the parameters.

1. Introduction

We consider a differentially heated cylindrical liquid volume of radius R under steady rotation of the hot upper disk, separated from the cold disk by a distance d , in the limit of zero capillary number and zero gravity. This *half-zone* models the float-zone crystal-growth process. The thermocapillary driving force is generated by vertical temperature difference ΔT along the cylindrical surface. Adiabatic condition is imposed along the free surface.

Re is the Reynolds number defined by $Re = \gamma \Delta T d / \rho_0 \nu^2$. The rotational Reynolds number for the hot disk rotation is defined as $Re_\Omega = \Omega d^2 / \nu$. The Prandtl number is $Pr = \nu / \kappa$, and the aspect ratio $\Gamma = d / R$.

2. Numerical methods

The basic steady axisymmetric flow (u_0, p_0, θ_0) is calculated by a mixed finite-difference and Chebyshev collocation method [1] and its stability is investigated by solving the linearized equations with normal modes $\sim e^{(\alpha + i\omega)t} e^{im\varphi}$. From the resulting generalized eigenvalue problem, the critical conditions are found by seeking the zero of the growth rate α over azimuthal wave numbers up to $m = 6$ and all normal modes. Typical grid sizes are $N_r \times N_z = 32 \times 100$. More details on the numerical methods are given in [1].

3. Axisymmetric steady state: vortex breakdown

Without hot disk rotation, there exists an axisymmetric toroidal thermocapillary flow directed downwards (towards the cold wall) on the free surface and upwards near the axis, as shown in Fig. 1a for $\Gamma = 1.0$ and $Pr = 0.02$. The thermocapillary flow is enhanced by the secondary flow due to the hot disk's rotation. At a constant rotation rate $Re_\Omega = 800$ of the hot disk, vortex breakdown appears on the axis if the Reynolds number Re exceeds a certain value, as can be seen in Fig. 1b. The separation bubbles grow as the Reynolds number increases, a behavior very similar to the one in lid-driven confined swirling flows [2]. While vortex breakdown can appear when the rotational Reynolds number Re_Ω is increased at a fixed Reynolds number Re , it can also disappear again on a further increase of Re_Ω .

4. Linear stability analysis

A linear stability analysis shows that the flows shown in Figs. 1e and 1a are neutrally stable; those in Figs. 1b-d are linearly stable. We find that rotation of the hot disk generally stabilizes the thermocapillary flow. Results on the critical Reynolds number Re_c are shown in Fig. 2. For low Pr and in the absence of rotation (Fig. 1a) the critical mode is steady [1] (with $m = 1$ for $Pr = 0.02$ and $\Gamma = 2$). When the hot boundary rotates, the critical mode becomes unsteady with a frequency growing linearly from $\omega_c = 0$. In some cases, we observe a change of the critical wave number between $m = 2$ and $m = 1$ (cf. Fig. 2a). In the case of high Prandtl numbers the critical mode for $Re_\Omega = 0$ is already oscillatory and there exists a pair of azimuthally traveling waves with frequencies $\pm\omega$. We find different actions of the rotation on the pair of traveling waves. The rotation of the hot disk monotonically stabilizes the thermocapillary flow when the rotation direction is the same as the one of traveling wave (prograde mode), while the rotation slightly destabilizes the flow when the rotation direction is opposite to the one of traveling wave (retrograde mode) near $Re_\Omega = 0$. On a further increase of Re_Ω , however, the flow becomes stabilized monotonically. The stability boundary of the retrograde mode is lower than that of the prograde mode, as shown in Fig. 2b.

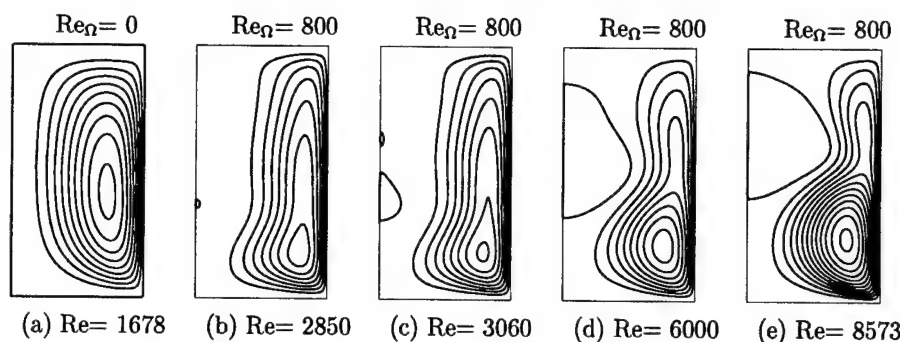


Figure 1: Streamlines of the meridional flow showing the appearance of vortex breakdown with increasing Reynolds number Re for $Re_\Omega = 800$, $Pr = 0.02$, and $\Gamma = 2.0$. Two breakdowns are visible in (c).

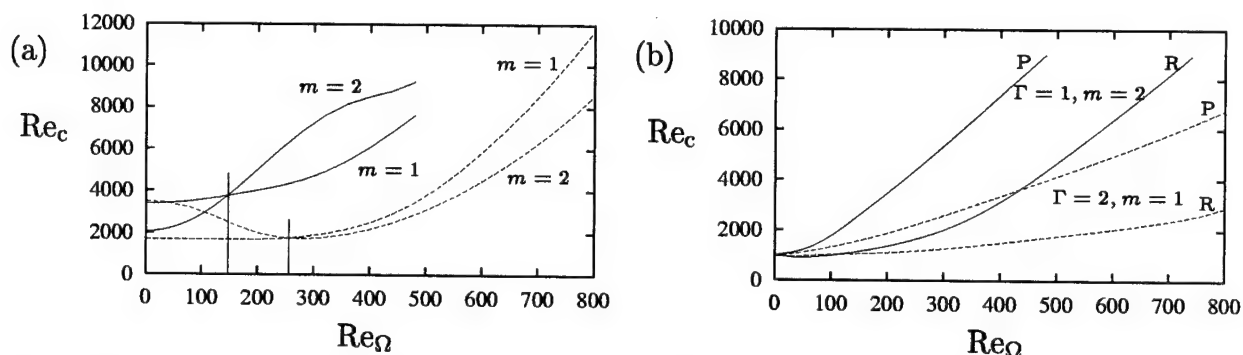


Figure 2: Dependence of the critical Reynolds number Re_c on the rotational Reynolds number Re_Ω . $\Gamma = 1$ —, $\Gamma = 2$ - - - - -. (a) $Pr = 0.02$, (b) $Pr = 4$. P indicates the prograde mode, R the retrograde mode.

5. Conclusion

It is shown that the vortex breakdown caused by the rotation of the hot disk is strongly affected by the thermocapillary flow in the Prandtl-number range $0.02 \leq Pr \leq 4$ and for aspect ratios $1 \leq \Gamma \leq 2$. A linear stability analysis reveals that the most dangerous perturbations are oscillatory with azimuthal wavenumber $m = 1$ or $m = 2$ depending on the parameters.

Acknowledgements

Support by KOSEF is gratefully acknowledged.

6. References

- 1 WANSCHURA, M.; SHEVTSOVA, V. M.; KUHLMANN, H. C.; RATH, H. J.: Convective instability mechanisms in thermocapillary liquid bridges. *Phys. Fluids* **7** (1995), 912–925.
- 2 GELFGAT, A. Y.; BAR-YOSEPH, P. Z.; SOLAN, A.: Stability of confined swirling flow with and without vortex breakdown. *J. Fluid Mech.* **311** (1996), 1–36.

Addresses: YOU-SEOP LEE, HENDRIK C. KUHLMANN, HANS J. RATH, Universität Bremen, ZARM, Am Fallturm, D-28359 Bremen

CHUNG-HWAN CHUN, Pohang University of Science and Technology, Department of Mechanical Engineering, San 31 Hyoja-Dong, Pohang 790-784, South Korea

M. MARCIC, M. ZGONIK, J. AVSEC

Combustion of the Diesel Fuel Spray

The paper deals with the computer simulation of the Diesel fuel spray combustion under the similar conditions as in Diesel engines. A mathematical model of the spray propulsion and combustion is treated which allows the observation of the phenomena in the spray during its movement through air. Fuel droplets of the spray are vaporized due to the transfer of heat from hot air. In a certain moment when required conditions are met selfignition of mixture occurs. In order to determine the points where selfignitions occurs first, we have introduced the term "ignition probability" referring to the local air ratio and fuel dispersion in the spray.

1. The Physical Model

The paper deals with the computer simulation of the Diesel fuel spray combustion under the similar conditions as in Diesel engines. The mathematical model of combustion consists of submodels describing individual combustion stages. The paper describes in detail only the fuel ignition stage. The mathematical model of the Diesel spray (Fig. 1) is obtained from the continuity and momentum equation. Spray is divided into small elementary volume. The mathematical model allows the computation of the quantity of fuel and fuel vapours, air, mean, maximum and minimum fuel droplet diameter [1] as well as their number in each elementary volume. Due to the varying fuel output velocity $u(t)$ from the nozzle and different positions of elementary volumes in the spray, their velocities differ one from another. We assume that inside each elementary volume all the droplets move at the same velocity.

The most efficient combustion with regard to the consumption and emission will be in those elementary volumes containing the stoichiometric air ratio and the fuel droplets with the lowest mean diameters. At the same time, there is a strong probability that under normal operating conditions in Diesel engines self-ignition the fuel vapour-air mixture occurs in those elementary volumes containing stoichiometric air ratio and fuel droplets with the lowest diameters. In order to determine the points or elementary volumes where self-ignition occurs first, we have introduced the term "ignition probability" Ψ referring to the local air ratio and fuel dispersion quality in the spray.

$$\Psi = \Psi_c \Psi_d \leq 1 \quad (1)$$

The term Ψ_c takes into account the local air ratio in the spray and has the highest value for stoichiometric air ratio. In the equation 2 m_g is mass of fuel and m_a is mass of air.

$$\Psi_c = \exp \left[-ABS \ln \frac{\Phi_r}{\Phi_s} \right] \quad \Phi_r = \frac{m_g}{m_a} \quad \Phi_s = \left(\frac{m_g}{m_a} \right)_{stoichiometric} \quad (2)$$

Ψ_d takes into account the fuel spray dispersion quality and has the maximum value at the droplet diameter $d_{opt} = 0.0065$ mm. This diameter is considered the optimum for combustion in Diesel engines. The droplets with the diameter 0.0065 mm may already be treated as those burning as a gas [2]. In the equation 3 d_m is a mean droplet diameter in each elementary volume.

$$\Psi_d = \frac{1}{3\sigma_0 (2\pi)^{\frac{1}{2}}} \exp \left[-\frac{1}{2} \left(\frac{d_m - d_{opt}}{3\sigma_0} \right)^2 \right] \quad \sigma_0 = ABS(d_m - d_{min}) \quad (3)$$

The points where Ψ has equal value are joint into curves so as to obtain the areas where the self-ignition probability is the strongest. In the point s_t (Fig.1), the fuel jet changes from the fully liquid into the spray containing air, fuel vapours and fuel droplets. To calculate the evaporation of fuel droplets we used the law of droplet evaporation[3].

2. Computer Simulation and Comparison with Measured Results

The simulation results of the combustion of Diesel spray injected into stagnant 832°C/10 bar air are presented. The injected fuel amount is 128 mm³/cycle and the duration of injection 1,84 ms. The highest probability of the

mixture self-ignition is at the end of the spray (Fig. 2) where the majority of the fuel has been evaporated, the droplets have very low diameters and the local air ratio is approximately one.

The experiments have been carried out in a combustion bomb allowing the measurements of spray diameter, concentration in spray, combustion temperature and combustion shooting. Fig. 3 shows the radial temperature distribution in the spray at the distance of 40 mm from the injection nozzle. The matching of the measured and computed temperatures is good over the entire cross section of the spray.

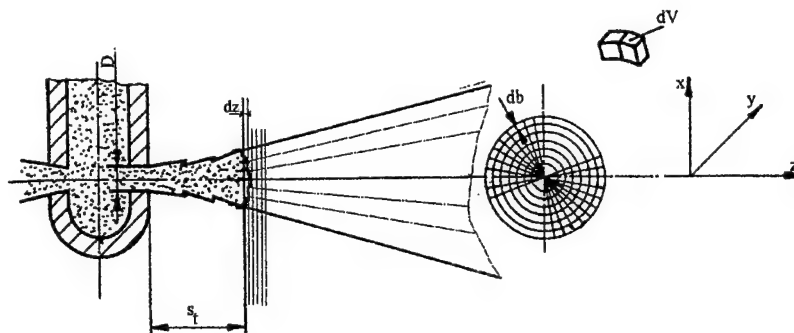


Fig. 1: Diesel spray

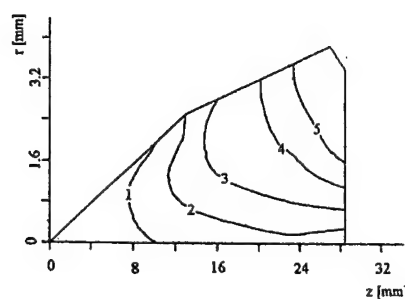


Fig. 2: Probability of the mixture self-ignition

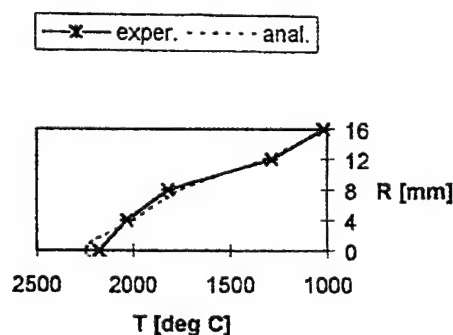


Fig. 3: Measured and computed temperature

3. References

- 1 Sinamon J. V., Lancaster A. N., Steiner I. C.: An Experimental and Analytical Study of Engine Fuel Spray Trajectories, SAE 800135
- 2 Chiger, N.: Energy and Combustion Science, Pergamon Press, London, New York, 1978.
- 3 Hiroyasu, H., Kadota, T., Arai, M., Development and Use of a Spray Combustion Modelling to predict Diesel Engine Efficiency and Pollutant Formation, JSME 26, No. 214, 1984, Part I, II, III.

Addresses: Milan Marcic, University of Maribor, Smetanova 17, 2000 Maribor

H. MOCIKAT, J. PRAŽÁK, ST. GÖPPERT, H. HERWIG

Konvektiver Wärmeübergang bei instationärer Anströmung

Der Einfluss instationärer Strömungen, z.B. rotierender oder pulsierender Prallstrahlen, auf den Wärmeübergang an einer angeströmten Platte wird mit Hilfe gemessener Temperatur- und Wärmestromfelder untersucht. Die Bewertung der Strömungsvarianten mit Wärmeübergangs-Koeffizienten α bzw. Nußelt-Zahlen Nu ist problematisch, weil α unstetig werden kann und die charakteristische Länge der Nu -Zahl für verschiedenste Düsenkonstruktionen schlecht vergleichbar ist. Deshalb wird eine neue Auswertung mit Hilfe der Parameter "Leistung des Prallstrahls" sowie einer Effektivitäts-Kennzahl E vorgestellt.

1. Einführung

Stationäre Prallstrahlen bewirken an den beaufschlagten Flächen einen sehr intensiven konvektiven Wärmeübergang und sind deshalb ausführlich untersucht worden [1]. Üblicherweise werden die experimentellen Ergebnisse in der Form $\alpha(Re, H/D, r/D)$ bzw. $Nu(Re, H/D, r/D)$ ausgewertet, mit dem Wärmeübergangs-Koeffizienten $\alpha(r) = \dot{q}(r)/[T(r) - T_L]$, der Nußelt-Zahl $Nu(r) = \alpha(r) \cdot D/\lambda$, der Reynolds-Zahl $Re = w \cdot D/\nu$, D : Düsendurchmesser, H : Abstand Düse - Wärmeübergangsfläche, r : Abstand Staupunkt - Messort, $\dot{q}(r)$: Wärmestromdichte, $T(r)$: Temperatur der Wärmeübergangsfläche, T_L : Luft-Temperatur.

Dabei treten Probleme auf, da die Temperaturdifferenz $[T(r) - T_L]$ sehr klein und sogar negativ werden kann und indem für den Vergleich mit komplizierten Düsengeometrien, wie sie z.B. mit Radialstrahl-Düsen [2] oder Düsen für pulsierende Prallstrahlen [3] gegeben sind, die charakteristischen Düsendurchmesser D nicht vergleichbar sind. Ein derartiger Vergleich ist aber erforderlich, wenn der Wärmeübergang mit Hilfe instationärer Prallstrahlen verbessert werden soll [4].

Als neue Größen zur Bewertung des Zusammenhangs "Düse - Strömungsfeld - Wärmeübergang" werden deshalb die Strahlleistung $P_D = \Delta p \cdot \dot{V}$ mit Düsen-Druckverlust Δp und dem Volumenstrom \dot{V} und eine Effektivitäts-Kennzahl E eingeführt.

2. Effektivitäts-Kennzahl E

Bei einer Wärmestromdichte $\dot{q}(r)$ stellen sich in einem Gebiet A bei natürlicher Konvektion eine Temperaturverteilung $T_{NK}(r, \varphi)$ und bei Prallstrahl-Anströmung eine Temperaturverteilung $T_{PS}(r, \varphi)$ ein. Die Wirkung des Prallstrahls besteht im Übergang $T_{NK} \rightarrow T_{PS}$. Im Gebiet A gilt nach experimenteller Beobachtung $T_{NK}(r, \varphi) \approx \text{const.}$. Weiterhin gilt $\dot{q} = \alpha_{NK} \cdot (T_{NK} - T_\infty)$, wobei T_∞ die Umgebungs-Lufttemperatur ist. Damit wird die Effektivitäts-Kennzahl E definiert:

$$E \equiv 1/A \cdot \int_A [(T_{NK} - T_{PS})/(T_{NK} - T_\infty)] dA$$

Werden die herkömmlichen α -Beziehungen eingesetzt, ergibt sich

$$E \equiv 1/A \cdot \int_A [1 - \alpha_{NK}/\alpha_{PS}] dA$$

E liegt im Wertebereich $0 \leq E \leq 1$. Die Versuchsergebnisse werden in der Form $E = E(P_D, H, r)$ ausgewertet.

3. Versuchsaufbau und -durchführung

Eine Messplatte von $400 \cdot 400 \text{ mm}^2$, die in 25 Einzelfelder unterteilt ist, wird elektrisch erwärmt und erlaubt die Messung der Oberflächentemperatur $T(r)$ und der konvektiven Wärmestromdichte $\dot{q}(r)$.

Die Düsenvarianten sind in der Tabelle aufgeführt. Der Düsen - Platten - Abstand wird im Bereich $20 \text{ mm} \leq H \leq 300 \text{ mm}$ variiert. Die Strahlleistung ergibt sich je nach Düse und Volumenstrom zu $0,5 \text{ W} \leq P_D \leq 750 \text{ W}$.

E wird für ein Gebiet $A = \pi \cdot R^2$ mit $R = 322 \text{ mm}$ bei mittleren Wärmestromdichten $\dot{q}_m \approx 400 \text{ W/m}^2$ berechnet.

Bezeichnung	Kürzel	Beschreibung	Strömung
Prallstrahl-Düse	FW	konvergente Düse, Querschnittsverjüngung von $D_a = 37\text{mm}$ auf $D = 10\text{mm}$	stationär, axialsymmetrisch
Ringstrom-Düse	RA	Düsenströmung ($D_i = 8\text{mm}$) konzentrisch von schnellerer Ringströmung umgeben ($D_r = 12\text{mm}$)	stationär, turbulent infolge freier Scherschicht
Pulsations-Düse	PA	innere Düse ($D_i = 8\text{mm}$) koaxial in äußerem Rohr ($D_a = 37\text{mm}$) um 110mm zurückgesetzt	instationär, schwach pulsierend
Pulsations-Düse	PB	wie PA, innere Düse um 270mm zurückgesetzt	instationär, stark pulsierend
Drallstrahl-Düse	FD	wie FW, aber mit Drallerzeugung in Düsenvorkammer ($D_a = 37\text{mm}$)	stationär, drallbehaftet
Präzessions-Düse	PD	wie FD, aber in äußerem Rohr ($D_a = 37\text{mm}$), mit Blende ($D_B = 10\text{mm}$) abgeschlossen	instationär, stochastisch präzessierend

Tabelle: Düsenvarianten und Strömungs-Charakteristika

4. Versuchsergebnisse und Diskussion

Abb. 1 zeigt mit $Re(P_D)$ den Zusammenhang von Strömungsfeld und Strahlleistung, wobei Re auf D bzw. D_r (s. Tab.) bezogen ist. Abb. 2 zeigt die größeren E -Werte für die stationären Strömungen, weil die instationären Strömungen offensichtlich noch nicht die charakteristischen Strouhal-Zahlen haben, um auf den Wärmeübergang einzuwirken. Zusätzlich sind die E -Werte über ein sehr großes Gebiet A gemittelt. Künftig werden die Ortsfunktionen $E = E(r)$ und zusätzlich die Parameter der Strömungsfelder gemessen und ausgewertet.

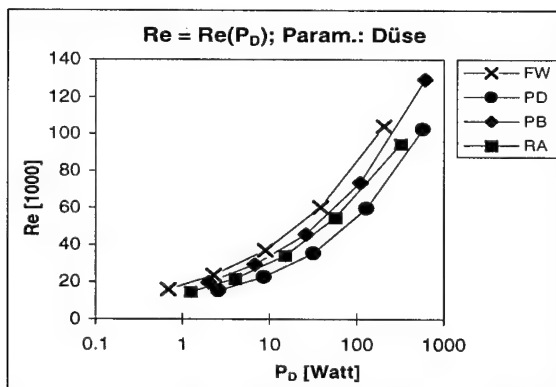


Abbildung 1: Reynolds-Zahl verschiedener Düsen bei Variation der Strahlleistung

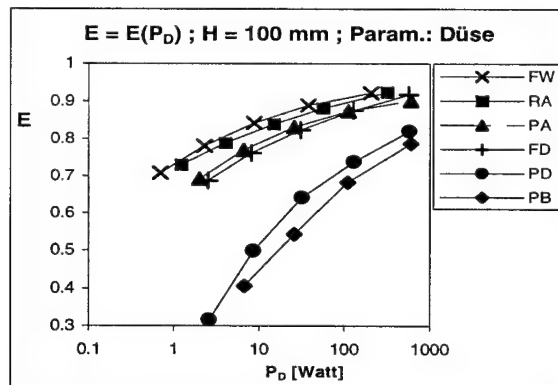


Abbildung 2: Effektivitäts-Kennzahl verschiedener Düsen bei Variation der Strahlleistung

Danksagung

Das Forschungsvorhaben wird von der Deutschen Forschungsgemeinschaft (DFG) unterstützt.

5. Literatur

- JAMBUNATHAN, K., LAI, E., MOSS, M.A., BUTTON, B.L.: A review of heat transfer data for single circular jet impingement. Int. J. Heat and Fluid Flow **13** (1992), 106–115.
- PEPER, F., LEINER, W., FIEBIG, M.: Impinging Radial and Inline Jets: A Comparison with Regard to Heat Transfer, Wall Pressure Distribution, and Pressure Loss. Exp. Thermal and Fluid Sci. **14** (1997), 194–204.
- SHERIFF, H.S., ZUMBRUNNEN, D.A.: Effect of Flow Pulsations on the Cooling Effectiveness of an Impinging Jet. ASME J. Heat Transfer. **116** (1994), 886–895.
- HERWIG, H., FRIEDRICH, I.: Concepts for unsteady convective heat transfer using devices without moving parts. ICHMT, Int. Symposium on Transient Convective Heat Transfer, Cesme, Turkey, 1996, pp. 19–26.

Adressen: DR. H. MOCIKAT, SIVUS gGmbH, Schulstrasse 38, D-09125 Chemnitz, Germany
 DR. J. PRAŽÁK, Acad. of Sciences, Inst. Thermomech., Dolejškova 5, CZ-18200 Prague 8, Czech Republic
 ST. GÖPPERT, Technische Thermodynamik, TU Chemnitz, D-09107 Chemnitz, Germany
 PROF. DR. H. HERWIG, Techn. Thermodynamik, TU Hamburg-Harburg, D-21073 Hamburg, Germany

NIENHÜSER, CH.; KUHLMANN, H. C.; RATH, H. J.

Instability of buoyant-thermocapillary flows in non-cylindrical liquid bridges

The flow driven by buoyancy and thermocapillarity in a liquid bridge between coaxial differentially heated disks held by surface tension forces is investigated. We numerically determine the stability of axisymmetric flows by a linear stability analysis. In the present approach, the influence of buoyancy forces on the flow stability is taken into account through static meniscus deformations as well as through internal buoyancy. To elucidate the physical instability mechanisms the energy balance given by Reynolds-Orr-like equations is considered term by term.

1. Model and numerical methods

The well-known half-zone model consists of a liquid bridge, bounded axially by two parallel concentric rigid disks. Their radii $r_i = R$ and their axial distance d define the aspect ratio $\Gamma = d/R$. Differential heating of the disks leads to a temperature gradient along the free fluid surface causing a variation of the surface tension. Since the surface tension of most liquids decreases with increasing temperature, a surface force directed from hot to cold surface areas drives a fluid motion (thermocapillary effect).

For the mathematical formulation we use the continuity-, the energy- and the Navier-Stokes equations together with appropriate boundary conditions. The characteristic numbers are the Prandtl number $Pr = \nu/\kappa$, the Reynolds number $Re = \gamma\Delta Td/\rho\nu^2$, and the Grashof number $Gr = g\beta\Delta Td^3/\nu^2$. In our scaling the Reynolds number gives the ratio of thermocapillary to viscous forces. The location of the free surface depends on the normal-stress balance. For liquid tin, which is considered here, the mean capillary pressure is large compared to the hydrodynamic one. Hence, the normal-stress balance can be approximated by the Young-Laplace equation, in which the static Bond number $Bo d^2 \rho g = \sigma_0$ gives the ratio of hydrostatic pressure to the mean capillary pressure. The Young-Laplace equation is solved for fixed contact lines and prescribed contact angle α at the hot corner.

Having determined the static free-surface shape by a shooting method the axisymmetric stationary 2D flow is calculated numerically. A streamfunction-vorticity formulation is discretized on a nonequidistant grid using second-order finite-differences. Geometrical grid compression towards the rigid walls and the free surface is applied to resolve gradients and boundary layers. By a linear analysis we determine the stability of the 2D basic state. Infinitesimal perturbations are represented by a complete set of normal modes with discrete wave numbers m in azimuthal direction. Neutral Reynolds numbers $Re_c(m)$ are determined by a vanishing real part of the growth rate. The critical mode with the wave number m_c is determined by the global minimum of $Re_c(m)$. We analyze the energy transfer rates to the perturbations using Reynolds-Orr-like equations. The identification of the most important terms and their local distributions can provide information about the instability mechanisms.

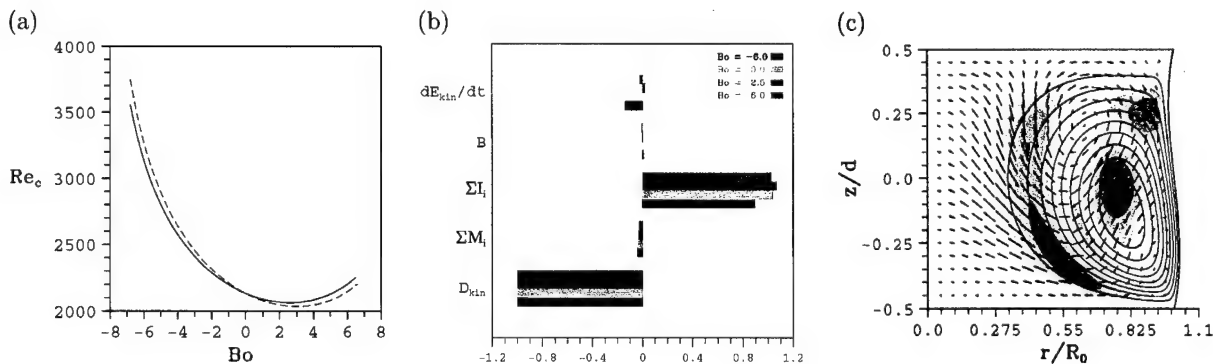


Figure 1: (a): Critical Reynolds number Re_c as function of the Bond number for $Gr = 0$ (dashed line) and $Gr \neq 0$ (full line). (b): Kinetic energy balance of the perturbations for different Bond numbers and for $Re = 2130$. (c): Local distribution of the integrand of $\sum I_i$ (shaded), the perturbation flow (arrows), and the stream function of the basic flow (full lines) for $Bo = 2.5$ and $Re = 2130$. The other parameters are $\Gamma = 1$, and $m_c = 2$.

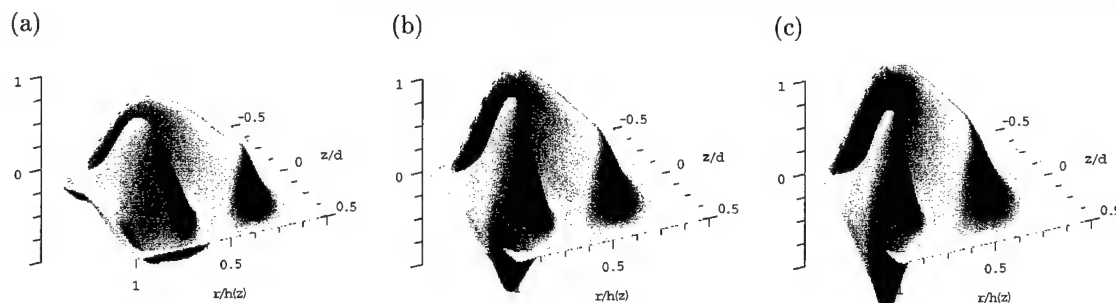


Figure 2: Local distribution of the integrand of $\sum I_i$ for $\Gamma = 1$, $Re = 2130$, $m = 2$, and $Bo = -6$ (a), $Bo = 2.5$ (b), and $Bo = 6$ (c).

2. Results

We present results for liquid tin, which is representative for most metals. The Prandtl number is $Pr = 0.02$ and the ratio of the dynamic Bond and the static Bond number is $Bd/Bo = Gr/BoRe = \gamma/\beta\sigma_0 \approx 0.27$. The sign of Gr and Bo distinguishes heating from above ($Gr, Bo > 0$), i.e. the gravitational acceleration is in direction of the thermocapillary drive, from heating from below ($Gr, Bo < 0$). Figure 1a shows the linear stability boundaries of the 2D flow as a function of the Bond number. The dashed line representing the results for $Gr = 0$ differs only slightly from the full line, which shows the results for non-zero Grashof number ($-6200 \lesssim Gr \lesssim 3900$). The (de)stabilization due to buoyancy for negative (positive) Grashof numbers is in agreement with results for the cylindrical half-zone [1] and dominating thermocapillary convection. Due to the small ratio of Bd/Bo the influence of buoyancy on the linear stability boundaries is small compared to that of the free-surface shape.

The kinetic energy balance of the perturbation for different Bond numbers, shown in fig. 1b, does not change qualitatively. The dissipation D_{kin} is mainly balanced by inertial terms $\sum I_i = -Re \int \vec{u}(\vec{u} \cdot \nabla) \vec{U}_0 dV$, which describe convective transport of basic-state momentum to the perturbation flow (basic-state velocity \vec{U}_0 , perturbation velocity \vec{u}). The local distribution of the integrand of $\sum I_i$ is shown in fig. 1c for $Bo = 2.5$ together with the basic-state vortex and the perturbation-flow field. One can identify one region of positive energy transfer near the basic-flow vortex-center, that is mainly fed by radial transport of axial basic-flow momentum. The contribution of this process decreases with increasing Bond number (fig. 2), when the basic-vortex center moves towards the convex part of the free surface near the cold corner. The other region of positive energy transfer extends, aligned with the basic-flow isolines, from the cold wall into the interior (fig. 1c). The underlying mechanism is the transport of momentum perpendicular to the basic-flow direction. Due to the 'no-slip' boundary-condition at the walls, which enhances the cross-stream gradient of \vec{U}_0 when the basic-vortex center moves towards the cold wall, this process becomes more efficient with increasing Bo . As functions of the Bond number, the change of efficiency of these two processes is opposite, where the latter one is dominating. This leads to a strong stabilization for large negative Bo and to a slight stabilization for large positive Bond numbers (fig. 1a).

Acknowledgements

This work was supported by NASDA in the framework of the Marangoni convection modeling research.

3. References

- 1 WANSCHURA, M.; KUHLMANN, H. C.; RATH, H. J. : Linear stability of two-dimensional combined buoyant-thermocapillary flow in cylindrical liquid bridges. *Phys. Rev. E* **55** (1997), 7036.

Addresses: CHRISTIAN NIENHÜSER, DR. HENDRIK C. KUHLMANN, DR. HANS J. RATH, ZARM – University of Bremen, Am Fallturm, 28359 Bremen, e-mail: nien@zarm.uni-bremen.de

SEVERIN, J., BECKERT, K., HERWIG, H.

Plane channel flow with heat transfer: stability analysis with a commercial CFD-code

Spatial development of small amplitude disturbances in plane Poiseuille flow is investigated numerically using a commercial CFD code (CFX 4.2). Small amplitude Tollmien-Schlichting waves known from an Orr-Sommerfeld analysis are superimposed as initial conditions on a fully developed laminar channel flow. The downstream spatial disturbances are calculated on the basis of the full Navier-Stokes equations (NSE). Results are compared to calculations based on the Orr-Sommerfeld equations (OSE). In a second step the thermal energy equation is solved in addition to the NSE to investigate temperature effects and especially the development of temperature disturbances.

1. Introduction

In our study we want to find out to what extent commercial CFD codes can be used today already for a direct numerical simulation (DNS) of flow stability characteristics. Plane Poiseuille flow is a "good candidate" since its mean flow is a parallel flow. Moreover, the analytical parabolic velocity profile is an exact solution of the full Navier-Stokes equations. Thus the Orr-Sommerfeld analysis, which we want to use as a reference theory, is an exact description of the linear stability behavior of (exponentially) small disturbances.

Since a spatial simulation of the problem under investigation needs a great amount of computer resources most previous studies have been performed in terms of a temporal simulation with periodic boundary conditions in the mean flow direction. In our study, however, we analyse the spatial development of Tollmien-Schlichting (TS) waves.

2. Our Approach

The basic setup of the problem is relatively simple and a sketch of it is shown in figure 1. Our computational domain is the rectangle $A - B - C - D$. We assume the flow to be fully developed, two-dimensional and incompressible. The basic equations solved by the program CFX 4.2 by AEA technology are the well known conservation equations for mass, momentum and, in the non-isothermal case, energy (see the CFX manual for details)

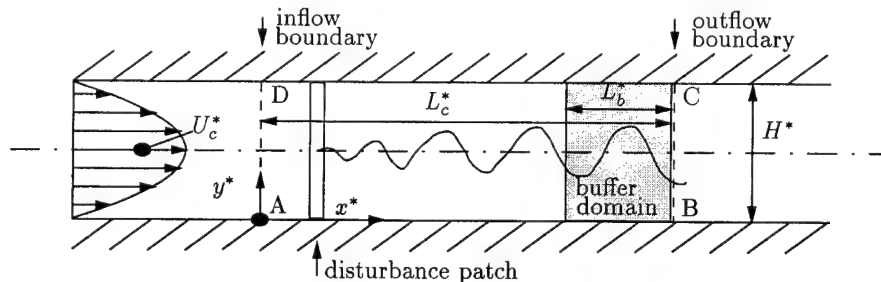


Fig. 1: Sketch of the channel flow and the computation domain for the NSE calculation.

In the present study the disturbances were introduced at some location downstream of the inflow boundary, on the "disturbance patch" ($x^* = x_{dp}^*$). Therefore, first the Orr-Sommerfeld solution for a given disturbance frequency and Reynolds number was calculated to get the amplitude functions of the $v^{*'}$ and $u^{*'}$ -components of the disturbance. Then the two-dimensional TS wave (only the $v^{*'}$ -component)

$$v^{*'}(x^* = x_{dp}^*, y^*, t^*) = A \text{ Real}(\hat{v}^* \exp(-i\omega^* t^*)) \quad (1)$$

was superimposed on the laminar parabolic velocity profile. Here, A is the amplitude of the TS wave, \hat{v}^* the dimensional amplitude function calculated from the Orr-Sommerfeld equation and ω^* the corresponding frequency.

Since CFX 4.2 does not provide direct access to the velocity field during the iteration process we had to model the disturbances on the disturbance patch by using source terms.

As a crucial element we introduced a so-called *buffer domain* in our NSE model (see Chung and Sung (1997) for this idea and more details). In this buffer domain the governing equations are modified to enforce strictly outgoing waves.

3. Results

In figure 2 NSE solutions for two different grid resolutions are compared to the corresponding OSE solution for the case $Re = 10000$, $\omega = 0,3302$ (nondimensional disturbance frequency). Since for these calculations a buffer domain was introduced the time periodic wave of the source was correctly transformed to a spatial disturbance. The corresponding OSE solution ($\hat{\alpha} = 1.0006 + i0.0109$) shows good agreement with the NSE solution with respect to the wavelength. The growth rate, however, still is too low. Obviously the grid resolution is insufficient.

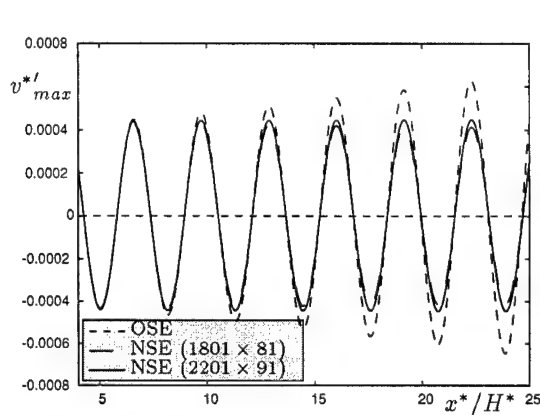


Fig. 2: v^*_{max} at the centerline: Comparison of NSE solutions (with buffer domain) with OSE solution

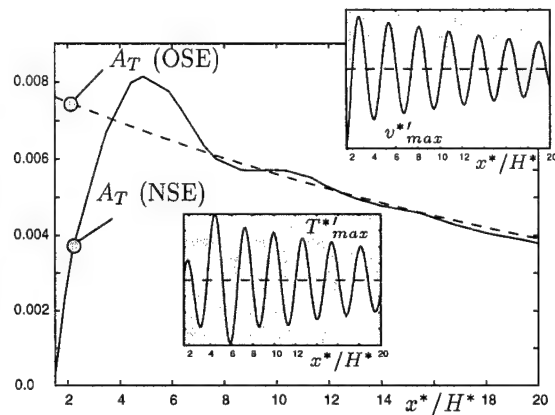


Fig. 3: Downstream development of $|T^*'|_{max}$ (absolute value of the amplitude of $T^{*'}_y$), grid resolution: 1651×81 , $Pr = 0.7$

In figure 3 the development of the amplitude of the temperature disturbance in downstream direction is shown for a Prandtl number $Pr = 0.7$. The gray shaded inserts show a typical downstream traveling wave of the temperature disturbance and the corresponding v -velocity disturbance at $y^* = H^*/2$.

After an overshoot a small adjustment zone is following before the disturbance reaches its final behaviour after approximately four wavelengths comparing well with the OSE results based on the so-called shape assumption (unique disturbance shape for flow and temperature).

All calculations were performed on a HP 9000/889 K460 workstation cluster. A typical number of 300 time steps, each of it with 4 iterations and 500 seconds of CPU time (grid resolution: 2001×81) thus took approximately 40 hours of total CPU time. Since computers with this specifications often are multi-user devices such calculations may last for days or weeks.

4. References

- 1 Y.M. CHUNG, H.J. SUNG, A.V. BOIKO: Spatial simulation of the instability of channel flow with local suction/blowing. Phys. Fluids 9(11) (1997), 3258-3266.

Address: DR.-ING. JAN SEVERIN, Siemens AG; Kruppstr. 16; D-45128 Essen

DR.-ING. KONRAD BECKERT, TU Chemnitz; Reichenhainer Str. 70; D-09126 Chemnitz

PROF.DR.-ING. HEINZ HERWIG, TU Hamburg-Harburg; Denickestr. 17; D-21073 Hamburg

STEINRÜCK, H.

Upstream travelling waves in the boundary layer of a horizontal mixed convection flow

The propagation of small disturbances in a mixed convection boundary layer flow over a horizontal plate is considered. Employing an asymptotic analysis with respect to a small buoyancy parameter $K = Gr/Re^2$ a triple deck structure of the perturbed flow field is found. Two effects contribute to the pressure perturbation in the lower deck: The displacement of the outer field and the buoyancy in the main deck. Linearizing the perturbation equations and taking the Fourier transform with respect to time and the coordinate parallel to the wall the dispersion relation is derived. Considering the case that the buoyancy induced pressure dominates the displacement induced pressure upstream travelling waves are found. These waves are confined to the boundary-layer and exist only in the case of the flow over a cooled plate. Furthermore a stationary downstream growing mode exists which indicates that the solution of the boundary layer equations is not unique.

We shall be concerned with the upstream propagation of small disturbances in the boundary layer of a mixed convection flow over a cooled horizontal surface. The upstream propagation of perturbations in a boundary-layer is nothing unusual [1]. But in most cases the boundary layer interacts with the outer flow field (triple-deck). Considering a mixed convection flow the upstream propagation can take place in the boundary layer for a certain parameter regime. In contrast to the triple-deck mechanism the pressure gradient is induced by the main deck. To understand that mechanism we have to look more closely onto the mixed convection flow:

Due to the cooling of the horizontal surface there is a temperature gradient normal to the wall in the fluid (figure 1). Corresponding to this temperature gradient, a hydro-static pressure gradient normal to the wall builds up. This pressure gradient influences the flow only indirectly. If the wall temperature is not uniform or the boundary layer thickness is growing, a horizontal pressure gradient results.

The governing equations are the Navier-Stokes equations for an incompressible fluid coupled to the energy equation. To account for buoyancy effects, the Boussinesq approximation is used. The equations are in dimensionless form using the velocity of the free stream, the boundary layer thickness and the temperature difference between the plate and the ambient fluid as reference values for velocities, lengths and temperature differences, respectively.

Thus the flow field is characterized by the Reynolds number Re and the buoyancy parameter $K = Gr/Re^2$. The Grashof number Gr and the Reynolds number Re are based on the boundary layer thickness δ . The third dimensionless parameter, the Prandtl number, is assumed to be of order unity.

The equations governing the propagations of small disturbances are derived under the following conditions: The length scale λ on which the perturbations vary parallel to the wall is assumed to be large compared with the boundary layer thickness. But it has to be small compared with the length scale on which the boundary layer thickness varies ($\lambda \ll Re$). Thus we consider the limit of a large wave length λ and a small amplitude ε of the perturbation. For the flow field we assume small buoyancy effects $K \ll 1$ and a large Reynolds number Re . Thus we consider the limit:

$$\varepsilon \rightarrow 0, \quad \lambda \rightarrow \infty, \quad Re \rightarrow \infty, \quad K \rightarrow 0. \quad (1)$$

To obtain meaningful limiting equations the following scaling conditions have to hold:

$$\lambda = K^3 Re \rightarrow \infty, \quad \varepsilon = O(\lambda^{-1}). \quad (2)$$

Under these conditions we obtain a triple deck structure of the perturbed flow field. But the scaling differs from the classical case. Depending on the magnitude of the buoyancy parameter K , we distinguish the following three cases:

buoyancy param. K	wave length λ	
$K \ll Re^{-1/4}$	$\lambda = Re^{1/4}$	triple deck
$K \sim Re^{-1/4}$	$\lambda = Re^{1/4}$	triple deck+buoyancy
$1 \gg K \gg Re^{-1/4}$	$Re \gg \lambda \gg Re^{1/4}$	waves in the boundary layer

Figure 1 shows the scaling for the third case. The wave number $1/\lambda$ of the perturbation is small compared to the buoyancy parameter K . In general, there are two contributions to the pressure perturbations: The outer flow field generates a pressure correction of the order $O(1/\lambda)$ due to displacement effects. In the main deck a second contribution to the pressure perturbation of magnitude $O(K)$ is induced due to buoyancy effects. Thus in the third case the pressure in the lower deck is dominated by the buoyancy induced contribution. In this parameter regime the outer flow field plays no active role. In the second case, where the buoyancy parameter $K = O(1/\lambda)$ is of the same magnitude as the wave number, the usual triple-deck scaling applies. Here both pressure contributions act onto the lower deck.

Assuming only small amplitudes of the perturbations, $\varepsilon \ll \lambda^{-1}$, $\varepsilon \ll K$, the perturbation equations can be linearized. Searching for harmonic waves of the form

$$u(x, y, t) = U(y)e^{i(ax/\lambda + \omega/\lambda K)}, \quad (3)$$

the perturbation equation can be solved in terms of the Airy function, and the dispersion relation can be derived. In the buoyancy dominated case we obtain:

$$\frac{1}{\sqrt{\omega}} \frac{\tau^2}{\Theta(0)} + \frac{1}{\sqrt{z_1} \text{Ai}'(z_1)} \int_{z_1}^{\infty} \text{Ai}(z) dz = 0, \quad (4)$$

with $z_1 = -\frac{i\omega}{(\tau a)^{2/3}}$, τ being the dimensionless wall shear stress of the basic flow and $\Theta(0)$ the dimensionless wall temperature. The dispersion relation is solved numerically, showing the existence of waves propagating upstream in case of a cooled plate (Fig 2). In the case of a heated plate these upstream-propagating modes are not present. One spatially growing, stationary mode exists in the case of buoyancy-dominated flow over a cooled plate. This mode has been described previously [3]. A consequence is the non-uniqueness of the solution of the steady-state mixed-convection boundary-layer equations and the influence of downstream conditions onto the boundary layer flow. This has been shown previously in [2] and for a different parameter regime in [3].

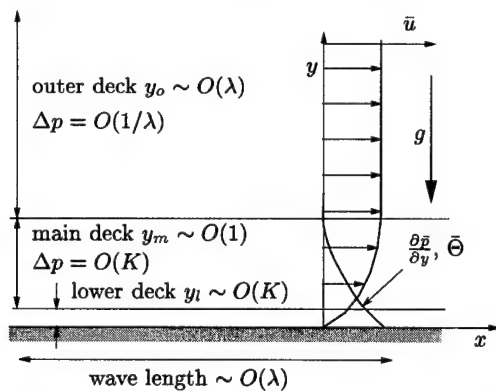


Fig.1: The triple-deck structure of the disturbed flow field and the undisturbed velocity, temperature and pressure distributions.

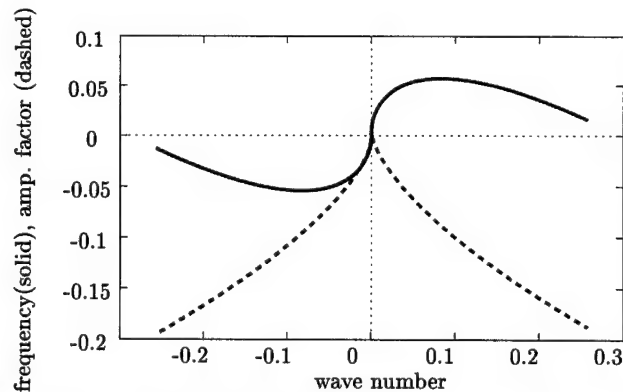


Fig.2: First branch of the dispersion relation in case of adverse indirect buoyancy.

References

- 1 SCHNEIDER, W.: Upstream propagation of unsteady disturbances in supersonic boundary layers, *J. Fluid Mech.* 63 (1974), 465-485.
- 2 LAGREE, P. Y.: Mixed convection at small Richardson number on triple deck scales, *C. R. Acad. Sci. Paris* 318, Serie II (1994), 1167-1173.
- 3 STEINRÜCK, H.: Mixed convection over a horizontal plate: self-similar and connecting boundary-layer flows, *Fluid Dyn. Res.* 15 (1995), 113-127.

Address: DR. HERBERT STEINRÜCK, TU Vienna, Institute of Fluid Mechanics and Heat Transfer, Wiedner Hauptstraße 7, A-1040 Vienna, Austria.

AVSEC, J.; MARCIC, M.

The Calculation of Velocity of Sound near the Liquid-Gas Transition

The paper features the mathematical model of thermodynamic functions of state in gas-liquid region for pure refrigerants with the help of classical thermodynamics and statistical thermodynamics. To calculate the thermodynamic properties of real fluid we used models on the base of Lennard-Jones intermolecular potential.

1. Introduction

Utilizing the semi-classical formulation of the partition function for the purpose of the canonical ensemble for the N indistinguishable molecules can be expressed as follows :

$$Z = \frac{1}{N!h^{NF}} \int \dots \int \exp\left(-\frac{H}{kT}\right) d\vec{r}_1 d\vec{r}_2 \dots d\vec{r}_N d\vec{p}_1 d\vec{p}_2 \dots d\vec{p}_N, \quad (1)$$

where F stands for the number of degrees of freedom of individual molecule, H designates the Hamiltonian of the molecule system. The canonical ensemble for the system of N molecules can be like this:

$$Z = Z_0 Z_{trans} Z_{vib} Z_{rot} Z_{ir} Z_{el} Z_{nuc} Z_{conf}. \quad (2)$$

Thus the partition function Z is a product of terms of the ground state (0), the translation (trans), the vibration (vib), the rotation (rot), the internal rotation (ir), the influence of electrons excitation (el), the influence of nuclei excitation (nuc) and the influence of the intermolecular potential energy (conf). Utilizing the canonical theory for computing the thermodynamic functions of the state can be put as follows [1]:

$$\text{Pressure: } p = kT \left(\frac{\partial \ln Z}{\partial V} \right)_T, \text{ Internal energy: } U = kT^2 \left(\frac{\partial \ln Z}{\partial T} \right)_V, \text{ Free energy } A = -kT \cdot \ln Z. \quad (3)$$

The term velocity of sound refers to the velocity of the mechanical longitudinal pressure waves propagation through a medium. It is very important parameter in the study of compressible fluids flows and in some applications of measurement (acoustic resonance level gauge). The propagation of sonic waves for real fluids is almost in all cases nearly isentropic. Therefore, we can calculate the isentropic speed of sound for the real fluid c_0 :

$$c_0 = \sqrt{-V^2 \left(\frac{\partial p}{\partial V} \right)_S \frac{1}{M}} = \sqrt{\frac{V^2 \frac{C_p}{T} \left(\frac{\partial p}{\partial V} \right)_p}{M \left[\left(\frac{\partial V}{\partial T} \right)_p - \frac{C_p}{T} \left(\frac{\partial T}{\partial p} \right)_V \right]}}, \quad (4)$$

where T is temperature, p is pressure, S is entropy, V is molar volume, C_p is the molar heat capacity at constant pressure.

2. Configurational integral

For the calculation of thermodynamical functions of state is the Lennard-Jones fluid the most widely used model. In the present paper those models were used which yielded favorable results in practical computations for a large number of components.

a) Johnson-Zollweg-Gubbins (JZG) model

For a real fluid the Johnson-Zollweg-Gubbins [2] model based on molecular dynamics and Monte Carlo simulations with the Lennard-Jones intermolecular potential we used. The JZG model contains 32 linear parameters and one non-linear parameter. On this basis we can express configurational free energy A_{conf} :

$$\frac{A_{conf}}{N\varepsilon} = \sum_i \frac{a_i \rho^{*i}}{i} + b_i G_i, \quad (5)$$

where are a_i , b_i and G_i the coefficients. The coefficients a_i and b_i are functions of temperature T only, the coefficient G_i is function of the reduced density ρ^* . N presents the number of molecules in the system, ε is Lennard-Jones parameter.

b) Revisited Cotterman model (CYJ) [3]

Revisited Cotterman EOS is based on the hard sphere perturbation theory. The average relative deviation for pressure and internal energy in comparison with Monte-Carlo simulations are 2.17% and 2.62% respectively for 368 data points [3]. The configurational free energy is given by:

$$A^{conf} = A^{HS} + A^{pert}, \quad (6)$$

where A^{HS} is configurational free energy on the base of hard sphere model and A^{pert} is perturbational part of free energy.

c) Tang-Tong-Lu model [4]

Tang-Tong-Lu model uses as the intermolecular potential a new two-Yukawa function. This function is found to mimic very closely the Lennard-Jones potential. Tang-Tong-Lu analytical model calculates thermodynamic functions of state on the base of solution of the Ornstein-Zernike equation with help of perturbation theory. The configurational free energy is given by:

$$\frac{A_{conf}}{NkT} = a_0 + a_1 + a_2, \quad (7)$$

where a_0 represents the free energy of the hard sphere fluid, a_1 and a_2 are perturbed first and second order parts.

3. Results and comparison with experimental data

Determining the equilibrium states between the liquid and the gaseous phases conditions for equilibrium are applied:

$$T' = T'', p' = p'', \mu' = \mu'', \quad (8)$$

where $'$ in equation (8) means the liquid phase, $''$ means the gaseous phase and μ constitutes the chemical potential. Due to the mathematical complexity of the equations in the model, the states on the coexistence curve are obtained numerically. By applying these states, thermodynamic properties in the two phase environment can be calculated. In the two-phase region the computation of thermodynamic functions of state are based on the mixing rule.

Table 1 shows the results for carbon dioxide (saturated vapour) and R 152a (boiling liquid). The computed velocity of sound conform well for all models, obtained by statistical thermodynamics, with the measured velocity of sound. Somewhat larger deviations can be found in the region of critical conditions due to the large influence of fluctuation theory and singular behaviour of some thermodynamic properties in the near-critical condition.

Table 1: Velocity of sound (m/s) for carbon dioxide (saturation curve) and for R152a (boiling curve).

CO ₂	263 K	273 K	283 K	293 K	301 K	R 152a	278.5 K	298.5 K	318.5 K	338.5 K	358.5 K
JZG	219.3	219.3	212.9	203.7	194.1	JZG	749.8	600.8	549.0	430.0	297.4
CYJ	223.8	219.9	213.8	204.2	191.0	CYJ	737.0	592.8	544.6	437.9	320.1
TTL	226.4	223.2	218.1	210.2	199.2	TTL	699.2	570.4	528.9	429.6	315.9
Exp.	217.5	212.7	206.3	197.9	189.8	Exp.	743	642	542	435	321

4. References

- 1 LUCAS, K., Statistical Thermodynamics, Springer-Verlag, 1992, New York.
- 2 JOHNSON, J.K., ZOLLWEG, J.A., GUBBINS, K.E.,: The Lennard-Jones Equation of State Revisited, Molecular Physics, 78 (1993), 591-618.
- 3 CHUNXI, L., YIGUI, L., JIUFANG, L.: Investigation and Improvement of Equations of State for Lennard-Jones Fluid, Fluid Phase Equilibria, 127 (1997), 71-81.
- 4 TANG, Y., TONG, Z., LU, B.C.-Y.,: Analytical Equation of State based on Ornstein-Zernike Equation, Fluid Phase Equilibria, 134 (1997), 21-42.

Addresses: Faculty of Mechanical Engineering, University of Maribor, Smetanova 17, Maribor, Slovenia

BAUMBACH, V.; DREYER, M.; RATH, H.J.

Coating by Capillary Transport through Porous Media

A coating device which works with the help of a porous medium is considered. The fluid of interest is a surfactant solution which passes a porous medium before it is deposited on a solid substrate. A hydrostatic model for the process is proposed which assumes the validity of DARCY's law as well as an approach for slot coaters developed by Higgins and Scriven (1980). Emphasis will also be placed on the experimental determination of the porous media permeability and porosity. Moreover the model is compared with experimental results.

1. Introduction

In numerous practical coating applications it is required that the process works without any auxiliary devices like pumps, valves and sensors. For such applications we have developed a coating device, which is shown in Fig. 1.

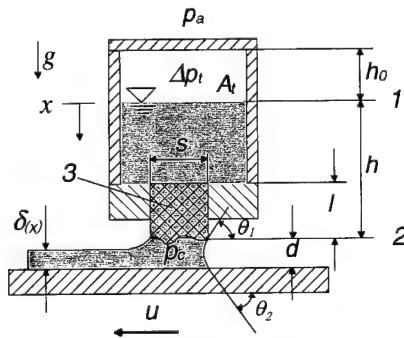


Fig. 1: Model of the process.

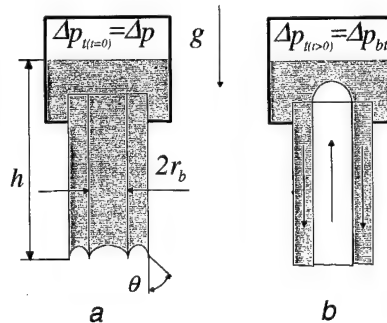


Fig. 2: a) Initial and b) gas break-through condition.

Here the coating device consists of a liquid tank which is filled up with a surfactant solution. A porous medium, made up of a fibrous package, with a measured porosity of $\epsilon = 0.21_{-0.01}^{+0.01}$, is fixed in the middle of the tank (Fig. 1, number 3). The fibres are aligned along x and have a diameter of $150\mu\text{m}$. Below a fleece is attached between the substrate surface and the fibrous package to guarantee a uniform contact. Provided that the porous media are fully saturated and applying a relative velocity u , a pressure gradient is generated which results in a flow of the coating liquid through the fibres onto the substrate surface.

For modelling the process we assume the validity of DARCY's law and that the system works in a range of small BOND numbers $\text{Bo} = \rho g d^2 / \sigma < 1$ and of small capillary numbers $\text{Ca} = u \mu / \sigma < 1$, where ρ , μ and σ are the fluid density, dynamic viscosity and surface tension respectively. Further on we assume that the remaining gas volume expands isothermally and we neglect surfactant diffusion in the liquid film. Moreover the transient coating process is going to be considered within the limiting conditions of two different bubble points. At $t = 0$, Fig. 2a), we can calculate the initial pressure $\Delta p = p_0 - p_a = -\rho g h - (2\sigma/r_b) \cos \theta$, where the first term on the r.h.s. counts for the hydrostatic pressure and the second one for the capillary pressure at the meniscus of the porous medium (see Fig. 2a). For $t > 0$, during the coating process, the biggest capillary in the fibrous package drains due to the expansion of gas within the tank. This is illustrated in Fig. 2b) where the system purges. After the gas break through Δp_{bt} a nearly steady state coating condition is achieved (see Fig. 3).

2. Modelling the Process

Access to the coating process provides the tank pressure, which can be both, measured and calculated via Eq. (1). Here the fractional term in the brackets refers to the isothermal expansion and is dependent on the gas volume and the change of the liquid level along the x co-ordinate, which is also designated in Fig. 1. For a more convenient

depiction the tank pressure is nondimensionalised by the first mentioned bubble point Δp .

$$P_t = \frac{\Delta p_t}{\Delta p} = \left[p_a - p_0 \frac{1}{1 + \frac{1}{h_0} x} \right] \frac{1}{\Delta p} \quad (1)$$

To predict the transient behaviour of the tank pressure till the system purges we need to develop the differential equation with respect to the x co-ordinate. For this we use the stationary BERNOULLI equation by neglecting also the convectonal term. Intergrating it along a streamline from the initial point 1 to the end point 2, as designated in Fig. 1, leads to the following equation:

$$\frac{\mu A_t l}{K s b} \dot{x} + p_a - p_c - p_0 \frac{1}{1 + \frac{1}{h_0} x} - \rho g (h - x) = 0 \quad (2)$$

Here the first term refers to the pressure drop over the porous media via DARCY's law, where K and b are the porous media permeability and the fibrous package depth respectively. With the aid of a correlation from Higgins and Scriven (1980) the pressure within the coating gap can be determined:

$$p_c = 1.34 \text{Ca}^{2/3} \frac{\sigma}{\delta(x)} + [\cos \theta_1 + \cos \theta_2] \frac{\sigma}{d} \quad (3)$$

The dynamic contact θ_2 can be estimated by the HOFFMAN-TANNER (1975, 1979) law, $\theta_2 = 4.54 \text{Ca}^{0.353}$, the contact angle θ_1 is approximated to zero. Reorganization of Eq. (1-3) and the utilization of conservation of mass $\dot{x} = \delta(x) b u / A_t$ leads to two equations for the two remaining unknown, the final film thickness $\delta(x)$ and the time derivation from x .

3. Comparison with Experimental Results

The only parameter which has to be determined experimentally is the porous medium permeability. With the aid of DARCY's law $K = Q l \mu / b s \Delta p_p$ and measuring the adjusted flow rate Q and the corresponding pressure drop Δp_p over the porous media one obtains a permeability of $K = 29.5 \times 10^{-12} \text{m}^2$, where the accuracy is in a range of 10%.

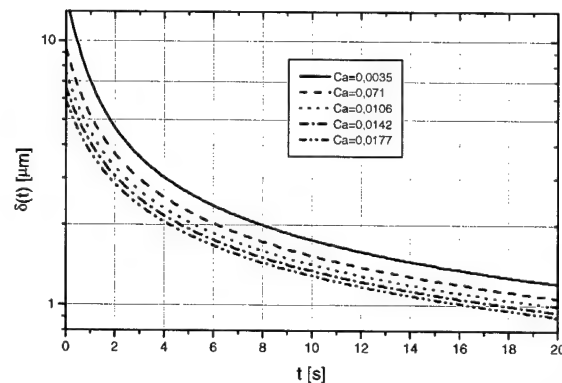
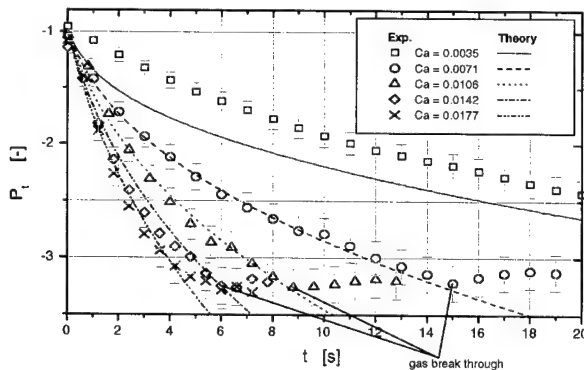


Fig. 3: Comparison of experimental data and of the model. Fig. 4: Calculated film thickness.

The diagrams shown in Fig. 3 and 4 depict the nondimensionalised tank pressure P_t and the film thickness $\delta(x)$ respectively over the time t for different capillary numbers. Apart from the experiment at the lowest capillary number we obtain for the remaining experimental data a good agreement with the model. This means that the model works properly for capillary numbers in a range of 7×10^{-3} to 1.8×10^{-2} . (This work is funded by the German Space Agency DLR under grant number 50TT9737 6)

4. References

- 1 B. HIGGINS, L. E. SCRIVEN: Chem. Ing. Sci. **35**, (1980), 673.
- 2 L. H. TANNER: J. Phys. D: Appl. phys. **12**, (1979), 1473.
- 3 R. L. HOFFMAN: J. Coll. Inter. Sci. **50**, (1975), 228.

Address: DIPL.-ING. VOLKER BAUMBACH, DR.-ING. MICHAEL DREYER, PROF. DR.-ING. HANS J. RATH,
ZARM, Universität Bremen, Am Fallturm, D-28359 Bremen

BIELERT, U.; KOTCHOURKO, A.; BURGETH, B.; BREITUNG, W.

Numerical simulation of large scale hydrogen explosions in complex geometries

Large hydrogen air clouds represent a serious hazard during severe accidents in nuclear power plants as well as in facilities of the developing hydrogen technology. The accident scenarios are dominated by large time and length scales with complicated boundary conditions. The combustion can proceed as an accelerating turbulent flame with possibly transition to detonation. Such problems require a careful selection of the physical and chemical models as a fully detailed calculation is not yet feasible. An extension of the well known eddy break-up model together with the k - ϵ -model was calibrated at a large set of experiments on different scales. It was demonstrated that this model gives good results for a large range of parameters.

1. Analysis procedure for safety applications

Today's computers do not allow to simulate a complete accident scenario in a nuclear power plant on a fine physical level. Therefore the whole process must be broken down into smaller problems which can be tackled by specialized methods. After the problem has been specified by selecting a plant design, a mitigation concept and an accident scenario, the first step is to calculate the hydrogen release and distribution in the containment. The creation of hydrogen inside the reactor vessel can be modeled by lumped parameter codes like MELCOR [1] which take into account the complex chemical reactions of the reactor materials but do not resolve the details of the flow. Once hydrogen has been created and is released into the containment the distribution of hydrogen and steam is simulated by the CFD code GASFLOW [2]. Depending on the type of accident this distribution phase can last for hours or even days. Therefore the heating of the structures and evaporation of water and condensation of steam must be considered also. During the distribution the hazard potential of the hydrogen-steam-air mixture must be assessed. This is done by applying three criteria. The first criterion are the ignition limits of the mixture. Only when the mixture is within the ignition limits combustion can be initiated. If the mixture can be ignited the next question is whether the flame can accelerate. From a large experimental database the σ -criterion has been derived [3]. Only if the expansion ratio of the burning mixture is higher than a certain threshold the flame can accelerate. If flame acceleration is possible the third criterion evaluates the possibility of a transition to a detonation (DDT). For DDT to occur the available space compared to the detonation cell size of the mixture must be large enough (λ -criterion). Depending on the results of the three criteria different combustion codes are used to calculate the further progress of the accident. If only the ignition criterion is fulfilled, the resulting slow flames are investigated with V3D. If flame acceleration is possible, COM3D [4] is used. And if DDT can not be excluded DET3D [5] can be used. The different combustion codes produce as result the loads on the containment structure. In case of a slow deflagration or a standing diffusion flame these are mainly thermal loads. For the faster combustion regimes mechanical loads are more important. The results of these calculations either verify that a given design is sufficient or give indications how the design must be modified, thus starting a new iteration through the whole sequence.

2. The computer code COM3D

For fast turbulent combustion processes the computer code COM3D is used. In this code the Favre-averaged Navier-Stokes equations are solved on a structured grid with constant cell size. Turbulence is modeled by either a standard k - ϵ -model or by the RNG k - ϵ -model. Combustion is described by the extended eddy-break-up model of Said and Borghi [6]. COM3D has been optimized to deal with complex three dimensional geometries with internal obstacles. A variety of explicit solvers including van Leer, Roe and various TVD schemes has been implemented. A more detailed description of the code can be found in [4].

3. Calibration and Validation of COM3D

The combustion model as well as the turbulence model in COM3D contain constants that must be specified. For the k - ϵ -model well known values for turbulent tube flow were used [7]. The single constant in the extended eddy-break-up model was calibrated against experiments performed in the FZK 12m tube. For this tube a large set of

experiments with different hydrogen-air mixtures and obstacle configurations is available. Experiments with different blockage ratios and different hydrogen concentrations were simulated with COM3D. For most of the experiments a value of $C_f = 6.0$ gave good agreement between calculation and measurement. For very lean mixtures the C_f values for best agreement deviated somewhat from this value. An important influence parameter is the geometrical scale of the problem. For larger scales a more violent combustion process can be expected. To cover this effect simulations of combustion processes on a larger scale in the RUT facility (63 m length) of the Kurchatov Institute were performed and compared to experimental data. It was found that these large scale experiments could be simulated with the same model constants as in the small scale experiments. During the simulation the length and time scales of turbulence and combustion were evaluated. This allows to locate the combustion process in the so called Borghi diagram. Collecting this information for many calculations allowed to identify the region in the Borghi diagram for which the extended eddy-break-up model has been calibrated.

4. Application of COM3D to a nuclear power plant containment

The length scale of the RUT facility is of the same order of magnitude as a typical nuclear power plant containment. But of course the total volume of the containment is much larger than the RUT facility. Thus it was possible to perform fast turbulent combustion calculations of a full size reactor containment. The grid for this simulation consisted of approximately 2100000 cells with a cell size of 0.4 m. The accident scenario chosen for the simulation was a small break loss of cooling accident (SBLOCA). In this scenario the release of hydrogen and the subsequent preconditioning of the hydrogen-steam-air mixture proceeds for a very long time. The gas distribution at the time of the proposed ignition were calculated with GASFLOW and then imported into COM3D. For the chosen scenario the simulation predicts maximum pressures on the outer containment shell of less than 3 bar. This maximum pressure is well below the design pressure of the containment of 5 bar. Higher pressure values are observed on internal structures in the containment, especially in the steam generator tower near the proposed ignition location.

5. Summary and Outlook

It has been shown that the combustion code COM3D is capable of predicting turbulent combustion processes in large geometric scales. Its application is not limited to nuclear safety investigations. Another possible application is the investigation of accident scenarios in the use of hydrogen as a future source of energy in transportation. However, there are several points that need further attention. The spatial resolution of the code should be increased to cover smaller details of the problem geometry and smaller details of the turbulent flow field. An adaptive grid refinement procedure is presently under development to achieve these goals. Another point for future work is the modeling of turbulent combustion. The extended eddy-break-up model used so far does not cover the whole area of interest in industrial applications. Therefore work is under way to supplement this model with a presumed β -PDF model.

6. References

- 1 R.O. GAUNTT ET AL. MELCOR Computer Code Manuals, Version 1.8.4 July 1997. NUREG/CR-6119, Vol. 1, Rev. 1; SAND97-2398; US Nuclear Regulatory Commission, Washington, DC, USA, 1998.
- 2 TRAVIS, J.R., ROYL, P., REDLINGER, R., NECKER, G., SPORE, J.W., LAM, K.L., WILSON, T.L., NICHOLS, B.D. AND MÜLLER, C. GASFLOW II: A three dimensional finite volume fluid-dynamics code for calculating the transport, mixing and combustion of flammable gases and aerosols in geometrically complex domains. Bericht FZKA-5994, LA-13357-M, Forschungszentrum Karlsruhe, 1997.
- 3 BREITUNG, W. AND DOROFEEV, S.B. Summary of DDT Criteria for Nuclear Power Plant Analysis. Jahrestagung Kerntechnik 99, Seiten 185-190, 1999.
- 4 KOTCHOURKO, A. AND BREITUNG, W. Numerische Simulation der turbulenten Verbrennung von vorgemischten Gasen in komplexen 3D-Geometrien. FZK Nachrichten Heft2, 2000.
- 5 REDLINGER, R. Numerische Simulation von Gasetonationen in komplexen 3D-Geometrien. FZK Nachrichten Heft2, 2000.
- 6 NAJI, H. SAID, R. AND BORGHİ, R. Towards a general turbulent combustion model for spark ignition engines. SAE 890672, SAE Technical Paper Series, 1989.
- 7 LAUNDER, B.E. AND SPALDING, D.B. The numerical computation of turbulent flows. Computer methods in Appl. Mech. and Eng., 3:269-289, 1974.

Addresses: DR. ULRICH BIELERT, DR. ALEXEI KOTCHOURKO, DR. BERNHARD BURGETH, DR. WOLFGANG BREITUNG Forschungszentrum Karlsruhe, Institut für Kern- und Energietechnik, Postfach 3640, 76021 Karlsruhe

DIEBELS, S.; EHLERS, W.; MARKERT, B.

Neglect of the Fluid Extra Stresses in Volumetrically Coupled Solid-Fluid Problems

Usually the fluid flow through porous media is described by Darcy's law or generalizations of it. In this contribution, Darcy's law is derived from the theory of porous media. To archive this, the fluid extra stress (frictional stress) is neglected in comparison with the momentum exchange (drag force) between the fluid phase and the solid skeleton of a two-phase model. This common assumption is motivated by the results obtained from a microscopic capillary model in combination with a dimensional analysis of the continuum mechanical model. This analysis shows that the influence of the fluid extra stress decreases with increasing number of capillary tubes per area element.

1. Macroscopic Model

The Theory of Porous Media may be used to derive Darcy's law. The theoretical approach is based on the concept of superimposed continua and on the concept of volume fractions. Details are given e. g. by Ehlers [2, 3] and others. The balance equations for a materially incompressible fluid-phase flowing through a porous medium read

$$(n^F)'_F + n^F \operatorname{div} \mathbf{x}'_F = 0, \quad \rho^F \mathbf{x}''_F = \operatorname{div} \mathbf{T}^F + \rho^F \mathbf{g} + \hat{\mathbf{p}}^F. \quad (1)$$

Therein, n^F is the porosity, $\rho^F = n^F \rho^{FR}$ is the partial fluid density, \mathbf{x}'_F and \mathbf{x}''_F are the macroscopic velocity and acceleration, respectively, \mathbf{T} , $\hat{\mathbf{p}}^F$ and \mathbf{g} are the fluid Cauchy stress tensor, the momentum exchange between the fluid and the porous skeleton, and the gravity. Eq. (1)₁ results from the balance of mass, if the effective density ρ^{FR} is assumed to be materially constant. According to thermodynamical investigations, the stress tensor and the momentum exchange are split into a term depending on the pore pressure p and so-called extra terms depending on the rate of deformation $\mathbf{D}_F = 1/2(\operatorname{grad} \mathbf{x}'_F + \operatorname{grad}^T \mathbf{x}'_F)$ and on the seepage velocity $\mathbf{w}_F = \mathbf{x}'_F - \mathbf{x}'_S$. In the physically linear case, the constitutive equations for the stress tensor and for the interaction force may be written as

$$\mathbf{T}^F = -n^F p \mathbf{I} + 2\mu^F \mathbf{D}_F, \quad \hat{\mathbf{p}}^F = p \operatorname{grad} n^F - \frac{(n^F)^2 \gamma^{FR}}{k^F} \mathbf{w}_F. \quad (2)$$

Therein, the dynamic viscosity of the fluid is μ^F , the bulk viscosity ζ^F is neglected for simplicity, γ^{FR} is the effective weight of the fluid, and, finally, k^F is the Darcy permeability describing the geometry of the pore-space as well as viscous properties of the fluid. The combination of (1)₂ and (2) yields Darcy's law provided that the processes are quasi-static, i. e. $\mathbf{x}''_F \approx 0$, and, furthermore, that the extra stresses $\mathbf{T}_E^F = 2\mu^F \mathbf{D}_F$ are neglected in comparison with the extra momentum exchange $\hat{\mathbf{p}}_E^F = -(n^F)^2 \gamma^{FR} \mathbf{w}_F / k^F$. In this case, Darcy's law is obtained in the following form:

$$n^F \mathbf{w}_F = -\frac{k^F}{\gamma^{FR}} (\operatorname{grad} p - \rho^{FR} \mathbf{g}). \quad (3)$$

2. Microscopic Model

An interpretation of the Darcy permeability in terms of the structure of the pore-space will be given in this section. Therefore, the flow through the pores is described by a simple capillary model. In this case, N capillary tubes crossing an area element of size A are taken into account. For simplicity, all tubes are assumed to be parallel and of the same diameter d and length l . For a Newtonian fluid, in each tube the flow is of Hagen-Poiseuille type, if inertia and gravitation are not taken into account. According to [5], the volume flux Q caused by a pressure difference Δp in one of the tubes may be expressed as

$$Q = -\frac{\pi d^4 \Delta p}{128 \mu^F l}. \quad (4)$$

The total volume flux of fluid crossing the area element A is then given by $Q_A = N Q$. On the other hand, it follows from the macroscopic model, that the flux of volume crossing an area element A is $Q_A = (n^F \mathbf{w}_F \cdot \mathbf{n}) A$, where \mathbf{n} is

the unit normal. If the volume fluxes according to the microscopic and to the macroscopic approach are equivalent, the Darcy permeability k^F may be computed in terms of the microscopic quantities as follows

$$Q = -N \frac{\pi d^4 \Delta p}{128 \mu^F l} = -\frac{k^F}{\gamma^{FR}} \frac{\Delta p}{l} \quad \rightarrow \quad k^F = \frac{n^F d^2 \gamma^{FR}}{32 \mu^F} \quad \rightarrow \quad K^S = \frac{\mu^F}{\gamma^{FR}} k^F = \frac{n^F d^2}{32}. \quad (5)$$

In (5), it is taken into account that the *Hagen-Poiseuille* flow is derived under the assumption of a constant pressure gradient $\Delta p/l$. In addition, it follows that the intrinsic permeability K^S is a function of the volume fraction n^F and of the diameter d of the capillary tubes only. Similar results have been presented previously, e. g. by Rusch [6]. These relations are applied in the next section within the framework of a dimensional analysis of the macroscopic model. As a consequence of this analysis, it will be shown that the neglect of the fluid extra stress in the continuum mechanical approach is justified.

3. Dimensional Analysis

For the following analysis, the motion of the solid skeleton is neglected, i. e. $\mathbf{w}_F \approx \mathbf{x}'_F$. The combination of the quasi-static balance of momentum according to (1)₂ and of the constitutive equations (2) may be written in a dimensionless form, if the position vector \mathbf{x} is scaled by a characteristic length L , $\mathbf{x} = L \mathbf{x}^*$, and the seepage velocity \mathbf{w}_F is scaled by a characteristic velocity V , $\mathbf{w}_F = V \mathbf{w}^*$. In the dimensionless form, the magnitude of the viscous forces $\mathcal{O}(\text{div} \mathbf{T}_E^F)$ resulting from the extra stress and the magnitude $\mathcal{O}(\hat{\mathbf{p}}_E^F)$ of the extra interaction force are given by the parameter combinations related to the dimensionless stress and to the dimensionless momentum exchange, respectively. The extra stress and the extra interaction may be compared in terms of a dimensionless number relating the order of magnitude of one to the other [1, 4]:

$$\Pi = \frac{\mathcal{O}(\text{div} \mathbf{T}_E^F)}{\mathcal{O}(\hat{\mathbf{p}}_E^F)} = \frac{\mu^F k^F}{(n^F)^2 \gamma^{FR} L^2}. \quad (6)$$

If it is assumed that the characteristic length scale is related to the characteristic area element, $L^2 = A$, and, furthermore, if the results of the microscopic model for the permeability according to (5) are substituted, it can be seen that the dimensionless number Π is proportional to N^{-1} :

$$\Pi = \frac{1}{8\pi N} = \mathcal{O}(1/N). \quad (7)$$

This result may be interpreted as follows: The macroscopic model validly describes the flow through the pore-space, if the pores are small compared with the macroscopic length scale. In this case, there is a large number N of capillary tubes per characteristic area A . Therefore, the value of Π is rather small, and, as a consequence, the extra stress is negligible with respect to the interaction force. This situation fits to the concepts behind the Theory of Porous Media and justifies the neglect of the fluid extra stress in the macroscopic approach. On the other hand, if there is only one tube per characteristic area, the interaction force and the fluid extra stress are of the same magnitude, and both of them must be taken into account in the framework of a microscopic model.

4. References

- 1 DIEBELS, S.: Mikropolare Zweiphasenmodelle: Formulierung auf der Basis der Theorie Poröser Medien. Habilitation, Bericht Nr. II-4 aus dem Institut für Mechanik (Bauwesen), Universität Stuttgart 2000.
- 2 EHLERS, W.: Constitutive Equations for Granular Materials in Geomechanical Context. In HUTTER, K.: Continuum Mechanics in Environmental Sciences, CISM Courses and Lectures No. 337, Springer-Verlag, Wien (1993), 313–402.
- 3 EHLERS, W.: Grundlegende Konzept in der Theorie Poröser Medien. Technische Mechanik **16** (1996), 63–76.
- 4 EHLERS, W.; ELLSIEPEN, P.; BLOME, P.; MAHNKOPF, D. & MARKERT, B.: Theoretische und numerische Studien zur Lösung von Rand- und Anfangswertproblemen in der Theorie Poröser Medien. Bericht aus dem Institut für Mechanik (Bauwesen) Nr. 99-II-1, Universität Stuttgart 1999.
- 5 PRANDTL, L.: Strömungslehre. 6. Auflage, Vieweg & Sohn, Braunschweig 1965.
- 6 RUSCH, K. C.: Dynamic Behavior of Flexible Open-cell Foams. The University of Akron, Ph. D. Thesis, Engineering, general, 1965.

Address: Dr.-Ing. STEFAN DIEBELS, Prof. Dr.-Ing. WOLFGANG EHLERS, Dipl.-Ing. BERND MARKERT, Universität Stuttgart, Institut für Mechanik (Bauwesen), Lehrstuhl II, Pfaffenwaldring 7, 70569 Stuttgart, Deutschland.

EHLERS, W., BLOME, P.

A multi-phase soil model including a soil-foundation interface

In the present contribution, the frictional material soil is considered within the well-founded framework of the Theory of Porous Media [1-3]. The model represents a multi-phase medium consisting of a solid skeleton, a pore-liquid (here water) and a pore-gas (here air). Concerning the solid skeleton, a general elasto-plasticity approach including a soil-foundation interface is presented. In particular, to describe granular soils like sand, a physically non-linear soil elasticity law [4] is taken into consideration. In the plastic domain, use is made of the single-surface yield function by Ehlers [2], which is extended towards isotropic work-hardening materials.

1. The soil model

The soil model is composed by the phases φ^α . These phases are φ^S , the soil skeleton, φ^L , a pore-liquid, and φ^G , a pore-gas. In case of fluid saturation, the saturation constraint holds. Thus,

$$n^S + n^L + n^G = 1 \quad \text{with the porosity} \quad n^F = n^L + n^G, \quad (1)$$

where n^α are the volume fractions of the constituents. It is assumed that the solid and the liquid are materially incompressible, whereas the gas phase is materially compressible according to the ideal gas law (Boyle's law).

The primary variables of the model are the solid displacement \mathbf{u}_S , the effective pore pressures p_E^{LR} of the liquid and p_E^{GR} of the gas exceeding the atmospheric pressure p_0 . For their numerical determination, the sum of the partial linear momentum balances of all constituents, the sum of the partial volume balances of the solid and the liquid and the sum of the partial mass balances of the solid and the gas are used. In the quasi-static case, the corresponding weak forms are

$$\int_{\Omega} \delta \mathbf{u}_S \cdot (\rho^S + \rho^L + \rho^G) \mathbf{b} \, dv - \int_{\Omega} \text{grad } \delta \mathbf{u}_S \cdot (\mathbf{T}^S + \mathbf{T}^L + \mathbf{T}^G - \rho^L \mathbf{d}_L \otimes \mathbf{d}_L - \rho^G \mathbf{d}_G \otimes \mathbf{d}_G) \, dv = - \int_{\Gamma} \delta \mathbf{u}_S \cdot \bar{\mathbf{t}} \, da. \quad (2)$$

$$\int_{\Omega} \delta p_E^{LR} [(n^S + n^L)'_S + (n^S + n^L) \text{div}(\mathbf{u}_S)'_S] \, dv - \int_{\Omega} \text{grad } \delta p_E^{LR} \cdot n^L \mathbf{w}_L \, dv = - \int_{\Gamma} \delta p_E^{LR} \bar{v}^L \, da, \quad (3)$$

$$\begin{aligned} \int_{\Omega} \delta p_E^{GR} [n^G (\rho^{GR})'_S + (1 - n^L) \rho^{GR} \text{div}(\mathbf{u}_S)'_S - \rho^{GR} (n^L)'_S] \, dv - \\ - \int_{\Omega} \text{grad } \delta p_E^{GR} \cdot n^G \rho^{GR} \mathbf{w}_G \, dv = - \int_{\Gamma} \delta p_E^{GR} \bar{q}^G \, da, \end{aligned} \quad (4)$$

Therein, \mathbf{T}^α is the partial Cauchy stress tensor related to each φ^α , \mathbf{d}_L and \mathbf{d}_G denote the diffusion velocities of the liquid and gas phases with respect to the local barycentric velocity $\mathbf{v}_F = (\rho^L \mathbf{v}_L + \rho^G \mathbf{v}_G)/(\rho^L + \rho^G)$ of the fluid mixture. $\rho^\alpha = n^\alpha \rho^{\alpha R}$ is the partial mass density given by the effective (true) mass density $\rho^{\alpha R}$ and the volume fraction n^α . The symbol $(\cdot)'_S$ characterizes the material time derivative following the motion of the solid phase. Furthermore, \mathbf{b} denotes the volume force per unit mass (gravity), \mathbf{w}_L and \mathbf{w}_G represent the seepage velocities of the respective fluids. Finally, $\delta \mathbf{u}_S$, δp_E^{LR} and δp_E^{GR} are test functions corresponding to the solid displacement and the excess pore pressures of the liquid and gas phases.

On the surface Γ of a considered domain Ω , there may act an external stress vector $\bar{\mathbf{t}} = \mathbf{T} \mathbf{n}$, a liquid volume efflux $\bar{v}^L = n^L \mathbf{w}_L \cdot \mathbf{n}$ or a gas mass efflux $\bar{q}^G = n^G \rho^{GR} \mathbf{w}_G \cdot \mathbf{n}$. Here, \mathbf{T} is the total stress tensor and \mathbf{n} the outward oriented unit surface normal on Γ .

According to the effective stress principle, the total stress tensor can be reformulated by

$$\mathbf{T} = \mathbf{T}_E^S - n^L/n^F p_E^{LR} \mathbf{I} - n^G/n^F p_E^{GR} \mathbf{I} - \rho^L \mathbf{d}_L \otimes \mathbf{d}_L - \rho^G \mathbf{d}_G \otimes \mathbf{d}_G, \quad (5)$$

where \mathbf{T}_E^S denotes the solid extra stress (effective stress). Furthermore, the filter velocities $n^L \mathbf{w}_L$ in (3) and $n^G \mathbf{w}_G$ in (4) are replaced by Darcy's general filter law. The dependence of the filter law on the soil deformation and on

the degree of fluid saturation has to be taken into consideration additionally.

The numerical implementation of the model leads to a differential-algebraic equation (DAE) of first order in time. The solution of this DAE by the FE method determines the solid deformation \mathbf{u}_S , the excess pore pressures p_E^{LR} and p_E^{GR} and therewith the seepage velocities \mathbf{w}_L and \mathbf{w}_G .

2. An elasto-plasticity material law for soils including a soil-foundation interface

The extra part \mathbf{T}_E^S of the solid stress is described in the framework of a geometrically linear theory by a physically non-linear elasticity law that is appropriate to describe the complex material behaviour of frictional soil materials:

$$\mathbf{T}_E^S = 2\mu^S(\varepsilon_{vp})\varepsilon_{Se}^D + k^S(\varepsilon_{ve}; \varepsilon_{vp}, \varepsilon_{v \min})(\varepsilon_{Se} \cdot \mathbf{I})\mathbf{I}. \quad (6)$$

Therein, μ^S and k^S are not the usual elastic constants. In particular, k^S is a function of the elastic volume strain ε_{ve} at a given state of plastic deformations. Thus, the plastic volume strain ε_{vp} and the maximal achievable volume contractancy $\varepsilon_{v \min}$ must be understood as parameters of the elastic process [4].

For the description of the plastic material behaviour, the model proceeds from a single surface yield criterion, isotropic work-hardening conditions and a non-associated flow rule [2, 4]:

$$F = \sqrt{\Pi_D (1 + \gamma \text{III}_D / (\Pi_D)^{3/2})^m + \frac{1}{2} \alpha \text{I}^2 + \delta^2 \text{I}^4 + \beta \text{I} + \epsilon \text{I}^2 - \kappa}, \quad (7)$$

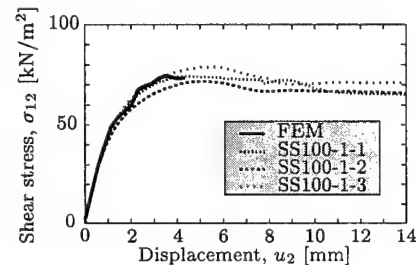
$$G = \sqrt{\psi_1 \Pi_D + \frac{1}{2} \alpha \text{I}^2 + \delta^2 \text{I}^4 + \psi_2 \text{I} + \epsilon \text{I}^2} \rightarrow (\varepsilon_{Sp})'_S = \Lambda \partial G / \partial \mathbf{T}_E^S. \quad (8)$$

The yield criterion, $F = 0$, is described by the first invariant I and the second and third deviatoric invariants Π^D and III^D of \mathbf{T}_E^S together with a set of seven material parameters. The subset $(\alpha, \beta, \delta, \epsilon, \kappa)$ refers to the shape of the yield curve in the hydrostatic plane of the principal stress space, whereas the subset (γ, m) refers to the deviatoric plane. For the consideration of work-hardening conditions, the parameters are developed as functions of the plastic work. In the framework of the non-associated plasticity concept, an additional plastic potential (8) is used, where the parameters ψ_1 and ψ_2 govern the plastic dilatation angle. Consequently, the flow rule is given with respect to G , where Λ is the plastic multiplier.

An interface formulation for the description of the contact zone between foundation and soil is considered necessary, when the material behaviour in this zone is substantially different from the material behaviour of the pure soil. Therefore, in the scope of a continuous formulation, the presented model is also applied in the contact zone using a modified set of material parameters. These modified parameters are generated by the reduction of the maximal plastic work taken by the material.

3. Example: numerical simulation of a shear test on Berlin sand

The numerical example considers a shear test with a vertical load of $\sigma_{11} = 100 \text{ kN/m}^2$. A parameter identification by experimental data from triaxial tests on dense *Berlin* sand was performed before [4]. Result of the numerical simulation of the interface "sand-sand" by the FE method is a shear stress-displacement curve that reproduces successfully the experimental findings up to the maximal shear stress. Ongoing, the interface "sand-concrete" is studied in a corresponding test.



4. References

- 1 DE BOER, R., EHLERS, W.: Theorie der Mehrkomponentenkontinua mit Anwendung auf bodenmechanische Probleme, Teil I; Forschungsberichte aus dem Fachbereich Bauwesen der Universität-GH-Essen 40, Essen 1986.
- 2 EHLERS, W.: Constitutive equations for granular materials in geomechanical context; in: K. Hutter (ed.), Continuum Mechanics in Environmental Sciences and Geophysics, CISM Courses and Lectures No. 337, Springer-Verlag, Wien 1993, 313-402.
- 3 EHLERS, W.: Grundlegende Konzepte in der Theorie Poröser Medien; Technische Mechanik 16 (1996), 63-76.
- 4 EHLERS, W., MÜLLERSCHÖN, H.: Parameter Identification of a Macroscopic Granular Soil Model Applied to Dense Berlin Sand; Granular Matter 2 (2000), to appear.

Addresses: PROF. DR.-ING. WOLFGANG EHLERS, DIPL.-ING. PETER BLOME, Universität Stuttgart, Institut für Mechanik (Bauwesen), Lehrstuhl II, Pfaffenwaldring 7, D-70569 Stuttgart, Germany.

FAVIER, V., VERVISCH, L.

Partial premixing in diffusion flame quenching

Using Direct Numerical Simulation, we focus on the development of partial premixing in laminar diffusion flame quenching. Calculations are performed in the configuration of a 2-D diffusion flame squeezed by a pair of vortices. First, the flame undergoes strong finite rate chemistry effects, linked to high levels of strain rate induced by vorticity. Then quenching develops, leading to edge-flames. During the creation of the hole within the reaction zone, the response of the laminar diffusion flame burning rate to strain rate variation is investigated. Depending on the flame structure, strong differences between DNS results and the behavior of a steady 1-D flamelet are observed, on account of partial premixing.

1. Introduction

Finite rate chemistry and quenching in diffusion flames lead to intermediate combustion regimes between fast chemistry and fast micromixing [1]. Modeling partially premixed combustion in industrial devices requires a good understanding of these phenomena, local quenching prohibits flame stabilization and modifies pollutants formation [2].

In order to study the quenching mechanisms and the flame structure bordering quenched locations, numerical simulations of diffusion flame quenching are investigated. It is shown that one may distinguish between conditions leading to transition from burning to quenching and conditions observed at a quenched location featuring different flame properties, related to combustion in a partially premixed regime.

2. Diffusion flame quenching, edge flame and partially premixed flamelets

Diffusion flames may be parametrized using the mixture fraction Z as a conserved scalar ($Z = 0$ in pure oxidizer and $Z = 1$ in pure fuel). The local Damköhler number Da is defined as the ratio of a diffusive time τ_χ to a chemical time [3]. When Da falls below a critical value Da_q^* , flame quenching occurs. τ_χ may be estimated from the scalar dissipation rate $\chi = D|\nabla Z|^2$ as $\tau_\chi \approx \chi^{-1}$ (D is a diffusion coefficient). Solutions of planar flame problems for a variety of χ , called flamelet library, provide the critical quenching value χ_q^* used in turbulent combustion models [1].

To study flamelet quenching without curvature of the stoichiometric line, we have further analyzed a Direct Numerical Simulation (DNS) database initially developed to focus on triple flame / vortices interaction [4]. The diffusion flame is initially stabilized within a 2-D domain following a procedure proposed in [5]. For strong vortices, the trailing diffusion flame is submitted to a high level of strain and χ leading to quenching of the 2-D planar diffusion flamelet (Fig. 1). We focus on the zone of the computational domain where quenching appears and where only diffusion combustion is concerned. For the simulated case, the vortices do not carry any hot gases and products remaining from their interaction with the partially premixed front and effects of unsteadiness are negligible in our analysis.

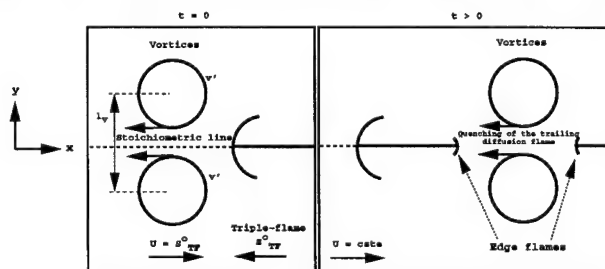


Figure 1: Schematic of the simulations of two-dimensional quenching.

A laminar flamelet library has been constructed using the same chemistry and transport than in the full Navier Stokes simulation. The reference quenching scalar dissipation rate χ_q^* , its corresponding quenching length $\delta_q = (D/\chi_q^*)^{1/2}$ and the scalar dissipation rate in the unperturbed trailing diffusion flame χ_{Diff} may be used as control parameters. The vortices are characterized by their radius R , velocity v' and the length l_v (Fig. 1). The reported simulations have been performed using a representative condition where diffusion flame quenching is found: $\chi_q^*/\chi_{Diff} \approx 100$, $l_v/\delta_q \approx$

12, $R/\delta_q \approx 5$, $v' / (\chi_q^* \delta_q) \approx 40$. Varying these numbers changes the streamwise position of quenching, but do not fundamentally modifies the presented results. The studied sequence may be decomposed in three stages (Fig. 2).

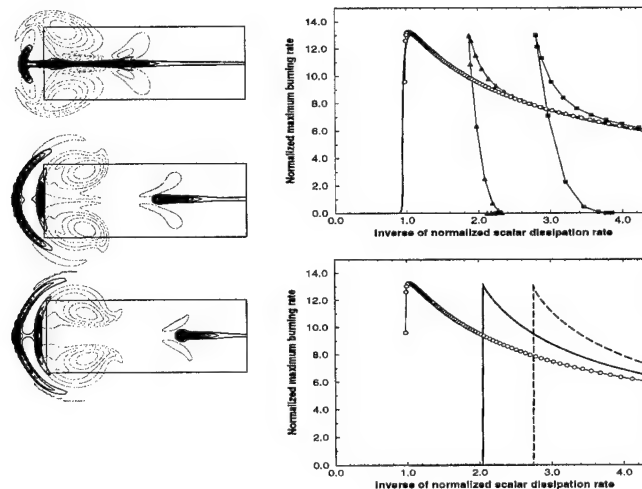


Figure 2: Three successive times of 2-D unsteady quenching of a planar diffusion flame pinched by a pair of vortices, configuration studied in [4]. Left, bold: iso-reaction rate, dotted: vorticity, frame: region of the flow where the centerline response of the flame versus inverse mixture fraction dissipation rate is studied. Right top, circle: 1-D flamelet library, line: top left 2-D flame, triangle: middle left 2-D flame, square: bottom left 2-D flame. Right bottom, circle: 1-D flamelet library, line: partially premixed flamelet $\phi_m = 0.16$, dash line: $\phi_m = 0.19$.

The planar diffusion flame is first squeezed by the vortices, then quenching occurs. Latter, premixed kernels develop at the reaction zone extremities. The centerline response of the burning rate shows that one should distinguish between the amount of scalar dissipation rate necessary to quench the diffusion flame χ_q , and, χ_{qEd} , the value measured at the extremity of the reaction zone, featuring an edge flame [6] (Fig. 2). In these unsteady simulations, the value χ_q that should be applied to transition from burning to quenching is found to be of the order of χ_q^* predicted by flamelet theory (Fig. 2 top right). In particular when $\chi > \chi_q^*$, quenching is observed. However, once a hole exists in the reaction zone, χ_{qEd} , the level of scalar dissipation rate necessary to maintain quenching, is always lower than the reference flamelet value χ_q^* . This is explained by multi-dimensional flux of species and heat at the flame tip combined with partial premixing of the reactants in the zone bordering the quenched location.

An indicator of the local degree of partial premixing is given by the product of reactants mass fractions $\phi_m = Y_F Y_O$. In a pure mixing situation: $\phi_m = Y_{F,o} Y_{O,o} Z(1 - Z)$, where $Y_{F,o}$ and $Y_{O,o}$ are the mass fractions of fuel and oxidizer in the feeding streams. Flamelet library are usually constructed using as boundary conditions for (Y_F, Y_O, Z) the values $(0, Y_{O,o}, 0)$ and $(Y_{F,o}, 0, 1)$. They may also be constructed for prescribed values of partial premixing ϕ_m . Fig. 2 (bottom right) suggests that steady partially premixed flamelets, parametrized with both ϕ_m and χ , reproduce the edge flame response after quenching has developed. A meaningful result for flamelet modeling of turbulent burners where strong finite rate chemistry and quenching occur, and have to be captured carefully.

3. References

- 1 PETERS, N.: Turbulent Combustion. Cambridge University Press.
- 2 VERVISCH, L., POINSOT, T.: Direct numerical simulation of non-premixed turbulent flame. *Annu. Rev. Fluid Mech.* **30** (1998), 655–692.
- 3 LIÑÁN, A.: The asymptotic structure of counterflow diffusion flames for large activation energies. *Acta Astronautica*. **1007** No.1 (1974).
- 4 FAVIER, V., VERVISCH, L.: Effects of unsteadiness in edge-flames and liftoff in non-premixed turbulent combustion. In 27th Symp. (Int.) on Combustion. The Combustion Institute (1998), 1239–1245.
- 5 RUETSCH, G.R., VERVISCH, L., LIÑÁN, A.: Effects of heat release on triple flame. *Phys. Fluids*, **6** No.7 (1995), 1447–1454.
- 6 BUCKMASTER, J., WEBER, R.: Edge-flame holding. In Proceedings of the 26th Symp. (Int.) on Combustion. The Combustion Institute, Pittsburgh (1996).

Addresses: V. FAVIER, PROF. L. VERVISCH, INSA - CNRS - CORIA - UMR 6614, Avenue de l'Université - BP 8, 76801 Saint Etienne du Rouvray Cedex, France. Contact e-mail: favier@coria.fr, vervisch@coria.fr

GEIß, S., SADIKI, A., MALTSEV, A., DREIZLER, A., JANICKA, J.

Investigations of Turbulence Modulation in Turbulent Particle Laden Flows

This paper presents the results of experimental and numerical analyses of high particle laden turbulent flows. The dispersed phase consists of non-reacting solid mono-dispersed particles with variable diameter between $60\mu\text{m}$ and $1500\mu\text{m}$. Experiments using Laser Doppler Anemometer (LDA) and Phase Doppler Anemometer (PDA) show in agreement with earlier investigations that small particles attenuate turbulence while large particles enhance turbulence. More detailed investigations are, however, needed to clearly identify and quantify such influences. In order to obtain preliminary information about the performance of the $k-\epsilon$ model, mostly used for the majority of the numerical models, in predicting the physical features of modulation, some numerical calculation results obtained by use of Euler / Lagrange method and a modified version of the $k-\epsilon$ model are compared to the experimental data.

1. Introduction

Particle laden flows or turbulent multiphase flows are frequently encountered in a variety of technical processes (injection, sprays, chemical or combustion processes, etc.). These processes include separated flows, bubble flows, gas-solid, gas-liquid or solid-liquid flows with or without chemical reactions. In such flows, the processes are considerably influenced by interactions between the turbulence of the carrier phase (the continuous phase) and the dispersed phase.

Three types of turbulence / dispersed phase interactions have been identified in the literature: a) turbulent dispersion of the dispersed phase; here, the particle motion is additionally influenced by interaction with the walls of the confinement; b) modification of the continuous phase turbulence characteristics by the dispersed phase or by interphase transport, the so-called turbulence modulation, and c) modification of interphase transport by turbulence. The third type of interaction is much less investigated and, consequently, less understood [1]. Several sources review the state of the art for the first two types of turbulence / dispersed phase interaction [2]. Although several models have been developed for turbulence modification besides recent direct numerical simulation [3], it appears that they have limited application as they all fail to predict the increase in turbulence energy experimentally observed for large particles. Careful experimentation and more appropriate models are still demanded to clearly identify, predict and quantify the mechanisms for turbulence in multiphase flows. This paper aims to investigate experimentally and numerically the turbulence modulation in turbulent particle laden flows without chemical reactions.

2. Experimental set-up and measurement techniques

For the experimental investigations a vertical closed test tunnel was designed and built up. This is a strongly modified test facility compared to Kulick et al. [4]. The carrier phase - driven by a radial compressor - circulates in a closed pipe system. The glass particles are dispersed in required doses by a sluice, generating the two phase flow. The flow passes a diffuser with an half-angle of $\alpha/2=4.1^\circ$ before reaching the settling chamber where diverse meshes (first mesh $\beta=0.37$, second mesh $\beta=0.60$; β : open area ratio) and honeycombs are integrated. Consequently a nozzle with a contraction ratio of 1,57:1 homogenises the flow. At the nozzle exit a turbulence grid and the measurement section are placed. In a following section the two phases are separated by use of a cyclone. The essential data of the set-up are: a) the measurement section is designed as a vertical square glass tunnel with inner dimensions of $0,2\text{m} \times 0,2\text{m} \times 2,0\text{m}$; b) the maximum mean velocity of the measurement section is 12m/s ; c) the particle size can be varied between $60\mu\text{m}$ and $1500\mu\text{m}$ (the maximum of the particle size is limited by the smallest used mesh size); d) the particle concentration is constant and can be chosen between $\mu=0-2$ (μ : ratio of mass of the particle phase and mass of the carrier phase; the maximum of the particle concentration is limited by the optical transparency of the flow).

For simultaneous measurements of velocity (mean velocity, higher moments), correlations, particle size and concentrations a two dimensional LDA/PDA set-up is used. The optical set-up consists of a fibre flow probe including a beam expansion; the beams are separated on the focusing lens ($f_{\text{LDA}}=310\text{mm}$) by $b_s=75,24\text{mm}$. For this optical configuration the measurement volume results in a diameter of $d_R=46\mu\text{m}$ and a length of $d_L=380\mu\text{m}$. For the PDA measurements the LDA measurement volume is combined with PDA receiving optic with a focal length of $f_{\text{PDA}}=400\text{mm}$ (PDA probe without beam expansion). Detailed descriptions of the measurement techniques can be found in [5].

3. General flow characteristics

For the investigations it is required that the flow field has to be isotropic and stationary. Grid generated turbulent flows approximate these requirements. Such flow fields decrease in intensity of the turbulent kinetic energy in the direction of the mean flow. The decay of turbulence is characterised by at least two distinct regions. The first region which is important in the present study is defined between 10 and 100 mesh length downstream the grid. The second region is located beyond 500 mesh lengths which is not investigated here.

In this study two different biplanar square turbulence grids are employed. The characteristics of the grids are: mesh length $M=6\text{mm}$ (1mm thickness of wire) and $M=12\text{mm}$ (2mm thickness of wire). The selection for both grids is based on the requirement to obtain a high level of turbulence but also to maintain a local isotropic flow field. In respect to these needs a solidity ratio (projected solid area over total area) of $s=0,31$ is chosen.

4. Results and discussions

For both types of turbulence grids the flow field in the wind tunnel is characterised in a first step without particles. The LDA measurements are performed over a fine point grid covering the core (8cm square area) of the wind tunnel to avoid the influence of the boundary layer. Gravitational effects are also negligible. The measurements span from at $x/M=10$ to $x/M=60$. The turbulence is found to be homogeneous in planes perpendicular to the mean flow direction up to $x/M=40$. To obtain the degree of local isotropy, the ratio of the mean square velocity fluctuation in streamwise direction u'^2 to that of the vertical v'^2 and horizontal w'^2 cross stream direction is computed. Throughout the test section, the local isotropy is found to be higher than 95% (see Fig. 1). Measurements of decay of the turbulent energy in the streamwise direction are found to agree well with that expected by the use of such grids. The corresponding behaviour is shown in Fig. 1 in addition to earlier experimental results [6] using different grids. For the investigation of particle laden flows identical measurement locations are taken. To illustrate the influence of a dispersed phase round glass particles (diameter $d_p=110\mu\text{m}\pm 10\mu\text{m}$) are used. The density of the particles is $\rho_p=2440\text{kg/m}^3$ and the particle concentration is set to $250\text{ particles/cm}^3$. Measurements of induced decay of the turbulence energy show that such small particles attenuate turbulence. A comparison with results obtained without particles is given in Fig. 2 in addition to numerical results. For these simulation purposes a modified k- ϵ model following [7] has been used and is not presented here.

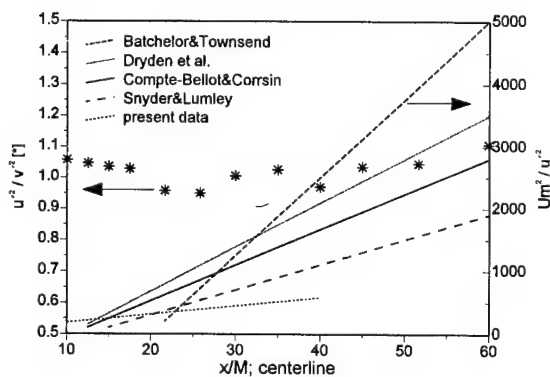


Figure 1

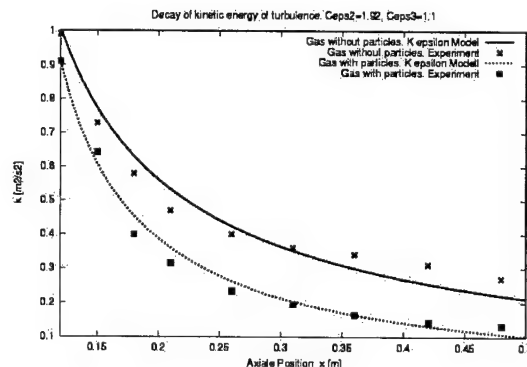


Figure 2

5. Conclusion

Detailed measurements obtained by means of LDA and PDA are used for comparison to standard numerical models for dispersed two phase flows. In particular, a simple modified k- ϵ model in the Euler / Lagrange framework is tested in order to obtain information about the performance of this model. This model compares well to experimental data which indicate that small particles attenuate turbulence. The effect of larger particles ($>1\text{mm}$) which augment turbulence on the continuous phase is the topic of further investigations.

Acknowledgements

The authors are grateful for the financial support by the German Research Foundation (DFG), contract no. JA544/11-2.

6. References

- 1 ISKENDER, G., CHAUEAU, C., SIMON, O.: *Mass transfer from liquid fuel droplets in turbulent flow*; The Combustion Institute, Elvier Science Publ. 1992.
- 2 CROWE, C.; SOMMERFELD, M., TSUJI, Y.: *Multiphase flows with droplets and particles*; CRC Press, NY., 1998.
- 3 ELGOBASHI, S. and TRUESDELL, G.C.: *On the two-way interaction between homogeneous turbulence and dispersed particles. I: Turbulence modification*, Phys. Fluids A, Vol. 5 (7) pp.1790-1801, 1993.
- 4 KULICK, J.D.; FESSLER, J.R., EATON, J.K.: *Particle response and turbulence modification in fully developed channel flow*; J. Fluid Mech., 277, pp. 109-134, 1994.
- 5 RUCK, B.: *Lasermethoden in der Strömungsmesstechnik*; AT-Fachverlag GmbH; Stuttgart; 1990.
- 6 WELLS, M.R. and STOCK, D.E.: *The Effects of Crossing Trajectories on the Dispersion of Particles in a Turbulent Flow*; J. Fluid Mech., 136, pp. 31-62, 1983.
- 7 KOHNEN, G. and SOMMERFELD, M.: *The effect of turbulence, Modelling on turbulence modification in two-phase flows using the Euler-Lagrange approach*, 11th Symp. On Turbulent shear flows, Grenoble, 1997.

Addresses: GEIß, S., SADIKI, A., MALTSEV, A., DREIZLER, A., JANICKA, J. Technische Universität Darmstadt, FG Energie- und Kraftwerkstechnik, Petersenstr. 30, 64287 Darmstadt, Germany

GERLINGER, W., SCHNEIDER, K., BOCKHORN, H.

Direct numerical simulation of three-dimensional flame instabilities

The evolution of premixed gas flames near extinction and stability limits is of primary interest for many applications in combustion technology. Under such conditions the flames are very sensitive, and exhibit quasi-steady state behaviour so that they are well-suited to determine flammability limits. We show three-dimensional numerical simulation of the transient behaviour of lean H_2 -air flames. The thermo-diffusive equations are solved by means of a parallelized Fourier-pseudospectral code. We compute the evolution of freely propagating spherical flames, whereby the influence of the initial flame radius is investigated. The results exhibit different behaviour as found in experimental studies under microgravity conditions, i.e. the splitting due to cellular instabilities, extinction, and stationary flame balls.

1. Introduction

Premixed gas flames near extinction and stability limits are of primary interest for many applications, e.g. the improvement of energy conversion engines or fire safety applications. For many reactive systems there is little knowledge about the very sensitive near-extinction conditions. Because the dominating significance of earth-generated buoyancy is excluded, microgravity (μg) conditions constitute a suitable environment to investigate the interaction of scalar transport, chemical reaction and radiation.

Many μg -experiments have been performed to study the extinction and flammability limits of premixed lean gas mixtures at small Lewis numbers [6]. These studies show different phenomena such as local extinction, cellular instabilities, and steady flame balls.

We present the studies on the non-stationary behaviour of flame balls in three dimensions by means of direct numerical simulation of the governing partial differential equations. The code was implemented and optimized on a massively parallel computer so that large scale problems using high resolutions can be solved. In particular, we are interested in the influence of the initial radius and the radiative heat loss onto the evolution of the flame structures.

2. Numerical method

Our research deals with the numerical simulation of two- and three-dimensional flame balls. As governing equations we employ the thermo-diffusive model in its dimensionless form [1],

$$\partial_t T - \nabla^2 T = \omega - \sigma, \quad (1)$$

$$\partial_t Y - \frac{1}{Le} \nabla^2 Y = -\omega, \quad (2)$$

$$\omega = \frac{\beta^2}{2Le} Y \exp\left(\frac{\beta(T-1)}{1+\alpha(T-1)}\right), \quad (3)$$

$$\sigma = s(T + (\alpha^{-1} - 1))^4 - s(\alpha^{-1} - 1)^4. \quad (4)$$

The physical quantities are nondimensionalized with the flame thickness, the flame velocity, and the burnt and unburnt state. The chemical reaction is modelled by single-step kinetics with the Zeldovich number β and a temperature ratio α . The heat loss due to radiation is represented by the Stefan-Boltzmann law with radiation constant s . The Lewis number Le is the ratio of the species and heat diffusion. The above model equations exclude convection and assume the density and other thermodynamic properties of the gas to be constant, as justified in [5].

As flame balls are not influenced by boundaries, we choose a periodic approximation in the simulations. As initial condition we take the asymptotic solution of the three-dimensional flame balls proportional to $1/r$ [2] with a small additional smoothing for large radii $r(x, y, z)$ to ensure periodicity.

The system (1)–(4) is discretized in time using exact time integration of the linear terms and a second order Adams-Bashforth extrapolation for the non-linear terms. The spatial discretization is done by a classical Fourier-

pseudospectral approach [3]. The equations are transformed into Fourier space using a parallel version of the Fast Fourier Transform (FFT). The non-linear terms are calculated by collocation in physical space. The main computational cost is caused by multidimensional FFT's between physical and coefficient space. To achieve high resolution without increasing computing time, the code was implemented on an IBM RS/6000 SP using the message passing interface (MPI) [1].

3. Results and Discussion

In the following computations, the thermodynamic parameters were $\beta = 10$, $\alpha = 0.64$, $T_b = 830\text{ K}$, $T_u = 300\text{ K}$, and $Le = 0.3$, corresponding to a 6.5 % H_2 -air flame. The radiation coefficient was $s = 0.1$. The computational box length was $L = 80$, and the time step was $\Delta t = 5 \times 10^{-4}$. The presented simulations were computed on 64 processors with a spatial resolution of 256^3 . This discretization is sufficient to resolve the narrow chemical reaction zone.

To study the influence of the different parameters, we carried out simulations varying the initial flame radius r_0 . The evolution of the flame ball is quantified by the integral reaction rate $R(t) = \int_V \omega dV$. Figure 1 summarizes the evolution of R for different initial radii. Configuration (a) exhibits a gradual splitting of the flame into more and more cells. Hence, the integral reaction rate is increasing. The evolution of a flame kernel with radius $r_0 = 4$ (b), also starts with increasing R and separating into cells, but later is extinguished because of increasing heat loss with growing radius. Larger initial radii (c) lead to direct extinction without splitting of the flame due to dominating radiation effects so that the integral reaction rate is decaying monotonously.

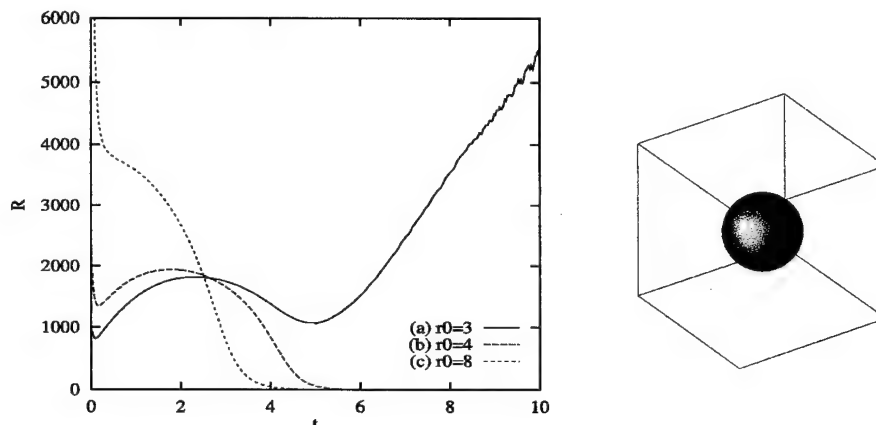


Figure 1: Left: Evolution of the integrated reaction rate R for simulations with different initial radii; right: temperature isosurface of an extinguishing spherical flame structure.

Acknowledgements

We thank the Rechenzentrum Karlsruhe for supplying the computation time on the IBM RS/6000 SP. Partial support by the Deutsche Forschungsgemeinschaft Contract No. Bo 693/8-1 is acknowledged.

References

- 1 BOCKHORN H., FRÖHLICH J., GERLINGER W., SCHNEIDER K.: Direct numerical simulation of flame balls. In: Keil, Mackens, Voss, Werther (eds.): *Scientific Computing in Chemical Engineering II*, Springer 2 (1999), 102–109.
- 2 BUCKMASTER J.: The structure and stability of laminar flames. *Ann. Rev. Fluid Mech.*, 25 (1993), 21.
- 3 CANUTO C., HUSSAINI M.Y., QUATERNIONI A., ZANG T.A.: *Spectral Methods in Fluid Dynamics*, Springer, Berlin, 1988.
- 4 GERLINGER W., SCHNEIDER K., BOCKHORN H.: Numerical Simulation of three-dimensional instabilities of spherical flame structures. to appear in: *Proc. Combust. Inst.* 28 (2000).
- 5 KAGAN L., SIVASHINSKI G.: Self-fragmentation of nonadiabatic cellular flames. *Combust. Flame*, 108 (1997), 220.
- 6 RONNEY P.D., WU M.-S., PEARLMAN H.G., WEILAND K.J.: Experimental study of flame balls in space: Preliminary results from STS-83. *AIAA Journal*, 36(8) (1998), 1361–1368.

Addresses: WOLFGANG GERLINGER, KAI SCHNEIDER, HENNING BOCKHORN,
Universität Karlsruhe (TH), Institut für Chemische Technik, Kaiserstr. 12, 76128 Karlsruhe, Germany.

GERLINGER, W., SCHNEIDER, K., BOCKHORN, H.

Mixing in two-dimensional turbulent reactive flows

Enhanced transport and mixing of scalars in turbulent flows are of major importance, in particular, when chemical time scales are smaller or of the same order as the mixing time. We present direct numerical simulation of the mixing of passive and reactive scalars in two-dimensional flows dominated by coherent vortices. These organized structures have a significant impact on the mixing dynamics in turbulence. By means of a Fourier-pseudospectral method the instationary equations are numerically integrated. To quantify the mixing, we consider statistical properties, i.e. the variance decay and histograms to approximate the probability density functions of the scalars. Also, the influence of a chemical reaction on mixing are investigated.

1. Introduction

Turbulent flows guarantee enhanced mixing of the transported quantities: momentum, mass, and energy, and lead to an accelerated diffusion. Moreover, there is a wide range of scales present in the flow which involves a large number of degrees of freedom. As the dynamics of such flows is mainly dominated by coherent vortices [1], they are of primordial importance for the mixing of scalars. We present the evolution of typical vortex arrangements, analyze their ability to mix scalars, and attribute the influence of vortices to the formation of spirals and to the vortex merging.

2. Governing equations and numerical treatment

We use a classical pseudo-spectral scheme to integrate numerically the Navier-Stokes equations together with the species' transport equations [2]. The semi-implicit time scheme consists of an Euler backwards treatment for the linear terms and an Adams-Bashforth extrapolation for the non-linear terms. The governing equations read in dimensionless form

$$\partial_t \vec{v} + \vec{v} \cdot \nabla \vec{v} - \frac{1}{Re} \nabla^2 \vec{v} + \frac{1}{\rho} \nabla p = 0, \quad (1)$$

$$\nabla \cdot \vec{v} = 0, \quad (2)$$

$$\partial_t c_i + \vec{v} \cdot \nabla c_i - \frac{1}{Re Sc} \nabla^2 c_i = -Da c_A c_B, \quad (3)$$

with the velocity \vec{v} , the hydrodynamic pressure p , the concentration c_i of two species $i = A, B$. The density ρ is set to 1. As non-dimensional parameters, the Reynolds number Re , the Schmidt number Sc and the Damköhler number Da are introduced. We consider a two-dimensional isothermal incompressible flow imposing periodic boundary conditions in both directions. In the reactive case, we implement a second order reaction between the species.

We calculate the temporal evolution of the physical quantities in a domain of $\Omega = [2\pi]^2$ using 600^2 grid points for the computation of about 10 eddy turnover times with a time step of 10^{-3} . The physical parameters are $Re = 10\,000$, $Sc = 1$.

3. Results

In [3] we examined typical coherent vortex structures and a fully developed turbulent flow in order to show how vortices promote the mixing of species. We showed two mechanisms which enhance the mixing process, the merging of co-rotating vortices, and the creation of quasi-singular structures, i.e. the formation of spirals. We conclude that the spiral formation and the vortex merging are important features to model turbulent flows.

In this paper, we focus on the influence of the merging on a second order chemical reaction of two species and on the histograms of the species in a fully developed turbulent field.

In the left picture of figure 1 the evolution of the volume integrated chemical reaction rate is shown for two different

vortex arrangements with increasing merging influence: case one is a homostrophic dipole consisting of two co-rotating and slowly merging vortices. The species boundary is located between these two vortices so that with the merging the boundary is elongated yielding an accelerated mixing. The second vortex configuration corresponds to case one but includes a third counter-rotating vortex with half the vorticity amplitude. This third vortex pushes the other two together and cares for a fast merging of the two co-rotating vortices. A comparison of the homostrophic dipole with the reference case yields similar reaction rate profiles until $t = 5$, but with initiating the merging process R increases significantly for the three vortex configuration.

Figure 1 (right) shows the histograms of c_A in the non-reactive and reactive case after about 30 vortex turnover times. A comparison with fitted β -functions, which are used in classical presumed shape PDF-models [5] for computing turbulent flows shows a good accordance.

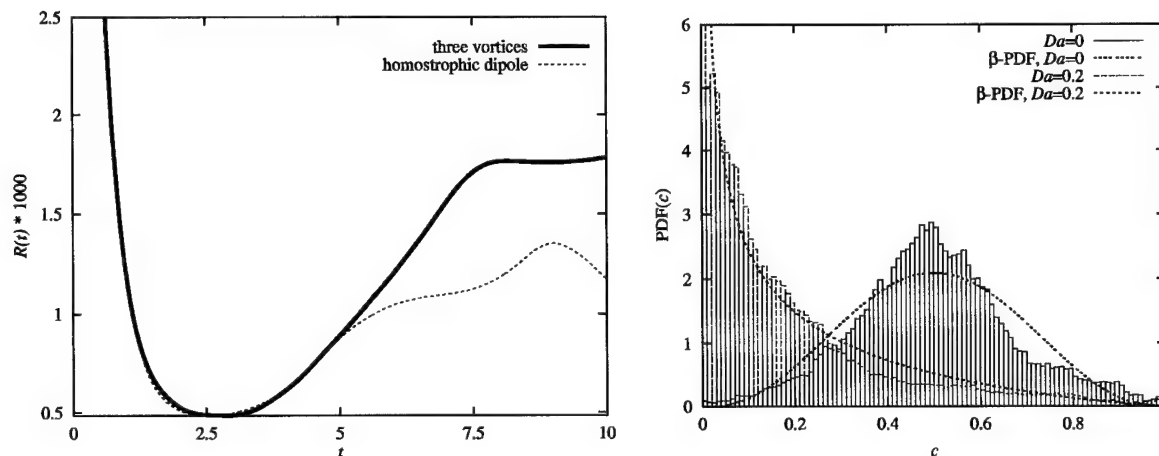


Figure 1: Left: Evolution of the chemical reaction rate for two vortex configurations: a slow merging homostrophic dipole and a fast merging three-vortex configuration; right: Histograms and approximated β -PDF's for a non-reactive ($Da = 0$) and a reactive ($Da = 0.2$) simulation after 30 eddy turnover times.

4. Conclusions

The present paper is concerned with the direct numerical simulation of the mixing in freely decaying, incompressible homogeneous isotropic turbulence in two dimensions. We showed the influence of the merging onto the mixing and hence on the evolution of the chemical reaction rate. Also, we showed the agreement of the histograms of passive and reactive scalars with commonly used β -PDF's.

Acknowledgements

We gratefully acknowledge partial support through the Deutsche Forschungsgemeinschaft (Contract DFG Bo 693/8-2).

5. References

- 1 MC WILLIAMS, J.C.: The emergence of isolated coherent vortices in turbulent flows, *J. Fluid Mech.* **146** (1984), 21–43.
- 2 CANUTO, C., HUSSAINI, M.Y., QUARTERONI, A., AND ZANG, T.A.: *Spectral Methods in Fluid Dynamics*, Springer, Berlin, 1988.
- 3 GERLINGER, W., SCHNEIDER, K., FALK, L., BOCKHORN, H.: Numerical simulation of the mixing of passive and reactive scalars in two-dimensional flows dominated by coherent vortices, *Chem. Eng. Sci.*, **55**, (2000), 1–15.
- 4 FLOHR, P., VASSILICOS, J.C.: Accelerated scalar dissipation in a vortex, *J. Fluid Mech.*, **348** (1997), 295–317.
- 5 FOX, R.O.: Computational methods for turbulent reactive flows in the chemical process industry, *Revue de l'Institut Francais du Pétrole* **51**(2) (1996), 215–242.

Addresses: WOLFGANG GERLINGER, KAI SCHNEIDER, HENNING BOCKHORN,
Universität Karlsruhe (TH), Institut für Chemische Technik, Kaiserstr. 12, 76128 Karlsruhe, Germany.

GUTHEIL, E.

Structure and Extinction of Laminar Ethanol/Air Spray Flames

The paper presents the structure and extinction of both mono- and bidisperse ethanol/air spray flames in the counterflow configuration. A similarity transformation for monodisperse spray flames is extended to polydisperse spray flames, and the resulting one-dimensional formulation accesses the use of detailed chemical reaction mechanisms as well as detailed transport. For the ethanol/air system, 38 species and 337 elementary reactions are used.

At high strain, the droplets cross the gas stagnation plane, reverse and return towards their injector. For this situation, the width of the chemical reaction zone of bidisperse and monodisperse sprays with the Sauter mean radius is almost the same. However, the droplet oscillation causes the spray flame of the bidisperse spray to strongly increase the total spray flame thickness. For the injection velocity of the spray studied here, the droplets returning to their injector hit the boundary of the computational domain as strain is increased whereas the monodisperse spray flame extinguishes at a considerably higher value of gas strain rate. Thus, the extinction behavior of the bidisperse spray flame is not represented by the monodisperse spray flame with the Sauter mean radius. The model is also suitable to predict pollutant formation.

1. Introduction

Structures of laminar spray flames in the counterflow configuration have been studied extensively in the last decade. Several research groups have presented papers on both experimental [1-5] and theoretical [6-11] investigations. The focus has been on polydisperse, nonreactive sprays [2,3] for the fuels methanol and n-heptane as well as on monodisperse spray flames [4-6,8,10,12]. A survey of the major publications until 1996 is given in a review paper by Li [13].

The most advanced theoretical study of polydisperse spray flames is that of Greenberg and Sarig [14] who investigate these flames using a simplified one-step chemical reaction step for decane/air. They find that the polydispersity has a strong influence on the reaction zone structure. However, a single-step chemical reaction system is not suitable to include effects of strain on the flame structure and in particular to predict flame extinction [10].

The focus of the present paper is the investigation of the fuel ethanol that has not yet been studied for spray flames in the counterflow configuration. Its chemical reaction mechanism of the gas phase, however, is known well enough [15] to predict reliable extinction conditions. Moreover, the liquid phase properties are available [16,17] which qualifies that system for the study presented in this paper. Also, bidisperse sprays are investigated, and both their structure and extinction conditions are presented.

2. Formulation

The mathematical formulation of the present study is an extension of previous work [10]. That paper concerned structures and extinction of both monodisperse methanol and n-heptane spray flames in air. However, it was pointed out already by Continillo and Sirignano [6] that the similarity solution employed in the formulation of the gas phase is also suitable to treat polydisperse sprays.

The thin spray is modeled using an Eulerian-Lagrangian formulation for the gas and the liquid phase, respectively. The major assumptions are steadiness of the gas phase, low Mach number, and the validity of the ideal gas law. The equations used here to present the gas phase are derived following the previous paper [10], where detailed transport and detailed chemical reactions are considered. The major difference is the consideration of a polydisperse spray. The spray characteristics is formulated using a discrete droplet model where each individual droplet group is represented by a single droplet for each axial position – the particles with equal properties lie perpendicular to the space coordinate. It should be pointed out here that all droplet size groups are treated separately, so that they maintain their individual characteristics presented by the equations for droplet heating, vaporization, and motion. Thus, for each droplet size group the corresponding equations are formulated [18].

The convective droplet transport for each droplet group is evaluated from the equations derived by Abramzon and Sirignano [19]. Thus, the equations given in the previous papers for a monodisperse spray are transferred to each droplet size group in the present paper individually which allows for independent heating, vaporization, and motion for each droplet group.

The gas phase equations are the well known twodimensional Navier Stokes equations where additional source terms due to interaction with the liquid phase appear. The similarity transformation is used to transform the twodimensional gas equations into onedimensional form. The transformed equations may be found in [10] for detailed transport and detailed chemical reactions.

The present paper concerns the ethanol/air system, and a detailed chemical reaction mechanism is used. It has been derived by Chevalier [15] and was found to be suitable to predict ignition delay as well as laminar flame speeds in gas flames. Moreover, it was successfully used in a study of ignition delay for monodisperse ethanol/air sprays [20]. The mechanism is employed here for atmospheric pressure, and it comprises 38 species and 337 elementary reactions. The transport properties are computed using CHEMKIN.

3. Results and Discussion

The computations concern both mono- and bidisperse ethanol/air spray flames in the axisymmetric counterflow configuration. If bidisperse sprays are investigated, the total liquid mass is distributed equally between the two size groups. For all flames the pressure is atmospheric, the spray is introduced with carrier gas air at an inlet temperature of 300 K, and the air stream that is directed against the spray flow has also 300 K. The influence of both equivalence ratio and initial spray velocity was studied in the previous paper [10]. The global equivalence ratio is unity here, and the initial spray velocity is fixed to a value of 0.44 m/s. The gas strain rate on the spray side of the configuration is varied from 55/s up to extinction for most cases. Moreover, the initial droplet size is varied.

Figure 1 shows the structure of two different spray flames for fixed strain rate $a = 55/s$. The spray enters from the left side, and the symbols show both the magnitude and position of droplets. The figure displays the outer flame structure of a bidisperse spray (left) where the initial droplet sizes are $R_{01} = 25\mu m$ and $R_{02} = 10\mu m$ whereas in the right part of Fig. 1 the structure of a monodisperse spray flame with $R_0 = 14.286\mu m$ which is the Sauter mean radius (SMR) of the bidisperse spray flame. A comparison of the structures shows that the flame temperature decreases as larger droplets are involved which is associated with an increased energy exchange between the gas and liquid. The same is true for momentum exchange which causes a substantial decrease in gas velocity. The large droplets of the bidisperse spray penetrate deeper into the configuration – this is associated with the increased momentum of these droplets. However, the monodisperse situation shows a considerably broader reaction zone which is due to the increased gas velocity and the high peak flame temperature. None of the flames shows droplet reversal. The monodisperse spray yields less interaction between spray and chemical reactions.

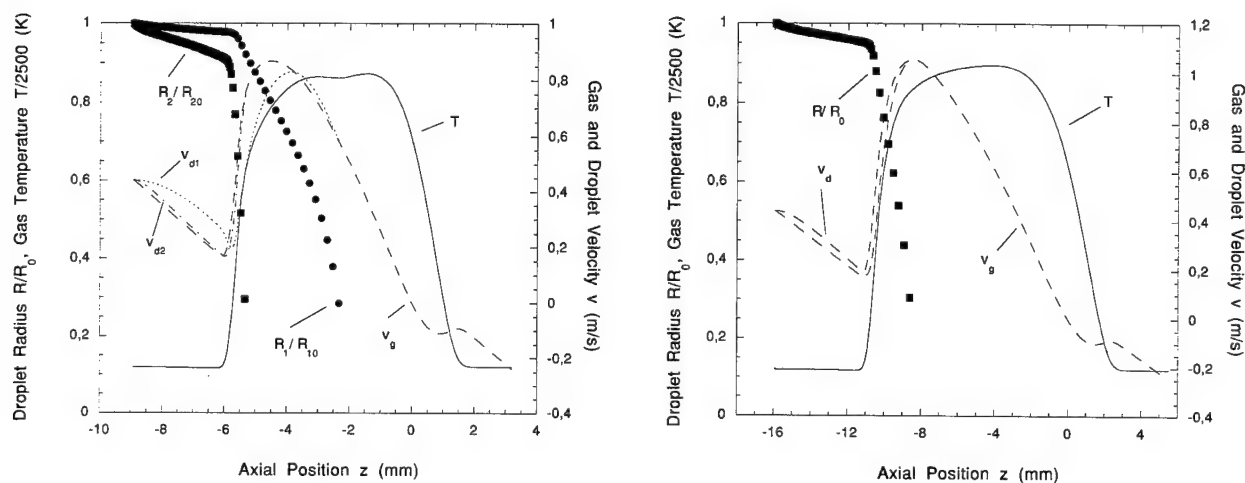


Figure 1: Outer structure of a bidisperse (left) and a monodisperse (right) spray flame where $R_{01} = 25\mu m$, $R_{02} = 10\mu m$, and $R_{SMR_0} = 14.286\mu m$, at $a = 55/s$.

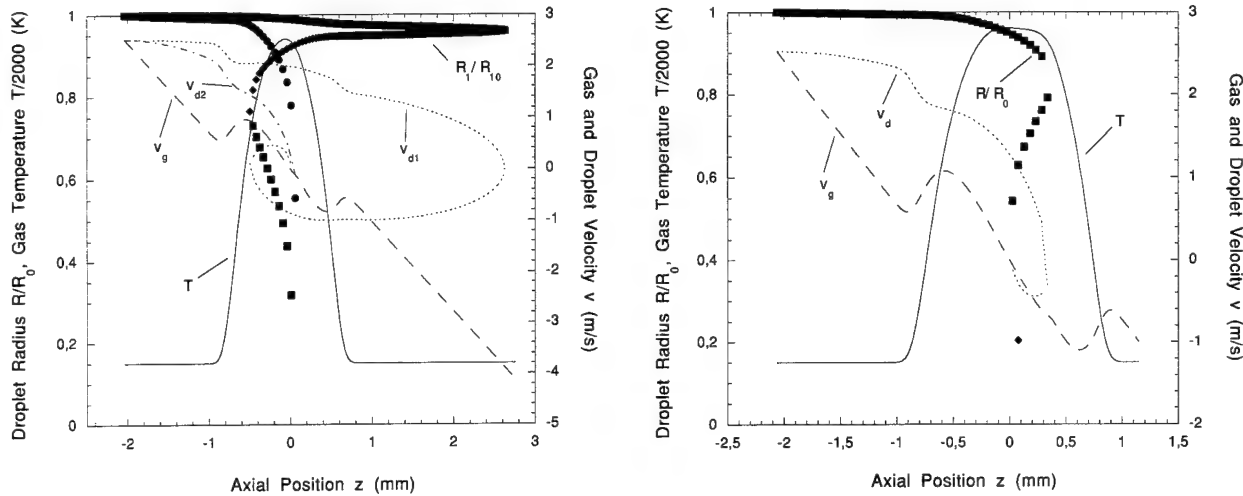


Figure 2: Outer structure of a bidisperse (left) and a monodisperse (right) spray flame where $R_{01} = 25\mu\text{m}$, $R_{02} = 10\mu\text{m}$, and $R_{SMR_0} = 14.286\mu\text{m}$, at $a = 1800/\text{s}$.

Figure 2 shows a comparison of the flame structure of the bidisperse and the monodisperse spray, respectively, at elevated strain ($a = 1800/\text{s}$). The figure shows the droplet oscillation of the large droplets of the bidisperse spray. Their complete evaporation occurs near the gas stagnation point whereas the droplets on the air side of the configuration do not contribute to the vaporization process. The large droplets determine the width of the spray flame whereas the small ones dominate the reaction zone characteristics. A comparison with the corresponding monodisperse spray on the right in Fig. 2 demonstrates that the width of the reaction zones of both flames is almost the same. The peak value of the vaporization rate of the small droplets of the bidisperse spray is about the same as monodisperse droplet vaporization (not shown). The peak gas temperature shown in Fig. 1 of the bidisperse spray, however, is about 50 K lower, and the difference increases as strain increases.

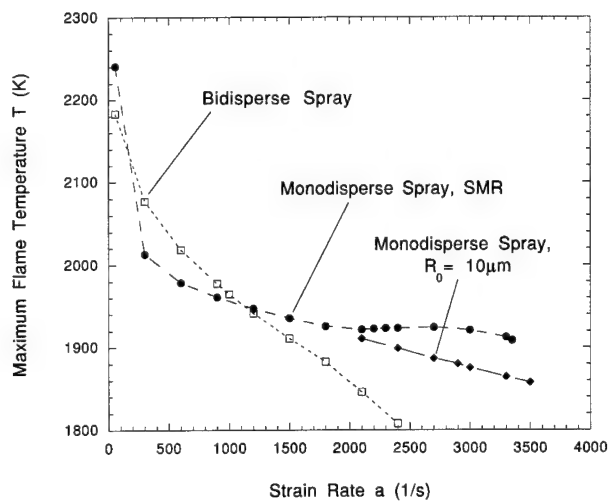


Figure 3: Maximum flame temperature versus gas strain rate on the fuel side where $R_{01} = 25\mu\text{m}$, $R_{02} = 10\mu\text{m}$, and $R_{SMR_0} = 14.286\mu\text{m}$.

A comparison is made to see if the reaction zone resembles that of a monodisperse spray having the small droplet size. The results are shown in Fig. 3. The structure of that flame is more similar to that of the bidisperse spray (not shown), but it is considerably stabler compared to the bidisperse situation. Note that this situation has not been carried to extinction – these flames, however, are more stable compared to the $R_0 = 14.286\mu\text{m}$ situation.

4. Conclusions

The structure and extinction of mono- and bidisperse ethanol/air spray flames have been presented. Large droplets of a bidisperse spray determine the width of the spray flame as well as its stability. The small droplets dominate the reaction zone characteristics and the width of the reaction zone. A comparison of the vaporization rates of the droplet size groups shows that large droplets contribute only about 10% to the total vaporization process at high strain. The results of the study show that the extinction characteristics of spray flames is not sufficiently well reflected by the Sauter mean radius of a spray with droplet reversal. The Sauter mean radius, however, may be suitable to describe polydisperse spray flames where no droplet reversal occurs.

If the laminar spray flame structures are to be used in turbulent flame computations employing the flamelet model for spray diffusion flames [21], the discrete droplet groups should be matched to laminar flame computations using that droplet size rather than using the Sauter mean radius for systems where droplet oscillation occurs. This procedure, of course, increases the computational effort of both laminar and turbulent flame simulations.

Acknowledgements

The author is indebted to Prof. Dr. W. A. Sirignano who participated in developing the code for methanol/air and n-heptane/air spray flames. The financial support of this study through the Deutsche Forschungsgemeinschaft through SFB 359 is gratefully acknowledged.

5. References

- 1 PURI, I. K., LIBBY, P. A., Combust. Sci. and Tech.: **66**, (1989) 267.
- 2 LI, S. C., LIBBY, P. A., WILLIAMS, F. A., Twenty-Fourth Symposium (International) on Combustion, The Combustion Institute, Pittsburgh, PA, (1992), 1503-1512.
- 3 LI, S. C., LIBBY, P. A., WILLIAMS, F. A., Combust. Flame **94** (1993), 161-177.
- 4 CHEN, G., GOMEZ, A., Twenty-Fourth Symposium (International) on Combustion, The Combustion Institute, Pittsburgh, PA, (1992), 1531-1539.
- 5 GOMEZ, A., CHEN, G., Combust. Sci. and Tech., **96**, (1994), 47-59.
- 6 CONTINILLO, G., SIRIGNANO, W. A., Combust. Flame: **81** (1990), 325-340.
- 7 CHEN, N.-H., ROGG, B., BRAY, K. N. C., Twenty-Fourth Symposium (International) on Combustion, The Combustion Institute, Pittsburgh, PA, (1992), 1513-1521.
- 8 LI, S. C., WILLIAMS, F. A., Twenty-Sixth Symposium (International) on Combustion, The Combustion Institute, Pittsburgh, PA, (1996), 1017-1025.
- 9 DARABIHA, N., LACAS, F., ROLON, J. C., CANDEL, S., Combust. Flame: **95** (1991), 261-275.
- 10 GUTHEIL, E., SIRIGNANO, W. A., Combust. Flame: **113** (1998), 92-105.
- 11 GREENBERG, J. B., SARIG, N., Combust. Flame: **104** (1996), 431-459.
- 12 CHEN, Z. H., LIU, T. H., SOHRAB, S. H., Combust. Sci. and Tech.: **60** (1988), 63-77.
- 13 LI, S. C., Prog. Energy Combust. Sci., **23** (1997), 303-347.
- 14 GREENBERG, J. B., SARIG, N., Twenty-Sixth Symposium (International) on Combustion, The Combustion Institute, Pittsburgh, PA, (1996), 1705-1711.
- 15 CHEVALIER, C., Ph.D. Thesis, Universität Stuttgart, Stuttgart (1993).
- 16 VARGAFTIK, N. B., Tables on the Thermophysical Properties of Liquids and Gases, 2nd Ed., John Wiley and Sons, (1975).
- 17 REID, R. C., PRAUSNITZ, J. M., POLING, B. E., Properties of Gases and Liquids. 4th Ed., McGraw Hill, New York, (1988).
- 18 SCHLOTZ, D., GUTHEIL, E., Combust. Sci. and Tech., 2000, to appear.
- 19 ABRAMZON, B., SIRIGNANO, W. A., Int. J. Heat Mass Transfer: **32**, 9 (1989), 1606-1618.
- 20 GUTHEIL, E.: Combust. Sci. and Tech.: **105** (1995), 265-278.
- 21 HOLLMANN, C., GUTHEIL, E., Combust. Sci. and Tech.: **135** (1998), 175-192.

Address: PROF. DR. EVA GUTHEIL, Interdisziplinäres Zentrum für Wissenschaftliches Rechnen, Universität Heidelberg, Im Neuenheimer Feld 368, D-69120 Heidelberg, Germany

THOMAS HULD AND HEINZ WILKENING

3D simulations of turbulent deflagrations using dynamic grid adaptation

We present a CFD code for simulating turbulent deflagrations in gas mixtures for studies of explosion accidents. A dynamic grid adaptation method is used to increase the accuracy of the calculation in regions of interest, such as at flame and shock fronts. The numerical simulations compared with experimental data and is shown to yield strongly improved results at at modest cost in computational time.

1. Models and numerical methods

The details of the basic physical equations and numerical methods have been described in [1]. The basis for the numerical methods is the set of compressible Navier-Stokes equations for the conservation of species' masses, momentum and total energy, coupled with the equation of state for an ideal mixture of Joule gases. The effects of turbulence are modeled by the compressible k - ϵ equations.

In turbulent deflagrations the chemical source terms are heavily influenced by the turbulence. A model must therefore be used to account for this influence. In the present work we have used a model based on the Eddy Dissipation Concept [2], with modifications due to Said and Borghi. In this model, the chemical time scales are assumed to be very much shorter than the turbulent time scales, so the combustion processes are limited by the turbulent rate of mixing at the flame front. The source term for the fuel component of the mixture is given by:

$$\omega_{fu} = -C_f \frac{\epsilon}{k} \rho Y_{lim} \quad (1)$$

where Y_{lim} is the mass fraction of the species which is present in lowest concentration, weighted stoichiometrically in the combustion process. ρ is the density, k is the specific turbulent kinetic energy and ϵ the dissipation rate of k . The factor C_f is calculated from the laminar burning velocity u_{lam} and the turbulent kinetic energy:

$$C_f = C_{f0} \left(1 + \frac{4.4}{1 + 3.2\sqrt{k}/u_{lam}} \right) \quad (2)$$

where C_{f0} is an empirical constant, which must be found by comparisons with experiments. The advantages of this combustion model are its simplicity and low computational costs. It does have limitations, however, in that it cannot account for important phenomena such as the transition from laminar to turbulent flames or the transition from deflagration to detonation.

The NS equations are discretized by dividing space into a set of tetrahedral elements. Control volumes are then formed around each vertex by equipartition of the tetrahedra [1]. The integral formulation of the equations is then solved by a finite-volume method, calculating the fluxes across control volume boundaries.

In order to improve the calculation accuracy, we have introduced a system for dynamic grid adaptation. New node points are inserted in regions of interest (defined by monitoring the spatial variation of one variable, for instance pressure or temperature). The new nodes are removed when the variation of the chosen variable becomes low enough. This avoid cluttering up the grid with useless grid points. A certain amount of "look-ahead" can be imposed, whereby the new grid points are inserted also in a region around the region of interest. In this way the grid can be "prepared" for the arrival of the flame front or shock, which avoids problems with interpolation.

2. Results and discussion

As a test of the code and the models, we chose to simulate the development of a turbulent deflagration in an explosion tube experiment performed at the Forschungszentrum Karlsruhe, Germany [3]. The tube has a length of 12m and a diameter of 0.35m. Inside the tube are ring-shaped obstacles, placed at intervals of 0.5m, blocking 30% of the tube cross-section. The tube was filled with a uniform mixture of hydrogen and dry air. Ignition occurred at the center of one endplate. Pressure and light transducers recorded the progression of the flame.

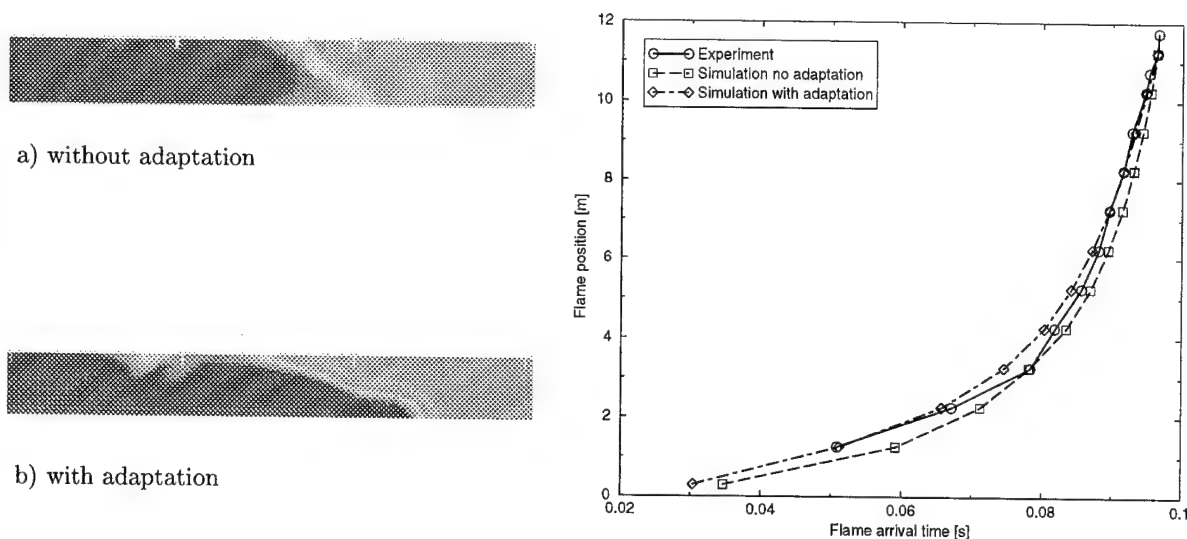


Figure 1: (a & b left) Isocolour plots of a flame propagating in an explosion tube with obstacles. The plots show temperature in a 2D cut in a section of the tube, with $4\text{m} < x < 5.5\text{m}$. One half of tube cross-section is shown. Results shown are without (a) and with (b) grid adaptation. Right graph shows comparison of flame arrival times vs. position between experimental values and simulations with and without grid adaptation.

Figure 1 shows a comparison between experimental results and numerical simulations for a case with an H_2 concentration of 12% by volume. The simulations were performed with an original grid of 40000 grid points. In the adaptive simulation, the number of grid points reached a maximum of 80000 grid points. For these calculations we chose a value of $C_{f0} = 6.0$.

Figures 1 a) and b) show clearly the improvement in the sharpness of the flame front due to the adaptive grid. In figure 1 in the graph the arrival time has been offset so that all arrival times coincide at $x = 11.25\text{m}$. Here we see that the adaptive calculation better captures the rapid acceleration in the first part of the tube and the subsequent reduced acceleration. The non-adaptive calculation is more prone to continue accelerating throughout the tube.

3. Conclusion

Dynamically adaptive grids provide a valuable tool for accurately simulating turbulent deflagrations in complex geometries. Much improved solutions may be obtained at moderate requirements in computational time. In the calculation presented in this paper an improved resolution of a factor of 3 in each dimension was obtained with a increase in computational nodes of less than a factor 2. This gave a much improved resolution of the flame front and better global prediction of the deflagration.

Acknowledgements

We would like to thank W. Breitung and co-workers at Forschungszentrum Karlsruhe for making their experimental data available for our research.

4. References

- 1 WILKENING H. AND HULD T.: An adaptive 3-D CFD solver for modeling explosions on large industrial environmental scales. *Combust. Sci. and Tech.*, **149**, 361-387 (1999)
- 2 HJERTAGER B. H.: Computer modeling of turbulent gas explosions in complex 2D and 3D geometries. *J. Hazardous Materials*, **34**, 173-197 (1993)
- 3 BREITUNG W., ROYL P. AND VESER A.: Results on Hydrogen Behaviour and Mitigation in Severe PWR Accidents. FZKA 5914, Karlsruhe, Germany (1997)

Addresses: Joint Research Centre of the European Commission
T.P. 723, I-21023 Ispra, Italy

INDENBIRKEN, M.; STRAUSS, K.

Zur Modellierung komplexer partikelbeladener Strömungen mit der kinetischen Theorie granularer Medien

Die Partikelbewegung in verdünnten feststoffbeladenen Gasströmungen wird häufig mit der kinetischen Theorie granularer Medien (engl.: kinetic theory of granular flows, KTGF) beschrieben. Dieses aus der kinetischen Gastheorie abgeleitete Modell basiert auf der Kontinuumsannahme für beide Phasen (dem sog. Euler/Euler-Ansatz) und ist in seiner ursprünglichen Formulierung vor allem für einfache Strömungsformen geeignet. Hier werden neue Ansätze vorgestellt, die die Verwendung der KTGF auch bei komplexen Strömungen mit ausgeprägten Partikel-Wand-Kollisionen ermöglichen. Dazu ist es erforderlich, die beschreibenden Kollisionsintegrale auszuwerten und die nicht elementar integrierbaren Ausdrücke zu approximieren. Als Resultat werden neuartige Randbedingungen sowie ein erweitertes Konzept zur Beschreibung der Partikel-Partikel-Wechselwirkungen vorgestellt.

1. Modellbildung

Die Motivation zur Entwicklung des hier vorgestellten Modells ergibt sich daraus, daß in der Verfahrenstechnik häufig partikelbeladene Strömungen vorliegen, in denen lokal begrenzt Wandkollisionen der Partikel auftreten. Entsprechende Beispiele sind die Durchströmung von Rohrkrümmern und die Umströmung von Wärmetauscherrohren. In den genannten Anwendungen werden die Partikel mit der Gasströmung in Richtung der begrenzenden Wand bewegt und kollidieren aufgrund ihrer Trägheit mit der Berandung, bevor sie der Bewegung des Fluids wieder folgen können. Derartige gerichtete Wandkollisionen können bei Verwendung des Euler/Euler-Ansatzes für die Partikelphase in Verbindung mit der KTGF nicht beschrieben werden.

Aus diesem Grunde wurde das Konzept entwickelt, den Feststoff auf mehrere Phasen aufzuteilen, wobei eine Phase durch die Partikel gebildet wird, die sich in die Richtung der zu untersuchenden Berandung bewegen. Eine weitere Phase enthält diejenigen Partikel, die bereits mit der angeströmten Wand kollidiert sind und sich wieder von ihr entfernen. Obwohl dieses Konzept bei wiederholten Wandkollisionen auf beliebig viele Partikelphasen erweitert werden kann, ist es sinnvoll, deren Anzahl auf maximal drei oder vier zu begrenzen. Insbesondere für Anwendungen, die eine große Zahl gerichteter Partikel-Wand-Kollisionen bedingen - wie z. B. der horizontale pneumatische Transport - ist dagegen das Lagrange-Verfahren zur Beschreibung der Partikelbewegung zu bevorzugen.

Aus der Konzeption des hier beschriebenen Verfahrens ergeben sich die Aufgaben, geeignete Randbedingungen für die jeweilige Partikelphase sowie Wechselwirkungsterme herzuleiten, die den Austausch von Masse, Impuls und Fluktuationsenergie zwischen den verschiedenen Partikelphasen beschreiben.

2. Randbedingungen

Zur Herleitung der Randbedingungen wird das Kollisionsintegral der jeweiligen Transportgröße gelöst. Dies bedeutet, daß alle Partikel berücksichtigt werden, deren wandnormale Geschwindigkeit $v_n (= V_n + v'_n)$ so groß ist, daß sie innerhalb des betrachteten Zeitintervalls die Berandung erreichen. Das Vorgehen wird exemplarisch am Beispiel des an der zu untersuchenden Wand zwischen zwei Partikelphasen ausgetauschten Massenstroms vorgestellt. Bei der Beschränkung auf eine zweidimensionale Darstellung ergibt sich unter Verwendung der Partikelmasse m_p , der Verteilungsfunktion f der Partikelgeschwindigkeiten (angenommen als Maxwell-Verteilung), der Fluktuationsenergie Θ (der sog. granular temperature) und der zur Wand tangentialen Geschwindigkeit v_t der ankommenden Partikel (Index A) der an die Phase der reflektierten Partikel (Index R) übertragene Massenstrom

$$\begin{aligned} \dot{m}_w &= -m_p \int_{-\infty}^{-V_{n,A}} \int_{-\infty}^{\infty} (V_{n,A} + v'_{n,A}) f_A dv'_{n,A} dv'_{t,A} \\ &= \Phi_A \varrho_p \left\{ \sqrt{\frac{\Theta_A}{2\pi}} \exp\left(-\frac{V_{n,A}^2}{2\Theta_A}\right) - \frac{V_{n,A}}{2} \left[1 - \operatorname{erf}\left(\frac{V_{n,A}}{\sqrt{2\Theta_A}}\right) \right] \right\}. \end{aligned}$$

Zur Formulierung der Randbedingung wird dieser flächenspezifische Massenstrom anstelle des konvektiven Flusses

in die Massenbilanzen beider Partikelphasen für ein an die Berandung angrenzendes Volumenelement eingesetzt.

Auf analoge Weise wird der an der Wand zwischen den Phasen übertragene Impuls bestimmt, wobei in der Bilanz der reflektierten Phase zusätzlich die Wandschubspannung zu berücksichtigen ist. Ebenso ist bei der Randbedingung für die Fluktuationsenergie zu beachten, daß es zur Dissipation von Fluktuationsenergie durch die Inelastizität der Wandkollisionen und zur Produktion aufgrund der Rotation der Teilchen nach dem Wandstoß kommt.

3. Wechselwirkungen der Partikelphasen

Durch die Anwesenheit von Partikeln anderer Phasen werden die kinetischen Größen wie Druck und Viskositäten der betrachteten Partikelphase beeinflusst. Entsprechende Modifikationen der beschreibenden Gleichungen sind von der Betrachtung polydisperser Suspensionen bekannt [1]. Auch Terme, die den Impulsaustausch mehrerer Phasen untereinander beschreiben, sind bereits vorgestellt worden (vgl. [2],[3]), enthalten jedoch im allgemeinen starke Vereinfachungen. Dagegen existieren keine entsprechenden Ausdrücke für den Austausch der Fluktuationsenergie Θ [1]. Bei der Herleitung dieser Terme - beispielhaft für den Impulsaustausch \vec{J}_{AR} zwischen beiden Partikelphasen vorgestellt - sind die Verteilungsfunktionen der beteiligten Phasen und die *radial distribution function* g_0 zu berücksichtigen. Es ergibt sich:

$$\vec{J}_{AR} = C_1 g_0 \int_{-\infty}^{\infty} \int_{-\infty}^{\infty} \int_{-\infty}^{\infty} \int_{-\infty}^{\infty} f_A f_R |\vec{v}_A - \vec{v}_R| \cdot (\vec{v}_A - \vec{v}_R) dv_{N,A} dv_{T,A} dv_{N,R} dv_{T,R}.$$

Die Lösung erfolgt, indem \vec{J}_{AR} für den Grenzfall $\Theta \ll (\vec{v}_A - \vec{v}_R)^2$ sowie für den Fall ausschließlich zentraler Stöße bestimmt wird. Diese Lösungen lassen sich schließlich zu dem folgenden Ausdruck ergänzen [4]:

$$\vec{J}_{AR} = C_2 g_0 \Phi_A \Phi_R \frac{\vec{V}_A - \vec{V}_R}{|\vec{V}_A - \vec{V}_R|} \cdot \left((\vec{V}_A - \vec{V}_R)^2 + \Theta_A + \Theta_R \right) \operatorname{erf} \sqrt{\frac{(\vec{V}_A - \vec{V}_R)^2}{2(\Theta_A + \Theta_R)}}.$$

In den beiden Gleichungen stellen C_1 und C_2 jeweils Konstanten dar, Φ repräsentiert die Volumenanteile. Ein analoges Vorgehen kann auch zur Berechnung des Austausches der Fluktuationsenergie Θ angewandt werden [4].

4. Ergebnisse

Als Anwendungsbeispiel für die beschriebene Methode wurde ein horizontaler Freistrahle betrachtet, der in eine verdünnte zirkulierende Wirbelschicht eingedüst wird. Unter dem Einfluß des einphasigen Gasstrahles werden die sich zunächst vertikal bewegenden Partikel in Richtung des Freistrahles abgelenkt und kollidieren schließlich mit der der Düse gegenüberliegenden Berandung. Von der Wand prallen die Partikel zurück in das Strömungsgebiet und wechselwirken mit den sich dort befindlichen Partikeln. Dieses aus eigenen experimentellen Untersuchungen bekannte Verhalten wird mit den beschriebenen Methoden sehr gut wiedergegeben.

Demgegenüber ist es mit der KTGF in ihrer ursprünglichen Formulierung nicht möglich, die wandnormale Bewegung und folglich die gerichteten Wandkollisionen der Partikel zu beschreiben. Der Impulsaustausch mit der Berandung ergibt sich daher bei Verwendung der klassischen KTGF ausschließlich aus der Fluktuationsbewegung der Partikel. Vergleiche mit Ergebnissen, die mit dem hier beschriebenen neuartigen Ansatz erhalten wurden, zeigen, daß bei Verwendung der ursprünglichen Formulierung der KTGF der Impulsaustausch mit der Wand in der vorliegenden Anwendung um bis zu 60% zu gering berechnet wird.

5. Literatur

- 1 BOEMER, A.: Euler/Euler-Simulation der Fluidodynamik blasenbildender Wirbelschichten. Dissertation, RWTH Aachen (1996).
- 2 ARASTOPOUR, H., LIN, S., WEIL, S. A.: Analysis of the vertical pneumatic conveying of solids using multiphase flow models. AICHE Journal 28, No. 3 (1982), 467-473.
- 3 SYAMLAL, M.: The particle-particle drag term in a multiparticle model of fluidization. Topical report DOE/MC/21353-2373, DE87 006500 (1987).
- 4 INDENBIRKEN, M.: Weiterentwicklung des Euler/Euler-Verfahrens zur Beschreibung berandeter Gas-Feststoff-Strömungen. Dissertation, Universität Dortmund (in Vorbereitung).

Adresse: DIPL.-ING. MATTHIAS INDENBIRKEN, PROF. DR.-ING. KARL STRAUSS, Lehrstuhl Energieprozeßtechnik und Strömungsmechanik, Fachbereich Chemietechnik, Universität Dortmund, D-44221 Dortmund

KEMPF, A.; FORKEL, H.; CHEN, J.-Y.; SADIKI, A.; JANICKA, J.

Large Eddy Simulation of a Counterflow Configuration

The aim of the present work is to extend the possibilities of predicting turbulent activity and mixing in counterflow burners. Such burners are well suited for the calibration and validation of combustion models. Because of their geometry, they allow simulations to be performed in only one dimension of space. This saves much computation time, rendering for example the simulation of detailed chemistry possible. Here, a three dimensional LES is applied without considering chemical reactions. Sub-grid fluctuations are modeled according to Smagorinsky. The model constant is determined dynamically by the well known Germano approach.

1. Introduction

The understanding of the flow structure and the mixing process is crucial for many fundamental and industrial applications. Numerical simulations of turbulent flows which are able to predict the instationary behaviour within reasonable computational efforts are highly needed. As far as combustion is concerned, LES has a greater potential for the simulation of turbulent flows than RANS, because fluctuations of velocity and chemical composition are resolved down to filter width. An accurate description of mixing, the driving mechanism of combustion in such systems, is therefore possible.

Although the extension of LES to reacting flows has already been the goal of many investigations (see [1] and other mentioned papers), it is well known that a good overall agreement of the flow and mixing field is a prerequisite for understanding the turbulence-chemistry interaction. For configurations which are well suited for calibration and validation of combustion models (e.g. counterflows), it appears very interesting to see how existing SGS-models perform in predicting turbulent flow and mixing. The aim of this work is to investigate the potential of LES to describe turbulent counter-flow with the view of advancing the use of LES in understanding complex systems.

In the numerical method, the density is considered to be independent of pressure. The subgrid distribution of the mixture fraction fluctuation is presumed to have the shape of a β function. To represent the sub-grid scale stresses and scalar flux, a Smagorinsky model is used [6]. The Smagorinsky coefficient is determined by the dynamic Germano procedure [2]. The subgrid-fluctuation of the mixture-fraction is modeled by the resolved variation of the mixture fraction in the neighbour-cells.

2. Configuration and Computational Parameters

The burner studied in this work is based on a design by Mastorakos [3] and Sardi [5], in which two opposed nozzles (30mm in diameter) are arranged in line, separated by a distance of 30mm. These nozzles create opposed jets. Their velocities are adjusted to balance momentum, so the mixing layer is located at half the nozzle distance.

Two straight pipes deliver the fluid. Short upstream of the nozzles, a perforated plate excites reproduceable turbulence. For the non-reactive case presented here, both nozzles spend plain air. In the experiments, the mixture fraction was determined by measuring the local temperatures. (One stream is heated 25 degrees over ambient.) In contrast, this work presents iso-thermal mixing.

A laminar coflow shields the opposed jets of outer influences.

Its height is defined by the nozzle distance, its radius was set to approximately 1.5 times the radius of the pipe. Thus, part of the Co-flow is simulated as well. This domain was discretized by 104.000 cells (65 axial, 25 radial, 64 tangential).

The nozzles and the Co-flows were described by a Dirichlet condition for both velocity and mixture fraction and a von Neumann condition for pressure. On the outer ring (coflow) steady laminar flow is forced, whereas velocities on the inner section fluctuate corresponding to the turbulent flow out of the nozzles. With this domain the turbulent inflow condition is of special importance for the entire flow-field, because there is no time for turbulence to develop before approaching the area of interest (the entire centerline). Thus, it appears to be necessary to predict the velocity

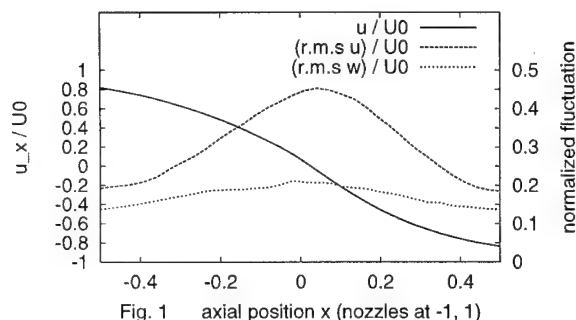


Fig. 1 axial position x (nozzles at -1, 1)

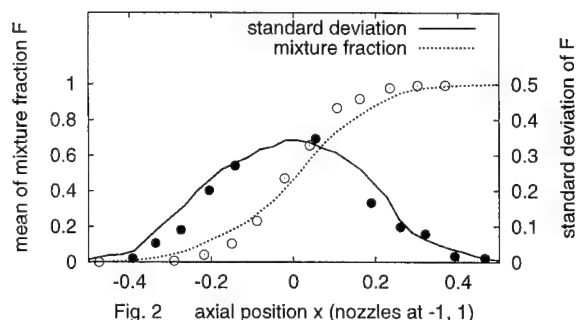


Fig. 2 axial position x (nozzles at -1, 1)

fields in the wake of the perforated plate and to copy these velocities onto the inflows. The flow out of the plate holes was described by a corresponding velocity profile which was forced onto the inflow of the feeding pipes. As boundary condition on the cylinder shell, a simple outflow condition was used (Dirichlet-condition for pressure, von Neumann-type condition for velocities and scalars). Negative outflow-velocities are cut-off to ensure stability.

3. Results, Discussions and Conclusions

For this study, it was relied on experimental data by K. Sardi [5]. The case considered features a Reynolds-number of 7,500. Results along the domain-centerline are presented in both Fig. 1 and Fig. 2. The first figure shows the normalized mean axial velocity and the fluctuations for both axial and radial velocity. The numerical solution for the mixture fraction (see Figure 2) proves that good results can be achieved by this approach. The fluctuation peak value seems to be predicted very well, while the fluctuations out of the middle are slightly overestimated. Although the experimental data presented in Figure 2 is not really sufficient to draw such conclusions, they are confirmed by data-items acquired at an increased Reynolds-number of 10,000 (presented in [5] as well). Because the mixing is determined by the state of the flow turbulence, it can be deduced that the flow quantities shown in Fig. 1 are predicted realistically as well. (No experimental data are available here.)

All in all, the results appear to be pretty promising for further investigation. Furthermore, they were achieved at a reasonable cost (3 days of CPU-time). Finally, it shall be stressed that the entire turbulent flow fields were computed by LES. No experimental data was used to describe the boundary conditions.

Acknowledgements

The authors gratefully acknowledge the financial support of the DFG-Graduiertenkolleg "Modellierung und numerische Beschreibung technischer Strömungen".

4. References

- 1 H. FORKEL, J. JANICKA: *Large-Eddy Simulation of a turbulent Hydrogen Diffusion Flame*, 1st Symposium on Turbulent Shear Flow Phenomena (1999)
- 2 M. GERMANO, U. PIOMELLI, P. MOIN AND W.H. CABOT: *A dynamic subgrid-scale eddy viscosity model*, Phys. Fluids A, 3, pp. 1760-1765 (1991)
- 3 E. MASTORAKOS, A. TAYLOR, J. WHITELAW: *Mixing in Turbulent Opposed Jet Flows*, Ninth Symposium on Turbulent Shear Flows (1993)
- 4 S.I. MÖLLER, E. LUNDGREN, C. FUREBY: *Large Eddy Simulation of Unsteady Combustion*, 26th Symposium (International) on Combustion, pp. 241-248 (1996)
- 5 K. SARDI, A. TAYLOR, J. WHITELAW: *Conditional scalar dissipation statistics in a turbulent counterflow*, Journal of Fluid Mechanics, vol. 361, pp. 1-24 (1998)
- 6 J.S. SMAGORINSKY: *General circulation experiments with the primitive equations, 1. The basic experiment*, Monthly Weather Rev., 91, pp. 99-164 (1963)

Addresses: DIPL.-ING. ANDREAS KEMPF, DR. RER. NAT. AMSINI SADIKI, PROF. DR.-ING. JOHANNES JANICKA
Technische Universität Darmstadt, Fachgebiet Energie- und Kraftwerkstechnik
Petersenstr. 30, 64287 Darmstadt, Germany

DR.-ING. HENDRIK FORKEL, AEA Technology, Otterfing, Germany

PROF. J.-Y. CHEN, UC-Berkeley, CA, USA

LANGE, MARC; WARNATZ, JÜRGEN

Parallel DNS of Turbulent Non-Premixed Flames with Adaptive Chemistry

Direct numerical simulations (DNS) have become one of the most important tools to study turbulent combustion. Computation time is still a main limiting factor for the DNS of reacting flows, especially in the case of using detailed chemical mechanisms. The computation of the chemical source terms is one of the most time-consuming parts in such DNS. An adaptive evaluation of the chemical source terms is used in the presented DNS of turbulent diffusion flames. This leads to a decrease of the time needed for this part of the computation by more than a factor of five without any significant loss of accuracy of the results.

1. DNS of Reacting Flows

Turbulent combustion processes are important for a wide range of applications like automotive engines, electrical power generation, and heating [1]. During the last few years, direct numerical simulation (DNS), i.e. the computation of time-dependent solutions of the compressible Navier-Stokes equations resolving the whole wave-number spectrum, has become one of the most important tools to study turbulent combustion. Due to the broad range of occurring length and time scales, DNS are far from being applicable to most technical configurations, but they can provide detailed information about turbulence-chemistry-interactions and thus aid in the development and validation of turbulent combustion models.

In the case of using detailed chemical reaction mechanisms, in addition to the conservation equations for mass, momentum, and energy, an equation for the species-mass of each of the N_S chemical species α

$$\frac{\partial(\rho Y_\alpha)}{\partial t} + \text{div}(\rho Y_\alpha \vec{u}) = M_\alpha \dot{c}_\alpha - \text{div} \vec{j}_\alpha \quad (1)$$

has to be solved. Herein ρ denotes the density and \vec{u} the velocity, Y_α , \vec{j}_α and M_α are the mass fraction, diffusion flux and molar mass of the chemical species α . The computation of the chemical source terms on the right-hand-sides of the species mass equations (1) is one of the most time-consuming parts in such DNS. The production rate \dot{c}_α of the chemical species α is given as the sum over the formation rate equations for all N_R elementary reactions,

$$\dot{c}_\alpha = \sum_{\lambda=1}^{N_R} k_\lambda (\nu_{\alpha\lambda}^{(p)} - \nu_{\alpha\lambda}^{(r)}) \prod_{\alpha=1}^{N_S} c_\alpha^{\nu_{\alpha\lambda}^{(r)}}, \quad (2)$$

where $\nu_{\alpha\lambda}^{(r)}$ and $\nu_{\alpha\lambda}^{(p)}$ denote the stoichiometric coefficients of reactants and products respectively, and c_α is the concentration of the species α . The chemical reaction mechanism for the $\text{H}_2/\text{O}_2/\text{N}_2$ system which has been used in the simulations presented contains $N_S = 9$ species and $N_R = 37$ elementary reactions [1].

2. Adaptive Computation of Chemical Source Terms

Figure 1 shows a snapshot of a typical DNS of a turbulent non-premixed flame. An initially planar laminar diffusion flame has been superimposed with homogeneous turbulence at the beginning of this simulation. A very fine grid is used to resolve the smallest turbulent length-scales everywhere in the computational domain. In a fully coupled simulation the complex chemistry model is normally computed on every point of the same grid although in big parts of the domain no or almost no reactions occur. Thus, computation time can be saved by computing the chemical source terms using the detailed chemical mechanism only in those regions in which reaction-rates are non-negligible. Criteria which can be fast evaluated are then needed to decide if a grid point belongs to such a region. For non-premixed and partially premixed reactive systems, it is possible to check the element mass fractions of fuel and oxidizer. If one of these two is nearly zero, no reactions will occur. As a test for this adaptive evaluation of the chemical source terms, a DNS of autoignition in a turbulent mixing layer has been performed. The initial temperature of the fuel stream consisting of 10% H_2 and 90% N_2 (mole fractions) was $T_1 = 298 \text{ K}$ and the initial temperature of the air stream was $T_2 = 1398 \text{ K}$. The turbulent Reynolds number based on the integral length-scale was $Re_\Lambda = \text{r.m.s.}(\vec{u}') \cdot \Lambda / \nu = 238$. The size of the domain is $18 \text{ mm} \times 18 \text{ mm}$ and the computational grid has 800×800 points. The temporal evolution of maximum heat release rate for this DNS is shown in Fig. 2. In the

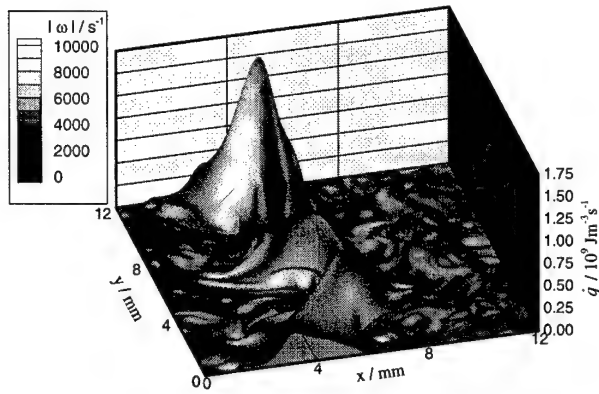


Figure 1: Snapshot of heat release rate \dot{q} and absolute vorticity $|\omega|$ in a turbulent non-premixed flame

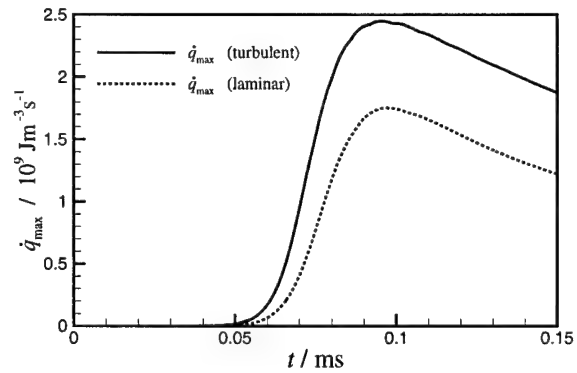


Figure 2: Maximum heat release rate \dot{q}_{\max} over time in a laminar and a turbulent mixing layer

adaptive computation for every timestep the chemical source terms have been set to $\dot{c}_\alpha = 0$ for all chemical species α at those points at which $Z_H < \epsilon_a$ or $Z_O < \epsilon_b$ with $\epsilon_a = \epsilon_b = 1 \cdot 10^{-5}$. The limiting values $\epsilon_{a,b}$ have been estimated from the results of a similar one-dimensional simulation. Another possibility would be the computation of a library of production-rates in homogeneous mixtures depending on temperature and pressure, from which limiting values for more general applications could be determined. In the following table the maxima of the relative errors

$$\delta_X^{\max}(t) = \max_{x,y}(\delta_X(x,y,t)) = \max_{x,y} \left(\frac{|X_{\text{full}}(x,y,t) - X_{\text{adapt}}(x,y,t)|}{\max_{x,y}(X_{\text{full}}(x,y,t))} \right) \quad (3)$$

of heat release rate and mass fractions of OH and HO₂, which are especially important for the ignition, are given:

$t/\mu\text{s}$	25	50	75	100	125	150
$\delta_q^{\max}(t)$	$1.8 \cdot 10^{-3}$	$7.2 \cdot 10^{-4}$	$1.6 \cdot 10^{-3}$	$1.2 \cdot 10^{-3}$	$1.4 \cdot 10^{-3}$	$1.4 \cdot 10^{-3}$
$\delta_{Y_{\text{HO}_2}}^{\max}(t)$	$1.5 \cdot 10^{-4}$	$4.6 \cdot 10^{-4}$	$2.6 \cdot 10^{-4}$	$1.7 \cdot 10^{-3}$	$4.4 \cdot 10^{-3}$	$4.1 \cdot 10^{-3}$
$\delta_{Y_{\text{OH}}}^{\max}(t)$	$6.7 \cdot 10^{-4}$	$6.0 \cdot 10^{-4}$	$1.7 \cdot 10^{-4}$	$8.6 \cdot 10^{-5}$	$1.7 \cdot 10^{-4}$	$2.0 \cdot 10^{-4}$

The maximum errors $\delta_X^{\max}(t)$ at times $t = 25 \mu\text{s}, 50 \mu\text{s}, \dots, 150 \mu\text{s}$ for x - and y -components of velocity u and v , pressure p , density ρ , and temperature T are all less than $2 \cdot 10^{-5}$, and those of the mass fractions Y_α of all chemical species except HO₂ are smaller than $1 \cdot 10^{-3}$. It can clearly be seen that no significant loss in accuracy is introduced by the adaptive computation of the chemical source terms.

As our DNS-code is parallelized using a domain-decomposition approach, a dynamic load-balancing has to be done to be able to benefit from the adaptive chemistry computation. The implemented load-balancing scheme performs a grid-point redistribution, based on differences of the times which had been needed by the processors for carrying out the last integration step on their subdomains. More details on the load balancing scheme and the DNS code in general can be found in [2]. The additional time needed for the load-balancing is typically small compared to the savings due to the adaptivity in the chemistry computation. In the described DNS of a turbulent mixing layer (carried out on 64 processors of a Cray T3E), the sum of the times needed for the load-balancing and for the computation of the chemical source terms in the adaptive computation is by a factor of five smaller than the time needed for the full computation of the chemical source terms.

Acknowledgements

We would like to thank the High-Performance-Computing Centres at Stuttgart (HLRS) and Jülich (NIC) for granting us access to their supercomputers.

3. References

- 1 WARNATZ, J., MAAS, U., DIBBLE, R.W.: Combustion. 2nd Ed., Springer, Heidelberg (1999)
- 2 LANGE, M., THÉVENIN, D., RIEDEL, U., WARNATZ, J.: DNS of Turbulent Reactive Flows Using Massively Parallel Computers. In: Parallel Computing (D'Hollander, E. et.al., Eds.), Elsevier, Amsterdam (1998), 287–295

Addresses: MARC LANGE, PROF. DR. DR.H.C. JÜRGEN WARNATZ, IWR, Universität Heidelberg, INF 368, D-69120 Heidelberg, Germany.

LUO, KAI

Some Recent Findings on Turbulent Diffusion Flames from DNS

Direct numerical simulation (DNS) is a valuable tool for the study of complex interactions between turbulence and combustion, thanks to its ability to resolve the wide range of time and length scales involved. Its application in the fundamental study of turbulent diffusion flames has been particularly fruitful in recent years, which led to some new findings, improved understanding of known phenomena and the development of new theories and models. This paper is concerned with the effects of heat release from finite-rate chemistry on compressible turbulence. The present DNS results reveal intricate interactions among combustion, turbulent transport and mixing.

1. Heat release effects on shear-layer growth rate

Turbulent diffusion flames are strongly dependent on the effectiveness of mixing between the fuel and the oxidizer, which is often measured by a shear-layer thickness. How such a thickness grows spatially and temporally will determine how a combustion process will proceed or whether it will take place at all. The reverse process, in which combustion influences the shear-layer growth, is equally important, through their non-linear interactions. Numerous studies were devoted to the topic, but conclusions were often contradictory. The shear-layer growth was seen to be inhibited by heat release in some cases [1, 2] but promoted in others [3]. In almost all cases, explanations were sketchy. Lately, the study of Luo [4] provided a full explanation of the observed phenomena on the basis of a mathematically exact relationship between the shear-layer growth rate and other flow quantities expressed as:

$$\frac{d\delta}{dt} = \frac{2}{\rho_1 U_{1,+}^2} \left[\int_{-\infty}^{+\infty} \left(-\rho u_1'' u_2'' \frac{\partial \tilde{u}_1}{\partial x_2} \right) dx_2 + \int_{-\infty}^{+\infty} \left(\bar{\sigma}_{12} \frac{\partial \tilde{u}_1}{\partial x_2} \right) dx_2 \right] \quad (1)$$

where the symbols have their usual meanings, that is, ρ for density, u_i for velocity and x_i for space coordinate in the i -direction. σ_{ij} stands for viscous stresses. A Reynolds average decomposition of a quantity ϕ is defined as $\phi = \bar{\phi} + \phi'$ whereas a Favre average decomposition is defined by $\phi = \bar{\phi} + \phi''$. Thus, the first term on the right-hand side is the integrated Reynolds stress production for the 11-component of the Reynolds stresses and the second term represents its viscous stress production. The shear-layer thickness is defined using the momentum thickness of a temporal mixing layer: $\delta(t) = 1/(\rho_1 U_{1,+}^2) \int_{-\infty}^{+\infty} \bar{\rho} (U_{1,+} - \tilde{u}_1)(\tilde{u}_1 - U_{1,-}) dx_2$ where $U_{1,+}$ and $U_{1,-}$ are the upper and lower free-stream velocities in the streamwise direction. Formulas identical to these and (1) can be written for a spatial mixing layer or jet.

It is clear from (1) that the shear-layer growth rate is affected by both turbulence and viscous effects. DNS results [4] show that combustion can either increase or reduce the growth rate, depending on the effects of non-linear interactions between heat release and turbulence on the two production terms in (1). On the one hand, heat release can increase the turbulent production through augmented velocity gradients and enhanced pressure-strain rates due to increased pressure fluctuations. On the other hand, heat release can increase viscous effects as a result of raised temperature. The interactions between the two opposing mechanisms are responsible for the diversity of phenomena reported in the literature. For modelling purposes, the viscous term in (1) can be ignored when the heat release is small and the Reynolds number is large. The advantage is that the growth rate can then be predicted solely by the turbulence production term, which is computed directly in a second-moment closure model. For the cases studied by Luo [4], neglecting the viscous term led to an error of up to 15% in the prediction of the growth rate. It is anticipated that the error will decrease with increasing Reynolds number but will increase with increasing heat release.

2. Countergradient diffusion

In the modelling of turbulent combustion, turbulent scalar fluxes are customarily approximated by gradient diffusion (GD) models. However, Bray *et al.* [5] predicted theoretically the existence of countergradient diffusion (CGD) in premixed turbulent flames. Recent DNS studies have produced evidence of CGD in both premixed [6] and non-premixed [7] turbulent combustion. Therefore, the use of GD models in reacting turbulent flow must be questioned. Luo [8] conducted further investigation into the mechanisms behind CGD, using DNS of non-premixed turbulent flames with different heat release rates. Local countergradient diffusion (LCGD) was observed in the turbulent fluxes

of both non-conserved and conserved scalars. The frequency, extent and duration of the occurrence of LCGD all increased with increasing heat release, although GD never broke down completely in all spatial locations and at all times. The appearance of such LCGD increases the complexity of the problem even further.

A detailed analysis of the transport equations for scalar fluxes in compressible reacting turbulent flow was performed by Luo [8], which revealed the driving forces for and against CGD. Both the mean and the fluctuating pressure gradients generated by combustion promote CGD, whereas the production terms due to the mean velocity and scalar gradients inhibit CGD. The viscous dissipation term also inhibits CGD although its magnitude is relatively small and its physical mechanism still unclear. It is highly likely that the viscous effects inhibit CGD by damping turbulent fluctuations. Finally, the term containing the reaction rate has a negligible effect on scalar transport. It explains why conserved and non-conserved scalars have very similar turbulent transport behaviour. On the basis of these results, a criterion for the occurrence of LCGD of the scalar flux $\overline{\rho\theta''u_j''}$ in the j -direction can be written as:

$$\frac{\partial p_e}{\partial x_j} \geq K \left(1 + \frac{1}{Pr_t} \right) \frac{\overline{\rho u_j'' u_k''}}{\sqrt{\overline{\theta'' \theta''}}} \frac{\partial \tilde{\theta}}{\partial x_j} \quad (2)$$

where K is a model constant, Pr_t a turbulent Prandtl number and p_e an "effective pressure gradient" defined as:

$$\frac{\partial p_e}{\partial x_j} = -\frac{1}{\sqrt{\overline{\theta'' \theta''}}} \left(\overline{\theta'' \frac{\partial p'}{\partial x_j}} + \overline{\theta''} \frac{\partial \bar{p}}{\partial x_j} \right) \quad (3)$$

The above criterion (2) states that LCGD or CGD occurs when the combustion-generated "effective pressure gradient" effect is larger than the effect of the gradient diffusion caused by the mean scalar gradient. It should be noted that the effects of mean velocity gradients have been incorporated into the turbulent Prandtl number Pr_t . Furthermore, the effective pressure gradient represents the total effects of combustion-generated mean and fluctuating pressure gradients. DNS results show that combustion-generated pressure gradients are highly sensitive to the level of heat release, which in turn depends on many factors. The next challenging task is to find a quantitative relationship between heat release and p_e through further simulation and modelling. In this sense, the criterion in (2) is a vital but first step in establishing a viable tool for predicting CGD in general. As discussed above, CGD or LCGD occurs due to a sufficiently large effect of the combustion-induced pressure gradient. It is therefore an intrinsic effect of the heat release process, which should be present in most practical flames. Provided the spatial and temporal accuracy of the simulation or measurement is sufficiently high, CGD or LCGD should be detected in more and more situations. Accordingly, combustion models must be built to be able to account for CGD and LCGD.

Acknowledgements

Supercomputing time from the UK EPSRC under grants No. GR/K93761 and No. GR/L67271 is gratefully acknowledged.

3. References

- 1 MCMURTRY, P.A., RILEY, J.J., METCALFE, R.W.: Effects of heat release on the large-scale structure in turbulent mixing layers; *J. Fluid Mech.* **199** (1989), 297-332.
- 2 GRINSTEIN, F.F., KAILASANATH, K.: Chemical energy release and dynamics of transitional, reactive shear flows; *Phys. Fluids A* **4**, No. 10 (1992), 2207-2221.
- 3 GIVI, P., MADNIA, C.K., STEINBERGER, C.J.: Effects of compressibility and heat release in a high speed reacting mixing layer; *Combust. Sci. and Tech.* **78** (1991), 33-67.
- 4 LUO, K.H.: Combustion effects on turbulence in a partially premixed supersonic diffusion flame; *Combustion and Flame* **119**, No. 4 (1999), 417-435.
- 5 BRAY, K.N.C., LIBBY, P.A., MASUYA, G., MOSS, J.B.: Turbulence production in premixed turbulent flames; *Combust. Sci. Technol.* **25** (1981), 127-140.
- 6 VEYNANTE, D., TROUVÉ, A., BRAY, K.N.C., MANTEL, T.: Gradient and counter-gradient scalar transport in turbulent premixed flames; *J. Fluid Mech.* **332** (1997), 263-293.
- 7 LUO, K.H., BRAY, K.N.C.: Combustion-induced pressure effects in supersonic diffusion flames; *Proceedings of the Combustion Institute* **27** (1998), 2165-2171.
- 8 LUO, K.H.: On local countergradient diffusion in turbulent diffusion flames; *Proceedings of the Combustion Institute* **28** (2000).

Addresses: DR. KAI H. LUO, Department of Engineering, Queen Mary and Westfield College, University of London, London E1 4NS, United Kingdom.

MACHU G.; MEILE, W.; NITSCHKE, L.; SCHAFLINGER, U.

The motion of a swarm of particles travelling through a quiescent, viscous fluid.

The motion and shape evolution of viscous drops made from a dilute suspension of microscopic, spherical glass beads sedimenting in an otherwise quiescent liquid is investigated for conditions of low Reynolds number and infinite Bond number. The key stages of deformation of single drops and pairs of interacting drops are identified. Of particular interest are (1) the coalescence of two trailing drops, (2) the subsequent formation of a torus, and (3) the break-up of the torus into two or more drops in a repeated cascade. All the phenomena described above can be explained within the realm of Stokes flow, without resort to interfacial tension or inertial effects.

1. Introduction

In the following, the shape evolution of single and interacting pairs of drops is investigated theoretically by means of discretizing the drop volumes with a swarm of small particles at a given volume fraction. The particles act simultaneously as generators of the flow field (because they are sedimenting relative to the local ambient flow) and tracers of shape and interface of the drops. The concept of shape and (fuzzy) interface is therefore a macroscopic interpretation of the result of a (microscopic) calculation of individual particle positions.

2. Governing equations

For a small drop Reynolds number (and an even smaller particle Reynolds number) and vanishing acceleration of the particles, the suspension drop can be modeled by using the equations of creeping flow. At low volume fractions the ratio of the particle radius to the smallest interparticle distance r is small. A good representation of hydrodynamic interactions between the particles is to therefore pretend that each particle at the position \underline{x}_m sediments essentially in isolation with the Stokes settling velocity relative to a local ambient velocity vector. This velocity vector is obtained by superposing the Stokeslet disturbance fields (determined by $\mathbf{F}(\underline{x})$) from all other particles at positions \underline{x}_n , each of these others being regarded as itself settling in isolation relative to its own local flow field. If we recast the governing equations (see [2] or [4]) by using R as the radius of the drop, a reference velocity U which is the Hadamard-Rybczynski (H-R) velocity for a drop of unit radius and time R/U , we obtain the velocity of the m -th particle in the swarm:

$$\frac{d\underline{x}_m}{dt} \approx \sum_{n=1}^M (6\pi\epsilon_g) \cdot \mathbf{F}(\underline{x}_m - \underline{x}_n), \quad \mathbf{F}(\underline{x}) = \frac{1}{8\pi r} (\mathbf{I} + \underline{\hat{x}}\underline{\hat{x}}), \quad \underline{\hat{x}} = r^{-1}\underline{x} \quad r = \underline{x}_m - \underline{x}_n$$

3. Results

We have proved rigorously (see [4]) the analogy in behaviour of drops containing finely dispersed particles and drops consisting of pure liquid (see also [3] for experiments). Therefore, all the results exhibited in this section also hold true for drops of pure liquid. In figure 1(a), the interaction of two horizontally displaced drops is presented. Due to the interaction (see [1]), the rear drop manages to catch up with the leading drop and eventually pokes through. During the further development both droplets mix due to the toroidal vortex. It is clearly visible that a large amount of surrounding clear liquid becomes entrained in the newly formed compound drop. This mechanism of entrainment is identified for being responsible for the subsequent torus formation presented in figure 1(b). The entrained liquid circulates in the compound drop and gives rise to a ring-like structure, a 'closed' torus. This initially formed torus is surrounded by an envelope of closed streamlines, as exhibited in figure 2. The torus undergoes a series of radial expansion and contraction cycles, with the expansion prevailing. Subsequently the flow field suddenly changes and the torus evolves into a so-called 'open' torus, with the streamlines passing through the hole in the center. The 'open' torus is unstable and disintegrates into two or three secondary drops, which themselves become unstable and break into tertiary drops - the cascade of ring disintegration.

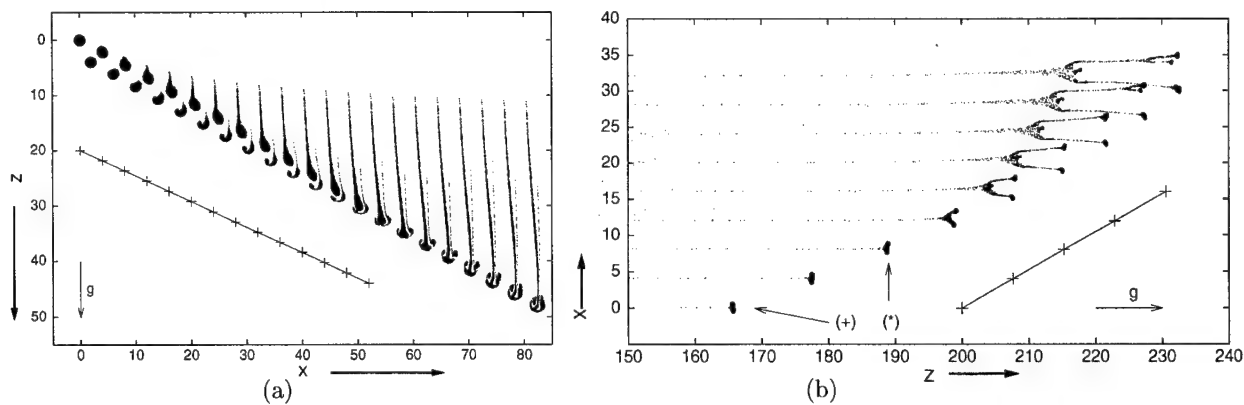


Figure 1: (a) The interaction of two horizontally displaced suspension drops in a sectional plane. Drop positions are shifted four units to the right at each dimensionless time interval of $\Delta t=1.84$. A H-R trajectory for a single drop of unit radius is drawn as a reference scale. (b) The cascade of ring disintegration in a (Z/X) diagram. Drop positions are shifted four units in X at each dimensionless time interval of $\Delta t=7.64$. The graph is turned 90 degrees counterclockwise from the vertical to make it compact.

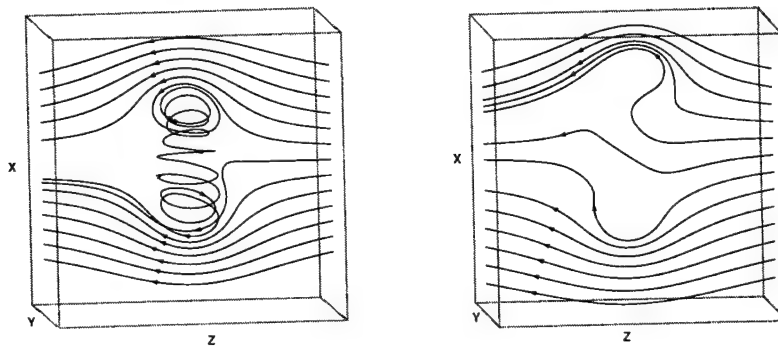


Figure 2: 3-d volume streamlines for the closed (+) and the open torus (*) marked as (+) and (*) in figure 1(b). The torus (not drawn here) is situated at the centre of the cubical volume. The streamlines start along a regular spacing at a line parallel to the X -axis in a sectional plane which intersects the centre of the torus.

4. References

- 1 MANGA, M., STONE, H. A.: Collective hydrodynamics of deformable drops and bubbles in dilute low Reynolds number suspensions. *J. Fluid Mech.* **300** (1995), 231–263.
- 2 NITSCHKE, J. M., BATCHELOR, G. K.: Break-up of a falling drop containing dispersed particles. *J. Fluid Mech.* **340** (1997), 161–175.
- 3 SCHAFLINGER, U., MACHU, G.: Interfacial phenomena in suspensions. *Chem. Eng. Technol.* **22** (1999), 617–619.
- 4 MACHU, G., MEILE, W., NITSCHKE, L. C., SCHAFLINGER, U.: Coalescence, torus formation and break-up of sedimenting drops: experiments and computer simulations. *J. Fluid Mech.*, submitted

Addresses: DIPL.-ING. GUNTHER MACHU, DR. WALTER MEILE, PROF. DR. UWE SCHAFLINGER, Institute of Fluid Mechanics and Heat Transfer, Technical University Graz, Inffeldgasse 25, A-8010 Graz, Austria.
 PROF. LUDWIG C. NITSCHKE, PhD, Department of Chemical Engineering, The University of Illinois at Chicago, 810 South Clinton Street, Chicago, IL 60607, USA

MEILE, W., MACHU, G., SCHAFLINGER, U.

Experimental investigation of viscous drop formation from a needle

The present paper focuses on the shape evolution and deformation of single drops and pairs of trailing drops made from dilute suspensions during gravitational sedimentation in an otherwise quiescent homogeneous liquid. The presented experimental results are only one part of a comprehensive investigation also including theoretical considerations and numerical simulations. This paper presents the characteristic phenomena through both flow visualization and detailed PIV-measurements including subsequent derivation of the streamline pattern.

1. Introduction

It became evident from previous investigations that both homogeneous liquid drops and suspension drops exhibit similar phenomena during sedimentation when effects of inertia and interfacial tension are negligible, i.e. zero drop Reynolds number

$$\mathcal{R}_d = \frac{U_d R}{\nu_f} \cong \frac{(\Delta \varrho) g R^3}{\varrho_f \nu_f^2}$$

and infinite Bond number

$$\mathcal{B} = \frac{(\Delta \varrho) g R^2}{\sigma}$$

Our recent theoretical studies yielded a rigorous mathematical proof of the striking analogy between liquid drops and suspension drops [3]. Here, $\Delta \varrho = \varrho_d - \varrho_f = \phi(\varrho_p - \varrho_f)$ denotes the density difference between the suspension drop and the ambient liquid, ϕ the volume fraction of solid particles, R the drop radius and σ the (vanishing) interfacial tension. For equal viscosities U_d is the Hadamard-Rybczyński settling velocity of the drop. The shape evolution of both (liquid drops and suspension drops) has been observed experimentally and results are given in a number of previous papers (e.g. [1], [2], [4], [6]). Despite the wide variety of experimental and theoretical treatments applying different methods, several important questions have remained. In particular, the formation and the possible break-up of the torus with respect to the initial conditions, and the subsequent cascade of following break-ups are of certain interest. Previous multiparticle simulations [5] have addressed the break-up of a spherical blob by a dispersive exodus of particles in a tail, but with no significant distortions in shape. However, this theoretical ideal of a strictly spherical drop is nearly impossible to produce in the laboratory.

2. Experimental setup

The suspension drops consisted of pure glycerine and a small fraction of glass beads with a mean radius of $a = 25 \mu\text{m}$ corresponding to volume concentrations of $0.04 < \phi < 0.08$. The premixed suspension was injected through a thin needle via a precisely controllable pump into the reservoir with the ambient fluid (pure glycerine). The laser light-sheet was created by an argon ion laser in combination with an electro-optical shutter and a polygon scanner. Light-sheet visualization and detailed measurements were performed with a complete DANTEC PIV-system including a cross-correlation camera, the Flow Map processor and the appropriate software package. Inside the drops the glass beads served as seeding particles, and the ambient liquid was seeded with polyamide particles of similar size. In addition, suspension drops with polyamide particles instead of glass beads were used for better performance of the correlation procedure.

3. Results

The individual pictures in Figures 1 and 2 show the shape evolution of a single suspension drop and a pair of horizontally displaced trailing drops, respectively. All pictures were recorded via light-sheet technique and are addressed in the following text from the left to the right (and from the upper row to the lower row in Fig. 1). The evolution of single drops is quite fundamental, and the different stages displayed in Fig. 1 are explained in greater detail, what follows. The first photograph of Fig. 1 shows the typical shape of the initial "drop" shortly after the downward injection of the suspension below the free surface of the liquid. The lower part of the suspension forms

a roughly hemispherical cap, while the upper (rear) part resembles the conical shape of the laminar jet due to the injection process. The corresponding streamline-pattern (streamlines cut through the rear part of the structure) indicates that clear liquid starts to become entrained at the rear. Furthermore, particles are swept out from the edges of the spherical part and form a second coaxial tail. Clear liquid circulates in the toroidal vortex and progresses towards the front stagnation point, eventually cuts through the surface and is carried back to the rear. This process leads to the mushroom shape with the leading cap and the depression region at the rear, as seen in the fourth photograph. At this stage a closed envelope of streamlines can be detected and both tails, the original and the coaxial, are left behind (c.f. [3]). During the following process also the leading cap is carried back (fifth photograph) and in time the shape becomes toroidal with an envelope of closed streamlines and two stagnation points in front and rear. To this configuration we refer as a *closed torus*. This initial torus is an intermediate outcome of a *range* of initial configurations; once it has formed, the further proceeding appears in two distinct phases: (1) a period of cyclic expansions and contractions, where the expansions prevail in time and the torus grows in horizontal direction; (2) at some point, the configuration changes to an *open torus* with streamlines passing through the central hole (see e.g. [3]). However, the open torus is unstable under the above-mentioned conditions which leads to the subsequent well-known break-up cascade. It is the *closed torus* that first forms and undergoes a periodic expansion and contraction cycle, but it is the *open torus* that eventually disintegrates. The experimental observations of pairs of trailing drops clearly display the flattening of the leading drop and a strong elongation of the trailing drop yielding a prolate shape with a long tail. The trailing drop moves at higher velocity, catches up with the leading drop and pokes through. In the further progress the toroidal vortex leads to a mixing of both drops and a compound spherical drop emerges. The tail gets disconnected and a closed torus is formed. Eventually a transition to an open torus takes place and this is followed by a cascade of break-ups. In case of horizontal displacement the trailing drop gets into alignment with the leading one and the further evolution is similar as described above (see Fig. 2).

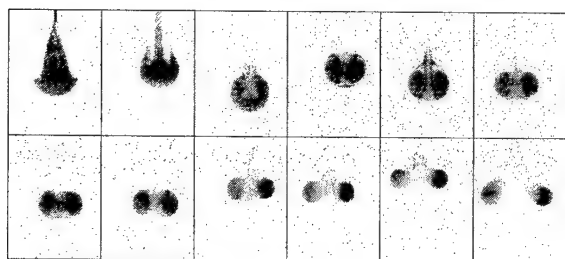


Figure 1: Evolution of a single suspension drop

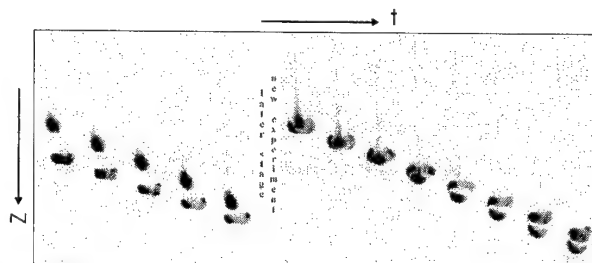


Figure 2: Two horizontally displaced suspension drops

Acknowledgements

WM, GM and US gratefully acknowledge the fruitful and enlightening cooperation with Prof. Ludwig C. Nitsche during his sabbatical visit to the Institute of Fluid Mechanics and Heat Transfer of Technical University Graz. The financial support of LCN from the Fulbright Commission and from the Christian Doppler Laboratory for Continuous Solidification Processes, Vienna, is gratefully acknowledged. Furthermore, the present work benefited from a series of helpful conversations with Prof. Johannes M. Nitsche, for which the authors are grateful.

4. References

- 1 ADACHI, K., KIRIYAMA, S., KOSHIOKA, N.: The behavior of a swarm of particles moving in a viscous fluid. *Chem. Eng. Sci.* **33** (1978), 115–121.
- 2 JOSEPH, D. D., RENARDY, Y. Y.: *Fundamentals of Two-Fluid Dynamics*. Springer-Verlag, New York, 1993.
- 3 MACHU, G., MEILE, W., NITSCHKE, L., SCHAFLINGER, U.: Coalescence, torus formation and break-up of sedimenting drops: experiments and computer simulations. *J. Fluid Mech.*, submitted.
- 4 MANGA, M., STONE, H. A.: Collective hydrodynamics of deformable drops and bubbles in dilute low Reynolds number suspensions. *J. Fluid Mech.* **300** (1995), 231–263.
- 5 NITSCHKE, J. M., BATCHELOR, G. K.: Break-up of a falling drop containing dispersed particles. *J. Fluid Mech.* **340** (1997), 161–175.
- 6 SCHAFLINGER, U., MACHU, G.: Interfacial phenomena in suspensions. *Chem. Eng. Technol.* **22** (1999), 617–619.

Addresses: DR. WALTER MEILE, DIPL.-ING. GUNTHER MACHU, PROF. DR. UWE SCHAFLINGER, Institute of Fluid Mechanics and Heat Transfer, Technical University Graz, Inffeldgasse 25, A-8010 Graz, Austria

DIRK MEINKÖHN

Liquid-Fuelled Rocket Propulsion: The Role of Atomization Processes in Combustion Chamber Instabilities

1. Introduction

Combustion instabilities are defined to be large-scale unsteady movements of the gas contained in a combustion chamber. They are unwanted and considered potentially dangerous since such chambers are designed for steady operating conditions. Combustion instabilities may evolve out of stationary chamber operations and are driven by feed-back from downstream chamber processes like combustion to upstream processes generally associated with how the propellants are fed into the combustion chamber. For liquid-fuelled propulsion, these supply processes involve liquid injection and atomization, and the feed-back loop comprising downstream combustion and upstream atomization has been identified as a major factor in generating combustion instabilities. In order to predict and thereby to avoid combustion instability in the case of liquid propellants, the physics of jet instability and disintegration of liquid sheets and ligaments needs to be thoroughly understood. Although motor designers in liquid-fuelled rocket propulsion are fully aware of this requirement, a predictive model is still unavailable. This is largely due to the fact that liquid disintegration and atomization are not readily describable in terms of continuum mechanics because the act of rupture by which a droplet eventually separates from a parent body of liquid violates basic assumptions of continuum theoretics. It is found, though, that the act of rupture by which a hole forms in a liquid sheet, or by which a droplet pinches off a liquid filament, is given in the form of an asymptotic limit of the appropriate field equations which comprise the Navier-Stokes equations, the equation of mass continuity, and an equation describing the kinematics of the transverse surfaces of the sheet. The lowest order in the corresponding asymptotic expansion gives a set of strongly coupled evolution equations which are degenerate-parabolic. This degeneracy causes the appearance of singularities in finite time which are associated with the act of rupture. Since the sheet curvature approaches large values, large values of the capillary pressure occur which lead to strong acceleration of the liquid elements of the sheet. Since their inertia prevents large regions of liquid to be affected, the act of rupture is given as a self-similar phenomenon.

Due to strong coupling and parabolic degeneracy, the mathematical treatment of the lowest order field equations is difficult. It is the intention of this paper to investigate free liquid sheets along with sheets which are supported by a solid surface. For both types, the physics of hole formation and droplet detachment are found to result from the same mechanism. Since surface-supported liquid sheets turn out to be mathematically more tractable, it is hoped that from their treatment insight is gained as to the more complicated case of free liquid sheets and filaments.

2. Hydrodynamics of Thin Liquid Sheets

In order to facilitate a comparison of supported and unsupported liquid sheets, symmetry conditions are imposed on the systems under consideration. For *supported sheets*, the supporting solid surface is required to be a plane. The sheet thickness h is measured in the normal direction, so that the outer surface of the sheet is given as: $z = h(x_1, x_2, t)$, where z is the transverse coordinate measured in the normal direction, t the time, and x_1, x_2 are coordinates in the longitudinal directions along the solid support. *Unsupported sheets* are assumed to be symmetrical with respect to an internal neutral plane. In this case, the film thickness is $2h$, and due to symmetry it suffices to restrict considerations to the upper half of the sheet, which is therefore bounded by the outer surface $z = h(x_1, x_2, t)$ and the neutral plane at $z = 0$. The evolution of both types of sheets is driven by capillary forces arising from the curvature of the outer surface of the sheet. These forces give rise to a flow field within the sheets, with a velocity $\vec{v} = \{u_1, u_2, w\}$. The two cases of supported and unsupported sheets essentially differ in the boundary condition for $z = 0$, i.e. at the supporting plane or the neutral plane, respectively. At the supporting plane the no-slip condition is imposed whereas for an unsupported film the velocity boundary condition at the neutral plane is a consequence of the imposed symmetry.

The field equations are as follows:

$$\text{Navier-Stokes} \quad \partial_t \vec{v} + (\vec{v} \cdot \nabla) \vec{v} = -\frac{1}{\rho} \nabla p + \nu \Delta \vec{v}$$

$$\begin{array}{ll} \text{mass continuity} & \nabla \cdot \vec{v} = 0 : \quad \nabla_s \vec{u} + \partial_z w = 0 \\ \text{surface kinematics} & z = h(x_1, x_2, t) : \quad \frac{\partial h}{\partial t} - |1 + (\nabla_s h)^2| v_n = 0 \end{array}$$

∇ = nabla operator, $\nabla_s = \{\partial_{x_1}, \partial_{x_2}, 0\}$ = surface nabla, v_n = normal velocity at the outer sheet surface $z = h(x_1, x_2, t)$, ρ = density, p = pressure, ν = kinematic viscosity, $\vec{u} = \{u_1, u_2, 0\}$ = surface velocity. If a characteristic thickness h_0 and a characteristic time t_0 are introduced, and if a characteristic velocity is defined by $v_0 = h_0/t_0$, and if the internal pressure is given by the capillary pressure: $p \simeq \sigma \nabla^2 h$, where σ is the surface tension, then the Navier-Stokes equation is obtained in nondimensional form as follows:

$$Re \left(\partial_t \vec{v} + (\vec{v} \cdot \nabla) \vec{v} \right) = \frac{1}{Ca} \nabla^3 h + \nabla^2 \vec{v}$$

Re = Reynolds number, Ca = capillary number which essentially expresses the ratio ν/σ . Sheet rupture is investigated in the distinguished limit $Re = \epsilon^2 \rightarrow 0$, with the supplementary condition $ReCa \sim O(1)$. Particularly, for a supported sheet: $ReCa = \epsilon^2 \rightarrow 0$, which expresses the physical fact that in this case large capillary forces can be dynamically equilibrated by internal friction and wall friction, whereas inertial forces are negligible in lowest order of approximation. The case of an unsupported sheet is different in that there is no wall friction, and inertial forces are therefore needed to equilibrate the capillary forces. In this case the supplementary condition must be: $ReCa = \epsilon \rightarrow 0$ whereby $1/Ca = \epsilon$.

In the limit of $\epsilon \rightarrow 0$ the field equations along with the boundary conditions are solved for the surface velocity $\vec{u} = \{u_1, u_2, 0\}$ and the sheet thickness h . For unsupported sheets, the field equations are:

$$\begin{aligned} \partial_t \vec{u} + (\vec{u} \cdot \nabla_s) \vec{u} &= \sigma \nabla_s^3 h + 4 \frac{1}{h} \nabla_s \cdot (h \nabla_s \cdot \vec{u}) \\ \partial_t h + \nabla_s \cdot h \vec{u} &= 0 \end{aligned}$$

For \vec{u} the following boundary conditions need to be satisfied: $\partial_z \vec{u} = 0$ at $z = 0$ and at $z = h$. The case of a supported sheet is simpler in that integration of the Navier-Stokes equation is straightforward, giving \vec{u} as a functional of h , so that a single field equation remains to be solved:

$$\partial_t h + \nabla_s \cdot \left[\frac{h^3}{3} \sigma (\nabla_s \nabla_s) \cdot \nabla_s h \right] = 0$$

Here, the velocity field \vec{u} satisfies the boundary conditions of $\partial_z \vec{u} = 0$ at $z = h$ and $\vec{u} = 0$ at $z = 0$

3. Field Equation Properties

The lowest-order approximation of the field equations amounts to a reduction of the initial 3-d sheet to a 2-d membrane or a 1-d filament. Due to this reduction the approximate equation system turns out to be nonlinear degenerate-parabolic because it is given in terms of transport operators of the following form: $\nabla_s \zeta(h) \vec{j}$. In this expression, \vec{j} is a flux given in terms of $\nabla_s h$ or $\nabla_s \vec{v}$ whereas $\zeta(h)$ designates a transport coefficient which is proportional to some power of the field variable h : $\zeta(h) \sim h^q$. The degeneracy arises since $h \rightarrow 0$ is admitted, in which case $\zeta \rightarrow 0$, which implies singular values of $\nabla_s h$ or $\nabla_s \vec{v}$. Degeneracy may lead to the appearance of *self-similar sharp waves* (similar to those which are known as *Barenblatt waves*) of finite speed of propagation, whilst in the case of nondegenerate parabolic systems the perturbations in the field variables propagate with infinite speed. Self-similar waves in nondegenerate parabolic systems correspond to a relaxation phenomenon by which initially steep gradients in the field variables are progressively smoothed out. For sharp waves a steep neck is propagated without losing its steepness, which is in close agreement with what is observed experimentally when liquid sheets and ligaments rupture. In the case of an unsupported sheet, the two field equations are strongly coupled since spatial derivatives of both h and \vec{u} occur in each of the two evolution equations.

In order to investigate why drops form preferentially by pinching off 1-d filaments, a right circular cylinder of radius R is chosen as supporting solid surface or as neutral surface, respectively. This generalizes the coordinate system to become curvilinear, which introduces an additional curvature effect since now even the outer surface of a liquid sheet of constant thickness possesses a mean curvature which is nonvanishing. It is found that this additional curvature favours sheet instability. In the limit of $R \rightarrow 0$ the two principal curvatures become infinite but there is a compensation since they differ as to their sign.

Addresses: PROF. DR. DIRK MEINKÖHN, Deutsches Zentrum für Luft- und Raumfahrt DLR
Institut für Raumfahrtantriebe, 74239 Hardthausen, FRG

Heiko Meironke, Janusz A. Szymczyk

Experimentelle Untersuchungen der Deformation einer Phasengrenze einer aufsteigenden Gasblase

1. Einleitung

In dieser Arbeit wird die Vorgehensweise, der Versuchsaufbau und die ersten Ergebnisse im Rahmen der experimentellen Untersuchungen der Deformation einer Phasengrenze einer aufsteigenden Luftblase präsentiert.

2. Theoretische Betrachtungen

Um das Spektrum der Untersuchungen bei der Blasendynamik einzugrenzen ist eine Gliederung der durchzuführenden Experimente sowie der Bezug auf relevante Kennzahlen nötig. Zur genauen Berechnung dieser Kennwerte, müssen daher die bestimmenden Größen mit einer höchst möglichen Genauigkeit erzielt werden. Im Allgemeinen kann man den Aufstieg der Blase vom Austritt bis zur Oberfläche in vier Bereiche unterteilen, die in Abhängigkeit von den Kennwerten der flüssigen Phase und den Dimensionen der gasförmigen Phase weniger oder zum Teil dominant ausgeprägt sind (Abb. 1). Um den Bereich der Pendelbewegung entlang einer Spiraltrajektorie eindeutig beschreiben zu können, ist es notwendig eine Reihe von Größen zu ermitteln, welche die lokale Lage der Blase im Raum sowie die spiralförmige Trajektorie charakteristisch beschreiben. Als wichtige Kennzahlen für das Auftreten von Instabilitäten der Oberfläche während des Blasenanstieges stehen unter anderen die Reynolds-, die Weber und die Mortonzahl. Eine kritische Reynoldszahl existiert für verunreinigte und hochviskose Flüssigkeiten ($Re=202$) und eine kritische Weberzahl für reine, niedrigviskose Flüssigkeiten ($We=1,26$) [1]. Es gibt jedoch bis jetzt keine exakte Methode, die eine eindeutige Aussage liefert, welches der beiden Kriterien in einer gegebenen Flüssigkeit überwiegt. Aus diesen Kriterien resultieren folgende Aufgabenstellungen für die Untersuchungen:

- I. Ermittlung der strömungsmechanischen Übergänge bei folgenden Phänomenen:
 - Existenz von Oszillationen der Oberfläche
 - Auftreten einer instabil verlaufenden Aufstiegsbahn (Pendelbewegungen)
 - Instabilitäten der Blasenform während des Aufstieges: Kugelform zum Ellipsoid, Ellipsoid-Form, Pilzform
 - Blasenzerfallprozeß (bei großen Öffnungsdurchmessern)
- II. Katalogisierung der Oszillationsmoden von aufsteigenden Blasen

3. Versuchsaufbau

Um die oben genannten Anforderungen hinsichtlich der Genauigkeit und der hohen zeitlichen und räumlichen Auflösung des Meßobjektes gerecht zu werden, sollen im Rahmen dieser Untersuchungen ein digitales Hochgeschwindigkeitsvideo-System (40500 Bilder/s) sowie ein 3D Stereo Particle Image Velocimetry-System eingesetzt werden. Zum Einsatz kamen Quarzglas-Kapillare, die einen Öffnungsdurchmesser von 0.2 mm bis zu 2 mm aufwiesen. Zur definierten Generierung der Blasen wird eine Kolbenpumpe eingesetzt, welche einen extrem langsamen Vorschub gewährleistet.

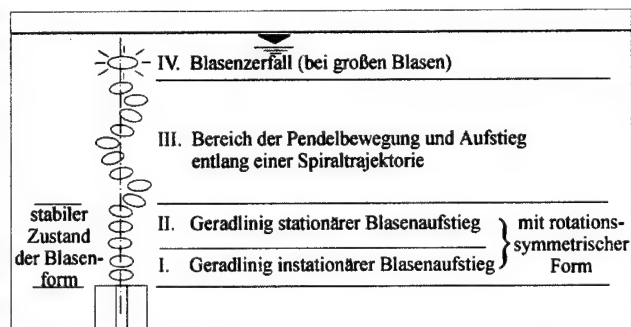


Abb. 1: Strömungsmechanische Übergänge

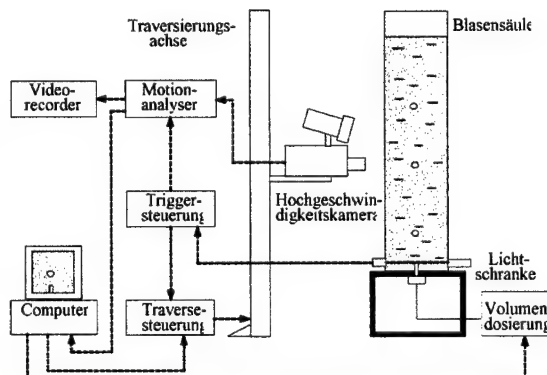


Abb. 2: Schematischer Versuchsaufbau

4. Präsentation der Ergebnisse

Als flüssiges Medium wurde ein 50% Glycerin / Wasser Gemisch (166 mm über Kapillare) und in einer weiteren Bildsequenz destilliertes Wasser (480 mm über Kapillare) untersucht. Die Blase wurde jeweils mit einem Volumenstrom von 47.1 $\mu\text{l/h}$ an einem Öffnungsdurchmesser von 1.11 mm generiert. Die Verfahrensgeschwindigkeit der Kamera wurde der Aufstiegsgeschwindigkeit der Blase annähernd angepaßt. Nach dem Abriß (Abb. 4 $t = 0.0\text{ms}$), befindet sie sich in der Beschleunigungsphase und ist durch den Abbau der Schwingungen, die durch den Ablösevorgang entstanden sind, gekennzeichnet. Hierbei ist die Blase rotationssymmetrisch und bewegt sich auf einer geradlinigen Bahn (bis $t \approx 100\text{ms}$). In dem II. Bereich bewegt sich die Blase geradlinig mit einer stationären Aufstiegsgeschwindigkeit entlang der vertikalen Achse und ist noch rotationssymmetrisch ($t < 259\text{ms}$). Mit Erreichen eines kritischen Punktes ($t = 259\text{ms}$; 49.7 mm über dem Austritt) endet die geradlinige Aufstiegsbahn und die Blase beginnt sich in einer Pendelbewegung und entlang einer Spiraltrajektorie nach oben zu bewegen. Kennzeichnend für dieses Fluid mit einem höheren Dämpfungseffekt aufgrund der Viskosität (Prandtl-Zahl = 46.1), ist eine bleibende rotationsymmetrische Form der Blase selbst. Bei der Pendelbewegung entlang einer Spiraltrajektorie ist aber die Symmetrieachse der Blase in einem Winkel gegenüber der vertikalen Achse geneigt. Weiterhin erfolgt auch eine pendelnde Rotation der Blase in horizontaler Richtung der Blasenachse.

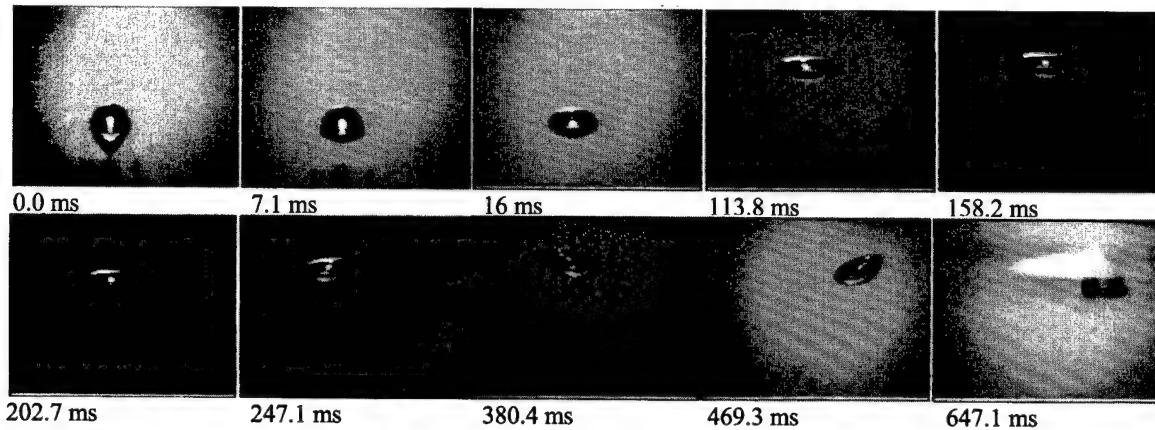


Abb. 3: Blasenauftstieg im 50 % Glycerin/Wasser-Gemisch - Aufnahmefrequenz: 1125 Bilder/s

Kennwerte im Bereich des geradlinigen stationären Aufstieges:

Volumen der Blase (nach Abriß)	= 40.87 mm ³	Kennzahlen:	Re = 155;	We = 0.26
Blasenäquivalentdurchmesser	= 4.27 mm		Mo = 3.66 10 ⁻⁸ ;	Pr = 46.1
Geschwindigkeit der Blase	= 192 mm/s			

5. Zusammenfassung und Ausblick

Zur Untersuchung der Deformation der Phasengrenzfläche einer aufsteigenden Blase wurde ein Versuchsstand entwickelt, der es ermöglicht, qualitative und quantitative Aussagen über die Blasenform und ihrer bestimmenden Parameter in einer hohen zeitlichen und räumlichen Auflösung zu gewährleisten. Die verschiedenen Verhaltensmuster der Gasblasen während des Blasenauftiegs wurden in Bereiche unterteilt, die durch strömungsmechanische Übergänge gekennzeichnet sind. Zur Optimierung des Untersuchungsaufwandes wurden bestimmende Kenngrößen zusammengefaßt und die Aufgabenbereiche in Abhängigkeit von diesen Kenngrößen beschrieben. Am Beispiel von zwei verschiedenen Fluiden wurden erste Aufnahmen erstellt und qualitativ interpretiert. Als Strömungsmeßtechnik wird die Particle Image Velocimetry zur Sichtbarmachung des Strömungsbildes um die Blase und zur quantitativen Auflösung der lokalen Geschwindigkeitskomponenten in der Umgebung der Phasengrenze zum Einsatz kommen.

Literatur

- [1] Hartunian, R. A. & Sears, W. R.: On the instability of small gas bubbles moving uniformly in various liquids. Journal of Fluid Mechanics, Vol. 3, 1957
- [2] Braeske H., Brenn G., Dornick J.: Experimentelle Grundlagenuntersuchungen zur Strömungsmechanik in Blasensäulen. Zwischenbericht zum Forschungsvorhaben Do 251/7-1. Lehrstuhl für Strömungsmechanik, Universität Erlangen-Nürnberg, 1996
- [3] Pahl, M. H. und Özkurt, M.: Aufstiegsverhalten von CO₂-Blasen unter verschiedenen Betriebsbedingungen. Monatsschrift für Brauwissenschaft, Heft 9/10, 1998
- [4] Szymczyk, J. A., Cieslinski, J. T., Meironke, H.: Visualisation of Bubble Growth using Particle Image Velocimetry. Tagungsband, 3rd Baltic Heat Transfer Conference 22.09.-24.09.1999

Adresse: Dipl.-Ing. H. Meironke, Fachhochschule Stralsund, FB Maschinenbau, Fachgebiet Strömungslehre und Strömungsmaschinen, Zur Schwedenschanze 15, 18435 Stralsund

J. NIEMANN, E. LAURIEN

Computing Virtual Mass by Direct Numerical Simulation

Bubbles resist acceleration with an apparent added mass. An improved knowledge of this virtual mass is desirable for accurate models of bubbly flows, for instance, in a two-fluid-model. A high-resolution, two-phase numerical code based on a volume-of-fluid method is used to compute the virtual mass of air and vapour bubbles in water. The dependency of virtual mass from void fraction is investigated. A well known analytically obtained equation of this dependency is confirmed and the hitherto undetermined quadratic term, which is of importance for medium and high void fractions, is established. A dependency on bubble size and shape is investigated.

1. Introduction

For the development of new models for technical two-phase flows, e.g. the Two-Fluid Model [1], it is necessary to determine model parameters. The virtual mass coefficient c_{vm} is one of these parameters. It takes account of the effect that bubbles resist acceleration stronger than is apparent from their actual mass. The virtual mass increases as the average volume fraction of gas x , or void fraction, increases. Because acceleration effects are difficult to measure experimentally, it is desirable to investigate them numerically. Virtual mass is often defined differently by different authors. The definition of the virtual mass coefficient used here is

$$c_{vm} = \left(1 - \frac{\rho_G}{\rho_L}\right) \cdot \frac{g}{a} - \frac{\rho_G}{\rho_L} \quad (1)$$

with ρ_G and ρ_L the gas and liquid densities, g the gravity and a the actual upward acceleration.

2. State of the Art

Several authors employed a potential theory to obtain similar formulas of the general form

$$c_{vm} = \frac{1}{2} + \frac{K}{2}x + O(x^2) \quad (2)$$

with K taking values of 2.78, 3 or 3.32 [2,3,4]. The neglecting of the quadratic term leads to large errors at medium and high void fractions ($x > 0.1$). Sangiani and Acrivos [5,6] derived an expression for medium void fractions. The logarithmic function used there can be approximated by the above quadratic polynomial.

3. Numerical Method

The numerical method used here is an incompressible Navier-Stokes code with a volume-of-fluid method for description of the free surface, a semi-implicit, multi-grid solver running parallel on a supercomputer (Cray T3E). It was originally designed for droplet collisions [7,8]. To simulate bubbles at high void fractions, a single bubble is placed into a cartesian box as the integration domain with periodic boundary conditions in the vertical direction and mirror boundary conditions in all other directions. Thus, a hexagonal array of bubbles is established. The simulations are run with 64^3 and 128^3 numerical cells for medium and low void fraction, respectively. The bubble is resolved with at least 16 cells across the bubble diameter.

4. Results

The acceleration is obtained by time derivation of the bubble position and has been computed for bubble arrays with void fractions between 1% and 35%. In the low void fraction regime, up to 10%, the results are in agreement with the linear approximation of equation (2). For medium void fractions, the quadratic dependency is obtained:

$$c_{vm} = \frac{1}{2} + \frac{3.26}{2}x + \frac{7.7}{2}x^2 \quad (3)$$

Variation of bubble diameter showed no influence on the result, whereas ellipsoidal bubbles showed that the area of the cross section perpendicular to the direction of motion determines the virtual mass. The diameter of this cross section becomes the determining quantity, shifting the coefficient c_{vm} towards higher void fractions by a factor in the order of the aspect ratio.

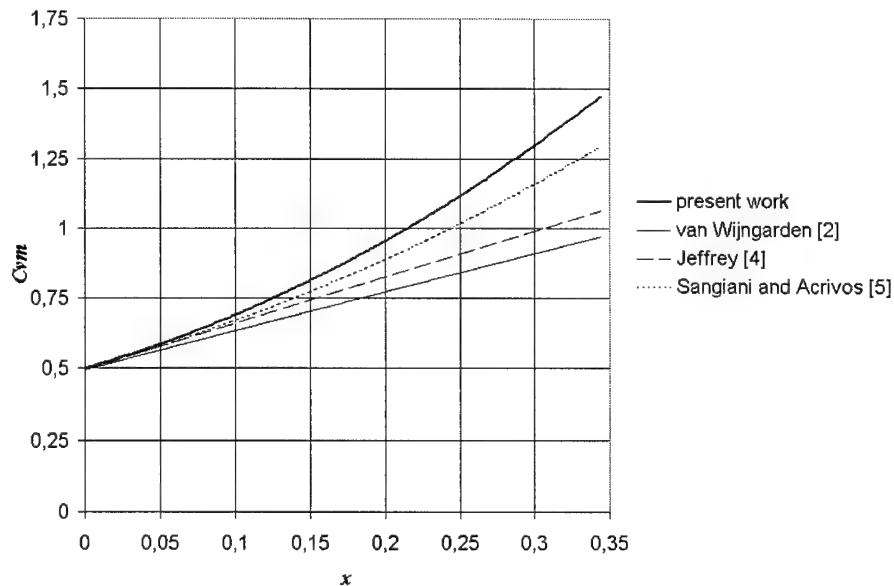


Figure 1: Diagram of the virtual mass coefficient versus void fraction

During acceleration, the pressure field around the bubble changes. This effect depends on void fraction. The pressure field at high void fractions is more deformed compared to the initial pressure field than at low void fraction. The virtual mass effect can be explained as a force acting to resist the change of the pressure field around the bubble.

5. Conclusion

Earlier formulas represent virtual mass only well for low void fractions. An improved formula for medium void fractions is presented. The phenomenon of virtual mass is interpreted as a force resisting the pressure change around the bubble's surface during the process of gaining speed.

Acknowledgements

The results presented in this paper have been computed with the numerical method developed by Dr.-Ing. M. Rieber.

6. References

- 1 DREW, A. : Mathematical Modelling of Two-Phase Flow, *Ann. Rev. Fluid. Mech.* **15** (1983), 261-291
- 2 VAN WIJNGARDEN, L. : Hydrodynamic interaction between gas bubbles in liquid, *J. Fluid Mech.* **77** (1976), 22-44
- 3 ZUBER, N. : On the dispersed two-phase flow in the laminar flow regime, *Chem. Eng. Sci.* **19** (1964), 897-917
- 4 JEFFREY, D. J. : Conduction through random suspension of spheres, *Proc. R. Soc.* **A335** (1973), 355-367
- 5 SANGIANI, A.S. AND ACRIVOS, A. : Slow Flow through a Periodic Array of Spheres, *Int. J. Multiphase Flow* **8** (1982), 343-360
- 6 SANGIANI, A.S. AND ACRIVOS, A. : The Effective Conductivity of a Periodic Array of Spheres, *Proc. R. Soc.* **A386** (1983), 263-275
- 7 RIEBER, M. AND FROHN, A. : Navier-Stokes Simulation of Droplet Collision Dynamics, *Proc. 7th Int. Symp. on Computational Fluid Dynamics*, Beijing, China (1997), 520-525
- 8 RIEBER, M. AND FROHN, A. : Parallel Computation of Interface Dynamics in Incompressible Two-Phase Flows, *High Performance Computing in Science and Engineering*, Krause, E. and Jaeger, W. (Eds.), Springer (2000), 241-252

Addresses: DIPL.-ING. J. NIEMANN, PROF. DR.-ING. E. LAURIEN, University of Stuttgart, IKE, Pfaffenwaldring 31, 70550 Stuttgart, Germany

RUMBERG, O; ROGG, B.

A Three Variable Formalism for Turbulent Reactive Sprays

A suitably defined PDF is set up for the statistical treatment of a liquid spray dispersed in a gaseous carrier phase. The formulation is full in the sense that the PDF allows for the mathematical description of the totality of all liquid-phase and gas-phase variables. The evolution of this PDF in time is governed by a PDF transport equation, which is modelled and solved via a Monte-Carlo method. The numerical results clearly indicate the usefulness of the method for laminar and turbulent reacting flows.

1. Introduction

In many technical applications, to enhance combustion liquid fuel is sprayed into hot gas, leading to a very large number of droplets with different properties. In numerical simulations it is impossible to track the droplets individually in a deterministic manner, thus in a certain sense the mathematical description has to be statistical. This concept leads to a joint probability density function (PDF) for the spray and a corresponding transport equation, which is referred to as *Williams' spray equation* [1]. For pure gaseous flows advantage is taken by setting up a joint probability density function, too. Here this approach has become popular and widespread through the work of *Pope*, see e.g. [2].

A natural way of modelling proceeds by considering both the droplet and the gas-phase motion as random processes and to describe the overall process via a suitably defined PDF. The formulation is "full" in the sense that there is a single joint-PDF for the totality of all gas-phase and liquid-phase dependent variables. Based on a general joint-PDF formulation of two-phase flow [3], the special case of a reactive spray is considered for which transport equations are derived. Next to the well-known advantages that using a PDF method for turbulent flows reaction and convection are given in closed form, in the formulation derived the interaction of liquid and gaseous fluid phase appears in closed form, too. Significant reduction in computational effort is achieved by assuming that the gas-phase combustion chemistry can be described by a global one-step reaction which leads to a formulation with only three scalar variables [4].

2. Statistical Formulation

Without loss of generality, for the joint PDF f the additive form $f = f_I + f_{II}$ is assumed [4]. Here f_I denotes the contribution to f of the liquid phase, f_{II} the contribution to f of the gas phase. For the systems and flames considered herein, $f_I = f_I(\underline{\hat{V}}, \hat{R}; \underline{x}, t)$ and $f_{II} = f_{II}(\underline{\hat{V}}, \hat{\zeta}, \hat{c}, \hat{\eta}; \underline{x}, t)$. Here carets are used to denote the phase variables of the respective stochastic quantities; $\underline{\hat{V}}$ is the phase-independent velocity vector (the phase being taken into account explicitly by distinguishing between f_I and f_{II}). For f_I the transport equation

$$\frac{\partial}{\partial t} \{ \rho_L f_I \} + \hat{V}_i \frac{\partial}{\partial x_i} \{ \rho_L f_I \} + \frac{\partial}{\partial \hat{V}_i} \{ W_i(\underline{\hat{V}}, \hat{R}) \rho_L f_I \} + \frac{\partial}{\partial \hat{R}} \{ Q_M(\underline{\hat{V}}, \hat{R}) \rho_L f_I \} = 0 \quad (1)$$

can be derived, for f_{II} the transport equation

$$\begin{aligned} & \frac{\partial}{\partial t} \{ \rho_G f_{II} \} + \hat{V}_i \frac{\partial}{\partial x_i} \{ \rho_G f_{II} \} + \frac{\partial}{\partial \hat{V}_j} \left\{ \left(-\frac{\partial \langle p \rangle}{\partial x_j} + \frac{\partial \langle \tau_{ij} \rangle}{\partial x_i} \right) f_{II} \right\} \\ & - \frac{\partial}{\partial \hat{c}} \left\{ \frac{\partial \langle J_i^c \rangle}{\partial x_i} f_{II} \right\} + \frac{\partial}{\partial \hat{c}} \{ w(\hat{\zeta}, \hat{c}, \hat{\eta}) f_{II} \} - \frac{\partial}{\partial \hat{\zeta}} \left\{ \frac{\partial \langle J_i^\zeta \rangle}{\partial x_i} f_{II} \right\} - \frac{\partial}{\partial \hat{\eta}} \left\{ \frac{\partial \langle J_i^\eta \rangle}{\partial x_i} f_{II} \right\} = \\ & + \frac{\partial}{\partial \hat{\zeta}} \left\{ \left\langle \frac{\partial J_i^{\zeta'}}{\partial x_i} \middle| \hat{\underline{\hat{z}}} \right\rangle f_{II} \right\} + \frac{\partial}{\partial \hat{c}} \left\{ \left\langle \frac{\partial J_i^{c'}}{\partial x_i} \middle| \hat{\underline{\hat{z}}} \right\rangle f_{II} \right\} + \frac{\partial}{\partial \hat{\eta}} \left\{ \left\langle \frac{\partial J_i^{\eta'}}{\partial x_i} \middle| \hat{\underline{\hat{z}}} \right\rangle f_{II} \right\} \\ & - \frac{\partial}{\partial \hat{V}_i} \left\{ \left\langle \left(-\frac{\partial p'}{\partial x_i} \right) \middle| \hat{\underline{\hat{z}}} \right\rangle + \left\langle \frac{\partial \tau'_{ij}}{\partial x_j} \right\rangle \right\rangle f_{II} \right\} + \langle \rho B | \hat{\underline{\hat{z}}}, \hat{\beta}^I \rangle f(\underline{\hat{V}}, \hat{\zeta}, \hat{c}, \hat{\eta}, \hat{\beta}^I; \underline{x}, t). \end{aligned} \quad (2)$$

In Eqs. (1) and (2) it is understood that $\hat{\underline{\hat{z}}} = (\underline{\hat{V}}, \hat{\zeta}, \hat{c}, \hat{\eta})^T$, $\rho_G = \rho_G(\hat{\zeta}, \hat{c}, \hat{\eta})$ and $\rho_L = \text{const.}$, respectively. The

last terms in Eqs. (1) and (2) account for evaporation. For general two-phase flows the last term in Eq. (2) needs modelling, but here – in the special case of a spray – it can be rewritten in closed form [4]; the exchange of mass, momentum and scalars due to evaporation is described physically correct even under turbulent flow conditions.

3. Numerical Method and Results

Equations (1) and (2) are solved using a particle method, where two sets of notional particles are assigned properties according to the inlet conditions and are tracked on their way through physical and state space. Details on the important questions of consistency and computation of a proper pressure gradient are addressed in [4]. The unclosed terms on the right hand side of Eq. (2) are approximated by standard models, which are a *modified mixing model* and a *stochastic reorientation model*, respectively [2]. Statistical moments up to all orders and of all variables of interest are computed through ensemble averaging at given physical position \underline{x} and time t .

The numerical simulation shown below is for turbulent, overall steady and one-dimensional flow in the limit $Re_G \rightarrow \infty$. At $x = 0$ the liquid droplets are injected into the flow. Both phases exchange momentum with an without the exchange of mass. For the latter a common drag-law is used; for evaporation a d^2 -law is assumed with the evaporation-rate parameter taken as $K/(R_0 V_G) = 2 \cdot 10^{-3}$. With respect to the gas phase other typical parameters read: $\rho_L/\rho_G = 500$, $V_G/V_L = 2$, $L/R_0 = 8 \cdot 10^3$. The reaction is characterised by a Zel'dovich number of $Ze = 6.5$ and a heat release parameter of $\alpha = 0.85$.

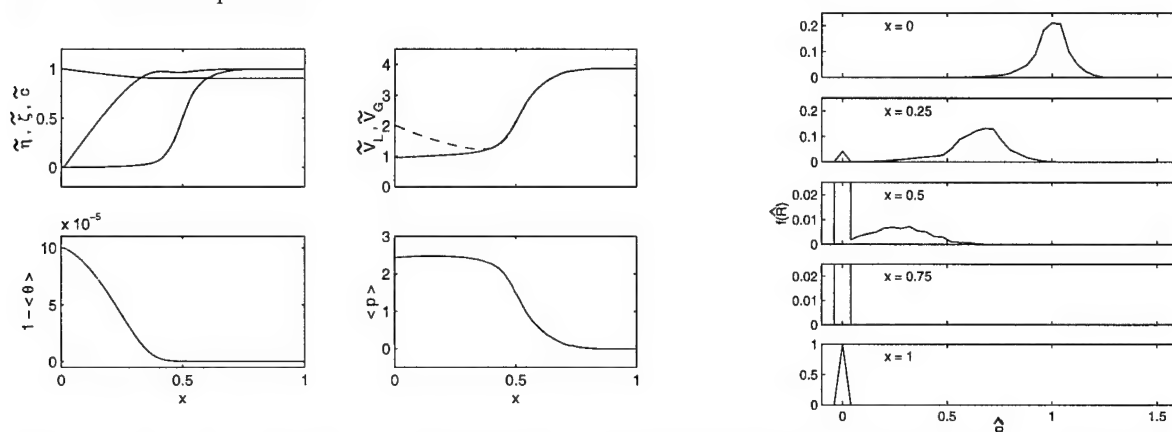


Figure 1: Numerical results for a one-dimensional, turbulent and reacting polydisperse spray; a) mean profiles of significant variables, b) droplet-size distribution at different axial positions x .

Figure 1a shows mean profiles of the gas-phase scalars $\bar{\eta}$, $\bar{\zeta}$ and \bar{c} , the velocities \bar{V}_L and \bar{V}_G , the void fraction $\bar{\theta}$ and the pressure distribution \bar{p} . It is seen that with evaporation the evaporation-progress variable $\bar{\eta}$ increases from zero to one and the void fraction $\bar{\theta}$ tends from its initial value to one; simultaneously the mixture fraction $\bar{\zeta}$ decreases. Whereas the evaporation is seen to set in immediately after injection, the combustion, indicated by the reaction-progress variable \bar{c} , develops further downstream. The kink in the profile of $\bar{\eta}$ is due to the onset of combustion and only present in turbulent flow. The right column of Fig. 1a plots the mean profiles of droplet and gas velocity and pressure. By exchange of momentum the droplets are decelerated, the gas accelerated and static pressure is recovered. Over the flame region the pressure drops to account for thermal expansion.

Figure 1b displays the marginal density function $f_I(\hat{R}; x, t)$ at different axial positions. Starting from an initial distribution the droplet radius is seen to decrease, changing the shape of its distribution and finally approaching $f(\hat{R}) = \delta(\hat{R})$.

4. References

- 1 WILLIAMS, F.A.: Progress in Spray-Combustion Analysis. 8th Symp. (Int.) Comb. (1962), 50–69.
- 2 POPE, S.B.: PDF Methods for Turbulent Reactive Flows. Prog. Energy Combust. Sci. **11** (1985), 119–192.
- 3 ZHU, M., BRAY, K.N.C., RUMBERG, O., ROGG, B.: PDF Transport Equations for Two-Phase Reactive Flows and Sprays. Comb. and Flame (2000), in press.
- 4 RUMBERG, O., ROGG, B.: Full PDF Modelling of Reactive Sprays via an Evaporation-Progress Variable. Comb. Sci. and Tech. (2000), in press.

Address: DIPL.-ING. O. RUMBERG, PROF. DR.-ING. B. ROGG, Ruhr-Universität Bochum, Lehrstuhl für Strömungsmechanik, Fakultät für Maschinenbau, Universitätsstr. 150, D-44780 Bochum, Germany.

D.SAPTOADI AND E.LAURIEN

Simplified Two-Fluid Model for the Simulation of Two Phase Bubbly Flows

An engineering application model to calculate two-phase bubbly flows is developed on the basis of the equations of the two-fluid model. With the used assumptions, the momentum and energy equation of the gas phase are always satisfied, and one has to solve only the continuity equation of the gas phase. The modeling of gas-liquid interaction will also be discussed. The simplified model is verified by comparison to an experimental investigation of a bubble column.

1. Introduction

Numerous theoretical and experimental investigations of bubbly flow systems have been carried out. [1] used the homogeneous model, with predefined gas volume (void) fraction distribution, to simulate a bubble column experiment [2]. The two-fluid model is used to simulate a bubble plume [3] and a pipe flow [4]. Either the accuracy, lack of ability to predict different types of flows, or the high computation time are drawbacks of the mentioned models. Therefore the present simplified two-fluid model is developed.

2. Simplified Two-Fluid Model

The simplified two-fluid model is based on the full two-fluid equations [5] with some assumptions: (1) Liquid and gas are both isothermal and incompressible with constant densities, ρ_L , ρ_G , (2) each bubble moves upwards relative to the liquid with constant terminal velocity u_T , (3) there is no virtual mass effect, and (4) there is no momentum or energy transfer among the bubbles. With these assumptions, the momentum and energy equations of the gas phase are always satisfied. The governing equations of the liquid phase are:

$$\rho_L \left\{ \frac{\partial \alpha_L}{\partial t} + \nabla(\alpha_L \tilde{u}^L) \right\} = \Gamma_L \quad m = 1, 2, 3 \quad (1)$$

$$\rho_L \left\{ \frac{\partial(\alpha_L \tilde{u}_m^L)}{\partial t} + \nabla(\alpha_L \tilde{u}^L \tilde{u}_m^L) \right\} = -\frac{\partial(\alpha_L \bar{p}^L)}{\partial x_m} + \nabla[\alpha_L (\bar{\tau}^L + \bar{\tau}^{Re,L})] + \tilde{u}_m^L \Gamma_L + M_{L,m}. \quad (2)$$

Where $\bar{\cdot}$ and $\tilde{\cdot}$ denote phase averaging and mass-weighted phase averaging of the gas (G) or the liquid (L) phase, respectively; the index $m = 1, 2, 3$ refers to the three coordinate directions, $\vec{x} = [x_1, x_2, x_3]$ is the space coordinate, $\tilde{u}^L = [\tilde{u}_1^L, \tilde{u}_2^L, \tilde{u}_3^L]$ is the velocity, α_L and α_G are the void fractions, \bar{p}^L is the pressure, $\bar{\tau}^L$ is the stress, $\bar{\tau}^{Re,L}$ is the Reynold stress tensor, Γ_L is the interfacial mass transfer, and $M_{L,m}$ is the interfacial momentum transfer term. Because of the following relationships,

$$\alpha_G = 1 - \alpha_L, \quad \tilde{u}^G = \tilde{u}^L + \vec{u}_T \quad \text{and} \quad \vec{u}_T = [0 \quad 0 \quad u_T]^T, \quad (3)$$

we have the continuity equation of the gas phase as follows:

$$\rho_G \left\{ \frac{\partial \alpha_G}{\partial t} + \frac{\partial(\alpha_G \tilde{u}_1^L)}{\partial x_1} + \frac{\partial(\alpha_G \tilde{u}_2^L)}{\partial x_2} + \frac{\partial(\alpha_G [\tilde{u}_3^L + u_T])}{\partial x_3} \right\} = -\Gamma_L. \quad (4)$$

The terms Γ_L and $M_{L,m}$ that appear in the equations describe the interaction between both phases, and have to be modeled to gain a realistic result. In the first step of the development, it is assumed that $\Gamma_L = 0$, and $M_{L,m}$ is represented by the drag force:

$$\vec{M}_{L,m} \equiv \vec{F}_D = \frac{3}{8} \frac{\alpha_G \rho_L C_D}{R_b} |\vec{u}_T| \vec{u}_T \quad (5)$$

where R_b is the bubble radius and C_D is the drag coefficient of a bubble. The terminal velocity u_T and the drag coefficient C_D are determined using balance between buoyancy and drag, and have to be evaluated consistently.

3. Numerical Method

The model is implemented into a single phase incompressible 2D-CFD code, with staggered grid [6] in cylindrical coordinates (r, z) . As dependent variables, $\alpha_L \tilde{u}_m^L$ and $\alpha_L \tilde{p}^L$ are used. The time derivative of equation (1) is omitted, making our implementation not time accurate.

4. Calculation Result

The simplified model is verified with the bubble column experiment [2]. The following parameters are used for the calculations: column radius $R = 0.05\text{ m}$ and height (A) $ZT = 0.278\text{ m}$ and (B) $ZT = 0.098\text{ m}$. The liquid is castor oil (viscosity $0.699 \cdot 10^{-3} \text{ m}^2 \text{ s}^{-1}$) and the gas is air with bubble radius $R_b = 3.0 \text{ mm}$, terminal velocity $u_T = 2.8 \text{ cm s}^{-1}$ and void fraction at the gas inlet $\alpha_{G0} = 0.0178$. The liquid velocity vector of the results and gas void fraction of experiment A for a transient and for a stationary state is shown in figure 1. The transient state is shown to illustrate the convergence history. The profile of the axial liquid velocity w normalized with bubble maximum velocity w_{bmax} for experiment B is shown in figure 2. Good agreement with the experiment is observed.

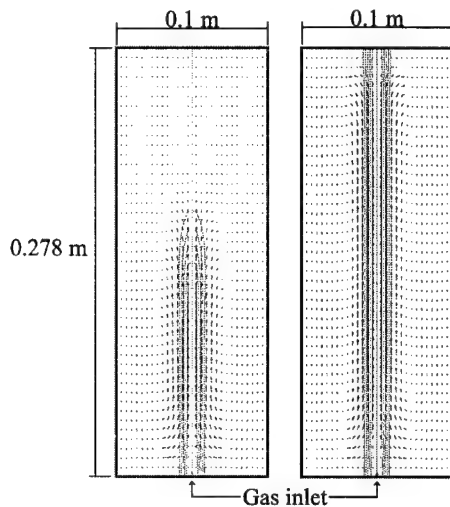


Figure 1: Liquid velocity vector and gas void fraction of experiment A, left: transient, right: stationary.

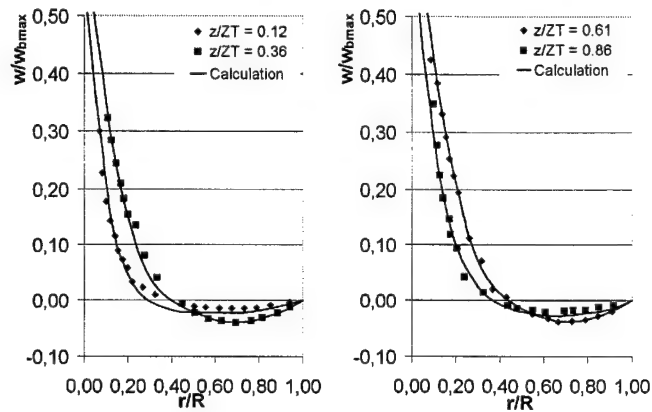


Figure 2: Liquid axial velocity profiles of experiment B.

5. Summary

A simplified two-fluid model for two-phase bubbly flow and its equation system have been described. The simulation of the bubble column experiment [2] has been presented. Without prior assumption of the void fraction distribution, as in [1], calculations show good agreement with the experiment.

6. References

- 1 CELIK, I AND WANG, Y.Z.: Numerical Simulation of Circulation in Gas-Liquid Column Reactor: Isothermal, Bubbly, Laminar Flow, Int. J. Multiphase Flow Vol. 20 No.6 (1994), 1053-51070.
- 2 DURST, F., et.al. : Experimental and Numerical Investigation of Bubble-Driven Laminar Flow in an Axisymmetric Vessel, Int. J. Multiphase Flow Vol.10 No.5 (1984), 557-569.
- 3 SMITH B.L AND MILELLI M.: An investigation of confined Bubble Plumes, ICMF'98, Lyon, France, June 8-12, 1998.
- 4 JANSSENS-MAENHOUT et.al.: Subcooled Nucleate Boiling at Low Pressure and Low Heat Flux, ICMF'98, Lyon, France, June 8-12, 1998.
- 5 DREW, D.A.: Mathematical Modeling of Two-Phase Flow, Ann. Rev. Fluid Mech. 15 (1983), 261-291.
- 6 AMSDEN AND HARLOW: The SMAC Method: A numerical Technique for Calculating Incompressible Fluid Flow, Los Alamos LA-4370, 1970.

Addresses: IR. D. SAPTOADI M.ENG. AND PROF. DR-ING. E. LAURIEN. University of Stuttgart, Institute of Nuclear Energy and Energy System, Pfaffenwaldring 31, 70555 Stuttgart, Germany.

J. SAUER, G.H. SCHNERR

Development of a New Cavitation Model based on Bubble Dynamics

This paper presents a numerical approach for a cavitation model that bases on a combination of the Volume-of-Fluid technique with a model predicting the growth and collapse process of bubbles. The cavitation model is applied for the simulation of cavitating nozzle flows and cavitating flow over a NACA 0015 hydrofoil and showed it's capability to resolve characteristic effects of cavitation such as the cyclic formation of the cavitation cloud, the formation of the re-entrant jet and the local occurrence of hydrodynamic pressure peaks due to bubble cloud collapse.

Introduction

The investigation of cavitation phenomena is of great interest for industry since its occurrence in hydraulic systems (pipes, pumps, etc.) can lead to damage and loss of performance. In the past, several models were developed to simulate cavitation, which do in general not model the complicated and highly transient bubble growth and collapse process. This process is responsible for the cavitation damage and therefore the location where the bubbles collapse is of great interest and the need for a cavitation model rises that also includes effects based on bubble dynamics. Since hydrofoils make up so many different types of machines - pumps, turbines, propellers- the study of as how to cavitation affects hydrofoil performance is of special interest. The type of cavitation most frequently observed for hydrofoils with a well-rounded leading edge is the so-called traveling bubble cavitation, where the nuclei reach the leading edge and grow to vapor bubbles while they are convected downstream. The bubbles are swept in the region of higher pressure and finally collapse. Essentially, the numerical model follows close this experimental observation and will be described in the following section.

2. Numerical Approach

In general, the bubble-liquid flow is treated as a homogeneous mixture, hence only one set of equations is used for description. Entering or leaving the cavitated region, the mixture density jumps from the pure liquid value to a much smaller value or vice versa. To overcome problems due to a discontinuous density distribution, the Volume-of-Fluid method (VoF) is used. The VoF-method requires in addition to the continuity and the momentum equations (which are coupled by a SIMPLE algorithm), the solution of a transport equation for the cell vapor fraction α , which is defined as the vapor volume/cell volume:

$$\frac{\partial \alpha}{\partial t} + \frac{\partial(\alpha u)}{\partial x} + \frac{\partial(\alpha v)}{\partial y} = \left(\frac{n_0}{1+n_0 \frac{4}{3}\pi R^3} \right) \frac{d}{dt} \left(\frac{4}{3}\pi R^3 \right)$$

The vapor production is taken into account by the source term on the right hand side of the equation. The change of the cell vapor fraction does now depend on the number of bubbles per cell volume (rhs:1st term) times the volume change of a single bubble (rhs:2nd term) and the convective transport. The parameter n_0 is defined as the nuclei concentration per unit volume of pure liquid. To model the bubble growth process, the Rayleigh relation is used which is well suited for the description of inertia controlled bubble growth:

$$\dot{R} = \sqrt{\frac{2}{3} \frac{p(R) - p_\infty}{\rho_L}},$$

where $p(R)$ is the pressure in the liquid at the bubble boundary and p_∞ is the pressure in the liquid at a large distance from the bubble. Within the scope of this model, $p(R)$ is set equal to the vapor pressure and p_∞ to the ambient cell pressure.

3. Results

The above described cavitation model is used to simulate the cavitating flow over a NACA 0015 hydrofoil at an angle of attack of 6° . The geometry and boundary conditions are shown in Fig.1. The mixture is assumed to be inviscid, the nuclei concentration n_0 is set to $10^8 \frac{\text{nuclei}}{\text{m}^3 \text{water}}$, the vapor fraction at the inlet to a value of $\alpha_0 = 10^{-5}$ which corresponds to a nucleus radius of $R_0 = 30 \mu\text{m}$. The inlet velocity U is set to 12m/s. The fluid is water, the water temperature is 293.15K and hence thermal effects are negligible.

The series of instantaneous pictures 1-8 (labeled from top to bottom) presented in Fig.3 shows the vapor fraction distribution during one cycle of the periodic formation and destruction of the vapor phase. The frequency is $f=11$ Hz, the time increment is $\Delta t = 0.011$ s. The corresponding times are also marked in Fig.2, which shows the lift and drag per [m span]. The vapor cavity starts growing at the leading edge and grows until a re-entrant jet forms and brakes off a part of the cavity (Fig 3, pics 1-3). The first part starts to collapse (pic. 4) and the second part of the cavity is swept downstream. A secondary vapor region forms (pic. 6), merges with the already existing vapor region and finally collapses. The growth and collapse of the vapor phase does significantly alter the pressure distribution and thus changes the lift and drag of the hydrofoil, Fig.2. The single phase calculation yields a lift of $L = 7300$ N per meter span and a drag of $D \sim 0$ N (inviscid calculation), compared to a time averaged lift of $L_c = 4200$ N and drag of $D_c = 750$ N under cavitating conditions. Due to cavitation, the lift of the hydrofoil has been substantially decreased (drag increased) which is in agreement with experimental observations.

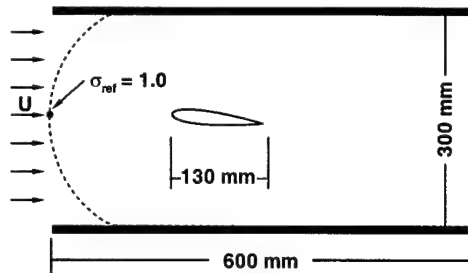


Fig.1: Cavitating NACA 0015 hydrofoil. Geometrical setup and boundary conditions

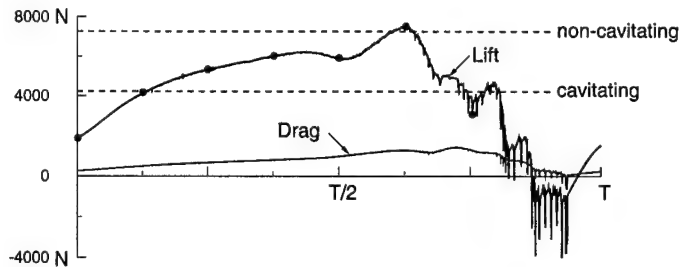


Fig.2: Unsteady lift and drag for one cavitation cycle.

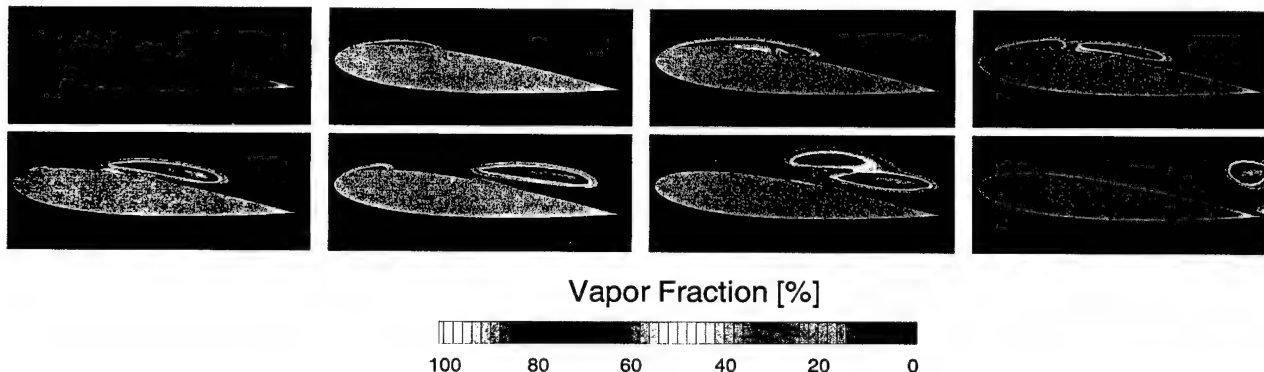


Fig.3: One cycle of the periodic formation and destruction of the vapor phase, $f = 11$ Hz.

4. Conclusions

A cavitation model based on a combination of the Volume-of-Fluid method with a relation to estimate vapor change due to bubble growth and collapse has been derived. The cavitation model was successfully applied to calculate cavitating flow over a hydrofoil and resolved characteristic flow phenomena associated with cavitation.

Acknowledgements

The authors gratefully acknowledge the support from the Deutsche Forschungsgemeinschaft (DFG) during performing this work in the Graduiertenkolleg "Energie- und Umwelttechnik" at the Faculty of Mech. Engineering of the University of Karlsruhe. Special thanks are given to Prof. Dr.-Ing. M. Peric and Dipl.-Phys. M. Krömer from the TU - Hamburg Harburg for providing the single phase version of the code.

Addresses: PROF. DR.-ING. HABIL. G.H. SCHNERR, DIPL.-ING. JÜRGEN SAUER, University of Karlsruhe, Fachgebiet Strömungsmaschinen, Kaiserstr.12, 76185 Karlsruhe, Germany, email: guenter.schnerr@mach.uni-karlsruhe.de.

H. STEINER AND W.K. BUSHE

Large Eddy Simulation of a Turbulent Reacting Jet-Flame

The high nonlinearity of the chemical reaction terms requires a closure model for the chemical source terms occurring in the spatially filtered scalar transport equations. Based on the Conditional Moment Closure hypothesis a new model was recently proposed for LES of non-premixed combustion. The new model was applied to an LES of a piloted jet flame to assess the model's robustness and predictive capabilities.

1. Equations

The LES set of equations is obtained by applying a density-weighted spatial filter to the governing differential transport equations. In chemically reacting flow the filtered transport equations for species and enthalpy read as follows:

$$\frac{\partial \bar{\rho} \tilde{Y}_j}{\partial t} + \nabla \cdot (\bar{\rho} \tilde{\mathbf{u}} \tilde{Y}_j) = \nabla \cdot \left[\bar{\rho} (\tilde{D}_l + \tilde{D}_t)_j \nabla \tilde{Y}_j \right] + \bar{\Omega}_j, \quad (1)$$

$$\frac{\partial \bar{\rho} \tilde{h}}{\partial t} + \nabla \cdot (\bar{\rho} \tilde{\mathbf{u}} \tilde{h}) = \nabla \cdot [(\tilde{\kappa}_l + \tilde{\kappa}_t) \nabla \tilde{T}] + \sum_{j=1}^J (\bar{\Omega}_j h_{0,j}). \quad (2)$$

Here, $\bar{\rho}$, $\tilde{\mathbf{u}}$, \tilde{h} , and \tilde{T} are the filtered density, velocity vector, enthalpy and temperature; \tilde{Y}_j is the mass fraction of species j , $h_{0,j}$ is its enthalpy of formation. The molecular diffusivity and thermal diffusivity of species j is represented by $\tilde{D}_{l,j}$ and $\tilde{\kappa}_l$, respectively. The eddy diffusivities, $\tilde{D}_{t,j}$ and $\tilde{\kappa}_t$, which account for the unresolved subgrid-scale turbulent transport, are modeled using the dynamic model proposed for compressible flows [1]. Constant specific heats, a uniform molecular Schmidt number and unity Lewis number were assumed for all species.

2. Model for chemistry

The rate of change of species mass fraction due to chemical reaction, $\bar{\Omega}_j$, appearing as source term in Eqs. (1) and (2) is a linear combination of the different reaction rates in which species j participates:

$$\bar{\Omega}_j = W_j \sum_{k=1}^K (\nu'_{jk} - \nu''_{jk}) \bar{\omega}_k. \quad (3)$$

Therein, K is the total number of reactions and ν'_{jk} and ν''_{jk} are the stoichiometric coefficients for species j in reaction k . The spatially filtered chemical reaction rates $\bar{\omega}_k$ in Eq. (3) were obtained using the Conditional Source-term Estimation (CSE) method [2]. CSE invokes the Conditional Moment Closure (CMC) hypothesis [3]

$$\langle \dot{\omega}_k | \zeta \rangle \approx f_k(\langle \rho | \zeta \rangle, \langle T | \zeta \rangle, \langle Y_j | \zeta \rangle), \quad (4)$$

where $\langle \dot{\omega}_k | \zeta \rangle$ denotes the average of the rate of reaction k conditioned on the mixture fraction having some value ζ and f_k is the Arrhenius-type equation for $\dot{\omega}_k$ evaluated with the conditionally averaged density $\langle \rho | \zeta \rangle$, temperature $\langle T | \zeta \rangle$, and mass fractions $\langle Y_j | \zeta \rangle$. The CMC hypothesis (4) has proven to give a fairly accurate approximation when compared to data from experiments and DNS. The conditional averages input to the RHS of (4) are computed by inverting integral equations, which, e.g., for the conditionally averaged mass fraction $\langle Y_j | \zeta \rangle$ reads

$$\int_0^1 \langle Y_j | \zeta \rangle \tilde{P}(\zeta; \mathbf{x}, t) d\zeta = \tilde{Y}_j(\mathbf{x}, t), \quad (5)$$

on planes of constant distance from the nozzle of the jet, on which statistical homogeneity, hence invariance, for the conditional averages can be assumed. The quantities on the RHS of (5) are provided by the spatially resolved LES flow field. $\tilde{P}(\zeta; \mathbf{x}, t)$ denoting the Favre-filtered density function (FDF) at some LES point \mathbf{x} and time t is assumed as a β -function determined by the mean $\tilde{Z}(\mathbf{x}_m, t)$ and variance $\tilde{Z}''^2(\mathbf{x}_m, t)$. The first can be expressed as linear

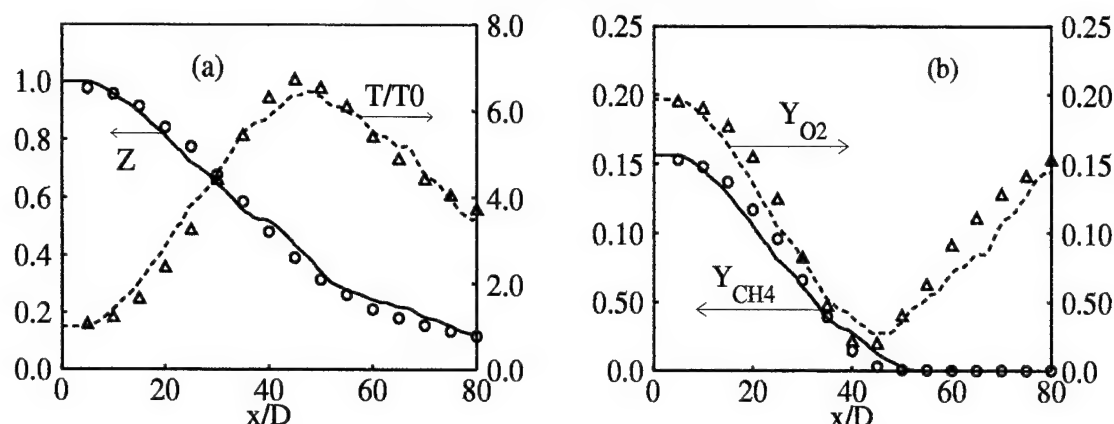


Figure 1: Centerline profiles versus downstream distance in nozzle diameters D : (a) mixture fraction Z and temperature T/T_0 normalized with the reference temperature $T_0 = 291K$, (b) fuel Y_{CH_4} and oxidizer Y_{O_2} ; symbols denote the experimental data.

combination of the reacting species, the latter is dynamically modeled [4]. Once the conditional reaction rate is obtained with (4), its unconditional counterpart is computed using

$$\bar{\omega}_k(\mathbf{x}_m, t) = \bar{\rho}(\mathbf{x}_m, t) \int_0^1 \frac{\langle \dot{\omega}_k | \zeta \rangle}{\langle \rho | \zeta \rangle} \tilde{P}(\zeta; \mathbf{x}_m, t) d\zeta. \quad (6)$$

3. Results

The present LES considered a piloted methane-air jet flame with the Reynolds number $Re = 22400$. It is known as the "Sandia D-Flame" [5]. The feed fuel stream is diluted with air such that the stoichiometric mixture fraction is $Z_{stoic} = 0.352$. A reduced two-step methane-air mechanism was employed as chemical kinetic scheme [6]. The good agreement in mixture fraction shown in Fig 1.a illustrates that the LES captures the mixing process very well. The fairly accurate predictions for temperature and reactive species (Fig 1.b) prove the CSE method as a reliable closure model for LES of non-premixed combustion.

Acknowledgements

The authors wish to thank B. Bilger, G. Košaly, A. Kerstein, N. Peters, J. Ferziger, H. Pitsch and the staff at the Center for Turbulence Research for their useful suggestions and discussions as well as the NASA-Ames Research Center for providing the required computing resources. H.S. gratefully acknowledges the financial support from the FWF Austria.

4. References

- 1 MOIN, P., SQUIRES, K., CABOT, W., LEE, S.: A dynamic subgrid-scale model for compressible turbulence and scalar transport, *Phys. Fluids A* **3** (1991), 2746–2757.
- 2 BUSHE, W. K., STEINER, H.: Conditional Moment Closure for Large Eddy Simulation of non-premixed turbulent reacting flows, *Phys. Fluids* **11** (1999), 1896–1906.
- 3 BILGER, R.W.: Conditional moment closure for turbulent reacting flow, *Phys. Fluids A* **5** (1993), 436–444.
- 4 PIERCE, C. D., MOIN, P.: A dynamic model for subgrid-scale variance and dissipation rate of a conserved scalar, *Phys. Fluids* **10** (1998), 3041–3044.
- 5 Information available at: www.ca.sandia.gov/tdf/Workshop.html
- 6 WILLIAMS, F. A.: Overview of Asymptotics for Methane Flames, in *Reduced Kinetic Mechanism and Asymptotic Approximations for Methane-Air Flames*, (Smooke, Eds.), Springer-Verlag, New York, (1991), 68–99.

Addresses: DR. HELFRIED STEINER, Institut für Strömungslehre und Wärmeübertragung, Technische Universität Graz, Inffeldgasse 25, A-8010 Graz, Austria.

ASS.-PROF. DR. WILLIAM KENDAL BUSHE, Department of Mechanical Engineering, University of British Columbia, 2324 Main Mall, Vancouver, B.C., V6T1Z4, Canada.

TEPPNER, R. AND SCHAFLINGER, U. †

Bubble Formation on Inclined Surfaces

Gas purging is used in metal casting processes to increase the product quality. We studied the influence of the surface inclination and the surface roughness on the bubble formation in experiments using water, air and teflon surfaces.

1. Introduction

In metal casting gas purging is used for impurity reduction. The impurities concentrate on the surface of the gas bubbles and are transported towards the slag by the ascending bubbles. Therefore, efficient flotation requires an optimal relation of the bubble volume and the bubble surface [1].

The aim of this work is to learn about the factors which influence the volume of the generated bubbles. We investigated the bubble formation on different porous media surfaces and studied the dependence of the bubble volume on the inclination angle of these surfaces.

In this context it is known that the bubble formation is strongly influenced by the non-wettability between the porous refractory and the melt. In our experiments we simulated this situation by using water, air and teflon surfaces. A comparison is possible since the systems water/air and melt/purging gas have similar physical properties because of equal Bond numbers and approximately equal kinematic viscosities. The surfaces we used were a single teflon orifice, a teflon grid, a wetted porous refractory and a non-wetted porous refractory.

2. Single Teflon Orifice

For these experiments we used a teflon plate with an orifice of 0.6 mm in diameter in its center. We investigated the influence of the inclination of the non-wetted surface on the volume and the shape of the detaching bubbles. Inclination angles from 0° up to 90° were examined in 15° steps. Figure 1 shows the bubble shape on the horizontal plane. The bubble is located right above the orifice. Figures 2 and 3 show bubbles at inclined planes, detached from the orifice. For inclined planes we generally observed that the bubbles do not grow symmetrically to the orifice because of the acting buoyancy forces. The bubbles separate earlier from the orifice and are therefore smaller than in the horizontal case. Figures 2 and 3 show the bubbles already separated from the orifice. This means that they have achieved their final volume. Figure 4 shows the average bubble volume in dependence of the inclination angle of the surface. 50% volume reduction can be achieved by inclining the surface from 0° to 45°. An inclination of 90° leads to a volume reduction of 67%.

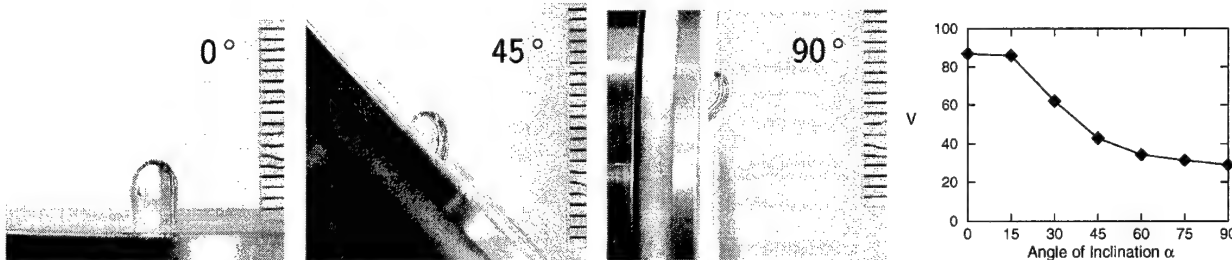


Fig.1

Fig.2

Fig.3

Fig.4

Figs. 1-4: Single teflon orifice, $\dot{V}=45 \text{ mm}^3/\text{s}$; comparison of the resulting bubble shapes. Fig. 1: Bubble at horizontal surface, above the orifice. Fig. 2, Fig. 3: Bubbles at inclined surfaces, detached from the orifice. The ruler shows a mm scale. Fig. 4: Dependence of the average bubble volume [mm³] on the angle of inclination.

3. Teflon Grid

A teflon grid with orifices of 0.6 mm in diameter was used. The rows were separated from each other by 3 mm. The actual number of emerging bubbles and their size is determined by the non-wettability of the surface [2]. We investigated the influence of inclining the grid surface on the bubble generation from 0° to 180° in 30° steps. The volume of the detached bubbles is not clearly dependent on the inclination angle of the grid surface. Possible explanations are the coalescence of bubbles and the aspiration of additional air while the bubbles are running over neighbouring orifices. In the special case of an inclination of 180° the bubbles are not able to detach. They merge to a very big bubble which detaches when it has reached a critical size.

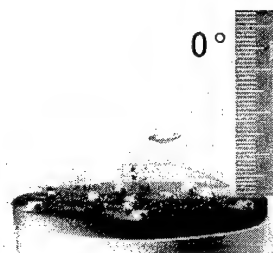


Fig.5

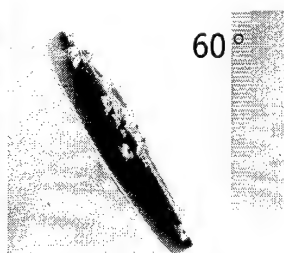


Fig.6

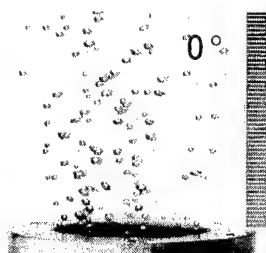


Fig.7

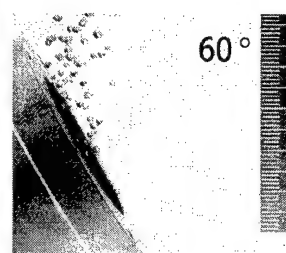


Fig.8

Figs. 5,6: Teflon grid, non-wetted, $\dot{V}=100 \text{ cm}^3/\text{min}$. Figs. 7,8: Porous refractory, non-wetted, $\dot{V}=120 \text{ cm}^3/\text{min}$.
In all four figures the ruler shows a mm scale and the gray scale is inverted.

4. Porous Refractory, wetted and non-wetted

We studied a porous refractory with a porosity of about 20%. For small volume flows only a small number of refractory pores is active. First, the refractory had a rough surface which was wetted by water. Analogously to a wetted sieve [2] the bubble size is determined by the pore radius and there is no coalescence of bubbles. We found that the bubble volume is independent of the refractory inclination. Second, in order to achieve non-wettability by water the surface of the refractory was coated with a teflon spray. Analogously to the wetted refractory we see small bubbles whose size is mainly determined by the pore radius. There is no coalescence and no dependence of the bubble volumina on the inclination angle.

Comparing the results for the non-wetted porous refractory with those for the teflon grid leads to the conclusion that the surface roughness prevents the contact line from spreading which results in smaller bubbles. The capillary length of the liquid/gas system is given by $l_{\sigma}^{li/gas} = \sqrt{\frac{\sigma_{li/gas}}{g(\rho_{li} - \rho_{gas})}}$. If the magnitude of the surface roughness is much smaller than $l_{\sigma}^{li/gas}$, then there is no influence on the spreading of the contact line (Fig. 9). If the surface roughness and $l_{\sigma}^{li/gas}$ have the same magnitude, there is a distinct influence on the spreading of the contact line (Fig. 10).

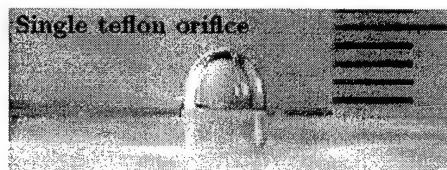


Fig. 9: The teflon surface is smooth compared to the capillary length $l_{\sigma}^{water/air} = 2,72 \text{ mm}$. There is no influence of the surface roughness on the spreading of the contact circle.

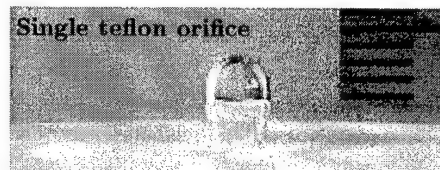


Fig. 10: The roughness of the teflon surface in the vicinity of the orifice was artificially increased to the magnitude of $l_{\sigma}^{water/air} = 2,72 \text{ mm}$. There is a distinct influence of this roughness on the spreading of the contact circle.

5. Conclusions

We investigated factors which are essential in the formation of air bubbles in water on teflon and porous refractory surfaces. For the single teflon orifice the surface inclination influences the bubble volume. However, for all studied porous media no distinct dependence of the bubble volume on the inclination angle of the surface was found. Comparing the experiments for the teflon grid with those for the non-wetted refractory we found that the surface roughness with respect to the capillary length of the system determines more the bubble size than the non-wettability.

6. References

- 1 WANG, L.; LEE, H.; HAYES, P.: Prediction of the Optimum Bubble Size for Inclusion Removal from Molten Steel by Flotation. ISIJ International **36** (1996), 7-16.
- 2 LOIMER, TH.; MACHU, G.; SCHAFLINGER, U.: Formation of Bubbles at Porous Walls. ZAMM **80** (2000), 723-724.

Addresses: MAG. RENATE TEPPNER, PROF. DR. UWE SCHAFLINGER †, Christian Doppler Laboratory for Continuous Solidification Processes, Technical University Graz, Inffeldgasse 25, A-8010 Graz, Austria.

THÉVENIN, D., GICQUEL, O. AND DARABIHA, N.

Computations of NO_x Emissions of Domestic Boilers

Due to severe regulations concerning pollutant emissions, practical devices using combustion to release energy must be designed from the start using accurate, predictive numerical tools. A partially premixed methane/air flame in a two-dimensional configuration is investigated in this work. This configuration is close to those used in real domestic gas boilers. The flame structure and flow pattern are calculated using complex chemistry and detailed transport models. A post-processing method is then used to predict NO emission.

Computations are performed for two configurations. The two cases have the same primary and secondary mass flow-rates and equivalence ratio. The only difference between them is the introduction of an insert inside the primary injector.

Both results have been compared to measurements. Calculations are found to be in good agreement with the flame shapes observed experimentally. The classical burner shows a Bunsen-type flame while the one with an insert has a totally different shape (butterfly-type flame). NO emission levels are also well predicted in both configurations. The butterfly flame induces a reduction in NO emission. This reduction seems to be due to the increased mixing between the burnt gases and the secondary air jet, which homogenizes the temperature distribution and reduces the maximum temperature.

1. Configuration and numerical methods

We consider here an idealised domestic boiler based on a 2D laminar partially-premixed methane/air burner. The boiler power input and performance are similar to those of a typical domestic boiler. Its specificity is that the primary and secondary air and gas flow-rates are independently controlled.

Two different cases are considered. The first test case is a classical Bunsen-type flame. In the second case an insert is added in the middle of the slot to alter the flow field. The flame is then transformed into a butterfly-type flame. In both cases the global methane/air mixture equivalence ratio is equal to $\phi_g = 0.714$ while the primary air equivalence ratio is equal to $\phi = 0.833$. The primary air inlet velocity is equal to 0.9776 m/s and the secondary air inlet velocity is equal to 0.051 m/s.

Computations of these partially-premixed 2D laminar methane-air flames are carried out by solving the Navier-Stokes equations discretized on an orthogonal and structured mesh. The discretization relies on the finite-volume method. The numerical resolution is based on a semi-implicit segregated solver. Two grids are used to solve the equations: a velocity grid (used to solve the density and the velocity), which nodes are located on the mesh intersection lines, and a pressure grid (to solve the pressure, the temperature and the species mass fractions), which nodes are located on the center of the cubes formed by the velocity grid nodes. In order to reduce the CPU time, the computations rely on the FPI (Flame prolongation of ILDM) technique [1]. The FPI technique uses a one-dimensional laminar flame as a prolongation of a one-dimensional ILDM manifold.

2. Post-processing technique

The numerical prediction of NO_x has been intensively studied in recent years. Detailed chemical schemes are now available, including about 50 species and more than 200 chemical reactions. Performing computations with such mechanisms requires a huge amount of CPU time and is not possible in an industrial environment.

To be still able to take into account all the information included in these detailed chemical mechanisms, several post-processing techniques have been developed. The chemistry is then described with reduced schemes in the fluid mechanics computation [2]. These mechanisms are obtained using the classical steady-state and partial equilibrium assumptions for species such as OH, O or CH₃. As the reactive nitrogen species usually represent a small percentage in mass in the flame and have only a small impact in the main reaction process, it is possible to decouple the nitrogen chemistry computation from the main flow field computation [2,3]. For the nitrogen species computations, the steady-state assumption is usually assumed for all species except for NO and HCN, which are determined with a standard transport equation [2]. This approach requires a good background in chemistry to generate an accurate

reduced scheme and implies many modifications in standard CFD codes to implement the equations describing the steady-state assumptions. It often leads to severe numerical problems.

In the present work, a first fluid mechanics computation was performed using a FPI look-up table corresponding to a skeletal mechanism without the nitrogen chemistry. Afterwards the velocity, the temperature, all the mass fractions of the species included in the mechanism and the density field are frozen. We then compute all the nitrogen species using standard transport equations. This increases the numerical stability and computational speed. It is with this method possible to take into account accurately the real transport phenomena associated to all species and to describe similarly the different ways to create NO such as thermal NO and prompt NO. We have checked the accuracy of our post-processing technique for a laminar freely-propagating premixed flame and for a counterflow diffusion flame. In both cases, the error in NO levels is well below 10% (3 ppm) and the prediction of species such as CN or NH_3 is also very satisfactory.

3. Results

It can be seen in this figure that the maximum level of NO is very similar for the two cases investigated, while the NO distribution in the whole burner is quite different. The computations are able to reproduce the differences

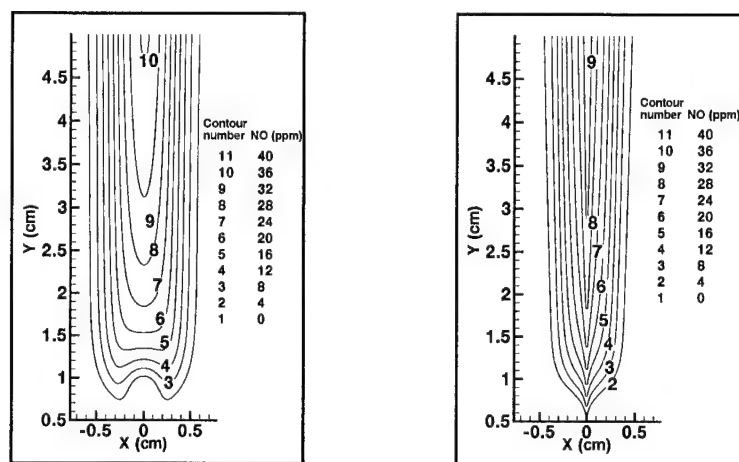


Figure 1: Field of NO in ppm corresponding to a Bunsen type flame (left) and to the corresponding butterfly-type flame (right).

observed experimentally between the two cases. The numerical NO emission index is about 30% lower than the one obtained experimentally, but the influence of the insert is perfectly reproduced. The computations were performed on a standard workstation. The initial computation without the NO_x chemistry takes 4 hours of CPU time and we need 30 more minutes to post-process NO. This is fully compatible with industrial constraints.

Acknowledgements

The results presented in this paper are part of a larger project involving Gaz de France. Interesting discussions with V. Quilichini are gratefully acknowledged.

4. References

- 1 GICQUEL, O., DARABIHA, N. AND THÉVENIN, D.: Laminar premixed hydrogen/air counterflow flame simulations using Flame Prolongation of ILDM with differential diffusion; *Twenty-eighth Symposium (International) on Combustion*, Edinburgh, accepted for presentation (2000).
- 2 GLARBORG, P., LILLEHEIE, N. I., BYGGSTOYL, S., MAGNUSSEN, B. F., KILPINEN, P., HUPA, M.: A reduced mechanism for nitrogen chemistry in methane combustion; *Proceedings of the Combustion Institute* **24** (1992), 889–898.
- 3 EGGELS, R.L.G.M.: Modelling of combustion processes and NO formation with reduced reaction mechanisms; PhD Thesis, Technische Universiteit Eindhoven, 1995.

Address: DR.-HABIL. DOMINIQUE THÉVENIN, EM2C Laboratory, École Centrale Paris,
Grande Voie des Vignes, F-92295 Châtenay-Malabry
France

M.E.H. VAN DONGEN, G. LAMANNA, B. PRAST

Condensing nozzle flows: Ludwig tube experiments and numerical/ theoretical modelling.

The present paper deals with homogeneously condensing flows of humid nitrogen in a Laval nozzle. The modelling of nonequilibrium condensation phenomena can be separated in two distinct processes: homogeneous nucleation and droplet growth. Our objective is to investigate the quality of a condensation model characterised by the following combination: the (corrected) Internally Consistent Classical Theory for the nucleation process and a generalised transitional growth model, with the droplet temperature calculated explicitly via the wet-bulb equation. Our theoretical predictions have been then compared with our experimental results on droplet sizing showing a good agreement.

1. Introduction

Supersonic nozzle flows of a condensable gas mixture are characterised by the spontaneous generation of a liquid droplet cloud, whose properties strongly depend on the coupling between the flow and the condensation process itself. Further, depending on the initial conditions, different flow regimes may occur ranging from steady to periodic oscillating motions. Along the years, many different models have been proposed and verified thoroughly with respect to the onset of condensation, shock position, frequencies, and modes of oscillations [1,2,3]. However no conclusive answer could be drawn due the lack of reliable experimental data on droplet sizes. This latter, in fact, constitutes a very sensitive parameter for assessing the quality of the proposed condensation models. The scarcity of reliable data is ascribable to the difficulties of retrieving the size information from the spectral data of a nanometre-size cloud. At the gas dynamics laboratory of Eindhoven University of Technology, a facility has been developed to determine the time dependent variation of the size distribution by means of a white light extinction method. Objective of this paper is to use these experimental results to validate condensation models and to corroborate the validity of the underlying theoretical assumptions.

The modelling of nonequilibrium condensation can be separated in two distinct processes, namely homogeneous nucleation and droplet growth. Therefore, its correctness relies simultaneously on the quality of the nucleation and growth model employed. The present paper focuses essentially on this latter. By comparing two different growth laws, the importance of simulating correctly the energy flux between the droplet and its environment is ascertained. The quality of nucleation models is, instead, more difficult to evaluate and is, therefore, only marginally addressed here [4]. It is important to realise, in fact, that significant uncertainty exist with regard to the surface tension of subcooled liquid water. This uncertainty makes the assessment of nucleation models extremely critical, since it strongly depends on the extrapolation of surface data to low temperatures. Here the analysis is limited to a temperature range of [245 ÷ 270] K, where accurate experimental data are available from literature [5].

2. Modelling

On the basis of Luijten's experiments [6] on water-nitrogen systems, the *Internally Consistent Classical Theory* (ICCT) was chosen to model the nucleation process. This latter differs from the *Classical Nucleation Theory* (CNT) for the presence of correction factors, as indicated below:

$$J = \frac{1}{S} \exp \Theta J_{CNT}; \quad \Theta = \frac{\sigma a_0}{k_B T}; \quad (1)$$

$$J_{CNT} = \frac{\rho_v^2}{\rho_l} \sqrt{\frac{2\sigma}{\pi m^3}} \exp \left[-\frac{4}{27} \frac{\Theta^3}{(\ln S)^2} \right]; \quad (2)$$

where $S = p_v/p^s(T)$ is the supersaturation, σ is the surface tension, a_0 is a molecular surface area, k_B is the Boltzmann constant, and Θ is a dimensionless surface tension. For an exhaustive review on nucleation models, the reader is referred to Luijten *et al.* [7]. Upon implementing the (ICCT) model to condensing nozzle flows, it resulted that a satisfactory agreement was found with a correction factor of about 0.01. Thus the implemented nucleation rate is $J_{ICCT} = \xi \cdot J$, where $\xi = O(10^{-2})$.

The process of droplet growth involves the net transfer of mass (vapour molecules) towards the droplet, and the

simultaneous net transfer of energy (latent heat) away from the droplets. The mechanism of these fluxes depends to a large extent on the Knudsen number Kn . This latter is defined as the ratio of mean free path of vapours molecules to the diameter of the droplet. For small Kn , the transfer is governed by diffusion; for large Kn growth is regulated by the kinetic process of impingement of vapour molecules onto the droplet (Hertz-Knudsen regime). On the basis of the analysis of Peeters *et al.* [8], the Gyarmathy model was chosen. In this model, the expressions for the energy and mass flux between the droplet and its environment are explicitly calculated for the continuum and kinetic regime. Then the expressions for these fluxes in the intermediate situations are simply found by means of an interpolating fit between these two regimes. This procedure yields a system of four equations containing an additional unknown represented by the droplet temperature T_d . This latter can be calculated by means of an energy balance on the droplet surface, which after some simple algebra can be expressed as

$$\dot{E} = -\dot{M}L + \dot{M}h_{vs}, \quad (3)$$

where L is the latent heat of condensation, \dot{E} , and \dot{M} are the energy and mass fluxes, and h_{vs} is the specific enthalpy of the vapour at equilibrium. The above equation is only valid in the assumption of quasi-equilibrium between mass and latent heat transfer and is known as the "wet-bulb" approximation. Since for moist air the most relevant growth occurs in the Knudsen regime, we devoid from describing the model in detail [9], [4] and concentrate only on the kinetic regime. Within this restriction, the growth law (wet-bulb) reduces to:

$$\left(\frac{dr}{dt}\right)_{wet-bulb} = -\frac{1}{\rho_l} \left[\frac{p_v}{\sqrt{2\pi R_v T}} - \frac{p_{v,r}(T_d, r_d)}{\sqrt{2\pi R_v T_d}} \right]. \quad (4)$$

For reference the "traditional" expression for the Hertz-Knudsen law (HK) is also reported:

$$\left(\frac{dr}{dt}\right)_{HK} = -\frac{1}{\rho_l} \left[\frac{p_v - p_{v,r}(T, r_d)}{\sqrt{2\pi R_v T}} \right]. \quad (5)$$

The question to be answered is whether and to what extent the inclusion of temperature differences between the gas phase and the liquid droplets is relevant for modelling the growth process. To answer this question, let us consider Fig. 1. Here the following two combinations are considered: J_{CNT} for the nucleation rate; while for the droplet growth, in one case Eq. (4) is adopted, in the other the Hertz Knudsen formula (Eq. 5) is employed. As it can be

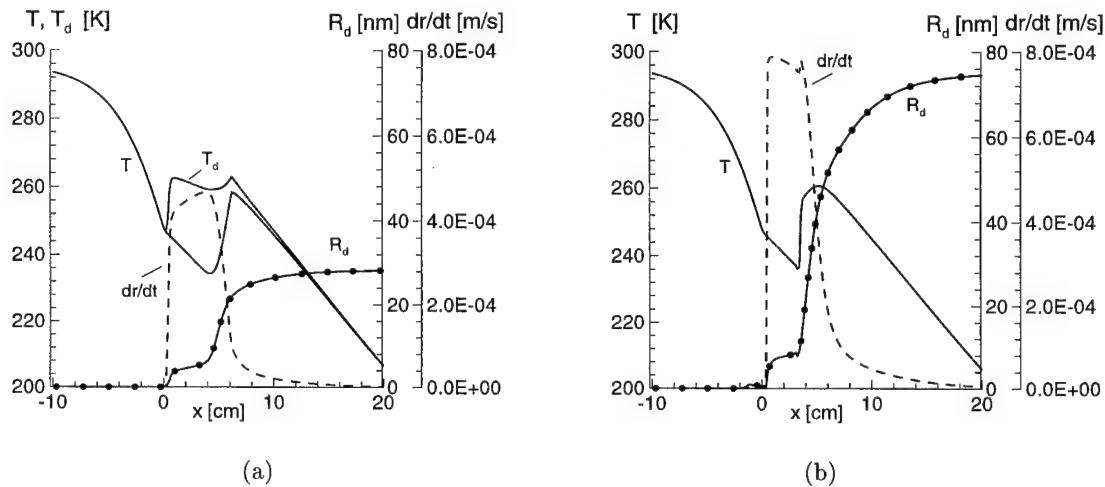


Figure 1: Axial distribution of temperatures T , T_d , modal radius R_d and droplet growth rate dr/dt . Models: Part (a) - J_{CNT} and wet-bulb equation ($T_d \neq T$). Part (b) - J_{CNT} and Hertz-Knudsen ($T_d = T$). Nozzle: G2. Stagnation conditions: $T_0 = 296.6$ K; $P_0 = 8.67 \cdot 10^4$ Pa; $S_0 = 0.50$.

inferred immediately from Fig. 1(a), large temperature differences are predicted in the initial part of the growth process by the wet-bulb model. This can be understood because while the gas temperature decreases rapidly due to the expansion, the droplet temperature increases due to the release of latent heat at the droplet surface. The macroscopic consequence of this is twofold. First, the temperature difference effectively damps the growth process: $(dr/dt)_{wet-bulb}$ is roughly two times smaller than $(dr/dt)_{HK}$. Second, smaller modal radii R_d are predicted by the wet-bulb law: since the rate of heat addition is considerably lower in this model, the nucleation rate is quenched a bit later. As a consequence, more critical cluster are produced while the total amount of liquid mass stays the same.

3. Experimental Set-up

The experiments are carried out in a Ludwig tube: it has a square cross-section of 0.01 m^{-2} , a length of 12 m, and is initially separated from a vacuum vessel by a diaphragm. A thermal control system allows to reach initial temperatures as high as 40°C . Upon rupturing of the diaphragm, an expansion wave is generated which accelerates the undisturbed mixture. The nozzle has a steady reservoir condition until the arrival of the reflected wave from the rear end of the tube, which occurs after roughly 50 ms. The droplet sizes are measured by means of a fully time resolved white light extinction method [4]. The technique is based on the simultaneous determination of the extinction coefficients β at seven different wavelengths λ . As an example, Fig. 2(a) shows the extinction coefficients as functions of time at three different wavelengths. On the basis of Mie theory, variations in β are directly connected to variations in droplet modal radius r_m and number density n_d . However, it is worth mentioning explicitly that in proximity of the regime of Rayleigh scattering, it is theoretically impossible to retrieve meaningful information on droplet size from the spectral data. To verify that this limiting condition is not met, the experimentally determined extinction efficiencies $g(\alpha)$ have been directly compared to their theoretically counterparts $Q_{ext}(\alpha)$, where $\alpha = 2\pi R_d/\lambda$ is the size parameter. In the hypothesis of a monodispersed distribution, $g(\alpha)$ is simply $\beta_{exp}(\alpha)/\pi n_d r_m^2$, where r_m and n_d are provided by the inversion procedure. Figure 2(b) shows this comparison in correspondence of the extinction peak at $t_i = 33.3 \text{ ms}$. The perfect match between Mie curve and $g(\alpha)$ guarantees first that the measured spectrum is definitely outside the regime of Rayleigh scattering. Second, it proves that the experimental determination of β and the solution of the inversion procedure are both accurate. It is, thus, on these points (i.e. extinction peaks), that the validation and analysis of condensation models is based.

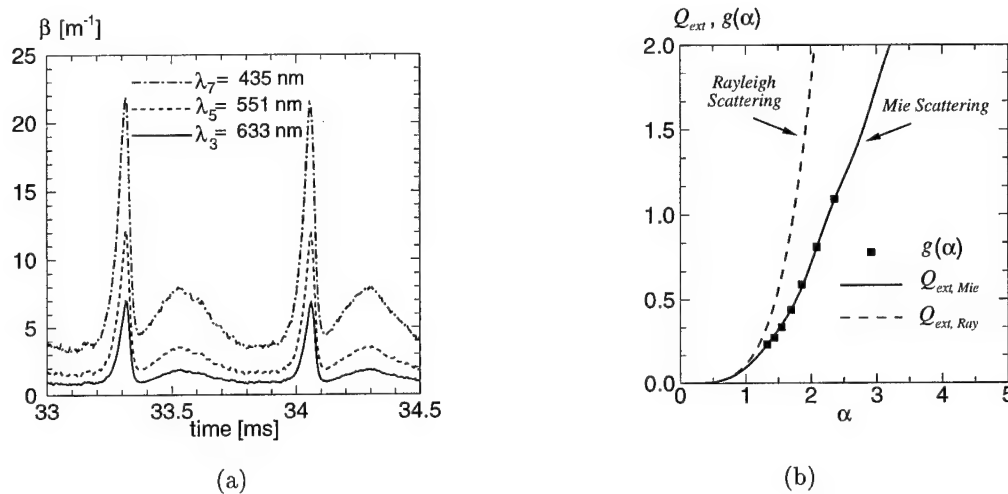


Figure 2: Part (a) - Experimentally determined extinction coefficients β versus time. Part (b) - Theoretical extinction efficiency Q_{ext} and spectral turbidity $g(\alpha)$ as function of the size parameter α . Nozzle: G2. Exp. 37 - Stagnation conditions: $P_o = 8.752 \cdot 10^4 \text{ Pa}$, $T_o = 296.6 \text{ K}$, $S_o = 1.188$.

4. Results

Objective of this section is to validate condensation models and to verify the correctness of the underlying theoretical considerations. In particular three different models were considered. The first (ICCT-wb) is proposed by the authors and described earlier. The second one (SD), proposed by Schnerr *et al.* [10], has been widely used for a variety of nozzle configurations. It uses CNT for the nucleation process, with a specific surface tension fit, and the Hertz-Knudsen formula for the droplet growth process. The third one (SD-wb) has the same nucleation model as the (SD) model, but it employs the wet-bulb correction for the droplet growth. The three models are compared with respect to frequencies of the oscillations and predicted maximum droplet radii. Figure 3(a) shows the results for the droplet radius. Clearly, regardless from the specific nucleation models, correct droplet sizes are predicted only when the wet-bulb approximation is implemented. In agreement with our theoretical consideration from the previous section, the HK growth rate is too strong and leads to an overestimation in droplet radii. Figure 3(b) is, instead, more difficult to interpret. We start observing that, while the (SD) and the (ICCT-wb) model agree fairly well with the experimental results, the (SD-wb) model clear underestimates the frequency values. By comparing the (ICCT-wb) with the (SD-wb) model, the influence of the correct expression for the nucleation rate becomes evident: the CNT theory is a bit weaker than the corrected ICCT one and this leads to the prediction of lower frequencies.

On the other hand, in the (SD) model, the stronger droplet growth law compensates for the weaker nucleation rates, thus leading, by a cancellation of errors, to the correct frequency value.

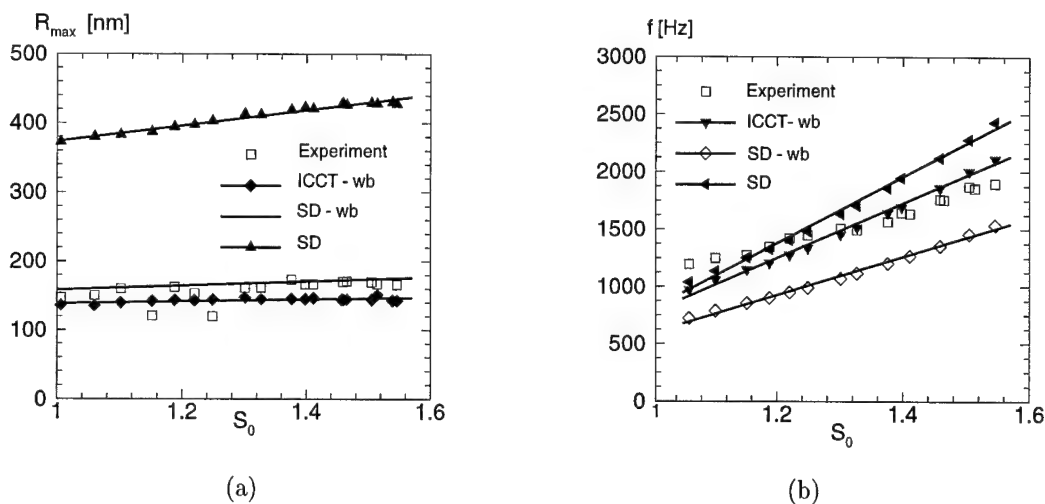


Figure 3: Frequency of oscillations (a) and maximum modal radius R_{max} (b) versus stagnation supersaturation. Nozzle: G2. Stagnation conditions: $T_0 = 296.8 \pm 0.4$ K; $P_0 = 8.69 \cdot 10^4 \pm 0.015$ Pa.

5. Conclusions

It has been shown that for the correct modelling of nonequilibrium condensation, it is essential to calculate explicitly the energy flux between the droplet and its environment. The simple assumption of equal temperatures between gas and liquid phase leads inevitably to an overestimation in droplet size, by at least a factor 2.5. Three condensation models were analysed and compared with our experimental results. From this study, it turned out that the best overall agreement was obtained with the (ICCT-wb) model.

Acknowledgements

The authors would like to express their gratitude to the Netherlands Foundation for Fundamental Research on Matter for supporting this work with grant no.97.1293.

6. References

- 1 WEGENER, P.P.: Gasdynamics of expansion flows with condensation, and homogeneous nucleation of water vapor; in Nonequilibrium flows I, Marcel Dekker, New-York, **1**, (1969), 162–243.
- 2 MOSES, C.A., STEIN, G.D.: On the growth of steam droplets formed in a Laval nozzle using both static pressure and light scattering measurements; J. Fluids. Eng. **100**, (1978), 311–322.
- 3 ADAM, S., SCHNERR, G.H.: Instabilities and bifurcation of nonequilibrium two-phase flows; J. Fluid. Mechanics. **348**, (1997), 1–28.
- 4 LAMANNA, G.: On nucleation and droplet growth in condensing nozzle flows; Ph.D. Thesis, Eindhoven University of Technology, (to appear).
- 5 HACKER, P.T.: Experimental values of the surface tension of supercooled water; NACA TN 2510, (1951).
- 6 LUIJTEN, C.C.M., VAN DONGEN, M.E.H.: Nucleation at high pressure. II. Wave tube data and analysis; J. Chem. Phys. **111**, No. 18 (1999), 8535–8544.
- 7 LUIJTEN, C.C.M., VAN DONGEN, M.E.H.: Nucleation at high pressure. I. Theoretical consideration; J. Chem. Phys. **111**, No. 18 (1999), 8524–8534.
- 8 PEETERS, P., LUIJTEN, C.C.M., VAN DONGEN, M.E.H.: Transitional droplet growth and diffusion coefficients; Int. J. Heat Mass Transfer (to be published).
- 9 PRAST, B.: Numerical modelling of condensation processes in Laval nozzle flows; Ph.D. Thesis, Eindhoven University of Technology, (to appear).
- 10 SCHNERR, G.H., DOHRMANN, U.: Transonic flow around airfoils with relaxation and energy supply by homogeneous condensation; AIAA J. **28**, No. 7, (1990), 1187–1193.

Addresses: PROF. DR. M.E.H. VAN DONGEN, G. LAMANNA, Dept. of Applied Physics, Eindhoven University of Technology, P.O. Box 315, 5600 MB Eindhoven, The Netherlands.
B.PRAST Stork Product Engineering BV, P.O. Box 379, 1000 AJ Amsterdam, The Netherlands.

C. VORTMANN, G.H. SCHNERR

A New Law of State Model for Cavitation at Non-Equilibrium

For practical reasons cavitating flow is often simulated using simple law of state models. These models are usually based on the assumption that the phase transition occurs if the pressures drops below the equilibrium vapor pressure. In order to improve the description of the cavitation process a new law of state model was developed that takes phase non-equilibrium effects into account. By postulating the variation of the free enthalpy for the phase mixture a rate equation for the dryness fraction is derived. Concerning the calculation of two-dimensional, unsteady cavitating flow the rate equation for dryness fraction is solved in combination with a modified Volume-of-Fluid algorithm.

1. Cavitation model and numerical scheme

In earlier studies [1] cavitation was predicted by a simple law of state model. Herein the thermodynamic state is fixed by coupling pressure and density at constant temperature. At ideal case the phase transition takes place at the equilibrium vapor pressure. Due to numerical stability the phase transition region is spread in these models across a certain pressure region. The physical modeling is however rude and has to be improved. Phase transition is stated as a molecular exchange process that develops during a finite time interval. Hence the liquid will not immediately evaporate completely if the equilibrium vapor pressure is reached but a time depending evaporation process starts. Such a non-equilibrium effect can be modeled by an approach suggested by Landau and Ginzburg. In this study the promising model of Müller and Achenbach [2] is modified with the purpose of application to fluid dynamics, especially for the description of cavitation phenomena.

In the following the underlying physical concept is explained. Equilibrium states can be calculated by minimizing the free enthalpy G . In equilibrium phase transition is indicated by equality of the free enthalpy values of each phase. For the modified non-equilibrium model of Müller and Achenbach the free enthalpy of a cluster of water molecules is introduced. The postulated variation of the free enthalpy consists of an energy potential corresponding to the liquid state and another one for the vapor. In between exists an energetic barrier that has to be passed by the cluster during the phase transition. The lower the energy potential of the corresponding phase the more probable the cluster will adopt this state. Based on this concept the following rate equation for the dryness fraction x can be derived

$$\frac{dx}{dt} = \underbrace{(1-x) \cdot K_{l \rightarrow v}}_{\text{Gain}} - \underbrace{x \cdot K_{v \rightarrow l}}_{\text{Loss}} \quad K_{l \rightarrow v} = \frac{\exp\left(-\frac{g(v_{bar}, T, p)}{k/m_c \cdot T}\right)}{\tau \cdot \int_{v_b}^{v_{bar}} \exp\left(-\frac{g(v, T, p)}{k/m_c \cdot T}\right) dv} \quad (1)$$

The gain of vapor clusters depends on the number of liquid clusters expressed by the liquid fraction $y = 1 - x = m_l/m$, and furthermore on the probability $K_{l \rightarrow v}$ that liquid clusters change their state of aggregation from liquid to vapor. This probability can be derived by the theory of thermally stimulated processes, if the form of the free enthalpy is postulated as described above. The probability $K_{v \rightarrow l}$ differs from $K_{l \rightarrow v}$ only concerning the integration boundaries that cover the region of the respective phase area. The time scale is controlled by the relaxation parameter τ and by the mass of a cluster m_c . The dryness fraction in Eqn. 1 is calculated by a routine that is particularly suited for stiff systems (Radau IIa from the book of Hairer and Wanner). The integral form of the 2-D Euler equations are numerically solved by an implicit Finite-Volume-Method at non-orthogonal structured, single-block grids with a collocated arrangement of variables as described by Perić [3]. The phase mixture is simulated as fluid with varying density, whereas the pure phases are treated incompressible. To overcome problems due to the huge density variation between vapor and liquid a modified Volume-of-Fluid algorithm is used

$$\frac{\partial \alpha}{\partial t} + \nabla \cdot (\alpha \vec{c}) = \rho \cdot \left(\frac{1}{\rho_l} - \frac{1}{\rho_v} \right) \cdot \frac{dx}{dt} \quad (2)$$

Herein evaporation resp. condensation is described by a source term on the right handside of the transport equation (Eqn. 2) for the void fraction $\alpha = V_v/V$. This source term is calculated by using Eqn. 1.

2. Results

Cavitating flow is investigated in a nozzle geometry shown in Fig. 1. Water at $T = 20^\circ\text{C}$ was chosen and the mass of a cluster is $m_c = 1.7 \cdot 10^{-24} \text{ kg}$. Figure 2 presents the total vapor content in the nozzle versus time for different values of the relaxation parameter τ . The decrease of τ to 10^{-4} s kg/m^3 leads to states that are related with equilibrium. As a consequence only small differences can be recognized compared to the bubble growth laws e.g. Rayleigh. For all parameters periodic behavior with the frequency $f=9.5 \text{ Hz}$ is observed after a single overshoot. Figure 3 shows one cycle of the cavitating flow at maximum non-equilibrium condition $\tau = 1.0 \text{ s kg/m}^3$. A re-entrant jet forms due to the sudden decrease of vapor fraction at the cavity tail. In that way a cavitation cloud arises which moves downstream where it finally collapses.

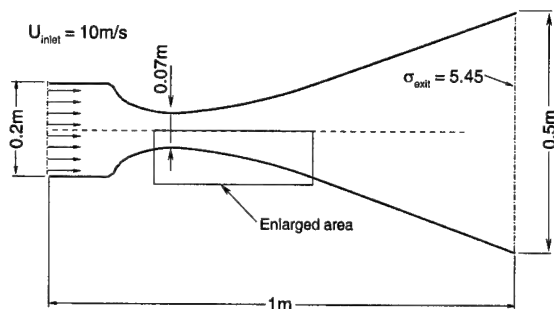


Fig. 1: Geometrical setup of 2-D plane nozzle.

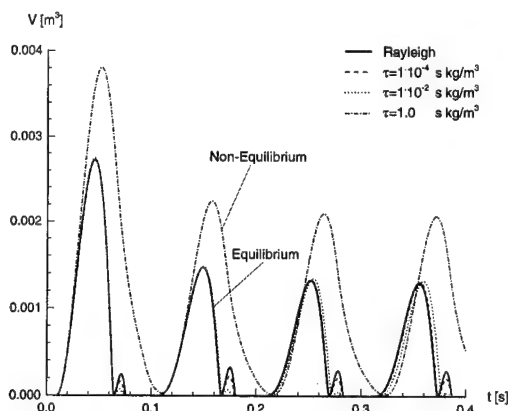


Fig. 2: Total vapor volume vs. time, Variation of the relaxation parameter τ for Müller-Achenbach Model and comparison with Rayleigh-Model.

Acknowledgements

Sincere thanks are given to Prof. Dr.-Ing. M. Perić from the TU - Hamburg Harburg and his former co-worker Dipl.-Phys. M. Krömer for committing the single-phase version of the numerical code to us. The authors are grateful for the cooperation with Prof. Dr. Dr. h.c. I. Müller and Dr.-Ing. S. Seelecke from the TU - Berlin.

3. References

- 1 G.H. SCHNERR, C. VORTMANN, J.SAUER. *Numerical Studies of Flow in Fuel Injector Nozzles - Interaction of Separation and Cavitation*. To appear in: Proc. DFG-Schwerpunktprogramm "Transiente Vorgänge in mehrphasigen Systemen mit einer oder mehreren Komponenten", Wiley-VCH, Weinheim 2000.
- 2 M. ACHENBACH, I. MÜLLER: Simulation of Material Behaviour of Alloys with Shape Memory. *Archives of Mechanics* **37**, 6 (1985), 573–585.
- 3 J. H. FERZIGER, M. PERIĆ. *Computational Methods for Fluid Dynamics*. Springer-Verlag, 1996.

Addresses: PROF. DR.-ING. HABIL. G.H. SCHNERR, DIPL.-ING. C. VORTMANN, University of Karlsruhe, Fachgebiet Strömungsmaschinen, Kaiserstr.12, 76185 Karlsruhe, Germany, e-mail: guenter.schnerr@mach.uni-karlsruhe.de.

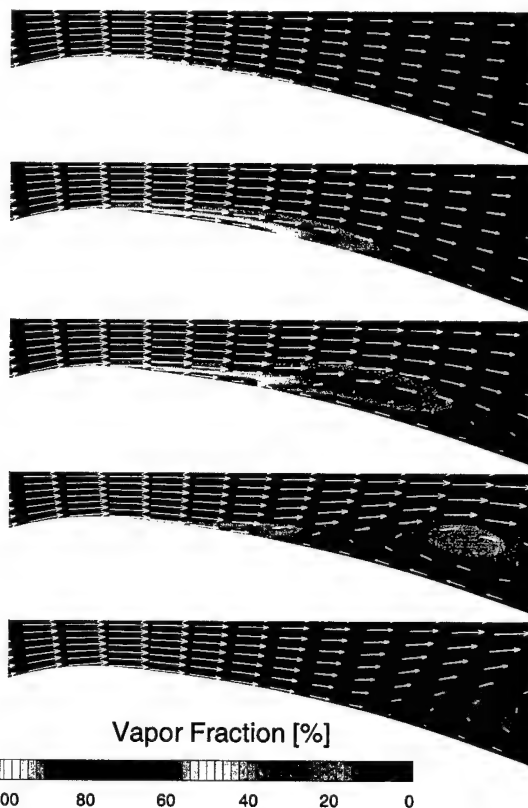


Fig. 3: Velocity vectors and vapor fraction, $\tau = 1.0 \text{ s kg/m}^3$.

G. WINKLER, M. HEILER, G.H. SCHNERR

Simulation of Condensation Processes in Turbines including Impurity Effects

Condensation processes are important for many technical applications such as in transsonic low pressure steam turbines. Impurities like dust particles or chemical deposits significantly affect the condensation process. Depending on the expansion rate the condensate formation is controlled by homogeneous or heterogeneous nucleation. Technical steam for example, used in power processes, typically consists of several impurities, which change due to lower expansion rates the condensation behaviour, so that a large fraction of the condensate mass is formed heterogeneously. Numerical parameter variations in the nozzle BA-1 were performed to study as how to the number of particles influences the condensation onset and the total amount of formed condensate mass. In comparison to the homogeneous case, a smaller supersaturation is reached if heterogeneous condensation dominates. The condensation occurs close to the equilibrium state and reduces losses caused by the pure non-equilibrium process.

1. Introduction

The expansion in the last stages of low pressure steam turbines crosses the thermodynamic state path and enters the metastable area. Hence the subsequent stages operate in a two-phase mixture of steam and droplets. Depending on the fluid contamination with impurities and the expansion rate, a superposition of homogeneous and heterogeneous condensation will occur [2,4,5]. As expected, the effects of homogeneous/heterogeneous condensation in the turbulent transonic steam flow behave similar to the already investigated inviscid nozzle flow of condensing moist air [2].

2. Physical modelling and numerical scheme

The homogeneous nucleation process is modeled according to the classical nucleation theory of Volmer, Frenkel, and Zel'dovich. The simulation of steam turbine flows requires droplet growth expressions which cover the whole Knudsen number range and does also take the temperature as a driving potential into account. A modified model of Gyarmathy shows good agreement with nozzle flow experiments of steam [1,3], which approximate very well steam turbine conditions. In addition the Hertz-Knudsen law, is used to model the droplet growth in moist air and well suited for very low partial vapor pressures.

The simulation is based on the time dependent 2-D Navier-Stokes equations which are solved in conservative form. Two additional conservation equations (wetness fraction, droplet number) are used to model the condensation process and the liquid phase. The k-R turbulence model, which is applied in our calculations, solves the equations for the turbulent kinetic energy k and the undamped eddy viscosity R . The solution is further based on a MUSCL-type Finite-Volume-Method on structured body fitted grids. The source terms for the condensate formation are treated by applying the fractional step method in order to split the equations into a homogeneous and an inhomogeneous part, so the scheme accounts for different time scales of the flow and of the condensation process, respectively. The solution of both sets of equations proceeds by an explicit second order accurate time integration. The fluxes at the cell interfaces are determined by a hybrid AUSM/van Leer flux vector splitting for imperfect gases assuming a frozen speed of sound. Finally the κ -scheme from van Leer with the van Albada limiter calculates the vector of unknowns at the cell interfaces.

3. Results

The influence of the homogeneous/heterogeneous condensation process on the transonic flow in the nozzle BA-1 is investigated. The numerically simulated Schlieren picture Fig. 1 a) shows a typical shock formation, associated with the homogeneous condensation process. By increasing stepwisely the particle number, the shock is weakened and moves further downstream until it finally vanishes completely. The distribution of physical relevant quantities along the nozzle axis (see Fig. 2) of the purely homogeneous and a purely heterogeneous case shows, that the homogeneous nucleation process is suppressed completely. Due to subsonic heat addition (see Fig. 2b)) the pressure distribution is changed along the whole nozzle length. The amount of the wetness fraction is increased compared to the homogeneously condensing flow. The investigation of the loss of efficiency shows a decrease with $n_{het,0} = 10^{16}$ in contradiction to the purely homogeneous case, even if the wetness fraction at the nozzle axis is increased.

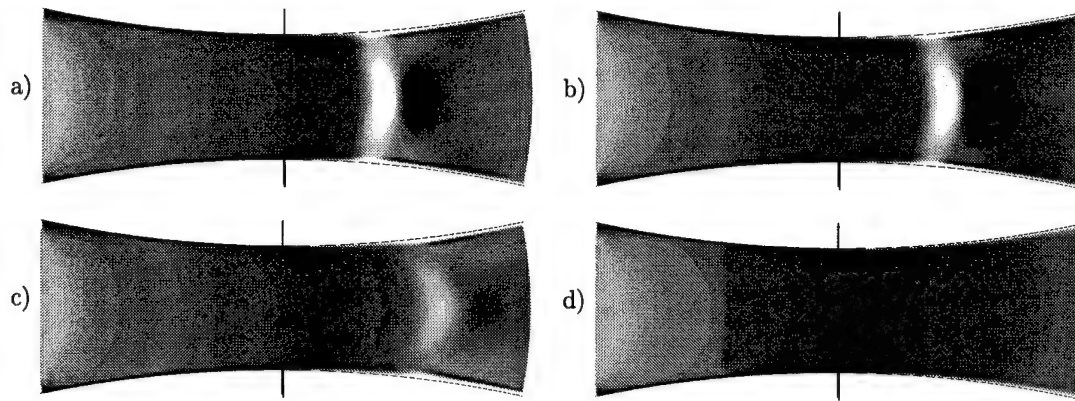


Fig. 1: Numerically simulated Schlieren pictures; reservoir conditions: $T_{01} = 380.55 \text{ K}$, $p_{01} = 0.784 \text{ bar}$; a) homogeneous, b) $n_{het,0} = 10^{14} \frac{1}{m^3 s}$, c) $n_{het,0} = 10^{15} \frac{1}{m^3 s}$, d) $n_{het,0} = 10^{16} \frac{1}{m^3 s}$, flow from left to right;

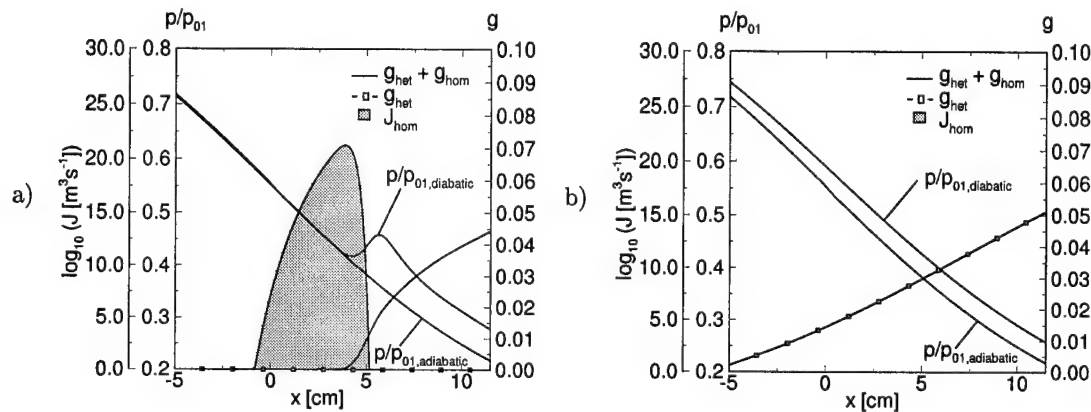


Fig. 2: Physical quantities along the nozzle axis: nondimensional pressure distribution (with and without condensation) p/p_{01} , homogeneous nucleation rate $\log_{10}(J_{hom} [m^{-3} s^{-1}])$, wetness fraction g ; reservoir conditions: $T_{01} = 380.55 \text{ K}$, $p_{01} = 0.784 \text{ bar}$, a) homogeneous, b) $n_{het,0} = 10^{16} \frac{1}{m^3 s}$, flow from left to right;

Acknowledgements

The authors would like to express their gratitude to the Deutsche Forschungsgemeinschaft (DFG) for supporting this research on condensing flows with contract 352 SCH/13-5.

4. References

- 1 HEILER, M.: Instationäre Phänomene in homogen/heterogen kondensierenden Düsen- und Turbinenströmungen, Dissertation, (1999), Fakultät für Maschinenbau, Universität Karlsruhe (TH).
- 2 Heiler, M., Winkler, G., Schnerr, G.H.: Homogeneous/Heterogeneous Condensation in Transonic Nozzle Flows: Proc. GAMM 1999 - Annual Meeting of the Gesellschaft für Angewandte Mathematik und Mechanik, April 12-16, Metz, France, ZAMM 80, pp. 284-285.
- 3 BARSCHDORFF, D.: Verlauf der Zustandsgrößen und gasdynamische Zusammenhänge der spontanen Kondensation reinen Wasserdampfes in Lavaldüsen, Forsch. Ing.-Wes., (1971), Vol. 37, No. 5.
- 4 STELTZ, W.G., LEE, P.K., LINDSAY, W.T. The verification of concentrated impurities in low pressure steam turbines, Journal of Eng. for Power, (1983), Vol. 105, pp. 192-198.
- 5 STASTNY, M., SEJNA, M. Numerical analysis of heterogeneous condensation of the steam flowing in turbine cascade, IMechE, Conference Transactions, (1999), Turbomachinery Vol. B, March 2-5, Royal National Hotel, London.

Addresses: PROF. DR.-ING. HABIL. GÜNTER H. SCHNERR, DIPL.-ING. GUNTER WINKLER, Fachgebiet für Strömungsmaschinen, Universität Karlsruhe (TH), Kaiserstrasse 12, D-76128 Karlsruhe, Germany, e-mail: guenter.schnerr@mach.uni-karlsruhe.de.

WÖLK, G.; DREYER, M.; RATH, H.J.

Gas/Liquid Two-Phase Flow under Low Gravity Conditions

A novel flow pattern map is developed based on five dimensionless parameters. The transition region from dispersed bubble to slug flow, from slug to frothy slug/annular flow and from frothy slug/annular to annular flow is presented and good agreement between theory and experimental data from the literature is obtained.

1. Introduction

Prediction of the flow pattern in a gas/liquid flow is one of the most important problems in two-phase flow. For the optimization of the design and the operation of two-phase flow systems, especially concerning the pressure drop and thermodynamical quantities, there is a need to predict accurately the existing flow patterns. In case of gas/liquid flow under low gravity conditions (μg_0) four major flow patterns, designated by Zhao & Rezkallah [1] as dispersed bubble flow, slug flow, frothy slug/annular flow and annular flow, can be observed.

2. Flow pattern maps

The aim of this investigation is to propose a flow pattern map for single-component two-phase flow as well as for two-component two-phase flow. A dimensional analysis was performed to identify the dimensionless groups which control flow pattern maps under low gravity (μg_0) condition. The parameters influencing gas/liquid flow under μg_0 -conditions in a smooth tube are the characteristic (superficial) velocities U_{GS} and U_{LS} , the densities ρ_L and ρ_G , the dynamic viscosities μ_L and μ_G , the surface tension σ and the tube diameter d_h . The subscripts L and G denote liquid and gas, respectively. Using the Π -theorem one gets five dimensionless groups which together with combinations of these groups could be relevant for presenting a flow pattern map in absence of gravity:

$$\frac{U_{GS}}{U_{LS}}, \frac{\mu_L}{\mu_G}, \text{We}_{GS} \left(= \frac{\rho_G U_{GS}^2 d_h}{\sigma} \right), \text{Re}_{GS} \left(= \frac{\rho_G U_{GS} d_h}{\mu_G} \right), \text{We}_{LS} \left(= \frac{\rho_L U_{LS}^2 d_h}{\sigma} \right). \quad (1)$$

Here, the Weber number represents the relative importance of inertial forces to surface tension forces and the Reynolds number represents the balance between inertial forces and viscous forces.

For the new developed flow pattern map, we use this five dimensionless groups and propose the following coordinates for the flow pattern map:

$$\begin{aligned} \text{for the abscissa:} & \quad \left(\frac{U_{GS}}{U_{LS}} \right)^X (\text{We}_{LS})^Z, \\ \text{for the ordinate:} & \quad \left(\frac{\mu_L}{\mu_G} \right)^X (\text{Re}_{GS})^Y (\text{We}_{GS})^Z, \end{aligned} \quad (2)$$

where the exponents X , Y and Z are adjustable parameters. In equation (2) we note that the same exponent Z applies to the gas and liquid Weber number; and that the same exponent X applies to the viscosity and velocity ratios. Additionally, if Z is much greater than both X and Y , the Weber number dominates the flow pattern prediction as published by Zhao & Rezkallah [1], without totally neglecting the other three dimensionless parameters. The values of the exponents, found by fitting to the experimental data collected by many researchers (e.g. Bousman [2], Colin et al. [3], Colin & Fabre [4], Dukler et al. [5], Lowe & Rezkallah [6], Reinarts [7], Rite & Rezkallah [8], Wölk et al. [9], Zhao & Rezkallah [1]), are $X = 0.50$, $Y = -0.25$ and $Z = 2.50$. Figure 1 shows the result of this approach as an overall flow pattern map for the gas/liquid two-phase flow in a circular tube. The flow regime data are depicted from papers [1]-[9] irrespectively concerning the used working fluids/gases and tube sizes. Overall a combination of 19 different experimental results (combinations of 5 different liquid/gas systems with 11 different tubes sizes) are shown in the map. However, only experimental data with a residual acceleration less than $10^{-2} g_0$ during the experimental observations are considered in this investigation. From Figure 1 one could directly see that four flow regime domains exist, with one flow regime being absolutely dominant in each domain. Inside the map, the grey bars display transition regions between two flow regimes. The proposed flow pattern map predicts: no dispersed

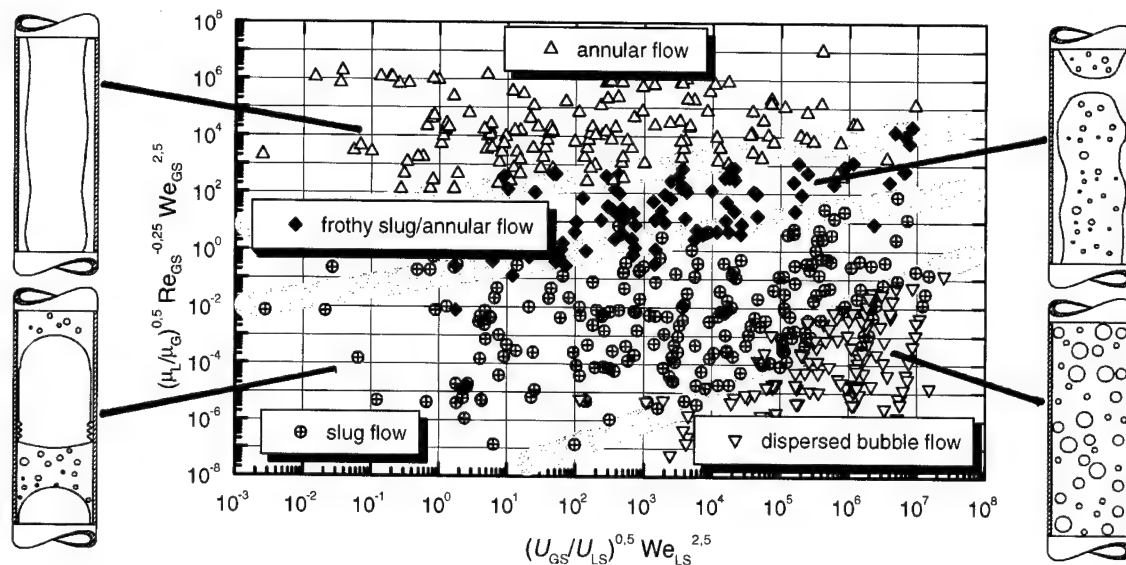


Figure 1: Overall flow pattern map for a gas/liquid two-phase flow under low gravity conditions. The grey bars display transition regions between two flow regimes. The flow pattern data are depicted from paper [1]-[9].

bubble flow pattern in the frothy slug/annular flow regime region and vice versa, no dispersed bubble flow pattern in the annular flow regime region and vice versa, and no slug flow pattern in the annular flow regime region and vice versa. Overall a good agreement between the new flow pattern map and the experimental data from the literature is obtained. The results of modeling the transition regions from disperse bubble to slug flow, from slug to frothy slug/annular flow and from frothy slug annular to annular flow is being discussed by Wölk et al. [10].

Acknowledgements

This work is supported by the German Space Agency DARA under grant number 50 WM 9443.

3. References

- 1 ZHAO, L., REZKALLAH, K.S.: Gas-liquid flow pattern at microgravity conditions. *Int. J. Multiphase Flow* **19** (1993), 751-763.
- 2 REINARTS, Rite & Rezkallah, Zhao & Rezkallah
- 3 BOUSMAN, W.S.: Studies of two-phase gas-liquid flow in microgravity. NASA Contractor Report 195434 (1995).
- 4 COLIN, C., FABRE, J., DUKLER, A.E.: Gas-liquid flow at microgravity conditions - I: dispersed bubble and slug flow; *Int. J. Multiphase Flow* **17** (1991), 533-544.
- 5 COLIN, C., FABRE, J.: Gas-liquid flow under microgravity conditions: influence of tube diameter on flow patterns and pressure drops; *Adv. Space Res.* **16** (1995), 137-142.
- 6 DUKLER, A.E., FABRE, J., MC QUILLAN, J.B., VERNON, R.: Gas-liquid flow at microgravity conditions: flow pattern and their transistions; *Int. J. Multiphase Flow* **14** (1988), 389-400.
- 7 LOWE, D.C., REZKALLAH, K.S.: Flow regime identification in microgravity two-phase flows using void fraction signals; *Int. J. Multiphase Flow* **25** (1999), 433-457.
- 8 REINARTS, T.R.: Adiabatic two phase flow regime data and modeling for zero and reduced (horizontal flow) acceleration fields; PhD Dissertation, Texas A&M University (1993).
- 9 RITE, R.W., REZKALLAH, K.S.: Local and mean heat transfer in bubbly and slug flows under microgravity conditions; *Int. J. Multiphase Flow* **23** (1997), 37-54.
- 10 WÖLK, G., DREYER, M., RATH, H.J.: Investigation on Two-Phase Flow in Small Diameter Non-Circular Channels under Low and Normal Gravity; Space Technology and Applications International Forum - 1999, Albuquerque, NM, AIP-Conference **458** (1999), 785 - 791.
- 10 WÖLK, G., DREYER, M., RATH, H.J.: Gas/liquid flow pattern maps for low gravity conditions; *Int. J. Multiphase Flow* (submitted 2000).

Address: DIPL.-ING. GERRIT WÖLK, DR.-ING. MICHAEL DREYER, PROF. DR.-ING. HANS J. RATH, ZARM, Universität Bremen, Am Fallturm, D-28359 Bremen

S. WURSTHORN, G.H. SCHNERR

Numerical Investigation of Performance Losses in a Centrifugal Pump due to Cavitation

Numerical simulations of cavitating pump flow in consideration of centrifugal and Coriolis force are performed. For the simulations a homogeneous model for the liquid-vapor two-phase flow is used. The pump investigated is a radial type of low specific speed ($n_q = 18$) with parallel shroud and hub. Numerical results such as detailed visualizations of the unsteady vapor distribution and time averaged pressure distribution in comparison with experiments are provided.

1. Introduction

In hydraulic machine systems cavitation is an important phenomenon. Due to the highly unsteady flow, cavitation causes noise, vibrations and damage of the material accompanied by performance losses. To get detailed insight and knowledge of this problem two phase simulations of unsteady cavitating flow are of great interest.

2. Numerical treatment

The calculations have been performed with the commercial CFD-software STAR-CD. The numerical treatment of the cavity flow is done with a modified Volume-of-Fluid algorithm. This means the liquid-vapor mixture described by a void fraction α is treated like a single fluid with varying density $\rho = \alpha\rho_v + (1 - \alpha)\rho_l$. The pure phases are treated incompressible. For α a transport equation is solved. The formation and disappearance of vapor is described by a source term in the reformulated continuity equation $\nabla \cdot \vec{c} = -\frac{1}{\rho} \frac{d\rho}{dt} = -\frac{1}{\rho} \frac{1}{a^2(\alpha)} \frac{dp}{dt}$ and in the transport equation for α : $\frac{\partial \alpha}{\partial t} + \nabla(\alpha \vec{c}) = \frac{d\alpha}{dt} + \alpha \nabla \cdot \vec{c} = \frac{1}{\rho_v - \rho_l} (2 - \frac{\rho_l}{\rho}) \frac{1}{a^2(\alpha)} \frac{dp}{dt}$. A simplified description of the vaporisation and condensation process is proposed through an empirical distribution of the speed of sound $a(\alpha)$ for the liquid-vapor mixture proposed by Wallis [1]. The minimum speed of sound at $\alpha = 0.5$ is fixed at $2m/s$. The pressure - velocity coupling is done by the PISO algorithm.

3. Results

The geometry of the pump is given in [2]. Inviscid calculations were performed in the rotating reference system with additional terms for Coriolis and centrifugal forces. Due to the diffuser ring it's sufficient to simulate only one vane with cyclic boundary conditions. Figure 1 shows the underlying computational mesh with the boundary conditions.

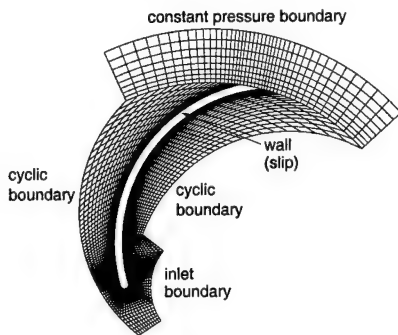


Fig. 1: Computational mesh with boundary conditions.

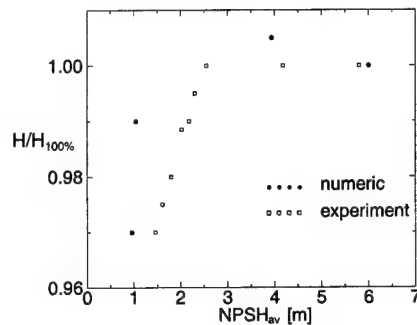


Fig. 2: Comparison of the experimental and numerically predicted NPSH-head-drop-curve at partial capacity ($\dot{V} = 272m^3/h$).

Figure 2 shows the numerically predicted NPSH-head-drop-curve in comparison with experimental measurements. It shows that the calculations are able to predict changes of the head due to cavitation. At high $NPSH_{av}$ -values the simulations show a gain of head. At lower $NPSH_{av}$ -values the head loss takes place suddenly and in a small range of $NPSH_{av}$. This unstable behaviour of the NPSH-head-drop-curve is caused by the lack of damping viscosity due to the inviscid calculations. Concerning the commonly used 3%-head-drop-criterion for acceptable cavitation,

the discrepancy of $NPSH_{3\%}$ is only 0.5 m. Figure 3 shows the vapor distribution of the periodic cavitating flow at $NPSH_{3\%}$. The cavitation is separated from the blade due to a vortex at this region. The influence of this vortex can also be seen in the surface pressure distribution (Fig. 4 right).

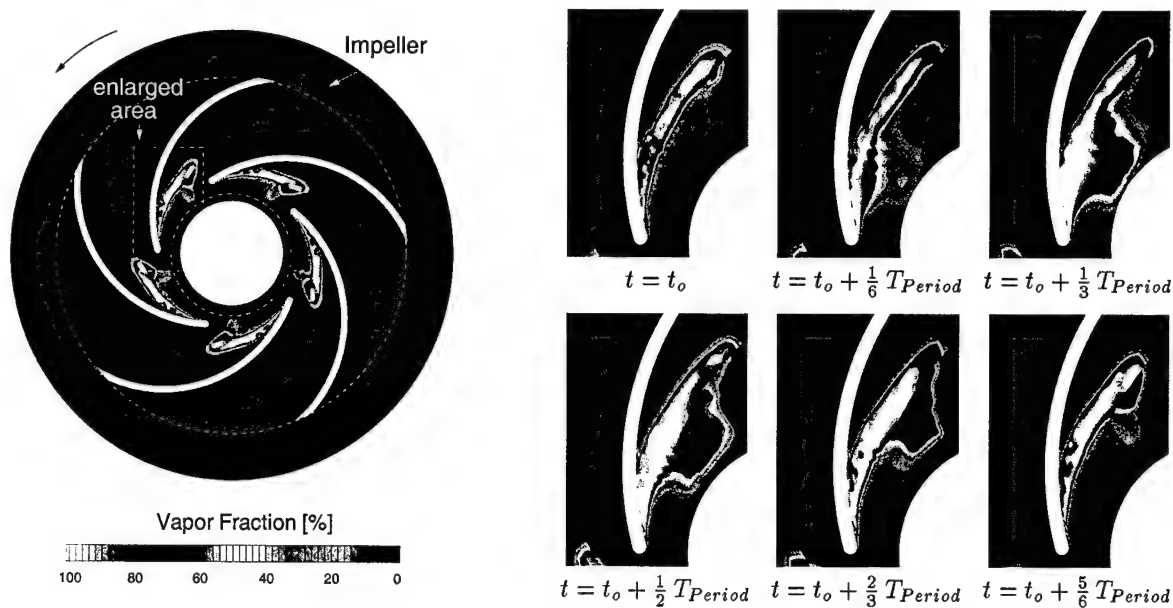


Fig. 3: Periodic cavitating pump flow. Vapor fraction in the flow field at 3% head loss. $f = 45\text{Hz}$, $\dot{V} = 272\text{m}^3/\text{h}$.

At Pfeiderer-Institut Braunschweig photographs of the cavitation area have been taken and pressure measurements in the rotating system have been performed [2]. Figure 4 shows qualitative good agreement concerning the vapor distribution and surface pressure.



Fig. 4: Comparison with experiment. Left: Instantaneous vapor distribution in the flow field (photograph by Pfeiderer-Institut Braunschweig). Right: Time averaged surface pressure $\bar{p} = \frac{p - p_{ref}}{\rho/2u^2}$ (s =position on the vane surface beginning at the leading edge).

Acknowledgements

The authors would like to express their gratitude to the Deutsche Forschungsgemeinschaft Bonn and the Graduiertenkolleg "Energie- und Umwelttechnik" for supporting this research. Sincere thanks are given to Prof. Dr.-Ing. G. Kosyna and Dipl.-Ing. J. Friedrichs from Pfeiderer-Institut Braunschweig for providing the experimental data.

4. References

- 1 A. WALLIS: One-dimensional Two-phase Flow, McGraw-Hill, 1969.
- 2 A. DREISS: Untersuchung der Laufradkavitation einer radialen Kreiselpumpe durch instationäre Druckmessungen im rotierenden System, Dissertation TU Braunschweig (1997).

Addresses: PROF. DR.-ING. HABIL. G.H. SCHNERR, DIPL.-ING. S. WURSTHORN, University of Karlsruhe, Fachgebiet Strömungsmaschinen, Kaiserstr.12, 76185 Karlsruhe, Germany, e-mail: guenter.schnerr@mach.uni-karlsruhe.de

W. YUAN, G.H. SCHNERR

Numerical Simulation of Cavitating Flow in Injector Nozzles

In this study high-velocity cavitating flows in injector nozzles are calculated using a modified Volume-of-Fluid method coupled with bubble dynamics. The calculations show that cavitation in injector nozzles may be unsteady and the interaction between the internal and external flow should be taken into account.

1. Introduction

In injector nozzles cavitation may occur due to violent pressure drops. This affects the fuel dispersion and combustion process in engines. The small size of the nozzle and the high velocity of the flow make experimental measurements of this internal flow extremely difficult. Numerical simulation provides an efficient method, to further understand this small scale flow. In this study the continuum method is used, which reduces the computational cost. For simplicity and also due to the successful application to classical cavitation in hydraulic machinery, the bubble dynamic model is straight forward extended to high velocity cavitating flows.

2. Description of numerical method

The bubble-liquid flow is treated as a homogeneous mixture, hence only one set of governing equations is used for description. The equations are solved applying a cell-centered Finite-Volume-Method. Laminar flow is assumed for the reason that we are interested in assessing the effect of cavitation on the flow; introduction of a turbulence model would couple the effects of both cavitation and turbulence. This simplification will be removed in the future. In order to couple the pressure and velocity using SIMPLE algorithm, the non-conservative form of the continuity equation is used. The mixture density is calculated using the vapor fraction: $\rho = (1 - \alpha)\rho_l + \alpha\rho_v$. The vapor fraction α is solved from his transport equation:

$$\frac{\partial \alpha}{\partial t} + \nabla \cdot (\alpha \vec{c}) = \frac{d\alpha}{dt} + \alpha \nabla \cdot \vec{c} = \frac{n_0}{1 + n_0 \cdot \frac{4}{3}\pi R^3} \frac{d}{dt} \left(\frac{4}{3}\pi R^3 \right), \quad (1)$$

where n_0 is defined as nuclei concentration per unit volume of pure liquid. This equation indicates that the vapor is presumed to consist of mini spherical cavitation bubbles. The bubble growth is governed by the Rayleigh relation: $\dot{R} = \sqrt{\frac{2}{3} \frac{p_{vap} - p_\infty}{\rho_l}}$. For the test cases in this study n_0 is set to be $10^{17} \frac{\text{nuclei}}{\text{m}^3 \text{water}}$ and $R_0 = 0.3 \mu\text{m}$. The pressure of local cell is used as p_∞ .

3. Numerical results

To verify the above described bubble dynamic model for injector nozzle flows, experimental test cases of Roosen and Genge of the RWTH Aachen are calculated. The fluid was water. The mesh and boundary conditions are shown in Fig. 1. Table 1 shows three test cases. In the table the units are bar for pressure and m/s for velocity.

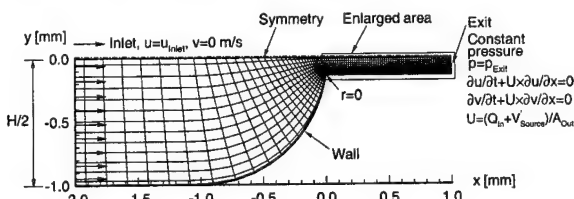


Table 1: Parameters of the test cases

Case	Experimental		$k = \frac{p_{inj} - p_v}{p_{inj} - p_{exit}}$	Computed	
	p_{exit}	p_{inj}		u_{inlet}	p_{inlet}
1	21	81	1.34	12.2	81
2	11	81	1.14	12.5	81
3	26		1.37	13.3	97 ± 2

Fig. 1: Sketch of the mesh and boundary conditions.

Figure 2 shows the experimental and computed (only half nozzle) cavitation distributions for case 1 (left) and case 2 (right). A nearly steady partial cavitation flow is obtained in case 1. Compared with the experimental observations, the calculated cavitation region is slightly longer due to lack of turbulence modeling and the fact that the nozzle

lip used for experiment was not truly sharp-edged. In the second case the cavitation number tends to unity and the cavitation region tends to the nozzle exit accompanied by a backflow, which indicates a fully flipped condition may occur. Once the condition with backflow is reached, the time accurate calculation is terminated due to the fact that the outflow boundary conditions under an unsteady flipping situation are not yet well defined. This problem should be solved in coupling with the external flow. This means, the interaction between the internal and external flow should be taken into account. Another interesting simulation is case 3. Calculations indicate that this flow is partially cavitating and periodic unsteady. A single period of this cavitation process is depicted in the Fig. 3. Figure 4 shows that the total vapor volume of this partially cavitating flow in the nozzle passage changes with a frequency of about 73.5 kHz, which is closely correlated with the time it takes a fluid element to traverse the nozzle passage.

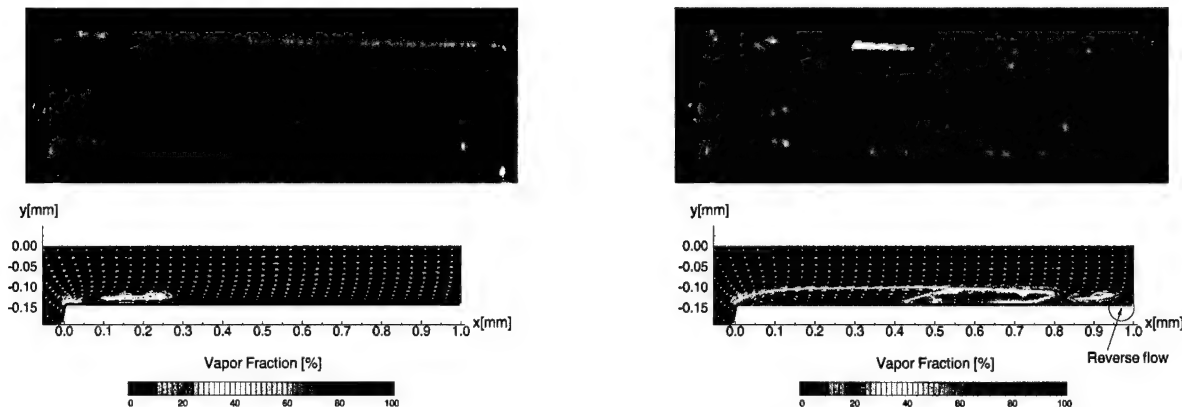


Fig. 2: Experimental (upper, from Roosen & Genge) and computed (lower) cavitation distributions for cases 1 & 2.

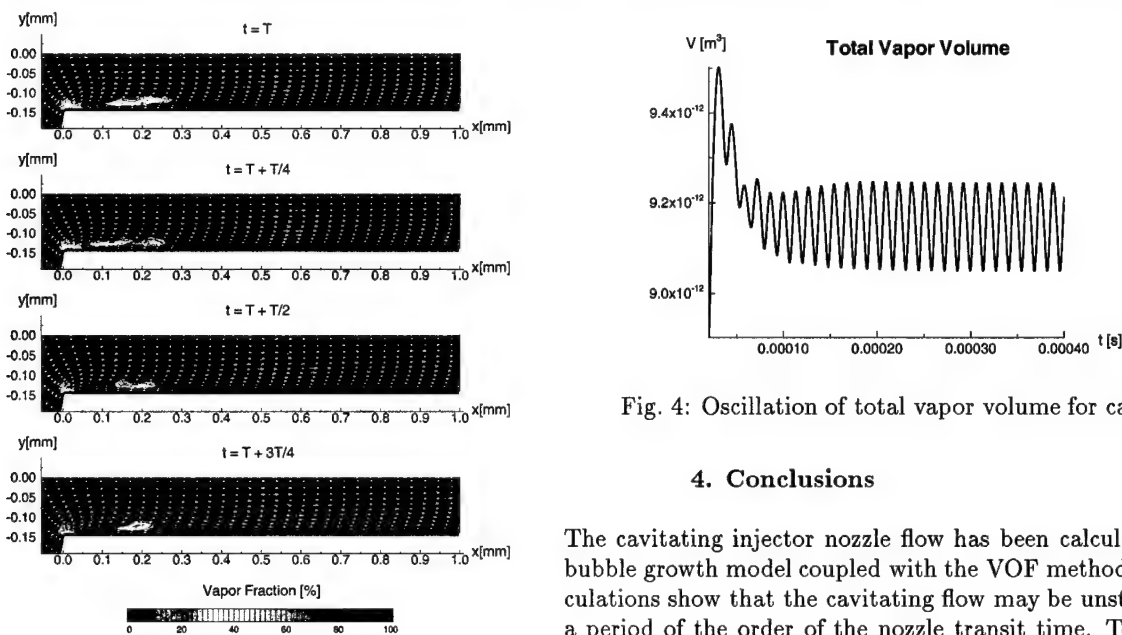


Fig. 3: Vapor fraction distribution and velocity vectors in the nozzle for case 3.

Fig. 4: Oscillation of total vapor volume for case 3.

4. Conclusions

The cavitating injector nozzle flow has been calculated using bubble growth model coupled with the VOF method. The calculations show that the cavitating flow may be unsteady with a period of the order of the nozzle transit time. To simulate the unsteady flipping situation, the complex outflow condition should be well treated.

Acknowledgements

The authors gratefully acknowledge the support from the Deutsche Forschungsgemeinschaft during performing this work. Sincere thanks are given to Dr.-Ing. P. Roosen and Dipl.-Ing. O. Genge of the Institute for Technical Thermodynamics of the RWTH Aachen (Germany) for providing the experimental data.

Addresses: PROF. DR.-ING. HABIL. GÜNTER H. SCHNERR, DR.-ING. WEIXING YUAN, University of Karlsruhe, Fachgebiet Strömungsmaschinen, Kaiserstr.12, 76185 Karlsruhe, Germany, e-mail: guenter.schnerr@mach.uni-karlsruhe.de.

DELFS, J.; GROGGER, H.; LAUKE, TH.; LUMMER, M.; YIN, J.

Numerical description of acoustic sources in airframe noise

The origin of airframe noise in subsonic flows is mainly related to vorticity perturbations which i) interact with geometric inhomogeneities (edges, steps, slots), ii) are subject to strong convective accelerations of the mean flow, iii) are strongly amplified in magnitude due to hydrodynamic instability of the mean flow. Therefore, apart from an appropriate modeling of the vorticity perturbations (e.g. causal or stochastic), a suitable Computational Aeroacoustics (CAA) method needs to describe accurately the conversion process from hydrodynamic to acoustic perturbations, i.e. the very noise generation. Aeronautics-related examples of numerically simulated airframe noise phenomena are presented which were obtained using DLR's CAA-code based on the high order spatial DRP scheme of Tam&Webb [1], the RK4 scheme in time and perfectly matched layers at the freefield boundaries Hu [2].

1. Simulation concept for airframe noise

In the study of (broadband) airframe noise one is not primarily concerned with the turbulence eigennoise, i.e. the sound produced by free turbulence. At subsonic flow Mach numbers a much more efficient source mechanism is represented through diffraction of the hydrodynamic pressure field at geometric inhomogeneities. Here part of the pressure associated with the vorticity fluctuations in the flow is converted into sound. For high Reynolds-number flows, two basically different approaches to the simulation of airframe noise are practical: a) the solution of a wave equation, derived from e.g. Lighthill's, Lilley's, Möhring's acoustic analogies. This approach requires the modeling of dedicated acoustic source terms; b) the solution of conservation equations, in which only the origin of the source, i.e. the vorticity perturbations is modeled, while the sound source is part of the simulation. For very complex flow situations as e.g. near the very noisy deployed high lift devices of a wing in approach conditions, the source modeling for a) may become overly complicated. For such situations approach b) is justified although the smaller amount of modeling has to be paid by considerably more computational effort.

In what follows, approach b) is considered exclusively. Two models of a different kind lend themselves to a reasonable representation of broadband vorticity disturbances: i) stochastic modeling, and ii) a causal modeling. In the first case a suitable stochastic representation of the velocity fluctuation field mimics the relevant features of turbulence. Causal modeling relies on imposing a spatially localized purely vortical disturbance upstream the source region in the steady mean flowfield. The computed acoustic response of aerodynamic bodies to such "vorticity pulses" defines their ability to convert vorticity into sound (i.e. their airframe noise characteristics), see also [4].

2. Governing equations

Simulating aeroacoustic sources of the mentioned kind necessitates the use of equations which describe simultaneously vortex dynamics and sound, and thus their interdependence. The compressible, unsteady Euler equations meet this requirement. They serve as the basic equations upon which a set of linear perturbation equations may be derived (see e.g. [3]), which describe the dynamics of small perturbations $q' := (\rho', v', p')$ about a given (quasi-) steady flow $q^0 := (\rho^0, v^0, p^0)$:

$$\frac{d^0 \rho'}{dt} + v' \cdot \nabla \rho^0 + \rho^0 \nabla \cdot v' + \rho' \nabla \cdot v^0 = \dot{m}' \quad (1)$$

$$\rho^0 \frac{d^0 v'}{dt} + \rho^0 v' \cdot \nabla v^0 + \rho' v^0 \cdot \nabla v^0 + \nabla p' = f' \quad (2)$$

$$\frac{d^0 p'}{dt} + v' \cdot \nabla p^0 + \gamma p^0 \nabla \cdot v' + \gamma p' \nabla \cdot v^0 = \dot{\theta}' \quad (3)$$

The equations are dimensionless with time $t = t^* a_\infty / l$, lengths $x_i = x_i^* / l$, density $\rho = \rho^* / \rho_\infty$, velocity vector $v = v^* / a_\infty$, pressure $p = p^* / \rho_\infty a_\infty^2$, some mass source density disturbance $\dot{m}' = \dot{m}'^* l / \rho_\infty a_\infty$, some force density disturbance $f' = f'^* l / \rho_\infty a_\infty^2$ and some entropic (e.g. heat) source density disturbance $\dot{\theta}' = \dot{\theta}'^* l / \rho_\infty a_\infty^3$. The asterisk denotes quantities bearing dimensions. A thermally and calorically perfect gas is assumed and γ denotes the isentropic exponent ($\gamma = 1.4$ for air). Moreover $\frac{d^0}{dt} := \frac{\partial}{\partial t} + v^0 \cdot \nabla$.

The spectrally tuned DRP-scheme of Tam&Webb [1] is the basis for the numerical representation of (1-3) to simulate the vortical, entropic and acoustic disturbance dynamics.

The boundary conditions for acoustically hard walls is equivalent to satisfying the non-penetration condition. With \mathbf{n} representing a vector locally normal to the wall at a given wall point it reads:

$$v_n := \mathbf{n} \cdot \mathbf{v}' = 0 \iff \frac{\partial p'}{\partial n} = (\rho^0(\mathbf{v}^0 \mathbf{v}' + \mathbf{v}' \mathbf{v}^0) + \rho' \mathbf{v}^0 \mathbf{v}^0) : \nabla \mathbf{n} \quad (4)$$

The boundary condition is implemented indirectly as a condition on the wall normal component of the pressure gradient $\frac{\partial p'}{\partial n}$ as indicated by the above equivalence. It says that the pressure gradient at a hard wall is – other than for acoustics in non-moving media – usually non-zero, namely the double contraction of the momentum flux with the local curvature tensor of the wall, i.e. centrifugal and coriolis components. The above statement is essential when dealing with the computation of the sound generation at aerodynamic bodies subject to flows which contain vorticity perturbations (e.g. inflow turbulence).

3. Results

First the effect of the presence of a flow field on scattering of a sound wave at a cylinder is illustrated in figure 1.

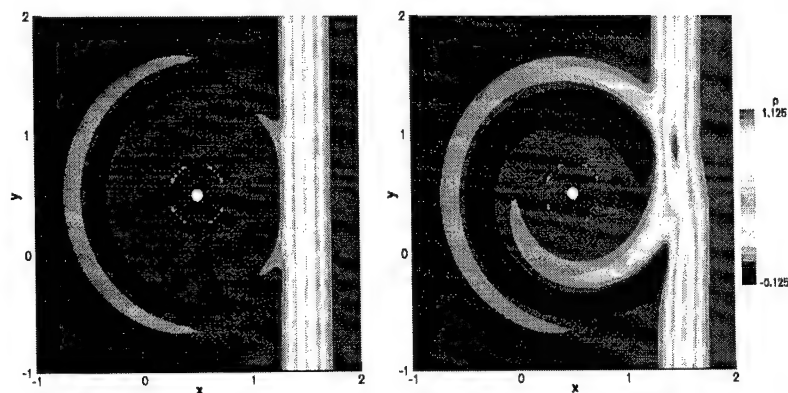


Figure 1: CAA-simulation of scattering of right-running plane Gaussian-shaped pressure pulse at cylinder. Left: no flow, right: Vortex flow around cylinder, $v_\varphi^0 = 0.5$ (white spots near cylinder due to plotting difficulties for overlapped grids). The primary plane wave experiences very small changes without flow and strong changes in the presence of flow. The radiation pattern is completely changed as well.

The effect of the nonhomogeneous condition for $\frac{\partial p'}{\partial n}$ on a noise generation problem is illustrated in fig. 2. It shows the numerical solution of (1-3) to simulate the aeroacoustic noise generation due to the interaction of a localized vorticity disturbance (test vortex seeded far upstream) with a Joukowski airfoil in a flow of Mach number $M_\infty = 0.5$. The initial linear vortex-disturbance is defined by its streamfunction, being a Gaussian of half-width $h_w = 0.1$, i.e. 10% of the airfoil's chord. It is seen that the visualized acoustic pressure pulse generated during the encounter of the airfoil's nose with the vortex appears strongly distorted when simulated using the condition $\frac{\partial p'}{\partial n} = 0$ as in classical acoustics. Other related edgenoise problems are dealt with in more detail in [3],[4].

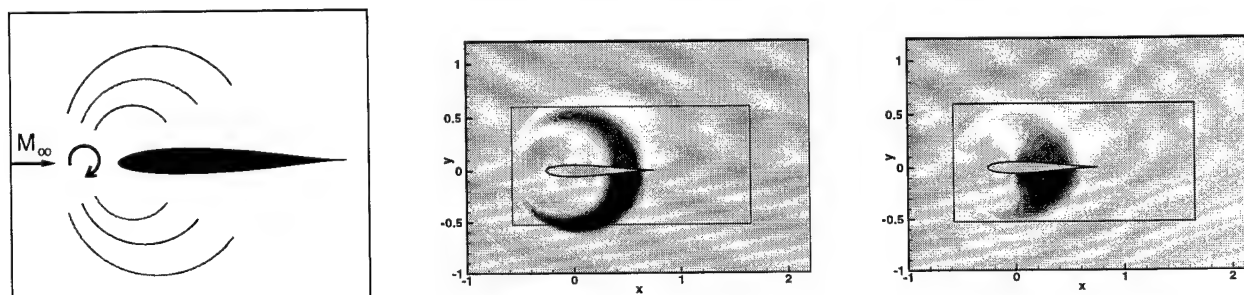


Figure 2: Pressure p' after airfoil-vortex encounter. Center: correct boundary condition due to (4), right: $\frac{\partial p'}{\partial n} = 0$.

4. References

- 1 TAM, C.K.W.; WEBB, J.C.: Dispersion-Relation-Preserving Finite Difference Schemes for Computational Aeroacoustics. J. Comp. Phys., Vol.107, pp. 262–281, 1993.
- 2 HU, F.Q.: On absorbing boundary conditions for linearized Euler equations by a Perfectly Matched Layer. J. Comp. Phys., Vol.129, 1996.
- 3 DELFS, J.; YIN, J.; LI, X.: Leading edge noise studies using CAA. AIAA Paper 99-1897, 1999.
- 4 YIN, J., DELFS, J.; GROGGER, H.; LAUKE, TH.; LUMMER, M.: Prediction of noise from interaction of vorticity with airfoils using CAA. Proceedings of ICAV7, Garmisch-Partenkirchen. To appear 2000.

Address: DR. JAN W. DELFS, ET AL.

Technical Acoustics Division, DLR, Lilienthalplatz 7, D-38108 Braunschweig, Germany.

DZIĘCIELAK, R.

Lamb's Problem for a Fluid-Saturated Porous Medium with a Structure

The Lamb's problem for a fluid-saturated porous medium has been considered by PHILIPPACOPOULOS [1] on the basis of BIOT'S [2] linear theory for porous fluid-saturated media. This author described structure of a medium by volume porosity only.

The aim of this paper is to present the results of the study of this problem for a fluid-saturated porous half-space with a structure. This problem is of interest in earthquake engineering applications. The medium consists of an isotropic elastic solid skeleton with pores filled by viscous compressible fluid. Usually in the soil and rock mechanics the structure of a porous medium is determined by single, the well known parameter, volume porosity f_v . However such description of a porous medium structure is too poor to describe the dynamic properties of this medium from the point of view of balance of momentum leading to the equations of motion. This is a reason to introduce so called double-parameter description of a porous medium structure. Complete description of a porous medium by two parameters has been given by KUBIK [3]. This author characterized the isotropic pore structure by two parameters: the volume porosity f_v and the structural permeability parameter λ or structure parameter $\kappa = \lambda/f_v$.

We confine our considerations to the elastic fluid-saturated porous medium described by the linear constitutive relations proposed by BIOT, [3],

$$\mathbf{T}^s = 2N\mathbf{E}^s + (A\text{tr}\mathbf{E}^s + Q\text{tr}\mathbf{E}^f)\mathbf{1} \quad \mathbf{T}^f = (Q\text{tr}\mathbf{E}^s + R\text{tr}\mathbf{E}^f)\mathbf{1} \quad (1)$$

where \mathbf{T}^s and \mathbf{T}^f are the stress tensors in the solid skeleton and in the fluid, respectively, A, N, Q, R are the material constants of a medium, \mathbf{E}^s and \mathbf{E}^f are the linear strain tensors

$$\mathbf{E}^s = \frac{1}{2}[\text{grad}\mathbf{u}^s + \text{grad}(\mathbf{u}^s)^T], \quad \mathbf{E}^f = \frac{1}{2}[\text{grad}\mathbf{u}^f + \text{grad}(\mathbf{u}^f)^T]. \quad (2)$$

\mathbf{u}^s and \mathbf{u}^f denotes the displacement vectors of the solid skeleton and the fluid, respectively, T denotes transposition.

Linearized equations of motion for the medium with a structure are of the form, [8],

$$\text{div}\mathbf{T}^s + b(\mathbf{v}^f - \mathbf{v}^s) = \rho_{11}(\kappa)\frac{\partial \mathbf{v}^s}{\partial t} + \rho_{12}(\kappa)\frac{\partial \mathbf{v}^f}{\partial t}, \quad \text{div}\mathbf{T}^f - b(\mathbf{v}^f - \mathbf{v}^s) = \rho_{12}(\kappa)\frac{\partial \mathbf{v}^s}{\partial t} + \rho_{22}(\kappa)\frac{\partial \mathbf{v}^f}{\partial t} \quad (3)$$

where:

$$\rho_{11}(\kappa) = \bar{\rho}^s + \frac{1-\kappa}{\kappa}\bar{\rho}^f, \quad \rho_{12}(\kappa) = -\frac{1-\kappa}{\kappa}\bar{\rho}^f, \quad \rho_{22}(\kappa) = \frac{1}{\kappa}\bar{\rho}^f. \quad (4)$$

\mathbf{v}^s and \mathbf{v}^f are the velocities of the solid skeleton and the fluid, respectively, b is the resistant coefficient for Poiseuille flow; for lower frequencies ($f < 1000$ Hz) which are especially met in seismology, the dependence of internal forces of interaction between components of the medium on the frequency can be neglected. The mass coefficients $\rho_{11}(\kappa)$, $\rho_{12}(\kappa)$, $\rho_{22}(\kappa)$ depend on the structure parameter κ . The considered in this paper influence of the structure of a medium stems from these terms of the equations of motion. The displacement equations are of the form

$$N\nabla^2\mathbf{u}^s + (A+N)\text{grad div}\mathbf{u}^s + Q\text{grad div}\mathbf{u}^f + b\left(\frac{\partial \mathbf{u}^f}{\partial t} - \frac{\partial \mathbf{u}^s}{\partial t}\right) = \rho_{11}(\kappa)\frac{\partial^2 \mathbf{u}^s}{\partial t^2} + \rho_{12}(\kappa)\frac{\partial^2 \mathbf{u}^f}{\partial t^2}, \quad (5)$$

$$Q\text{grad div}\mathbf{u}^s + R\text{grad div}\mathbf{u}^f - b\left(\frac{\partial \mathbf{u}^f}{\partial t} - \frac{\partial \mathbf{u}^s}{\partial t}\right) = \rho_{12}(\kappa)\frac{\partial^2 \mathbf{u}^s}{\partial t^2} + \rho_{22}(\kappa)\frac{\partial^2 \mathbf{u}^f}{\partial t^2} \quad (6)$$

Now we apply a Helmholtz resolution of each of the two displacement vectors, of the form

$$\mathbf{u}^s = \text{grad}\varphi + \text{rot}\mathbf{h}, \quad \mathbf{u}^f = \text{grad}\psi + \text{rot}\mathbf{g}, \quad (7)$$

to the displacement equations (5), (6) and we obtain the system of wave equations.

To simplify the study of the influence of a porous medium structure on Lamb's problem we confine our further considerations to one-dimensional problem of the uniformly distributed load

$$p(r, t) = P_0 e^{i\omega t} \quad (8)$$

on the boundary of the half-space; ω is the circular frequency of the surface load. The vertical displacements u and w of the solid skeleton and the fluid, respectively, are of the form

$$u_z = -(A_1 l_1 e^{-l_1 z} + B_1 l_2 e^{-l_2 z}) e^{i\omega t}, \quad w_z = -(A_1 \delta_1 l_1 e^{-l_1 z} + B_1 \delta_2 l_2 e^{-l_2 z}) e^{i\omega t}, \quad (9)$$

where l_1 and l_2 are the wave numbers. The displacements indicate that the dynamical load of the boundary of half-space causes, as usually in such a medium, the propagation of two longitudinal waves: the wave of the first kind and the wave of the second kind with the phase velocities

$$v_1 = \frac{\omega}{\text{Im} l_1}, \quad v_2 = \frac{\omega}{\text{Im} l_2} \quad (10)$$

Both of these waves are attenuated and attenuation coefficients are

$$\beta_1 = \text{Im} l_1, \quad \beta_2 = \text{Im} l_2 \quad (11)$$

In order to estimate the influence of a medium structure on the propagation of longitudinal waves in a fluid-saturated porous medium with a structure the numerical calculations were performed taking the data for water-saturated Bere'a sandstone and for oil-saturated sandstone.

Numerical solution of the dispersion equation gives us the phase velocities and the attenuation coefficients of the wave of the first kind and the wave of the second kind as a functions of the structural permeability parameter. The results of the numerical calculations made for two kinds of media let us to formulate interesting conclusions concerning the properties of these waves in the fluid-saturated porous medium with a structure. The dependence of the dimensionless phase velocities of the wave on the structure parameter κ is presented in Figure 1. The influence of a medium structure on the phase velocities and on the attenuation coefficients is stronger at higher frequencies of the waves. The phase velocity of the wave of the second kind is a little more sensitive on the medium structure than the phase velocity of the wave of the first kind. The attenuation coefficient of the wave of the first kind is influenced by a medium structure much stronger than the attenuation coefficient of the wave of the second kind. Practically, the phase velocity is not sensitive to the wave frequency thus the dispersion is not observed in the range of frequencies met in seismology

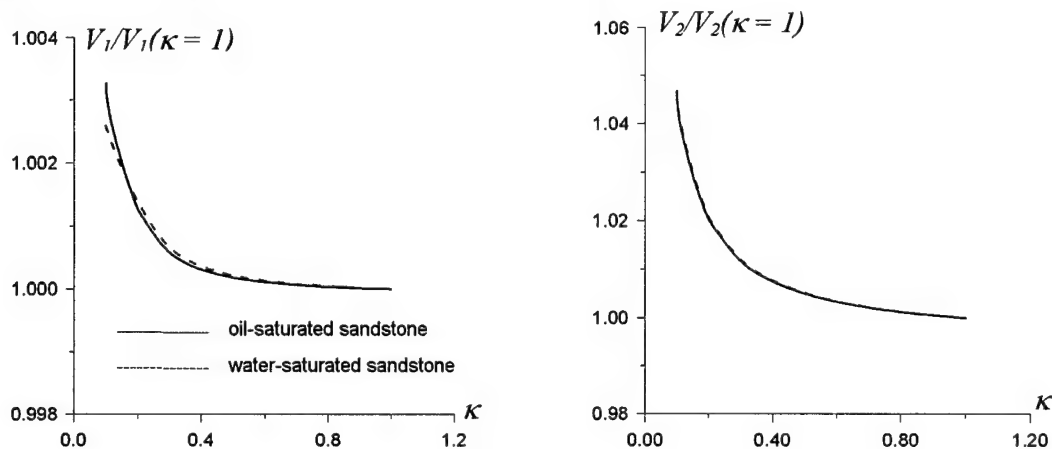


Fig. 1. Dimensionless phase velocities of the wave of the first kind and the wave of the second kind

References

1. PHILIPPOPOULOS, A.J.: Lamb's problem for fluid-saturated porous media. *Bull. Seism. Soc. Am.* **78** (1988), 908-923.
2. KUBIK, J.: Pore structure in dynamic behaviour of saturated materials. *Transport in Porous Media* **9** (1992), 15-24.
3. BIOT, M.A.: Theory of elasticity and consolidation for a porous anisotropic solid. *J. Appl. Phys.* **26** (1955), 182-185.

Address : Doc. R. DZIĘCIELAK, Poznań University of Technology, Institute of Applied Mechanics, ul. Piotrowo 3, 60-965 Poznań, Poland

PETR KONÍČEK, MICHAL BEDNAŘÍK, MILAN ČERVENKA

Nonlinear Effects in the Sound Field of the Circular Piston

This paper deals with the numerical modelling of the directional sound beams in the tube. The solution of KZK equation with and without the boundary layer is presented. The importance of boundary layer in directional sound beams modelling is shown here.

1. Khokhlov-Zabolotskaya-Kuznetsov equation

The KZK equation is the most widely used model equation for describing the combined effects of diffraction, nonlinearity and absorption in directional sound beams. KZK equation accounts for diffraction at the same order as dissipation and nonlinearity. In the case of axial symmetry it can be written as [1]

$$\frac{\partial^2 w}{\partial \sigma \partial \tau} = \alpha r_0 \frac{\partial^3 w}{\partial \tau^3} + \frac{r_0}{2l_d} \frac{\partial^2 w^2}{\partial \tau^2} + \frac{1}{4} \left(\frac{1}{\xi} \frac{\partial}{\partial \xi} + \frac{\partial^2}{\partial \xi^2} \right) w \quad (1)$$

where $w = v/v_m$ is the dimensionless velocity, $\sigma = z/r_0$ is the dimensionless coordinate in the direction of propagation, $\xi = r/R_0$ is the dimensionless coordinate perpendicular to the direction of propagation, $\tau = \omega t - kz$ is the dimensionless retarded time, α is the linear coefficient of diffusion, l_d the shock formation distance for the plane wave, r_0 is the Rayleigh distance (the beginning of the far field region) and R_0 is the tube diameter.

2. Numerical solution

The equation (1) was solved in the frequency domain where we obtain the system of nonlinear equations which was solved by means of a simple iteration method.

3. Frequency correction

When the wave approaches the shock wave, numerical instability rises (Gibbs oscillations). It is given by the finite number of terms in the Fourier series. This problem was solved by using the frequency correction term for each harmonics in the Fourier series [2]

$$\psi_n = \text{sinc}(n/H). \quad (2)$$

It is necessary to set an appropriate value of H to eliminate Gibbs oscillations and not to affect the higher part of the frequency spectrum significantly.

4. Boundary conditions

The equation (1) was solved with two different boundary conditions which were compared each other. The following boundary condition was used for the ideal fluid in the tube:

$$\frac{\partial w}{\partial r} = 0. \quad (3)$$

The second boundary condition taking into account a boundary layer was applied for real fluids:

$$\frac{\partial w}{\partial r} = -\frac{B}{c_0} \sqrt{\frac{2}{\pi}} \frac{\partial}{\partial \tau} \int_{-\infty}^{\tau} \frac{\partial w}{\partial \tau'} \frac{d\tau'}{\sqrt{\tau - \tau'}} \quad (4)$$

where $B = \sqrt{2\nu[1+(\gamma-1)/\sqrt{Pr}]} / 2c_0$, $\nu = \eta'/\rho_0$ is the kinematic viscosity, $Pr = \eta'c_p/\kappa$ is the Prandtl's number, κ is the heat conduction coefficient. This formula was derived by Blackstock from the Stokes equation for the boundary layer [1].

5. Results

The courses of three velocity harmonics in the dependence on ξ and σ are shown in the figures below. Each figure contains three dependencies for various combinations of the frequency correction factor H and the boundary value coefficient $U_0 = BR_0\omega^{3/2}/c_0$. All calculation were done for Gaussian sources.

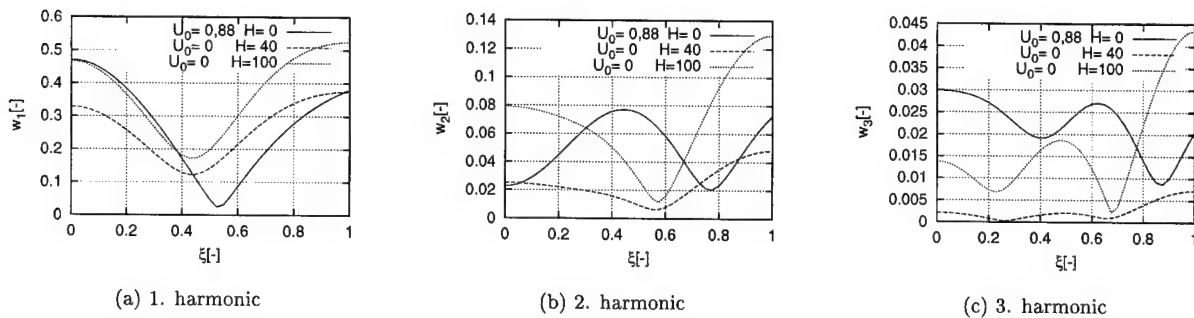


Figure 1: Dependence of the harmonics on the radius ξ for $\sigma = 1, 0$.

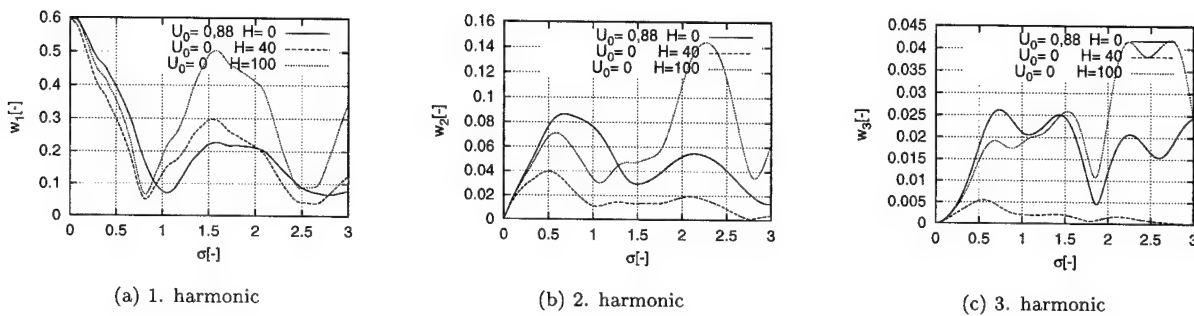


Figure 2: Dependence of the harmonics on the σ coordinate for $\xi = 0, 5$.

6. Conclusion

The velocity harmonics dependence of the sound beam in the tube on σ and ξ axes was shown. These dependencies demonstrated nonlinear, diffraction and dissipation effects in the tube. If we compute the velocity time dependence, we can observe the influence of dispersion effects on it very well. From the comparison of results with and without the boundary layer we see the importance of the boundary layer for the modelling the directional sound beams in the tube.

Acknowledgements

The work was supported by the Grant Agency of the Czech Republic, grant number 313/97/P117

7. References

- 1 HAMILTON, M.F., BLACKSTOCK, D.T.: Nonlinear Acoustics, Academic Press, USA 1997.
- 2 LANZOS, C.: Linear Differential Operators, Van Nostrand, New York, 1961.

Addresses: DR. MGR. PETR KONICEK, DR. ING. MICHAL BEDNARIK, ING. MILAN CERVENKA, Czech Technical University in Prague, Department of Physics, Technicka2, Prague 6, 166 27, Czech Republic.

S. LANGER, H. ANTES

Schalltransmission durch Isolierfenster

Der Nachweis der Schalldämmwirkung von Isolierfenstern erfolgt bisher im Allgemeinen durch Messungen unter normierten Bedingungen, obwohl eine numerische Simulation schneller und effektiver wäre. Deshalb wird dafür hier ein Berechnungsmodell entwickelt, dass die Schallwellenausbreitung und den Schalldurchgang durch zweifach-verglaste Fenster sowie alle auftretenden dynamischen Wechselwirkungsvorgänge beinhaltet.

Dazu wird sowohl für die Biege- als auch die als elastische, dünne Kirchhoff-Platten modellierten Glasscheiben wie für die Schalldruckwellen in der Luft der Scheibenzwischenräume und des Gebäudeinnenraums die Finite-Element-Methode (FEM) verwendet. Die Umgebung ausserhalb des Gebäudes stellt ein halbumendliches Gebiet dar, so dass wegen der Abstrahlbedingung dort die Randelementmethode (REM) bevorzugt wird. Die Kopplung der Fluidgebiete mit den Glasscheiben erfolgt jeweils über die virtuellen Arbeiten an den Koppelflächen. Die Lösung liefert sowohl das dynamische Verhalten der Glasscheiben wie die Schalldruckverteilung in der Luft. Damit ist dort der Schallpegel bekannt und kann das Schalldämm-Maß des Fensters ermittelt werden.

1. Theoretische Grundlagen

Die Finite-Element-Gleichungen für eine mit der Frequenz ω angeregte elastische Kirchhoff-Platte (5) und für ein ideales kompressibles Fluid (4) können aus der folgenden, auf dem Hamilton'schen Prinzip basierenden Variationsgleichung hergeleitet werden:

$$\delta(E_{kin} - E_{pot}) + \delta W = 0 \quad (1)$$

Die Variation von kinetischer bzw. potenzieller Energie führt auf die Steifigkeitsmatrizen \mathbf{K} und \mathbf{K}_1 bzw. die Massenmatrizen \mathbf{M} und \mathbf{K}_2 . Die Durchbiegung η der Platte wird dabei in jedem finiten Element der diskretisierten Platte durch $\eta = \mathbf{N}_s \mathbf{u}$, der Schalldruck in jedem finiten Element des diskretisierten Fluids durch $p = \mathbf{N}_a \mathbf{p}$ approximiert (vgl. [1]). Mit dem Term δW können die strukturellen und die akustischen Freiheitsgrade gekoppelt und damit deren Wechselwirkungen erfasst werden (vgl. [2]). Er ergibt sich für die Fluidgleichung (4) mit Variation des Schalldrucks δp zu (2) bzw. für die Strukturgleichung (5) mit der Variation der Plattendurchbiegungen δw zu (3).

$$\delta W = - \int \delta p w \, d\Gamma^{(i1)} \quad (2) \quad \delta W = - \int p \delta w \, d\Gamma^{(i1)} \quad (3)$$

Für die Kopplung müssen vorab die Verformungsfreiheitsgrade $\mathbf{u} = (w, w_x, w_y, w_{xy})$ der Kirchhoff-Platte kondensiert werden, so dass nur die Durchbiegungsfreiheitsgrade w zurückbleiben. Die beiden miteinander gekoppelten FE-Gleichungssysteme lauten dann:

$$\left(\mathbf{K}_1 - k^2 \mathbf{K}_2 \right) \mathbf{p} = -\rho \omega^2 \mathbf{C}^T \mathbf{w}^{(i1)} \quad (4) \quad \left(\mathbf{K} - \omega^2 \mathbf{M} \right)^* \mathbf{w} = -\mathbf{C} \mathbf{p}^{(i1)} \quad (5)$$

wobei $(\mathbf{K} - \omega^2 \mathbf{M})^*$ die dynamische Steifigkeitsmatrix der Platte nach der Kondensation ist. Die Knotenwerte der Durchbiegung und des Schalldrucks in der Koppelfläche sind in den Vektoren $\mathbf{w}^{(i1)}$ und $\mathbf{p}^{(i1)}$ zusammengefasst. Grenzt an beide Seiten der Platte ein Fluidgebiet, stellt $\mathbf{p}^{(i)} = \mathbf{p}_{(hinter)} - \mathbf{p}_{(vor)}$ den Schalldrucksprung an der Koppelfläche dar. $\mathbf{C} = \int \mathbf{N}_s^T \mathbf{N}_a \, d\Gamma^{(i1)}$ ist die Kopplungsmatrix der ersten Koppelfläche $\Gamma^{(i1)}$, also der inneren Fensterscheibe, die an die abgeschlossenen, luft- bzw. gasgefüllten Gebiete des Gebäuderaums bzw. des Scheibenzwischenraums grenzt.

Bei Schallausbreitungsproblemen in unendlich ausgedehnten Gebieten muß die Sommerfeld'sche Abstrahlbedingung erfüllt sein, d.h. die Wellen müssen im Unendlichen auslaufen. Am Diskretisierungsrand eines Finite-Elementgebietes kann es zu Reflexionen kommen, so dass die Abstrahlung nur durch zusätzlichen Aufwand, z. B. durch die Verwendung von infiniten Elementen (vgl. [3]), sichergestellt werden kann. Die Randelementmethode erfüllt im Gegensatz dazu implizit diese Bedingung. Die Randintegralgleichung für Schallausbreitungsprobleme ist in Gleichung (6) gegeben, wobei p^* die sogenannte Fundamentallösung und q^* deren Schallfluß bedeutet (vgl. [4]).

$$c(\xi)p(\xi) + \int_{\Gamma} q^*(\mathbf{x}, \xi)p(\mathbf{x}) \, d\Gamma_{\mathbf{x}} = \int_{\Gamma} p^*(\mathbf{x}, \xi)q(\mathbf{x}) \, d\Gamma_{\mathbf{x}} \quad (6) \quad \mathbf{G} \mathbf{q} - \mathbf{H} \mathbf{p} = \mathbf{0}. \quad (7)$$

Diskretisierung des Randes Γ und Approximierung von Schalldruck und -fluß durch $p = \mathbf{N}_p \mathbf{p}$ und $q = \mathbf{N}_q \mathbf{q}$ in jedem Randelement sowie Kollokation in jedem Randelementknoten führt auf die Randelementgleichung (7).

Die äußere Glasscheibe, also die zweite Koppelfläche $\Gamma^{(2i)}$, grenzt an den gasgefüllten Scheibenzwischenraum

(SZR) und das unendlich ausgedehnte Außengebiet. Während die FE/FE-Kopplung von SZR und Platte analog zur ersten Koppelfläche erfolgen kann (8), muß für die FE/RE-Kopplung von Platte und Außenraum für beide Freiheitsgrade der REM, den Schalldruck und den Schallfluß, eine Koppelbedingung eingeführt werden. Dort müssen jedoch die Beschleunigungen der elastischen Partikel der Platte und die der Fluidpartikel gleich sein, woraus als Bedingung für die Kopplung der strukturellen Durchbiegungen mit dem Schallfluß $\mathbf{q} = \frac{\partial \mathbf{p}}{\partial n} = \rho_F \omega^2 \mathbf{w}^{(i2)}$ und damit Gl. (10) folgt. Die Anwendung des Prinzips der virtuellen Arbeit in der Form $\delta W = -(p_h - p_v) \delta w \, d\Gamma^{(i2)}$ führt auf die Kopplung mit dem Schalldruck (vgl. (9)).

Es ergibt sich damit das folgende Gleichungssystem, wobei Randelement-Knoten, die nicht auf der Koppelfläche liegen, Dirichlet- oder Neumann-Randbedingungen aufweisen müssen (vgl. (11)). Für den Fall, dass für die Finiten Elemente und die Randelemente die gleichen Ansatzfunktionen gewählt werden, sind die Kopplungsmatrizen $\mathbf{C}_{(FE)}$ und $\mathbf{C}_{(RE)}$ gleich.

$$\left(\mathbf{K}_1 - k^2 \mathbf{K}_2 \right) \mathbf{p} = -\rho \omega^2 \mathbf{C}^T \mathbf{w}^{(i2)} \quad (8) \quad \left(\mathbf{K} - \omega^2 \mathbf{M} \right)^* \mathbf{w} = -\mathbf{C}_{(RE)} \mathbf{p}_{(RE)}^{(i2)} + \mathbf{C}_{(FE)} \mathbf{p}_{(FE)}^{(i2)} \quad (9)$$

$$\rho_F \omega^2 \mathbf{G} \mathbf{w}^{(i2)} - \mathbf{H} \mathbf{p} = 0 \quad (10) \quad \mathbf{G} \mathbf{q} - \mathbf{H} \mathbf{p} = 0 \quad (11)$$

2. Numerische Beispiele

Zur Erprobung des Verfahrens wird die Schalldämmwirkung eines mit fester Einspannung gelagerten Fensters der Größe $1\text{ m} \times 1\text{ m}$ untersucht, das einen $1\text{ m} \times 1\text{ m} \times 0,5\text{ m}$ großen Raum mit ansonsten schallweichen Wänden (Reflexionsfaktor = -1 und Absorptionsgrad = 0) vom Außenraum trennt. Die Belastung erfolgt durch einen konstanten Schalldruck der Größe $1 \frac{\text{N}}{\text{m}^2}$ auf der dem Fenster abgewandten Stirnfläche des Raumes. Die maßgebende Bauteilkenngröße ist das Schalldämm-Maß, das sich aus den Schalldruckverteilungen p_1 bzw. p_2 vor bzw. hinter dem Fenster zu $R = L_1 - L_2 = 20 \lg \frac{p_1}{p_2} \text{ [dB]}$ berechnen läßt, wobei mit L_1 und L_2 die Schalldruckpegel am Sende- bzw. Empfangsort bezeichnet werden.

Zum Vergleich wurden Berechnungen mit unterschiedlichen Dicken der Glasscheiben durchgeführt und die Gasfüllung des Scheibenzwischenraums (SZR) variiert (vgl. Abb.1). Die Berechnungen zeigen, dass Fenster mit einem edelgasgefüllten SZR (I) ein besseres Schalldämm-Maß aufweisen als Fenster mit Luftfüllung (III). Ebenso ist die schalldämmende Wirkung eines solchen luftgefüllten Fensters mit asymmetrischem Scheibenaufbau (III) besser als eines mit identischer Gesamtscheibendicke und SZR-Füllung aber symmetrischem Scheibenaufbau (II).

Diese akustischen Einflüsse konstruktiver Änderungen werden beim Entwurf von Isolierfenstern ausgenutzt und können mit dem vorgestellten Verfahren simuliert werden.

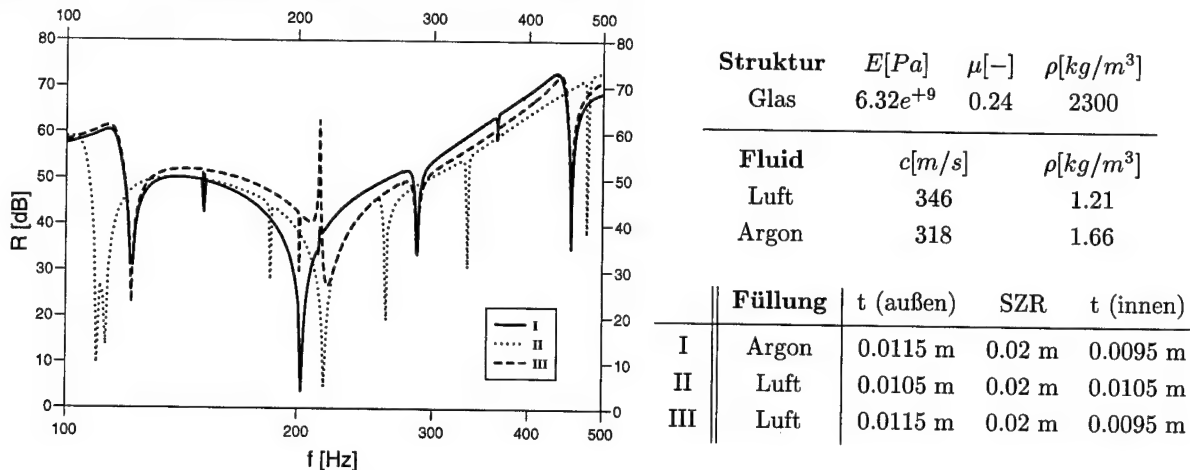


Abbildung 1: Einfluß des Fensteraufbaus bzw. der Zwischenraumfüllung auf das Schalldämm-Maß

3. References

- 1 O. C. ZIENKIEWICZ, R. L. TAYLOR: The finite element method; McGraw-Hill (1989).
- 2 F. FAHY: Sound and Structural Vibration; Academic Press (1985).
- 3 P. BETTRESS: Infinite Elemente; Penshaw Press (1992)
- 4 H. ANTES: Anwendungen d. Methode d. Randelemente in d. Elastodynamik und d. Fluidodynamik; B.G. Teubner (1988)

Adresse: DIPL.-ING. SABINE LANGER, PROF. DR.RER.NAT. HEINZ ANTES, Technische Universität Braunschweig, Institut für Angewandte Mechanik, Postfach 3329, D-38023 Braunschweig

SCHANZ, M.; CHENG, A.H.-D.

Wave propagation in a one-dimensional poroelastic column

In Biot's theory of porous media a second compressional wave, known as the slow wave, has been identified. An analytical solution in the Laplace transform domain is obtained showing clearly two compressional waves. For the special case of an inviscid fluid, a closed form exact solution in time domain is obtained using an analytical inverse Laplace transform. For the general case of a viscous fluid, solution in time domain is evaluated using the Convolution Quadrature Method of Lubich. Using properties of two different real materials, the wave propagating behavior, in terms of stress, pore pressure, displacement, and flux, are examined. Of most interest is the identification of second compressional wave and its sensitivity of material parameters.

1. Analytical solution

For a wide range of fluid infiltrated materials, such as water saturated soils, oil impregnated rocks, or air filled foams, Biot's theory of poroelasticity is used. Among the significant findings in this theory was the identification of three waves for a 3-d continuum, two compressional waves and one shear wave. This extra compressional wave, known as the slow wave, will here be confirmed numerically.

A 1-d poroelastic column of length ℓ is considered. It is assumed that the side walls and the bottom are rigid, frictionless and impermeable. Hence, the displacements normal to the surface are blocked and the column is otherwise free to slide parallel to the wall. At the top, the total stress σ and the pore pressure p and at the bottom the longitudinal displacement u and the flux q are prescribed. Due to these restrictions the governing set of differential equations is reduced to two scalar coupled ordinary differential equations in Laplace domain (denoted by $\hat{\cdot}$) with parameter s)

$$E\hat{u}_{,xx} - (\alpha - \beta)\hat{p}_{,x} - s^2(\varrho - \beta\varrho_f)\hat{u} = 0 \quad \frac{\beta}{s\varrho_f}\hat{p}_{,xx} - \frac{\phi^2 s}{R}\hat{p} - (\alpha - \beta)s\hat{u}_{,x} = 0, \quad (1)$$

with the abbreviation $\beta = \frac{\phi^2 s \kappa \varrho_f}{\phi^2 + s \kappa (\varrho_a + \phi \varrho_f)}$, the modulus E , the porosity ϕ , the bulk density $\varrho = \varrho_s(1 - \phi) + \phi \varrho_f$ and the permeability κ . The apparent mass density ϱ_a is assumed to be frequency independent as $\varrho_a = 0.66\phi \varrho_f$. Biot's effective stress coefficient α and R complete the set of material parameters.

Due to the neglected body forces this is a system of homogeneous ordinary differential equations with inhomogeneous boundary conditions. Such a system can be solved by the exponential ansatz $\hat{u}(x) = Ue^{\lambda s x}$, $\hat{p}(x) = Pe^{\lambda s x}$. This leads to an Eigenvalue problem where the characteristic equation has four complex roots, and, therefore, the complete solution of the homogeneous problem is $\hat{u}(x) = \sum_{i=1}^4 U_i e^{\lambda_i s x}$, $\hat{p}(x) = \sum_{i=1}^4 P_i e^{\lambda_i s x}$. Using the Eigenvectors a system of four equations for four unknowns is achieved. Finally, for stress boundary conditions $\hat{\sigma}(x = \ell) = -P_0$ and $\hat{u}(x = 0) = \hat{q}(x = 0) = \hat{p}(x = \ell) = 0$ the results for the displacement and the pressure is obtained

$$\hat{u}(s, x) = \frac{P_0}{E(d_1 \lambda_3 - d_3 \lambda_1)} \left[\frac{d_3 (e^{-\lambda_1 s(\ell-x)} - e^{-\lambda_1 s(\ell+x)})}{s(1 + e^{-2\lambda_1 s \ell})} - \frac{d_1 (e^{-\lambda_3 s(\ell-x)} - e^{-\lambda_3 s(\ell+x)})}{s(1 + e^{-2\lambda_3 s \ell})} \right] \quad (2)$$

$$\hat{p}(s, x) = \frac{P_0 d_1 d_3}{E(d_1 \lambda_3 - d_3 \lambda_1)} \left[\frac{(e^{-\lambda_1 s(\ell-x)} + e^{-\lambda_1 s(\ell+x)})}{1 + e^{-2\lambda_1 s \ell}} - \frac{(e^{-\lambda_3 s(\ell-x)} + e^{-\lambda_3 s(\ell+x)})}{1 + e^{-2\lambda_3 s \ell}} \right]. \quad (3)$$

Note, due to the dependence of β to the Laplace parameter s , the roots λ_i and consequently $d_i = \frac{E\lambda_i^2 - (\alpha - \beta)\lambda_i}{(\alpha - \beta)\lambda_i}$ are dependent of s . Therefore, an analytical inverse Laplace transform of the solutions above is in general not possible. However, if the damping due to the relative motion of the fluid and the solid is neglected, i.e. the permeability tends to infinity $\kappa \rightarrow \infty \Rightarrow \beta \approx \frac{\phi^2 \varrho_f}{\varrho_a + \phi \varrho_f}$, an analytical inverse Laplace transform can be found [2]. For an arbitrary value of κ a numerical inverse Laplace transformation is necessary. Here, it is preferable to take the 'Convolution Quadrature Method' proposed by LUBICH [1]. This method approximates a convolution integral numerically by a quadrature formula whose weights are determined with the help of the Laplace transformed impulse response functions $\hat{u}(s, x)$ and a linear multistep method.

2. Results

Next, wave propagation in the 1-d column is studied using the developed solutions. Two very different materials, a rock (Berea sandstone) and a soil (coarse sand) are chosen to represent a wide range of porous materials. To unambiguously capture the slow wave, we examine an 'infinite' column to avoid wave reflections. This is achieved by using a column length of $\ell = 1000 \text{ m}$ and a short observation time. In Fig. 1 we record the pressure, $p(t, x = 995 \text{ m})$, five meters behind the excitation point ($x = \ell = 1000 \text{ m}$). It is assumed that the time history of the stress loading is a Heaviside step function. Since this is the first time that we expect to observe such wave, it is compared with the

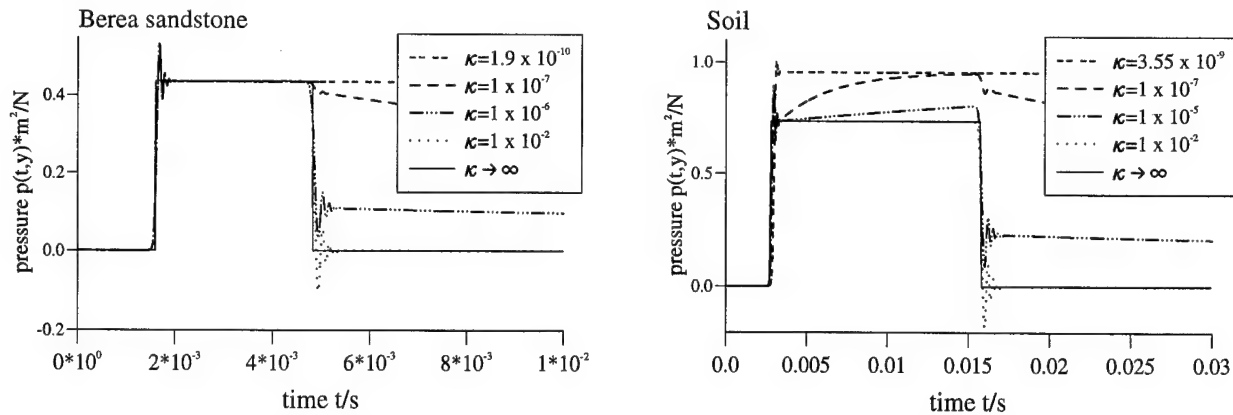


Figure 1: Pressure $p(t, x = 995 \text{ m})$ versus time for different values of κ compared with the analytical solution

exact time domain solution for $\kappa \rightarrow \infty$ [2], shown as solid lines in Fig. 1 for the two materials, to gain confidence. To make the comparison, an arbitrarily large value, $\kappa = 1 \times 10^{-2}$, is chosen in the Convolution Quadrature solution, with results plotted in dashed lines in Fig. 1. It is observed that, except for some fluctuations at wave fronts, which are generally unavoidable for all numerical inversion methods, the two solutions compare very well.

The phenomenon exhibited in Fig. 1 can be rationalized as follows. We first observe the arrival of the first wave at 5 m that causes the step jump. The second wave, arriving at a later time, is of negative amplitude and cancels exactly the first wave as indicated by the exact solution. The arrival time of the two waves is independent of κ as its limit has been taken.

To obtain and understand the solution of the realistic cases, we start to decrease κ values. Fig. 1 shows a sequence of reduction that lead to the real values. As κ decreases, we observe that both the amplitude and the arrival time of the waves are affected. The effect is strongest for the second wave. For some intermediate values of κ , we observe that when the second wave arrives, its amplitude is diminished. Hence the pressure does not drop to zero at the passage of the wave front. We also observe that the second wave is dispersive as it does not arrive as a sharp front with constant value in some cases. Rather, the pressure continues to decline as seen in some curves. Also, the comparison shows the different behavior of the two different materials on changing the permeability. For rock, the wave amplitude of the first wave is nearly independent from the permeability, contrary to the soil.

Summarizing, two compressional waves are clearly identified in the limiting case of an infinite permeability. For some intermediate permeability cases the second wave is also present. However, for the actual permeabilities of the tested materials the effect of the second wave vanishes after a short distance. This paper does not test all practical materials, natural and man-made. There exist some materials, particularly those with small fluid viscosity and large medium permeability, in which the second wave effect can be significant.

3. References

- 1 LUBICH, C.: Convolution Quadrature and Discretized Operational Calculus. I. Numerische Mathematik. **52** (1988), 129–145.
- 2 SCHANZ, M.; CHENG, A.H.-D.: Transient Wave Propagation in a One-Dimensional Poroelastic Column. Acta Mechanica. (submitted), 1999.

Addresses: MARTIN SCHANZ, Technical University Braunschweig, Institute of Applied Mechanics, P.O. Box 3329, 38023 Braunschweig, Germany
A.H.-D. CHENG, University of Delaware, Department of Civil & Environmental Engineering, Newark, Delaware 19716, USA

ZIEGLER, F.

THE 3-D DYNAMIC GREEN FUNCTIONS EXPANDED IN PLANE WAVES

Basic equations

The Helmholtz decomposition of the displacements in a homogeneous and isotropic solid yields the set of wave equations for P- and S-waves,

$$u = \text{grad } \phi + \text{curl } \psi, \quad \Delta \phi = c^{-2} \ddot{\phi}, \quad \Delta \psi = C^{-2} \ddot{\psi}, \quad \text{div } \psi = 0 \quad (1)$$

Furthermore the three components of stresses, given by Hooke's law enter the "internal" boundary value problems to be considered below

$$\sigma_{zz} = \lambda c^{-2} \ddot{\phi} + 2\mu \left(\frac{\partial^2 \phi}{\partial z^2} + \frac{\partial^2 \psi_y}{\partial x \partial z} - \frac{\partial^2 \psi_x}{\partial y \partial z} \right), \quad \sigma_{zx} = \mu \left[-C^{-2} \ddot{\psi}_y + 2 \left(\frac{\partial^2 \phi}{\partial x \partial z} - \frac{\partial^2 \psi_x}{\partial x \partial y} + \frac{\partial^2 \psi_y}{\partial x^2} \right) \right], \quad \sigma_{zy} = \mu \left[-C^{-2} \ddot{\psi}_x + 2 \left(\frac{\partial^2 \phi}{\partial y \partial z} - \frac{\partial^2 \psi_z}{\partial x \partial z} + \frac{\partial^2 \psi_x}{\partial z^2} \right) \right] \quad (2)$$

Vertical instant single force

Laplace-transformation in time, Fourier transformations with respect to the horizontal (x, y) coordinates, render the solution via the three conditions provided by the internal b. v. problem

$$z=0: \quad \bar{\sigma}_{zz}(\xi, \kappa, s) = -\frac{1}{2} \varepsilon_z Q_z \bar{f}(s), \quad u_x = u_y = 0 \quad (3)$$

in terms of the P- and S-wave potentials, expanded into plane waves and in the form of the Weyl-Sommerfeld integrals, the phase - time relationship has been indicated, note the emittance functions, see also [1] and [2],

$$\begin{aligned} \bar{\phi}^z(x, y, z, s) &= s^2 Q_z \bar{F}(s) \int_{-\infty}^{\infty} \int_{-\infty}^{\infty} S_P^z \exp(s g_P) d\xi d\kappa, \quad \bar{\psi}_j^z(x, y, z, s) = s^2 Q_z \bar{F}(s) \int_{-\infty}^{\infty} \int_{-\infty}^{\infty} S_{Sj}^z \exp(s g_S) d\xi d\kappa, \\ -t = g_P &= i\xi x + i\kappa y - \eta |z - z_0|, \quad \eta = \sqrt{c^{-2} + \xi^2 + \kappa^2}, \quad -t = g_S = i\xi x + i\kappa y - \zeta |z - z_0|, \quad \zeta = \sqrt{C^{-2} + \xi^2 + \kappa^2}, \quad j = x, y \\ \bar{F}(s) &= \bar{f}(s) / 8\pi^2 s^2 \rho, \quad S_P^z = -\varepsilon_z, \quad S_{Sx}^z = -\frac{i\kappa}{\zeta}, \quad S_{Sy}^z = \frac{i\xi}{\zeta}, \quad \bar{\psi}_z^z(x, y, z, s) = 0 \end{aligned} \quad (4)$$

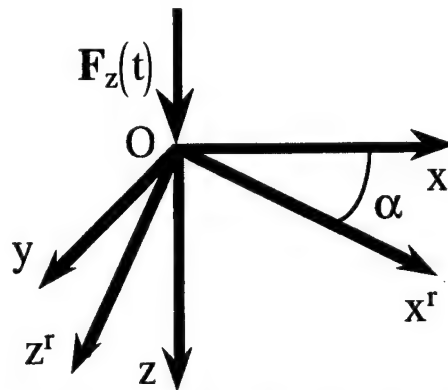


Fig. 1 Vertical force in infinite space. Rotation of coordinates about the y -axis

The potentials, Eq. (4), are easily referred to rotated coordinates, see Fig. (1), by enforcing the following invariance conditions for the plane wave amplitudes and phases, P or S waves are understood,

$$S d\xi d\kappa = S^r d\xi^r d\kappa^r, \quad -t = g = g^r = i\xi x + i\kappa y - (\eta, \zeta) |z| = i\xi^r x^r + i\kappa^r y - (\eta, \zeta^r) |z^r| \quad (5)$$

However, the transformed 3-dimensional solution cannot be interpreted to represent the potentials of the counter-rotated (horizontal) force by putting $\alpha = \pi/2$. Violation of the condition of axisymmetry is the major reason, - the interpretation works for the 2-dimensional case of line loads, see again [1].

Horizontal instant single forces

The instantaneous forces are considered in the x - and y -directions and the internal b. v. problems yield alternated emittance functions, listed in Table 1,

$$z=0: \bar{\sigma}_{zx}(\xi, \kappa, s) = -\frac{1}{2} \varepsilon_z Q_x \tilde{f}(s), \quad u_z = u_y = 0, \quad z=0: \bar{\sigma}_{zy}(\xi, \kappa, s) = -\frac{1}{2} \varepsilon_z Q_y \tilde{f}(s), \quad u_z = u_x = 0. \quad (6)$$

Putting alternatively $j = x, y$ in the displacement potentials, note the coupling by the characteristic determinants,

$$\bar{\phi}^j(x, y, z, s) = s^2 Q_j \tilde{F}(s) \int_{-\infty}^{\infty} \int_{-\infty}^{\infty} S_{Sj}^j \exp(s g_S) d\xi d\kappa, \quad \bar{\psi}_x^j(x, y, z, s) = s^2 Q_x \tilde{F}(s) \int_{-\infty}^{\infty} \int_{-\infty}^{\infty} S_{Sx}^j \exp(s g_S) d\xi d\kappa \quad (7)$$

$$\bar{\psi}_y^j(x, y, z, s) = s^2 Q_y \tilde{F}(s) \int_{-\infty}^{\infty} \int_{-\infty}^{\infty} S_{Sy}^j \exp(s g_S) d\xi d\kappa, \quad \bar{\psi}_z^j(x, y, z, s) = s^2 Q_x \tilde{F}(s) \int_{-\infty}^{\infty} \int_{-\infty}^{\infty} S_{Sz}^j \exp(s g_S) d\xi d\kappa \quad (8)$$

and considering Table 1 renders the desired solutions. Note the vector potential with all three components present.

Table 1 Emittance functions of horizontal forces

$$\begin{aligned} S_P^x &= C^{-2} \frac{i\xi}{\eta} \frac{\eta}{\Delta_x}, \quad S_{Sx}^x = \varepsilon_z \xi \kappa \frac{\eta - \zeta}{\Delta_x}, \quad S_{Sy}^x = \varepsilon_z & S_P^y &= C^{-2} \frac{i\kappa}{\eta} \frac{\eta}{\Delta_y}, \quad S_{Sx}^y = -\varepsilon_z, \quad S_{Sy}^y = -\varepsilon_z \xi \kappa \frac{\eta - \zeta}{\Delta_y} \\ S_{Sz}^x &= i\kappa \frac{\eta \zeta - \xi^2 - \kappa^2}{\Delta_x}, \quad \Delta_x = \eta(\zeta^2 - \xi^2) - \zeta \kappa^2 & S_{Sz}^y &= -i\xi \frac{\eta \zeta - \xi^2 - \kappa^2}{\Delta_y}, \quad \Delta_y = \eta(\zeta^2 - \kappa^2) - \zeta \xi^2 \end{aligned}$$

The oblique instant force

Since a common time source function is understood in the above given solutions, the potentials are summed to render the so called source ray. We note exemplary the emitted P-wave

$$\bar{\phi}(x, y, z, s) = s^2 \tilde{F}(s) \int_{-\infty}^{\infty} \int_{-\infty}^{\infty} S_P \exp(s g_P) d\xi d\kappa, \quad S_P = Q_x \frac{i\xi}{C^2 \Delta_x} - Q_y \frac{i\kappa}{C^2 \Delta_y} - Q_z \varepsilon_z \quad (9)$$

The oblique surface force

Buried source and receiver, where $z - z_0 > 0$, in the half-space are considered first with source ray, Eq. (11), and reflected rays, (first segment pointing upwards) P_p and P_s , superposed. In that solution, the limit of the source depth to zero is performed to render the proper emittance functions of the surface force, the reflection coefficients for potentials are derived in [3],

$$\bar{\phi}_p = \bar{\phi}_0 + \lim_{z_0 \rightarrow 0} \left(\bar{\phi}_{P_p} + \sum_k \bar{\phi}_{S,kp} \right), \quad S_p = S_{0p} + S_P R^{Pp} + \sum_k S_{S,k} R^{S,kp}, \quad k = x, y, z \quad (10)$$

$$\bar{\psi}_{sj} = \bar{\psi}_{0j} + \lim_{z_0 \rightarrow 0} \left(\bar{\psi}_{P_sj} + \sum_k \bar{\psi}_{S,k sj} \right), \quad S_{sj} = S_{0sj} + S_P R^{Psj} + \sum_k S_{S,k} R^{S,k sj}, \quad j = x, y, z \quad (11)$$

Similarly, the source in the interface between a surface layer and an underlying dissimilar half space is considered.

References

- 1 PAO, Y.-H.; GAJEWSKI, R. R.: The generalized ray theory and transient responses of layered elastic solids. In: MASON, W. P.; THURSTON, R. N. (eds.): *Physical Acoustics* 13. Academic Press, New York 1977, Ch. 6, pp. 183-265.
- 2 BOREJKO, P.; ZIEGLER, F.: Pulsed asymmetric point force loading of a layered half-space. In: GURAN, A.; BOSTRÖM, A.A.; LEROY, O.; MAZE, G. (eds.): *Acoustic Interactions with Submerged Elastic Structures*, Part 4, Ch. 11. World Scientific, Singapore (in press)
- 3 BOREJKO, P.: Reflection and transmission coefficients for three-dim. plane waves. *Wave Motion* 24 (1996), pp. 371-393

Address: ZIEGLER, F., Techn. Universität Wien, Wiedner Hauptstr. 8-10/201, A-1040 Wien, Austria

CHEŁMIŃSKI, KRZYSZTOF

On Noncoercive Models in the Theory of Inelastic Deformations with Internal Variables

In the theory of inelastic deformations with internal variables, H.-D. Alber has defined an important class of models called models of monotone type. For the subclass containing coercive models, the existence of global in time solutions is known. Unfortunately, in practice the coerciveness condition fails very often. Therefore we consider here noncoercive problems. In this note we study a subclass of models of monotone type for which the so-called coercive approximation converges to a solution of the original noncoercive problem.

1. Introduction and the existence result for coercive models

Let $\Omega \subset \mathbb{R}^3$ be a bounded region with the smooth boundary $\partial\Omega$. The system of equations modelling inelastic deformations of metals can be written in the form:

$$\rho v_t = \operatorname{div}_x \mathcal{D}(\varepsilon - Bz) + F, \quad \varepsilon_t = \frac{1}{2}(\nabla_x v + \nabla_x^T v), \quad z_t \in g\left(-\rho \nabla_z \psi(\varepsilon, z)\right) \quad (\text{MS})$$

where $v : \Omega \times (0, T) \rightarrow \mathbb{R}^3$ is the velocity field, $\rho > 0$ is the constant mass density, ε is the strain tensor, $\mathcal{D} : \mathcal{S}^3 \rightarrow \mathcal{S}^3 = \mathbb{R}_{\text{sym}}^{3 \times 3}$ denotes the elasticity tensor which we assume to be constant, symmetric and positive definite. $z = (\varepsilon^p, \bar{z}) : \Omega \times (0, T) \rightarrow \mathbb{R}^N$ is the vector of internal variables containing the plastic strain tensor ε^p . The operator $Bz = B(\varepsilon^p, \bar{z}) = \varepsilon^p$ is the projector of the vector z on the ε^p -direction. $g : D(g) \subset \mathcal{S}^3 \times \mathbb{R}^N \rightarrow \mathcal{P}(\mathbb{R}^N)$ is the given constitutive multifunction, $F : \Omega \times (0, T) \rightarrow \mathbb{R}^3$ describes external forces acting on the material and finally $\psi(\varepsilon, z)$ is the free energy function associated with the model. The system (MS) is considered with the Dirichlet or the Neumann boundary condition

$$v(x, t) = g_D(x, t), \quad \text{or} \quad T(x, t) n(x) = g_N(x, t) \quad \text{for } x \in \partial\Omega \text{ and } t \geq 0$$

and the initial conditions are: $v(x, 0) = v^0(x)$, $\varepsilon(x, 0) = \varepsilon^0(x)$, $z(x, 0) = z^0(x)$, compatible with the boundary data (where $T = \mathcal{D}(\varepsilon - Bz)$ denotes the stress tensor).

Definition 1. We say that the model (MS) is of **monotone type** if the constitutive multifunction $g : D(g) \subset \mathbb{R}^N \rightarrow \mathcal{P}(\mathbb{R}^N)$ is monotone and additionally satisfies $0 \in g(0)$, and the free energy function is in the form

$$\rho \psi(\varepsilon, z) = \frac{1}{2} \mathcal{D}(\varepsilon - Bz) \cdot (\varepsilon - Bz) + \frac{1}{2} Lz \cdot z$$

where B is the projector on the ε^p -direction and $L \in \mathbb{R}_{\text{sym}}^{N \times N}$ is positive semi-definite. Moreover, L is so chosen that the symmetric matrix $B^T D B + L$ is positive definite ($\Rightarrow \ker L \subset \text{range } B$ if $\text{range } L \supset \ker B$).

Let us denote by $\langle \cdot, \cdot \rangle_{\mathcal{E}}$ the following bilinear form generated by the total energy function \mathcal{E}

$$\langle (v, \varepsilon, z), (\bar{v}, \bar{\varepsilon}, \bar{z}) \rangle_{\mathcal{E}} = \int_{\Omega} (\rho v \cdot \bar{v} + [\mathcal{D}(\varepsilon - Bz)] \cdot (\bar{\varepsilon} - B\bar{z}) + Lz \cdot \bar{z}) dx.$$

If the bilinear form $\langle \cdot, \cdot \rangle_{\mathcal{E}}$ induces a scalar product in $L^2(\Omega; \mathbb{R}^3 \times \mathcal{S}^3 \times \mathbb{R}^N)$ then we say that the problem (MS) is **coercive**. In [1] and [3] is proved the following existence result:

Theorem 1. If the problem (MS) is coercive and the monotone multifunction $g : D(g) \subset \mathbb{R}^N \rightarrow \mathcal{P}(\mathbb{R}^N)$ is maximal monotone then the system (MS) possesses global large solutions to all initial data from the L^2 -domain of the operator generated by the right-hand side of the system (MS).

2. Safe-load condition and the main result

Following [2], for noncoercive models we define the coercive approximation and require that the sequence $(v^k, \varepsilon^k, z^k)$ satisfies the system

$$v_t^k = \operatorname{div}_x \mathcal{D}\left(\varepsilon^k - Bz^k + \frac{1}{k} \varepsilon^k\right) + F, \quad \varepsilon_t^k = \frac{1}{2}(\nabla v^k + \nabla^T v^k), \quad z_t^k \in g\left(-\rho \nabla_z \psi^k(\varepsilon^k, z^k)\right) \quad (\text{CA})$$

with $v^k(x, t) = g_D(x, t)$ or with $\mathcal{D}(\varepsilon^k - Bz^k + \frac{1}{k}\varepsilon^k)(x, t) \cdot n(x) = g_N(x, t)$ for $x \in \partial\Omega$ and $t \geq 0$, and with the initial conditions $v^k(0) = v_k^0$, $\varepsilon^k(0) = \varepsilon_k^0$, $z^k(0) = z_k^0$. The quadratic form ψ^k is now defined by

$$\rho\psi^k(\varepsilon^k, z^k) = \frac{1}{2}\mathcal{D}(\varepsilon^k - Bz^k) \cdot (\varepsilon^k - Bz^k) + \frac{1}{2}Lz^k \cdot z^k + \frac{1}{2k}\mathcal{D}\varepsilon^k \cdot \varepsilon^k.$$

Definition 2. We say that g_D or g_N satisfies the **safe-load condition** if the problem

$$\rho v_t^* = \operatorname{div}_x \mathcal{D}(\varepsilon^* - Bz^*), \quad \varepsilon_t^* = \frac{1}{2}(\nabla_x v^* + \nabla_x^T v^*), \quad z_t^* = 0,$$

with $v^* = g_D$, or $\mathcal{D}(\varepsilon^* - Bz^*) \cdot n = g_N$ on $\partial\Omega$, and with the initial conditions $(v^*(0), \varepsilon^*(0), z^*(0)) = (v_*^0, \varepsilon_*^0, z_*^0)$ compatible with the boundary data, possesses a solution $(v^*, \varepsilon^*, z^*)$ satisfying:

$$\left. \begin{aligned} \exists \delta > 0 \quad \forall |\sigma| < \delta \quad (-\rho \nabla_z \psi(\varepsilon^*, z^*) + \sigma) \in D(g) \quad \text{and} \\ \forall |\sigma| < \delta \quad \exists z_\sigma^* \in g(-\rho \nabla_z \psi(\varepsilon^*, z^*) + \sigma) \quad \left\| \sup_{|\sigma| < \delta} |z_\sigma^*| \right\|_{L^2} < C(T). \end{aligned} \right\} (SLC)$$

Theorem 2. $(SLC) \Rightarrow \|z_t^k\|_{L^\infty(L^1)} < C(T)$.

Proof. By the monotonicity of g

$z_t^k \cdot \sigma \leq z_t^k \cdot (-\rho \nabla_z \psi^k(\varepsilon^k, z^k) + \rho \nabla_z \psi(\varepsilon^*, z^*) - z_\sigma^* \cdot (-\rho \nabla_z \psi^k(\varepsilon^k, z^k) + \rho \nabla_z \psi(\varepsilon^*, z^*) - \sigma))$. Next we take the supremum with respect to σ and use the energy estimate. For more details see [3].

Let us assume for simplicity that $\ker L = \operatorname{range} B$. Then the limit functions satisfy the following limit problem:

$$\begin{aligned} \rho v_t &= \operatorname{div}_x \mathcal{D}(\varepsilon - Bz) + F \quad \text{in } L^\infty(L^2) & \varepsilon_t &= \frac{1}{2}(\nabla v + \nabla^T v) \quad \text{in } L^\infty(\mathcal{M}_{\text{sym}}^{3 \times 3}) \\ \varepsilon_t^p &= w - \lim_{k \rightarrow \infty} \varepsilon_t^{p,k} = \chi^p \quad \text{in } L^\infty(\mathcal{M}_{\text{sym}}^{3 \times 3}) & \tilde{z}_t &= w - \lim_{k \rightarrow \infty} \tilde{z}_t^k = \tilde{\chi} \quad \text{in } L^\infty(L^2). \end{aligned}$$

where $\mathcal{M}_{\text{sym}}^{3 \times 3}$ denotes the space of bounded Radon measures with values in the space \mathcal{S}^3 . Hence it only remains to prove that $(\chi^p, \tilde{\chi})$ satisfies the nonlinear inelastic constitutive equation. First we improve our convergence result.

Theorem 3. For models of monotone-gradient type, $(g(z) = \partial M(z))$ and $M : \mathbb{R}^N \rightarrow \mathbb{R}_+$ is convex, the sequence $\{\nabla_z \psi^k(\varepsilon^k, z^k)\}$ converges strongly to $\nabla_z \psi(\varepsilon, z)$ in $L^\infty(L^2)$.

Now we have to define the product $(\varepsilon_t^p, T) \Leftrightarrow$ to define $(\varepsilon_t - \mathcal{D}^{-1}T_t, T) \Leftrightarrow$ to define (ε_t, T) :

$$\left\langle \frac{1}{2}(\nabla v + \nabla^T v) \cdot T, \phi \right\rangle \stackrel{\text{df}}{=} - \int_\Omega \operatorname{div} T \cdot v \phi \, dx - \int_\Omega T \cdot (v \otimes \nabla \phi) \, dx$$

for $\phi \in C_0^\infty(\Omega; \mathbb{R})$. Thus we have defined the product (ε_t, T) as a distribution ($T \in L^2(\operatorname{div})$ and $v \in L^2$).

Theorem 4. Suppose that the model (MS) is of monotone-gradient type with a maximal monotone multifunction g and the given boundary data satisfies the safe-load condition, then $\forall (\omega^p, \tilde{\omega}) \in g((w^p, \tilde{w}))$ the expression

$$(\varepsilon_t^p - \omega^p, \mathcal{D}(\varepsilon - \varepsilon^p) - w^p) - (\tilde{z}_t - \tilde{\omega}, \tilde{L}\tilde{z} + \tilde{w})$$

is a nonnegative scalar distribution. Hence the inelastic constitutive equation is satisfied in the sense of distributions.

Acknowledgements

This work was supported by the Sonderforschungsbereich 298.

3. References

- 1 ALBER, H.-D.: Materials with Memory; Lecture Notes in Math. **1682** Springer, Berlin Heidelberg New York, (1998).
- 2 CHELMIŃSKI, K.: Coercive limits for a subclass of monotone constitutive equations in the theory of inelastic material behaviour of metals; Roczniki PTM App. Math. **40** (1997), 41–81.
- 3 CHELMIŃSKI, K., GWIAZDA, P.: Nonhomogeneous initial-boundary value problems for coercive and self-controlling models of monotone type; Fach. Math. TU Darmstadt Preprint Nr. **2059**, submitted to Contin. Mech. Thermodyn.

Address: DR. HAB. KRZYSZTOF CHELMIŃSKI, Technische Universität Darmstadt, Fachbereich Mathematik, Schlossgartenstrasse 7, 64289 Darmstadt, Germany

GASSER, I.

The Small Debye Length Limit in a Hydrodynamic Model for Charged Fluids

The small Debye length limit is studied in a hydrodynamic model for charged fluids. The problem is studied on two different time scales. The limiting problems are identified.

1. Introduction

We consider a bipolar hydrodynamic model (HD) for charged fluids in one space dimension. This kind of models are used in semiconductor physics, plasma physics, etc. (see MARKOWICH ET AL. or SITENKO-MALNEV). Denoting by $n, p, j, g, P(n), Q(p)$ the charge densities, current densities and pressures of the two - negatively and positively charged - fluids, respectively, the scaled equations of the bipolar HD model are given in $x \in \mathbb{R}, t \geq 0$ by

$$\begin{aligned} n_t + j_x &= 0 & p_t + g_x &= 0 \\ j_t + (j^2/n + P(n))_x &= nE - j/\tau & g_t + (g^2/p + Q(p))_x &= -pE - g/\tau \\ \lambda^2 E_x &= n - p - C, \end{aligned} \quad (1)$$

where E is the electric field satisfying the Poisson equation, which is the only coupling between the two fluids. $C = C(x)$ is a given fixed background charge. λ is the so called Debye length. We prescribe initial conditions

$$n(t=0, x) = n_0(x), \quad j(t=0, x) = j_0(x), \quad p(t=0, x) = p_0(x), \quad g(t=0, x) = g_0(x). \quad (2)$$

We assume a damping mechanism of relaxation type with relaxation time τ . In the semiconductor context the relaxation term models the influence of the underlying semiconductor lattice. In the case of a plasma the relaxation term describes the influence of the non-ionised part of the fluid. Global in time existence of weak solutions for this model was obtained by NATALINI.

Typically, the scaled quantities τ and λ are very small in many standard scalings. Therefore, in the following we consider the limits $\tau \rightarrow 0, \lambda \rightarrow 0$ on two significant time scales. In both cases we assume the relation $\lambda^2 = \tau^{1+\alpha}$ with $-1 < \alpha < 1$.

2. The small Debye length limit

The first scaling we consider is given by

$$\begin{aligned} s_1 &= \frac{t}{\tau^\alpha}, & J^\tau(s_1, x) &= \tau^\alpha j(\tau^\alpha s_1, x), & G^\tau(s_1, x) &= \tau^\alpha g(\tau^\alpha s_1, x), \\ F^\tau(s_1, x) &= \tau^{1+\alpha} E(\tau^\alpha s_1, x), & n^\tau(s_1, x) &= n(\tau^\alpha s_1, x), & p^\tau(s_1, x) &= p(\tau^\alpha s_1, x), \end{aligned} \quad (3)$$

where the superscript τ denotes the dependence on the parameter. The rescaled equation read

$$\begin{aligned} n_{s_1}^\tau + J_x^\tau &= 0 \\ \tau^{1-\alpha} J_{s_1}^\tau + (\tau^{1-\alpha} \frac{(J^\tau)^2}{n^\tau} + \tau^{1+\alpha} P(n^\tau))_x &= n^\tau F^\tau - J^\tau \\ p_{s_1}^\tau + G_x^\tau &= 0 \\ \tau^{1-\alpha} G_{s_1}^\tau + (\tau^{1-\alpha} \frac{(G^\tau)^2}{p^\tau} + \tau^{1+\alpha} Q(p^\tau))_x &= -p^\tau F^\tau - G^\tau \\ F_x^\tau &= n^\tau - p^\tau - C. \end{aligned} \quad (4)$$

We Assume τ independent initial data and perform the limit $\tau \rightarrow 0$. The (formal) limit problem - which is a short (long) time approximation for positive (negative) values of α - is given by

$$n_{s_1} = -(nF)_x, \quad p_{s_1} = (pF)_x, \quad F_x = n - p - C, \quad (5)$$

with initial data n_0 and p_0 for n and p . Here n, p, F denote the limits of n^τ, p^τ, F^τ as $\tau \rightarrow 0$. Alternatively, the limit system can be written as inhomogeneous (inviscid) Burgers equation

$$F_{s_1} + \left(\frac{F^2}{2}\right)_x = -FC. \quad (6)$$

In GASSER-MARCATI-1 this limit is justified rigorously in the setting of weak entropy solutions for values $\gamma_n = \gamma_p > 2$.

3. The quasi-neutral limit

The second scaling we consider is given by

$$s_2 = \tau t, \quad J^\tau(s_2, x) = \frac{j(\frac{s_2}{\tau}, x)}{\tau}, \quad G^\tau(s_2, x) = \frac{g(\frac{s_2}{\tau}, x)}{\tau}, \quad n^\tau(s_2, x) = n(\frac{s_2}{\tau}, x), \quad p^\tau(s_2, x) = p(\frac{s_2}{\tau}, x). \quad (7)$$

This scaling corresponds to a long time analysis. For $C \equiv 0$ The rescaled equations read

$$\begin{aligned} n_{s_2}^\tau + J_x^\tau &= 0 \\ \tau^2 J_{s_2}^\tau + (\tau^2 \frac{(J^\tau)^2}{n^\tau} + P(n^\tau))_x &= n^\tau E^\tau - J^\tau \\ p_{s_2}^\tau + G_x^\tau &= 0 \\ \tau^2 G_{s_2}^\tau + (\tau^2 \frac{(G^\tau)^2}{p^\tau} + Q(p^\tau))_x &= -p^\tau E^\tau - G^\tau \\ \tau^{1+\alpha} E_x^\tau &= n^\tau - p^\tau. \end{aligned} \quad (8)$$

In this scaling the limit $\tau \rightarrow 0$ is a quasi-neutral limit, since the two differently charged fluid in the limit become a single neutral fluid. The formal limit problem is given by the nonlinear diffusion equation

$$w_{s_2} = \frac{1}{2}(P(w) + Q(w))_{xx}, \quad w(s_2 = 0, x) = \frac{n_0(x) + p_0(x)}{2}, \quad (9)$$

where w denotes the limits of n^τ and p^τ , which are the same due to the Poisson equation. This limit is known to be very delicate. The only results regarding quasi-neutral limits in hydrodynamic models concern the limit for classical solutions given in CORDIER-GRENIER or special traveling wave solutions in CORDIER-DEGOND-MARKOWICH-SCHMEISER. In GASSER-MARCATI-2 the result is performed for general weak entropy solutions.

Acknowledgements

The author acknowledges partial support from the european TMR network Asymptotic Methods in Kinetic Theory (contract number ERB FMRX CT97 0157).

4. References

- 1 CORDIER, S., GRENIER, E.: Quasineutral limit of Euler-Poisson systems arising from plasma physics. Preprint LAN R96030, Université Paris 6 (1996).
- 2 CORDIER, S., DEGOND, P., MARKOWICH, P.A., SCHMEISER, C.: Quasineutral limit of travelling waves for the Euler-Poisson model. in Gary (ed.), Mathematical and numerical aspects of wave propagation. Proceedings of the third international conference, Mandelieu-La Napoule, France, April 24-28, (1995), 724-733.
- 3 GASSER, I.: The Initial Time Layer Problem and the Quasineutral Limit in a Nonlinear Drift Diffusion Model for Semiconductors. To appear in Nonlin. Diff. Eq. Appl. NoDEA (2000).
- 4 GASSER, I., MARCATI, P., 1: The Combined Relaxation and Vanishing Debye Length Limit in the Hydrodynamic Model for Semiconductors. Preprint DMPA 04-00, Università degli Studi dell'Aquila (2000).
- 5 GASSER, I., MARCATI, P., 2: In preparation (2000).
- 6 MARKOWICH, P.A., RINGHOFER, C., SCHMEISER, C.: Semiconductor Equations. Springer, Wien (1990).
- 7 NATALINI, R.: The Bipolar Hydrodynamic Model for Semiconductors and the Drift-Diffusion Equations, J. of Math. Anal. and Appl. 198 (1996), 262-281.
- 8 SITENKO, A., MALNEV, V.: Plasma Physics Theory. Chapman & Hall, London (1995).

Addresses: DR. GASSER INGENUIN, Fachbereich Mathematik, Universität Hamburg, Bundesstrasse 55, 20146 Hamburg, Germany.

GWIAZDA, PIOTR

On the Model Chan-Bodner-Lindholm in the Theory of Inelastic Deformation

We prove global in time existence and uniqueness of large solutions for a problem in the nonlinear theory of inelastic deformations with internal variables for nonhomogeneous boundary conditions. The proof is based on the nonlinear nonautonomous semigroup method.

1. Introduction

We shall consider the dynamic problem for a system of equations modelling the non-elastic deformation of metal. The model proposed by K.S. Chen, S.R. Bodner, U.S. Lindholm [2] is an extension of the Bodner-Partom model [1]. The extension is based on introducing directional hardening properties. All main results proved in this article are also true for the Bodner-Partom model (which is a special case of our model). The system of equations, which we consider consists of linear partial differential equations (the balance of momentum) and nonlinear ordinary differential equations for internal variables (constitutive equations describing the dependence of the material's properties on its deformation history). The set of internal variables consists of two matrix variables (ε_p, β) and one scalar variable y . ε_p describes the plastic part of the deformation tensor. β is the directional hardening and y is the isotropic hardening. We consider materials with constant density $\rho = 1$ and use the assumption of small deformation, which allows the balance of momentum to be linearized. We assume that the stress-elastic strain relation is generated by a bilinear, strictly positive, symmetric form. The problem which we study can then be written in the form: Let $\Omega \subset \mathbb{R}^3$ be an open, connected set with smooth boundary $\partial\Omega$, find the velocity field $v : \Omega \times \mathbb{R}_+ \rightarrow \mathbb{R}^3$, the stress tensor $T : \Omega \times \mathbb{R}_+ \rightarrow \mathbb{R}_{\text{sym}}^{3 \times 3}$ and the internal variables $(\varepsilon_p, \beta, y) : \Omega \times \mathbb{R}_+ \rightarrow \mathbb{R}_{\text{sym}}^{3 \times 3} \times \mathbb{R}_{\text{sym}}^{3 \times 3} \times \mathbb{R}_+$ which satisfy the following system of equations

$$\begin{aligned} \frac{\partial}{\partial t} v(x, t) &= \operatorname{div}_x T(x, t) + F(x, t) \\ \frac{\partial}{\partial t} \varepsilon(x, t) &= \frac{1}{2} (\nabla_x v(x, t) + (\nabla_x v(x, t))^T) \\ \frac{\partial}{\partial t} \varepsilon_p(x, t) &= \mathcal{G} \left(\frac{|\sigma(x, t)|}{y_c(x, t)} \right) \frac{\sigma(x, t)}{|\sigma(x, t)|} \\ \frac{\partial}{\partial t} y(x, t) &= \gamma(y(x, t)) \mathcal{G} \left(\frac{|\sigma(x, t)|}{y_c(x, t)} \right) |\sigma(x, t)| - A\delta(y(x, t)) \\ \frac{\partial}{\partial t} \beta(x, t) &= m \left(r \frac{\sigma(x, t)}{|\sigma(x, t)|} - \beta(x, t) \right) \mathcal{H} \left(\frac{|\sigma(x, t)|}{y_c(x, t)} \right) - B\eta(|\beta(x, t)|) \frac{\beta(x, t)}{|\beta(x, t)|}. \end{aligned} \quad (\text{CBL})$$

Here $T = \mathcal{D}(\varepsilon - \varepsilon_p)$, $\sigma = T - \frac{1}{3}(\operatorname{tr} T) \cdot I$ is the stress deviator, $\mathcal{G}, \mathcal{H}, \eta : \mathbb{R}_+ \rightarrow \mathbb{R}_+$, $\gamma : D(\gamma) \subset \mathbb{R}_+ \rightarrow \mathbb{R}_+$, $\delta : D(\delta) \subset \mathbb{R}_+ \rightarrow \mathbb{R}_+$ are given functions and $A, B, m, r \geq 0$ are given material constants, moreover the constitutive equation for $y_c = y + \frac{\sigma}{|\sigma|} \beta$ holds.

In the present paper we impose the Dirichlet or Neumann nonhomogeneous boundary condition

$$v(x, t)|_{\partial\Omega} = (g_D)_t(x, t) \text{ or } T(x, t) \cdot n(x)|_{\partial\Omega} = g_N(x, t) \quad (\text{BC})$$

and initial conditions

$$u(x, 0) = u^0(x), \quad \frac{\partial}{\partial t} u(x, 0) = u^1(x), \quad \varepsilon_p(x, 0) = \varepsilon_p^{(0)}(x), \quad y(x, 0) = y^{(0)}(x), \quad \beta(x, 0) = \beta^{(0)}(x). \quad (\text{IC})$$

Now we shall describe properties of the functions $\mathcal{G}, \mathcal{H}, \gamma, \delta, \eta$, which yield all nonlinearities to the system. To prove our theorems we need that the functions $\mathcal{G}, \mathcal{H}, \gamma, \delta, \eta$ satisfy:

Assumptions

$$1. \mathcal{G}(p), \mathcal{H}(p) \in \mathbb{C}^2(\mathbb{R}_+) \cap \mathbb{C}^0(\mathbb{R}) \text{ (for all } p < 0 \mathcal{G}(p) = 0 \text{ and } \mathcal{H}(p) = 0), \quad \frac{\mathcal{G}(p)}{p}, \frac{\mathcal{H}(p)}{p} \in \mathbb{C}^2(\mathbb{R}_+, \mathbb{R}_+) \quad (\text{A1})$$

$$2. \exists_{g>0, h>0} \forall_{p \in IR_+} \mathcal{G}(p) < g, \mathcal{H}(p) < h \text{ (}\mathcal{G}, \mathcal{H} \text{ are bounded)}, \quad (A2)$$

$$3. \forall_{p \in IR_+} \mathcal{G}'(p) \geq 0, \mathcal{H}'(p) \geq 0 \text{ (}\mathcal{G}, \mathcal{H} \text{ are nondecreasing)}. \quad (A3)$$

$$4. \exists_{g'>0, h'>0} \forall_{p \in IR_+} \mathcal{G}'(p)p^2 < g', \mathcal{H}'(p)p < h', \quad (A4)$$

$$5. D(\gamma) = D(\delta) = [y_2, y_1] \text{ where } 0 < y_2 < y_1 \text{ and } \gamma(p), \delta(p) \text{ are } C^\infty(D(\gamma), IR_+) \text{ functions}, \quad (A5)$$

$$6. D(\eta) = [0, R] \text{ and } \eta(p) \text{ is } C^\infty(D(\eta), IR_+) \quad (A6)$$

$$7. \forall_{p \in [y_2, y_1]} \gamma'(p) \leq 0 \text{ (}\gamma \text{ is nonincreasing)}, \quad (A7)$$

$$8. \gamma(y_2) > \gamma(y_1) = 0, \delta(y_2) = 0 \text{ and } \forall_{p \in (y_2, y_1]} \delta(p) > 0, \quad (A8)$$

$$9. \forall_{p \in D(\eta)} \eta(p) > 0. \quad (A9)$$

2. Main result

To consider our problem as the abstract problem in the Hilbert space:

$$H = \{(v, \varepsilon, \varepsilon_p, y, \beta) \mid v \in \mathbb{L}^2(\Omega; IR^3), \varepsilon \in \mathbb{L}^2(\Omega; IR^{3 \times 3}_{sym}), \varepsilon_p \in \mathbb{L}^2(\Omega; IR^{3 \times 3}_{sym}), y \in \mathbb{L}^2(\Omega; IR^1), \beta \in \mathbb{L}^2(\Omega; IR^{3 \times 3}_{sym})\},$$

we define the scalar product:

$$\langle (v, \varepsilon, \varepsilon_p, y, \beta), (\bar{v}, \bar{\varepsilon}, \bar{\varepsilon}_p, \bar{y}, \bar{\beta}) \rangle_H = \int_{\Omega} v \cdot \bar{v} + [D(\varepsilon - \varepsilon_p)] \cdot (\bar{\varepsilon} - \bar{\varepsilon}_p) + \varepsilon_p \cdot \bar{\varepsilon}_p + y \cdot \bar{y} + \beta \cdot \bar{\beta} \, dx.$$

Definition 1. We say that the initial data are admissible if and only if: $(v^{(0)}, \varepsilon^{(0)}, \varepsilon_p^{(0)}, y^{(0)}, \beta^{(0)}) \in H$, $(\operatorname{div}_x \mathcal{D}(\varepsilon^{(0)} - \varepsilon_p^{(0)}), \nabla_x v^{(0)} + (\nabla_x v^{(0)})^T) \in \mathbb{L}^2(\Omega; IR^3 \times IR^{3 \times 3})$, and initial data are compatible with boundary data.

Theorem 1. Let us assume, that $F \in \mathbb{W}^{1,1}((0, T); \mathbb{L}^2(\Omega; IR^3))$, $g_D \in \mathbb{W}^{1,\infty}((0, T); \mathbb{H}^{\frac{3}{2}}(\partial\Omega; IR^3))$, or $g_N \in \mathbb{W}^{1,\infty}((0, T); \mathbb{H}^{\frac{1}{2}}(\partial\Omega; IR^3))$. Moreover for the Dirichlet problem $(g_D)_{tt} \in \mathbb{W}^{1,1}((0, T); \mathbb{L}^2(\partial\Omega; IR^3))$, or for the Neumann problem $(g_N)_{tt} \in \mathbb{L}^1((0, T); \mathbb{L}^2(\partial\Omega; IR^3))$, and the initial data are admissible.

Then there exists the solution $(v, \varepsilon, \varepsilon_p, y, \beta) \in \mathbb{W}^{1,\infty}((0, T); H)$ to the problem (CBL).

Proof. : Main idea is to use the results of nonlinear semigroup method (see [6]) for the sum of a monotone operator and a Lipschitz operator. For the full proof with the homogeneous boundary data see [4], and with the nonhomogeneous boundary data see [5].

Acknowledgements

This work was supported by the Sonderforschungsbereich 298.

3. References

- 1 BODNER, S.R., PARTOM, Y.: Constitutive Equations for Elastic-Viscoplastic Strain-Hardening Materials; J. of Appl Mech. (1975), 385-389
- 2 BODNER, S.R., CHAN, K.S. LINDHOLM, U.S.: Phenomenological Modeling of Hardening, and Thermal Recovery in Metals; J. of Engineering Materials and Technology JANUARY 1988, Vol. 110/1
- 3 CHELMIŃSKI, K., GWIAZDA, P.: Nonhomogeneous initial-boundary value problems for coercive and self-controlling models of monotone type; Fach. Math. TU Darmstadt Preprint Nr. 2059, in press, Contin. Mech. Thermodyn.2000
- 4 GWIAZDA P.: Existence and Uniqueness Theorem for the Chan-Bodner-Linholm Model; Math. Meth. App. Sci. 22 (1999), 285-300
- 5 GWIAZDA P.: Nonhomogeneous boundary value-problem for the Chan-Bodner-Linholm model; in press Math. Meth. App. Sci. 2000
- 6 PAVEL H. NICOLAE: Nonlinear Evolution Operators and Semigroups- Applications to Partial Differential Equations; Lectures Notes in Mathematics 1260 Springer; Berlin Heidelberg New York London Paris Tokyo (1987)

Addresses: DR. PIOTR GWIAZDA, Technische Universität Darmstadt, Fachbereich Mathematik, Schlossgartenstrasse 7, 64289 Darmstadt, Germany

KNOBLOCH, S.

Zur Behandlung des Elastizitätsproblems in Gebieten mit Ecken

Betrachtet wird ein Randwertproblem aus der linearen ebenen Elastizitätstheorie in einem Gebiet mit einer Ecke, deren Innenwinkel $> \pi$ ist. Die Lösung gehört nicht zu H^2 , was für die numerische Behandlung problematisch ist. Als Ausweg dient die Zerlegung in einen singulären Teil mit singulären Funktionen und Spannungsintensitätsfaktoren und einen reguläreren Teil, der zu H^2 gehört. Kennt man die singulären Funktionen und die Spannungsintensitätsfaktoren, kann man Randwertprobleme für den Teil, der zu H^2 gehört, numerisch lösen und die eigentlich gesuchte Lösung durch Hinzufügen der singulären Teile erhalten. Es werden Formeln zur Berechnung der Spannungsintensitätsfaktoren bereitgestellt, in die aber die unbekannte Lösung eingeht, so daß ein iterativer Algorithmus vorgeschlagen wird.

1. Einleitung

Betrachtet wird eine Aufgabe der linearen Elastizitätstheorie für ein homogenes, isotropes und elastisches Material:

$$-\sum_{j=1}^2 \frac{\partial}{\partial x_j} \sigma_{ij}(\vec{u}) = f_i(x) \quad \text{in } \Omega \subset \mathbb{R}^2, \quad i = 1, 2, \quad \vec{u} = \vec{0} \quad \text{auf } \partial\Omega. \quad (1)$$

Es bezeichnen $\vec{u}(x)$ die Verschiebung, $f_i(x) \in L_2(\Omega)$, $i = 1, 2$, die Komponenten des gegebenen äußeren Kraftfeldes, $\mu > 0$ und $\lambda > 0$ die Lamé-Konstanten und $\sigma_{ij}(\vec{u})$, $i, j = 1, 2$, die Komponenten des Spannungstensors mit

$$\sigma_{ii}(\vec{u}) = 2\mu \cdot \frac{\partial u_i}{\partial x_i} + \lambda \cdot \left(\frac{\partial u_1}{\partial x_1} + \frac{\partial u_2}{\partial x_2} \right), \quad i = 1, 2, \quad \sigma_{12}(\vec{u}) = \sigma_{21}(\vec{u}) = \mu \cdot \left(\frac{\partial u_1}{\partial x_2} + \frac{\partial u_2}{\partial x_1} \right).$$

Ist der Rand des Gebietes Ω glatt, dann gilt $\vec{u} \in [C^2(\bar{\Omega})]^2$. Hat der Rand Ecken, ist das nicht mehr der Fall. Ist das Gebiet konvex, dann gilt noch $\vec{u} \in [H^2(\Omega)]^2$, was nicht mehr gilt, wenn das Gebiet nicht konvex ist, siehe [3]. Die Regularität der Lösung ist für die numerische Behandlung von Randwertproblemen von Bedeutung, da die Konvergenzrate und der Fehler eines numerischen Verfahrens von der Regularität abhängen. Ist das Gebiet ein konvexes Polygon, gibt es für die Lösung des Elastizitätsproblems mit der Finite-Elemente-Methode Fehlerabschätzungen der Größenordnung $O(h)$ bzw. $O(h^2)$, siehe [2].

Das Gebiet Ω habe eine Ecke mit einem Winkel $\omega > \pi$, die im Koordinatenursprung liege. In der Nähe dieser Ecke stimme Ω mit einem Kreissektor überein. An möglicherweise weiteren vorhandenen Ecken seien die Eckwinkel $< \pi$.

2. Zerlegung der Lösung und Formeln für die Spannungsintensitätsfaktoren

Um trotz fehlender Regularität zu günstigen numerischen Verfahren zu gelangen, nutzen wir die Zerlegung von \vec{u} in einen singulären und einen regulären Teil, siehe [3]:

$$\vec{u} = c_{z_1} \cdot \vec{S}_{z_1} + c_{z_2} \cdot \vec{S}_{z_2} + \vec{w}, \quad \vec{w} \in [H^2(\Omega)]^2. \quad (2)$$

c_{z_1} und c_{z_2} sind Konstanten, die sogenannten Spannungsintensitätsfaktoren. Die singulären Funktionen sind

$$\vec{S}_{z_i}(r, \theta) = \tau(r) \cdot r^{z_i} \cdot \vec{\Phi}_{z_i}(\theta), \quad 0 < z_i < 1, \quad \text{mit einer glatten Funktion } \tau(r) = \begin{cases} 1, & \text{falls } r \text{ klein} \\ 0, & \text{falls } r \text{ groß} \end{cases}, \quad (3)$$

Zahlen z_i , die $\sin^2 z_i \omega = z_i^2 \cdot \sin^2 \omega \cdot \left(\frac{\lambda + \mu}{\lambda + 3\mu} \right)^2$ erfüllen, und glatten Funktionen $\vec{\Phi}_{z_i} = \vec{\Phi}_{z_i}(\theta, \omega, \lambda, \mu, z_i)$, die in [3] zu finden sind. r, θ sind die Polarkoordinaten bezüglich des Koordinatenursprungs. Für $\omega > \pi$ gilt $0 < z_1 < \frac{\pi}{\omega} < z_2 < 1$. Wären c_{z_1} und c_{z_2} bekannt, könnte man das Problem

$$-\sum_{j=1}^2 \frac{\partial}{\partial x_j} \sigma_{ij}(\vec{w}) = \hat{f}_i(x) \quad \text{in } \Omega, \quad \vec{w} = \vec{0} \quad \text{auf } \partial\Omega \quad \text{mit } \hat{f}_i = f_i + \sum_{m=1}^2 c_{z_m} \cdot \left(\sum_{j=1}^2 \frac{\partial}{\partial x_j} \sigma_{ij}(\vec{S}_{z_m}) \right), \quad i = 1, 2, \quad (4)$$

numerisch lösen. Da $\vec{w} \in [H^2(\Omega)]^2$, hat man bei Verwendung der Finite-Elemente-Methode eine $O(h)$ -Fehlerabschätzung, siehe [1]. Mit \vec{w} ist \vec{u} aus (2) berechenbar. Es werden Formeln für die Spannungsintensitätskoeffizienten benötigt.

Theorem 1. Es gelten

$$c_{z_1}(\vec{u}) = \frac{\Psi_1(z_1, \lambda, \mu, \vec{u}, \vec{f})}{I_1(z_1, \lambda, \mu, \omega)} \quad \text{und} \quad c_{z_2}(\vec{u}, \vec{v}) = \frac{\Psi_2(z_2, \lambda, \mu, \vec{u}, \vec{v}, \vec{f})}{I_2(z_2, \lambda, \mu, \omega)} \quad \text{mit} \quad \vec{v}(\vec{u}) = \vec{u} - c_{z_1}(\vec{u}) \cdot \vec{S}_{z_1}, \quad (5)$$

$$\Psi_1 = \int_{\Omega} \sum_{i=1}^2 \left(f_i(x) \cdot \vec{S}_{-z_1, i} + u_i \cdot \sum_{j=1}^2 D_j \sigma_{ij}(\vec{S}_{-z_1}) \right) dx, \quad (6)$$

$$I_i = 2z_i \cdot \int_0^{\omega} I_{ii}(\theta, \lambda, \mu) d\theta, \quad i = 1, 2, \quad (7)$$

$$I_{ii} = (\lambda + \mu) \cdot \{ \cos \theta \cdot \Phi_{z_i, 1}(\theta) + \sin \theta \cdot \Phi_{z_i, 2}(\theta) \}^2 + \mu \cdot \{ \Phi_{z_i, 1}^2(\theta) + \Phi_{z_i, 2}^2(\theta) \}, \quad i = 1, 2, \quad (8)$$

$$\Psi_2 = \int_{\Omega} \sum_{i=1}^2 \left(\tilde{f}_i(x, \vec{u}) \cdot \vec{S}_{-z_2, i} + v_i \cdot \sum_{j=1}^2 D_j \sigma_{ij}(\vec{S}_{-z_2}) \right) dx, \quad (9)$$

$$\tilde{f}_i(x, \vec{u}) = f_i(x) + c_{z_1}(\vec{u}) \cdot \sum_{j=1}^2 D_j \sigma_{ij}(\vec{S}_{z_1}), \quad i = 1, 2, \quad (10)$$

$$\vec{S}_{-z_i}(r, \theta) = \tau(r) \cdot r^{-z_i} \cdot \vec{\Phi}_{z_i}(\theta), \quad i = 1, 2, \quad (\text{duale singuläre Funktionen}). \quad (11)$$

Die Formeln (5) lassen sich mit (2) und mit Hilfe der Greenschen Formel in Gebieten $\Omega \setminus B_{\rho}(0)$ herleiten, wenn $B_{\rho}(0)$ Kreise um 0 mit kleinen Radien $\rho > 0$ bezeichnen, siehe [4]. Die Greensche Formel wird zunächst für \vec{u} und \vec{S}_{-z_1} aufgestellt, um die Formel für c_{z_1} zu gewinnen. Dann wird die Greensche Formel für \vec{v} und \vec{S}_{-z_2} genommen und die Formel für c_{z_2} erhalten. Bei den Betrachtungen treten Integrale über das Randstück $r = \rho$ auf, die unabhängig von ρ sind und auf (7) mit (8) führen. Für andere auftretende Integrale über $r = \rho$ läßt sich mit $\vec{w} \in [H^2(\Omega)]^2$ und Sobolev'schen Einbettungssätzen zeigen, daß sie für $\rho \rightarrow 0$ gegen 0 gehen. Beim Grenzübergang $\rho \rightarrow 0$ wird aus $\Omega \setminus B_{\rho}(0)$ das Gebiet Ω .

3. Algorithmus

- 1.) für $k = 0$: Anfangsnäherung \vec{u}_0 als Lösung des Randwertproblems (1) numerisch bestimmen
für $k = 1, 2, \dots$: $\vec{u}_k = \vec{w}_{k-1} + c_{z_1}(\vec{u}_{k-1}) \cdot \vec{S}_{z_1} + c_{z_2}(\vec{u}_{k-1}, \vec{v}(\vec{u}_{k-1})) \cdot \vec{S}_{z_2}$ berechnen
- 2.) $c_{z_1}(\vec{u}_k)$ mit (5) und \vec{u}_k aus 1.) berechnen
- 3.) $\vec{v}(\vec{u}_k) = \vec{u}_k - c_{z_1}(\vec{u}_k) \cdot \vec{S}_{z_1}$ und $\tilde{f}_i(\vec{u}_k) = f_i(x) + c_{z_1}(\vec{u}_k) \cdot \sum_{j=1}^2 D_j \sigma_{ij}(\vec{S}_{z_1})$ berechnen
- 4.) $c_{z_2}(\vec{u}_k, \vec{v}(\vec{u}_k), \tilde{f}(\vec{u}_k))$ mit (5), \vec{u}_k aus 1.), $\vec{v}(\vec{u}_k)$ und $\tilde{f}_i(\vec{u}_k)$ aus 3.) berechnen
- 5.) $\hat{f}_i(\vec{u}_k, \vec{v}(\vec{u}_k), \tilde{f}(\vec{u}_k)) = \tilde{f}_i(\vec{u}_k) + c_{z_2}(\vec{u}_k, \vec{v}(\vec{u}_k), \tilde{f}(\vec{u}_k)) \cdot \sum_{j=1}^2 D_j \sigma_{ij}(\vec{S}_{z_2})$ berechnen
- 6.) \vec{w}_k als Lösung des Randwertproblems (4) mit rechter Seite $\hat{f}_i(\vec{u}_k, \vec{v}(\vec{u}_k), \tilde{f}(\vec{u}_k))$ aus 5.) numerisch bestimmen
- 7.) $k := k + 1$ setzen und bei 1.) fortfahren

Das Randwertproblem für $\vec{u} \notin [H^2(\Omega)]^2$ wird nur einmal numerisch gelöst. Die Anfangsnäherung \vec{u}_0 wird verbessert, indem Randwertprobleme für $\vec{w} \in [H^2(\Omega)]^2$ gelöst werden. Außerdem erhält man Näherungen für c_{z_1} und c_{z_2} .

4. References

- 1 BRENNER, S. C., SCOTT, L. R.: The mathematical theory of finite element methods (1994).
- 2 BRENNER, S. C., SUNG, L.-Y.: Linear finite element methods for planar linear elasticity. Mathematics of Computation 59 (1992), 321 – 338.
- 3 GRISVARD, P.: Singularities in Boundary Value Problems. Springer-Verlag (1992).
- 4 KNOBLOCH, S.: Zur Behandlung des Elastizitätsproblems in Gebieten mit Ecken mittels der Spannungsintensitätsfaktoren, eingereicht

Addresses: DR. SUSANNE KNOBLOCH, Universität Essen, Fachbereich 10 - Bauwesen, Arbeitsgruppe Ingenieurmathematik, Universitätsstraße 3, 45117 Essen, Germany

KUNZE, M.

On the Period of Periodic Motions of a Particle in a Scalar Wave Field

It is shown that a periodic solution of the nonlinear infinite-dimensional Hamiltonian system describing a particle in a scalar wave field can have only certain discrete periods that are related to zeroes of the Fourier transform of the function that realizes the coupling.

1. Introduction

For the motion of a charged particle $q(t) \in \mathbb{R}^3$ subject to its self-generated field, a simplified model is governed by the equations

$$\begin{aligned} \dot{q}(t) &= \frac{p(t)}{\sqrt{1+p(t)^2}}, & \dot{p}(t) &= -\nabla V(q(t)) + \int d^3y \phi(y, t) \nabla \rho(y - q(t)), \\ \dot{\phi}(x, t) &= \pi(x, t), & \dot{\pi}(x, t) &= \Delta \phi(x, t) - \rho(x - q(t)), \end{aligned} \quad (1)$$

with $x \in \mathbb{R}^3$ and $t \in \mathbb{R}$. Here $\dot{q}(t)$ and $p(t) = (1 - \dot{q}(t)^2)^{-1/2} \dot{q}(t) \in \mathbb{R}^3$ are the velocity and the momentum of the particle, respectively, and $\phi(x, t) \in \mathbb{R}$ denotes the (scalar) field. If the wave equation $\ddot{\phi} = \Delta \phi - \rho(x - q(t))$ in (1) were replaced by the full Maxwell equations for electric and magnetic fields $E(x, t), B(x, t) \in \mathbb{R}^3$, then (1) would be the more general and well-known Maxwell-Lorentz model, also called Abraham model; see [8] for an up-to date review. An important role is played by the function ρ in (1), since it accounts for considering the particle a charged sphere with charge ρ rather than a point particle: If one formally sets $\rho = \delta_0$, then the wave equation $\ddot{\phi} = \Delta \phi - \delta(x - q(t))$ means that there is only charge at the point $x = q(t)$ where the particle sits. For ρ we assume

$$\rho \in C_0^\infty(\mathbb{R}^3), \quad \rho(x) = 0 \quad \text{for } |x| \geq R_\rho, \quad \rho(x) = \rho_r(|x|), \quad (C)$$

to be satisfied.

Our goal is to investigate the long-time behaviour of (1) as a dynamical system on the state-space $\mathcal{E} = D^{1,2}(\mathbb{R}^3) \oplus \mathbb{R}^3 \oplus L^2(\mathbb{R}^3) \oplus \mathbb{R}^3$, with the canonical norm, where $D^{1,2}(\mathbb{R}^3) = \{\phi \in L^6(\mathbb{R}^3) : |\nabla \phi(x)| \in L^2(\mathbb{R}^3)\}$. Assuming here and in the sequel that $V \in C^2(\mathbb{R}^3)$ with $\inf_{q \in \mathbb{R}^3} V(q) > -\infty$, it is known from [4; Lemma 2.1] that for data $Y_0 = (\phi_0, q_0, \pi_0, p_0) \in \mathcal{E}$ there exists a unique global (weak) solution $t \mapsto Y(t) \in \mathcal{E}$ of (1), $Y(t) = (\phi(\cdot, t), q(t), \pi(\cdot, t), p(t))$, such that $Y(0) = Y_0$.

It became apparent that for the dynamics of (1) a particularly important role seems to be played by the Fourier transform

$$\hat{\rho}(k) = (2\pi)^{-3/2} \int d^3x e^{-ik \cdot x} \rho(x), \quad k \in \mathbb{R}^3,$$

of ρ . In case that $\hat{\rho}(k) \neq 0$ for all $k \in \mathbb{R}^3$, it was also shown in [4] that solutions of (1) for *any* data $Y_0 \in \mathcal{E}$ (with a certain decay at $|x| \rightarrow \infty$) will approach the set of all equilibria of (1), in the topology on \mathcal{E} generated by the seminorms induced by restriction of integrals over $\{x \in \mathbb{R}^3 : |x| \leq R\}$, $R > 0$. This corresponds to the fact that the particle is accelerated by the potential V and hence radiates energy in x -space. Therefore, if a fixed ball $\{x \in \mathbb{R}^3 : |x| \leq R\}$ is considered, then all energy should be dissipated from this ball as $t \rightarrow \infty$.

Contrary to this satisfactory answer, from a rigorous viewpoint the situation is much less clear if $\hat{\rho}$ admits zeroes, for simplicity we suppose

$$\hat{\rho}(k) = 0 \quad \text{for } k \in \mathbb{R}^3, |k| = a > 0, \quad \hat{\rho}(k) \neq 0, \quad |k| \neq a; \quad (2)$$

note that since ρ is radially symmetric, so is $\hat{\rho}$. In this case, linearizing (1) about a fixed point, it can be seen that the linearized system possesses periodic solutions, of period $T = 2\pi/a$. It has been proved in [5] that, due to the coupling to the continuous spectrum, these "linearized periodic solutions" do not generate periodic solutions of the

non-linear problem, in a certain sense. This somehow excludes the existence of periodic solutions to (1) close to equilibrium points, but it remained open whether there are periodic solutions at all, e.g., with large energy.

In the present note we will prove that if a periodic solution to (1) does exist, then necessarily it is of period $T = (2\pi/a)n$ for some $n \in \mathbb{N}$. More precisely, we show

Theorem 1. Assume (C) and (2) are satisfied, and let $Y(t) = (\phi(\cdot, t), q(t), \pi(\cdot, t), p(t))$ be a solution to (1) with data $Y_0 = (\phi_0, q_0, \pi_0, p_0) \in \mathcal{E}$ such that for some $R_0 > 0$ the functions $\phi_0(x)$ and $\pi_0(x)$ are C^2 and C^1 -differentiable, respectively, outside the ball $\{x \in \mathbb{R}^3 : |x| \leq R_0\}$, and for $|x| \rightarrow \infty$

$$|\phi^0(x)| + |x| \left(|\nabla \phi_0(x)| + |\pi_0(x)| \right) + |x|^2 \left(|\nabla \nabla \phi_0(x)| + |\nabla \pi_0(x)| \right) = \mathcal{O}(|x|^{-\sigma}) \quad (3)$$

holds, with some $\sigma > 1/2$. Then, if $q(\cdot)$ is periodic of period $T > 0$ and non-constant, we already must have $T = (2\pi/a)n$ for some $n \in \mathbb{N}$.

Remark 1. (i) Since (1) is a nonlinear infinite-dimensional Hamiltonian system, the fact that there should be periodic solutions of only discrete periods seems to be somewhat unlikely. Typically one would expect periodic solutions of "very many" periods, cf. e.g. [2]. Perhaps this indicates that there are no periodic solutions at all, and that every trajectory has to tend to the set of all equilibria in the long-time limit.

(ii) For the choice $\rho(x) \cong \delta(|x| - b)$, which means that the charge is uniformly distributed over the sphere $|x| = b$, an analogous (but quite formally derived) result has been obtained in [7]; see also the remarks in [6; p. 937]. For this ρ the existence of a periodic solution is claimed in [1], but the argument is non-rigorous. Note, however, that in this case (C) is not satisfied, and $\hat{\rho}(k) \cong \frac{\sin kb}{kb}$.

(iii) The decay assumption (3) is the one already used in [4].

2. Proof of Theorem 1

The following result from [4; Prop. 3.1] will play the main role in the proof.

Lemma 1. In the situation described in Theorem 1,

$$\int_0^\infty dt \int_{|\omega|=1} d^2\omega |R_\omega(t)|^2 < \infty, \quad \text{with} \quad R_\omega(t) = \int d^3x \rho(x - q(t + \omega \cdot x)) \frac{\omega \cdot \ddot{q}(t + \omega \cdot x)}{(1 - \omega \cdot \dot{q}(t + \omega \cdot x))^2}.$$

This estimate obtains from a careful analysis of how much energy does leave a ball $\{x \in \mathbb{R}^3 : |x| \leq R\}$ as $t \rightarrow \infty$, and it reflects the fact that there is energy dissipated in quantitative terms. Note that due to the a priori bound $\sup_{t \in \mathbb{R}} |\dot{q}(t)| = \sup_{t \in [0, T]} |\dot{q}(t)| \leq \bar{v} < 1$, see [4], we always have $|\omega \cdot \dot{q}(t + \omega \cdot x)| \leq \bar{v}$ for $|\omega| = 1$, whence $R_\omega(t)$ is well-defined.

Now we can proceed to show Theorem 1.

Proof. Since q is T -periodic, so are \dot{q} and \ddot{q} . Whence $R_\omega(\cdot)$ is T -periodic as well, for each $|\omega| = 1$, and thus the same holds for $t \mapsto \int_{|\omega|=1} d^2\omega |R_\omega(t)|^2$. Utilizing Lemma 1 we find that this is only possible in case that $R_\omega(t) = 0$ for all $|\omega| = 1$ and $t \in [0, T]$. To rewrite $R_\omega(t)$ appropriately, we introduce the 1D version $\rho_{(1)}(\xi) = \int_{\mathbb{R}^2} \rho(x_1, x_2, \xi) dx_1 dx_2$ of ρ , with $\xi \in \mathbb{R}$. We perform a change of variables

$$\mathbb{R}^3 \ni x \mapsto (\omega_1 \cdot (x - \varphi(\omega \cdot x)), \omega_2 \cdot (x - \varphi(\omega \cdot x)), \omega \cdot x) = z \in \mathbb{R}^3,$$

with $\varphi(\xi) = q(t + \xi) \in \mathbb{R}^3$, and $\omega_1, \omega_2 \in \mathbb{R}^3$ are chosen in such a way that $\{\omega_1, \omega_2, \omega\}$ is an orthonormal base of \mathbb{R}^3 . Then it may be calculated that

$$|\det(\frac{dz}{dx})| \equiv 1 \quad \text{and} \quad |x - \varphi(\omega \cdot x)| = |(z_1, z_2, z_3 - \omega \cdot \varphi(z_3))|,$$

hence

$$\rho(x - q(t + \omega \cdot x)) = \rho(z_1, z_2, z_3 - \omega \cdot \varphi(z_3))$$

due to (C). Thus we obtain

$$R_\omega(t) = \int d^1\xi \rho_{(1)}(\xi - \omega \cdot q(t + \xi)) \frac{\omega \cdot \ddot{q}(t + \xi)}{(1 - \omega \cdot \dot{q}(t + \xi))^2} = 0, \quad |\omega| = 1, \quad t \in [0, T].$$

Writing $r(t) = \omega \cdot q(t)$, this yields, due to $\rho_{(1)}(-\xi) = \rho_{(1)}(\xi)$,

$$\begin{aligned} 0 &= \int d^1\xi \rho_{(1)}(\xi - r(t + \xi)) \frac{\ddot{r}(t + \xi)}{(1 - \dot{r}(t + \xi))^2} = \int d^1\xi \rho_{(1)}(t - [\xi - r(\xi)]) \frac{\ddot{r}(\xi)}{(1 - \dot{r}(\xi))^2} \\ &= \int d^1\theta \rho_{(1)}(t - \theta) \frac{\ddot{r}(\xi(\theta))}{(1 - \dot{r}(\xi(\theta)))^3}, \end{aligned}$$

the latter through the substitution $\theta = \xi - r(\xi)$, $\frac{d\theta}{d\xi} = 1 - \dot{r}(\xi)$; recall that $|\dot{r}(\xi)| \leq \bar{v} < 1$, hence $\xi \mapsto \theta(\xi)$ is a diffeomorphism with inverse $\theta \mapsto \xi(\theta)$. Since this is a convolution, we can summarize that

$$(\rho_{(1)} * g_\omega)(t) = 0, \quad |\omega| = 1, \quad t \in [0, T], \quad \text{with} \quad g_\omega(\theta) = \frac{\omega \cdot \ddot{q}(\xi(\theta))}{(1 - \omega \cdot \dot{q}(\xi(\theta)))^3}, \quad (4)$$

see also [4]. Due to the assumed periodicity we may as well write " $t \in \mathbb{R}$ " instead of " $t \in [0, T]$ ". According to (2),

$$\hat{\rho}_{(1)}(k) = 0 \quad \text{for} \quad k \in \mathbb{R}, \quad |k| = a > 0, \quad \hat{\rho}_{(1)}(k) \neq 0, \quad |k| \neq a. \quad (5)$$

From (4) and (5) we want to conclude that $T = (2\pi/a)n$ for some $n \in \mathbb{N}$. We will use the following lemma, the proof of which is certainly known, but since we didn't find a precise reference we will include some details.

Lemma 2. *If $\rho_{(1)} \in C_0^\infty(\mathbb{R})$ satisfies (5), and if $g \in C_b(\mathbb{R})$ is such that*

$$(\rho_{(1)} * g)(t) = 0, \quad t \in \mathbb{R},$$

then either $g \equiv 0$ or $g(t) = A \sin(at + \theta)$, $t \in \mathbb{R}$, for some $A, \theta \in \mathbb{R}$.

Proof. (of Lemma 2). Define the finite measure $\mu(A) = \int_A \rho_{(1)}(\xi) d\xi$ for $A \in \mathcal{B}(\mathbb{R})$, the Borel σ -algebra on \mathbb{R} . Then $\rho_{(1)} * g \equiv 0$ can be rewritten as $\mu * g \equiv 0$. With the notation $\sigma(g) = \bigcap_{f \in N(g)} \{k \in \mathbb{R} : \hat{f}(k) = 0\}$, where $N(g) = \{f \in L^1(\mathbb{R}; \mathbb{C}) : f * g \equiv 0\}$, it is thus known from [3; Thm. 15.4.6(vii)] that

$$\sigma(g) \subset \{k \in \mathbb{R} : \hat{\mu}(k) = 0\} = \{k \in \mathbb{R} : \hat{\rho}_{(1)}(k) = 0\} = \{-a, +a\},$$

the latter by (5). Hence there are not many possibilities for the spectrum $\sigma(g)$ of g . If $\sigma(g) = \emptyset$, then $g \equiv 0$ by [3; Thm. 15.4.7]. In case that $\sigma(g) = \{-a\}$, $\sigma(g) = \{a\}$, or $\sigma(g) = \{-a, a\}$, it follows from [3; Thm. 15.4.17(iii)] that g has the form $g(t) = \alpha e^{-iat} + \beta e^{iat}$ for some $\alpha, \beta \in \mathbb{C}$. Since g is real-valued, we arrive at

$$g(t) = [\operatorname{Re} \alpha + \operatorname{Re} \beta] \cos(at) + [\operatorname{Im} \beta - \operatorname{Im} \alpha] \sin(at) = A \sin(at + \theta), \quad t \in \mathbb{R},$$

for suitable A, θ . This completes the proof of Lemma 2.

To continue with the proof of Theorem 1, we now can apply Lemma 2 to each $g_\omega(\cdot)$ from (4). Hence for each $|\omega| = 1$ we find $A_\omega, \theta_\omega \in \mathbb{R}$ such that

$$\frac{\omega \cdot \ddot{q}(\xi(\theta))}{(1 - \omega \cdot \dot{q}(\xi(\theta)))^3} = g_\omega(\theta) = A_\omega \sin(a\theta + \theta_\omega), \quad \theta \in \mathbb{R}.$$

Setting $\theta = \theta(\xi)$, the inverse of $\theta \mapsto \xi(\theta)$, we infer

$$\frac{\omega \cdot \ddot{q}(t)}{(1 - \omega \cdot \dot{q}(t))^3} = A_\omega \sin(a[t - \omega \cdot q(t)] + \theta_\omega), \quad t \in \mathbb{R}, \quad (6)$$

where we wrote t instead of ξ . To deduce further information from this implicit ODE for q , we re-introduce $u(t) = t - \omega \cdot q(t)$, i.e., $u = \theta$. Then (6) reads as

$$\ddot{u} + A_\omega \sin(au + \theta_\omega) \dot{u}^3 = 0, \quad t \in \mathbb{R}.$$

Writing this as $\dot{u} = z$, $\dot{z} = -A_\omega \sin(au + \theta_\omega)z^3$, it follows that

$$\frac{du}{dz} = -\frac{1}{A_\omega \sin(au + \theta_\omega)z^2}.$$

Hence integration reveals that for all $|\omega| = 1$ there exists $C_\omega \in \mathbb{R}$ such that

$$\omega \cdot q(t) = A_\omega \sin(a[t - \omega \cdot q(t)] + \theta_\omega) + C_\omega, \quad t \in \mathbb{R}. \quad (7)$$

This finally gives the claim of the theorem, since due to T -periodicity of q for all $t \in \mathbb{R}$

$$\begin{aligned} A_\omega \sin(aT + a[t - \omega \cdot q(t)] + \theta_\omega) &= A_\omega \sin(a[t + T - \omega \cdot q(t + T)] + \theta_\omega) = \omega \cdot q(t + T) - C_\omega \\ &= \omega \cdot q(t) - C_\omega = A_\omega \sin(a[t - \omega \cdot q(t)] + \theta_\omega). \end{aligned} \quad (8)$$

From (7) we conclude that it is not possible to have $A_\omega = 0$ for all $|\omega| = 1$, as in this case

$$\frac{4\pi}{3} q(t) = \int_{|\omega|=1} d^2\omega (\omega \cdot q(t))\omega = \int_{|\omega|=1} d^2\omega C_\omega \omega$$

is independent of t , i.e., q is constant. Thus for one $|\omega| = 1$ with $A_\omega \neq 0$ it follows from (8) that

$$\sin(aT + \bar{u}(t)) = \sin(\bar{u}(t)), \quad t \in \mathbb{R},$$

with $\bar{u}(t) = a[t - \omega \cdot q(t)] + \theta_\omega$, $t \in \mathbb{R}$. Since $\bar{u} : \mathbb{R} \rightarrow \mathbb{R}$ is onto, we finally find

$$\sin(aT + \tau) = \sin(\tau), \quad \tau \in \mathbb{R},$$

hence $T = (2\pi/a)n$ for some $n \in \mathbb{N}$ as was to be shown.

Acknowledgement

I am grateful to A. KOMECH and H. SPOHN for discussions.

3. References

- 1 BOHM, D., WEINSTEIN, M.: The self-oscillation of charged particles; *Physical Review* **74** (1948), 1789-1798.
- 2 CRAIG, W., WAYNE, C.E.: Newton's method and periodic solutions of nonlinear wave equations; *Comm. Pure Appl. Math.* **46** (1993), 1409-1498.
- 3 GRIPENBERG, G., LONDEN, S.-O., STAFFANS, O.: *Volterra Integral and Functional Equations*, Cambridge University Press, Cambridge-New York 1990.
- 4 KOMECH, A., SPOHN, H., KUNZE, M.: Long-time asymptotics for a classical particle interacting with a scalar wave field; *Comm. Partial Differential Equations* **22** (1997), 307-335.
- 5 KUNZE, M.: Instability of the periodic motion of a particle interacting with a scalar wave field; *Comm. Math. Phys.* **195** (1998), 509-523.
- 6 PEARLE, P.: Absence of radiationless motions of relativistically rigid classical electron; *Foundations of Physics* **7** (1977), 931-943.
- 7 SCHOTT, G.A.: *Phil. Mag. Suppl.* **7** (1933), 752.
- 8 SPOHN, H.: *Dynamics of Charged Particles and Their Radiation Field*, preprint 1999.

Address: MARKUS KUNZE, Mathematisches Institut der Universität Köln, Weyertal 86, 50931 Köln,
email: mkunze@mi.uni-koeln.de

PATRIZIO NEFF

A model describing small elastic deformations and Korn's inequality with nonconstant coefficients

This contribution is concerned with the formulation and mathematical investigation of a model for small elastic deformations which arises from multiplicative theories of elasto-plasticity. In a natural way it leads to a linear elliptic system with nonconstant coefficients for the deformation u . In contrast to infinitesimal plasticity the model should be valid for both large plastic deformations F_p and large deformation gradients F . The arising linear partial differential system is proved to have unique solutions by means of a generalized Korn's inequality.

1. Motivation

In the nonlinear theory of elasto-plasticity at large deformation gradients it is often assumed that the deformation gradient $F = \nabla u$ splits multiplicatively into an elastic and plastic part $\nabla u(x) = F(x) = F_e(x) \cdot F_p(x)$, $F_e, F_p \in GL(3, \mathbb{R})$ where F_e, F_p are explicitly understood to be incompatible configurations, i.e. $F_e, F_p \neq \nabla \Psi$ for any $\Psi : \Omega \subset \mathbb{R}^3 \mapsto \mathbb{R}^3$. In our context we assume that this decomposition is uniquely defined up to a rigid rotation. This ansatz is micromechanically motivated by the kinematics of single crystals where dislocations move along fixed slip systems through the crystal lattice. The source for the incompatibility are those dislocations which did not completely transverse the crystal and consequently give rise to an inhomogeneous plastic deformation. Therefore it seems reasonable to introduce the deviation of the plastic intermediate configuration F_p from compatibility as a kind of plastic **dislocation density**. This deviation should be related somehow to the quantity $\text{Rot} F_p$ and indeed later on we see the important role which is played by $\text{Rot} F_p$, see [4] for more on this subject and for applications of this theory in the engineering field look e.g at [2,3].

2. Metal Plasticity

It is known that any homogeneous, isotropic and material objective energy with stress free reference configuration \mathbb{I} admits the representation

$$\bar{W}(F) = \lambda \|F^T F - \mathbb{I}\|^2 + \mu \text{tr}(F^T F - \mathbb{I})^2 + o(\|F^T F - \mathbb{I}\|^2) \quad (1)$$

near \mathbb{I} . Here $\lambda, \mu > 0$ denote the Lamé constants. When dealing with metal-plasticity it is observed that elastic deformations remain small in the sense that $\|F_e^T F_e - \mathbb{I}\|$ remains pointwise small. Accordingly taking \bar{W} and inserting F_e instead of F and skipping the higher order term $o(\|F_e^T F_e - \mathbb{I}\|^2)$ the following St. Venant-Kirchhoff ansatz for a hyperelastic free energy should be a reasonable first choice:

$$\hat{W} = \hat{W}(F_e) = \lambda \|F_e^T F_e - \mathbb{I}\|^2 + \mu \text{tr}(F_e^T F_e - \mathbb{I})^2. \quad (2)$$

However, \hat{W} would still lead to a problem which is neither linear in F nor elliptic. Therefore invoking the smallness of $\|F_e^T F_e - \mathbb{I}\|$ again we see with the aid of the polar decomposition that F_e is approximately a rotation R_e . If we set $F_e = (F_e - R_e) + R_e$, insert this formula into the free energy \hat{W} and cancel terms which are of second order in $(F_e - R_e)$ we are left with the following elastic energy:

$$W(F, F_p, R_e) = \lambda \|R_e^T F F_p^{-1} + F_p^{-T} F^T R_e - 2 \cdot \mathbb{I}\|^2 + \mu \text{tr}(R_e^T F F_p^{-1} + F_p^{-T} F^T R_e - 2 \cdot \mathbb{I})^2. \quad (3)$$

Note that W is quadratic with respect to F if F_p, R_e are assumed to be known. The new energy W is still material objective since $Q \cdot F = Q \cdot F_e \cdot F_p$ implies $R_e(Q \cdot F_e) = Q \cdot R_e(F_e)$ and $W(Q \cdot F, F_p, Q \cdot R_e) = W(F, F_p, R_e) \forall Q \in O(3)$. Let $\Omega \subset \mathbb{R}^3$ be a smooth bounded domain with boundary $\partial\Omega$. In the absence of body forces and in the quasistatic setting the problem to be solved is: find the deformation $u : [0, T] \times \Omega \mapsto \mathbb{R}^3$ and the plastic deformation gradient $F_p : [0, T] \times \Omega \mapsto GL(3, \mathbb{R})$ such that

$$\text{div } D_F W(F(x, t), F_p(x, t), R_e(x, t)) = 0 \quad x \in \Omega \quad (4)$$

$$\frac{d}{dt} F_p^{-1} = f(F, F_p^{-1}) \quad (5)$$

$$R_e(x, t) = \text{polar}(F_e(x, t)) \quad (6)$$

$$F(x, t) = F_e(x, t) \cdot F_p(x, t) \quad (7)$$

$$F_p^{-1}(x, 0) = F_{p_0}^{-1}(x) \quad (8)$$

$$u|_{\partial\Omega}(x, t) = g(x, t) \quad (9)$$

where $f: M^{3 \times 3} \times M^{3 \times 3} \mapsto M^{3 \times 3}$ is some function governing the plastic evolution, g is the given Dirichlet boundary data and $F_{p_0}^{-1}$ is the initial condition on the plastic flow. Here $\text{polar}: GL(3, \mathbb{R}) \mapsto O(3)$ is the function which gives the unique rotation of its argument according to the polar decomposition. Observe that the complete system is still nonlinear in F altogether due to the appearance of $\text{polar}: GL(3, \mathbb{R}) \mapsto O(3)$. Some simple computations reveal that the above equilibrium system is a linear elliptic system with nonconstant coefficients at fixed values F_p, R_e in contrast to the elliptic system with constant coefficients in infinitesimal plasticity. Note that R_e represents in a natural way deformation induced anisotropy. It is natural to ask whether at fixed time t_0 the equilibrium equation $\text{div } D_F W(F, F_p, R_e) = 0$ has a unique solution if the data g, F_p, R_e at t_0 are known. The answer is given in

Theorem 1. *Let $\Omega \subset \mathbb{R}^3$ be a bounded smooth domain with smooth boundary and let $F_p, R_e \in C^2(\bar{\Omega}, GL(3, \mathbb{R}))$. Moreover assume that $g \in H^1(\Omega, \mathbb{R}^3)$. Then*

$$\text{div } D_F W(F, F_p, R_e) = 0 \quad x \in \Omega \quad (10)$$

$$u|_{\partial\Omega} = g \quad (11)$$

admits a unique solution $u \in H^1(\Omega, \mathbb{R}^3)$.

Proof. The proof uses the key idea to interpret the equilibrium equation as the Euler-Lagrange equation of the functional $I: H^1(\Omega, \mathbb{R}^3) \times C^2(\bar{\Omega}, GL(3, \mathbb{R})) \times C^2(\bar{\Omega}, GL(3, \mathbb{R})) \mapsto \mathbb{R}$ with $I(u, F_p, R_e) := \int_{\Omega} W(\nabla u, F_p^{-1}, R_e) dx$. Evaluating the second derivative of I with respect to u we have the following estimate

$$D_u^2 I(u, F_p, R_e) \cdot (\phi, \phi) \geq 2\lambda \int_{\Omega} \|F_p^{-T} \nabla \phi^T R_e + R_e^T \nabla \phi F_p^{-1}\|^2 dx. \quad (12)$$

In [1] it is shown by proving a generalized Korn's inequality that there exists some positive constant $c^+ > 0$ such that for all $\phi \in H_0^1(\Omega, \mathbb{R}^3)$ we have

$$\int_{\Omega} \|F_p^{-T} \nabla \phi^T R_e + R_e^T \nabla \phi F_p^{-1}\|^2 dx \geq c^+ \cdot \|\phi\|_{H^1(\Omega)}^2 \quad (13)$$

which implies the strict convexity of I with respect to u . By the direct methods of the calculus of variations it is clear that there exists a unique minimizer of I over the space $H^1(\Omega)$ together with the boundary condition. In the prove of this assertion a prominent role is played by the quantity $\text{Rot} F_p$ which to our opinion shows clearly the importance of the dislocation density concept approach in elasto-plasticity.

Observe that our model is at variance with models already proposed for small elastic deformations, which essentially are defined by making the physically linear ansatz $S_2 = D \cdot (C - C_p)$ where D is a fourth order positiv definite symmetric elasticity tensor, $C = F^T F$ and C_p is some plastic variable. It turns out however that the associated equilibrium equations are neither linear in F nor in general elliptic. There may even be no solution of the equilibrium system due to the possible formation of microstructure. This may indicate that our approach of defining a model for small elastic deformations is more likely to lead to well posed problems and to stable numerical algorithms.

3. References

- 1 NEFF, P.: On Korn's inequality with nonconstant coefficients. Fachb. Math. TU Darmstadt Preprint Nr. 2080, submitted to Proc. Roy. Soc. Edinb.
- 2 MIEHE, C.: A theory of large-strain isotropic thermoplasticity based on metric transformation tensors, Archive Appl. Mech. **66** (1995), 45-64.
- 3 SIMO, J.C.: Numerical analysis and simulation of plasticity, Handbook of numerical analysis, (P.G. Ciarlet and J.L. Lions eds.) Elsevier, Amsterdam, 1998.
- 4 STEINMANN, P.: Views on multiplicative elastoplasticity and the continuum theory of dislocations, Int. J. Engng. Sci. **34** (1996), 1717-1735

Address: DR. PATRIZIO NEFF, Technische Universität Darmstadt, Fachbereich Mathematik,
Schlossgartenstrasse 7, 64289 Darmstadt, Germany
email: neff@mathematik.tu-darmstadt.de

ANDRIJA RAGUŽ

Compensated compactness for higher order differential relations

In this paper we present two compensated compactness results which generalise well known results of Tartar and Murat. The first result generalises the basic compensated compactness theorem in quadratic case to differential relations of arbitrary order m . A particular result of this type has already been used in the homogenisation theory for elastic materials (Antonić and Balenović, 1999). The other result treats the case where differential relations are of different order, and therefore cannot be reduced to the above form. Nevertheless, we obtain a result showing that we can pass to the limit in the product of two weakly converging sequences.

1. Some notation

The abbreviation LPDO is used for a linear partial differential operator (with constant coefficients), and $n(A)$ denotes the order of LPDO A , while A^* stands for the LPDO adjoint to A . \mathcal{F} stands for the Fourier transform on $L^2(\mathbf{R}^d)$, and Ω denotes a bounded open set in \mathbf{R}^d .

2. Main results

Theorem 1. (generalised compensated compactness in the quadratic case)

Let us fix $d, r, m \in \mathbf{N}$. Consider real quadratic form $Q: \mathbf{R}^r \rightarrow \mathbf{R}$ satisfying $Q(\lambda) \geq 0$, $\lambda \in \Lambda$, where

$$\Lambda := \left\{ \lambda \in \mathbf{R}^r : (\exists \xi \in \mathbf{R}^d \setminus \{0\}) \sum_{j=1}^r \sum_{k_1, \dots, k_d} A_{ijk_1 \dots k_d} \xi_{k_1} \dots \xi_{k_d} \lambda_j = 0, i = 1, \dots, q \right\}, \quad (1)$$

and the sum is taken over all $k_1, \dots, k_d \in \{0, \dots, d\}$ satisfying the constraint $k_1 + \dots + k_d = m$. Let us assume that

$$(i) \ U^n \xrightarrow{L^2_{loc}(\Omega; \mathbf{R}^r)} U^\infty$$

$$(ii) \ \sum_{j=1}^p \sum_{k_1, \dots, k_d} A_{ijk_1 \dots k_d} \frac{\partial^m U_j^n}{\partial^{k_1} x_{k_1} \dots \partial^{k_d} x_{k_d}} \text{ is pre-compact in } H_{loc}^{-m}(\Omega) \text{ (strongly), for } i = 1, \dots, q.$$

Then from $Q \circ U^n \xrightarrow{\text{vague}} \mu$ it follows $\mu \geq Q \circ U^\infty$.

Proof. Firstly, following [4], we note that without loss of generality we can assume (after suitable extension of U^n and U^∞ by zero to the whole space) that the sequence $V^n := U^n - U^\infty$ (where we keep the same notation for extended functions) satisfies $\text{supp } V^n \subseteq K$ for some compact $K \subseteq \mathbf{R}^d$, and also $V^n \xrightarrow{L^2(\mathbf{R}^d; \mathbf{R}^r)} 0$, as well as

$$\sum_{j=1}^r \sum_{k_1, \dots, k_d} A_{ijk_1 \dots k_d} \frac{\partial^m V_j^n}{\partial^{k_1} x_{k_1} \dots \partial^{k_d} x_{k_d}} \xrightarrow{H^{-m}(\mathbf{R}^d)} 0. \quad (2)$$

After taking the Fourier transform, we have $\mathcal{F}V^n \xrightarrow{L^2(\mathbf{R}^d; \mathbf{C}^r)} 0$ and

$$\frac{1}{1 + |\xi|^m} \sum_{j=1}^r \sum_{k_1, \dots, k_d} A_{ijk_1 \dots k_d} \frac{\partial^m \mathcal{F}V_j^n}{\partial^{k_1} \xi_{k_1} \dots \partial^{k_d} \xi_{k_d}} \xrightarrow{H^{-m}(\mathbf{R}^d)} 0. \quad (3)$$

Furthermore, by Plancherel's theorem it suffices to prove that

$$\liminf_{n \rightarrow \infty} \int_{\mathbf{R}^d} \bar{Q}(\mathcal{F}U^n(\xi)) d\xi \geq 0, \quad (4)$$

where \bar{Q} is the hermitian form on \mathbf{C}^r associated to Q . By construction we have

$$\mathcal{F}V^n \xrightarrow{L^2_{loc}(\mathbf{R}^d; \mathbf{C}^r)} 0. \quad (5)$$

Next we split the integral over \mathbf{R}^d in (4) into integral over the unit ball and over its complement. By (5), the integral over the ball tends to 0 when $n \rightarrow \infty$, and it remains to consider the integral over $|\xi| \geq 1$. We recall the following useful inequality (as in [4], Theorem VII.5): For any $\varepsilon > 0$ there exists $C_\varepsilon > 0$ such that for all $\mathbf{W} \in \mathbf{C}^r$ and $\eta \in \mathbf{R}^d \setminus \{0\}$

$$\operatorname{Re} \tilde{Q}(\mathbf{W}) \geq -\varepsilon |\mathbf{W}|^2 - C_\varepsilon \sum_{i=1}^q \left(\sum_{j=1}^p \sum_{k_1, \dots, k_d} A_{ijk_1 \dots k_d} W_j \frac{\eta_1 \dots \eta_d}{|\eta|^m} \right)^2. \quad (6)$$

For $M := \limsup_n \|V^n\|_{L^2}$, $\mathbf{W} := \mathcal{F}U^n(\xi)$ and $\eta := \xi$, where $|\xi| \geq 1$, by (6) we get

$$\liminf_{n \rightarrow \infty} \int_{|\xi| \geq 1} \operatorname{Re} \tilde{Q}(\mathcal{F}U^n(\xi)) d\xi \geq -\varepsilon M^2, \quad (7)$$

and when $\varepsilon \rightarrow 0$ we obtain (4).

Corollary 1. *If $Q(\Lambda) = \{0\}$, then, under the assumptions of the theorem, $Q \circ U^n \xrightarrow{\text{vague}} Q \circ U^\infty$.*

Theorem 2. (non-symmetric case) *Suppose that Ω has sufficiently smooth boundary, and that $B : \mathcal{D}'(\Omega; \mathbf{R}^d) \rightarrow \mathcal{D}'(\Omega; \mathbf{R})$ and $H : \mathcal{D}'(\Omega; \mathbf{R}^d) \rightarrow \mathcal{D}'(\Omega; \mathbf{R}^d)$ are given LPDOs. Furthermore, let us assume that $D^n \xrightarrow{L^2(\Omega; \mathbf{R}^d)} D$, $E^n \xrightarrow{L^2(\Omega; \mathbf{R}^d)} E$, and that (BD^n) is pre-compact in $H^{-n(B)+1}(\Omega; \mathbf{R})$, while (HE^n) is pre-compact in $H^{-n(H)+1}(\Omega; \mathbf{R}^d)$. If there exist LPDOs $K : \mathcal{D}'(\Omega; \mathbf{R}^d) \rightarrow \mathcal{D}'(\Omega; \mathbf{R})$ and $A : \mathcal{D}'(\Omega; \mathbf{R}^d) \rightarrow \mathcal{D}'(\Omega; \mathbf{R}^d)$ satisfying*

$$(i) \quad n(B) + n(K) = n(A) + n(H)$$

$$(ii) \quad L := B^*K - AH \text{ is an elliptic LPDO,}$$

then $D^n \cdot E^n \xrightarrow{\text{vague}} D \cdot E$.

Proof. Let us consider a new sequence $u_n \in H_0^{n(L)}(\Omega; \mathbf{R}^d)$ such that $Lu_n = E^n$. Then, by a standard elliptic regularity argument (cf. [3]) we immediately conclude that

$$Hu_n \xrightarrow{H_0^{n(A)+1}} Hu \quad \text{and} \quad Ku_n \xrightarrow{H_0^{n(B)+1}} Ku. \quad (8)$$

On the other hand:

$$\int_{\Omega} E^n \cdot \varphi D^n = \int_{\Omega} Ku_n \cdot B\varphi D^n + \int_{\Omega} Ku_n \cdot \varphi BD^n - \int_{\Omega} Hu_n \cdot A^* \varphi D^n - \int_{\Omega} Hu_n \cdot \varphi A^* D^n. \quad (9)$$

Assumptions (i) and (ii) allow us to pass to the limit in all integrals, and after performing the reverse calculation we conclude that $\int_{\Omega} E^n \cdot \varphi D^n \rightarrow \int_{\Omega} E \cdot \varphi D$.

Acknowledgements

The author would like to thank prof. Nenad Antonić for constant encouragement while writing this paper.

3. References

1. N. ANTONIĆ, N. BALENOVIĆ *Optimal design for plates and relaxation*, Math. Communications, 4 (1999) 111–119.
2. N. ANTONIĆ, A. RAGUŽ AND M. VRDOLJAK *Homogenisation of nonlinear elliptic systems*, to appear
3. D. GILBARG, N. S. TRUDINGER *Elliptic Partial Differential equations of Second Order*, Springer 1983.
4. L. TARTAR *Homogenization, Compensated Compactness, H-measures*, unpublished lecture notes.

Addresses: ANDRIJA RAGUŽ University of Zagreb, Department of Mathematics, Bijenička c. 30, 10000 Zagreb, Croatia; Presently on leave at Max Planck Institute for Mathematics in the Sciences, Inselstrasse 22-26, D-04103 Leipzig, Germany.

BERGER, A.

Regular and chaotic motion of a kicked pendulum: A Markovian approach

Mechanical devices subject to impulsive excitation may exhibit very complicated dynamics. Though desirable, a complete analysis of the statistical morphogenesis of (the maps induced by) such systems usually is highly demanding. We therefore focus on a special class of maps nevertheless wide enough to comprise a number of interesting examples. Furthermore, an approximation technique tailored to this specific class is shown to improve Markovian approximation techniques discussed in the literature.

1. Statistical stability

Let $(I, \mathcal{B}, \lambda)$ denote the unit interval together with the σ -algebra of its Borel subsets and Lebesgue measure; furthermore, assume that the measurable map $T : I \rightarrow I$ be non-singular, i.e. $\lambda(T^{-1}(B)) = 0$ whenever $\lambda(B) = 0$. The uniquely determined linear operator P_T on L^1 satisfying

$$\int_{T^{-1}(B)} f d\lambda = \int_B P_T f d\lambda \quad \text{for all } B \in \mathcal{B} \text{ and } f \in L^1$$

is called the *Frobenius-Perron operator* associated with T . This positive, non-expansive operator constitutes a major tool in the statistical analysis of dynamical systems ([1,4]). According to [4] the map T is termed *statistically stable* if there exists a unique P_T -invariant density $f^* \in L^1$ and $P_T^n f \rightarrow f^*$ as $n \rightarrow \infty$ for every density f . Conditions implying statistical stability (as well as the weaker form of asymptotic periodicity) are extensively studied in the literature. In view of the application below we state the following result which may be considered a slight modification of the classical Lasota-Yorke theorem ([4]).

Theorem Assume that for a finite number of points $0 = a_0 < a_1 < \dots < a_{r-1} < a_r = 1$ the map $T : I \rightarrow I$ is C^2 on $]a_{i-1}, a_i[$ and has a C^1 -extension to $[a_{i-1}, a_i]$ for all $i = 1, \dots, r$. Then T is statistically stable if only $\lim_{x \nearrow a_i} T(x) = 0$ for all $i = 1, \dots, r$ and $\sup_{x \in I} T'(x) \leq -\tau$ for some $\tau > 1$.

In order to deal with the mechanical application below we consider a special class of maps on I . Let $f : I \rightarrow [0, \infty[$ be a strictly decreasing C^2 function with $f(1) = 1$ and $\beta > 1$. The map \tilde{T} on $[0, \infty[$ defined as

$$\tilde{T}(x) := \begin{cases} f(x) & \text{if } x \in I, \\ \beta^{-1}x & \text{if } x \notin I, \end{cases}$$

induces a measurable map T on I according to $T(x) := \tilde{T}^{n(x)}(x)$ where $n(x) := \min\{l \in \mathbb{N} \mid \tilde{T}^l(x) \in I\}$. A short calculation yields $T(x) = f(x)\beta^{-\lfloor \log_\beta f(x) \rfloor}$; consequently $T(I) \subseteq [\beta^{-1}, 1]$, and the analysis of T may be restricted to the latter interval.

Corollary Let f and β be as above. If the induced map T is expanding, i.e. $\inf_x |T'(x)| > 1$ on $[\beta^{-1}, 1]$, then it is statistically stable.

2. An example: The kicked pendulum

We shall statistically investigate the dynamics of a kicked *long* pendulum with linear friction (see figure 2). The linearized equation of motion reads $ml^2\ddot{\varphi} + k\dot{\varphi} + mgl\varphi = 0$. In order to keep the pendulum in motion a kick is exerted whenever the pendulum's angular velocity does not exceed ω_0 as the pendulum goes through the vertical position from the right to the left, i.e. whenever $0 < -\dot{\varphi}|_{\varphi=0} < \omega_0$; specifically, we assume that at each kick the angular velocity $\dot{\varphi}^-$ is instantaneously enlarged to $\dot{\varphi}^+ = K(\dot{\varphi}^-) > \dot{\varphi}^-$. After introducing the non-dimensional quantities $x := \dot{\varphi}^-/\omega_0$ as well as $\rho := \frac{k}{2ml^2} \sqrt{\frac{l}{g}}$ and $\sigma := \frac{2\pi\rho}{\sqrt{1-\rho^2}}$ we are more or less in the situation discussed above with $f(x) := K(\omega_0 x)/\omega_0$ and $\beta = e^\sigma$. (For simplicity the damping is assumed to be *weak*, i.e. $0 < \rho < 1$.) Clearly, any measurable map on the unit interval could be obtained in this way by appropriately specifying the kick-law K . In the sequel we shall, however, exclusively deal with the affine rule $f(x) := 1 + \alpha(1 - x)$ where $\alpha > 0$. Intuitively a

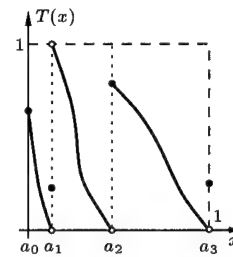


Fig.1 A map satisfying the assumptions of the modified Lasota-Yorke theorem

kick due to this law is the stronger the slower the pendulum and the larger the parameter α . Depending on the parameters σ and α the dynamics of the resulting map $T_{(\sigma,\alpha)}$ on I may differ quite considerably.

By introducing the boundary functions $b_s^-(\xi) := (e^{s\xi} - e^\xi)/(e^\xi - 1)$ and $b_s^+(\xi) := e^{s\xi}$ ($s \in \mathbb{N}$), it is easy to see that $T_{(\sigma,\alpha)}$ has an attracting fixed point x^* whenever $(\sigma, \alpha) \in B_s := \{(\xi, \eta) \in \mathbb{R}_+^2 \mid b_s^-(\xi) < \eta < b_s^+(\xi)\}$ for some $s \in \mathbb{N}$. In the latter case $X_s := \{x \in I \mid T_{(\sigma,\alpha)}^n(x) \not\rightarrow x^*\}$ turns out to be a Cantor set if $s \geq 3$. Its Hausdorff dimension can be calculated as $\dim_H(X_s) = \log_\beta Z$ where Z denotes the unique solution in $[1, \beta]$ of $z + z^2 + \dots + z^{s-1} = z^{\log_\beta \alpha}$. (If $(\sigma, \alpha) \in B_s$ then $\dim_H(X_s) < 1$; on the boundary b_s^- one finds $\dim_H(X_s) = 1$ while on b_s^+ the relation $\dim_H(X_s) = \frac{\sigma_s^*}{\sigma} \leq 1$ holds, with σ_s^* being uniquely defined by $b_s^-(\sigma_s^*) = b_s^+(\sigma_s^*)$.) Furthermore, $(X_s, T_{(\sigma,\alpha)}|_{X_s})$ is easily seen to be topologically conjugate to the full shift on $s-1$ symbols (cf. [2]). The sets B_s ($s \geq 3$) thus provide "tongues" of transient chaos (see figure 3).

If $(\sigma, \alpha) \notin \bigcup_{s \in \mathbb{N}} \overline{B_s}$ the map $T_{(\sigma,\alpha)}$ is piecewise expanding and therefore statistically stable by the above corollary. In general the unique $T_{(\sigma,\alpha)}$ -invariant density f^* will be rather complicated. (Since $T_{(\sigma,\alpha)}$ is piecewise affine one could write down an explicit formula for f^* which in fact turns out to be hardly illuminating, [3].) Probably the most convenient way of discussing f^* and its morphogenesis under varying (σ, α) consists in approximating $T_{(\sigma,\alpha)}$ by a Markov map. By definition, such a map sends each interval $[a_{i-1}, a_i]$ to a union of such intervals. It is well known that the analysis of P_T reduces to a matter of finite-dimensional linear algebra, if T is an expanding, piecewise affine Markov map. In particular, there always exists an invariant density which is piecewise constant. Moreover, a lot of approximation techniques have been discussed in the literature (see [1] and the references cited therein). However, the computational effort due to these methods usually grows *exponentially* with the number of approximation steps that have to be performed. As far as the present problem is concerned, a much better approximation can be found. Although $T_{(\sigma,\alpha)}$ will not be Markovian in general, it might be so with respect to a refined partition: assume that $T_{(\sigma,\alpha)}^n(0) \in \{a_0, \dots, a_r\}$ for some $n \in \mathbb{N}$. It is easy then to see that $T_{(\sigma,\alpha)}$ is a Markov map with respect to $\{a_0, \dots, a_r\} \cup \{T_{(\sigma,\alpha)}(0), \dots, T_{(\sigma,\alpha)}^{n-1}(0)\}$. Consequently, the unique solution of $P_{T_{(\sigma,\alpha)}} f^* = f^*$ can be found by solving a linear equation in \mathbb{R}^{r+n-2} . (Observe that the dimension of the latter problem grows *linearly* with n .) For the system under consideration it is easily seen that the set made up by those parameters (σ, α) which give rise to a Markov map is in fact *dense* in \mathbb{R}_+^2 . It therefore should not come as a surprise that our Markovian analysis provides a rather complete picture of the system's statistical morphogenesis. A few results in this direction are summarized by figure 3. It is worth noting that due to the discontinuities in the family $T_{(\sigma,\alpha)}$ there can be observed more dramatic dynamical changes than for other, more regular families. For example, if α crosses one of the lines b_s^+ from below, an immediate transition from transient to full chaos takes place via a continuum of two-periodic points; following [2] we call this effect a *chaotic explosion*.

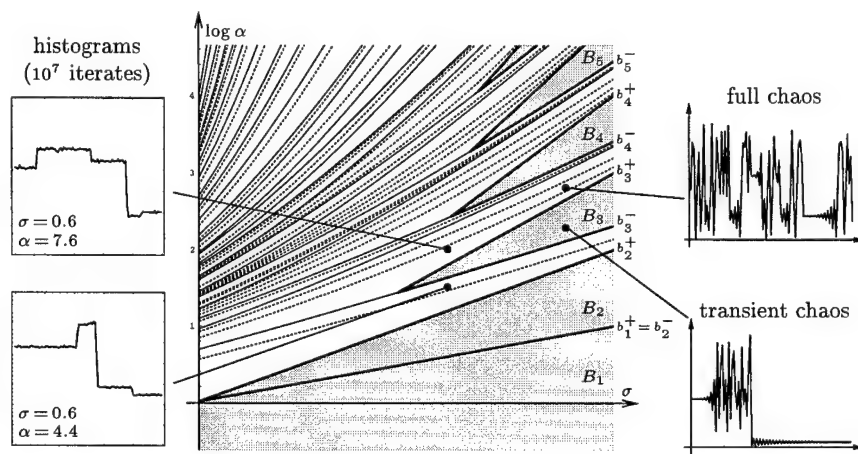


Fig.3 Statistical analysis in the parameter plane; a few first and second order Markovian situations are indicated by solid and broken lines respectively.

3. References

- 1 BOYARSKY, A.; GORA, P. : Laws of Chaos, Birkhäuser, 1997.
- 2 DEVANEY, R.L. : An Introduction to Chaotic Dynamical Systems, Addison-Wesley, 1989.
- 3 KOPF, C. : Invariant measures for piecewise linear transformations of the interval, Appl. Math. Comput. **39** (1990), 123-144.
- 4 LASOTA, A.; MACKEY, M. : Chaos, Fractals and Noise, Springer, 1993.

Address: DR. ARNO BERGER

Vienna Univ. of Technology, Institute of Mechanics, Wiedner Hauptstrasse 8-10, A-1040 Vienna, Austria

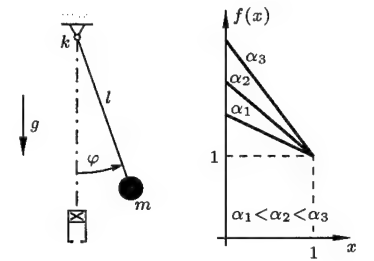


Fig.2 The pendulum model (left) and the non-dimensional kick law f

CALLIES, M.; CALLIES, R.

Hochgenaue Konturliniengenerierung

Automatisierte Meßverfahren tasten Gegenstände mit hoher Genauigkeit ab. Die entstehenden Datenmengen sind für eine direkte Weiterverarbeitung in FE-Programmen zu umfangreich. Ein datenreduzierender, auf multivariaten NURBS basierender Ansatz wird vorgestellt, mit dem sich Konturkurven und -flächen mit hoher Präzision aus Meßwerten ableiten lassen. Die Approximationsqualität wird strikt an die Größe der Meßfehler angepaßten mathematischen Nebenbedingung, unter der die primären Zielfunktionale zu optimieren sind. Lokal adaptive Verfeinerungen erhöhen signifikant die Flexibilität der Ansätze. Alle Schritte unterliegen einer strikten Optimierung über SQP-Verfahren. Beispielhaft wird die automatische Präzisionsauswertung von Schichtbildern aus der Computertomographie vorgestellt. Man erreicht Approximationsgenauigkeiten der Konturlinien von 0.05 mm bei einer Datenreduktion um mehr als den Faktor 5.

1. Bestimmung der zu approximierenden Punkte und zulässigen Gebiete

Die Computertomographie generiert eine Folge von Einzelbildern für parallele Schichten. Jedes Einzelbild besteht aus $q \cdot r$ quadratischen Pixeln endlicher Ausdehnung, jedem Pixel ist ein fester Grauwert zugeordnet (Typisch: 4096 diskrete Graustufen). Alle Grauwerte unterhalb eines festgelegten Schwellwertes S werden als Untergrund interpretiert, alle Werte oberhalb als Material bzw. (in der Medizin) als Gewebesubstanz.

Im Vorverarbeitungsschritt wird ein regelmäßiges Gitter durch die Zentren der Graufächen gelegt. Man erhält eine $q \cdot r$ -Matrix aus Flächenpunkten $X(u_\mu, v_\nu) \in \mathbb{R}$, $\mu = 1 \dots q$, $\nu = 1 \dots r$; je 4 Punkte bilden eine Zelle. Ziel ist die Bestimmung der zu approximierenden Punkte d_j , $j = 0, \dots, m$ durch lineare Interpolation entlang der Gitterlinien sowie die Approximation der Konturlinie durch einen Polygonzug als Verbindungslinie der d_j .

Eine polygonale Höhenlinie tritt entlang einer Kante in eine Zelle ein und verläßt sie wieder entlang einer der anderen Kanten; der Austrittspunkt kann durch Betrachtung der restlichen Kanten und anschließende Interpolation bestimmt werden. Eine nichtganzzahlige Wahl von S verhindert, daß die Konturlinie durch die Ecke einer Zelle oder entlang einer Zellenkante verläuft. Die in Abb. 1 beispielhaft dargestellte Eindeutigkeitsforderung löst das Vier-Punkte-Problem und sichert die Eindeutigkeit des Algorithmus. Zentrale Forderung ist, daß die Verbindungslinie von

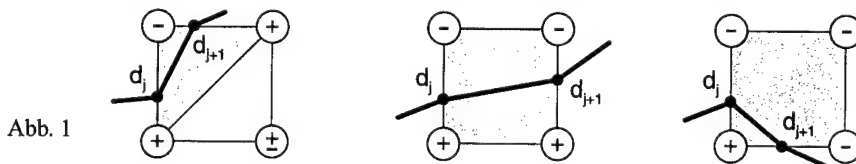


Abb. 1

$X(u_\mu, v_\nu) > S$ und $X(u_{\mu+1}, v_{\nu+1}) > S$ durch den Polygonzug nicht geschnitten wird. Die Bedingung verhindert in Grenzfällen das Zerfallen in mehrere Einzelobjekte und basiert auf dem Prinzip der minimal extrahierten Information [1]. Neben der Festlegung der Approximationspunkte werden die in der Abb. 1 schattierten Bereiche bestimmt, in denen die approximierende Konturlinie verlaufen darf (Beschränkung, die Selbstdurchdringung verhindert!)

2. Optimierung der approximierenden NURBS

NURBS: Gegeben sei ein Intervall $[u_0, u_f] \subset \mathbb{R}$ mit der Unterteilung $u_0 \leq u_1 \leq \dots \leq u_{n+p+1} = u_f$, ferner Gewichte $0 \leq w_i \in \mathbb{R}$ und Kontrollpunkte $P_i := (x_i, y_i)^T \in \mathbb{R}^2$. Dann ist die parametrisierte NURBS-Kurve vom Grad p definiert als

$$C(u) = \frac{\sum_{i=0}^n w_i P_i N_{i,p}(u)}{\sum_{i=0}^n w_i N_{i,p}(u)}.$$

Die B-Spline-Basisfunktionen $N_{i,p}(u) \in \mathbb{R}$ sind rekursiv über dem Knotenvektor $U := (u_0, u_1, \dots, u_{n+p+1})^T \in \mathbb{R}^{n+p+2}$ definiert (Cox-de Boor).

NURBS-basierte Darstellungen ermöglichen sowohl die Beschreibung von Freiformflächen als auch die exakte Darstellung analytischer Standardformen (Kegel, Quadriken, Drehflächen). Durch die Variation von Kontrollpunkten, Knoten, Gewichten und der Parametrisierung erreichen die NURBS eine hohe Flexibilität und sind zur Approximation komplizierter Geometrien besonders geeignet [2].

Optimierungsproblem: Gegeben sind die Datenpunkte $d := (d_j(\tau_j) \in \mathbb{R}^2 \mid j = 0, \dots, m)$. Gesucht wird hier das Minimum der nichtlinearen Zielfunktion $\Phi = \sqrt{\frac{1}{m+1} \sum_{j=0}^m G_j (C(\tau_j; P, w, u) - d_j(\tau_j))^2} \stackrel{!}{=} \min$, $G_j > 0$ (andere Zielfunktionen sind problemlos implementierbar) mit folgenden Variablen:

Kontrollpunkte $P := (P_i \in \mathbb{R}^2 \mid i = 0, \dots, n)$, Gewichte $w := (w_i \in \mathbb{R} \mid i = 0, \dots, n)$, Knoten $u := (u_i \in \mathbb{R} \mid i = 0, \dots, n + p + 1)$ sowie Datenparametrisierung $\tau := (\tau_j \in \mathbb{R} \mid j = 0, \dots, m)$.

Für die Komponenten von P, w, u und τ sind jeweils Grenzen vorgegeben. Die inneren Knoten müssen die lineare Beschränkung $u_{i+1} - u_i \geq 10^{-2}$ erfüllen. Im Fall geschlossener Kurven gilt zusätzlich $P_0 - P_n = 0 \wedge w_0 - w_n = 0$. Die Bereichsbeschränkung aus Abb. 1 und der vorgegebene maximale Abstand der Konturlinie von den Datenpunkten bilden die nichtlinearen Beschränkungen.

SQP-Verfahren: Die Lösung des Optimierungsproblems geschieht mit Hilfe des SQP-Verfahrens NPSOL [3]. Dabei wird eine Folge $\{x_k\}$ konstruiert, die gegen die optimale Lösung x^* konvergiert. In jedem Haupt-Iterationsschritt sind die Variablen und die Lagrange-Multiplikatoren neu zu bestimmen:

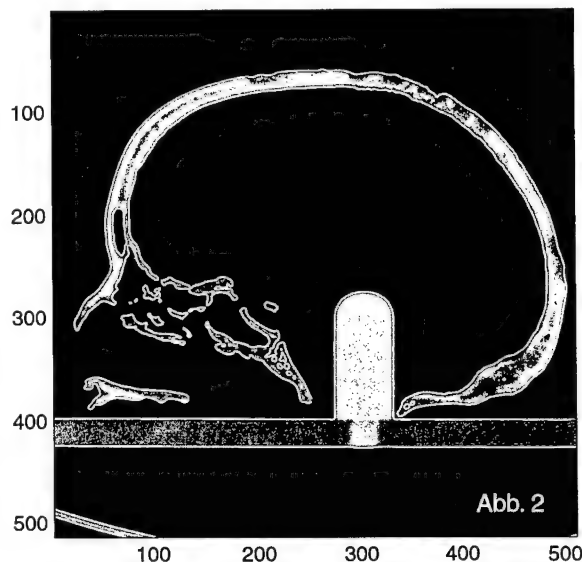
$$x_{k+1} = x_k + \alpha_k p_k, \quad \lambda_{k+1} = \lambda_k + \alpha_k \xi_k, \quad (\xi_k \text{ Suchrichtung für Multiplikatoren})$$

Zur Bestimmung der Suchrichtung $p_k \in \mathbb{R}^n$ entwickelt man die Lagrange-Funktion $\mathcal{L}(x, \lambda) := f(x) - \lambda^T r(x)$ und die Beschränkungen um den Punkt $\{x_k\}$ und bricht die Taylorentwicklung nach dem quadratischen bzw. nach dem linearen Term ab. Das entstandene quadratische Optimierungsproblem wird in den Neben-Iterationen gelöst. Der Relaxationsfaktor $\alpha_k \geq 0$ ergibt sich als Ergebnis einer skalaren Liniensuche mit dem Ziel einer „signifikanten“ Reduktion der erweiterten Lagrange-Gütefunktion $L(x, \lambda, s) := f(x) - \sum_i \lambda_i (c_i(x) - s_i) + 1/2 \sum_i \rho_i (c_i(x) - s_i)^2$. Am Ende jedes Haupt-Iterationsschrittes ist eine neue Näherung für die Hessematrix $\nabla_x^2 \mathcal{L}(x_{k+1}, \lambda_k)$ zu bestimmen. Um die Effizienz des Verfahrens zu erhöhen, werden die erforderlichen Ableitungen analytisch vorgegeben.

3. Anwendungsbeispiel

In Zusammenhang mit der Restauration der Gebeine der seligen Gisela (erste ungarische Königin, ca. 980–1055 n. Chr.) entstanden hochgenaue Aufnahmen des Schädels mit einem neuentwickelten Spiral-CT der Firma Siemens Medizintechnik. Die einzelnen Schichten sind 1 mm dick, ihr Abstand beträgt 0.5 mm. Insgesamt liefert das CT 512 Schichten zu je 512×512 Bildpunkten in 4096 Graustufen (Aufnahmevervolumen: $200 \times 200 \times 250$ mm).

Die beschriebenen Verfahren ermöglichen die computer-gestützte Rekonstruktion des Schädels, exemplarisch dargestellt an einer Schichtaufnahme (vgl. Abb. 2). Es treten in diesem Fall 29 geschlossene Kurven und 5 randbegrenzte Kurvenstücke mit insgesamt 6224 Konturpunkten auf. Die Schädeldecke bildet mit 2605 Punkten das größte Objekt. Die NURBS-Approximation besitzt eine Genauigkeit von weniger als 0.05 mm, die Datenmenge der Kontur wird um den Faktor 5.01 komprimiert. Auch kritische Bereiche wie z. B. die poröse Knochenstruktur der Schädeldecke werden mit hoher Genauigkeit rekonstruiert.



Danksagung

Herrn Prof. Dr. Dr.h.c. R. Bulirsch danken wir für seine Unterstützung. Die Arbeit wurde von der Bayerischen Forschungsförderung im Rahmen des Forschungsverbundes für Med. Bildgebung und Med. Bildverarbeitung (ForBild) großzügig gefördert.

4. Literaturverzeichnis

- 1 CALLIES, R.: Entwurfsoptimierung und optimale Steuerung. Differential-algebraische Systeme, Mehrgitter-Mehrzielsätze und numerische Realisierung, Habilitationsschrift, TU München, 2000.
- 2 PIEGL, L. AND TILLER, W.: The NURBS book, Springer-Verlag Berlin, Heidelberg, New York 1995.
- 3 GILL, P., MURRAY, W., SAUNDERS, M.A. AND WRIGHT, M.H.: User's guide for NPSOL 5.0: A FORTRAN package for nonlinear programming, Technical Report SOL 94, Stanford 1995.

Anschrift: MECHTILD CALLIES, DR. RAINER CALLIES,
Zentrum Mathematik, Technische Universität München, D-80290 München,

KOHOUT, M., SCHREIBER, I. AND KUBÍČEK, M.

Numerical continuation of homo/heteroclinic orbits with an oscillatory approach to stationary point

We formulate a boundary value problem to locate homoclinic or heteroclinic orbits approaching a stationary point in an oscillatory manner so that velocity vectors on the orbit close to the stationary point are used rather than eigenvectors. A Newton method combined with multiple shooting can be used to numerically find the orbit truncated to a finite time interval. This is an extension of an earlier method proposed for 'nonoscillatory' homo/heteroclinics [1,2]. We have incorporated this procedure into a continuation algorithm, so that a parameter dependence can be obtained. The method has been applied to Rössler system and can be applied to travelling waves.

1. Method for calculation and continuation of 'oscillatory' homoclinic orbits

Homoclinic orbits are asymptotic to a stationary point of a vector field. When the orbit is oscillatory it approaches the stationary point within a two-dimensional stable/unstable manifold. There are several numerical methods dealing with the problem of accurately locating homoclinic orbits with a two-dimensional (un)stable manifold [3-5]. These methods rely in some way on stable/unstable eigenspaces at the stationary point. In contrast, our method is using velocity vectors on the orbit close to stationary point avoiding thus the manipulation with the Jacobian. Despite this, the method seems quite efficient. Let

$$\frac{dx}{dt} = f(x; \alpha, \beta), \quad x \in \mathbb{R}^n, \quad (1)$$

be a system of ODEs determined by the vector field $f(x)$ with a stationary point x^S , α and β are parameters. A homoclinic orbit $x(t)$ satisfies the boundary conditions

$$t \rightarrow \pm\infty : x(t) \rightarrow x^S. \quad (2)$$

To find such an orbit numerically implies a truncation to a finite time interval $t \in [0, T]$ and replacing (2) by a suitably chosen substitute. We do this by choosing small distances $\varepsilon_1, \varepsilon_2$ from the ends of the truncated orbit to x^S and using $f(x)$ at the endpoints. Oscillations are embedded in a plane near x^S , so we need two endpoints at the oscillatory side. A homoclinic orbit is a codimension one bifurcation phenomenon that plays a major role in the Shil'nikov transition to deterministic chaos [3]. Therefore a curve of loci of homoclinics in a parameter plane is desired and we have implemented the method for computing homoclinics into the continuation package CONT [6]. This system of equations truncated to a finite interval $t \in [0, T]$ is ($\psi(t, x)$ is the flow of (1), $T_1 = 0, T_N = T$):

$$x^1 - x^N = \varepsilon_2 \frac{f(x^N; \alpha, \beta)}{\|f(x^N; \alpha, \beta)\|} + \varepsilon_1 (c_1 \frac{f(x^1; \alpha, \beta)}{\|f(x^1; \alpha, \beta)\|} + c_2 \frac{f(x^0; \alpha, \beta)}{\|f(x^0; \alpha, \beta)\|}), \quad (3)$$

$$\psi(T_{i+1} - T_i, x^i) - x^{i+1} = 0, \quad i = 1, \dots, N-1, \quad (4)$$

$$f(x^S; \alpha, \beta) = 0, \quad (5)$$

$$\|x^1 - x^S\| = \varepsilon_1, \quad \|x^S - x^N\| = \varepsilon_2, \quad (6)$$

$$\psi(T_0, x^0) - x^1 = 0, \quad \|x^0 - x^S\| = \frac{1}{2}\varepsilon_1, \quad (7)$$

$$G^T G \begin{pmatrix} c_1 \\ c_2 \end{pmatrix} = G^T \begin{pmatrix} \frac{x^1 - x^S}{\|x^1 - x^S\|} \\ \vdots \\ \frac{x^N - x^S}{\|x^N - x^S\|} \end{pmatrix}, \text{ where } G = \begin{pmatrix} \frac{f_1(x^1; \alpha, \beta)}{\|f(x^1; \alpha, \beta)\|} & \frac{f_1(x^0; \alpha, \beta)}{\|f(x^0; \alpha, \beta)\|} \\ \vdots & \vdots \\ \frac{f_n(x^1; \alpha, \beta)}{\|f(x^1; \alpha, \beta)\|} & \frac{f_n(x^0; \alpha, \beta)}{\|f(x^0; \alpha, \beta)\|} \end{pmatrix}. \quad (8)$$

Here Eq. (3) represents the boundary conditions. The initial point x^1 on the truncated orbit is assumed to be at ε_1 distance from the stationary point x^S , see Eq. (6). The approach to x^S is assumed oscillatory and thus an auxiliary point x^0 at distance $\varepsilon_1/2$ is introduced so that x^1 is reached in time T_0 from x^0 , see Eqs. (7). The vectors $f(x^1)$ and $f(x^0)$ provide approximately a basis of a plane of oscillations and a linear combination of the two vectors is sought so that points x^S and x^1 are connected. At the endpoint x^N of the orbit a nonoscillatory approach to x^S is assumed

in the direction of $f(x^N)$; the distance from x^N to x^S is chosen according to Eq. (6) to be ε_2 . Eqs. (4) define the multiple shooting procedure and Eq. (5) defines the stationary point. Finally, Eq. (8) represents a Gauss-Newton procedure for finding best fit of the linear overdetermined problem for the oscillatory plane. Since this is a codim one problem, a solution is found for a particular value of parameter α . By introducing another parameter β , we obtain a continuation problem solved by a predictor-corrector method [7].

2. Example

A simple example may be provided by a variant of a model of abstract chemical kinetics due to Rössler [8]. It is represented by three ODEs:

$$\frac{dx_1}{dt} = -(x_2 + x_3), \quad \frac{dx_2}{dt} = x_1 + Ax_2, \quad \frac{dx_3}{dt} = Bx_1 - Cx_3 + x_1x_3, \quad (9)$$

where A, C are external parameters. For sufficiently large C there is a Hopf bifurcation giving rise to a periodic solution which in turn approaches an oscillatory homoclinic orbit as A is increased. An initial estimate for this orbit has been obtained by continuation of the periodic orbit to sufficiently high period. Then a curve of homoclinics in the A, C plane has been calculated by applying continuation method to Eqs. (3–8), see Fig. 1a. The sequence of selected homoclinic orbits along this curve is shown in Fig. 1b. As C is decreased the orbit shrinks and approaches a point which is a kind of degenerate Bogdanov-Takens singularity. This happens when another bifurcation curve of branch stationary points is met, see inset in Fig. 1a. The numerical procedure seems to converge quadratically.

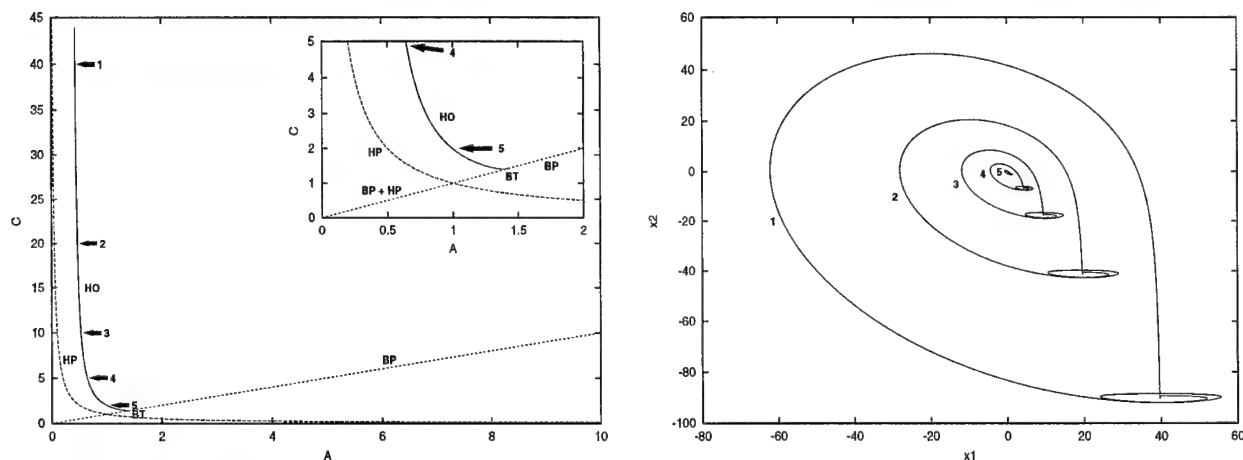


Figure 1. left panel – bifurcation diagram in A - C plane, full line – locus of homoclinic orbits (HO), dashed line – locus of Hopf bifurcation points (HP), dotted line – locus of branch points (BP), BT – Bogdanov-Takens like point; right panel – a series of homoclinic orbits along the line indicated by numbers in the left panel

Acknowledgements: This work has been supported by the project No. VS96073 of the Czech Ministry of Education and grants No. 201/98/0220 and 203/98/1304 of the Czech Grant Agency.

3. References

- 1 SCHREIBER, I., KOHOUT, M., KUBÍČEK, M.: in: Scientific Computing in Chemical Engineering II, F. Keil et al. eds., Springer, Berlin (1999), 200–207.
- 2 KUBÍČEK, M., SCHREIBER, I.: ZAMM 78 Suppl. 3 (1998), 981–982.
- 3 KUZNETSOV, Y. A.: Elements of Applied Bifurcation Theory. Springer Verlag, New York 1995.
- 4 BEYN, W. J.: IMA J. Numer. Anal. 10 (1990), 379–405.
- 5 FRIEDMAN, M. J., DOEDEL, E. J.: SIAM J. Numer. Anal. 28 (1991), 789–808.
- 6 MAREK, M., SCHREIBER, I.: Chaotic Behaviour of Deterministic Dissipative Systems. Cambridge University Press 1995.
- 7 KUBÍČEK, M., MAREK, M.: Computational Methods in Bifurcation Theory and Dissipative Structures. Springer Verlag, New York 1983.
- 8 RÖSSLER O. E.: Phys. Lett. 57 A (1976), 397–398.

Addresses: MARTIN KOHOUT: Dept. of Chem. Eng., Prague Inst. of Chem. Technology, Technická 5, CZ-166 28 Prague 6. E-mail: kohoutm@tiger.vscht.cz, schrig@vscht.cz, kubicek@vscht.cz

ANNA KUCABA-PIETAL.

Squeeze film of micropolar fluid - theory and application

The squeeze flow of micropolar fluid between two plates is considered. The upper plate is rigid and the lower is porous. The analytical solution to the problem is derived for the general form of boundary conditions imposed on microrotation vector on the wall.

1. Foundations

Experiments have shown that when liquids flow through narrow passages then there are many anomalies and nonlinearity of rheological phenomena that the classical Newtonian continuum theory is not able to explain. Eringen's theory of micropolar fluids describes such flows very well. The reviews of research and results in the field to date can be found in the books of MIGOUN, PROKHORENKO [5] and LUKASZEWICZ [3]. Micropolar squeeze films between two plates have been investigated theoretically by several authors due to its applicability in modelling lubrication and biolubrication processes. The problem of squeeze film bearing with micropolar fluid as lubricant has been studied by MATH [4]. Several authors considered the system of squeezing plates as an approximation for the lubrication in the weight bearing synovial fluids under conditions when the area of contact is maximum such as in standing and jumping. NIGAM [6] considered squeeze flow between parallel plates with the reference to human joints. The lower plate was porous and consisted of three layers of different porosities which modelled cartilage. The results were obtained under the assumption, that microrotation vector vanishes on the wall. The problem, concerning the effect of non-zero values of microrotation vector on the walls on squeeze film behavior of micropolar fluid was studied by KUCABA-PIETAL, MIGOUN [2] and results shown, that the effect is considerable and strongly depend on the parameters characterising the fluid micropolarity. This motivated the paper.

2. Formulation of the problem and solution

We consider squeezing flow of micropolar fluids between two parallel plates. The lower plate is stationary and a porous solid consisting of three layers of different porosities. The upper one, which is parallel to the stationary plate is rigid and moves normal to itself towards the lower plate with the velocity U . In the Cartesian coordinate system (x, y, z) the lower plate is described as $y = 0$ and the upper one as $y = h$. The translational velocity of the plate is $(0 - U, 0)$. The motion is very slow. Each of three layers is described by parameter k_i , which denotes Darcy's coefficient, and H_i , which denotes width of the layer, $i = 1, 2, 3$. The fluid leaves the domain between the plates in two directions, through the open boundary at $x = a$ and $x = -a$. So the model may be considered as a two region flow model of (i) squeeze film lubrication between two approaching surfaces with micropolar fluid and (ii) flow of viscous fluid in a porous matrix. In this note we solve (i) problem for general boundary conditions imposed on microrotation vector and using solution by NIGAM [6] in the porous region (ii).

Denoting by $\mathbf{v} = (u, v, 0)$ the velocity, by $\boldsymbol{\nu} = (0, 0, \omega)$ the microrotation and by p - the pressure, the flow in the region (i) can be described by the following system of equations [2]:

$$\frac{\partial p}{\partial x} = \frac{1}{2}(2\mu + \kappa) \frac{\partial^2 u}{\partial y^2} + \kappa \frac{\partial \omega}{\partial y}, \quad \frac{\gamma \partial^2 \omega}{\partial y^2} - 2\kappa\omega - \kappa \frac{\partial u}{\partial y} = 0, \quad \frac{\partial p}{\partial y} = 0. \quad (1)$$

Symbols κ, γ, μ denote rheological constants of micropolar fluid. The boundary conditions for the problem are:

$$\mathbf{v} = U, \quad \boldsymbol{\nu} = \frac{1}{2}(\alpha) \text{rot} \mathbf{v}, \quad (2)$$

for $y = h$, and

$$\mathbf{v} = \mathbf{u}, \quad \boldsymbol{\nu} = \frac{1}{2}(\alpha) \text{rot} \mathbf{v} \quad (3)$$

for $y=0$. h is the gap width between the two plates, $0 \leq \alpha \leq 1$, and $\mathbf{u} = (u_1, v_1, 0)$ denotes velocity resulting from porosity of the lower wall. From analysis of the flow in porous layer flow given by NIGAM it follows that:

$$u_1 = \frac{k_i}{\mu} \frac{\partial p_1}{\partial x}, \quad v_1 = \frac{k_i}{\mu} \frac{\partial p_1}{\partial y} \quad (4)$$

Solving (1) subject to boundary conditions (2)-(4) we get

$$u(x, y) = - \left[(-1 + \cosh(ky)) \frac{\kappa}{k} X + \sinh(ky) \frac{\kappa}{k} Y + \frac{1}{2\mu} y^2 + 2Vy + \frac{k_1}{\mu} \right] PE(x), \quad (5)$$

$$\omega(x, y) = \left[X \sinh(ky) + Y \cosh(ky) + V - \frac{1}{2\mu} y \right] PE(x) \quad (6)$$

Functions which appeared in the formula are defined below:

$$Y = \frac{-(V(1+2\alpha))}{\alpha\kappa+1}, \quad X(\cosh(kh)-1) = -\frac{1+2\alpha}{\alpha\kappa+1} V \sinh(kh) - \frac{hk}{\kappa} (2V + h \frac{h}{2\mu^N}), \quad (7)$$

$$N = \sqrt{\frac{\kappa}{2\mu+\kappa}}, \quad L = \frac{h}{l}, \quad l = \sqrt{\frac{\gamma}{4\mu}}, \quad k = N \frac{L}{h}, \quad (8)$$

$$V = \frac{(-VP1 + \alpha VP2)}{(\alpha VP3 - VP4) + (1+2\alpha)(\cosh(kh)-1)}, \quad VP4 = \frac{2\alpha+1}{\alpha\kappa+1}, \quad (9)$$

$$VP1 = \frac{h}{2\mu} (-1 + ct \frac{hk}{\kappa}), \quad VP2 = \frac{h}{2\mu} (2 - ct hk), \quad VP3 = ct(-\kappa) (\frac{1+\alpha}{\alpha\kappa+1} \sinh(kh) - 2 \frac{hk}{\kappa}), \quad (10)$$

$PE(x)$ denotes $\frac{dp}{dx}$ and $ct = \coth(ky/2)$; From the equation of continuity and analysis of porous layer flow in the region (ii) [6] we get

$$\frac{d}{dx} \int_0^h u dy = U + H \frac{d^2 p}{dx^2} \quad (11)$$

where $H = (H_1 + \frac{k_2}{k_1} H_2 + \frac{k_3}{k_2} H_3)$. Integrating (11) with respect to x and using the boundary conditions (2)-(4) the pressure is given:

$$p - p_0 = \frac{-U(a^2 - x^2)}{\left[\frac{1}{6\mu} h^3 + (1 - \cosh(kh)) \frac{\kappa}{k^2} Y + (-\sinh(kh) + h) \frac{\kappa}{k^2} X - h^2 V + 6k_1 h + 12\mu H \right]}. \quad (12)$$

After differentiation (12) we receive $\frac{dp}{dx}$ which appears in the expressions (5), (6) defining solution to the problem. Having it done we are able to obtain all tribological characteristics of the bearing system: load L and time of approach T . For the case $\alpha = 0$ obtained solution cover the case considered by NIGAM.

3. References

- 1 ERINGEN, A. C.: Theory of Micropolar Fluids; J. Math. Mech. **16** 1966 1-16.
 - 2 KUCABA-PIETAL, A., MIGOUN P.N.: Effects of non-zero values of microrotation vector on the walls on squeeze film behavior of micropolar fluid; Int. J. Nonlin. Sci. Num. Simulation, (2000), to appear.
 - 3 LUKASZEWICZ, G.: Micropolar fluids. Theory and Application. ;Birkhouser, Berlin 1999.
 - 4 MATI, G.: Micropolar Squeeze Film Bearing; Jap. J. Appl. Phys. **13** (1974), 1440 -1443.
 - 5 MIGOUN N.P., PROHORENKO P.P. : Hydrodynamics and Heat Transfer of Gradient Flows of Micropolar Fluids . Minsk 1988 (in Russian).
 - 6 NIGAM, K.M. MANOHAR, K., JAGGI, J.: Micropolar Fluid Film Lubrication Between Two Parallel Plates With Reference To Human Joints; Int.J. Mech. Sci. **24** (1982), 661-671.
- Address: DR. ANNA KUCABA-PIETAL, Department of Fluid Mechanics and Aerodynamics, Rzeszow University of Technology, Powstancow Warszawy 8 35-359 Rzeszow Poland

DIRK LANGEMANN

Numerical analysis of the polygonalization of railway wheels

The formation of irregular wear patterns on wheels in high-speed trains is an important problem because it affects negatively the convenience of passengers and increases maintenance costs. Finally, nonhomogeneous contact geometry leads to considerable variations of loading conditions and is hence a security hazard.

An algorithm is presented to analyze the development of irregular wear patterns quantitatively and to predict wear formation of wheel/rail-systems. It is based on the concept of ergodicity and it is time-expensive but reliable. The algorithm is applied on a 3D-model using different parameters.

1. The coupled system of multiple time-scales

Let us regard a mechanical system, e. g. a wheelset, which undergoes wear on a surface of a body due to contact with another body. The generalized coordinates $q \in \mathbb{R}^l$ with the time derivatives $\dot{q} \in \mathbb{R}^l$ describes the motion of the mechanical system. The wearing surface S is parameterized by $x \in \mathbb{R}^k$, ($k < l$) and $u(x, t)$ is the depth of the total material loss at the point $x \in S$ until the time t . Every position q of the mechanical system implies a set of contact points, we shortly note $x = y(q)$ if $x \in S$ is a point in contact depending on the position q . Now, we get the coupled system of the equation of motion (ODE)

$$m\ddot{q} = f(q, \dot{q}, \lambda) + \lambda \nabla_q g(q, u) \quad \text{with } g(q, u) = 0 \quad (1)$$

with the mass matrix m , the outer force f , the LAGRANGEian multiplier λ and the geometrical constraints g depending on u . Using the actual wear $w(q, \dot{q}, \lambda)$ at $y(q)$, we formulate the evolution equation of the surface (PDE)

$$u_{,t}(y(q), t) = w(q, \dot{q}, \lambda) \quad (2)$$

In practice, exact knowledge about the wear of a material pair is lacking, and thus the actual wear is assumed to be proportional to the dissipated energy. In general, the values of w and y are functions over S , but for reasons of simplicity we will handle them as single values.

The dynamical behaviour of the system, s. Eq. (1), and the wear evolution, s. Eq. (2), have completely different time-scales, e. g. the wear speed of a railway wheel is about $5 \cdot 10^{-11}$ m/s. That is why we neglect a second LAGRANGEian multiplier with respect to the change of u and why the accurate numerical solution of the hybrid system (1), (2) is impossible in time intervals relevant for wear. On the other hand, most realistic mechanical systems, in particular rolling wheelsets, behave ergodically in time relevant for wear, although they are deterministic in short time intervals, cf. [4].

2. Adaptation and decoupling of the time-scales

The standard method to handle this problem is the adaptation of the time-scales by introducing a slow time $\tau = \beta^{-1}t$ and by enlarging the actual wear by the amplification factor β in the range of 10^4 up to 10^7 , cf. [3]. But this leads to considerable errors if $\dim S > 1$, cf. [2].

We propose the introduction of a density $\mathcal{W}(x, \tau)$ of wear intensity at the point x and the slow time τ . With a solution of Eq. (1) for fixed geometry $u(\tau)$, we regard the measure of the wear intensity on $\Theta \subset S$

$$\nu(\Theta, \tau) = \lim_{T \rightarrow \infty} \int_0^T w(q, \dot{q}, \lambda) \gamma_\Theta(y(q)) dt \quad (3)$$

with the characteristic function $\gamma_\Theta(x) = 1$ if $x \in \Theta$ and $\gamma_\Theta(x) = 0$ else. Due to the ergodic property the transient phase of the motion does not influence the measure ν , and on its support, ν is absolutely continuous to the EUKLIDIAN measure of Θ . The density of ν is $\mathcal{W}(x, \tau)$ and we replace Eq. (2) by

$$u_{,\tau}(x, \tau) = \beta \mathcal{W}(x, \tau). \quad (4)$$

Now, the solution of Eq. (1) acts as an input to the right hand side of the evolution equation (4).

3. Numerical technique

Eq. (4) can be handled by standard methods for evolution problems, e. g. by a semi-discretization in x with $x_i \in \Theta_i$, and the patches $\{\Theta_i\}$ form a partition of S . The evaluation of the right hand side consists in the solution of Eq. (1) with $t \in [0, T]$ for fixed $u(\tau)$, and $\nu(\Theta_i, \tau)$ is approximated, s. Eq. (3). The approximation is to accept if the relative change of ν with respect to T is neglectable. This procedure is time expensive but provides reliable results, cf. [2].

4. Results

It can be proven that the occurrence of wavy wear patterns is the generic case and not the exception. In the simulation, TRUE's wheelset model was chosen as a relatively simple 3D-wheelset with a complex behaviour of motion, cf. [4]. In particular, it has treads which are extended in two dimensions.

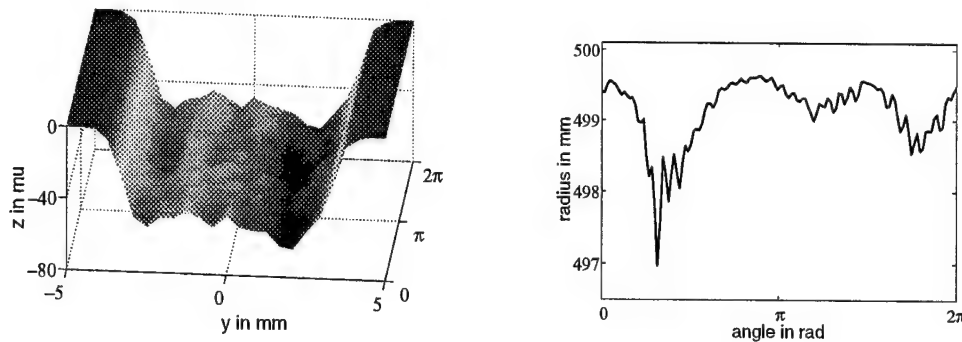


Figure 1: typical worn polygonalized tread; radius of a strongly worn wheel

In Fig. 1, a typical worn tread is shown on the left and a strongly worn contour of a wheel on the right. We remark three maxima of wear over the circumference and more material loss at the margins of the surface which comes potentially in contact with the rail. Both effects fit to the measurements of real polygonalized wheels.

The *slip* is the mean relative velocity of the particles in contact on the wheel and the support to each other, it is regarded as an important system parameter, cf. [1]. The influence of the slip, the conicity of the wheels et al. on the total material loss and on the strength of the polygonalization effect is investigated by first parameter studies.

The total material loss is strongly increasing with the absolute slip of the rolling wheel in the case of fixed vehicle speed and slightly decreasing with the speed in the case of a fixed slip. This holds if the actual wear increases with the dissipated energy in the used wear law (2). It is to mention that no single valued relation between the total material loss and the relative slip (slip per speed) could be exposed.

On the other hand, a total material loss is acceptable if the wheel stays round. We find a non-monotonous dependency of the unroundness on the slip, the speed and the conicity of the wheels, i. e. there are some rare parameter combinations which cause wheels staying nearly round. Nevertheless most of them effect unround wheels, and re-smoothing combinations were not found. The number of three fundamental radius maxima over the circumference is relatively stable. We have found ergodicity as a second fundamental property of wearing mechanical systems, beside the feed-back between different time-scales.

Acknowledgements

The results presented in this paper are based on a joint project sponsored by the German Research Council (DFG) together with DR. KURT FRISCHMUTH, Rostock.

5. References

- 1 KISILOWSKI, J., KNOTHE, K.: Advanced Railway Vehicle System Dynamics, Warsaw, 1991
- 2 LANGEMANN, D.: Numerische Analyse abrasiv verschleißender mech. Systeme. Fortschritt-Berichte VDI 12.392, 1999
- 3 LINDNER, C.: Verschleiß von Eisenbahnradern mit Unrundheiten. Zürich, 1997
- 4 TRUE, H.: Dynamics of a rolling wheelset. Applied Mechanics Review 46, No. 7 (1993)

Addresses: DR. DIRK LANGEMANN, University of Rostock, Dept. of Mathematics, D-18051 Rostock, Germany

RIEDER, A.

How to scale reconstruction filters in 2D-computerized tomography

The state-of-the-art reconstruction algorithm in 2D tomography is the filtered backprojection algorithm. The quality of the reconstructed density function depends crucially on the proper scaling of the reconstruction filter in relation to the discretization step size. We show how to do it the right way in the parallel scanning geometry.

1. Introduction

Tomographic reconstruction allows to look inside a closed object without destroying it, for instance, the human body in medical imaging. Speaking in mathematical terms we have to find a density distribution f supported in the unit ball Ω from all its line integrals.

The analytic basis of tomography in 2D is the reconstruction formula

$$f = (2\pi)^{-1} \mathbf{R}^* \Lambda \mathbf{R} f. \quad (1)$$

Here $\mathbf{R} : L^2(\Omega) \rightarrow L^2(Z)$, $Z =]-1, 1[\times]0, \pi[$, denotes the *Radon transform*,

$$\mathbf{R}f(s, \vartheta) := \int_{L(s, \vartheta) \cap \Omega} f(x) \, d\sigma(x),$$

mapping a function to its integrals over the lines $L(s, \vartheta) = \{\tau \omega^\perp(\vartheta) + s \omega(\vartheta) \mid \tau \in \mathbb{R}\}$, $s \in]-1, 1[$, $\omega(\vartheta) = (\cos \vartheta, \sin \vartheta)^t$ and $\omega^\perp(\vartheta) = (-\sin \vartheta, \cos \vartheta)^t$ for $\vartheta \in]0, \pi[$. This parameterization of lines hitting Ω gives rise to the *parallel scanning geometry*.

The *backprojection operator* $\mathbf{R}^* : L^2(Z) \rightarrow L^2(\Omega)$ is the adjoint to \mathbf{R} . Formally, Λ is the square root of the negative 1D Laplacian $-\Delta$: $\Lambda = (-\Delta)^{1/2}$. In (1), Λ acts on the variable s of $\mathbf{R}f$. For a proof of (1) see, e.g., [1].

As Λ amplifies high frequencies instabilities occur very likely in reconstructing f from noisy Radon data $\mathbf{R}f$ using (1) directly. Therefore, an algorithmic realization of tomographic reconstruction is based on (\star denotes convolution and \star_s denotes convolution with respect to the variable s)

$$f \star e_\gamma = \mathbf{R}^*(v_\gamma \star_s \mathbf{R}f), \quad e_\gamma = \mathbf{R}^* v_\gamma, \quad (2)$$

where $e_\gamma(x) = e(x/\gamma)/\gamma^2$, $\gamma > 0$, and $e = e_1$ is a smooth function with normalized mean value (called a *mollifier*). Hence, $f \star e_\gamma$ is a smoothed or mollified approximation to f . The convolution of the tomographic data $\mathbf{R}f$ with the *reconstruction kernel* or *reconstruction filter* v_γ implements a low pass filtered version of $\Lambda \mathbf{R}f$. A discretization of (2) leads to the filtered backprojection algorithm, see, e.g., [1, Chap. V].

In the following we will investigate how to choose γ depending on the discretization step size h used in the filtered backprojection algorithm. However, we will first comment on the computation of v_γ from e_γ .

2. Reconstruction filters

The reconstruction formula (1) holds true for all f in the L^2 -Sobolev space $H_0^{1/2}(\Omega)$ with zero boundary conditions. With $e_\gamma \in H_0^{1/2}(\Omega)$ we therefore define

$$v_\gamma := \Lambda \mathbf{R} e_\gamma / (2\pi) \quad (3)$$

which yields the required relation $e_\gamma = \mathbf{R}^* v_\gamma$. Restricting ourselves to radial symmetric mollifiers we may express (3) by

$$v_\gamma(s) = \frac{1}{\pi} \int_0^\infty \sigma \hat{e}_\gamma(\sigma, 0) \cos(s\sigma) \, d\sigma, \quad (4)$$

where \hat{e} is the Fourier transform of e being radial symmetric as well. Please note that $v_\gamma(s) = v_1(s/\gamma)/\gamma^2$. We therefore need to evaluate the integral in (4) only for $\gamma = 1$. This can be done analytically for several useful

mollifiers e .

Let us look at an example. We define a family $\{e^\nu\}_{\nu>0}$ of radial mollifiers by $e^\nu(x) := (1 - \|x\|^2)^\nu$ for $x \in \Omega$ and $e^\nu(x) := 0$, otherwise, which gives rise to the reconstruction kernels

$$v^\nu(s) = \frac{1}{2\pi^2} \begin{cases} 2(\nu+1) {}_2F_1(1, -\nu; 1/2; s^2) & : |s| \leq 1 \\ -{}_2F_1(1, 3/2; \nu+2; 1/s^2)/s^2 & : |s| > 1 \end{cases}$$

where ${}_2F_1$ is the *hypergeometric series*. For other examples see [2].

3. Scaling the filters

Here we model the filtered backprojection algorithm with discretization step size $h = 1/q$, $q \in \mathbb{N}$, by

$$f_R = \mathbf{R}^* \mathbf{I}_h(w \overset{h}{\star} g), \quad g = \mathbf{R}f,$$

see (2), where $\overset{h}{\star}$ denotes the *discrete convolution*,

$$\left(w \overset{h}{\star} g(\cdot, \vartheta)\right)_l = h \sum_k w_{l-k} g(hk, \vartheta) \quad \text{with } w_k = \begin{cases} v_\gamma(hk) & : k = -2q, \dots, 2q \\ 0 & : \text{otherwise} \end{cases}.$$

Above $\mathbf{I}_h : \ell^2(\mathbb{Z}) \rightarrow L^2(\mathbb{R})$ is the piecewise linear *interpolation operator*, $\mathbf{I}_h a(s) = \sum_k a_k B_h(s - hk)$, $B_h(s) = B(s/h)$, with B being the linear B-spline supported in $[-1, 1]$.

We will now investigate the difference (χ denotes the indicator function of the interval $[-2, 2]$)

$$\delta f := f_R - \mathbf{R}^*(\chi v_\gamma \star g) = \mathbf{R}^*\left(\mathbf{I}_h(w \overset{h}{\star} g) - \chi v_\gamma \star g\right)$$

which coincides with the reconstruction error $f_R - f \star e_\gamma$ in the region of interest Ω .

Theorem 1. *Let f be in $C_0^\infty(\Omega)$ and let v_γ be an even function. Then,*

$$\widehat{\delta f}(\xi) = 2\pi \frac{\widehat{f}(\xi)}{\|\xi\|} \left(\mathbf{T}_h v_\gamma(\|\xi\|) - \sqrt{2\pi} \widehat{\chi v_\gamma}(\|\xi\|) \right) + 2\pi \mathbf{T}_h v_\gamma(\|\xi\|) \sum_{l \neq 0} \frac{\widehat{f}(\|\xi\| - 2\pi l/h) \xi / \|\xi\|}{\|\xi\|}$$

with $\mathbf{T}_h v_\gamma(\sigma) = h(v_\gamma(0) + 2 \sum_{k=1}^{2q} v_\gamma(hk) \cos(hk\sigma)) \operatorname{sinc}^2(h\|\xi\|)$.

A closer look at $\widehat{\delta f}$ shows that term $\widehat{f}(\xi)/\|\xi\|$ is the critical one. In general $\widehat{f}(\xi)/\|\xi\|$ is far being absolutely small for small $\|\xi\|$. Therefore, we have know the behavior of the difference $\mathbf{T}_h v_\gamma(\sigma) - \sqrt{2\pi} \widehat{\chi v_\gamma}(\sigma)$ as σ tends to 0.

Lemma 2. *We have that*

$$\lim_{\sigma \searrow 0} \sigma^{-1} \left| \operatorname{sinc}^2(h\sigma) \mathbf{T}_h v_\gamma(\sigma) - \sqrt{2\pi} \widehat{\chi v_\gamma}(\sigma) \right| = 0$$

if and only if

$$h \left(v_\gamma(0) + 2 \sum_{k=1}^{2q} v_\gamma(hk) \right) = \int_{-2}^2 v_\gamma(s) \, ds. \quad (5)$$

Selecting γ for fixed h as a solution of equation (5) guarantees tomographic reconstructions without artefacts due to wrong scaling of the reconstruction filter.

All proofs omitted in this short note as well as numerical experiments and further references can be found in [2].

4. References

- 1 NATTERER, F.: The mathematics of computerized tomography. Wiley, Chichester, 1986.
- 2 RIEDER, A.: Principles of reconstruction filter design in 2D-computerized tomography. Work in progress, 2000.

Address: PROF. DR. ANDREAS RIEDER, Institut für Wissenschaftliches Rechnen und Mathematische Modellbildung, Universität Karlsruhe (TH), 76128 Karlsruhe, Germany,
email: andreas.rieder@math.uni-karlsruhe.de.

SCHAGERL, M.; BERGER, A.

On the appropriate treatment of singularly perturbed wave equations

Engineers frequently find themselves concerned with the following situation: One is not interested in certain effects of a model, expecting them to have no significant influence, and one therefore simply neglects them – even if the type of the governing equations is changed. Having obtained a sound knowledge about the thus simplified problem one would nevertheless like to take into account the effects neglected at first, preferably as some sort of small perturbation. By means of an example from dynamics we point out that such an approach may necessitate some careful analysis: More often than not the perturbations turn out to be of rather singular type.

1. The elastic pendulum: a multiple scales approach

We consider a light elastic rod with high stiffness, i.e. $\frac{mg}{EA} \ll 1$; in addition we also include linear viscous damping D (see Fig. 1a). For simplicity we assume the rod's configuration to remain perfectly straight. By $r = r(s, t)$ we denote the distance from the fixation point to the material point being at position s in the unstrained configuration. The pendulum's motion due to gravity, elasticity and damping is governed by

$$mr_{tt} - EA r_{ss} - Dr_{ts} = mr\dot{\varphi}^2 + mg \cos \varphi, \quad (1a)$$

$$I\ddot{\varphi} = -Sg \sin \varphi; \quad (1b)$$

here the first and second order moments have been denoted by $S(t) := m \int_0^1 r(s, t) ds$ and $I(t) := m \int_0^1 r^2(s, t) ds$, respectively. As the free endpoint isn't subjected to any tension, the solution has to satisfy the boundary condition $EA(r_s(1, t) - 1) + Dr_{ts}(1, t) \equiv 0$; at the fixation point obviously $r(0, t) \equiv 0$. Motivated by the high stiffness – and perhaps numerical problems when evaluating (1) – one may neglect the longitudinal extension. This naturally gives rise to the study of an inextensible rod, i.e. $r(s, t) \equiv s$. Clearly this reduction process yields the numerically well-behaved system (1b). Having obtained a solution of the reduced problem, the following question arises: Which properties of the former persist if the neglected effect is taken into account as small perturbation?

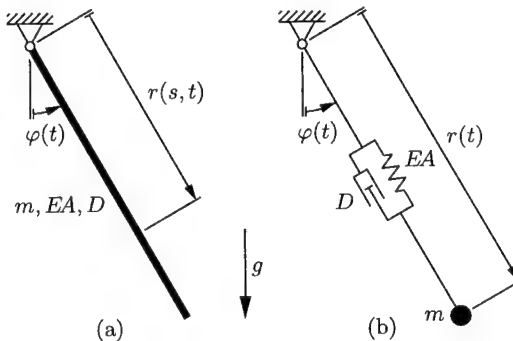


Fig. 1. A continuous visco-elastic pendulum (a) and its discrete analogon (b).

For the sake of technical lucidity we shall not consider the complicated partial differential equation (1a) in the sequel. Anticipating the result of a discretization procedure applied to (1), e.g. a simple finite difference scheme, it is sufficient to consider the analogous but finite dimensional system of a spring pendulum (Fig. 1b) in order to discuss an appropriate perturbation technique. The pendulum's governing equations with $r = r(t)$ then reads

$$m\ddot{r} + EA(r - 1) + D\dot{r} = mr\dot{\varphi}^2 + mg \cos \varphi \quad (2)$$

whereas the equation for φ is just (1b) with $I := mr^2$ and $S := mr$. Scaling time by \sqrt{g} and introducing the non-dimensional parameters $\epsilon^2 := \frac{mg}{EA}$ and $2\lambda := \frac{D}{m\sqrt{g}}$ we substantially have to discuss an equation

$$\epsilon^2 \ddot{r} + 2\lambda \epsilon^2 \dot{r} + r = 1 + \epsilon^2(ar + b).$$

We associate the limit $\epsilon \rightarrow 0$ to passing from an elastic to a rigid pendulum by increasing the former's stiffness. This clearly yields a singular perturbation problem ([2]): Setting $\epsilon = 0$ turns our governing differential equation into an algebraic one ($r(t) \equiv 1$). Since the latter trivial solution is always present in our model, we prefer introducing

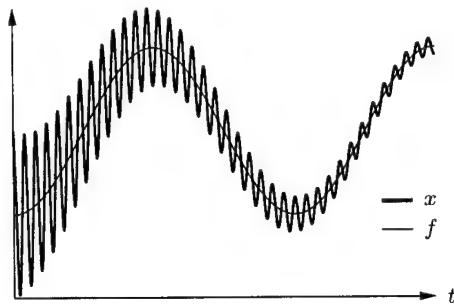


Fig. 2. A Solution of (3) for $\epsilon = 0.02$ and $f(t) = 1 + \sin^2 t$. The fast oscillations are persistent for long times.

a new variable x according to $r = \epsilon^2 x + 1$. In physical terms, x is just the ratio of the force in the pendulum's spring and the weight of the endmass. Subsequently we shall thus discuss the singularly perturbed initial value problem

$$\epsilon^2 \ddot{x} + 2\lambda \epsilon^2 \dot{x} + (1 - a\epsilon^2)x = f, \quad x(0) = \bar{x}, \quad \dot{x}(0) = \bar{v}; \quad (3)$$

here a and f are assumed to be given functions of t . Expecting the dynamics of typical solution of (3) to take place on different time scales t (slow) and $\tau := \frac{t}{\epsilon}$ (fast; see Fig. 2) we insert the asymptotic expansion

$$x(t) = x_0(t, \tau) + \epsilon x_1(t, \tau) + \epsilon^2 x_2(t, \tau) + O(\epsilon^3) \quad \text{as } \epsilon \rightarrow 0 \quad (4)$$

into (3). Balancing terms of zeroth, first and second order of ϵ respectively then yields

$$O(1): \quad x_{0,\tau\tau} + x_0 = f, \quad x_0(0, 0) = \bar{x}, \quad x_{0,\tau}(0, 0) = 0, \quad (5a)$$

$$O(\epsilon): \quad x_{1,\tau\tau} + x_1 = -2x_{0,t\tau} - 2\lambda x_{0,\tau}, \quad x_1(0, 0) = 0, \quad x_{1,\tau}(0, 0) = -x_{0,t}(0, 0) + \bar{v}, \quad (5b)$$

$$O(\epsilon^2): \quad x_{2,\tau\tau} + x_2 = -2x_{1,t\tau} - 2\lambda x_{1,\tau} - 2\lambda x_{0,t} - x_{0,tt} + ax_0, \quad x_2(0, 0) = 0, \quad x_{2,\tau}(0, 0) = -x_{1,t}(0, 0). \quad (5c)$$

According to the idea of two-timing, the variables t und τ have to be considered independent ([4]). Hence we have to solve the set of partial differential equations (5) successively. From the lowest order equation (5a) we simply get $x_0(t, \tau) = a_0(t) \cos \tau + b_0(t) \sin \tau + f(t)$. Note that the functions a_0 and b_0 are not specified yet. They are determined from the vital requirement that x_0 must not cause any fast resonance on the right hand side of (5b), $-2x_{0,t\tau} - 2\lambda x_{0,\tau} = 2(\dot{a}_0(t) + \lambda a_0(t)) \sin \tau - 2(\dot{b}_0(t) + \lambda b_0(t)) \cos \tau$; imposing initial conditions then yields $a_0(t) = (\bar{x} - f(0))e^{-\lambda t}$ and $b_0(t) \equiv 0$. From the $O(\epsilon)$ equation (5b) we obtain $x_1(t, \tau) = a_1(t) \cos \tau + b_1(t) \sin \tau$. Again we choose the functions a_1 and b_1 in such a way that the trigonometric terms are non-resonant for (5c). From the initial data we finally get the asymptotic relation

$$x(t) = f(t) + (\bar{x} - f(0))e^{-\lambda t} \cos \frac{t}{\epsilon} + \epsilon \left[(\bar{x} - f(0)) \left(\lambda + \frac{1}{2} \lambda^2 t + \frac{1}{2} \int_0^t a(\nu) d\nu \right) + \bar{v} - \dot{f}(0) \right] e^{-\lambda t} \sin \frac{t}{\epsilon} + O(\epsilon^2)$$

as $\epsilon \rightarrow 0$. Note that the first term is the solution of the reduced problem, i.e. $\epsilon = 0$ in (3). The singular nature of (3) is highlighted by the fact that there is – even on order $O(1)$ – an additional term in the approximate solution not visible in (3) with $\epsilon = 0$. We further point out that contrary to (4) separating asymptotic expansions like

$$x(t) = x_0(t) + \epsilon^2 x_2(t) + \epsilon^4 x_4(t) + \epsilon^2 (X_0(\tau) + \epsilon^2 X_2(\tau)) + O(\epsilon^6) \quad \text{with } \tau = \frac{t}{\epsilon^2} \quad (6)$$

(as advocated e.g. by [3]) would fail. Instead of (5a) expansion (6) would lead to $X_0'' + x_0 = f$ from which no reasonable insight on the function X_0 could be gained. Notice that such a treatment would nevertheless suggest the solution $x_0 = f$ of the reduced problem.

2. The role of damping

Expansion (6) is often used in initial layer problems where, due to strong damping, the solution quickly converges to the one of the reduced problem. One could therefore be tempted to justify the usage of (6) even for our problem by increasing the damping parameter λ in (3). However, this justification only works if $1/\lambda(\epsilon) = o(\epsilon)$ as $\epsilon \rightarrow 0$, e.g. $2\lambda(\epsilon) := c\epsilon^{-2}$. In the latter case, inserting (6) in (3), would yield on lowest order

$$O(1): \quad X_0'' + cX_0' + x_0 = f, \quad x_0(0) = \bar{x}, \quad \dot{x}_0(0) + X_0'(0) = \bar{v}. \quad (7)$$

At this point one can assume that the initial layer correction X_0 is fast decaying and hence can be neglected. This yields $x_0(t) = \int_0^t f(\nu) e^{(\nu-t)/c} d\nu + \bar{x}e^{-t/c}$ and in turn, after inserting this result into (7), $c^2 X_0(\tau) = (f(0) - \bar{x} - c\bar{v})e^{-c\tau}$ which justifies the convergence assumption. However, we point out that assuming $\lambda(\epsilon)\epsilon^2 = \text{const.}$ (or more generally $1/\lambda(\epsilon) = o(\epsilon)$ as $\epsilon \rightarrow 0$) is quite unreasonable from a physical point of view. Usually, materials like steel or polymers behave just the other way round: the higher the stiffness the lower the internal damping ([1]). We thus conclude that a thorough and realistic analysis of our model (as well as of the original wave propagation problem) definitely requires the use of multiple scales.

3. References

- 1 ASHBY, M. F.: Materials Selection in Mechanical Design. Pergamon Press, Oxford 1993.
- 2 HOLMES, M. H.: Introduction to Perturbation Methods. Springer-Verlag, New York 1995.
- 3 KUHN, A.: Numerische Behandlung von *Tethered Satellite Systems* unter besonderer Berücksichtigung längssteifer Verbindungsseile. Dissertation, TU Wien 1995.
- 4 O'MALLEY, R. E.: Introduction to Singular Perturbations. Academic Press, New York 1974.

Address: Dr. MARTIN SCHAGERL, Dr. ARNO BERGER

Technische Universität Wien, Institut für Mechanik, Wiedner Hauptstraße 8-10, A-1040 Wien, Austria

VRDOLJAK, M.; JANKOVIĆ, S.

Aircraft performance obtained from modified point mass model

1. Introduction

Complete motion of the rigid aircraft is described with the 6-degrees-of-freedom model (6DOF) [1]. This model is complex and requires large sets of data for modeling the aerodynamics, mass and propulsion. For the application of aircraft performance analysis we need to analyze the motion of the aircraft's center of gravity with the mass as a function of time due to the fuel consumption in order to determine some global characteristics of that motion. The flight regimes of the interest for the aircraft performance are quasi steady straight flight and sustained turn. In this paper a modified point mass model which describes only the motion of the center of the gravity will be presented and analyzed. Notation used here will be from [2] if not mentioned otherwise.

2. Modified point mass model

Since the airplane doesn't have the constant mass, we have to apply the theory of Gantmakher [3]

$$m(t) \cdot \frac{d\vec{V}_K}{dt} = \vec{R}^A + \vec{F} + m(t) \cdot \vec{g}. \quad (1)$$

This theory gives us the components of the propulsion force \vec{F} along the principal axes of inertia $[T \cos \alpha_T \quad 0 \quad T \sin \alpha_T - F_{P\sigma}(\alpha_P - \alpha_T)]^T$ as described in [4]. Here T is product of a mass flow and a velocity of the flow. The part $F_{P\sigma}(\alpha_P - \alpha_T)$ can be neglected in respect to the $T \sin \alpha_T$. We accept that there is no wind ($V_K = V$, $\gamma_a = \gamma$ and $\chi_a = \chi$) and with sideslip angle $\beta = 0$. In this case we can project the vector equation (1) on the velocity axis system denoted by "V" with x axis along the velocity, z axis in vertical plane through the velocity

$$m \cdot \begin{bmatrix} \dot{V} \\ V \cos \gamma \cdot \dot{\chi} \\ -V\dot{\gamma} \end{bmatrix} = \mathbf{L}_{VA} \cdot \begin{bmatrix} -D \\ 0 \\ -L \end{bmatrix} + \mathbf{L}_{VF} \cdot \begin{bmatrix} T \cos \alpha_T \\ 0 \\ T \sin \alpha_T \end{bmatrix} = m \cdot \mathbf{L}_{VO} \cdot \begin{bmatrix} 0 \\ 0 \\ g \end{bmatrix}. \quad (2)$$

Using the transformation matrices $\mathbf{L}_{VA} = \mathbf{L}_X(-\mu_A)$, $\mathbf{L}_{VF} = \mathbf{L}_X(-\mu_A) \cdot \mathbf{L}_Z(\beta) \cdot \mathbf{L}_Y(-\alpha)$ and $\mathbf{L}_{VO} = \mathbf{L}_Y(\gamma) \cdot \mathbf{L}_Z(\chi)$ we get

$$\begin{aligned} \dot{V} &= \frac{T}{m} \cos(\alpha_T - \alpha) - g \cdot \sin \gamma - \frac{D}{m} & \dot{x} &= V \cdot \cos \gamma \cdot \cos \chi \\ \dot{\chi} &= \left[\frac{L}{m} - \frac{T}{m} \sin(\alpha_T - \alpha) \right] \frac{\sin \mu_A}{V \cos \gamma} & \dot{y} &= V \cdot \cos \gamma \cdot \sin \chi \\ \dot{\gamma} &= \left[\frac{L}{m} - \frac{T}{m} \sin(\alpha_T - \alpha) \right] \frac{\cos \mu_A}{V} - \frac{g \cdot \cos \gamma}{V} & \dot{h} &= V \cdot \sin \gamma \\ \dot{m} &= -C_p \cdot P_{eng} \quad \text{or} \quad \dot{m} = -C_T \cdot T_{eng}. \end{aligned} \quad (3)$$

The angle μ_A can be related to the roll angle ϕ of the aircraft as described in [4] with

$$\tan \mu_A = \frac{\sin \phi}{\cos \alpha \cdot \cos \phi + \sin \alpha \cdot \tan \vartheta}. \quad (4)$$

Even for high values of roll angle ϕ and pitch angle ϑ at some usual value of angle of attack α , ϕ is very close to μ_A and can be used instead of it in (3).

Model (3) reduces the number of differential equations with respect to the 6DOF model and moreover we have the reduction in data sets needed for its solution. So for the aerodynamic model we need only the lift and drag force or in dimensionless form for lift $C_L = C_{L_0} + C_{L_\alpha} \alpha + C_{L_{\delta_m}} \delta_m$ and for drag force we have $C_D = C_{D_{\min}} + K \cdot (C_L - C_{L_{\min}})^2 \approx C_{D_0} + K \cdot C_L^2$. In case of trimmed flight the pitching moment is $C_m = C_{m_0} + C_{m_\alpha} \alpha + C_{m_{\delta_m}} \delta_m = 0$. From this equation we can determine the angle of attack α as the function of elevator deflection angle δ_m . Therefore from

the set of aerodynamic data we need: C_{D0} , K , C_{L0} , $C_{L\alpha}$, $C_{L\delta_m}$, C_{m0} , $C_{m\alpha}$, $C_{m\delta_m}$. Also for the mass model we need only the initial mass and specific fuel consumption coefficient. The power or the thrust of the engine can be regulated with the throttle command $\delta_{throttle}$ and in general as in [5] we can take the power for propeller engine $P_{eng} = P_{eng}(V, h, \delta_{throttle})$ and the thrust for jet engine $T_{eng} = T_{eng}(V, h, \delta_{throttle})$. For specific fuel consumption we have similar relations $C_P = C_P(V, h, \delta_{throttle})$ and $C_T = C_T(V, h, \delta_{throttle})$.

3. Results and Discussion

Presented model can be used for analyzing the quasi steady motion and in this paper we will restrict ourselves to regimes of straight and sustained turn flight. In straight flight we have $\gamma = const$, $\mu_A = 0$, $\alpha = const$, $\beta = 0$ and $V(t)$ with command $\delta_{throttle}(t)$. For example in range calculations airspeed and throttle setting have small variations with time. In this flight regime angular velocities are equal to zero and we can say that modified point mass model (3) is equal to the 6DOF model.

In sustained turn we have $V = const$, $\gamma = const$, $\mu_A = const$, $\beta = 0$ with small variations in time of $\alpha(t)$, or $\delta_m(t)$, and throttle setting $\delta_{throttle}(t)$. In turn we have angular velocities of the aircraft $\left[\frac{V}{R} \sin \alpha \quad \frac{V}{R} \cos \alpha \sin \phi \quad -\frac{V}{R} \cos \alpha \cos \phi \right]^T$ which cause additional parts to the forces that are not included in the presented model. Therefore in this flight regime some differences between presented model and 6DOF occur. Diagram on Fig.1 presents the results for modified point mass model in comparison with 6DOF model [6] for the trajectory of the center of gravity for big transport aircraft in sustained turn with given airspeed V and load factor n (which defines the roll angle ϕ) in climb at given angle γ . Even with the neglected angular velocities modified point mass model is still good approximation of the motion of aircraft's center of gravity in sustained turn. Difference between the results of these two models for the case from Fig.1 is less than 2% of the turn radius.

For the analysis of the aircraft performances modified point mass model can be applied because it describes the motion of the aircraft's center of gravity with the mass change and it is a good approximation of 6DOF model. The advantage of using this model instead of the 6DOF model is in simplification of the model itself, its calculation requirements, smaller data sets and simpler trim processes. Modified point mass model presented here can be used, beside for the performance analysis, possibly for the flight traffic management simulations because of its simplicity and possibility of simple modeling of different aircrafts.

Acknowledgements

The authors gratefully acknowledge the support from Soko Z.I. with the FLSIM software and the financial support from GAMM2000 Organizing Committee.

4. References

- 1 ETKIN, BERNARD: Dynamics of Atmospheric Flight, John Wiley & Sons, New York 1972.
- 2 ISO Concepts, Quantities and Symbols for Flight Dynamics, Part 1: Aircraft motion relative to the air, ISO/DIS 1151/1, and Part 2. Motion of the aircraft and the atmosphere relative to the Earth, ISO/DIS 1151/2, 1988.
- 3 GANTMAKER, F.R. AND LEVIN, L.M.: The Flight of Uncontrolled Rockets, Pergamon Press, Oxford 1964.
- 4 JANKOVIĆ, S.: Mehanika leta zrakoplova, Fakultet strojarstva i brodogradnje, Zagreb 2000.
- 5 VINH, NGUYEN X.: Flight Mechanics of High-Performance Aircraft, University Press, Cambridge 1993.
- 6 FLSIM Reference Manual v.7.0, Virtual Prototypes Inc., 1998.

Addresses: M.SC. MILAN VRDOLJAK, Institute for Defense Studies, Research and Development, p.p.252, HR-10002 Zagreb, Croatia, e-mail: mvr dolja@jagor.srce.hr
 PROF.DR. SLOBODAN JANKOVIĆ, Department of Aerospace, Faculty of Mechanical Engineering and Naval Architecture, I.Lučića 5, HR-10000 Zagreb, Croatia, e-mail: slobodan.jankovic@zg.tel.hr

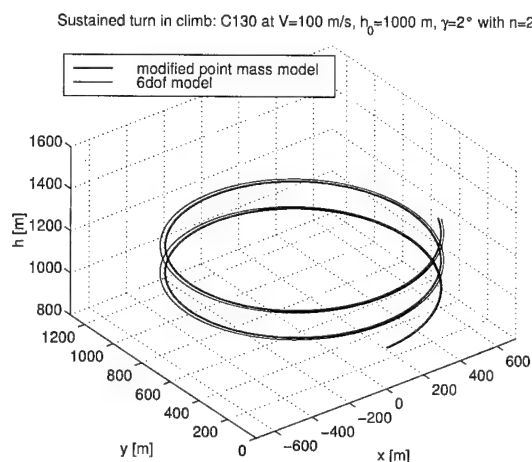


Figure 1: Results for sustained turn in climb

GERTON LUNTER

A generalization of Gröbner bases helps to compute singularity theory transformations

According to singularity theory, many functions admit (local) normal forms under suitable equivalence transformations. Motivated by a dynamical systems problem, where we are interested in symbolically computing bifurcation curves, our goal is to compute the normalizing transformation explicitly.

Its computation proceeds stepwise, and resembles Newton's root-finding algorithm, with the derivative replaced by the tangent space to the orbit under equivalence transformations. At each step we need a solution of a linear equation involving the tangent space, analogous to Newton's algorithm requiring the inverse of the derivative.

If the equivalences are right-transformations, the tangent space is an ideal, and the linear equation is solved by the normal form or 'division' algorithm of Gröbner bases. If left-right transformations are used, the tangent space consists of sums of ideal and algebra elements. The resulting linear equation can be solved analogously by suitably extending the notions of Groebner basis and canonical subalgebra (SAGBI) basis. See [9] for an extended overview, [8] for the details.

1. Motivation

The research reported here has its roots in a dynamical systems problem. Our overall goal is to symbolically compute bifurcation curves of a certain low-degree-of-freedom Hamiltonian dynamical system (see [4,3]). This is accomplished by simplifying the Hamiltonian system in a two-step reduction process. The first step is ordinary Birkhoff normalization, leaving a family of planar Hamiltonian systems. We shall focus on the second step, which uses singularity theory to simplify the Hamiltonian system by subjecting it to certain equivalence transformations. Bifurcation curves of the resulting (polynomial) normal form are easy to find, and pulling back these curves through the coordinate transformations yield bifurcation curves for the original dynamical system.

To compute symbolic bifurcation curves, we need explicit coordinate transformations in both reduction steps. The standard Birkhoff procedure (see e.g. [5]) also computes the transformation. For the second step, an algorithm of Kas and Schlessinger [7] can be used. It linearizes the nonlinear singularity theory equations and solves it iteratively for increasing degree, in the same way as Newton's root-finding algorithm uses the linearized equation to solve a nonlinear one.

We use two different equivalence classes, right-equivalences and left-right equivalences. The first leads to an equation of the form $F(x) = G(\phi(x))$, where $F, G : \mathbb{R}^n \rightarrow \mathbb{R}^k$, to be solved for $\phi : \mathbb{R}^n \rightarrow \mathbb{R}^n$. The tangent space to the orbit of G under right-transformations is an ideal, and the related linearized equation appearing in Kas and Schlessinger's algorithm, called the *infinitesimal stability equation* in this context, is of the form

$$f(x) = \sum_i \frac{dG}{dx_i} h_i(x),$$

to be solved for the h_i . In the ring of truncated formal power series, this is a linear equation in the coefficients of the h_i , and is solved efficiently using standard bases, a variant of Gröbner bases tailored to local rings [1,2,6]. In the case of left-right equivalences, the central equation is

$$F(x) = A(G(\phi(x))),$$

to be solved for $A : \mathbb{R}^k \rightarrow \mathbb{R}^k$ and ϕ . The left-right tangent space contains sums of ideal and subalgebra elements, and the related infinitesimal stability equation is

$$f(x) = \alpha(G_1(x), \dots, G_k(x)) + \sum_i \frac{dG}{dx_i} h_i(x),$$

to be solved for $\alpha : \mathbb{R}^k \rightarrow \mathbb{R}^k$ and the h_i . Again, this equation is linear in the coefficients of the h_i and of α . Straightforwardly solving it is inefficient due to the large matrices involved. We here propose a method for solving

the equation that uses the subalgebra and ideal structure, analogous to how the ideal structure is used in the standard basis approach. This method brings Gröbner bases, standard bases and SAGBI bases [11] under one umbrella.

2. Solving the infinitesimal stability equation

Given a basis for truncated formal power series ring, an ideal basis can be associated to a matrix representing a linear map whose image is the ideal. A standard basis then corresponds to this matrix being in row-echelon form. Linear equations involving such a matrix can be solved efficiently. This method can be generalised, by building a linear map Ψ whose image is required space, e.g. an ideal plus a subalgebra, and checking whether the corresponding matrix is in row-echelon form. The necessary conditions to check, analogous to S -polynomials reducing to 0, are related to the generators of the kernel of a certain linear map (the *monomial mapping*) associated Ψ .

In the case of the left-right tangent space, these generators are of three types: either S -polynomials associated to the ideal, or SAGBI-syzygies related to the subalgebra, or 'mixed' syzygies. This last type encodes situations where leading terms of ideal generators cancel those of subalgebra elements. Computing S -polynomials is trivial, while computing the two other types of syzygies is essentially a combinatorial problem. Gröbner bases can be used to solve this combinatorial problem, cf. [10].

Buchberger's algorithm has an analogue in this generalized setting: Adding nonzero reducts of syzygies to the basis improves the basis in a precise sense. Under some conditions, which are met in the case of truncated formal power series, this procedure is finite.

3. Results and conclusions

Using the approach sketched, we were able to compute symbolic bifurcation curves for certain dynamical systems. The results agreed with numerical data within measurement errors. Explicit computation of singularity theory transformations beyond simple right transformations may find application in other areas. The method can be used for automatic computation of codimension of singularities under various equivalence classes, and may be useful in automatic classification algorithms as well. Finally, the unified approach to Gröbner bases, standard bases and SAGBI bases may be helpful for expository purposes.

Acknowledgements

The author gratefully acknowledges help from Henk Broer, Karin Gatermann, Igor Hoveijn, Hans de Jong, Gert Vegter and Evgeni Verbitskii.

4. References

- 1 BECKER, T. Stability and Buchberger criterion for standard bases in power series rings. *J. of Pure and Applied Algebra* **66** (1990), 219–227.
- 2 BECKER, T. Standard bases and some computations in rings of power series. *J. Symb. Comp.* **10** (1990), 165–178.
- 3 BROER, H. W., HOVEIJN, I., LUNTER, G. A., AND VEGTER, G. Resonances in the spring-pendulum, a case study in equivariant singularity theory. *Nonlinearity* **11** (1998), 1569–1605.
- 4 BROER, H. W., LUNTER, G. A., AND VEGTER, G. Equivariant singularity theory with distinguished parameters, two Hamiltonian case studies in resonance. *Physica D* **112** (1998), 64–80.
- 5 DEPRIT, A., HENRARD, J., PRICE, J. F., AND ROM, A. Birkhoff's normalization. *Cel. Mech.* **1** (1969), 222–251.
- 6 GREUEL, G.-M., AND PFISTER, G. Gröbner bases and algebraic geometry. In *Gröbner Bases and Applications*, B. Buchberger and F. Winkler, Eds., vol. 251 of *LNS*. Springer-Verlag, 1988.
- 7 KAS, A., AND SCHLESSINGER, M. On the versal deformation of a complex space with an isolated singularity. *Math. Ann.* **196** (1972), 23–29.
- 8 LUNTER, G. A. *Bifurcations in Hamiltonian systems, computing singularities by Gröbner bases*. PhD thesis, University of Groningen, 1999.
- 9 LUNTER, G. A. Computing normalizing transformations for Hamiltonian systems in resonance. In *SPT98 – Symmetry and Perturbation Theory II* (2000), A. Degasperis and G. Gaeta, Eds., World Scientific, pp. 202–210.
- 10 STURMFELS, B. *Gröbner bases and convex polytopes*. AMS, 1996.
- 11 VASCONCELOS, W. V. *Computational Methods in Commutative Algebra and Algebraic Geometry*, vol. 2 of *Algorithms and Computation in Mathematics*. Springer, 1998.

Address: GERTON LUNTER, University of Groningen, Dept. of Mathematics, P.O. Box 800, 9700 AV Groningen, The Netherlands. Email: gerton@math.rug.nl

SEILER, W.M.

Index Concepts for General Systems of Partial Differential Equations

We proposed recently some index concepts for general systems of partial differential equations [12] based on the so-called formal theory. In this note we discuss their meaning in the context of semi-discretisations. It is shown for some simple examples that the involution index of the original partial differential equations provides a lower bound for the index of the differential algebraic equations obtained by a semi-discretisation.

1. Involutive Systems of Differential Equations

Differential algebraic equations have now been studied intensively for more than 20 years [1]. However, the extension of this theory to partial differential equations has only just begun and encounters many difficulties. We went recently the opposite direction and demonstrated that the formal theory of differential equations provides a powerful framework for studying general systems of partial differential equations, i. e. systems that do not necessarily satisfy the conditions of the Cauchy-Kowalevsky theorem, and that its specialisation to ordinary differential equations recovers much of the standard index theory of differential algebraic equations [12].

The notion of an *involutive system* of differential equations is central for the formal theory. It is beyond the scope of this short note to give a rigorous definition of it. For this we must refer to the literature [8,11]. In this section we will try to explain, in as simple words as possible, some of the basic ideas behind involution. We will restrict to linear systems, although from a theoretical point of view there is no fundamental difference between linear and non-linear systems in this context. The first step towards an involutive system of differential equations is *formal integrability*. The name stems from the fact that for formally integrable systems it is straightforward to construct order by order formal power series solutions. This will be the case, iff there are no *integrability conditions* hidden in the system. Such a condition represents a differential equation that is automatically satisfied by any solution of the given system but that is nevertheless algebraically independent of it.

For ordinary differential equations only one mechanism for the generation of integrability conditions exists: the system contains equations of differing order and the differentiation of the lower order ones leads to new equations. A simple example is $\dot{u} = v$ and $u + v = 0$. Differentiating the second equation and substituting the first one yields $\dot{v} = -v$. As for first order systems lower order equations are in fact algebraic equations, the name *differential algebraic equations* has become costumery for such systems.

For partial differential equations a second mechanism exists consisting in the simplest case of cross-differentiations. Consider the system $u_{zz} = u_y$ and $u_{zy} = u_x$. By subtracting the y -derivative of the first equation from the z -derivative of the second one, we see that any solution of this system must also satisfy the equation $u_{yy} = u_{xz}$. This equation cannot be constructed by performing only algebraic manipulations of the original system; it is crucial that we differentiate. More generally, integrability conditions arise, if it is possible to take linear combinations of differentiated equations such that all derivatives of highest order cancel. If we cannot generate any new equation this way, no matter how often we differentiate, then our system is formally integrable. One can show that in our example above addition of the integrability condition yields a formally integrable system.

A formally integrable system is called *involutive*, if it possesses in addition a somewhat abstract property of a more combinatorial nature. This property sounds very bizarre at first sight, but there rests a surprising power in it which explains much of the importance of involution. As we assume that we are dealing with a linear system, we can solve each equation in it for a derivative of maximal order. With some algebraic manipulations we can achieve that each equation is solved for a different derivative and thus we may consider each equation as a unique rule to determine a certain derivative. But when we start to differentiate the equations, we loose in general this uniqueness. In our example above, the integrability condition arises from the fact that there are two possibilities to determine u_{zzy} and we must of course require that both yield the same result.

Assume now that, somehow, we knew already that the given system was formally integrable, so that, whenever there exist several possibilities to compute a derivative, all of them lead to the same result (modulo the equations contained in the system). Involution concerns a certain "recipe" to choose in such cases a unique way to determine each derivative. It requires an ordering of the independent variables; so let us call them x_1, \dots, x_n . If $u_{x_{i_1} x_{i_2} \dots x_{i_q}}$ is a derivative of order q with $i_1 \leq i_2 \leq \dots \leq i_q$, we call i_1 the *class* of the derivative.

If an equation in our system is solved for a derivative of class k , we differentiate it only with respect to the variables x_1, \dots, x_k . It is not so difficult to see that if one has chosen carefully the derivatives for which each equation is solved (this means basically that one has taken derivatives of as high class as possible), all equations one obtains by these differentiations are algebraically independent, as they are still all solved for different derivatives. The decisive question is now whether we can construct *all* possible differentiated equations this way or whether we perhaps miss some. If we indeed get all equations, we call the system involutive.

We demonstrate this idea with two simple examples. Consider first the system $u_{x_2x_2} = 0$ and $u_{x_1x_2} = 0$. The first equation is of class 2 and we allow all possible differentiations of it. The second equation is of class 1 and thus may be differentiated only with respect to x_1 . But this restriction has no consequences: the equation $u_{x_1x_2x_2} = 0$ can also be obtained by an "allowed" differentiation of the first equation with respect to x_1 . Thus we have an involutive system. Now we take the system $u_{x_2x_2} = 0$ and $u_{x_1x_1} = 0$. Again the first equation is of class 2 and the second of class 1. But now the restriction to "allowed" differentiations prohibits us to derive the equation $u_{x_1x_1x_2} = 0$. So we have here an example of a system that is not involutive.

2. Completion and Indices

Involutive systems share a number of useful properties. For example, in the case of analytic systems one can prove an existence and uniqueness theorem for analytic solutions of the Cauchy problem, the *Cartan-Kähler theorem*. Involutive systems may also be considered as a kind of generalisation of the well-known Gröbner bases of polynomial ideals [2] to differential equations. In fact, for linear systems this relation can be made precise. Reinterpreting any derivative $u_{x_1x_2\dots}$ as a monomial $x^2y\dots$, we can associate to every linear system with constant coefficients a set of polynomials. If the system is involutive, this set represents not only a Gröbner basis of the ideal generated by it but even a very special kind, a so-called involutive basis, possessing many interesting properties [3,13].

If a given system of differential equations is not involutive, the *Cartan-Kuranishi theorem* asserts that we can make it involutive by differentiating it finitely often and by adding a finite number of integrability conditions. The proof of this theorem even leads straightforwardly to an algorithm for this *completion to involution*. An efficient version of it and its implementation in the computer algebra system MuPAD will be described in two forthcoming publications [5,6]. For lack of space we cannot discuss this interesting problem any further.

The basic insight of [12] was that differentiation indices, as they are often used to classify differential algebraic equations, basically only count the number of steps this completion algorithm requires; we thus prefer to speak of the *involution index*. As the Cartan-Kuranishi theorem holds for ordinary and for partial differential equations, we obtain this way automatically an index concept that can be applied independently of the number of variables. One can show that for linear differential algebraic equations it coincides with the *strangeness index*¹ introduced in [7].

For ordinary differential equations the theory becomes rather trivial, as for them there is no difference between involution and formal integrability and one can omit all the complicated combinatorial considerations. So it is not surprising that the completion algorithm restricted to this case has been rediscovered many cases, see e.g. [9,10]. For Hamiltonian systems with constraints one recovers the classical Dirac theory [14].

It should be emphasised that we speak here exclusively about *differentiation indices* and not about *perturbation indices* as introduced by Hairer et al. [4]. For the latter class of indices it is still an open question how they can be formulated for partial differential equations. Involution should play here an important role, too, as the involution index gives a sharp upper bound for the order of the derivatives of the perturbations that enter the involutive system and thus its solution.

3. Semi-Discretisations

Much of the currently existing literature on designing indices for general systems of partial differential equations is based on semi-discretisations, i.e. one reduces to a differential algebraic system for which many index concepts exist. We will present now two examples as evidence for a conjecture: *the involution index of a system of partial differential equations provides a lower bound for the index of any differential algebraic system arising from it by a semi-discretisation*.

In a first simple example we demonstrate the effect of the existence of integrability conditions in a system of partial differential equation on its semi-discretisation. Not very surprising, one rediscovers discretised versions of the integrability conditions as "hidden" constraints of the arising differential algebraic system. Consider the following

¹Due to a slightly different way of counting the strangeness index is actually always 1 less than the involution index.

linear over-determined system of second order partial differential equations for an unknown function $u = u(t, x)$:

$$u_{tt} = u_x, \quad u_{xt} = 0. \quad (1)$$

This system is not formally integrable, as a trivial cross differentiation yields the integrability condition $u_{xx} = 0$. Addition of this equation yields an involutive system, so we can conclude that the involution index of (1) is 1.

Now we perform a semi-discretisation of (1) by substituting central differences for the x -derivatives. We omit a discussion of initial or boundary conditions — not only for simplicity but also because for a non-involutive system it is not so obvious what conditions can be imposed. In our example, it is easy to see that the general solution of system (1) is given by $u(t, x) = 2Ax + At^2 + Bt + C$ with three arbitrary real constants A, B and C . Thus only three conditions at *points* could be imposed. The semi-discretisation yields the following differential algebraic system

$$2h\ddot{u}_i = u_{i+1} - u_{i-1}, \quad \dot{u}_{i+1} - \dot{u}_{i-1} = 0 \quad (2)$$

where h denotes the step width of the x -discretisation and $u_i = u_i(t)$ approximates the values of $u(t, x)$ at the i -th grid point. In order to determine the differentiation index of (2), we must check what happens, if we differentiate the second equation. After some trivial manipulations we get the algebraic equation

$$u_{i+2} - 2u_i + u_{i-2} = 0 \quad (3)$$

which represents just a central difference approximation (with grid size $2h$) of the integrability condition $u_{xx} = 0$ of the original system (1). It is easy to check that differentiation of (3) does not yield any new equations, so that the index of the differential algebraic system (2) is 1 and thus equal to the involution index of (1).

One should note that this result does not depend on the fact that we used central differences. It is easy to see that no matter what kind of difference formula is used to approximate the x -derivatives, one will always obtain a differential algebraic system consisting of second and first order equations and the differentiation of the first order equations will yield some algebraic constraints. Thus the differentiation index is always at least 1.

While this result is no big surprise, it is perhaps less obvious that when one discretises a formally integrable but not involutive system of partial differential equations the arising differential algebraic system will contain hidden constraints, too. As a simple example for this effect, we consider again a linear over-determined system of second order partial differential equations for an unknown function $u = u(t, x)$.

$$u_{tt} = 0, \quad u_{xx} = 0. \quad (4)$$

This system is formally integrable, as it obviously cannot generate any integrability conditions. But it is *not* involutive; it becomes involutive only after one differentiation to third order. So we find an involution index of 1.

As above we perform a semi-discretisation by approximating the x -derivative by a central difference and obtain the differential algebraic system

$$\ddot{u}_i = 0, \quad u_{i+1} - 2u_i + u_{i-1} = 0. \quad (5)$$

Obviously, we get new first order equations by differentiating the algebraic equations:

$$\dot{u}_{i+1} - 2\dot{u}_i + \dot{u}_{i-1} = 0. \quad (6)$$

It is easy to check that differentiating (6) does not yield any new equations and thus the index of the differential algebraic system (5) is 1, too.

Finally, let us consider the differentiation of (4) to third order. It yields the following *involutive* system

$$u_{ttt} = 0, \quad u_{ttx} = 0, \quad u_{txx} = 0, \quad u_{xxx} = 0. \quad (7)$$

Approximating the x -derivatives by central differences leads to the differential algebraic system

$$u_i^{(3)} = 0, \quad \ddot{u}_{i+1} - \ddot{u}_{i-1} = 0, \quad \dot{u}_{i+1} - 2\dot{u}_i + \dot{u}_{i-1} = 0, \quad u_{i+2} - 2u_{i+1} + 2u_{i-1} - u_{i-2} = 0. \quad (8)$$

It is left as an exercise for the reader that differentiation of any of the lower order equations in (8) does not yield anything new. Thus there are no hidden constraints and both (7) and (8) are of index 0.

4. Conclusions

We have outlined some ideas from the formal theory of differential equations and how they are related to index concepts for differential algebraic equations. Based on two simple examples we have formulated a conjecture on the

behaviour of the index under semi-discretisation. Attempts to prove this conjecture lead to interesting questions in Commutative Algebra related to *syzygies*.

All examples in this note are completely artificial and have no relevance for concrete applications. But there exist very important systems of partial differential equations which are not in Cauchy-Kowalevsky form. *Maxwell's equations* governing electromagnetic fields

$$\partial_t \vec{E} = \text{rot } \vec{B}, \quad \partial_t \vec{B} = -\text{rot } \vec{E}, \quad \text{div } \vec{E} = 0, \quad \text{div } \vec{B} = 0 \quad (9)$$

form an involutive system, although they are over-determined. The *incompressible Navier-Stokes equations*

$$\partial_t u + (u \cdot \nabla) u = -\text{div } p + \Delta u, \quad \text{div } u = 0 \quad (10)$$

have an involution index of 2 because of the peculiar way the pressure p enters. There is one non-trivial integrability condition, namely the well-known Poisson equation for the pressure

$$\Delta p + \nabla \cdot (u \cdot \nabla) u = 0. \quad (11)$$

It has been shown in [15] that any semi-discretisation of the Navier-Stokes equations indeed leads to a differential algebraic equation with a strangeness index of at least 1 and thus an involution index of at least 2.

In general, one expects that a semi-discretisation leads to a differential algebraic system with an index equal to the one of the original system of partial differential equations. In fact, one should take care that this is the case. The index is an important structural property of a differential system. If it is changed by the semi-discretisation, one must expect that other properties of the system may be changed, too, and so the obtained numerical approximation might be not very reliable.

Acknowledgements

This work has been supported by Deutsche Forschungsgemeinschaft.

5. References

- 1 BRENNAN, K.E., CAMPBELL, S.L., PETZOLD, L.R.: Numerical Solution of Initial-Value Problems in Differential-Algebraic Equations. SIAM, Philadelphia 1996.
- 2 COX, D., LITTLE, J., O'SHEA, D.: Ideals, Varieties, and Algorithms. Springer, New York 1992.
- 3 GERDT, V.P., BLINKOV, YU.A.: Involutive Bases of Polynomial Ideals. Math. Comp. Simul. 45 (1998), 519–542.
- 4 HAIRER, E., LUBICH, C., ROCHE, M.: The Numerical Solution of Differential-Algebraic Systems by Runge-Kutta Methods. Springer, Berlin 1989.
- 5 HAUSDORF, M., SEILER, W.M.: An Efficient Algebraic Algorithm for Geometric Completion to Involution. In preparation.
- 6 HAUSDORF, M., SEILER, W.M.: Differential Equations in MuPAD II: A Completion Package. In preparation.
- 7 KUNKEL, P., MEHRMANN, V.: Canonical Forms for Linear Differential-Algebraic Equations. J. Comp. Appl. Math. 56 (1994), 225–251.
- 8 POMMARET, J.F.: Systems of Partial Differential Equations and Lie Pseudogroups. Gordon & Breach, London 1978.
- 9 RABIER, P.J., RHEINOLDT, W.C.: A Geometric Treatment of Implicit Differential Algebraic Equations. J. Diff. Eq. 109 (1994), 110–146.
- 10 REICH, S.: On an Existence and Uniqueness Theory for Nonlinear Differential-Algebraic Equations. Circ. Sys. Sig. Proc. 10 (1991), 343–359.
- 11 SEILER, W.M.: Analysis and Application of the Formal Theory of Partial Differential Equations. Ph.D. Thesis, Lancaster University 1994.
- 12 SEILER, W.M.: Indices and solvability for non-normal systems of differential equations; Computer Algebra in Scientific Computing — CASC '99, V.G. Ghanza, E.W. Mayr, E.V. Vorozhtsov (eds.), Springer, Berlin 1999, 365–385.
- 13 SEILER, W.M.: A Combinatorial Approach to Involution and δ -Regularity. Preprint, Universität Mannheim 2000.
- 14 SEILER, W.M., TUCKER, R.W.: Involution and constrained dynamics I: The Dirac theory. J. Phys. A: Math. Gen. 28 (1995), 4431–4451.
- 15 WEICKERT, J.: Navier-Stokes Equations as a Differential-Algebraic System. Preprint SFB393/96-08, Universität Chemnitz 1996.

Addresses: WERNER M. SEILER, Lehrstuhl für Mathematik I, Universität Mannheim, 68131 Mannheim

WICHMANN, T.

Computer Aided Generation of Approximate DAE Systems for Symbolic Analog Circuit Design

The behavior of nonlinear analog circuits is described by a set of differential algebraic equations (DAE). We are developing simplification and approximation methods which can be applied to this DAE system in order to generate a reduced symbolic system, where a user given error bound is assured automatically. Either the reduced system can be analyzed further to achieve a better understanding of the circuit's behavior or it can be used as a behavioral model which can be solved numerically easier and faster. In the following we will focus on two aspects of the algorithm: simplification of subexpressions and monitoring of the index during simplification.

1. Introduction

Mathematically the behavior of an analog circuit can be described by a set f of differential equations and a set g of algebraic constraints, such that

$$f(x(t), x'(t), y(t), u(t); p) = 0 \quad \text{for all } t \in I \quad (1)$$

$$g(x(t), y(t), u(t); p) = 0 \quad \text{for all } t \in I. \quad (2)$$

Here, $u : \mathbb{R} \rightarrow \mathbb{R}^r$ denotes the inputs, $x = (v, i) : \mathbb{R} \rightarrow \mathbb{R}^k$ denotes the vector of internal voltages and currents, $y : \mathbb{R} \rightarrow \mathbb{R}^s$ denotes the outputs, and $I \subset \mathbb{R}$ denotes an interval. We are working with symbolic equations, i. e., f and g are parameterized by symbolic parameters $p = (p_1, \dots, p_N)$. The equations originate from Kirchhoff's current and voltage laws and the circuit element characteristics and form a nonlinear differential algebraic equation system (DAE) $F = (f, g)$. Even for small circuits the symbolic system of equations is getting very large, so the desire for an algorithm to reduce the complexity of the system arises.

DAE systems originating from analog circuits are often linear in the differential variable, i. e., $F(x, x', y, u; p) = A(x, u, y; p)x' + h(x, u, y; p)$ where A is a matrix valued function. To analyze the circuit's behavior, there are several standard techniques like DC, AC, or transient analysis. Since those are numerical analysis methods, a numerical design point $\pi \in \mathbb{R}^N$ has to be inserted for the symbolic parameters p .

2. The Simplification Algorithm

To simplify the symbolic DAE system, several different simplification methods are applied, including mathematical exact operations like elimination of variables. Additionally, operations which substitute the original system by an approximate one are applied, such as cancellation of terms, substituting of terms by constant values, or deletion of variables' time derivatives. One key aspect of the algorithm is the calculation of a suitable order, in which the different parts of the system are affected within one simplification method. An optimized order (*ranking*) yields both a better result and a higher performance of the algorithm. For different simplification techniques and different analysis methods several ranking algorithms have been developed. We refer to [1], [4], and [6] for a more detailed description of the simplification algorithm as well as of the ranking methods.

We found that the combination of algebraic elimination and cancellation of terms in most cases reduces the complexity of the equation system significantly. But it also turned out that the notion of *term* as introduced in [1] is sometimes not suitable: after the deletion of a term the maximum error exceeded, whereas subexpressions of this term could be simplified without significant influence on the error. So the algorithm was extended towards simplification not only of "top-level"-terms but also of subexpressions hereof. Fortunately the DC-ranking mentioned in [4] (which uses the linearization of F) can be adopted to the cancellation of terms in nested subexpressions: For this let the DAE systems $F = (f_1, \dots, f_n)$ and $\tilde{F} = (\tilde{f}_1, \dots, \tilde{f}_n)$, such that $\tilde{f}_i = f_i$ for $i \neq l$, $\tilde{f}_l = h + \tilde{r}$, and $f_l = h + r$ for an index l . Here r and \tilde{r} denote top-level terms in the l th equation of F and \tilde{F} which differ in the cancellation of a subexpression (for example, $r = \exp(x_1 + x_2)$ and $\tilde{r} = \exp(x_1)$). Then the Jacobian of \tilde{F} can be expressed in terms of the Jacobian of F as $J_{\tilde{F}} = J_F + uv^T$ where $u = e_l$ denotes the l th unit vector and $v = \text{grad}(\tilde{r} - r)$. Both Jacobians differ by a rank-one modification, such that the Sherman-Morisson formula can be applied for an efficient

calculation of $J_{\tilde{F}}$. As in the top-level case, the DC ranking gives a very good prediction of the error influence for subexpression deletion, too.

3. Index Observer

The so-called *index* plays an important role in the theory of DAEs and there exist a number of different index concepts in the literature, e. g., the global, the perturbation, the differential, or the tractability index. In this work we will focus on the latter one, so if we are talking of *the* index we are speaking of the tractability index ([3]). It is known that solving initial value problems for DAEs with index greater than one numerically is an ill-posed problem. DAEs originating from electrical networks theoretically can be of arbitrary index but in real world problems they are usually of index one or two. Since the simplification algorithm modifies the DAE system one can not rule out the possibility of an index change during simplification, which has to be avoided.

In [5] structural properties have been stated an electrical network has to fulfill in order to assure index one. By means of C-V-loops and L-I-cutsets it is possible to predict the index based on the network topology without analyzing the equation system. But this result is not suitable for our algorithm: After some simplification steps, say cancellation of terms, the resulting system of equations may not be re-interpreted as an electrical network. For example, Kirchhoffs current law may be violated for some nodes. So the index has to be calculated based on the equation system.

The quasilinear DAE $f(x, x') = A(x)x' + h(x)$ is said to be *index-1* (or *tractable*) if the matrix $A + BQ$ is regular, where $B = D_x f$, and Q denotes a projector onto $\ker A$. The projector Q can be computed numerically for example using the Gram-Schmidt orthogonalization or the singular value decomposition of A . Yet another way is the following: Let $S = \{x \in \mathbb{R}^n \mid Bx \in \text{im} A\}$, then it can easily be shown that $A + BQ$ is regular if and only if $S \cap \ker A = \{0\}$ (see [3]). Without loss of generality we may assume the following matrix structure:

$$A = \begin{pmatrix} A_1 & A_2 \\ 0 & 0 \end{pmatrix}, \quad B = \begin{pmatrix} B_1 & B_2 \\ B_3 & B_4 \end{pmatrix}, \quad (3)$$

where A_1 is regular. Then some simple computations show that $S \cap \ker A = \{0\}$ if and only if $\det(B_4 - B_3 A_1^{-1} A_2) \neq 0$.

So the idea is to check whether after some simplifications the DAE system is still index-1 using one of this methods to compute the index. If the index increased, we undo these simplifications because they changed the structural properties of the DAE system.

4. Conclusions

The extension of the algorithm towards simplification of subexpressions in many examples showed to be the key step to explicitly solve static circuit equations for the output variables. Furthermore, satisfactory results could be achieved applying the DC-ranking to those simplifications. Using the index observer it is now possible to avoid numerical problems for the simplified equation system caused by an increased index.

Acknowledgements

This work has been carried out within the MEDEA project A409 "SADE", supported by the Deutsches Ministerium für Bildung, Wissenschaft, Forschung und Technologie under contract no. 01M3037F and by Infineon Technologies.

5. References

- 1 C. BORCHERS: The Symbolic Behavioral Model Generation of Nonlinear Analog Circuits. In: IEEE Transactions on Circuits and Systems, **45** (1998), 1362–1371.
- 2 K. E. BRENAN, S. L. CAMPBELL, L. R. PETZOLD: The Numerical Solution of Initial Value Problems in Ordinary Differential-Algebraic Equations. North Holland Publishing Co., 1989.
- 3 E. GRIEPENTROG, R. MÄRZ: Differential-Algebraic Equations and Their Numerical Treatment. BSB Teubner, 1986.
- 4 R. POPP, W. HARTONG, L. HEDRICH, AND E. BARKE: Error Estimation on Symbolic Behavioral Models of Nonlinear Analog Circuits, Proc. Fifth Int. Workshop on Symbolic Methods and Applications in Circuit Design (SMACD), 1998.
- 5 D. E. SCHWARZ AND C. TISCHENDORF: Structural Analysis for Electric Circuits and Consequences for MNA. To appear in Journal of Circuit Theory and Applications.
- 6 T. WICHMANN, R. POPP, W. HARTONG, L. HEDRICH: On the Simplification of nonlinear DAE Systems in Analog Circuit Design. In: Computer Algebra in Scientific Computing. Springer, 1999.

Address: TIM WICHMANN, Institut für Techno- und Wirtschaftsmathematik e. V., 67663 Kaiserslautern, Germany

ZERZ, E.

Some Applications of Gröbner Bases in Multidimensional Systems Theory

The aim of algebraic systems theory is to study systems of differential equations with algebraic tools. This approach is also called "Algebraic Analysis." In the following, we will deal exclusively with linear systems of partial differential equations with constant coefficients:

$$R(\partial)w := R(\partial_1, \dots, \partial_n)w = 0. \quad (1)$$

Observe that a characteristic polynomial matrix R is associated to any such system: $R \in \mathcal{D}^{q \times q}$, where $\mathcal{D} = \mathbb{K}[\partial_1, \dots, \partial_n]$ and $\mathbb{K} = \mathbb{R}$ or $\mathbb{K} = \mathbb{C}$. The solution space of system (1) is defined as

$$\mathcal{B} = \ker_{\mathcal{A}}(R) = \{w \in \mathcal{A}^q \mid R(\partial)w = 0\}. \quad (2)$$

Here, \mathcal{A} denotes a function space with \mathcal{D} -module structure, for example, the space of smooth functions C^∞ or the space of distributions \mathcal{D}' .

We have the following natural Galois connection between \mathcal{D} -modules in $\mathcal{D}^{1 \times q}$ and \mathcal{D} -modules in \mathcal{A}^q (the \mathcal{D} -module structure of $N \subset \mathcal{D}^{1 \times q}$ is given by the usual multiplication in the polynomial ring, whereas the \mathcal{D} -module structure on $\mathcal{B} \subset \mathcal{A}^q$ is given by partial derivation). It is convenient here to introduce the notation

$$\cdot R : \mathcal{D}^{1 \times q} \rightarrow \mathcal{D}^{1 \times q}, \quad x \mapsto xR.$$

To a polynomial module $N = \text{im}(\cdot R) \subset \mathcal{D}^{1 \times q}$, we associate the behavior $N^\perp := \ker_{\mathcal{A}}(R)$ as in (2). Conversely, for $\mathcal{B} \subset \mathcal{A}^q$, we define $\mathcal{B}^\perp := \{r \in \mathcal{D}^{1 \times q} \mid r(\partial)w = 0 \ \forall w \in \mathcal{B}\}$. The mappings $(\cdot)^\perp$ are inclusion-reversing and we have $N \subseteq N^{\perp\perp}$ and $\mathcal{B} \subseteq \mathcal{B}^{\perp\perp}$.

Oberst [4] showed that for $\mathcal{A} = C^\infty, \mathcal{D}'$ this Galois correspondence induces a duality, i.e., a behavior $\mathcal{B} = \ker_{\mathcal{A}}(R)$ and the module $N = \text{im}(\cdot R)$ are in fact equivalent data. The following two sections show, in terms of two examples, how this may be exploited for gaining information on the solution spaces by studying the associated polynomial modules.

1. Interconnection of Systems

Given two solutions spaces $\mathcal{B}_i = \ker_{\mathcal{A}}(R_i) \subset \mathcal{A}^q$ ($i = 1, 2$), we define their interconnection (see Willems [7]) as $\mathcal{B} = \mathcal{B}_1 \cap \mathcal{B}_2$. In terms of the associated modules, we have $N = N_1 + N_2$.

Let us consider the following task from control theory: Given a system \mathcal{B}_1 and a desired behavior \mathcal{B} , design another system (a "controller") \mathcal{B}_2 such that $\mathcal{B}_1 \cap \mathcal{B}_2 = \mathcal{B}$ and $\mathcal{B}_1 + \mathcal{B}_2 = \mathcal{A}^q$. In terms of the associated modules: Given N_1 and N , design (if possible) N_2 such that $N = N_1 \oplus N_2$!

Our data are two polynomial modules $N_1 = \text{im}(\cdot R_1)$ and $N = \text{im}(\cdot R)$. An obvious necessary condition for the problem to be solvable is that $N_1 \subseteq N$. We shall make this assumption in the following. Then we have to decide whether N_1 is a direct summand of N , that is, whether the exact sequence $0 \rightarrow N_1 \hookrightarrow N \rightarrow N/N_1 \rightarrow 0$ splits. This is true if and only if there exists a polynomial solution Y to the linear matrix equation

$$A(YR_1 - R) = 0.$$

In that case, we already have a solution, namely $N_2 := \text{im}(\cdot YR_1 - R)$. The matrix A is obtained from computing a free resolution of the module N/N_1 , that is, an exact sequence

$$\dots \rightarrow F_1 \xrightarrow{A} F_0 \rightarrow N/N_1 \rightarrow 0$$

where F_i are free \mathcal{D} -modules. In other words, A is such that $N/N_1 \simeq \text{coker}(\cdot A)$. Note that the assumption $N_1 \subseteq N$ implies the existence of a polynomial matrix D such that $R_1 = DR$. Moreover, since $N/N_1 = \text{im}(\cdot R)/\text{im}(\cdot DR) \simeq \mathcal{D}^{1 \times q}/\text{im}(\cdot D) + \ker(\cdot R)$, we may compute the matrix A based on the following Gröbner basis techniques:

- For computation of D with $R_1 = DR$, we compute a row Gröbner matrix for R , that is, a matrix R^G whose rows are a Gröbner basis of the module generated by the rows of R . The extended Gröbner basis algorithm also yields a polynomial transition matrix X with $R^G = XR$. Now we may compute the normal form of each row of R_1 with respect to R^G . Storing each reduction towards the normal form (which is zero by assumption), this yields a representation $R_1 = D^G R^G = D^G XR$.
- The computation of a polynomial matrix Q with $\ker(\cdot R) = \text{im}(\cdot Q)$ is implemented in computer algebra systems such as SINGULAR [2].

Finally, we set $A = [D^T, Q^T]^T$. Now, for checking solvability of $A(YR_1 - R) = 0$, we rewrite it as $\text{vec}(AYR_1) = (R_1^T \otimes A)\text{vec}(Y) = \text{vec}(AR)$ (see e.g. [1]). Thus we have to test whether $\text{vec}(AR) \in \text{im}(R_1^T \otimes A)$. To this, one computes a column Gröbner matrix for $R_1^T \otimes A$ and the normal form of $\text{vec}(AR)$ with respect to it. Our problem is solvable if and only if this normal form is zero. The extended version of the division with remainder algorithm also provides a solution Y (if it exists). Then we put $R_2 := YR_1 - R$, and have $\text{im}(\cdot R_1) \oplus \text{im}(\cdot R_2) = \text{im}(\cdot R)$ as desired.

2. Parameterizability

The following result is fundamental in Algebraic Analysis [5]: Let $\mathcal{A} = C^\infty$ oder $\mathcal{A} = \mathcal{D}'$. If

$$\mathcal{D}^{1 \times g} \xrightarrow{\cdot R} \mathcal{D}^{1 \times q} \xrightarrow{\cdot M} \mathcal{D}^{1 \times m}$$

is exact, then so is $\mathcal{A}^g \xleftarrow{\cdot R} \mathcal{A}^q \xleftarrow{\cdot M} \mathcal{A}^m$, i.e.,

$$R(\partial)w = 0 \quad \Leftrightarrow \quad \exists v : w = M(\partial)v. \quad (3)$$

This motivates the following definition: A system $R(\partial)w = 0$ is said to be parameterizable if there exists a polynomial matrix M such that (3) holds. In view of Oberst's duality theorem [4], the following are equivalent [8]:

1. $\mathcal{B} = \ker_{\mathcal{A}}(R)$ is parameterizable;
2. $N = \text{im}(\cdot R)$ is a syzygy module, i.e., its rows generate the kernel of a polynomial matrix: $N = \ker(\cdot M)$;
3. $\mathcal{B} = \ker_{\mathcal{A}}(R)$ with a polynomial matrix R that is left prime in the following sense: If $R = DR_1$ with $\text{rank}(R) = \text{rank}(R_1)$, then there exists E such that $R_1 = ER$ (R_1 , D , and E are supposed to be polynomial matrices).

Based on the computation of syzygies [2], it is now easy to design a parameterizability test.

Classical examples are the parameterizations $\text{div}(w) = 0 \Leftrightarrow \exists v : w = \text{curl}(v)$, $\text{curl}(w) = 0 \Leftrightarrow \exists v : w = \text{grad}(v)$, and the Maxwell equations:

$$\left. \begin{aligned} \frac{\partial \vec{B}}{\partial t} + \nabla \times \vec{E} &= 0 \\ \nabla \cdot \vec{B} &= 0 \end{aligned} \right\} \Leftrightarrow \exists \vec{A}, \phi : \begin{cases} \vec{B} &= \nabla \times \vec{A} \\ \vec{E} &= -\frac{\partial \vec{A}}{\partial t} - \nabla \phi. \end{cases}$$

But there are also examples whose parameterizability has been decided only a few years ago [6], e.g. the linearized Einstein equations $\partial_{ij}\omega^{rs}\Omega_{rs} + \omega^{rs}\partial_{rs}\Omega_{ij} - \omega^{rs}(\partial_{ri}\Omega_{sj} + \partial_{rj}\Omega_{si}) - \omega_{ij}\omega^{rs}\omega^{uv}(\partial_{uv}\Omega_{rs} - \partial_{ru}\Omega_{sv}) = 0$. Does this 10×10 system of linear constant-coefficient PDEs admit a generic potential like the Maxwell equations? It is virtually impossible to do the calculations by hand, but with modern computer algebra systems such as SINGULAR [2] we are now able to obtain the answer (which is negative) within seconds.

3. References

- 1 BREWER, J. W.: Kronecker Products and Matrix Calculus in System Theory, *IEEE Trans. Circ. Syst.* **25** (1978), 772–781.
- 2 GREUEL, G. M., PFISTER, G., AND SCHÖNEMANN, H.: Singular Reference Manual, in: *Reports on Computer Algebra* **20**, Centre for Computer Algebra, University of Kaiserslautern (1998). URL: <http://www.mathematik.uni-kl.de/~zca/Singular>
- 3 LOMADZE, V. AND ZERZ, E.: Control and Interconnection Revisited, *Proc. NDS 2000*, Czocha Castle, Poland, 2000.
- 4 OBERST, U.: Multidimensional Constant Linear Systems, *Acta Applicandae Mathematicae* **20** (1990), 1–175.
- 5 PALAMODOV, V. P.: *Linear Differential Operators with Constant Coefficients*, Springer-Verlag, 1970.
- 6 POMMARET, J. F.: Einstein Equations Do Not Admit a Generic Potential, *Proc. Int. Conf. Diff. Geom. Appl.*, Brno, Czech Republic, 1995.
- 7 WILLEMS, J. C.: On Interconnections, Control, and Feedback, *IEEE Trans. Aut. Cont.* **42** (1997), 326–339.
- 8 ZERZ, E.: Primeness of Multivariate Polynomial Matrices, *Systems and Control Letters* **29** (1996), 139–145.

Address: DR. EVA ZERZ, Fachbereich Mathematik, Universität Kaiserslautern, 67663 Kaiserslautern, Germany.

KOLESNIK, A.D.

On Diffusion at Finite Speed in a Plane

We consider a diffusion generated by random motions at finite speed v in a plane with n , $n \geq 2$, directions controlled by a homogeneous Poisson process of rate $\lambda > 0$. The diffusion approximation theorem for the transition functions of this process is given.

1. Introduction

In the classical mathematical models of heat and mass transfer it is supposed that the diffusion is generated by chaotically moving particles making a Brownian motion. As is well known, such a process is being described by *parabolic* heat equations, which give a good approximation to the experimental data if the diffusion speed is sufficiently large. However, it is also known from physical experiments that parabolic equations are not satisfactory in many respects when we deal with a slow diffusion. This fact can be easily explained remembering that parabolic equations usually arise under the assumptions, which are equivalent to the infinite speed of Brownian particles. On the other hand, the Brownian trajectories are continuous and non-differentiable almost everywhere. This means that Brownian particle is exposed to the *infinite* number of collisions during a unit of the time, and it has not any free run. Clearly it is not like this in real physical processes. In reality the particle is subject to a *finite* number of collisions during a given time what entails changes of direction of the particle motion, and it moves with a *finite* velocity between two consequent collisions.

A new approach to the diffusion processes has recently been proposed in which these two idealized mathematical assumptions concerning infinite speed and number of collisions have been omitted. It was proposed to interpret the diffusion with *finite* velocity as a process of random motion of the particles moving with finite speed. This has led not to the parabolic equations, but to the hyperbolic ones. In this case the classical parabolic diffusion arises as a limit of the hyperbolic one under some natural conditions (that should be expected). This approach gives a new insight of many physical processes from the probabilistic point of view.

2. Main Result

The subject of our interests is the following planar stochastic motion. A particle moves with some constant finite speed v in the plane R^2 . At every time instant it has one of n , $n \geq 2$, possible directions of motion E_0, E_1, \dots, E_{n-1} , where the direction E_k , $k = 0, 1, \dots, n-1$, forms the angle $2\pi k/n$ with x -axis. In other words, the direction E_k is orientated like the vector $(\cos(2\pi k/n), \sin(2\pi k/n))$, $k = 0, 1, \dots, n-1$, $n \geq 2$. The motion is controlled by a homogeneous Poisson process with rate $\lambda > 0$ as follows. When a Poisson event occurs, the particle instantly takes on a new direction with probability $1/(n-1)$ and continues its motion in the chosen direction with the same speed v until the next Poisson event occurs, then it takes on a new direction again, and so on.

Let $\Theta(t) = (X(t), Y(t))$ denote the particle position in the plane at some instant t . It was shown in Kolesnik and Turbin (1998) that the transition law of the process $\Theta(t)$ is governed by the n -th order hyperbolic equation with constant coefficients

$$\left[\frac{\partial}{\partial t} \sum_{k=1}^{[(n+1)/2]} (-1)^{k-1} \binom{n-k}{k-1} Z^{n-2k+1} Q^{k-1} - 2 \sum_{k=1}^{[n/2]} (-1)^{k-1} \binom{n-k-1}{k-1} Z^{n-2k} Q^k - \right. \\ \left. 2 \left(-\frac{v}{2}\right)^n \sum_{k=0}^{[n/2]} (-1)^k \binom{n}{2k} \left(\frac{\partial}{\partial x}\right)^{n-2k} \left(\frac{\partial}{\partial y}\right)^{2k} \right] f = 0, \quad (1)$$

$$Z = \frac{\partial}{\partial t} + \frac{\lambda n}{n-1}, \quad Q = \frac{v^2}{4} \Delta,$$

with Δ being the two-dimensional Laplace operator, $[*]$ means the integer part of a number.

It was also proved that if the following so-called Kac's condition

$$v \rightarrow \infty, \quad \lambda \rightarrow \infty, \quad \frac{v^2}{\lambda} \rightarrow c, \quad c > 0, \quad (2)$$

is fulfilled then for $n \geq 3$ the hyperbolic equation (1) turns into the classical parabolic diffusion equation in the plane. This suggests that under the condition (2) the planar random motion described above is asymptotically a Wiener process in R^2 .

The behaviour of the transition laws of $\Theta(t)$ is of a special interest as the intensity of transitions λ of the switching Poisson process tends to infinity and, according to λ , the particle speed v increases as well. The accordance between the growth rates of λ and v is determined by the Kac's condition (2).

Here we present a diffusion approximation theorem stating that under the Kac's condition (2) the transition functions of the process $\Theta(t)$ weakly converge to the transition function of the two-dimensional Brownian motion with explicitly given generator (see Kolesnik (2001)).

Diffusion Approximation Theorem. *Let the Kac's condition (2) be fulfilled. Then in the Banach space of twice continuously differentiable functions with compact support the semigroups generated by the transition functions of the process $\Theta(t)$ converge to the semigroup generated by the transition function of the Wiener process in R^2 with generator*

$$G_n = \frac{c(n-1)}{2n} \Delta,$$

where Δ is the two-dimensional Laplace operator.

3. References

- 1 KOLESNIK, A.D., TURBIN, A.F. The equation of symmetric Markovian random evolutions in a plane. Stoch. Proc. Appl., **75** (1998), 67-87.
- 2 KOLESNIK, A.D. Weak convergence of a planar random evolution to the Wiener process. J. Theor. Prob., (2001). (To appear)

Addresses: DR. ALEXANDER KOLESNIK, Institute of Mathematics of the Academy of Sciences of Moldova, Academy Street 5, Kishinev 277028, Moldova.

MAZUR-ŚNIADY K., ŚNIADY P.

Reliability of the beam with variable cross – section under stochastic excitation

The paper presents the problem of reliability of a beam with periodically variable geometry under stochastic excitation. The approach is based on concepts of the nonasymptotic tolerance averaged model [3]. In this way we formulated the averaged equations of the structured beam which describe the length-scale effect [1,2]. Using these averaged equations we obtain the probabilistic characteristics of the beam with periodically variable geometry. We will solve the problem of reliability of this beam as the problem of the first crossing.

1. Foundations

We consider stochastic vibrations of the periodic-like straight beam with a variable cross-section and a finite length L . The equation of the beam has well known form (under assumptions of the Euler-Bernoulli linear elastic beam theory)

$$[B(x)v''(x,t)]'' + c(x)\dot{v}(x,t) + \rho(x)\ddot{v}(x,t) = p(x,t), \quad (1)$$

where $v(x,t)$ is the deflection of the beam axis, $B(x)$ is the flexural beam stiffness, $c(x)$ is the damping coefficient, $\rho(x)$ is the mass density per unit length, $p(x,t)$ is the stochastic process. The standard methods of analyzing of beam dynamics are effective only if coefficients in the equation above are constant or slowly varying. We consider beams in which the rapidly varying functional coefficients B, c, ρ are represented by periodic-like functions. It means that there exist a slowly varying function $l=l(x)$, $x \in \langle 0, L \rangle$, where $\max l(x) \ll L$, such that in every interval $\Delta x = (x-l(x)/2, x+l(x)/2)$, $\Delta x \in \langle 0, L \rangle$, functions B, c, ρ can be approximated respectively by certain $l(x)$ -periodic functions. Functions will be averaged by means of the

formula $\langle \varphi \rangle = \frac{1}{l} \int_{x-l/2}^{x+l/2} \varphi(\xi) d\xi$, $x \in \Omega^0$, $\Omega^0 = \{x \in \Omega : \Delta(x) \in \Omega\}$. We base on the physical assumptions that the

deflection of the l -periodic-like beam axis is an l -periodic-like function $v(x,t) \in PL(l)$. Let us define the averaged deflection $w(x,t)$ by means of formula $w(x,t) = \langle \rho \rangle^{-1} \langle \rho v \rangle(x,t)$. The total deflection of the beam can be represented by a sum $v(x,t) = w(x,t) + d(x,t)$, where $w(x,t) \in SV(l)$. The deflection disturbance function $d(x,t)$ will be assumed in the form of the series $d(x,t) = h^A(x)\psi_A(x,t)$, (summation convention over $A=1,2,\dots$ holds), where $h^A(x)$ —the global mode shape functions are the known a priori oscillating l -periodic-like functions (with the weight ρ), [1], having at every $x \in \Omega^0$ the periodic approximation $h_x^A(\xi)$, $\xi \in \bar{\Delta}(x)$ and the new unknowns amplitudes of the shape functions $\psi_A(x,t) \in SV(l)$. Based on concepts of the tolerance averaged model, [3] and [1], we obtain the averaged equations of the beam in form of a set $n+1$ differential equations with slowly varying or (for l -periodic beam) constant coefficients:

$$\langle B \rangle w^{IV}(x,t) + \langle B(h^A) \rangle'' \psi_A''(x,t) + \langle c \rangle \dot{w}(x,t) + \langle c h^A \rangle \dot{\psi}_A(x,t) + \langle \rho \rangle \ddot{w}(x,t) = \langle p \rangle(x,t), \quad (2)$$

$$\begin{aligned} \langle B(h^B) \rangle'' w''(x,t) + \langle B(h^B) \rangle'' (h^A)'' \psi_A''(x,t) + \langle c h^B \rangle \dot{w}(x,t) + \\ + \langle c h^B h^A \rangle \dot{\psi}_A(x,t) + \langle \rho h^B h^A \rangle \ddot{\psi}_A(x,t) = \langle p h^B \rangle(x,t). \end{aligned} \quad (3)$$

The boundary conditions are similar to that formulated in the Euler-Bernoulli beam theory. For the initial-value problem two initial conditions for ψ_A and w should be also known.

2. Stochastic excitation

We assume that $p(x,t) = P(x) \cdot F(t)$, where $P(x)$ is deterministic function of x and $F(t)$ is stationary stochastic process.

We consider the simply supported beam with periodic-variable cross-section. In this case we assume the following form of

the solution: $w = \sum_{i=1}^{\infty} y_i(t) \sin \frac{i\pi x}{L}$, $\psi_A = \sum_{j=1}^{\infty} q_{Aj}(t) \sin \frac{j\pi x}{L}$.

For $A=1$, $h^A = h^1 = h$ we have equations (2,3) in the matrix form $M\ddot{Y}^{(k)} + C\dot{Y}^{(k)} + K^{(k)}Y = \bar{R}^{(k)}F(t)$, where $k=1,2,\dots$,

$$\bar{Y}^{(k)} = \begin{bmatrix} y^{(k)}(t) \\ q^{(k)}(t) \end{bmatrix}, \quad M = \begin{bmatrix} \langle \rho \rangle, & 0 \\ 0, & \langle \rho h^2 \rangle \end{bmatrix}, \quad C = \begin{bmatrix} \langle c \rangle, & 0 \\ 0, & \langle c h^2 \rangle \end{bmatrix} = \eta M,$$

$$\bar{R}^{(k)} = \begin{bmatrix} \langle P \rangle^{(k)} \\ \langle Ph \rangle^{(k)} \end{bmatrix} = \begin{bmatrix} \int_0^L \langle P \rangle \sin \frac{k\pi x}{L} dx \\ \int_0^L \langle Ph \rangle \sin \frac{k\pi x}{L} dx \end{bmatrix}, \quad K^{(k)} = \begin{bmatrix} \langle B \rangle \left(\frac{k\pi}{L} \right)^4, & -\langle Bh'' \rangle \left(\frac{k\pi}{L} \right)^2 \\ -\langle Bh^4 \rangle \left(\frac{k\pi}{L} \right)^2, & \langle B(h'')^2 \rangle \end{bmatrix}.$$

We solve the eigenvalue problem to apply another eigenvalue transformation: $[K^{(k)} - (\omega^{(k)})^2 M] \bar{Z}^{(k)} = 0$. We find the frequency ω from equation $\det[K^{(k)} - (\omega^{(k)})^2 M] = 0$. Introducing new variables $\bar{r}_\beta^{(k)}(t) = \begin{bmatrix} r_1^{(k)}(t) \\ r_2^{(k)}(t) \end{bmatrix}$, $\bar{Y}^{(k)} = Z_\beta^{(k)} \bar{r}_\beta^{(k)}(t)$, $\beta =$

1, 2, we receive uncoupled set of equations: $\ddot{r}_\beta^{(k)} + 2\alpha_\beta^{(k)} \dot{r}_\beta^{(k)} + (\Omega_\beta^{(k)})^2 r_\beta^{(k)} = a_\beta^{(k)} F(t)$, (4)

where $2\alpha_\beta = \frac{C_\beta^{(k)}}{m_\beta^{(k)}}$, $(\Omega_\beta^{(k)})^2 = \frac{\kappa_\beta^{(k)}}{m_\beta}$, $a_\beta^{(k)} = [Z_\beta^{(k)}]^T Q^{(k)}$, $m_\beta^{(k)} = [Z_\beta^{(k)}]^T M Z_\beta^{(k)}$, $c_\beta^{(k)} = [Z_\beta^{(k)}]^T C Z_\beta^{(k)}$, $\kappa_\beta^{(k)} = [Z_\beta^{(k)}]^T K^{(k)} Z_\beta^{(k)}$.

The solution to equations (4) has form: $r_\beta^{(k)}(t) = a_\beta^{(k)} \int_0^t g_\beta^{(k)}(t-\tau) F(\tau) d\tau$, where $g_\beta^{(k)}(t) = \frac{1}{\Omega_\beta^{(k)}} e^{-\alpha_\beta^{(k)} t} \sin \Omega_\beta^{(k)} t$, $(\Omega_\beta^{(k)})^2 = (\Omega_{d\beta}^{(k)})^2 - (\alpha_\beta^{(k)})^2$. We assume the loading process $F(t)$ as stationary stochastic process.

The expectation and variance of the response have following forms: $E[r_\beta^{(k)}] = a_\beta^{(k)} \int_0^t g_\beta^{(k)}(t-\tau) E[F(\tau)] d\tau$,

$(\sigma_{r_\beta^{(k)}}(t))^2 = (a_\beta^{(k)})^2 \int_0^t \int_0^t g_\beta^{(k)}(t-\tau_1) g_\beta^{(k)}(t-\tau_2) C_{FF}(\tau_1-\tau_2) d\tau_1 d\tau_2$. The variance of the velocity of the response is:

$(\sigma_{\dot{r}_\beta^{(k)}}(t))^2 = (a_\beta^{(k)})^2 \int_0^t \int_0^t \dot{g}_\beta^{(k)}(t-\tau_1) \dot{g}_\beta^{(k)}(t-\tau_2) C_{FF}(\tau_1-\tau_2) d\tau_1 d\tau_2$. For steady state of the vibration the average number of

crossing the level s is given by the Rice's formula $\nu_s^+ = \frac{1}{2\pi} \frac{\sigma_{\dot{r}_\beta^{(k)}}}{\sigma_{r_\beta^{(k)}}} e^{-\frac{s^2}{2\sigma_{r_\beta^{(k)}}^2}}$. For white noise $C_{FF}(t_1-t_2) = \sigma_F^2 \delta(t_1-t_2)$ the

steady state solutions have form: $[\sigma_{r_\beta^{(k)}}]^2 = \frac{(a_\beta^{(k)})^2 \sigma_{FF}^2}{4\alpha_\beta^{(k)} (\omega_\beta^{(k)})^2}$, $[\sigma_{\dot{r}_\beta^{(k)}}]^2 = \frac{(a_\beta^{(k)})^2 \sigma_{FF}^2}{4\alpha_\beta^{(k)}}$, $\nu_s^+ = \frac{1}{2\pi} \omega_\beta^{(k)} \exp \left[-\frac{s^2 \sqrt{\alpha_\beta^{(k)} \omega_\beta^{(k)}}}{\alpha_\beta^{(k)} \sigma_{FF}} \right]$.

3. Conclusions

Problem of the stochastic excitations of the beam with periodically variable geometry is described by an equation with the rapidly varying coefficients. In this case the dynamic stochastic analysis and the estimate of reliability are rather difficult to obtain. In the framework of the tolerance averaging approach, it is possible to describe the problem in the form of the averaged differential equation system with constant coefficients. This approximation describes the effect of the beam segment length on the global dynamic behaviour (this effect disappears in classical homogenization solutions). We have reached the effective solution by double expansion into the eigen-functions and eigen-vectors.

4. References

1. MAZUR-ŚNIADY K.: On the formulation of the dynamics models of the beam with the periodic-like structure, XXXIX-th Symposium of Model. In Mech., Wisła 2000.
2. MAZUR-ŚNIADY K., ŚNIADY P.: Stochastic vibrations of micro-periodic, ZAMM, Acad. Verlag vol.77, 1997, Supplement 2.
3. WOŹNIAK C.: A Model for Analysis of Micro-Heterogeneous Solids. Tolerance Averaging versus Homogenization, Mechanic Berichte IAM, 1, 1999.

Addresses: PH.D. KRYSZYNA MAZUR-ŚNIADY, PROF. PAWEŁ ŚNIADY, Institute of Civil Engineering, Wrocław University of Technology, Wybrzeże Wyspiańskiego 27, 50-370 Wrocław, Poland.

RICHTER, M.; VOM SCHEIDT, J.; STARKLOFF, H.-J.

Moment Functions for Solutions of Random Boundary Value Problems

Boundary value problems for a class of ordinary differential operators with random coefficients are investigated. The random influences to the differential operators and the inhomogeneous terms are modelled by the class of weakly correlated processes. Using a perturbation method the random solutions can be represented as integral functionals of weakly correlated processes. It is possible to find approximations for the moment functions of the solutions by means of expansions in powers of the correlation length ε of the input processes. Especially asymptotic expansions for second-order moments of the solutions are presented. The results determined analytically are compared with Monte-Carlo simulations.

1. Random boundary value problems with weakly correlated stochastic influences

In this paper, random boundary value problems for ordinary differential equations

$$\begin{aligned} L(\omega)u &= g(x, \omega), & 0 \leq x \leq 1, \\ U_k[u] &= 0, & k = 1, 2, \dots, 2n, \end{aligned} \quad (1)$$

are considered, where $L(\omega)$ is given by

$$L(\omega)u := \sum_{i=0}^n (-1)^i \left[f_i(x, \omega) u^{(i)} \right]^{(i)}, \quad x \in [0, 1],$$

and the boundary conditions U_k are assumed to be non-random.

For the purpose of simplification, the function $f_n(x, \omega)$ is assumed to be non-random, $f_n(x, \omega) = f_n(x)$, the more general stochastic case is investigated in [3]. The paths of the considered random functions are assumed to be sufficiently smooth. Furthermore, the condition $f_n(x) \neq 0$ for all $x \in [0, 1]$ and the positive definiteness of $L(\omega)$ are supposed. Further assumptions, especially to the boundary conditions, are necessary, see [3]. Hence, the operator $L(\omega)$ is assumed to be symmetric with respect to all admissible functions (these are those functions, which possess $2n$ continuous derivatives and satisfy the boundary conditions). An example for suitable boundary conditions is given by $u(0) = u'(0) = \dots = u^{n-1}(0) = u(1) = u'(1) = \dots = u^{n-1}(1) = 0$.

The random influences to the considered problem are defined as follows, $g_\varepsilon(x, \omega) := g(x, \omega) - \langle g(x) \rangle$; $f_{i\varepsilon}(x, \omega) := f_i(x, \omega) - \langle f_i(x) \rangle$ ($i = 0, 1, \dots, n-1$), whereby $\langle \cdot \rangle$ denotes the expectation operator. It is assumed, that the random perturbations to $L(\omega)$ are sufficiently small, $|f_{i\varepsilon}(x, \omega)| \leq \eta$ a.s., $i = 0, 1, \dots, n-1$. Such as in [1], [3] and [4] boundary value problems are investigated, where the vector process $(g_\varepsilon(x, \omega), f_{0\varepsilon}(x, \omega), f_{1\varepsilon}(x, \omega), \dots, f_{n-1\varepsilon}(x, \omega))$ is assumed to be weakly correlated connected with correlation length ε . Weakly correlated functions can be characterized as functions without "distance effect". The definition and a detailed presentation of the theory of this class of random functions is presented in [4]. The essential property of a weakly correlated connected vector process $(h_{1\varepsilon}(x, \omega), h_{2\varepsilon}(x, \omega))$ reflects in the behaviour of the expectation and correlation functions, which are given by

$$\langle h_{i\varepsilon}(x) \rangle = 0 \quad \text{and} \quad \langle h_{i\varepsilon}(x) h_{j\varepsilon}(y) \rangle = \begin{cases} R_{ij\varepsilon}(x, y) & |x - y| \leq \varepsilon \\ 0 & |x - y| > \varepsilon \end{cases}, \quad i, j = 1, 2.$$

2. Asymptotic expansions of second-order moments of the solutions

Using a perturbation approach, it is possible to find the stochastic solution $u(x, \omega)$ of problem (1) in form of an expansion $u(x, \omega) = u_0(x) + \sum_{j=1}^{\infty} u_j(x, \omega)$. Thereby, $u_0(x)$ denotes the solution of the averaged problem (which arises by substituting the random input functions by their expectations) and $u_j(x, \omega)$ ($j = 1, 2, \dots$) denotes the term of $u(x, \omega)$, which is homogeneous of j -th order as to $g_\varepsilon(x, \omega)$, $f_{i\varepsilon}(x, \omega)$ ($i = 0, 1, \dots, n-1$). Consequently, the terms $u_j(x, \omega)$ can be represented as integral functionals of the weakly correlated connected input process.

The basis for the consideration of the stochastic behaviour of the solutions of (1) are asymptotic expansions of moments of integral functionals of weakly correlated processes ($\varepsilon \rightarrow 0$) which were given in [4] and which were (under

a special weak assumption) refined in [5]. In the following, exemplarily the second-order moments are investigated. Based on limits theorems given in [4], Theorem 1 can be derived. For a detailed presentation of the used perturbation method and the proof of the theorem it is referred to [3].

Theorem 1. Let $G(x, z)$ denote the Green's function associated with the averaged operator L_0 (defined by $L_0 u := \sum_{i=0}^n (-1)^i [(f_i(x)) u^{(i)}]^{(i)}$ and the boundary conditions) and let $u_0(x) = \int_0^1 G(x, z) \langle g(z) \rangle dz$ be the solution of the averaged problem. Then it holds

$$\begin{aligned} \langle (u(x_1) - u_0(x_1)) (u(x_2) - u_0(x_2)) \rangle = \varepsilon \cdot \left\{ \int_0^1 G(x_1, z) G(x_2, z) a_{gg}(z) dz \right. \\ \left. - \sum_{i=0}^{n-1} \int_0^1 \left(G(x_1, z) \frac{\partial^i G(x_2, z)}{\partial z^i} + G(x_2, z) \frac{\partial^i G(x_1, z)}{\partial z^i} \right) u_0^{(i)}(z) a_{gi}(z) dz \right. \\ \left. + \sum_{i_1, i_2=0}^{n-1} \int_0^1 \frac{\partial^{i_1} G(x_1, z)}{\partial z^{i_1}} \frac{\partial^{i_2} G(x_2, z)}{\partial z^{i_2}} u_0^{(i_1)}(z) u_0^{(i_2)}(z) a_{i_1 i_2}(z) dz \right\} + o(\varepsilon), \end{aligned} \quad (2)$$

whereby $a_{i_1 i_2}(z)$ ($i_1, i_2 = 0, 1, \dots, n-1$) denotes the intensity between the components $f_{i_1 \varepsilon}$ and $f_{i_2 \varepsilon}$ of the weakly correlated connected input process, $a_{i_1 i_2}(z) := \lim_{\varepsilon \downarrow 0} \frac{1}{\varepsilon} \int_{-\varepsilon}^{\varepsilon} \langle f_{i_1 \varepsilon}(z) f_{i_2 \varepsilon}(z+x) \rangle dx$, and $a_{gg}(z)$ and $a_{gi}(z)$ are defined accordingly.

Example 1. We consider the random boundary value problem

$$-u'' + (1 + f_0 \varepsilon(x, \omega)) u = 1 + g \varepsilon(x, \omega), \quad u(0) = u(1) = 0.$$

The vector process $(g \varepsilon(x, \omega), f_0 \varepsilon(x, \omega))$ is assumed to be a weakly correlated connected process, which can be simulated. Such processes are investigated in [2], [3] and [4]. The corresponding intensities are constants and chosen as $a_{gg} = 1.67 \cdot 10^{-7}$, $a_{g0} = 1.67 \cdot 10^{-6}$ and $a_{00} = 1.67 \cdot 10^{-5}$, respectively. On the left hand side of Figure 1 the approximation result for $V(x_1, x_2) := \lim_{\varepsilon \downarrow 0} \frac{1}{\varepsilon} \cdot \langle (u(x_1) - u_0(x_1)) (u(x_2) - u_0(x_2)) \rangle$ which is derived from (2) is shown. On the right hand side the result of a corresponding Monte-Carlo simulation is presented, which coincides very well to the approximation obtained from Theorem 1.

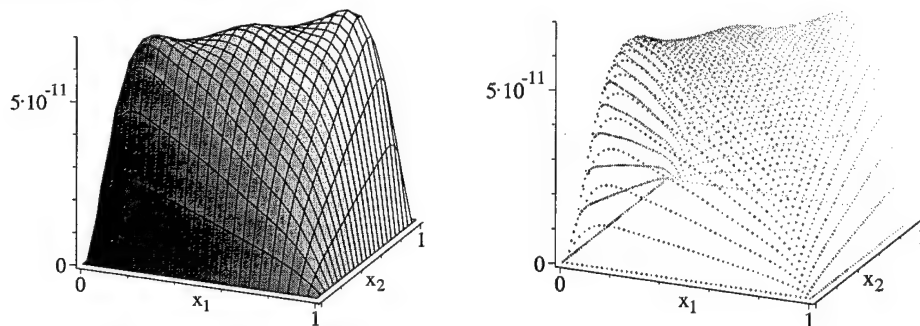


Figure 1: approximation and simulation results of $V(x_1, x_2)$

3. References

- 1 BOYCE, W. E.; XIA, N.-M.: The Approach to Normality of the Solutions of Random Boundary and Eigenvalue Problems with Weakly Correlated Coefficients; Quarterly of Appl. Math. XL 4, 419-445, 1983.
- 2 MEHLHOSE, S.: Eigenwerte zufälliger Matrizen von Integralfunktionalen schwach korrelierter Prozesse; Doctoral Thesis, TU Chemnitz, 1997.
- 3 RICHTER, M.: Wahrscheinlichkeitstheoretisches Verhalten der Lösungen stochastischer Randwertprobleme; Doctoral Thesis, TU Chemnitz, 1999.
- 4 VOM SCHEIDT, J.: Stochastic Equations of Mathematical Physics; Akademie-Verlag, Berlin, 1990.
- 5 VOM SCHEIDT, J.; STARKLOFF, H.-J.; WUNDERLICH, R.: Asymptotic expansions of integral functionals of vector valued ε -correlated processes, Preprint 99-3, TU Chemnitz, Faculty of Mathematics, 1999.

Addresses: DR. MATTHIAS RICHTER, Bauhaus-University Weimar, Faculty of Civil Engineering, D-99421 Weimar, Germany

PROF. DR. JÜRGEN VOM SCHEIDT, DR. HANS-JÖRG STARKLOFF, Chemnitz University of Technology, Faculty of Mathematics, D-09107 Chemnitz, Germany

SIENIAWSKA R., WYSOCKA A., ŻUKOWSKI S.

Reliability of Elastic-Plastic Bar Systems Loaded Dynamically

An approach for calculating the reliability and sensitivity of elastic-plastic systems loaded dynamically is presented. The algorithm integrates the random nature of static and dynamic load with elastic-plastic strains of the structure. For the dynamic calculations the COSMOS system has been used and for calculating the reliability index and sensitivities the STRUREL system has been applied. Some example results of a roof grid are shown.

1. Formulation and solution of the problem

Let's consider a plane or space bar structure made of an elastic-perfectly-plastic material of random parameters. Let's assume that the configuration of the structure elements is deterministic, the load does not change their location, acts on the structure in the static manner (for example the dead load, the weight of machines) and in dynamic manner (for example the load of working machines). Let's assume also that the dynamic load is an excitation of a harmonic type and the magnitudes of all kinds of loads are described by random variables of known probability distribution. The structure is so designed that the fundamental frequency of its natural modes is larger than the expected frequency of the loading function. Furthermore, we assume that the damage of the structure can be caused by the incremental growth of plastic strains in these cross-sections in which the extreme bending moments are equal to the cross-section capacities (plastic limit moments). The number of plastic hinges, which appear in the damaged cross-sections, must be so that it makes the construction collapse. The problem of the construction shakedown can be formulated in a kinematic way starting from the unshakedown Neal's theorem or in a static way starting from the Melan's shakedown theorem in both cases completed with the "dynamic" (sufficient) shakedown theorem (Ceradini [1], Ho [2]).

From the kinematic formulation follows that the structure will fail if there exists a failure mechanism which satisfies the following condition:

$$\sum_i (\max M_i^e \cdot \Theta_i^+ - \min M_i^e \cdot \Theta_i^-) \geq \sum_i M_{oi}^T \cdot (\Theta_i^+ + \Theta_i^-) \quad (1)$$

where M_{oi} are the plastic limit moments (capacities) in the i -th critical cross-section, Θ_i^+ , Θ_i^- are the strains in the i -th plastic hinges, $\max M_i^e = M_i^e(g) + \max M_i^e(p)$, $\min M_i^e = M_i^e(g) + \min M_i^e(p)$, are the maximum and minimum values of the bending moments, that occur due to given load in the i -th critical cross-section of the elastic system, respectively. From the static theorem it follows that the structure adopts to the changing loads if, for each cross-section, following conditions are satisfied:

$$\begin{aligned} \sum_{j=1}^{n_h} \bar{M}_i^j \cdot X_j^r + \max M_i^e - M_{oi}^+ &< 0 \\ - \sum_{j=1}^{n_h} \bar{M}_i^j \cdot X_j^r - \min M_i^e - M_{oi}^- &< 0 \end{aligned} \quad (2)$$

where \bar{M}_i^j is the bending moment in the i -th cross-section caused by the j -th unity hyperstatic force, X_j^r is the j -th residual hyperstatic force, n_h is a degree of the static indeterminacy.

For further considerations, as the reliability measure we assume the probability p_r that the construction does not fail. A reliability index β exists, which corresponds to this measure. We assume also that the random values that describe the types of load (dead load, operational etc.) and structure capacity are mutually independent.

2. Example results

The reliability and sensitivity of a roof grid built of 4 beams loaded by the dead load and static and dynamic operational load caused by working machines have been calculated. First, using the COSMOS system, the construction has been solved in the elastic range due to static and dynamic loads and the extreme bending moments have been found. Then, the shakedown conditions have been built and input to the STRUREL system for calculating the reliability and sensitivity of the structure.

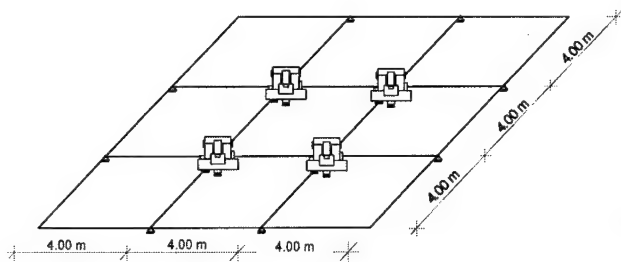


Fig. 1. Model of the structure

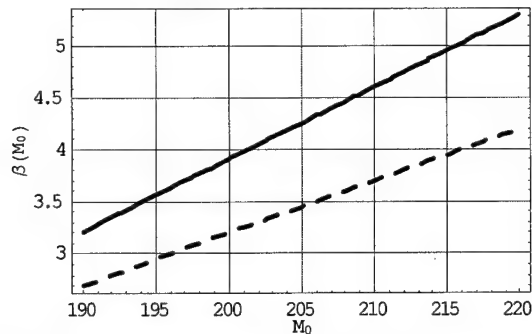


Fig. 3. The reliability index vs. the structure capacity calculated for the elastic state (dashed line) and for the shakedown state (solid line).

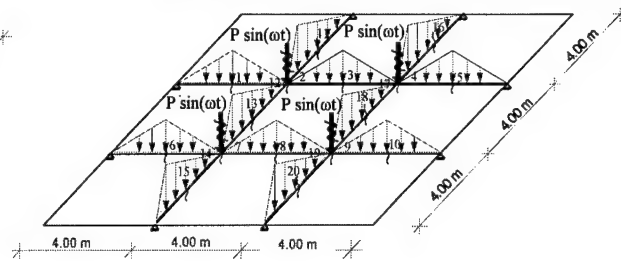


Fig. 2. Model of the load

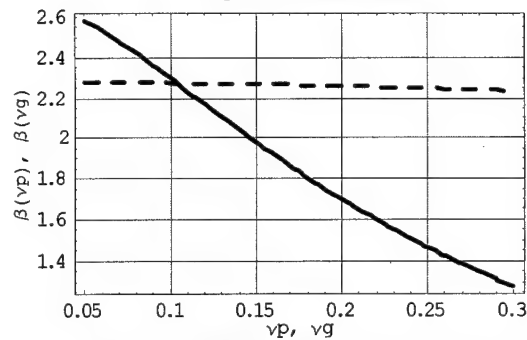


Fig. 4. The reliability index vs. the coefficients of variation (static load - solid line, dynamic load - dashed line)

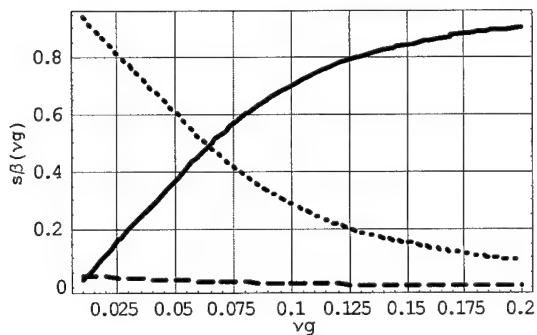


Fig. 6. The dimensionless sensitivities of the reliability index vs. the coefficient of variation of the static load (due to the change of the variation coefficient of the static load - solid line, due to dynamic load - dashed line, due to capacity - dotted line)

3. Conclusions

The algorithm presented is a whole probabilistic approach, it gives the possibility for taking into account both the randomness of the load and construction and also the plastic reserve and can be useful in estimating the reliability of existing or newly designed structures. From the calculations shown follows that: in a case such as presented, when the shapes of failure mechanisms are easy to determine the kinematic approach seems to be more effective as the static approach. The reliability index depends very strongly on the coefficient of variation of the static load and structure capacity and not much on the coefficient of variation of the dynamic load, because in this example the static load was much greater than the dynamic load.

4. References

- 1 CAPURSO M., Extended Displacement Bound Theorems for Continua Subjected to Dynamic Loading, *J. Mech. Phys. Solids*, 1975, Vol.23, 113-122
- 2 CERADINI G., Dynamic Shakedown in Elastic-Plastic Bodies, *J. of the Eng. Mech. Division, ASCE, EM3*, 1980, 481-499
- 3 HO HWA-SHAN, Shakedown in Elastic-Plastic Systems under Dynamic Loadings, *J. of Applied Mech. Division*, vol.39, 1972, 416-421
- 4 POLIZZOTTO C., Dynamic Shakedown by modal analysis, *Meccanica*, vol. 19, 1984, 133-144

Addresses: DR RÓŻA SIENIAWSKA, M. SC. ALINA WYSOCKA, DR. STANISŁAW ŻUKOWSKI, Institute of Civil Engineering, Wrocław University of Technology, W. Wyspiańskiego 27, 50 - 370 Wrocław, Poland

ŚNIADY P., SIENIAWSKA R., ŻUKOWSKI S.

Random Response of a System Due to Periodic Excitation with Gaussian and Non-Gaussian Disturbances

The vibrations of a linear system due to periodic excitation with some Gaussian and non-Gaussian disturbances are studied. The disturbances are modelled by the white noise and by compound Poisson stochastic processes. The Ito formula for the white noise process and the general Ito formula for the compound Poisson process are applied to get the equations for calculating the probabilistic moments of the system response.

1. Formulation and solution of the problem

Let's consider vibrations of a structure made of an elastic material with deterministic material and geometrical parameters. Let the vibrations be caused by a harmonic excitation with some stochastic disturbances of its amplitude and phase, caused, for example, by the wind pressure or by working machines. After making eigen transformation, the vibrations of a linear, multi-degree of freedom system can be described by the separated set of equations

$$y_n(t) + 2\alpha_n y_n(t) + \omega_n^2 y_n(t) = p_n [1 + \sigma \xi(t)] \sin \varphi(t) \quad (1)$$

Let's consider two types of disturbances: one of the gaussian type and one of non-gaussian type. In the first case the phase disturbance is described by

$$\frac{d\varphi(t)}{dt} = \bar{\omega} + \sigma_2 \xi_2(t) \quad (2)$$

where $\xi(t)$ and $\xi_2(t)$ are stochastic processes of the "white noise" type. The equation (2) can be written in the shape

$$d\varphi(t) = \bar{\omega} dt + \xi_2 dW_2(t) \quad (3)$$

where $W_2(t)$ is a unit Wiener stochastic process. Above problem has been considered in the paper [1].

In the second case the phase disturbance is as follows

$$\frac{d\varphi(t)}{dt} = \bar{\omega} + \sum_{k=1}^{N(t)} \Delta \omega_k \quad (4)$$

where $N(t)$ is the Poisson stochastic process with parameter λ and for further calculations we assume that $E[N(t)] = \lambda t$,

$E[\Delta \omega_k^i] = E[\Delta \omega^i] = \text{const}$, $i = 1, 2, 3$, $E[\Delta \omega_k] = 0$.

For calculating the probabilistic moments of the system response a set of Ito equations can be derived from the equation (1) after introducing some new variables [1] and taking into account the expressions (3) or (4). For the first case of excitation we introduce 4 new variables and for the second case of excitation 5 new variables

$$z_1(n, t) = y_n(t), \quad z_2(n, t) = \dot{y}_n(t), \quad z_3(t) = \sin \varphi(t), \quad z_4(t) = \cos \varphi(t), \quad z_5(t) = \sum_{k=1}^{N(t)} \Delta \omega_k. \quad (5)$$

The first 4 variables are the same in both cases.

After applying the Ito's differentiation formula for the gaussian excitation and the generalised Ito formula for the non-gaussian excitation one receives a hierarchical set of differential equations for calculating the probabilistic moments of the variables $z_i(t)$, ($i = 1, 2, \dots, 4, 5$).

2. Example results

Some probabilistic characteristics of an example system due to harmonic excitation with gaussian and non-gaussian disturbances have been calculated. The results are shown in Figures 1 to 4.

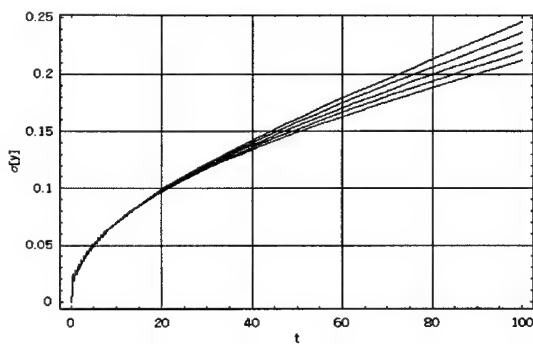


Fig. 1. Standard deviation of y for gaussian disturbance
(for stiffness parameters $k = a \cdot \frac{EI}{L^3}$, $a = 2 \div 6$)

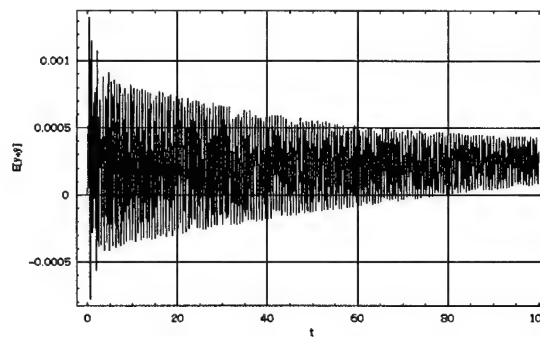


Fig. 3. Expected value of y and its velocity
calculated for gaussian disturbances

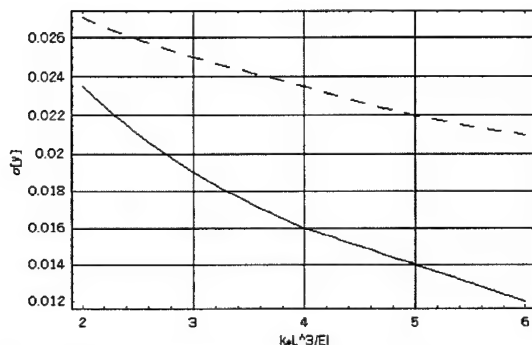


Fig. 3. Maximum and minimum values of standard deviation of y vs. for non-gaussian disturbances

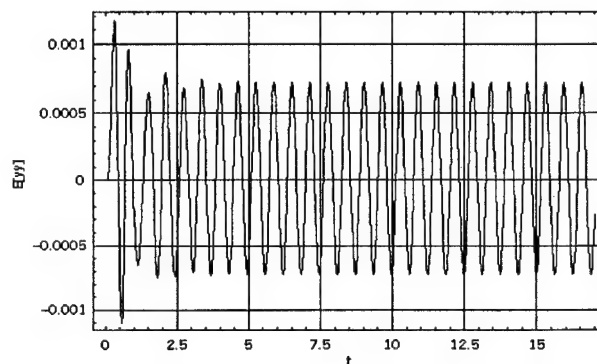


Fig. 4. Expected value of y and its velocity vs. structure stiffness calculated for non-gaussian disturbances

3. Conclusions

The problem presented seems to be interesting from the theoretical and practical point of view. The harmonic excitation with gaussian and non-gaussian types of disturbances can be an appropriate model for the wind load in the case when it causes the Benard-Karman vortices. In the case of harmonic vibrations with stochastic disturbances the problem is difficult to solve in both theoretical and numerical way. When analysing the problem numerically one can see that the results depend very strongly on the precision of calculations.

While solving the hierarchical set of differential equations for calculating the probabilistic moments of the system response a closure procedures is required. For any closure procedure, however, additional numerical verifications must be done. One of the closure procedures is to assume zero value for all probabilistic moments of orders higher than calculated. Another of the closure procedures is such that the higher order probabilistic moments, which have appeared in the equations, can be treated as a product of adequate probabilistic moments of lower order. Another proposition is to set the appropriate cumulants to zero.

4. References

- 1 HOU Z., ZHON Y., DIMENTBERG M.F., NOORI M., A stationary model of periodic excitation with uncorrelated random disturbances, Probabilistic Engineering Mechanics, 11, Elsevier Science Ltd., pp. 191-203, 1996.
- 2 SOBCZYK K., Stochastic Differential Equations, Kluwer Academic Publishers, Dordrecht, Boston, London, 1991

Addresses: PROF. DR PAWEŁ ŚNIADY, DR RÓŻA SIENIAWSKA, , DR. STANISŁAW ŻUKOWSKI, Institute of Civil Engineering, Wrocław University of Technology, W. Wyspiańskiego 27, 50 - 370 Wrocław, Poland

LESŁAW SOCHA

Statistical Linearization of the Duffing Oscillator under non-Gaussian Excitations with Criteria in Probability Density Function Space

The concept of statistical linearization with probability density criteria for nonlinear oscillator under non-Gaussian excitations is considered in this paper. New criteria of linearization and an approximate approach is proposed.

1. Introduction

In almost all studies of statistical linearization different moment criteria and nonlinear systems under Gaussian excitations have been considered. Also the application of statistical linearization to the Duffing oscillator in the case of moment criteria and non-Gaussian excitations [1] and in the case criteria in probability density space and Gaussian excitations [2] have been shown. The objective of this paper is to combine the both approaches for continuous excitations modelled by a polynomial of Gaussian coloured noises.

2. Problem statement

Consider a nonlinear Duffing oscillator described by

$$dx_1 = x_2 dt, \quad dx_2 = [-2\zeta\omega_0 x_2 - f(x_1)]dt + \eta dt, \quad (1)$$

where $f(x_1) = y = \omega_0^2 x_1 + \epsilon x_1^3$; ω_0, ζ , and ϵ are constant parameters; $\eta(t)$ is assumed to be a non-Gaussian stochastic process modelled by

$$\eta(t) = \sum_{i=1}^M \alpha_i y^i(t), \quad dy(t) = -\alpha y(t)dt + q d\xi, \quad (2)$$

where $\alpha, \alpha_i, (i = 1, \dots, M)$ and q are constant parameters, $y(t)$ is a one-dimensional coloured Gaussian process, and $\xi(t)$ a standard Wiener process. An equivalent linearized system for the Duffing oscillator has the form

$$dx_1 = x_2 dt, \quad dx_2 = [-2\zeta\omega_0 x_2 - \omega_e^2 x_1 - \epsilon_e]dt + \eta dt, \quad (3)$$

where $\omega_e^2 = k_e$ and $\epsilon_e = k_0 - k_e E[x_1(t)]$, k_0 and k_e are linearization coefficients. Two basic criteria of linearization in probability density functions space are introduced.

$$I_1(k_0, k_e) = \int_{-\infty}^{+\infty} (g_N(y) - g_L(y))^2 dy, \quad I_2(k_0, k_e) = \int_{-\infty}^{+\infty} |y|^2 |g_N(y) - g_L(y)| dy, \quad (4)$$

where $g_N(y)$ and $g_L(y)$ are probability density functions of variables of the outputs of nonlinear and linearized variables in equations (1) and (3), respectively.

3. Main results

One can show that for variables $y = \omega_0^2 x_1 + \epsilon x_1^3$ and $y = \omega_e^2 x_1 + \epsilon_e$ the corresponding functions $g_N(y)$ and $g_L(y)$ are

$$g_N(y) = \frac{1}{6a\epsilon} \left[\frac{y+a}{v_1^2} + \frac{y-a}{v_2^2} \right] g_I(h_N(y)), \quad g_L(y) = \frac{1}{|k_e|} g_I(h_L(y)), \quad (5)$$

where

$$g_I(x) = \frac{1}{\sqrt{2\pi}\sigma_x} \exp\left\{-\frac{(x-m_x)^2}{2\sigma_x^2}\right\} \left[1 + \sum_{\nu=3}^N \frac{c_\nu}{\nu!} H_\nu\left(\frac{x-m_x}{\sigma_x}\right)\right] \quad (6)$$

$$h_N(y) = v_1 + v_2, \quad h_L(y) = \frac{1}{k_e}(y - \epsilon_e) = \frac{1}{k_e}(y - k_0 + k_e E[y(t)]), \quad (7)$$

$v_1 = [\frac{1}{2\epsilon}(y + \sqrt{y^2 + 4\omega_0^6/27\epsilon})]^{1/3}$, $v_2 = [\frac{1}{2\epsilon}(y - \sqrt{y^2 + 4\omega_0^6/27\epsilon})]^{1/3}$, $m_x = E[x]$, $\sigma_x^2 = E[(x - m_x)^2]$; $c_\nu = E[G_\nu(x - m_x)]$, $\nu = 3, 4, \dots, N$ are quasi-moments, $H_\nu(x)$ and $G_\nu(x)$ are one-dimensional Hermite's polynomials. The quasi-moments of the response c_ν are uniquely determined by corresponding moments $E[x_1^{p_1} x_2^{p_2}]$ for $p_1 + p_2 = 0, 1, 2, \dots, \nu$.

We approximate the moments that are needed for the calculation of the linearization coefficients by the corresponding ones of the linearized system. One can show that for system (3) the moment equations are determined in closed form [1]. In this case, the following algorithm for the determination of the linearized system can be formulated:

1. Substitute $\epsilon = 0$ i.e. $k_0 = E[x_1] = 0$, $k_e^2 = \omega_0^2$ into equation (3) and calculate probability density function of linearized element (one dimensional) defined by (5) for $\sigma_x^2 = \sigma_L^2 = q^2/4\zeta\omega_0^2$
2. Calculate stationary moments for the solution of system (3) and next the probability density function $g_I(x)$ defined by (6)
3. Consider criterion I_1 or I_2 , where $g_N(y)$ and $g_L(y)$ are defined by (5) for $h_N(y)$ and $h_L(y)$ given by (7) and find the coefficient k_{min} which minimizes the considered criterion (4). Next, substitute $k_e = k_{min}$
4. Calculate stationary moments for the solution of system (3) and next the probability density function $g_I(x)$ by substituting $E[x_1^{p_1} x_2^{p_2}]$ and functions $g_N(y)$ and $g_L(y)$. Go to step 3 until k_e and $E[x_1^2]$ converge.

Example. We show a comparison of stationary mean-square displacements of linearized systems obtained by applying statistical linearization with criteria: mean-square error of displacements, mean-square error of potential energies, criteria I_1 , I_2 and by simulation. The numerical results denoted by lines with crosses, squares, triangles, circles and stars, respectively are presented in Figure 1.

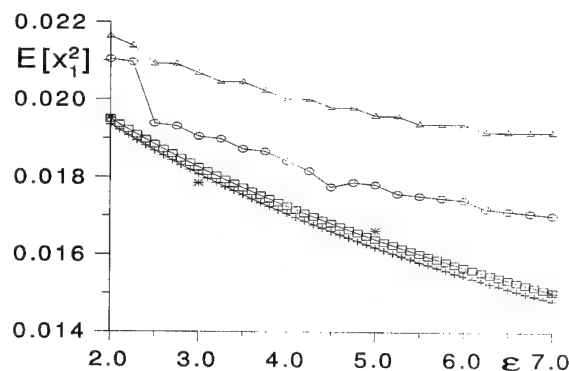


Figure 1: The comparison of stationary mean-square displacements of linearized systems vs. parameter ϵ with $\omega_0 = 1$, $\zeta = 0.05$, $q^2 = 0.1$, $\alpha = 1$, $M = 3$, $\alpha_1 = \alpha_2 = \alpha_3 = 0.25$

Acknowledgements

The author gratefully acknowledges research support from the Humboldt Foundation

4. References

- 1 SOBIECHOWSKI, C., SOCHA, L.: Statistical linearization of the Duffing oscillator under non-Gaussian external excitations; J.Sound Vib. **231** (2000), 19–35.
- 2 SOCHA, L.: Statistical and equivalent linearization techniques with probability density criteria; J.Theor. Appl. Mech. **37** (1999), 369–382.

Addresses: DR. SOCHA LESLAW, Silesian Technical University, Institute of Transport, ul.Krasinskiego 8, 40-019 Katowice, POLAND.

STARKLOFF, H.-J.; VOM SCHEIDT, J.; WUNDERLICH, R.

Random Vibration Systems with Weakly Correlated Random Excitation

In the paper asymptotic expansions for second-order moments of solutions to ordinary differential equations with weakly correlated random inhomogeneous terms are presented. Such equations arise e.g. in the mathematical modeling of vibration systems with an external random excitation. The given expansions allow an efficient approximative computation of moment functions of the solution process, particularly when the number of degrees of freedom is large.

1. Asymptotic expansions for correlation functions of integral functionals

Let us consider a system of random linear ordinary differential equations

$$\dot{y} = Ay + x \quad (1)$$

with a deterministic constant matrix A , which is assumed to be stable (i.e. all eigenvalues have negative real parts) and a centered wide-sense stationary random process x . Then a wide-sense stationary random solution process

$$y(t) = \int_{-\infty}^t \exp(A(t-s))x(s) ds = \int_0^{\infty} \exp(Au)x(t-u) du \quad (2)$$

exists (see e.g. [1]). In the present paper the case of an ε -correlated random excitation $x(s) = {}^{\varepsilon}f(s)$ will be treated. The random process ${}^{\varepsilon}f$ is characterized by a small correlation length $\varepsilon > 0$ in the sense, that for the matrix correlation function it holds $R_{{}^{\varepsilon}f}({}^{\varepsilon}f(s), t) = 0$ for values s, t with $|s - t| \geq \varepsilon$ [2,3]. In order to get approximations to second-order characteristics of the corresponding solution process, the process ${}^{\varepsilon}f$ is embedded in a family $({}^{\varepsilon}f), \varepsilon > 0$ of random processes and asymptotic expansions as $\varepsilon \rightarrow 0$ are derived. In a more general framework we can consider integral functionals of the type

$${}^{\varepsilon}g(t) = \int_{-\infty}^t Q(t-s){}^{\varepsilon}f(s) ds = \int_0^{\infty} Q(u){}^{\varepsilon}f(t-u) du.$$

Theorem 1. [4,6] *Let $({}^{\varepsilon}f(s), s \in \mathbb{R})$ be centered vector-valued wide-sense stationary ε -correlated processes with correlation functions $R_{{}^{\varepsilon}f}({}^{\varepsilon}f)$ which are generated by a continuous correlation function of a 1-correlated process, i.e.*

$$R_{{}^{\varepsilon}f}({}^{\varepsilon}f(s)) = R_{1f}({}^{\varepsilon}f\left(\frac{s}{\varepsilon}\right)) = R\left(\frac{s}{\varepsilon}\right) \quad (3)$$

and let Q be a deterministic matrix-valued function which is N -times continuously differentiable, $N \in \mathbb{N}_0 = \{0, 1, 2, \dots\}$, $Q^{(N)}$ is absolutely continuous on \mathbb{R}_+ and $Q^{(j)} \in L^2(\mathbb{R}_+) \cap L^1(\mathbb{R}_+)$, $j = 0, \dots, N+1$. Then the following asymptotic expansions for fixed values τ as $\varepsilon \rightarrow 0$ are valid:

$$\begin{aligned} R_{{}^{\varepsilon}g}({}^{\varepsilon}g(0)) &= \sum_{j=0}^N \frac{\varepsilon^{j+1}}{j!} \left\{ \int_0^{\infty} Q^{(j)}(u) \nu_j^+ Q^*(u) du + \left[\int_0^{\infty} Q^{(j)}(u) \nu_j^+ Q^*(u) du \right]^* \right\} + o(\varepsilon^{N+1}), \\ R_{{}^{\varepsilon}g}({}^{\varepsilon}g(\tau)) &= \sum_{j=0}^N \frac{\varepsilon^{j+1}}{j!} \int_0^{\infty} Q(u) \mu_j^* [Q^{(j)}(u+\tau)]^* du + o(\varepsilon^{N+1}) \end{aligned}$$

for $\tau > 0$ and $R_{{}^{\varepsilon}g}({}^{\varepsilon}g(\tau)) = R_{{}^{\varepsilon}g}({}^{\varepsilon}g(-\tau))$ for $\tau < 0$.

The quantities μ_j , ν_j^+ and ν_j are called correlation moments [4,6] and are defined by

$$\mu_j = \int_{-\infty}^{\infty} s^j R(s) ds, \quad \nu_j = \int_{-\infty}^{\infty} |s|^j R(s) ds, \quad \nu_j^+ = \int_0^{\infty} s^j R(s) ds,$$

where R denotes the generating correlation function from (3).

2. Application

Choosing $Q(u) = \exp(Au)$ one finds the asymptotic expansion for the matrix correlation function $R_{\varepsilon_y \varepsilon_y}(\tau)$ for the stationary solution process (2) of system (1) with excitation $x(t) = \varepsilon f(t)$.

Example 1. In the case of a one-degree of freedom random vibration system

$$\ddot{y} + 2\delta\theta_0\dot{y} + \theta_0^2 y = x, \quad 0 < \delta < 1$$

one gets for the general stationary solution (4) and the corresponding asymptotic expansions if $x = \varepsilon f$

$$\begin{aligned} R_{yy}(\tau) &= \frac{1}{4\delta\sqrt{1-\delta^2}\theta_0^3} \int_{-\infty}^{\infty} \exp(-\delta\theta_0|\tau-u|) \sin(\theta_d|\tau-u| + \varphi_\delta) R_{xx}(u) du \\ R_{\varepsilon_y \varepsilon_y}(0) &= \sum_{j=0}^N \frac{(-1)^{j+1} \theta_0^{j-3} \nu_j \varepsilon^{j+1}}{4j! \delta \sqrt{1-\delta^2}} \sin((j-1)\varphi_\delta) + o(\varepsilon^{N+1}) \\ R_{\varepsilon_y \varepsilon_y}(\tau) &= \sum_{j=0, j \text{ even}}^N \frac{\theta_0^{j-3} \mu_j \varepsilon^{j+1}}{4j! \delta \sqrt{1-\delta^2}} \exp(-\delta\theta_0|\tau|) \sin(\theta_d|\tau| - (j-1)\varphi_\delta) + o(\varepsilon^{N+1}) \quad (\tau \neq 0) \end{aligned} \quad (4)$$

with $\theta_d = \theta_0\sqrt{1-\delta^2}$ and $\varphi_\delta = \arctan(\frac{\sqrt{1-\delta^2}}{\delta})$.

Example 2. Investigating a multi-degree of freedom vibration system (1) with a stable diagonalizable matrix A , i.e. $A = V\Lambda V^{-1}$ with $\Lambda = \text{diag}(\lambda_1, \dots, \lambda_n)$, $\text{Re}(\lambda_i) < 0$, one can find for fixed values τ the asymptotic expansions

$$\begin{aligned} R_{\varepsilon_y \varepsilon_y}(0) &= \sum_{j=0}^N \frac{\varepsilon^{j+1}}{j!} \{j_q + j_q^*\} + o(\varepsilon^{N+1}) \\ R_{\varepsilon_y \varepsilon_y}(\tau) &= \sum_{j=0}^N \frac{\varepsilon^{j+1}}{j!} j_q(\tau) + o(\varepsilon^{N+1}) \quad (\tau > 0) \\ \text{with} \\ j_q &= -V \left(\frac{j b_{kl} \lambda_k^j}{\lambda_k + \bar{\lambda}_l} \right)_{k,l=1,2,\dots,n} V^*, \quad (j b_{kl})_{k,l=1,2,\dots,n} = V^{-1} \nu_j^+ [V^{-1}]^*, \\ j_q(\tau) &= -V \left(\frac{j c_{kl} \exp(\bar{\lambda}_l \tau) \bar{\lambda}_l^j}{\lambda_k + \bar{\lambda}_l} \right)_{k,l=1,2,\dots,n} V^*, \quad (j c_{kl})_{k,l=1,2,\dots,n} = V^{-1} \mu_j^* [V^{-1}]^* \end{aligned}$$

Further expansions of second-order moment functions for integral functionals of weakly dependent random processes and other related results can be found in [2,3,4,5,6].

Acknowledgements

The support by the Deutsche Forschungsgemeinschaft is greatly appreciated.

3. References

- 1 PREUMONT, A.: Random Vibration and Spectral Analysis; Kluwer Academic Publishers, Dordrecht, 1994.
- 2 VOM SCHEIDT, J.: Stochastic Equations of Mathematical Physics; Akademie-Verlag, Berlin, 1990.
- 3 VOM SCHEIDT, J.; FELLEBERG, B.; WÖHRL, U.: Analyse und Simulation stochastischer Schwingungssysteme; B. G. Teubner, Stuttgart, 1994.
- 4 VOM SCHEIDT, J.; STARKLOFF, H.-J.; WUNDERLICH, R.: Asymptotic Expansions of Integral Functionals of Vector Valued ε -correlated Processes, Preprint 99-3, TU Chemnitz, Faculty of Mathematics, 1999.
- 5 VOM SCHEIDT, J.; STARKLOFF, H.-J.; WUNDERLICH, R.: Integral Functionals of ε -correlated Random Fields, Preprint 99-4, TU Chemnitz, Faculty of Mathematics, 1999.
- 6 VOM SCHEIDT, J.; STARKLOFF, H.-J.; WUNDERLICH, R.: Asymptotic Expansions of Integral Functionals of Weakly Correlated Random Processes, ZAA, 19 (2000), 255-268

Addresses: DR. HANS-JÖRG STARKLOFF, PROF. DR. JÜRGEN VOM SCHEIDT, DR. RALF WUNDERLICH, Chemnitz University of Technology, Faculty of Mathematics, D-09107 Chemnitz, Germany

WUNDERLICH, R.; VOM SCHEIDT, J.; STARKLOFF, H.-J.

Low-Dimensional Approximations of Random Vibration Systems

The paper considers the computation of moment functions of the response of large-scale randomly excited vibration systems. Since standard methods fail because of enormous computational problems dimension reduction techniques are applied. We find approximations of the desired response characteristics of the large-scale system by solving a suitable reduced-order system.

1. Introduction

Mathematical modeling of real-world vibration systems (e. g. rotating generator shafts excited by random fluctuations of the generator torque, vehicles moving on a rough road) often results in the following system of equations

$$\dot{\mathbf{y}}(t) = \mathcal{F}(\mathbf{y}(t)) + \mathbf{B}\mathbf{h}(t, \omega); \quad \mathbf{z}(t) = \mathbf{T}\mathbf{y}(t) \quad (1)$$

with an r -dimensional input or excitation \mathbf{h} , an n -dimensional state \mathbf{y} and an n' -dimensional output or response \mathbf{z} , $r, n, n' \in \mathbb{N}$. The above equations are called state and output equation, respectively. \mathcal{F} is an n -dimensional mapping, \mathbf{B} and \mathbf{T} are $n \times r$ and $n' \times n$ matrices, respectively.

The excitation $\mathbf{h}(t, \omega)$ is assumed to be a stationary random vector function. For the description of the long-term behaviour of the above system under continuously acting excitations so-called stationary solutions \mathbf{y} and the corresponding output \mathbf{z} are used. A stationary solution is a random vector function which satisfies the state equation and which is stationarily related to \mathbf{h} . We are interested in conditions for the existence of stationary solutions \mathbf{y} and the computation of moment functions (as mean, variance, correlation function and spectral density) of the output \mathbf{z} . If \mathcal{F} is linear, i.e. $\mathcal{F}(\mathbf{y}) = \mathbf{A}\mathbf{y}$ with some $n \times n$ matrix \mathbf{A} , then the stability of \mathbf{A} is a sufficient condition for the existence of stationary solutions. For systems with additional polynomial nonlinear perturbations the papers [2,4] provide corresponding conditions. For the computation of moment functions we refer to [1,3,4].

In this paper we consider large-scale systems with a large number n of state equations. This case arises in the semi-discretization of continuous vibration systems which can be described by PDEs. Procedures for the computation of moment functions of \mathbf{z} (as well as for \mathbf{y}) become intractable because of enormous computational problems. Therefore, we try to find approximations of \mathbf{z} using the following system with a suitable low-dimensional state equation which still can be handled numerically

$$\dot{\mathbf{y}}_m(t) = \mathcal{F}_m(\mathbf{y}_m(t)) + \mathbf{B}_m\mathbf{h}(t, \omega); \quad \tilde{\mathbf{z}}(t) = \mathbf{T}_m\mathbf{y}_m(t). \quad (2)$$

Here, \mathbf{y}_m is an m -dimensional state, $m < n$, \mathbf{B}_m an $m \times r$ matrix, \mathbf{T}_m an $n' \times m$ matrix and \mathcal{F}_m an m -dimensional mapping. The n' -dimensional output $\tilde{\mathbf{z}}$ is called reduced-order approximation of \mathbf{z} and system (2) is called reduced-order system of (1).

2. Reduced-order systems

To describe the investigated reduction technique we restrict to the case $n' = n$ and $\mathbf{T} = \mathbf{I}_n$, i.e. $\mathbf{z} \equiv \mathbf{y}$. Assume the state space to be \mathbb{C}^n and let $\mathbf{v}_1, \dots, \mathbf{v}_n$ be a set of linear independent elements with unit norm forming a basis of \mathbb{C}^n . Denote by x_1, \dots, x_n the new coordinates of \mathbf{y} with respect to the above basis, i.e.

$$\mathbf{y}(t, \omega) = \sum_{k=1}^n x_k(t, \omega) \mathbf{v}_k = \mathbf{V}\mathbf{x}(t, \omega)$$

where $\mathbf{x} = (x_1, \dots, x_n)^T$ and $\mathbf{V} = (\mathbf{v}_1, \dots, \mathbf{v}_n)$. With respect to the transformed coordinates the original system (1) reads as

$$\dot{\mathbf{x}}(t) = \mathcal{G}(\mathbf{x}(t)) + \mathbf{D}\mathbf{h}(t, \omega); \quad \mathbf{z}(t) = \mathbf{V}\mathbf{x}(t) \quad (3)$$

where $\mathcal{G}(\mathbf{x}) := \mathbf{V}^{-1}\mathcal{F}(\mathbf{V}\mathbf{x})$ and $\mathbf{D} := \mathbf{V}^{-1}\mathbf{B}$. The approximation idea consists in the assumption, that the basis elements are chosen such that the last $n-m$ coordinates x_{m+1}, \dots, x_n are "small", i.e. approximately zero. Replacing

these variables by zero and truncating the corresponding state equations in (3) a reduced-order system (2) arises with $\mathcal{F}_m(\mathbf{y}_m) = \mathcal{G}_m \left(\begin{pmatrix} \mathbf{y}_m \\ \mathbf{0}_{n-m} \end{pmatrix} \right)$, $\mathbf{B}_m := \mathbf{D}_m$, $\mathbf{T}_m := (\mathbf{v}_1, \dots, \mathbf{v}_m)$. Here, \mathcal{G}_m and \mathbf{D}_m denote the first m rows of \mathcal{G} and \mathbf{D} , respectively.

In order to assess the approximation accuracy and to find suitable basis elements $\mathbf{v}_1, \dots, \mathbf{v}_n$ error criterions have to be defined. Since the main interest is to compute the correlation function $\mathbf{R}_{\mathbf{z}\mathbf{z}}(\tau) = \mathbf{E} \{ \mathbf{z}(t) \mathbf{z}^*(t + \tau) \}$ and the corresponding spectral density $\mathbf{S}_{\mathbf{z}\mathbf{z}}(\alpha)$ we define

$$\Delta^{\mathbf{R}}(\mathbf{z}, \tilde{\mathbf{z}}) := \int_{\mathbb{R}} \sum_{i,j=1}^n |\mathbf{R}_{z_i z_j}(\tau) - \mathbf{R}_{\tilde{z}_i \tilde{z}_j}(\tau)| \Psi_{ij} \theta(\tau) d\tau \text{ and } \Delta^{\mathbf{S}}(\mathbf{z}, \tilde{\mathbf{z}}) := \int_{\mathbb{R}} \sum_{i,j=1}^n |\mathbf{S}_{z_i z_j}(\alpha) - \mathbf{S}_{\tilde{z}_i \tilde{z}_j}(\alpha)| \Psi_{ij} d\alpha$$

where $\Psi = \{\Psi_{i,j}\}_{i,j=1,\dots,n}$ is a weighting matrix with non-negative entries and $\sum_{i,j=1}^n \Psi_{ij} = 1$ while θ is a non-negative weighting function with $\int_{\mathbb{R}} \theta(\tau) d\tau = 1$. In [4] the following upper bound for the introduced error criterions has been found

$$\Delta^{\mathbf{R}}(\mathbf{z}, \tilde{\mathbf{z}}), \Delta^{\mathbf{S}}(\mathbf{z}, \tilde{\mathbf{z}}) \leq \sqrt{\Delta_0(\mathbf{z}, \tilde{\mathbf{z}})} \left(2\sqrt{\mathbf{E} \{ \|\tilde{\mathbf{z}}\|^2 \}} + \sqrt{\Delta_0(\mathbf{z}, \tilde{\mathbf{z}})} \right)$$

where $\Delta_0(\mathbf{z}, \tilde{\mathbf{z}}) := \mathbf{E} \{ \|\mathbf{z} - \tilde{\mathbf{z}}\|^2 \}$. For the computation of the upper bound means and covariances of $\tilde{\mathbf{z}}$ and $\mathbf{z} - \tilde{\mathbf{z}}$ are needed, only. The above inequality suggests, that those basis elements $\mathbf{v}_1, \dots, \mathbf{v}_n$ provide small values of $\Delta^{\mathbf{R}}(\mathbf{z}, \tilde{\mathbf{z}})$ and $\Delta^{\mathbf{S}}(\mathbf{z}, \tilde{\mathbf{z}})$ for which the term $\Delta_0(\mathbf{z}, \tilde{\mathbf{z}})$ is small. This idea leads to the following suggestions for the selection of basis elements (see [4]).

1. Choose $\mathbf{v}_1, \dots, \mathbf{v}_n$ as the eigenvectors of the covariance matrix $\mathbf{\Gamma} := \mathbf{E} \{ \mathbf{y}(t) \mathbf{y}^*(t) \}$ such that for the corresponding eigenvalues $\sigma_1^2, \dots, \sigma_n^2$ it holds $\sigma_1^2 \geq \dots \geq \sigma_n^2$.
2. In case of a linear mapping $\mathcal{F}(\mathbf{y}) = \mathbf{A}\mathbf{y}$ choose $\mathbf{v}_1, \dots, \mathbf{v}_n$ as the eigenvectors of \mathbf{A} such that for the second-order moments of the transformed state variables x_1, \dots, x_n it holds $\mathbf{E} \{ |x_1|^2 \} \geq \dots \geq \mathbf{E} \{ |x_n|^2 \}$.

3. Application

The introduced dimension reduction procedures have been applied to a large-scale linear system (1) resulting from the semi-discretization of a PDE describing axial vibrations of a thin homogeneous beam of length 1 with a free end and a random excitation at the other end. The dynamics of the axial deflection $u(t, x, \omega)$ is governed by the equation

$$b_1 u_{tt} + b_2 u_t - b_3 u_{xx} - b_4 u_{txx} = 0$$

with the boundary conditions $u(t, 0, \omega) = \rho(t, \omega)$, $u_x(t, 1, \omega) = 0$. Here, b_1, b_2, b_3, b_4 are some positive constants and $\rho(t, \omega)$ is a stationary random process. Approximating the derivatives with respect to x by finite differences using the values of $u(t, x, \omega)$ at grid points $x_k = \frac{k}{N+1}$, $k = 0, \dots, N+1$, leads to a system (1) with $n = 2N$ state equations. Numerical experiments in [4] indicate that reduced-order systems using only a few ($m = 14 \dots 20$) properly chosen state equations provide a very accurate description of the random dynamics of the considered infinite dimensional vibration system.

4. References

- 1 VOM SCHEIDT, J., FELLEBERG, B., WÖHRL, U.: Analyse und Simulation stochastischer Schwingungssysteme. Teubner, Stuttgart 1994
- 2 VOM SCHEIDT, J., STARKLOFF, H.-J., WUNDERLICH, R.: Stationary solutions of random differential equations with polynomial nonlinearities. Stochastic Analysis and Applications, accepted for publication
- 3 Soong, T.T., Grigoriu, M.: Random vibration of mechanical and structural systems. PTR Prentice Hall, Englewood Cliffs NJ 1993
- 4 WUNDERLICH, R.: Systems of random differential equations and model reduction. Habilitation Thesis, TU Chemnitz 1999

Addresses: DR. RALF WUNDERLICH, PROF. DR. JÜRGEN VOM SCHEIDT, DR. HANS-JÖRG STARKLOFF
Chemnitz University of Technology, Faculty of Mathematics, D-09107 Chemnitz, Germany

AURNHAMMER A.; MARTI, K.

Adaptive Optimal Stochastic Trajectory Planning in real-time using neural network approximations

In Optimal Stochastic Trajectory Planning (OSTP) of industrial robots, the problem can be represented by a variational problem under stochastic disturbances. Using deterministic substitute problems obtained from stochastic optimisation theory, the corresponding deterministic substitute variational problem can be solved approximatively via mathematical programming techniques. However, due to the computationally expensive algorithms involved, these techniques can be used for off-line calculations only. Hence, neural networks are trained to solve the trajectory-planning problem in real-time and to provide suitable solutions for on-line applications.

1. Introduction

The point-to-point Adaptive Optimal Stochastic Trajectory Planning Problem (AOSPTP) for industrial robots can at every stage j , after a time-path parameter transformation $s: [t_j, t_f^{(j)}] \mapsto [s_j, s_f]$, be represented by [1]:

$$\min_{\beta, q_e} \int_{s_j}^{s_f} \mathcal{E}(f(s, q_e, q'_e, q''_e, \beta, \beta', p) | \mathcal{A}_{t_j}) ds \quad (1a)$$

s.t.

$$P(\tau_{min} \leq a\beta' + b\beta + c \leq \tau_{max} | \mathcal{A}_{t_j}) \geq \alpha_u, \quad s_j \leq s \leq s_f, \quad (1b)$$

$$q_{min} \leq q_e(s) \leq q_{max}, \quad \dot{q}_{min} \leq q'_e(s) \sqrt{\beta(s)} \leq \dot{q}_{max}, \quad s_j \leq s \leq s_f, \quad (1c)$$

$$\beta(s) \geq 0, \quad s_j \leq s \leq s_f, \quad (1d)$$

$$q_e(s_j) = q_j, \quad q_e(s_f) = q_f, \quad (1e)$$

$$q'_e(s_j) \sqrt{\beta(s_j)} = \dot{q}_j, \quad \beta(s_f) = 0, \quad (1f)$$

where $q_e = q_e(s)$ is the geometric path in configuration space, $\beta = \beta(s) := s^2(t)$ the velocity profile and (1b,c) are control, position and velocity constraints for the path to be optimised subject to the expected performance index (1a). Since in the coefficients $a = a(p, q_e, q'_e)$, $b = b(p, q_e, q'_e, q''_e)$ and $c = c(p, q_e)$ of (1b), as well as in the objective (1a), stochastic parameters $p = p(\omega)$, like e.g. the payload mass are included, the constraint is according to stochastic optimisation theory written as a probabilistic constraint, that has to be fulfilled with a certain minimum reliability of α_u . Furthermore, (1e,f) denote initial and terminal positions and velocities for the robot joints.

2. Solution of (AOSPTP)

Let $\tilde{f}(s, p)$ denote the objective in (1a) and $\bar{p}^{(j)}$ the conditional expectation of the parameter vector p subject to the available information \mathcal{A}_{t_j} at stage j , the expected objective can be approximated by the following Taylor expansion:

$$\mathcal{E}(\tilde{f}(s, p) | \mathcal{A}_{t_j}) \approx \tilde{f}(s, \bar{p}^{(j)}) + \sum_{i=1}^n \frac{1}{i!} \frac{\partial^i \tilde{f}}{\partial p^i}(s, \bar{p}^{(j)}) \mu_i, \quad (2)$$

where μ_i is the system of the i -th conditional central moments. Moreover, for calculating (1b), the condition for the torques is split into one-sided inequalities, and the inverse of the conditional distribution function is applied. Finally, using B-spline basis functions, the optimal solution $(q_e^{(j)}(s), \beta^{(j)}(s))$ can be approximated by $(\sum_{i=1}^{n_{q_e}} \gamma_i^{q_e} B_i^{q_e}(s), \sum_{k=1}^{n_\beta} \gamma_k^\beta B_k^\beta(s))$. Substituting these linear combinations of known basis functions into problem (1a-f), and discretising the path parameter s , finally yields a finite nonlinear parameter minimisation problem for $\gamma := (\gamma_i^{q_e}, \gamma_k^\beta)$, $i = 1, \dots, n_{q_e}$, $k = 1, \dots, n_\beta$, that can be solved by a mathematical programming algorithm. However,

since mathematical programming does not provide real-time solution capability for (AOSPPT), which is necessary due to the short cycle times of industrial robots, we solve many problems (1a-f) with $\zeta = (s_j, \mathcal{A}_{t_j}, q_j, \dot{q}_j)^T$ as input at the different stages j and use the solutions to train Neural Networks.

3. Example

Consider the following time-optimal point-to-point problem for the industrial robot Manutec r3 [2], where the payload is supposed to be stochastic with a uniform distribution on an interval $[m_l - \Delta m_l, m_l + \Delta m_l]$. The initial information is given by $q_0 = (0.0, -1.5, 0.0)^T$, $q_f = (1.0, -1.95, 1.0)^T$, $m_l = 7.5$, $\Delta m_l = 4.0$ and $\alpha_u = 0.99$, and the trajectory is adapted once at time $t_1 = 0.2229$ sec with new information $m_l = 5.0$ and $\Delta m_l = 2.66$. This leads on a SUN Ultra-Sparc II with a 200 MHz processor to the following numerical and graphical results for the first joint:

	stage j	t_j	m_l	Δm_l	$t_f^{(j)}$	CPU-time in seconds
Mathematical programming:	0	0.0	7.5	4.0	0.5689	3.57
Mathematical programming:	1	0.2229	5.0	2.66	0.5577	6.44
Neural Network:	1	0.2229	5.0	2.66	0.5553	0.02

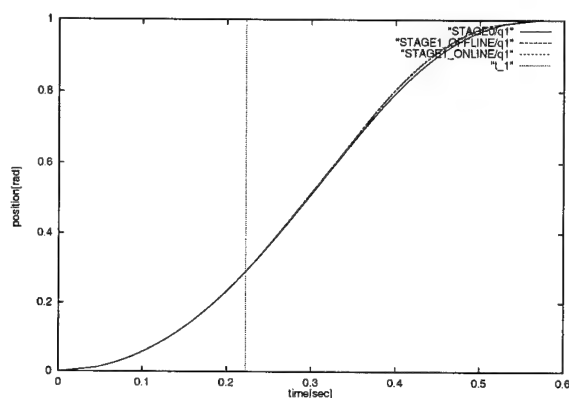


Figure 1: Position $q_1(t)$.

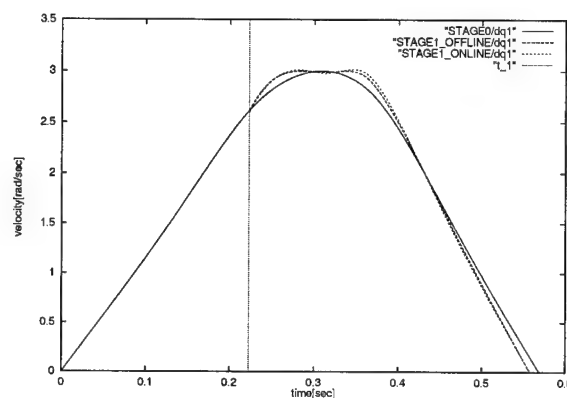


Figure 2: Joint velocity $\dot{q}_1(t)$.

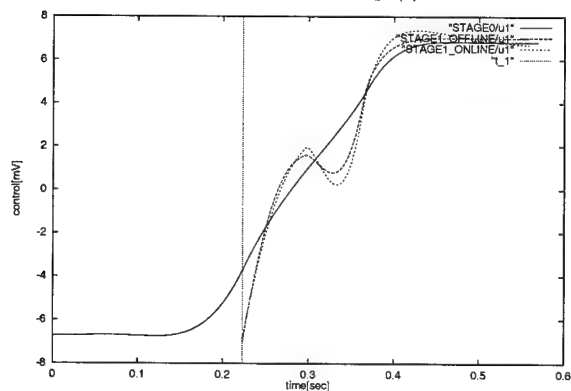


Figure 3: Control $\tau_1(t)$.

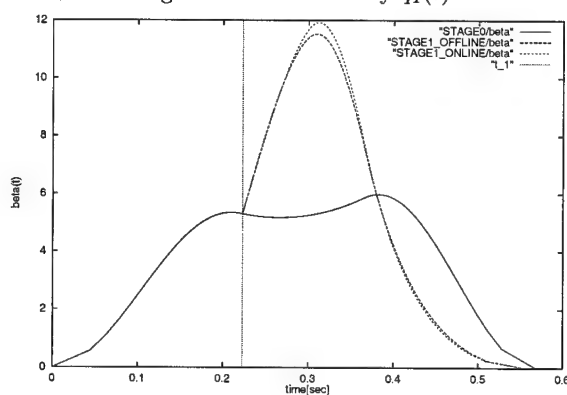


Figure 4: Velocity profile $\beta(t)$.

As the above table and Fig. 1-4 indicate, the neural network solution can be obtained very fast, and at the same time the optimal trajectory is approximated with a high precision.

4. References

- MARTI, K.: Path Planning for Robots under Stochastic Uncertainty, *Optimization* 45 (1999), 163-195.
- TÜRK, M.: Zur Modellierung der Dynamik von Robotern mit rotatorischen Gelenken, VDI-Verlag, Düsseldorf, 1990.

Addresses: DIPL.-MATH. ANDREAS AURNHAMMER, PROF. DR. KURT MARTI, Aero-Space Engineering and Technology, Federal Armed Forces University, 85577 Neubiberg/Munich, Germany.

BITTNER, L.

Shortest Curves for Vehicles on Surfaces of Celestial Bodies

The classical problem, to find the shortest line connecting two given points of a given surface, does not take account of 1) obstacles, i. e. forbidden regions (islands, icebergs, foreign territories a. s. o.) through which the curve must not run, 2) alterations of the shape of the surface in the course of time (tides, tectonic displacements a. s. o.), 3) the fact that the length of the curve, described by a vehicle moving on the surface, has eventually to be measured with respect to a primary inertial coordinate system emitting the control signals. The surface system may change its position relating to the primary system.

Let f_1, f_2, f_3 be the orthonormal unit vectors of the surface system and $P \hat{=} y$ be a point of the surface represented by a parametric description

$$y = r(t, v) = \sum_{i=1}^3 r_i(t, v) f_i$$

depending on the time t and the Gaussian parameter vector $v = (v_1, v_2)$. As a rule $r(t, v) = r^0(v) + d(t, v)$, where $r^0(\cdot)$ is the parametric representation of a reference surface and $d(t, v)$ is a deviation vector relatively small compared with $r^0(v)$.

Let e_1, e_2, e_3 be the orthonormal unit vectors of the primary system and let

$$a(t) = \sum_{j=1}^3 a_j(t) e_j$$

denote the distance vector from the origin of primary system to the origin of the surface system.

Since the unit vectors f_i of the surface system are definite functions

$$f_i = f_i(t) = \sum_{j=1}^3 \varphi_{ij}(t) e_j$$

of the (constant) unit vectors e_j we obtain

$$r(t, v) = s(t, v)$$

with

$$s(t, v) = \sum_j s_j(t, v) e_j, \quad s_j(t, v) = \sum_i r_i(t, v) \varphi_{ij}(t).$$

Assume

$$y(t) = r(t, v(t)), \quad t_i \leq t \leq t_f,$$

to be the actual position of the vehicle with respect to the surface system, hence

$$x(t) = a(t) + s(t, v(t)), \quad t_i \leq t \leq t_f,$$

the actual position with respect to the primary system. The initial point of the curve be $P_0 \hat{=} y^0$,

$$y^0 = r(t_0, v^0), \quad v^0 = v(t_0),$$

the final point be $P_f \hat{=} y^f$,

$$y^f = r(t_f, v^f), \quad v^f = v(t_f)$$

with respect to the surface system.

The length of the curve with respect to the surface system is

$$\begin{aligned} L_1 &= \int_{t_0}^{t_f} |y'(t)| dt = \int_{t_0}^{t_f} \left| \sum_i \frac{dr_i}{dt}(t, v(t)) f_i \right| dt \\ &= \int_{t_0}^{t_f} \left(\sum_{i,j=0}^2 g_{ij}(t, v(t)) \dot{v}_i(t) \dot{v}_j(t) \right)^{\frac{1}{2}} dt, \end{aligned}$$

where $v_0 = t$, $v_0(t) = t$ and g_{ij} denotes the scalar product $\frac{\partial r}{\partial v_i} \cdot \frac{\partial r}{\partial v_j}$. The length of the curve with respect to the primary system is

$$\begin{aligned} L_2 &= \int_{t_0}^{t_f} |\dot{x}(t)| dt = \int_{t_0}^{t_f} \left| \dot{a}(t) + \frac{d}{dt} s(t, v(t)) \right| dt \\ &= \int_{t_0}^{t_f} \left(|\dot{a}(t)|^2 + 2\dot{a}(t) \cdot \frac{d}{dt} s(t, v(t)) + \sum_{i,j=0}^2 h_{ij}(t, v(t)) \dot{v}_i(t) \dot{v}_j(t) \right)^{\frac{1}{2}} dt, \end{aligned}$$

where h_{ij} denotes the scalar product $\frac{\partial s}{\partial v_i} \cdot \frac{\partial s}{\partial v_j}$.

Either L_1 or L_2 has to be minimized by an appropriate choice of an absolutely continuous, two-dimensional function $v(\cdot)$, taking account of boundary, phase and slope (control) conditions B, Ph, Sl.

B) Let the moments t_0 , t_f and the points $P_0 \hat{=} y^0$, $P_f \hat{=} y^f$ be given, assume $y^0 = r(t_0, v^0)$, $y^f = r(t_f, v^f)$. Then a feasible function $v(\cdot)$ has to fulfill $v(t_0) = v^0$, $v(t_f) = v^f$. Alternatively

B') Let t_0 and $y^0 = r(t_0, v^0)$ be given, but t_f be free. Let the end point $P_f \hat{=} y^f(t) = r(t, v^f(t))$ be a variable target for $t \geq t_0$. Then a feasible function has to fulfill $v(t_0) = v^0$ and $v(t_f) = v^f(t_f)$ for some $t_f \geq t_0$.

Ph) The allowed region $A(t)$, to which the point $y(t) = r(t, v(t))$ has to belong, is supposed to be defined by

$$A(t) = \{y = r(t, v) \mid h_l(t, v) \geq 0 \quad (l = 1, \dots, L)\},$$

where the h_l are sufficiently smooth real functions. Therefore a feasible function $v(\cdot)$ has to satisfy

$$h_l(t, v(t)) \geq 0 \quad (l = 1, \dots, L).$$

Sl) Restrictions concerning $\dot{v}(t)$, f. e. $|\dot{v}(t)| \leq c$ f. a. t , are assumed to be defined by inequalities

$$g_k(t, \dot{v}(t)) \geq 0, \quad (k = 1, \dots, K) \text{ a. e.,}$$

where the g_k are sufficiently smooth real functions too.

In order to apply tools of optimal control the derivative $\dot{v}(t)$ is introduced as control $u(t)$. A simplified example (only one coordinate system, minimization of L_1 , ...) for such a solution procedure is presented in L. BITTNER, *Kürzeste Wege auf einer Fläche beim Vorhandensein von Hindernissen*, in Mathematik-Interdisziplinär, Shaker-Verlag, Aachen 2000.

Address: PROF. LEONHARD BITTNER, Institut für Mathematik und Informatik, Ernst-Moritz-Arndt-Universität Greifswald, D-17489 Greifswald, Germany

BLACHUT, J.

Optimal design of steel barrelled shells

The Simulated Annealing, SA, technique is applied to maximize the magnitude of external hydrostatic pressure for bowed out shells for which, the shape of the meridian is sought. A global maximum offers a 40% increase in load carrying capacity over the mass equivalent cylindrical shell of the same mass whilst the SA heuristic proves to be computationally affordable.

1. Background

Simulated annealing has been primarily explored in areas such as Operational Research, Computer Science and Artificial Intelligence. A comprehensive bibliography, containing 1380 entries, on heuristics can be found in [9]. In addition to SA it also covers genetic algorithms, tabu search and other search strategies. Apart from referencing past research effort into SA, this bibliography provides references for applications covering the following problems: assignment, combinatorial, design, function optimization, graph, placement, location and allocation, manufacturing, production planning, load balancing, multi-objective optimization, networks and telecommunications, routing and transportation, scheduling and statistical. It transpires from the detailed listing and available literature that structural optimization problems have rarely adopted the SA methodology. Known work in this area includes references [1-3, 7, 8, 10-12].

This paper explores the possibility of applying SA heuristic to structural optimization of shells subjected to stress and static stability constraints.

2. Neighbourhood Configuration and Problem Description

The following variable step method has been adopted for generation of candidate points in the design space. One starts with the initial, feasible, point X_0 and the next point is generated using the following relation:

$$X_{\text{new}} = X_0 + rv_h e_h, \quad (1)$$

where r is a random number generated in the range $[-1, 1]$, v_h is the component of the step vector along the h^{th} direction given by the vector e_h . If the h^{th} component of X_{new} falls outside the bounded domain given by constraints then a fresh random search takes place until a feasible point X_{new} is obtained. The magnitude of vector v is related to the acceptance ratio $\text{acc} \equiv n/N_k$, where n is the number of accepted moves and N_k is the total number of evaluated moves (\equiv epoch length). Both n and N_k are at a given temperature. For each direction, h , the new step vector component is taken as:

$$v_h = v_h^0(1 + c(n/N_k - 0.6)/0.4), \text{ if } n > 0.6N_k; \quad v_h = v_h^0(1 + c(0.4 - n/N_k)/0.4), \text{ if } n < 0.4N_k; \text{ or } v_h = v_h^0 - \text{otherwise} \quad (2)$$

The parameter c denotes a constant. The purpose of these variations in step length is to maintain the average percentage of accepted moves at about 50% of the total number of moves, at a given temperature. References [5,6] provide a more detailed discussion on choosing a step size for the continuum domain.

Let us consider a bowed out steel shell subjected to static external pressure. The shape of the barrelled out geometry is assumed to be given by the following generalised ellipse:

$$\left(\frac{x}{R_0 + \Delta}\right)^{n_1} + \left(\frac{y}{0.5L_0 + n_3}\right)^{n_2} = 1 \quad (3)$$

Exponents n_1 , n_2 and n_3 are taken as design variables and Δ denotes the amount of bowing out - see Ref. [4]. It is assumed in this paper, that bowed-out mild steel shells have the same radii, R_0 , at the top and bottom edges as the initial, and mass equivalent, cylindrical shell of length L_0 .

The load carrying capacity of the above shells is characterised by yield load, p_y , static bifurcation buckling, p_{bif} , or axisymmetric collapse, p_c . The bowed-out configuration capable of supporting the maximum external, hydrostatic pressure is sought, i.e.

$$p_{\text{opt}} = \max \min [p_y, p_{\text{bif}}, p_c], \quad n_1, n_2, n_3 \quad (4)$$

subject to the following constraints:

$$\begin{aligned} &\text{- lower and upper bounds on the design variables: } n_1^L \leq n_1 \leq n_1^U; \quad n_2^L \leq n_2 \leq n_2^U; \quad n_3^L \leq n_3 \leq n_3^U; \\ &\text{- constant mass of barrelled shell: } m_{\text{barrel}} = \text{const} (\equiv m_{\text{cylinder}}). \end{aligned} \quad (5)$$

(6)

Structural response of the above axisymmetric shells is calculated using BOSOR5 and ABAQUS codes. No axial deflection is allowed at the mid-length of barrels. Also, at the top and bottom edges only, axial displacements are allowed and the magnitude of all other variables is set to zero. Shells are assumed to be made from mild steel with Young's modulus $E = 210$ GPa, Poisson's ratio $\nu = 0.3$ and the yield point of material $\sigma_{yp} = 300$ MPa. Structural analyses are based on linear elastic, perfectly-plastic modelling of material (with isotropic strain hardening).

3. Solution Details, Results and Conclusions

There is very little a priori knowledge about the design space and the quality of cost function. It is known from past experience however that the cost function may not be continuous at the transition regions between axisymmetric collapse and bifurcation buckling, for example.

The following values were assumed for lower and upper bounds on design variables: $1.0 \leq n_1 \leq 10.0$; $1.0 \leq n_2 \leq 10.0$ and $1.0 \leq n_3 \leq 10.0$. The search process started from a random point X_0 with all subsequent new configurations generated using Eqn (2). Parameter c was taken to be 10. The epoch length, $N_k = 20$, was constant at all temperature levels. A geometric

schedule for lowering temperature was used with the parameter $\alpha = 0.99$ and the initial temperature $T_0 = 50.0$. The number of cooling cycles was not fixed and the annealing process was allowed to continue until there was no change of the cost function in 10 consecutive cycles.

Detailed computations were performed for the reference cylindrical geometry given by $L_0/R_0 = 1.0$ and $R_0/t_0 = 33.33$. The maximum hydrostatic pressure $p_{opt} = 14.71$ MPa, is associated with the axisymmetric collapse. The optimal design vector $(n_1, n_2, 2n_3/L_0)_{opt}$ equals $(2.2, 2.0, 1.0)$. Yielding starts on the inner surface of the barrel at both top and bottom edges and the maximum, effective plastic strain at the collapse reaches 3.2%. A section through the barrel, at collapse pressure, is

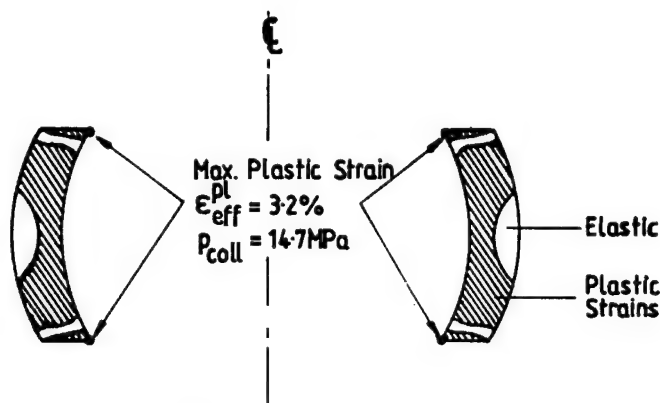


Fig. 1 Section through optimally shaped barrel.

depicted in Fig. 1 where it is seen that 71% of the cross section has yielded at the optimum load. The ratio of p_{opt} to the bifurcation buckling pressure of mass equivalent cylinder, p_{bif} is $p_{opt}/p_{bif} = 1.4$.

Computational effort of a single re-analysis is such that a predominantly sequential optimization tool, such as SA, is capable to navigate through the design space in an affordable amount of time.

4. References

- 1 BALLING, R.J.: Optimal steel frame design by simulated annealing, *J of Structural Eng*, **117**, (1991), 1780-1795.
- 2 BALLING, R.J.: Application of the simulated annealing algorithm to structural design, in 'Emergent Computing Methods in Engineering Design', (eds) D.E. Grierson and P. Hajela, Springer, Berlin, 1996, pp. 283-293.
- 3 BENNAGE, W.A., DHINGRA, A.K.: Single and multiobjective structural optimization in discrete-continuous variables using simulated annealing, *Int J Numer Meth Engng*, **38**, (1995), 2753-2773.
- 4 BLACHUT, J., WANG, P.: Barrelled shells subjected to external hydrostatic pressure, in *Proc. of the ASME PVP Conference*, Seattle, July 2000.
- 5 BOHACHEWSKY, I.O., JOHNSON, M.E., STEIN, M.L.: Generalised simulated annealing for function optimization, *Technometric*, **28**, (1986), 209-217.
- 6 CORANA, A., MARCHESI, M., MARTINI, C., RIDELLA, S.: Minimizing Multimodal functions of continuous variables with the simulated annealing algorithm, *ACM Trans on Mathematical Software*, **13**, (1987), 262-280.
- 7 LEITE, J.P.B., TOPPING, B.H.V.: Parallel simulated annealing for structural optimization, *Computers Struct.*, **73**, (1999), 545-564.
- 8 MAY, S.A., BALLING, R.J.: A filtered simulated annealing strategy for discrete optimization of a 3D steel frameworks, *Struct. Optimization*, **4**, (1992), 142-148.
- 9 OSMAN, I.H., LAPORTE, G.: Metaheuristics: a bibliography, *Annals of Operational Res*, **63**, (1996), 513-623.
- 10 SHIM, P.Y., MANOOCHEHRI, S.: Generating optimal configurations in structural design using simulated annealing, *Int J Numer Meth Engng*, **40**, (1997), 1053-1069.
- 11 SHIM, P.Y., MANOOCHEHRI, S.: A hybrid deterministic/stochastic optimization approach for the shape configuration design of structures, *Structural Optimization*, **17**, (1999), 113-129.
- 12 TZAN, S.R., PANTELIDES C.P.: Annealing strategy for optimal structural design, *J Struct Engineering*, *Trans of the ASCE*, **122**, (1996), 815-827.

Address: J. Blachut, The University of Liverpool, Mechanical Engineering, Liverpool L69 3GH, UK.

R. BURGMAIR; F. PFEIFFER

Prozeßspezifische Roboteroptimierung

Es werden Zielfunktionen und Nebenbedingungen zur numerischen Optimierung der Lage, Reglerkoeffizienten und der Fügerichtung von Robotern, die Objekte mit großen Auslenkungen montieren, vorgeschlagen. Das nichtlineare Vektoroptimierungsproblem wird mit einem SQP-Algorithmus gelöst, Optimierungsergebnisse werden gezeigt.

1. Einleitung

Seit langem gibt es große Bemühungen die in der automatisierten Montage auftretenden Handhabungsprozesse zu optimieren, u.a.[1],[2]. Da die bei Montageprozessen auftretenden Kräfte oft starken nichtlinearen Charakter zeigen, ist es naheliegend zur geeigneten Definition von Gütekriterien den Fügeprozeß selbst mit einfließen zu lassen. In [3] wurde auf solche Weise der Montageprozeß bezüglich eines Bolzen-Loch-Problems optimiert. Hier soll der Schwerpunkt auf Fügeprozesse mit großen Auslenkungen liegen.

2. Robotermodell

Grundlage für die Berechnung der Gütekriterien ist das mechanische Modell des Roboters (PUMA560, 6 Achsen). Je nach betrachtetem Gütekriterium werden die ersten drei Getriebe starr oder elastisch (Feder-Dämpfer-Element) modelliert. Im elastischen Fall erhält man $f = 9$ Freiheitsgrade, 3 Motor- und 6 Armwinkel, im starren Fall die $f = 6$ Freiheitsgrade der Armwinkel. Der Vektor der generalisierten Koordinaten ergibt sich im elastischen Fall zu $\bar{q} := [\gamma_{M,1}, \gamma_{M,2}, \gamma_{M,3}, \gamma_{A,1}, \dots, \gamma_{A,6}]$, im starren Fall zu $\bar{q} := [\gamma_{A,1}, \dots, \gamma_{A,6}]$. Allgemein lassen sich die Bewegungsgleichungen folgendermaßen hinschreiben:

$$M(\bar{q})\ddot{\bar{q}} + h(\bar{q}, \dot{\bar{q}}) = B\tau + J^T(\bar{q})\lambda, \quad (1)$$

mit $M \in \mathbb{R}^{f,f}$ als Massenmatrix, $h \in \mathbb{R}^{f,1}$ als gyroskopische, Zentrifugal- und Corioliskräfte, $B \in \mathbb{R}^{f,6}$ als Übersetzungsmatrix, $\tau \in \mathbb{R}^{6,1}$ als Motormomente, $J \in \mathbb{R}^{f,6}$ als Jacobimatrix bezüglich dem Greiferkoordinatensystem und dem System der Minimalkoordinaten \bar{q} , und $\lambda \in \mathbb{R}^{6,1}$ als auf den Greifer wirkende Kräfte und Momente. Jedes Gelenk ist PID geregelt: $\tau = -K_i \int (\gamma_M - \gamma_{M,S}) dt - K_p(\gamma_M - \gamma_{M,S}) - K_d(\dot{\gamma}_M - \dot{\gamma}_{M,S})$, mit $\gamma_M \in \mathbb{R}^{6,1}$ als Ist-Motorwinkel, $\gamma_{M,S} \in \mathbb{R}^{6,1}$ als Soll-Motorwinkel, und $K_{i,p,d} \in \mathbb{R}^{6,6}$ als Reglermatrizen. Bei Annahme kleiner Bahnlängen, verglichen zu den Roboterabmaßen, kann um einen Arbeitspunkt linearisiert werden: $\bar{q} = q_0 + q$. Man erhält ein gewöhnliches DGL-System 2.Ordnung.

3. Optimierungsproblem

Parameter: Optimierungsparameter sind die Armwinkel, die Reglerkoeffizienten, und die Orientierung des Fügekoordinatensystems (F) bezüglich des Greiferkoordinatensystems (G)(Kardan-Winkel).

Gütekriterien:

-Störverhalten: Durch Anregungen am Greifer und durch die Motoren wird der Roboter in Schwingungen versetzt. Um diese zu minimieren wird ein Integralkriterium $G_S = \int_0^\infty \Delta x^T(t) G_S \Delta x(t) dt$ definiert. Hierbei ist Δx der Vektor der Bahnabweichungen in F und G_S ist die Gewichtungsmatrix. Die Simulation erfolgt mit dem elastischen Modell. Da eine optimale Dämpfung der Schwingungen unendlich hohe Reglerkoeffizienten zur Folge hätte, müssen die benötigten Motormomente berücksichtigt werden: $G_\tau = \int_0^\infty \tau^T(t) G_\tau \tau(t) dt$, mit G_τ als Gewichtungsmatrix. Das Kriterium für Störverhalten ergibt sich zu $G_1 = 0.5(G_S + G_\tau)$.

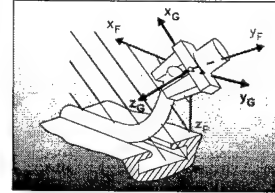
-Beschleunigungsvermögen (BV): Um auf ein Ereignis (z.B. Knicken) schnell reagieren zu können ist das BV eine wichtige Kenngröße. In [4] wird ein 'Dynamic Manipulability Ellipsoid' eingeführt, welches das räumliche BV charakterisiert. Die Begrenzungen der Motormomente gehen dort nicht ein. Da diese jedoch das BV wesentlich bestimmen, werden sie hier berücksichtigt. Ausgangspunkt sind die linearisierten Bewegungsgleichungen des starren Modells für $q = \dot{q} = \int q dt = 0$ und $\lambda = 0$: $\hat{M}\ddot{q} + \hat{h} = B\tau$. Eliminiert man hieraus \ddot{q} mit $J\ddot{q} = b = G_b e b$, erhält man nach weiterem Umformen die maximale gewichtete Beschleunigung b_{max} entlang einer vorgegebenen Richtung e :

$$b_{max} = \min_{i=1,\dots,6} \left\{ \frac{(B\tau_{ex} - \hat{h})_i}{((\hat{M}J^{-1})G_b e)_i} \right\}, \quad (2)$$

mit $b = \sqrt{b^T b}$, $e = b/b$, $G_b = \text{diag}(g_b)$ und $g_b \in \mathbb{R}^{6,1}$ als Gewichtungsvektor. $\tau_{ex,i} \in \{\tau_{min,i}, \tau_{max,i} | b > 0\}$, für $i = 1, \dots, 6$. Als Kriterium wird der Kehrbruch des von $eb_{max}(e)$ aufgespannten Volumens V_b definiert: $G_2 = 1/V_b$. -Fügekräfte: Da es sich bei Fügeobjekten mit großen Auslenkungen oft um gummiartige Materialien handelt, die große Reibkräfte verursachen, ist die zur Verfügungstellung genügend großer Fügekräfte wichtig. Ausgangspunkt sind wieder die linearisierten Bewegungsgleichungen des starren Modells, jetzt für $q = \dot{q} = \int q dt = 0$ und $\ddot{q} = 0$: $\hat{h} = B\tau + J^T\lambda$. Eliminiert man hieraus λ mit $\lambda = G_\lambda e\lambda$ erhält man analog zu G_2 das Kriterium $G_3 = 1/V_\lambda$.

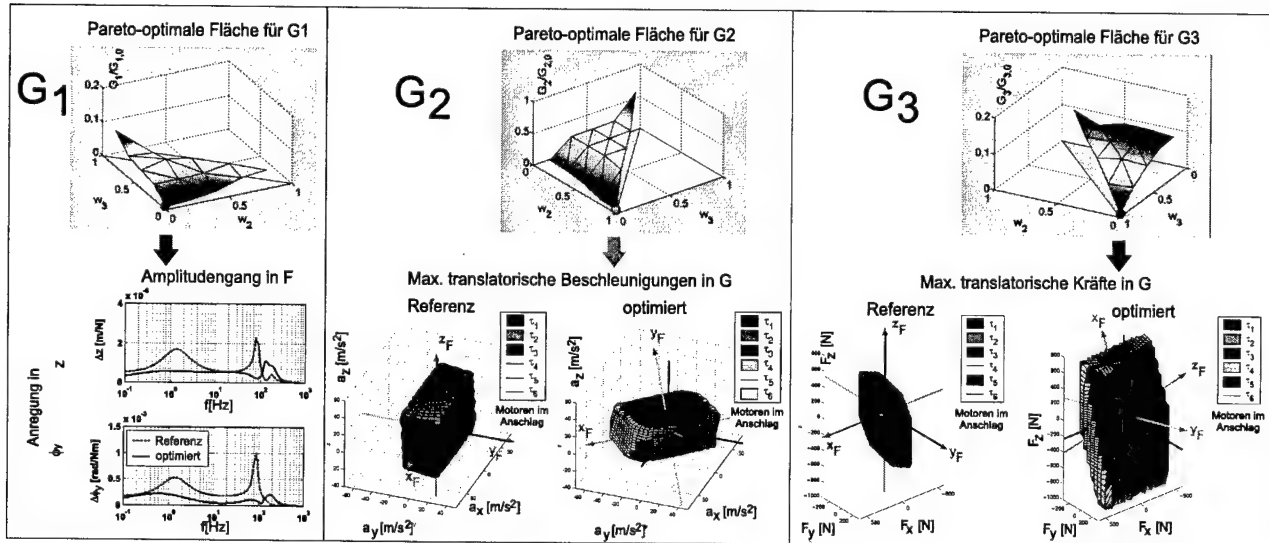
Nebenbedingungen sind Gelenkwinkelbeschränkungen, beschränkte Motormomente, Forderung der Reglerstabilität, genügend große Entfernung zu Singularitäten und Beschränkungen in Lage und Orientierung von F.

Lösung erfolgt mit einem SQP-Algorithmus, unter Verwendung automatisch generierter, analytischer Ableitungen der Gütekriterien und der Nebenbedingungen. Die Pareto-optimale Fläche wird mit der Methode der gewichteten Summe berechnet.



4. Ergebnisse

Für das Beispiel des Fügens einer Gummidichtung in einen Kanal (vgl. Abb. oben) werden geeignete Gewichtungen gewählt (Fügebene $x_F - z_F$). Das Ergebnis der Mehrkriterien Optimierung ist unten dargestellt. Für angezeigte Punkte wird ein Vergleich des jeweiligen Gütekriteriums bezüglich Referenz- und optimierter Parameter gezeigt. Angemerkt sei, daß die charakteristische Form des BV im Raum, durch Einbeziehung der Motormomentbeschränkungen, von Ellipsoid- (vgl. [4]) in Polyederform übergeht.



Danksagung

Die hier vorgestellte Arbeit wurde mit freundlicher Unterstützung der DFG finanziert (SFB336).

5. Literatur

- 1 O. KHATIB, "REAL-TIME OBSTACLE AVOIDANCE FOR MANIPULATORS AND MOBILE ROBOTS," *Int. J. of Robotics Research*, Vol. 5, No.1, pp. 90-98, 1986.
- 2 F. PFEIFFER, K. RICHTER, "OPTIMAL PATH PLANNING INCLUDING FORCES AT THE GRIPPER," *J. of Intelligent Robotic Systems*, 3, pp. 251-258, 1990.
- 3 G. PROKOP, F. PFEIFFER, "IMPROVED ROBOTIC ASSEMBLY BY POSITION AND CONTROLLER OPTIMIZATION," *Proc. of IEEE Intl. Conf. on Robotics and Automation*, MINNEAPOLIS, APRIL 22.-28., pp. 2182-2187, 1996.
- 4 T. YOSHIKAWA, "DYNAMIC MANIPULABILITY OF ROBOT MANIPULATORS," *Proc. of the 1985 IEEE Int. Conf. on Robotics and Automation*, pp. 1033-1038, 1985.

Adressen: PROF. DR.-ING. DR.H.C. F. PFEIFFER, R. BURGMAIR, Technische Universität München, Lehrstuhl B für Mechanik, Boltzmannstr.15, 85748 Garching, Deutschland.

IZTOK, CIGLARIC, SIMON KRASNA, IVAN PREBIL

Optimal path synthesis of the four-bar mechanism

Four-bar mechanisms are widely used in different devices as leading mechanisms that have to provide desired and often complicate motion and sustain substantial forces, accelerations and jerks. As the four-bar mechanism seems to be a simple device, it is well known that dimensional synthesis is an exacting piece of work. One has to determine the proportions of link lengths needed to accomplish the specified motion and force transformation. Paper discusses optimal synthesis of four-bar mechanism. The objective of this approach is to determine the optimal values of the mechanism link lengths, to minimize the difference between the trajectory "T" of the arbitrary point C on the mechanism coupler link and prescribed trajectory "P", while hinge forces have to remain within the prescribed values.

1. Mechanical model of four-bar mechanism

The vector notation [1] is particularly suitable for analyzing planar four-bar mechanisms depicted in Figure 1 by using symbolic manipulations [2]. To solve the kinematics, the loop closure condition needs first to be written [1], and represented as a system of two scalar equations

$$\begin{aligned} r_3 \cos \theta_3 &= r_1 \cos \theta_1 + r_4 \cos \theta_4 + r_2 \cos \theta_2 \\ r_3 \sin \theta_3 &= r_1 \sin \theta_1 + r_4 \sin \theta_4 + r_2 \sin \theta_2 \end{aligned} \quad (1)$$

with unknowns θ_3 and θ_4 . The angles θ_3 and θ_4 in terms of parameter θ_2 are obtained by summing squared equations (1) and after some additional algebraic manipulation. Figure 1 clearly demonstrates the relation between the angles θ_3 and θ_5 .

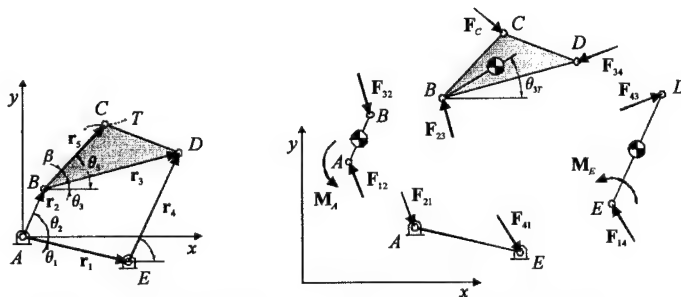


Figure 1: Notation and discretization of the four-bar mechanism

In order to perform kinetic analysis, the discretization approach is used. Figure 1 depicts, how mechanism links are considered as free bodies. An external force F_C is applied in point C and an external moment M_A is applied in point A. Newton-Euler equations of motion can be represented in the following matrix form

$$\begin{bmatrix} 1 & 0 & -1 & 0 & 0 & 0 & 0 & 0 & 0 \\ 0 & 1 & 0 & -1 & 0 & 0 & 0 & 0 & 0 \\ 0 & 0 & 1 & 0 & -1 & 0 & 0 & 0 & 0 \\ 0 & 0 & 0 & 1 & 0 & -1 & 0 & 0 & 0 \\ 0 & 0 & 0 & 0 & 1 & 0 & -1 & 0 & 0 \\ 0 & 0 & 0 & 0 & 0 & 1 & 0 & -1 & 0 \\ a_{71} & a_{72} & a_{73} & a_{74} & 0 & 0 & 0 & 0 & 0 \\ 0 & 0 & a_{83} & a_{84} & a_{85} & a_{86} & 0 & 0 & 0 \\ 0 & 0 & 0 & 0 & a_{95} & a_{96} & a_{97} & a_{98} & 1 \end{bmatrix} \begin{bmatrix} F_{12} \\ F_{12} \\ F_{23} \\ F_{23} \\ F_{34} \\ F_{34} \\ F_{41} \\ F_{41} \\ M_E \end{bmatrix} = \begin{bmatrix} m_2 a_{2T_x} \\ m_2 (a_{2T_y} + g) \\ m_3 a_{3T_x} - F_{Cx} \\ m_3 (a_{3T_y} + g) - F_{Cy} \\ m_4 a_{4T_x} \\ m_4 (a_{4T_y} + g) \\ J_{2T} \ddot{\theta}_2 - M_A \\ J_{3T} \ddot{\theta}_3 - e_1 F_{Cx} - e_2 F_{Cy} \\ J_{4T} \ddot{\theta}_4 \end{bmatrix} \quad (2)$$

The equations (1), together with equations (2), fully describe the four-bar mechanism motion and forces that produced motion or are the result of prescribed motion and should be understood as system equations.

2. Formulation and solution of nonlinear programming problem

Hydraulic support [5], depicted in Figure 2, is a part of mining industry equipment, considered for protection of working environment. The aim of research is optimal design of the leading four-bar mechanism $ABDE$ in order to ensure desired motion of hydraulic support top part with minimal transversal displacements, while the hinge forces have to be less than $F_{\max} = 1500.0 \text{ kN}$. The applied external vertical load in point C is 1178.4 kN . The nonlinear programming problem is defined as

$$\min \max |x_C(t) - 65|, \quad t \in [0, \tau] \quad (3)$$

$$\text{subject to } g_i(\mathbf{a}, \mathbf{u}, t) = |\mathbf{F}_i(\mathbf{a}, \mathbf{u}, t)| - F_{\max} \leq 0, \quad i = A, B, D, E, \quad t \in [0, \tau], \quad (4)$$

$$g_5(\mathbf{a}) = (a_3 + a_4) - (a_1 + a_2) \leq 0, \quad (5)$$

$$g_6(\mathbf{a}) = (a_2 + a_3) - (a_1 + a_4) \leq 0, \quad (6)$$

$$a_j \in [\widetilde{a}_j, \widehat{a}_j], \quad j = 1, 2, 3, 4, \quad (7)$$

where $\mathbf{a} = [a_1, a_2, a_3, a_4]^T := [r_1, r_2, r_3, r_4]^T$ is design variable vector and $\mathbf{u} = [u_1, u_2]^T := [x_C, y_C]^T$ is system variable vector. Hinge forces $\mathbf{F}_i(\mathbf{a}, \mathbf{u}, t)$, $i = 1, 2, 3, 4$ are calculated in symbolic form by using system equations (1) and (2). Formulation (3-7) enables one to minimize the maximal difference between the trajectory T of point C on the coupler of the four-bar mechanism $ABDE$ and the prescribed linear trajectory $P: x = 65$. Constraint functions (4) ensure the four-bar mechanism hinge forces to be less than prescribed value, while constraint functions (5) and (6) represent well known Grashoff conditions, which prevent from complete rotational movement of the links. Certain upper and lower bounds are imposed on design variables. Formulation (3-7) is not soluble with today known methods of mathematical programming. The issue of this problem is operator **max** in the objective function and time dependent constraint functions. As shown in [3], we involve an artificial design variable to eliminate operator **max** and time discretization of time dependent functions in the formulation (3-7) to obtain soluble form. The formulation (3-7) is solved by using global optimization method. The Adaptive Grid Refinement algorithm (AGR) is applied [4]. The optimal leading four-bar mechanism $ABDE$ is specified with parameters vector $\mathbf{a}^* = [718.5, 1361.9, 407.2, 1311.9]^T \text{ mm}$. The trajectory of point C and hinge force in E are depicted in Figure 2 as solid lines. Comparing previous existing solution (dashed lines) [5] with calculated optimal solution (solid lines) one could see slight increase of transversal displacements from $\Delta x_{\max} = 12.16 \text{ mm}$ to $\Delta x_{\max}^* = 12.53 \text{ mm}$. However, maximal hinge forces $F_{A \max}^* = 1234.41 \text{ kN}$, $F_{B \max}^* = 1234.30 \text{ kN}$, $F_{D \max}^* = 1493.97 \text{ kN}$ and $F_{E \max}^* = 1494.60 \text{ kN}$ for optimal design vector are decreased over 12% in critical joints D and E compared to previously existing solution. The external load is therefore more equally distributed between joints, consequently this means more improved and safer design.

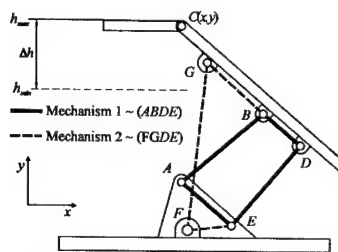


Figure 2: Hydraulic support

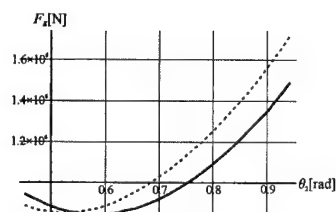
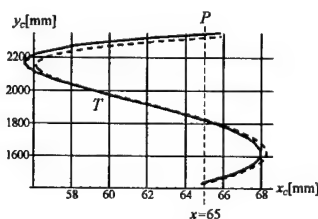


Figure 3: Trajectory of point C and hinge force F_E

3. References

- 1 SHABANA A.A.; Computational dynamics, John Wiley & Sons Inc., New York, 1994.
- 2 WOLFRAM S.; Mathematica - A system for doing mathematics by computers. Champaign, IL: Wolfram Research Inc, 1996.
- 3 HSIEH C. AND ARORA J.; Design sensitivity analysis and optimization of dynamic response. Computer methods in applied mechanics and engineering 43. p.p. 195-219, 1984.
- 4 LOEHLE ENTERPRISES; Global nonlinear optimization using Mathematica; University of Chicago, 1998.
- 5 KRASNA S.; Four-bar linkage synthesis using global optimization algorithm; Graduate thesis (in slovenian language); University of Ljubljana, 2000.

Addresses: Iztok Ciglaric, Ivan Prebil, Simon Krasna, University of Ljubljana, Faculty of Mechanical Engineering, Askerceva 6, Slovenia

H. ENGELS, W. BECKER

Optimization of Patch Reinforcements around Circular Holes in Isotropic and Anisotropic Plates

For various technical reasons cutouts like holes in thin-walled structures are often inevitable. Applied loads lead to an undesired stress concentration and respective strength degradation in the hole vicinity. In order to reattain the requested strength in practice a local hole reinforcement is applied. The techniques of mathematical structural optimization have been applied in order to determine an optimal design for the hole reinforcement.

1. Introduction

For many technical applications the frequent structural mechanical problem of cutouts like holes is inevitable. Any arbitrary load leads to an undesired stress concentration and strength degradation in the hole vicinity which results in a possible premature failure. By virtue of the mentioned strength degradation in practice a local hole reinforcement by doublers (Fig. 1) is employed. The application of the hole reinforcement leads to the question of an optimal doubler design with a minimum weight and maximal strength. For that purpose an optimization problem has been formulated which is solved by the techniques of mathematical structural optimization.

2. Problem Definition

For the subsequent investigations a circular hole in an infinitely extended plate consisting of isotropic or anisotropic material is assumed. Furthermore the settings of linear elasticity are presumed. For the analysis of the hole situation several analytical solutions (complex potential method and the Airy stress function) and of course numerical approaches like the finite element method are available. Analysing the stress distribution of the circumferential stress along the hole edge leads to the well-known stress concentration factor K [4]. Its numerical value depends on the investigated load case and thus in the present study the uniaxial tensile load case, shear load case and the biaxial tensile load case are considered. With respect to the shape and design of the doubler various alternatives are possible. In the present study a circular doubler, an elliptical doubler with fixed thickness t_d and an elliptical doubler with adjustable thickness t_d have been investigated.

3. Treatment of the Optimization Problem

In order to determine an optimized doubler design a clearly defined optimization problem has to be set up. First it is necessary to have a mathematical model for the structure which provides the required structural response and defined state variables. In the present case the structural model is given by a detailed finite element model. Second the optimization model itself has to be set up which includes the respective design variables, objective function as well as equality and inequality constraints. The doubler radius r_d , the elliptical aspect ratios a , b , the orientation angle θ of the ellipse and the doubler thickness t_d are possible design variables depending on the particular doubler alternative.

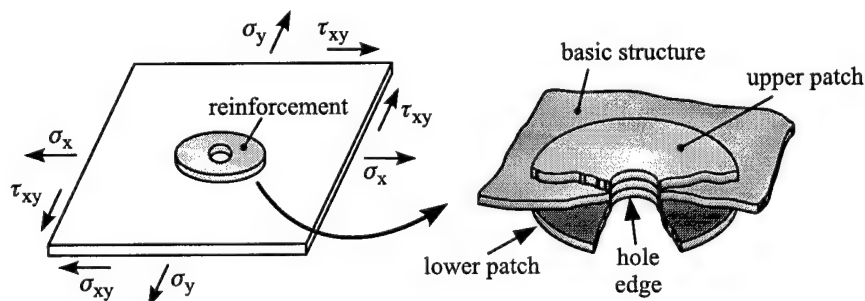


Figure 1: Hole reinforcement by doublers

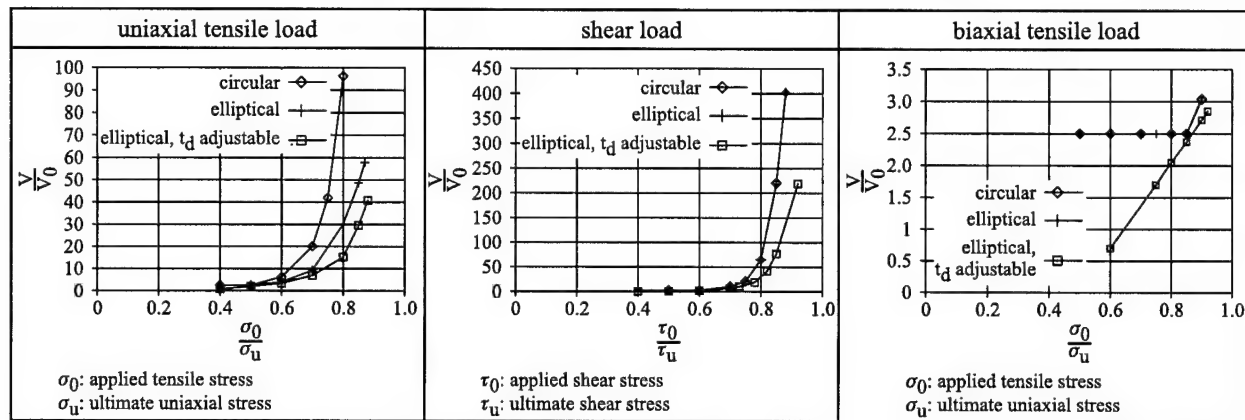


Figure 2: Optimization results

As objective function the doubler mass is chosen and is to be minimized. The necessary inequality constraints are given by the respective strength constraints along the hole edge and along the interior as well as exterior reinforcement boundary. Third the mathematical optimization problem has to be solved by an appropriate optimization algorithm [6]. The combined application of the sequential linearization and generalized reduced gradients turned out to be efficient. The derived optimization procedure can be applied for an anisotropic material in terms of a composite laminate as well [1,5]. In this case the ply angles and thickness of the respective doubler layup may be introduced as new additional design variables. For the strength constraints the Tsai-Wu failure criterion [5] is used in order to avoid first-ply-failure.

4. Results and Discussion

Figure 2 illustrates the determined optimization results for the considered load cases and doubler types assuming isotropic material. The minimal required doubler volume is shown in dependence of the obtainable strength for each load case. Obviously the required doubler volume depends significantly on the applied doubler type. Furthermore the obtainable strength differs with respect to the investigated doubler alternatives. The doubler volume can be reduced significantly by introducing the doubler thickness t_d as an additional design variable. The obtained optimization results for a composite laminate demonstrate well their effective use in regard of the adaptability to different load cases by well-adjusted doubler designs.

5. Conclusions

The techniques of mathematical structural optimization have been used successfully to the problem of hole reinforcements and reveal significant optimization potential. The implemented procedure works with good reliability. It turns out that the required doubler volume and the obtainable strength are highly dependent on the applied doubler type. Increasing strength requirements go along with a corresponding growth of the doubler volume.

6. References

- 1 ENGELS, H.; BECKER, W.: Optimization of Hole Reinforcements by Doublers. Accepted for publication in: Structural Optimization, Springer-Verlag.
- 2 ESCHENAUER, H.; SCHNELL, W.: Elastizitätstheorie: Grundlagen, Flächentragwerke, Strukturoptimierung. Mannheim: BI-Wissenschaftsverlag 1993.
- 3 GÖLDNER, H.: Lehrbuch Höhere Festigkeitslehre. Leipzig: Fachbuchverlag Leipzig 1991.
- 4 JONES, R. M.: Mechanics of Composite Materials. Tokyo: McGraw-Hill 1975.
- 5 VANDERPLAATS, G. N.: Numerical Optimization Techniques for Engineering Design. New York: McGraw-Hill 1984.

Addresses: H. ENGELS, W. BECKER
 University of Siegen,
 Department 11, Paul-Bonatz-Str. 9-11,
 D-57068 Siegen, Germany

CHRISTOPH GLOCKER

Spatial Friction as Standard NLCP

Coulomb friction problems can be stated as quasi-variational inequalities. These are variational expressions of certain non-smooth pseudo-potentials which have to be minimized in the sense of a two-person non-cooperative constrained game, consisting of the normal and the tangential player. In this paper we show that spatial Coulomb friction applied to the rolling contact problem in rigid body dynamics may be formulated as a nonlinear complementarity problem in standard form, i.e. as $0 \leq \mathbf{x} \perp \mathbf{f}(\mathbf{x}) \geq 0$ with continuous and differentiable $\mathbf{x} \rightarrow \mathbf{f}(\mathbf{x})$.

1. The spatial rolling contact problem

We investigate a multibody system (mass matrix \mathbf{M} , generalized velocities \mathbf{u} , applied forces and gyroscopical accelerations \mathbf{h}) with one spatial contact. Terms indexed by N and T refer to the normal of and to two orthogonal directions in the contact plane, respectively. The kinetic and kinematic equations for such a configuration are

$$\mathbf{M}\dot{\mathbf{u}} - \mathbf{h} - \mathbf{w}_N \lambda_N - \mathbf{W}_T \boldsymbol{\lambda}_T = 0, \quad \dot{\gamma}_N = \mathbf{w}_N^T \dot{\mathbf{u}} + \bar{w}_N, \quad \dot{\gamma}_T = \mathbf{W}_T^T \dot{\mathbf{u}} + \bar{\mathbf{w}}_T \quad (1)$$

with $(\lambda_N, \boldsymbol{\lambda}_T)$, (γ_N, γ_T) and $(\mathbf{w}_N, \mathbf{W}_T)$ being the values of the contact forces, the relative velocities and the generalized force directions of the contact. Only the rolling contact problem is considered. For the contact laws we assume impenetrability in the normal and Coulomb friction in the tangential directions, and we characterize the set of the admissible tangential forces $\boldsymbol{\lambda}_T$ by the friction disk D_T in \mathbb{R}^2 with normal cone $N_{D_T}(\boldsymbol{\lambda}_T)$,

$$D_T := \{\boldsymbol{\lambda}_T \mid |\boldsymbol{\lambda}_T| \leq \mu \lambda_N\} \Rightarrow N_{D_T}(\boldsymbol{\lambda}_T) = \begin{cases} \kappa \mathbf{e} & \text{for } 0 < |\boldsymbol{\lambda}_T| = \mu \lambda_N \\ 0 & \text{for } 0 \leq |\boldsymbol{\lambda}_T| < \mu \lambda_N \\ \mathbb{R}^2 & \text{for } 0 = |\boldsymbol{\lambda}_T| = \mu \lambda_N \end{cases} \quad (2)$$

Here, μ is the coefficient of friction, $\mathbf{e} = \boldsymbol{\lambda}_T / |\boldsymbol{\lambda}_T|$ the direction of the tangential force, and $\kappa \geq 0$. For a closed contact and $\gamma_N = \gamma_T = 0$, the impenetrability condition and Coulomb's law on the acceleration level become

$$\lambda_N \geq 0, \quad \dot{\gamma}_N \geq 0, \quad \lambda_N \dot{\gamma}_N = 0, \quad -\dot{\gamma}_T \in N_{D_T}(\boldsymbol{\lambda}_T), \quad (3)$$

and we may state the following problem: For \mathbf{M} , \mathbf{h} , $(\mathbf{w}_N, \mathbf{W}_T)$, $(\bar{w}_N, \bar{\mathbf{w}}_T)$ given, find $\dot{\mathbf{u}}$, $(\lambda_N, \boldsymbol{\lambda}_T)$, $(\dot{\gamma}_N, \dot{\gamma}_T)$ such as to satisfy (1) and (3).

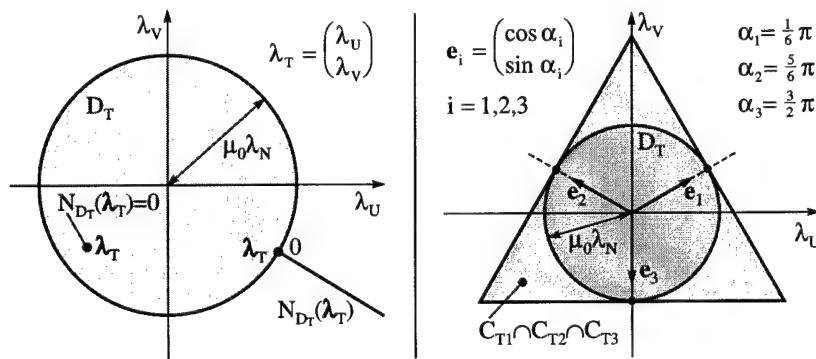


Fig. 1: Friction disk D_T . Left: Normal cone $N_{D_T}(\boldsymbol{\lambda}_T)$ at different points $\boldsymbol{\lambda}_T \in D_T$ according to (2). Right: Additional constraints C_{Ti} in (4) defined by three unit vectors \mathbf{e}_i .

2. An alternative representation of Coulomb's law

To formulate (1) and (3) as a nonlinear complementarity problem in standard form, an alternative representation of the tangential contact law $-\dot{\gamma}_T \in N_{D_T}(\boldsymbol{\lambda}_T)$ in (3) is needed. For this purpose we define

$$\begin{aligned} C_{Ti} &= \{\boldsymbol{\lambda}_T \mid \sigma_i(\boldsymbol{\lambda}_T) \geq 0\} & \text{with } \sigma_i(\boldsymbol{\lambda}_T) &= \mu \lambda_N - \mathbf{e}_i^T \boldsymbol{\lambda}_T, \quad i = 1, 2, 3 \\ D_T &= \{\boldsymbol{\lambda}_T \mid \sigma_D(\boldsymbol{\lambda}_T) \geq 0\} & \text{with } \sigma_D(\boldsymbol{\lambda}_T) &= \mu^2 \lambda_N^2 - |\boldsymbol{\lambda}_T|^2 \end{aligned} \quad (4)$$

Note that the friction disk D_T is now characterized by a parabolic function σ_D with vanishing gradients at $\lambda_T = 0$, but accompanied by three additional linear inequalities C_{Ti} which will take over the job to satisfy the friction law also at $\lambda_T = 0$. By setting

$$C_T := \bigcap_{i=1}^3 C_{Ti} \cap D_T \equiv D_T; \quad N_{C_T}(\lambda_T) = \sum_{i=1}^3 N_{C_{Ti}}(\lambda_T) + N_{D_T}(\lambda_T) \equiv N_{D_T}(\lambda_T) \quad (5)$$

we obviously obtain the identity $N_{C_T}(\lambda_T) \equiv N_{D_T}(\lambda_T)$, and may hence write the friction law as $-\dot{\gamma}_T \in N_{C_T}(\lambda_T)$. This inclusion can be rewritten as a system of inequalities [4]

$$-\dot{\gamma}_T = \sum_{i=1}^3 \mathbf{e}_i \kappa_i + 2\lambda_T \kappa_D \quad \text{with } \kappa_j \geq 0, \sigma_j \geq 0, \kappa_j \sigma_j = 0, \quad j = 1, 2, 3, D, \quad (6)$$

where equivalence with $-\dot{\gamma}_T \in N_{D_T}(\lambda_T)$ has been proven in [1].

3. An NLCP formulation of the rolling contact problem

By using the representation of the tangential contact law from section 2, the rolling contact problem may now be stated in the following form: We need the kinetic and kinematic equations (1), the normal contact law in (3), the definition of the friction saturations σ_i and σ_D in (4), and equation (6), i.e.

$$\begin{aligned} \mathbf{M}\dot{\mathbf{u}} - \mathbf{h} - \mathbf{w}_N \lambda_N - \mathbf{W}_T \lambda_T &= 0, & \dot{\gamma}_N &= \mathbf{w}_N^T \dot{\mathbf{u}} + \bar{w}_N, & \dot{\gamma}_T &= \mathbf{W}_T^T \dot{\mathbf{u}} + \bar{w}_T \\ \sigma_i &= \mu \lambda_N - \mathbf{e}_i^T \lambda_T \quad (i = 1, 2, 3), & \sigma_D &= \mu^2 \lambda_N^2 - |\lambda_T|^2, & -\dot{\gamma}_T &= \sum_{i=1}^3 \mathbf{e}_i \kappa_i + 2\lambda_T \kappa_D \\ \lambda_N &\geq 0, \dot{\gamma}_N &\geq 0, \lambda_N \dot{\gamma}_N &= 0, & \sigma_j &\geq 0, \kappa_j \geq 0, \sigma_j \kappa_j = 0 \quad (j = 1, 2, 3, D). \end{aligned} \quad (7)$$

We now eliminate $\dot{\mathbf{u}}$, $\dot{\gamma}_T$, λ_T from (7) such that as unknowns only the five complementary pairs $(\lambda_N, \dot{\gamma}_N)$ and (σ_j, κ_j) ($j = 1, 2, 3, D$) remain. By setting $\sigma_P := (\sigma_1 \sigma_2)^T$, $\kappa_P := (\kappa_1 \kappa_2)^T$, $\mu_P := (\mu \mu)^T$, $\mathbf{I}_P := (\mathbf{e}_1 \mathbf{e}_2)^T$, this yields

$$\begin{aligned} \begin{pmatrix} \dot{\gamma}_N \\ \kappa_P \\ \sigma_3 \\ \sigma_D \end{pmatrix} &= \begin{pmatrix} \mathbf{w}_N^T \mathbf{M}^{-1}(\mathbf{w}_N + \mathbf{W}_P \mu_P) & -\mathbf{w}_N^T \mathbf{M}^{-1} \mathbf{W}_P & 0 & 0 \\ -\mathbf{W}_P^T \mathbf{M}^{-1}(\mathbf{w}_N + \mathbf{W}_P \mu_P) & \mathbf{W}_P^T \mathbf{M}^{-1} \mathbf{W}_P & -\mathbf{I}_P^{-1} \mathbf{e}_3 & 0 \\ \mu - \mathbf{e}_3^T \mathbf{I}_P^{-T} \mu_P & \mathbf{e}_3^T \mathbf{I}_P^{-T} & 0 & 0 \\ 0 & 0 & 0 & 0 \end{pmatrix} \begin{pmatrix} \lambda_N \\ \sigma_P \\ \kappa_3 \\ \kappa_D \end{pmatrix} \\ &+ \begin{pmatrix} 0 \\ -2\mathbf{I}(\mu_P \lambda_N - \sigma_P) \kappa_D \\ 0 \\ \mu^2 \lambda_N^2 - \|\mu_P \lambda_N - \sigma_P\|_I^2 \end{pmatrix} + \begin{pmatrix} \mathbf{w}_N^T \mathbf{M}^{-1} \mathbf{h} + \bar{w}_N \\ -\mathbf{W}_P^T \mathbf{M}^{-1} \mathbf{h} - \bar{w}_P \\ 0 \\ 0 \end{pmatrix}. \end{aligned} \quad (8)$$

Here we have also used $\mathbf{W}_P := \mathbf{W}_T \mathbf{I}_P^{-T}$, $\bar{w}_P := \mathbf{I}_P^{-1} \bar{w}_T$ and $\mathbf{I} := \mathbf{I}_P^{-1} \mathbf{I}_P^{-T}$, where \mathbf{I} is a symmetric and positive definite 2×2 matrix. The NLCP (8) is of the form $\mathbf{y} = \mathbf{f}(\mathbf{x})$, $\mathbf{y} \geq 0$, $\mathbf{x} \geq 0$, $\mathbf{y}^T \mathbf{x} = 0$ with $\mathbf{f}(\mathbf{x}) = \mathbf{A}\mathbf{x} + \mathbf{g}(\mathbf{x}) + \mathbf{c}$ and generalizes the cases discussed in [2,3]. Since $\mathbf{f}(\mathbf{x})$ is continuous and differentiable we may finally state its Jacobian $D_x \mathbf{f} = \mathbf{A} + D_x \mathbf{g}$. We denote by $\lambda_P(\lambda_N, \sigma_P) := \mu_P \lambda_N - \sigma_P$ and obtain for $D_x \mathbf{g}$ explicitly depending on λ_N , σ_P and κ_D with $\mathbf{I} = \mathbf{I}^T$ the expression

$$D_x \mathbf{g} = \begin{pmatrix} 0 & 0 & 0 & 0 \\ 0 - 2\mathbf{I} \mu_P \kappa_D & 2\mathbf{I} \kappa_D & 0 & -2\mathbf{I} \lambda_P \\ 0 & 0 & 0 & 0 \\ 2\mu^2 \lambda_N - 2\lambda_P^T \mathbf{I}^T \mu_P & 2\lambda_P^T \mathbf{I}^T & 0 & 0 \end{pmatrix}. \quad (9)$$

4. References

- 1 GLOCKER, CH.: Formulation of spatial contact situations in rigid multibody systems. *Comput. Methods Appl. Mech. Engrg.* **177** (1999), 199–214.
- 2 KLARBRING, A.: A mathematical programming approach to three-dimensional contact problems with friction. *Comp. Meth. Appl. Mech. Engrg.* **58** (1986), 175–200.
- 3 PANG, J.S.; TRINKLE, J.C.: Complementarity formulations and existence of solutions of dynamic multi-rigid-body contact problems with Coulomb friction. *Mathematical Programming* **30** (1996), 199–226.
- 4 ROCKAFELLAR, R.T.: *Convex Analysis*. Princeton University Press, Princeton, New Jersey, 1970.

Addresses: DR. CHRISTOPH GLOCKER, Lehrstuhl B für Mechanik, TU München, D-85747 Garching, Germany.

HANSEL, W.; BECKER, W.

Weight-Minimal Laminate Structures Under Stress Constraints

The determination of weight-minimal laminate structures requires the well-aimed employment of structural optimization. In contrast to the common parameter optimization in which the design variables fiber orientation and layer thickness are varied continuously, a layerwise topology optimization offers more flexibility. Starting from an initial laminate lay-up with sufficient strength, the topology of each individual ply is varied by removing unnecessary material. The final design is well adapted to the local load fluxes.

1. Introduction

During the last decades, the use of unidirectional CFRP (carbon fiber reinforced plastics) got well established for lightweight construction of aircraft and spacecraft applications. The special anisotropic properties of composite materials allow tailoring the laminate behavior to the given structural needs. In order to receive weight minimal structures, structural optimization is needed. Traditionally, properties like fiber orientations or layer thicknesses are used as design variables which are varied continuously. Often this kind of optimization leads to weight-optimal laminate designs, which are difficult to manufacture. Therefore in the present work an optimization algorithm is presented that leads to designs which are easy to manufacture. The main idea of the layerwise topology optimization is to remove locally the whole ply material within regions where it is not seriously needed. With regard to a low-cost manufacturing the choice of orientation angles is limited to 0° , $\pm 45^\circ$ and 90° and the ply thickness is fixed to the discrete values 0 (no material) and h (material). The required structural analyses have been performed with the finite element program ANSYS and also the optimization algorithm has been implemented by ANSYS macros.

2. Problem formulation

As the initial design, we consider a symmetric laminate under pure inplane loading. In order to keep the manufacturing costs low a common quasi-isotropic lay-up $[0^\circ / \pm 45^\circ / 90^\circ]_S$ with the initial layer thicknesses h_i is used. The material orientation angles Θ_i are fixed and cannot be varied during optimization. The objective function of the optimization problem is to minimize the total weight m of the structure.

The strength constraints of the optimization problem are given by the TSAI-WU failure criterion in the form

$$\frac{\sigma_1^2}{X_t X_c} - \frac{\sigma_1 \sigma_2}{\sqrt{X_t X_c Y_t Y_c}} + \frac{\sigma_2^2}{Y_t Y_c} + \frac{\sigma_{12}^2}{S^2} + \sigma_1 \left(\frac{1}{X_t} - \frac{1}{X_c} \right) + \sigma_2 \left(\frac{1}{Y_t} - \frac{1}{Y_c} \right) \leq 1 \quad (1)$$

with the longitudinal and transverse strengths X and Y in tension (index t) and compression (index c). As design variables the thicknesses of the finite elements with the discrete values h and $\varepsilon \ll h$ are taken. The small value $\varepsilon \neq 0$ is chosen to avoid singularity problems within the performed finite element analyses.

3. Optimization algorithm

The contrived heuristic optimization algorithm is based on an iterative process with two phases in which the thicknesses of the single elements are varied. Within the first phase the principal directions φ and $\varphi + 90^\circ$ of the averaged stresses of the total laminate $[0^\circ / \pm 45^\circ / 90^\circ]$ are determined and compared with the four layer orientation angles Θ_i . The optimal load-carrying capacity of a single element is reached if that element is essentially loaded in the direction of its orientation angle. On the other hand this means that a single ply element is not optimally loaded, if its orientation angle differs significantly from the principal stress direction φ . Those elements can be removed, e.g. material in the $\pm 45^\circ$ -layers can be removed if the stress direction is in the range $-\Delta\varphi < \varphi < +\Delta\varphi$. The parameter $\Delta\varphi$ is an arbitrary threshold parameter that is increased during the first phase of the optimization process.

In the second optimization phase the weight saving potential is further exploited. For that purpose material is removed in those regions where the principal stresses σ_I and σ_{II} of the single elements are below a threshold parameter σ_0 . A low value of $\sigma_{I/II}$ suggests that the corresponding element is not loaded significantly. The threshold stress value σ_0 is increased successively until the load carrying capacity of the laminate is attained.

For some more flexibility two options are implemented in the algorithm to fit in again removed material. By a first

criterion material is fitted in if the principal stress of a removed element (thickness ϵ) is "large" and if simultaneously the TSAI-WU criterion is lower than 1. In a second criterion it is checked if at any location where failure occurs other layer elements exist whose orientation angles correspond in a better way to the calculated principal stress directions.

4. Optimization examples

The effectiveness of the proposed optimization method has been tested and verified in a number of example problems. In a first example the weight of a rectangular laminate plate is to be minimized when the plate is clamped along the left edge and is loaded by a single force at the upper right corner. The other edges are free. Each of the four layers is discretized into 20×40 quadrilateral plane eight-node elements. Thus, in all there are 3200 elements with 12400 degrees of freedom. In fig. 1 the final design after 35 iterations is shown. The weight could be reduced from 31.6g in the initial design to 3.81g in the final design.

In a second example the optimal design of a reinforcement for a $[0^\circ/90^\circ]_S$ -cross-ply laminate plate with a hole under a uniaxial tensile load is determined. As a reinforcement two quasi-isotropic $[0^\circ/\pm 45^\circ/90^\circ]$ doublers are chosen. The objective function is to minimize the total weight of the doublers. Because of symmetry only one-quarter of the problem is regarded (fig. 2). In the final design elements in the 0° - and $+45^\circ$ -layers are almost completely removed and only a small ring of the -45° -layer around the hole is remaining to reduce the circumferential stresses $\sigma_{\varphi\varphi}$. In order to transfer the tensile load predominantly material in the 90° -layer is required. The determined laminate structure is then optimally adapted to the local load fluxes.

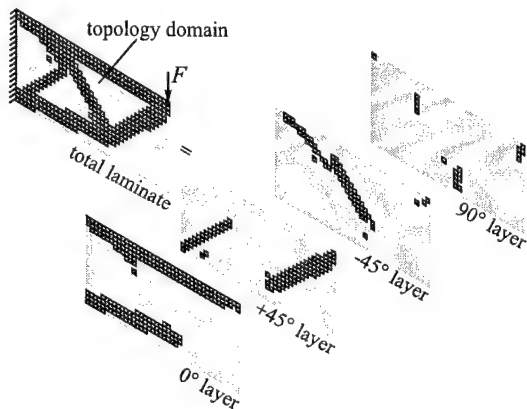


Figure 1: A cantilever plate

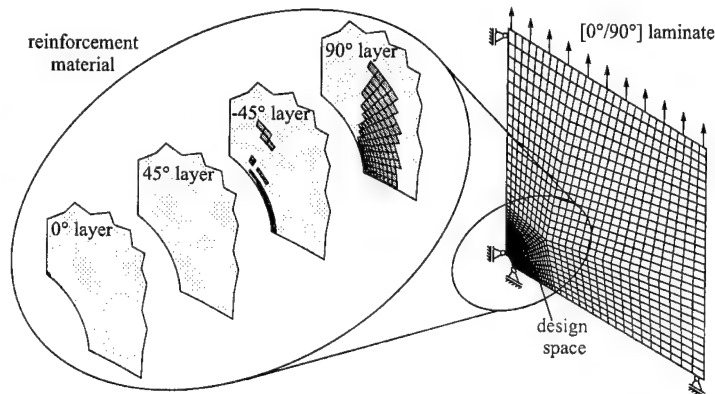


Figure 2: Optimal material distribution of reinforcement

5. Conclusions

The present work gives a novel concept of topology optimization for laminate structures, where the optimal topology is determined for each individual layer. The final design is easy to manufacture from standard prepreps by tailoring each layer individually and subsequent curing. In many cases the weight of the laminate design can be significantly reduced and the resultant structure is well-adapted to the structural needs. The numerical effort keeps reasonably low, because in contrary to a formal mathematical optimization no sensitivity analyses are needed.

6. References

- 1 HANSEL, W.; BECKER, W.: Layerwise Adaptive Topology Optimization of Laminate Structures. *Engineering Computations* **16** (1999), 841–851.
- 2 HINTON, E.; SIENZ, J.: Fully Stressed Topological Design of Structures Using an Evolutionary Approach. *Engineering Computations* **12** (1995), 229–244.
- 3 XIE, Y.M.; STEVEN, G.P.: A Simple Evolutionary Procedure for Structural Optimization. *Computers and Structures* **49** (1993), 885–896.

Addresses: WILFRIED HANSEL, WILFRIED BECKER, Universität-GH Siegen, Institut für Mechanik und Regelungstechnik, Paul-Bonatz-Str. 9-11, D-57068 Siegen, Germany.

HÖRNLEIN, H. R. E. M.

Effiziente semi-analytische Gradientenberechnung in der Strukturoptimierung

Bei der Lösung von Strukturoptimierungsaufgaben werden fast immer Gradientenverfahren der Mathematischen Optimierung eingesetzt. Die Bereitstellung der ersten Ableitungen beansprucht den größten Teil der Gesamtrechnenzeit. Der Erfolg der Optimierung hängt aber auch von der numerischen Genauigkeit der Ableitungen ab. Hier wird auf einen entscheidenden Nachteil der favorisierten semi-analytischen Sensitivitätsanalyse aufmerksam gemacht, gleichzeitig wird aber gezeigt wie dieser Nachteil zu beheben ist.

1. Bestandsaufnahme

In der Anwendung auf Sizing-Optimierungsprobleme ist die semi-analytische Berechnung der Gradienten unumstritten. Bei der Shape-Optimierung ist das nicht so, hier ist die Genauigkeit der Ableitungen fragwürdig. In der Literatur wurde an Beispielen gezeigt, daß die konventionelle semi-analytische Sensitivitätsanalyse (SA) mit großen numerischen Fehlern behaftet ist, siehe [1], [2], [3], [5]. In dem Bericht [8] sind diese Aktivitäten übersichtlich zusammengefaßt. In [2] wurde gezeigt, daß die Starrkörperrotationen der biege steifen Elemente (Balken, Platten, Schalen) für diesen Fehler verantwortlich sind. In [9] wird dieser Fehler durch die Berücksichtigung der Starrkörperrotation im Pseudo-Lastvektor vermieden. Bei der Improved Semi-Analytical Sensitivity Analysis (ISA) wird die Genauigkeit durch eine NEUMANN-Reihenentwicklung der perturbierten inversen Steifigkeitsmatrix verbessert, [4].

2. Verbesserte semi-analytische Sensitivitätsanalyse (ISA)

Das linear elastisches Gleichgewicht $\mathbf{K}(\mathbf{x})\mathbf{u} = \mathbf{p}$, $\mathbf{x} \in \mathbb{R}^n$ wird durch eine CHOLESKY-Zerlegung $\mathbf{K} = \mathbf{L}\mathbf{L}^T$ mit anschließender Vorwärts-Rückwärts-Substitution (VRS) nach den Verschiebungen \mathbf{u} gelöst. Für die Ableitung der Verschiebungen werden drei wesentlich verschiedene Möglichkeiten zur Berechnung der Gradienten betrachtet:

Analytisch (A)	Semi-Analytisch (SA)	Finite Differenzen (OFD)
$\frac{\partial \mathbf{u}}{\partial x_i} = -\mathbf{K}^{-1} \frac{\partial \mathbf{K}}{\partial x_i} \mathbf{u}$	$\frac{\partial \mathbf{u}}{\partial x_i} = \lim_{\Delta x_i \rightarrow 0} -\mathbf{K}^{-1} \frac{\Delta \mathbf{K}_i}{\Delta x_i} \mathbf{u}$	$\frac{\partial \mathbf{u}}{\partial x_i} = \lim_{\Delta x_i \rightarrow 0} \frac{\mathbf{u}(\mathbf{x} + \mathbf{e}_i \Delta x_i) - \mathbf{u}(\mathbf{x})}{\Delta x_i}$

Der Codierungsaufwand der analytischen Ableitungen ist für die Vielzahl von FE-Elementtypen und Variablenarten nicht vertretbar. Semi-analytische Ableitungen nach geometrischen Entwurfsvariablen sind bei der Anwendung auf biege steife Strukturen ungenau. Finite Differenzen (OFD) sind i.a. hinreichend genau aber zu rechenintensiv weil die CHOLESKY-Dekomposition für alle x_i durchgeführt werden muß. Die Konstruktionsidee für die ISA basiert auf einem Lemma von CARL NEUMANN:

Für lineare Operatoren $\mathbf{B} \in \mathbf{L}(\mathbb{R}^n)$ mit dem Spektralradius $\rho(\mathbf{B}) < 1$ existiert die Inverse $(\mathbf{I} + \mathbf{B})^{-1}$ und läßt sich als Reihe darstellen: $(\mathbf{I} + \mathbf{B})^{-1} = \lim_{k \rightarrow \infty} \sum_{j=0}^k (-1)^j \mathbf{B}^j$.

Für die inkrementierte Steifigkeitsmatrix $\mathbf{K}_+ = \mathbf{K}(\mathbf{x} + \mathbf{e}_i \Delta x_i) = \mathbf{K} + \Delta \mathbf{K}_i$ erhält man mit der Äquivalenz $\mathbf{K}_+^{-1} = (\mathbf{I} + \mathbf{K}^{-1} \Delta \mathbf{K}_i)^{-1} \mathbf{K}^{-1}$ und dem NEUMANN Lemma, die Verschiebung der gestörten Struktur als Reihendarstellung:

$$\mathbf{u}_+ = \mathbf{K}_+^{-1} \mathbf{p} = (\mathbf{I} + \mathbf{K}^{-1} \Delta \mathbf{K}_i)^{-1} \underbrace{\mathbf{K}^{-1} \mathbf{p}}_{\mathbf{u}} = \sum_{j=0}^{\infty} (-1)^j (\mathbf{K}^{-1} \Delta \mathbf{K}_i)^j \mathbf{u} = \mathbf{u} + \sum_{j=1}^{\infty} (-1)^j \underbrace{(\mathbf{K}^{-1} \Delta \mathbf{K}_i)^j \mathbf{u}}_{\boldsymbol{\vartheta}_{j+1}} \quad (1)$$

Die Auswertung der Reihe (1) läßt sich mit der Rekursion: $\sum_{j=1}^k (-1)^j (\mathbf{K}^{-1} \Delta \mathbf{K}_i)^j \mathbf{u} = \sum_{j=1}^k (-1)^j \mathbf{K}^{-1} \Delta \mathbf{K}_i \boldsymbol{\vartheta}_j$ einfach und schnell mit nur einer CHOLESKY-Dekomposition durchführen: $\mathbf{K} \boldsymbol{\vartheta}_{j+1} = \Delta \mathbf{K}_i \boldsymbol{\vartheta}_j$ und $\boldsymbol{\vartheta}_1 = \mathbf{u}$.

Eine Verallgemeinerung auf nichtlineare Rechthandseiten $\mathbf{p} = \mathbf{f}(\mathbf{u}^e)$ mit der elastischen Verschiebung \mathbf{u}^e der Aeroelastik ist einfach und kann beim Autor mit dem vollständigen Bericht als E-mail abgefragt werden.

Als Alternative zur ISA werden im Programmsystem LAGRANGE der DaimlerChrysler AG die gemittelten finiten Differenzen (GD) für $\Delta K/\Delta x_i$ verwendet. Neben den zentralen (GD2) Differenzen werden die vierten gemittelten Differenzen (GD4) aus den Taylorreihenentwicklungen für K bei $x + e_i \varepsilon$ mit $\varepsilon \in \{\pm \Delta x_i, \pm \Delta x_i/2\}$ berechnet.

3. Numerische Verifikation am Beispiel

Der in Abb. 1 gezeigte Kragbalken verformt sich unter der Einheitslast $M_z = 1$ nach der analytischen Lösung um $v = (M_z L^3)/(2EI_z)$. Die Geometrie und der Werkstoff ist mit $L = I = E = 1$ so gewählt, daß für die Verschiebungsableitung $\partial v/\partial L = 1.0$ gilt. Zur Simulation mit der FE-Rechnung wurden $m = 100$ Balkenelemente verwendet. In der Abb. 1 sind die Ergebnisse der konventionellen- (SA), der voll numerischen- (OFD), der verbesserten- (ISAk) und der gemittelten- (GDn) Gradienten für eine Perturbation von $\Delta L = 10^{-4}$ gegenübergestellt.

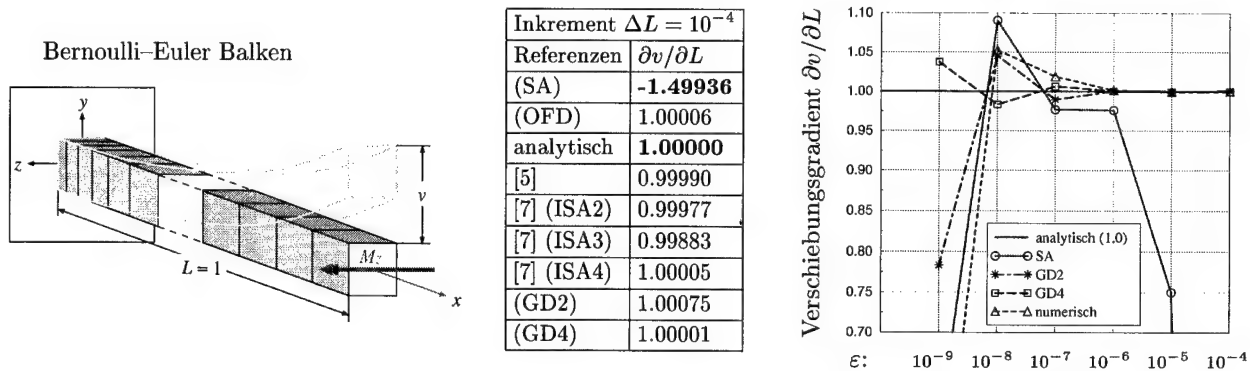


Abbildung 1: Vergleich des Verschiebungsgradienten $\partial v/\partial L$ am Kragbalken

In der Strukturoptimierung hat sich gezeigt, daß die superlinear konvergenten quasi-NEWTON-Verfahren der mathematischen Optimierung, z.B. die Sequentielle Quadratische Optimierung (SQP), sehr genaue Gradienten benötigen um die zweiten Ableitungen aufzubauen. Für den Anwender stellt sich also die Frage nach dem zu wählenden Inkrement ε , das klein genug sein muß um den Abschneidefehler klein zu halten aber auch nicht zu klein ist, um den Rundungsfehler zu vermeiden. Um dieses *numerische Fenster* zu treffen sind ε -Parameterstudien erforderlich. Die im Beispiel verwendete Perturbation ist mit $\varepsilon = 10^{-4}$ für Computerrechnungen zu groß gewählt, sie wurden hier verwendet um den SA-Fehler zu demonstrieren. Die Parameterstudie zeigt jedoch, daß der SA-Fehler auch mit kleinerem Inkrement nicht beseitigt werden kann. Es gibt für die SA *kein brauchbares numerisches Fenster*: die konventionelle semi-analytische Sensitivitätsanalyse ist für die praktische Anwendung nicht zu gebrauchen.

4. Referenzen

- 1 B. BARTHELEMY, R. T. HAFTKA: Accuracy of the semi-analytical method for shape sensitivity calculations. In *Structures, Structural Dynamics and Materials Conference*, pages 562–581. 29th AIAA/ASME/ASCE/ASC, Part 1, 1988.
- 2 G. CHENG, N. OLHOFF: New method of error analysis and detection in semi-analytical sensitivity analysis. In G. I. N. Rozvany, editor, *Optimization of large structural systems*, pages 361–383, Berchtesgaden, Germany, 1991. Lecture Notes NATO-DFG Advanced Study Institute, Dordrecht: Kluwer.
- 3 N. OLHOFF AND J. RASMUSSEN: Study of inaccuracy in semi-analytical sensitivity analysis: A model problem. *Structural Optimization*, 3:203–213, 1991.
- 4 H. R. E. M. HÖRNLEIN: Strukturoptimierung: Vom Problem zum System, Anhang 2, Semianalytische Sensitivitätsanalyse. Lecture notes, COMETT Seminar: Computer Aided Optimal Design of Structures, Thurnau, May 18.–22. 1992.
- 5 H.-P. MLEJNEK: Accuracy of semi-analytical sensitivities and its improvement by the natural method. *Structural Optimization*, 4:128–131, 1992.
- 6 K. YAMAZAKI AND G. VANDERPLAATS: Design sensitivity analysis with iso-parametric shell elements. *Structural Optimization*, 5(3):152–158, 1993.
- 7 S. ORAL: An improved semi-analytical method for sensitivity analysis. *Structural Optimization*, 11(1):67–69, 1996.
- 8 F. VAN KEULEN, R. HAFTKA, AND X.-Y. QU.: Review of options for structural sensitivity calculations. In *41th Structures, Structural Dynamics, and Materials Conference and Exhibit*, AIAA/ASME/ASCE/AHS/ASC. Atlanta, USA, April 2000, AIAA-00-1351, ISBN 1-56347-435-2.
- 9 K. VERVENNE AND H. DE BOER F. VAN KEULEN: Accuracy and implementation of refined second order semi-analytical design sensitivities. to appear in the proceedings GAMM 2000.

Adresse: HERBERT R. E. M. HÖRNLEIN, DaimlerChrysler Aerospace AG, Military Aircraft, D-Munich, Germany,
e-mail: herbert.hoernlein@m.dasa.de

ISTRATIE, V.

OPTIMAL RENDEZVOUS WITH CONSTRAINTS ON CIRCULAR AND ELLIPTICAL ORBITS

This work studies the optimum rendezvous with minimum fuel consumption two space vehicles on circular and elliptical orbits, the surveyor vehicle being equipped with a low thrust installation, their motion equations being written in the three-dimensional space, in relative motion; the space origin being the target vehicle. Optimal controls to be determined being the acceleration due to thrust related to the minimum fuel consumption. By means of the Legendre-Clebsch condition it is demonstrated that the formulated optimization problem is, indeed, a minimum problem.

1. Problem Formulation. Motion Equations of the State

Considering the Axy system: the z axis in the direction of the vectorial radius (that links the origin of the inertial system with the origin A of the moving system), the x axis is counter rotating, and the y axis perpendicular on them, related to the A target which evolves on an already known circular or elliptical orbit the motion equations of the surveyor (because the motion takes place out of the atmosphere the aerodynamic forces are neglected) are:

$$\begin{aligned}\frac{dx}{dt} &= V_x, \quad \frac{dV_x}{dt} = -\frac{2\mu\epsilon\sin\phi}{r_0^3}z + \frac{\mu p}{r_0^4}x + 2\frac{\sqrt{\mu p}}{r_0^2}V_z - \mu\frac{x}{[x^2 + (r_0 + z)^2 + y^2]^{3/2}} + a_x, \quad \frac{dz}{dt} = V_z \\ \frac{dV_z}{dt} &= \frac{\mu}{r_0^2} + \frac{2\mu\epsilon\sin\phi}{r_0^3}x + \frac{\mu p}{r_0^4}z - 2\frac{\sqrt{\mu p}}{r_0^2}V_x - \mu\frac{r_0 + z}{[x^2 + (r_0 + z)^2 + y^2]^{3/2}} + a_z, \quad \frac{dy}{dt} = V_y, \\ \frac{dV_y}{dt} &= -\mu\frac{y}{[x^2 + (r_0 + z)^2 + y^2]^{3/2}} + a_y, \quad \frac{d\phi}{dt} = \sqrt{\frac{\mu}{p^3}}(1 + \epsilon\cos\phi)^2\end{aligned}$$

where r_0 is radius planet, μ - gravitational parameter, p - focal parameter, ϵ - eccentricity orbit ($\epsilon=0$ for circular orbit), a_x, a_z, a_y - control variables (the accelerations due to the thrust) and (the state variables) are: x, z, y - coordinates, V_x, V_z, V_y - velocities, ϕ - elliptical anomaly, with the initial conditions at the time $t=0$:

$$x(0) = x_0, z(0) = z_0, y(0) = y_0, V_x(0) = V_{x_0}, V_z(0) = V_{z_0}, V_y(0) = V_{y_0}, \phi(0) = 105 \text{ degree} \quad (2)$$

and final conditions at $t=t_f$:

$$x(t_f) = z(t_f) = y(t_f) = V_x(t_f) = V_z(t_f) = V_y(t_f) = 0 \quad (3)$$

$\phi(t_f)$ is free. For the control variables C_L and γ we impose the constraints $|a_x| \leq a, |a_z| \leq a, |a_y| \leq a$ where for orbits in around of Earth, $a=10^{-3}g$, g - the gravity acceleration. The problem can be stated is: Let us find a control function $u=(a_x, a_z, a_y): [0, t_f] \rightarrow R^3$ and a state function $x=(x, z, y, V_x, V_z, V_y): [0, t_f] \rightarrow R^6$ for the circular orbits and $x=(x, z, y, V_x, V_z, V_y, \phi): [0, t_f] \rightarrow R^7$ for elliptical orbits, which minimize functional

$$J(u) = \int_0^{t_f} (a_x^2 + a_z^2 + a_y^2) dt \quad (4)$$

subject to the differential equations of motion (1) with the initial conditions (2) and the final conditions (3).

2. Optimizing Problem. Boundary Value Problem

Optimizing the problem by the minimum principle. The above defined problem of optimal control is transformed in a well-known¹ into a two point boundary problem. For this, the Hamiltonian is

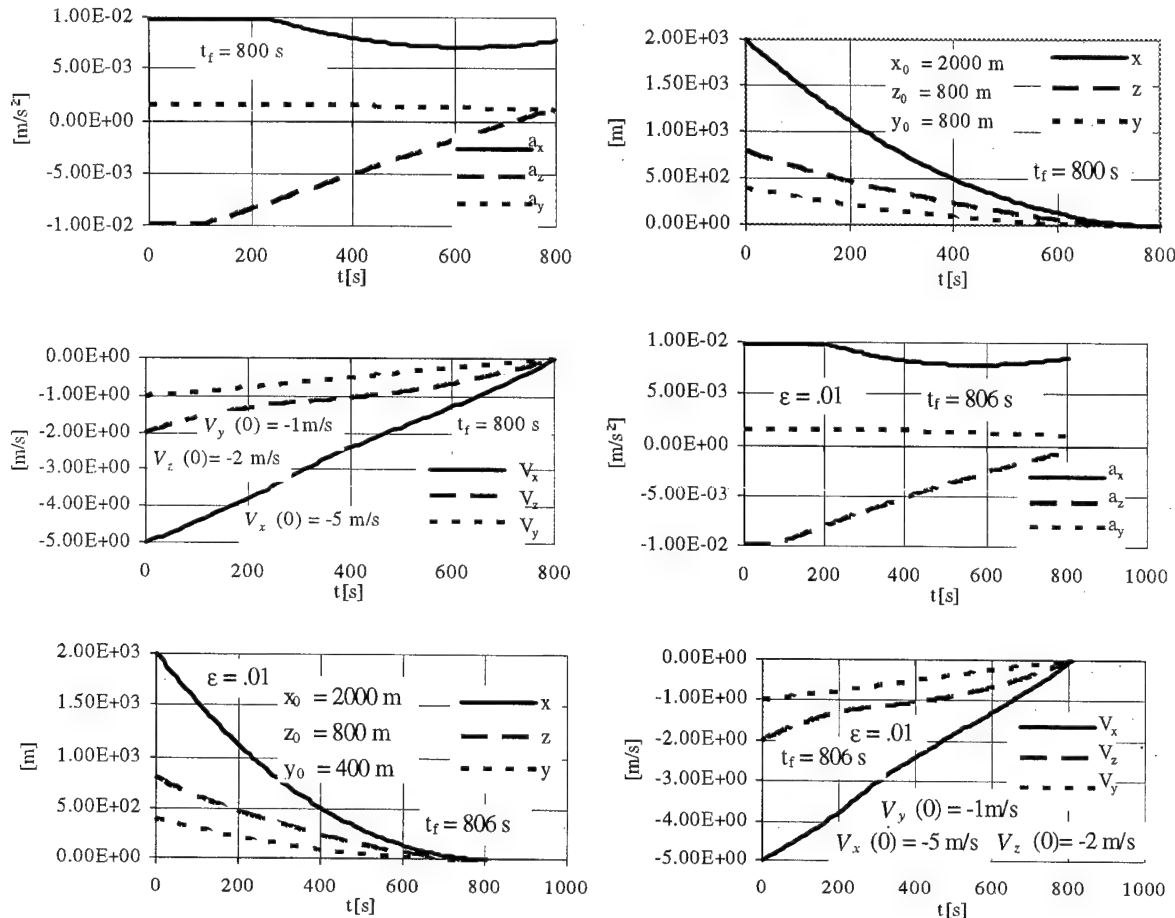
$$H = -f_0 + p_x f_x + p_{V_x} f_{V_x} + p_z f_z + p_{V_z} f_{V_z} + p_y f_y + p_{V_y} f_{V_y} + p_\phi f_\phi \quad (5)$$

where f_0 is the function under the integral (4), $x, p_{V_x}, p_z, p_{V_z}, p_y, p_{V_y}, p_\phi$ are the adjoint variables corresponding of the state variables $x, V_x, z, V_z, y, V_y, \phi$, and also, $f_V, f_\theta, f_\eta, f_z, f_\phi, f_\lambda, f_\phi$ are the functions defining the motion equations system of the state variables $x, V_x, z, V_z, y, V_y, \phi$, respectively.

By means of the Hamiltonian, the canonic equations that is the differential equations of the state variables (the above mentioned equations), the differential equations of the adjoint variables. The algebraic equations of the controls (the optimality conditions) are deduced for (a_x, a_z, a_y) the interior point. for H from $H_u = 0$ ($a_x = p_{V_x}/2$, $a_z = p_{V_z}/2$, $a_y = p_{V_y}/2$) and must fulfill the Legendre-Clebsch condition, that is $H_{uu} > 0$.

3. Solving of the Problem. Numerical Application

Practically, the analytical solution could not be determined due to the non-linear structure of the equations which form this system, so because of this we shall also solve this problem using the *shooting* type numerical method³. Calculations were performed (calculus was performed on a PC-486 computer having computational program elaborated in this respect according to the method *shooting*) for circular and elliptical ($\epsilon = .01$) orbits around the Earth, the final time being imposed.



4. Conclusions

1. The calculations performed using based on the non-linear theory presented in this work show that the differences between the results obtained for circular orbits and the elliptical ones are small if the eccentricity of them are also small.
2. The initial value of the target real anomaly does not significantly influence the results even in case the target reaches the proximity of the orbit apogee

5. References

1. Bryson, A. E., Ho, Y. C., *Applied Optimal Control*, Revised Printing, Hemisphere Publishing Corp., Washington D. C., 1975.
2. Istratie, V., "Shooting type methods for solving the two point boundary value in the optimization of the flight vehicles evolutions. Journal ZAMM, 1997.

Address: VASILE ISTRATIE, National Aerospace Research Institute, Bd. I. Maniu 220, 77538 Bucharest, Romania

KEGL, M.

An efficient shape parameterization concept for structural optimization

This paper describes a shape parameterization concept that may be used efficiently in structural shape optimization. It relies on the assumption that the finite element mesh is defined as a convective mesh, following automatically the shape changes of a conveniently parameterized body. Suitable parameterization of the body is achieved by combining the design element technique and a convenient design element. The design element in turn is defined as a rational (tensor-product) Bézier body. It represents a general-purpose design element, serving as the geometrical data provider for the response and sensitivity analysis for virtually any finite element type.

1. Introduction and fundamentals

Efficient parameterization of the structure, or more precisely of the finite element (FE) mesh, is the key to successful shape optimization. An efficient parameterization should provide enough flexibility of the structure with a minimum set of independent design variables. Additionally, it is most desirable that any geometrical requirements, imposed by the designing engineer, may be fulfilled automatically without extending the design problem with additional constraints. The proposed approach meets these requirements to a great extent.

This work represents a generalization of the concepts proposed in [1,2]. The fundamental idea can be briefly explained as follows [3]: let us consider a generic FE mesh of a structure. Let the hull of the mesh represent the boundary surface of a body B . We assume that we can build up some mapping Ω that maps some standard domain U into B . Once we have the mapping Ω , it is possible to define the FE mesh by defining its pre-image in the domain U rather than directly in the real 3-D space. Now we invoke the design variables \mathbf{b} as parameters of the mapping Ω . In this way, we get a 'convective' FE mesh that follows automatically the changes of the body B caused by changing the design variables \mathbf{b} . In that way, we can expect to be able to optimize the shape of the structure efficiently.

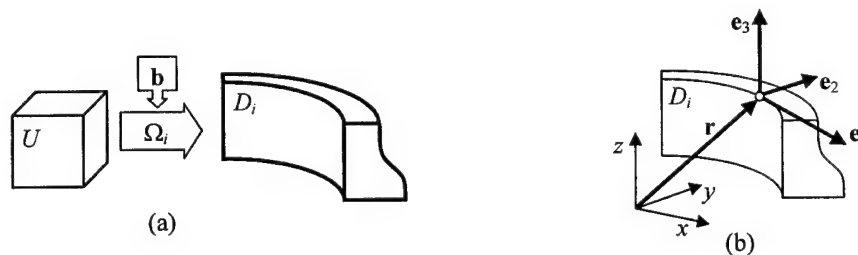


Figure 1: Design element mapping (a) and required geometrical data (b)

By adopting the above set-up, the most important question that naturally arises is how can we establish a convenient mapping Ω in a systematic way, suitable for the general case. It is proposed to employ the design element technique (see [3] and the references cited therein) by which B is regarded as an assemblage of smaller bodies with simple shape - the design elements D_i . Thus, we have $B = \bigcup_{i=1}^N D_i$ where N is the number of all design elements. Since D_i is assumed to have a simple shape, we can choose a convenient standard mapping Ω_i that maps U into D_i (Fig. 1a). The set of all mappings Ω_i defines fully the needed mapping Ω .

2. A convenient design element

We assume that all of the design element mappings Ω_i are of the same type and that only the values of their parameters are different. In this case we have to choose such a type of Ω_i that free-form shapes as well as classical shapes (e.g. bodies defined by surfaces of revolution) can be described in a rather convenient and simple way. Therefore, in our work Ω_i is defined to be a rational Bézier body mapping [3]. In other words, the position vector \mathbf{r}

of a point of $D_i \subseteq B$ is expressed as

$$\mathbf{r} = \Omega_i(\mathbf{s}, \mathbf{b}); \quad \Omega_i(\mathbf{s}, \mathbf{b}) = \frac{\sum_{j=1}^J \sum_{k=1}^K \sum_{l=1}^L B_j^J(s_1) B_k^K(s_2) B_l^L(s_3) \omega_{jkl}^i(\mathbf{b}) \mathbf{q}_{jkl}^i(\mathbf{b})}{\sum_{j=1}^J \sum_{k=1}^K \sum_{l=1}^L B_j^J(s_1) B_k^K(s_2) B_l^L(s_3) \omega_{jkl}^i(\mathbf{b})}$$

where $\mathbf{s} = [s_1 \ s_2 \ s_3]^T$ is the position vector of a point in a unit cube U , representing the domain of Ω_i . The symbol B denotes the Bernstein polynomial [4], \mathbf{q}_{jkl}^i is a position vector of a control point and ω_{jkl}^i is its corresponding weight. The symbols J , K and L denote the number of control points in corresponding parametric directions.

The geometrical data for the FE mesh can now be retrieved quite easily for any given \mathbf{b} . For a generic FE node \mathbf{s}_n , we usually need its position vector in the real 3-D space as well as sometimes some director (e.g. for a shell element). The position vector is given by $\mathbf{r} = \mathbf{r}(\mathbf{s}_n, \mathbf{b})$ while the director can be expressed in terms of $\mathbf{e}_i = \partial \mathbf{r} / \partial s_i(\mathbf{s}_n, \mathbf{b})$, representing the vectors being tangent to the parametric directions of the body D_i (Fig. 1b). The design derivatives $\partial \mathbf{r} / \partial \mathbf{b}$ and $\partial \mathbf{e}_i / \partial \mathbf{b}$ at $(\mathbf{s}_n, \mathbf{b})$, needed for the sensitivity analysis, can also be evaluated easily. The necessary expressions are given in [3].

3. A numerical example

Let us consider a classical test design problem of a plate in Fig. 2. A rigorous description of the problem can be found in [3]. In brief, the objective is to find the best possible shape of a hole in a square plate with uniform distributed forces applied on its edges, such that the Von Mises stresses along the hole boundary are minimized. Due to symmetry, only a quarter of the plate is modeled (Fig. 2). The solution is expected to be close to an ellipse that represents the analytical solution for an infinite plate under a biaxial stress field. In order to describe the structural geometry, one needs two design elements DE1 and DE2 (Fig. 2) with $3 \times 3 \times 1 = 9$ control points each. The shape of the hole boundary A-B depends on 6 design variables related to the control points and to their weights.

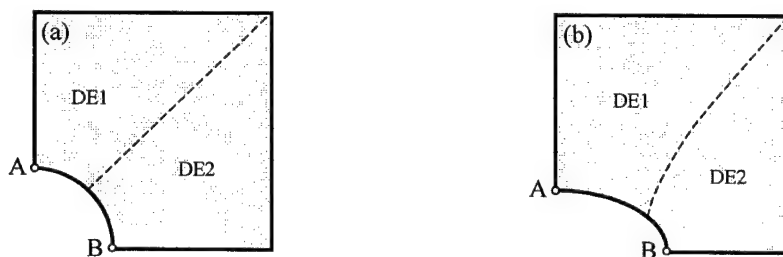


Figure 2: Starting (a) and optimized (b) boundary A-B of the plate

The optimization was started with the initial design corresponding to a circular hole with radius equal to 1, (Fig. 2a). The solution procedure was very stable and after a few iterations, the boundary A-B became almost an exact quarter of an ellipse (Fig. 2b). The ratio of the maximum to the minimum Von Mises stress along A-B, was reduced from 1.8726 to 1.0175. A more detailed discussion on the results can be found in [3].

Acknowledgements

This research was supported by the Ministry of Science and Technology of Republic of Slovenia.

4. References

- 1 KEGL, M.; BUTINAR, B.J.; OBLAK, M.M.: Shape optimal design of elastic planar frames with non-linear response. *Int. j. numer. methods eng.* **38** (1995), 3227–3242.
- 2 KEGL, M.; ANTES, H.: Shape optimal design of elastic space frames with non-linear response. *Int. j. numer. methods eng.* **43** (1998), 93–110.
- 3 KEGL, M.: Shape optimal design of structures: An efficient shape representation concept. *Int. j. numer. methods eng.* (in print).
- 4 FARIN, G.: *Curves and surfaces for computer aided geometric design*, 2nd edn, Academic Press, New York 1990.

Addresses: DOC. DR. MARKO KEGL, Faculty of Mechanical Engineering, Smetanova 17, SI-2000 Maribor, Slovenia

KIRIAZOV, PETKO

On Optimal Control of Mobile Robots

There are continuously increasing demands to mobile robots (MR) for faster operation, higher accuracy, and lower energy cost. A unified direct-search optimization approach is proposed which employs parameterized control laws consistent with the Pontryagin Maximum principle. We define mostly appropriate input-output pairs and transform the given two-point boundary-value problem into a system of shooting equations. The control parameters which are not in the input-output pairs are used for time/energy optimization. Existence of solutions is guaranteed under a weak and reasonable condition. The approach is applied on a dynamic model of a MR having two independently driven wheels.

1. Problem statement

MR are highly non-linear and difficult to model, identify and control mechanical systems due to dynamic couplings, friction, backlash, actuator saturation, and external disturbances. For control design purposes, we can consider the following dynamic model

$$\ddot{q} = M^{-1}(Bu - R(q, \dot{q})), \quad (1)$$

where the coordinates of the vector q are generalized coordinates with respect to a vehicle frame; M is the inertia matrix; B is a matrix which represents the location of actuator forces u ; $R(q, \dot{q})$ stands for all other forces;

To consider the robot motion in the real space (the state with respect to an absolute reference frame denoted by x), we use the following equation for the generalized velocities

$$\dot{q} = D\dot{x}, \quad (2)$$

where matrix D depends on the orientation of the vehicle with respect to the absolute reference frame.

The required motion task is how to take MR from a given state x^0 at a time-moment t^0 to a required state x^f at a time-moment t^f in the best possible way. It means that the movement is optimal in time or energy and the existing control (and state) constraints are not violated.

The complex vehicles' dynamics and the continuously increasing performance requirements give rise to problems which can not be efficiently solved by the classical control theory. In this study, we propose a direct-search optimization approach which leads to solutions which are not so sensitive to modelling errors as those obtained by the classical, gradient-based methods.

2. Time/energy optimal control

Robot point-to-point motion can be efficiently optimized applying a direct-search approach, [1], [2], with the following main steps: 1. Choose a set of appropriate test control functions; 2. Input-output pairing; 3. Solving shooting equations.

The term "appropriate" concerns the structure and the shape of the test control functions. Simple linear-spline control functions of "bang-bang", "bang-pause-bang", or "bang-slope-bang" types can be employed as such forms of the control laws are consistent with Pontryagin's Maximum Principle when a time/energy functional is the performance index.

Among all the control parameters, we find those n mostly effecting the reached final state $F = x(t^f)$. Denote this vector by p^f and make input-output pairing (p_i^f, F_i) in the sense that F_i is most sensitive to p_i^f for any $i = 1, \dots, n$. All the remaining parameters are taken to be components of the vector p^{opt} if the performance index depends, to some extent, on all of them. The proper choice of the control parameters can be done by using a mathematical model, or merely by engineering intuition.

Then, we have to perform the following two-level control synthesis procedure:

first level: with fixed p^{opt} , solve the given boundary value problem transformed into the shooting equation

$$F(p^f) = q^f \quad (3)$$

second level: optimize the performance index with respect to p^{opt} .

3. Existence of feasible solutions

In most practical cases, the reached final state F can be considered as a continuous function of any control parameter vector p . But for Eq.(2) to have a solution, the so-called independent parameter controllability (IPC) condition has to be fulfilled.

Definition 1. A parallelepiped $P = p : p_i \in [p_i^-; p_i^+]$, $i = 1, \dots, n$ is called to be a margin of IPC for V with control parameters p_i , if for any pair of points p and \bar{p} on the boundary of P , symmetrical about the centre of P , $\exists i$ such that $F_i(p)F_i(\bar{p}) < 0$.

As has been proven (see [1]), the IPC-condition is sufficient for the existence of solutions of Eq.(3). This condition is the weakest general condition for solution existence because in the linear case it is also necessary. Applying the non-negative matrix theory, it can be easily proven that a MR can fulfil the IPC-condition if its control transfer matrix $M^{-1}B$ is generalized diagonally dominant. Numerous verifications indicate that this property can take place for any MR having properly located actuators.

In our performance optimization scheme, the algorithms most appropriate for solving the problems at the two stages are those of one- or multi-dimensional bisections. Unlike classical gradient methods, they are globally convergent, robust to modelling errors, optimal as regards the number of trial movements, and natural for implementation in the real control systems. Since the control constraints are inherently satisfied with the choice of the test control functions, we should verify only if the solutions of the given boundary-value problem satisfy the state constraints. The performance optimization is carried out over the set of all feasible solutions.

4. Example: MR having two independently driven wheels

Consider the minimum time control problem. Such a problem for a simple (idealistic) model of MR with independently driven wheels has been solved in [3]. The authors have proven that the optimal controls are "bang-bang" and the total number of switch times for the two driving motors is three when MR orientation at the point of destination is not specified, and this number is four in the other case. We accept these reasonable shape and structure for the test control functions employed in the full-dynamics case.

The input-output pairing in the case when MR orientation at the point of destination is not specified is done as follows. To reach the required final position, we have to control the following two outputs (polar coordinates of a MR reference point): the direction of motion and the distance travelled. Correspondingly, the control parameters are: the first switch time and the mean value of the other two switch times. After the last switch time, the trajectory is linear and MR is decelerating until it stops. As the numerical experiments show, the required values of these control parameters can be easily found after a relatively small number of trial movements. This control learning procedure can be applied on the robot itself for final adjustment of the control parameters.

Acknowledgements

The financial support from the German Research Foundation is gratefully acknowledged.

5. References

- 1 KIRIAZOV, P.: Controllability of a class of dynamic systems, ZAMM 75 (1995) SI, 85–86.
- 2 KIRIAZOV, P. AND SCHIEHLEN, W.: On direct-search optimization of biped walking, CISM Courses, 381, Eds. A. Morecki, G. Bianchi, and C. Rzymkowski, SpringerWienNewYork, (1997), 133–140.
- 3 REISTER, D.B. AND F.G. PIN: Time-optimal trajectories for mobile robots with two independently driven wheels, Int. J. of Robotics Research, Vol. 13, No.1, (1994), 38–54.

Address: ASSOC. PROF. P. KIRIAZOV, Institute of Mechanics, Bulgarian Academy of Sciences, Acad.G.Bonchev Str., bl.4, BG-1113 Sofia, Bulgaria. E-mail: kiriazov@imbm.bas.bg

JANA KONÍČKOVÁ

Sufficient condition of basis stability of an interval linear programming problem

The contribution deals with basis stability of an interval linear programming (ILP) problem. We consider the coefficients of the matrix, right-hand side values and cost vector values to vary independently in the given intervals. We present the new necessary and sufficient condition, and the sufficient condition of basis stability of ILP problem.

1. Introduction

We study a family of linear programming problems

$$\max\{c^T x; Ax = b, x \geq 0\}, \quad (1)$$

$$A \in A^I, b \in b^I, c \in c^I, \quad (2)$$

where $A \in \mathbb{R}^{m \times n}$, $b \in \mathbb{R}^m$ and $c \in \mathbb{R}^n$. An interval matrix A^I is the set $\{A; \underline{A} \leq A \leq \bar{A}\}$. It can be written in the form $A^I = [\underline{A}, \bar{A}] = [A_c - \Delta, A_c + \Delta]$, where $A_c = \frac{1}{2}(\underline{A} + \bar{A})$ is the center matrix of A^I and $\Delta = \frac{1}{2}(\bar{A} - \underline{A})$ is the radius matrix of A^I . The interval vectors b^I , c^I are defined analogously: $b^I = \{b; \underline{b} \leq b \leq \bar{b}\} = [\underline{b}, \bar{b}] = [b_c - \delta, b_c + \delta]$, $c^I = \{c; \underline{c} \leq c \leq \bar{c}\} = [\underline{c}, \bar{c}] = [c_c - \gamma, c_c + \gamma]$. In this paper the new necessary and sufficient condition of basis stability, and the new sufficient condition of basis stability are established.

Definition 1. The problem (1), (2) is called [strongly] *B-stable* (basis stable) with basis B if each problem (1) with data satisfying (2) has a [unique] nondegenerate basic optimal solution with basic variables x_j , $j \in B$.

2. Necessary and sufficient condition of basis stability

We introduce the set $Y = \{y \in \mathbb{R}^m; |y_j| = 1 \text{ for } j = 1, \dots, m\}$, and for each $y \in Y$ we denote by T_y the diagonal matrix with diagonal vector y (i.e. $(T_y)_{ii} = y_i$ for each i and $(T_y)_{ij} = 0$ for $i \neq j$). In addition to the set $Y \subset \mathbb{R}^m$ we introduce also the set $Z_B = \{z \in \mathbb{R}^n; |z_j| = 1 \text{ for } j \in B, z_j = 1 \text{ for } j \notin B, j = 1, \dots, n\}$, so that Z_B has 2^m elements. For each $y \in Y$, $z \in Z_B$ we define the matrices A_{yz} , A_y and the vectors b_y , c_z by

$$\begin{aligned} A_{yz} &= A_c - T_y \Delta T_z, & b_y &= b_c + T_y \delta, \\ A_y &= A_c - T_y \Delta, & c_z &= c_c + T_z \gamma. \end{aligned}$$

Theorem 1 (Rohn, [1]). Problem ILP is [strongly] *B-stable* if and only if for each $y \in Y$, $z \in Z_B$ the linear programming problem $\max\{c_z^T x; A_{yz} x = b_y, x \geq 0\}$ has a [unique] nondegenerate basic optimal solution with basic variables x_j , $j \in B$.

This theorem characterizes basis stability by means of the 2^{2m} linear programming problems. In the following we formulate a new criterion of basis stability.

Theorem 2. The ILP problem is [strongly] *B-stable* if and only if the following conditions are satisfied: (i) system $(A_y)_B x_B = b_y$ has a unique positive solution $(x_y)_B$ for each $y \in Y$, (ii) for each $z \in Y$ the following system has a unique solution p_z :

$$T_z((A_c)_B^T p - (c_c)_B) = \Delta_B^T |p| + \gamma_B, \quad (3)$$

$$(A_c)_N^T p - \Delta_N^T |p| \geq \bar{c}_N, \quad (4)$$

[in system (4) sharp inequality holds]. Assertions in the square brackets are related to the case of strong basis stability.

This theorem is the consequence of the Theorem 1 and of its proof, which is given in [1].

To check the basis stability by means of the above criterion it is necessary to solve the 2^m systems of linear equations $(A_y)_B x_B = b_y$, and the 2^m systems of nonlinear equations (3). These nonlinear systems correspond with

the solution set of the system of interval linear equations $(A_B^T)^I p = c_B^I$. The convex hull of the solution set of this system is equal to the convex hull of the 2^m vectors p_z , which are the solutions of the corresponding nonlinear systems (3). We can use the "sign-accord algorithm" (Rohn, [2]) for computing all vectors p_z . Generally, this algorithm solves the 2^m systems of linear equations to find the vector p_z . In most cases one system only is solved. Also, it is necessary to solve at least the 2^{m+1} systems of linear equations, and the $2^m + 2^{2m}$ systems in the worst case.

3. Sufficient condition of basis stability

Let us denote $X_B = \{x_B; A_B x_B = b, A \in A^I, b \in b^I\}$, $P_B = \{p; A_B^T p = c_B, A \in A^I, c \in c^I\}$. The corresponding interval hulls are denoted by $[x_B, \bar{x}_B]$, $[p, \bar{p}]$. These interval hulls are the exact interval solutions of appropriate system of interval linear equations. The verification of the following sufficient condition is easier than the verification of the necessary and sufficient condition, because it is necessary to compute only the interval hulls of the sets X_B and P_B .

Theorem 3. Let A_B^I be a nonsingular interval matrix. Let $\underline{x}_B > 0$. Let N denote the index set of all nonbasic columns of matrix A^I . Let the inequality

$$\sum_{i=1}^m \min\{a_{ij} p_i, a_{ij} \bar{p}_i, \bar{a}_{ij} p_i, \bar{a}_{ij} \bar{p}_i\} \geq \bar{c}_j \quad (5)$$

hold for each $j \in N$. Then the ILP problem is B -stable with basis B . If the inequality (5) holds sharply, then the ILP problem is strongly B -stable.

Proof. The assumptions of nonsingularity of A_B^I and $\underline{x}_B > 0$ imply that the system $A_B x_B = b, x_B > 0$ has a unique solution for each $A \in A^I, b \in b^I$. Moreover, the nonsingularity of A_B^I implies that the system $A_B^T p = c_B$ has a unique solution for each $A \in A^I, c \in c^I$. We shall show that this solution satisfies $A_N^T p \geq c_N$. In the following relation we use the interval arithmetic:

$$(A^T p)_j = \sum_{i=1}^m a_{ij} p_i \geq \sum_{i=1}^m \min\{a_{ij} p_i, a_{ij} \bar{p}_i, \bar{a}_{ij} p_i, \bar{a}_{ij} \bar{p}_i\} \geq \bar{c}_j \geq c_j$$

holds for each $j \in N$. Hence, it follows from the duality theory and complementary slackness condition of linear programming that each problem (1) under (2) has a nondegenerate basic optimal solution and therefore the ILP problem is B -stable. If the inequality (5) holds sharply, then the previous inequality holds sharply too, which means that each problem (1) under (2) has a unique nondegenerate basic optimal solution, hence the ILP problem is strongly B -stable. The proof is complete.

4. Conclusion

Checking basis stability of ILP problem is important. In basis stable case it is very simple to find the set of all optimal solutions and the set of all optimal values. In this case the set X^* of all optimal solutions of ILP problem is described by means of the system of linear inequalities (Beeck, [3]) $X^* = \{x; \underline{A}_B x_B \leq \bar{b}, \bar{A}_B x_B \geq \underline{b}, x_B \geq 0, x_N = 0\}$. The set of all optimal values of ILP problem is the interval $[f, \bar{f}]$, which can be obtained by solving of two linear programming problems (Beeck, [3]) $\underline{f} = \min\{\underline{c}^T x; x \in X^*\}$, $\bar{f} = \max\{\bar{c}^T x; x \in X^*\}$.

Acknowledgements

This contribution has been supported by GACR grant No. 103/98/P025.

5. References

- 1 ROHN, J.: Stability of the optimal basis of a linear program under uncertainty. *Operations Research Letters* **13** (1993), 9–12.
- 2 ROHN, J.: Systems of linear interval equations. *Linear Algebra and Its Applications* **126** (1989), 39–78.
- 3 BEECK, H.: Linear programming with inexact data. Report TUM-ISU-7830, Technical University, Munich (1978).

Addresses: DR. MGR. JANA KONÍČKOVÁ, Department of Mathematics, Faculty of Civil Engineering, Czech Technical University, Prague, Thákurova 7, 166 29 Praha 6 - Dejvice, Czech Republic

KRAJNC, ALEŠ; BEG, DARKO

A Priori Constraint Elimination

The problem of steel frames optimal design, when it is written in mathematical programming form, gives a moderate number of unknowns and a huge number of constraints. A typical frame has about 50 unknowns and 20000 constraints. The large number of constraints, which are complex functions of many parameters, represents a problem for most non-linear programming solvers. In order to reduce the number of constraints, we developed a method, which eliminates a large portion of constraints without their costly evaluation. The method is based on the problem specific constraints organization, where the constraints are organized into sets. It turns out that we can remove individual constraints from a set by simply comparing constraint parameters.

1. Introduction

The optimization problems from the field of mechanics are always non-linear and complex. They combine two steps that are usually done separately: finite element analysis step and design step. During the finite element analysis we obtain internal forces and displacements. These results serve as a base for the design step, where initial structural dimensions are verified. The form of the design step depends on the structure type and the theory used during the analysis step. In general two approaches are possible: (i) A very detailed material and geometrical non-linear analysis using shell or 3D finite elements. Here, the results only need to be checked against their limit values in the design step. (ii) The finite element analysis using some simplified theory, e.g. beam elements. The results (internal forces and displacements) are then verified using rules from the design codes, e.g. [1].

The first approach has a clear mechanical background and is an obvious choice of the future. Today, unfortunately, it still can not be applied to solve everyday problems in the structural design practice¹. Namely, the modelling of the problem is too complex, the analysis is time consuming and requires high computational power. The second approach has only modest computational requirements, the modelling is easy, the analysis is fast. However, in the design step we have to deal with complex design rules. These rules are the cause for large number of constraints in our problem. Since our *steel frame optimization* problem is practically oriented, we are using the second approach.

Regardless of the approach used, the optimization solution of some mechanical problem is obtained in an iterative procedure where the following steps are taken:

1. Initially, assign some values to the initial solution of the problem and perform full finite element analysis.
2. Evaluate constraint functions and rank them according to criticality. Retain only those constraints that are critical or potentially critical. Only the retained constraints enter into further design cycle.
3. Perform the sensitivity analysis to calculate gradients of retained constraints and objective function.
4. Take the gradients and create an optimization problem. Solve the problem using either general purpose solver (if it could be used) or derive a problem specific solver, e.g. [2].
5. Update the analysis data with the solution obtained by the solver. Perform the the full finite element analysis and evaluate the quality of current design. If the solution has converged, terminate. Otherwise go back to step 2.

As it can be seen from the procedure, the elimination of the constraints is performed in step 2. First all constraints are evaluated, ranked and then selected according to some criterion. E.g. $g_i(\bar{x}) < -0.3$. We call such elimination a posteriori elimination (constraints are eliminated after their evaluation).

2. A Priori Constraint Elimination Background

The constraints in our problem have special organization, which enables us to eliminate them before they are actually evaluated. For one element (steel beam) in the frame, there are a few hundred constraints that come from nine different constraint families. We define a family as a set of constraints that have the same mathematical form, but

¹It can, however, be applied for solving some special engineering problems.

each set element has different parameters. E.g., set $G = \bigcup_{i=1}^n g_i$ has n elements in a form of $g_i(\vec{x}, \vec{p}_i) \leq 0$. Here, \vec{x} represents the vector of optimization unknowns and \vec{p}_i the vector of known parameters.

Mathematically speaking, let us have a set G that holds n constraints of the same function family g , which differ only in their parameters \vec{p} . $G = \{g_1(\vec{x}, \vec{p}_1), g_2(\vec{x}, \vec{p}_2), \dots, g_n(\vec{x}, \vec{p}_n)\}$. Let X denote the set of all feasible solutions of the problem. Let $g(\vec{x}, \vec{p})$ be increasing function for each component of \vec{p} for any fixed $\vec{x} \in X$. In this case $g_a(\vec{x}, \vec{p}_a) > g_b(\vec{x}, \vec{p}_b)$ if and only if $\vec{p}_a > \vec{p}_b$. Using the latter relation, we can build an elimination algorithm for constraints in set G based only on parameters \vec{p} . We can easily extend the validity of the algorithm for constraints that have one or more components p_j of \vec{p} , such that g is decreasing on p_j for any fixed \vec{x} . We can alter the decreasing behavior into an increasing one by introducing a new parameter $\bar{p}_j = -p_j$ that replaces j -th component of the parameter vector \vec{p} .

3. Algorithm

The algorithm below describes the process of the *a priori elimination*:

Input: n constraints $g_i(\vec{x}, \vec{p}_i); i = 1 \dots n$ of the same family.

Output: Sets G^+ and G^- that hold potentially critical and eliminated constraints, respectively.

1. Initialization: $G = \{g_1(\vec{x}, \vec{p}_1), g_2(\vec{x}, \vec{p}_2), \dots, g_n(\vec{x}, \vec{p}_n)\}$, G^- is an empty set. Set G^+ initially holds the first constraint g_1 . Let $i \leftarrow 2$ be an index.

2. Elimination I: Compare g_i with the elements in G^+ . If g_j^+ exists, an element in G^+ , such that corresponding $\vec{p}_j^+ \geq \vec{p}_i$, then \vec{p}_i becomes a new member of G^- and continue with step 4. If this is not the case, g_i will become a member of G^+ , but first we must check the existing elements in G^+ against their possible elimination by \vec{p}_i .

3. Elimination II: For each element in G^+ , let it be denoted by g_j^+ , check the corresponding parameter vector \vec{p}_j^+ for relation $\vec{p}_j^+ \leq \vec{p}_i$. If this is true, take g_j^+ from the set G^+ and put it into set G^- . When all elements in G^+ are checked, put g_i into the set G^+ .

4. Termination: $i \leftarrow i + 1$. Until $i < n$ go back to step 2. Otherwise the algorithm is completed and set G^+ holds critical and potentially critical constraints, while G^- holds the eliminated constraints.

4. Performance & Conclusions

We used the algorithm in many practical calculations and it gave very good results in all cases. The algorithm usefulness is revealed from the following topics:

- There are nine beam related constraint families in our problems. Only one family does not fulfill the *increasing* criterion, and thus we are not able to apply a priori elimination algorithm on it.
- For other eight families, the rate of elimination is up to 99.9% for the simple constraint function and down to 80% for the most complex constraint functions. This is far better than it is obtained by using a posteriori elimination.
- The a priori elimination algorithm is much faster than the evaluation of constraints – we get about 20% shorter overall computation times.
- We are able to eliminate constraints that are almost critical without any risk of being wrong, which is not the case in the a posteriori elimination.
- For complicated constraints we were not able to get an analytical proof for the constraint being an increasing / decreasing function over feasible area X . In such cases, the constraint must be numerically verified.

5. References

- 1 CEN, EUROPEAN COMMITTEE FOR STANDARDISATION: European Prestandard ENV 1993-1-1, Eurocode 3: Design of steel structures, 1992.
- 2 KRAJNC A., BEG D.: Optimal Design of Planar Steel Frames, Fifth Pacific Structural Steel Conference, Seoul (1998), Volume 1, 385–390

Address: DR. ALEŠ KRAJNC, PROF. DARKO BEG: Faculty of Civil and Geodetic Engineering, University of Ljubljana, Jamova 2, SI-1000 Ljubljana, Slovenia; e-mail: ainet@siol.net, dbeg@fgg.uni-lj.si

KUTYŁOWSKI R.

The ε - Relaxed Approach in Topology Optimization for Various ε Functions

The inspiration of this contribution was a paper written by Cheng and Guo [1] where the ε -relaxed approach for structural topology optimization was applied and a second one paper by Duysinx and Bendsoe [2] where continuum structure with stress constraints was considered. In this contribution various ε functions are proposed and discussed for continuum structure from the convergence point of view. The problem is illustrated by FEM examples.

1. Introduction

Generally, the topology optimization gives us an answer: from which regions in the design domain the material must be taken away and where it has to be left. The main goal of this ε -relaxed approach is to eliminate the singular optima from the topology optimization problem formulation. In this paper, by relaxing the mass constraints put on these designed points in which during the optimization process the strain energy is relatively small we modify the shape of the structure within fixed design domain. Based on [3] the variation approach is used. The objective is defined as the total strain energy of the structure. It is minimizing under the constraints put on the mass of the structure. These constraints say that the mass of the structure in j -th step is less or equal to available mass. Available mass is defined as $m_0 = \alpha m$, where α is less than one. The following formulation of the updating the density in every design point is used:

$$E(\rho_i) = E^0 \left(\frac{\rho_i}{\rho^0} \right)^3 \quad (1)$$

where ρ_i is the density in i element, ρ^0 is the initial density equal to the α parameter and E^0 is the initial Young's modulus. The optimization procedure, which was proposed in [4] is used here. This procedure uses the threshold functions to cut the density in the elements with relatively small strain energy. In current paper the threshold function works in the base form (2a) and in the weaken form - eight times less (2b):

$$a) \quad TF = 0.1 j \rho^0, \quad b) \quad TF = 0.0125 j \rho^0 \quad (2)$$

where j means the number of the topology optimization step during the process. The mass constraints are formulated as:

$$0 \leq m_j \leq m_0 \quad (3)$$

where m_0 is the available mass. This can be written globally in FE notation (4a) and for each one element separately with introduced the lower bound of the mass in (4b) form. Finally ε is assumed as the lower bound of the density (4c).

$$a) \quad 0 \leq \sum_{i=1}^N \rho_i V_i \leq \sum_{i=1}^N \rho^0 V_i \quad b) \quad \rho^L V_i \leq \rho_i V_i \leq \rho^U V_i \quad c) \quad \varepsilon = \rho^L \quad (4)$$

2. Formulation of the ε -relaxed functions and FE examples

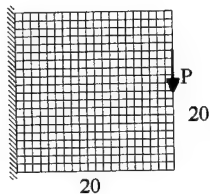


Fig. 1 Benchmark example with finite element mesh

The main problem in this paper is to define in proper way the ε -relaxed functions, to obtain the optimal topology within possible small step number. Clamped cantilever beam loaded by a force P as a benchmark of the problem is considered as an example (Fig.1). The available mass is assumed as $m_0 = 0.3m$, what means that the total mass in this case is 120 for considered finite element mesh (20×20). The figures in this paper are presented in number mode and in colour mode (from white through the shades of grey to black colour). White colour means void, the black colour - material and the shades of grey the intermediate density. In [1, 2] ε was assumed in the ranges from 10^{-3} to 10^{-9} and from 10^{-1} to 10^{-6} respectively. ε was relaxing by for example dividing by two in the subsequent steps. In this paper the following ε -relaxed functions are considered:

$$a) \quad \varepsilon = \text{const.} \quad \varepsilon = \{10^{-4} \dots 10^{-7}\}, \quad b) \quad \varepsilon(j) = \frac{\beta}{j^n}, \quad \beta = 10^{-3} \text{ or } 10^{-4}, \quad (5)$$

$$c) \quad \varepsilon(j) = \frac{10^{-3}}{j^2 + 100j}, \quad d) \quad \varepsilon(j) = \frac{10^{-3}}{0.1j^3 + j^2 + j}, \quad e) \quad \varepsilon(j, \rho^0) = \frac{10^{-3}}{(\rho^0)^2 j^2}.$$

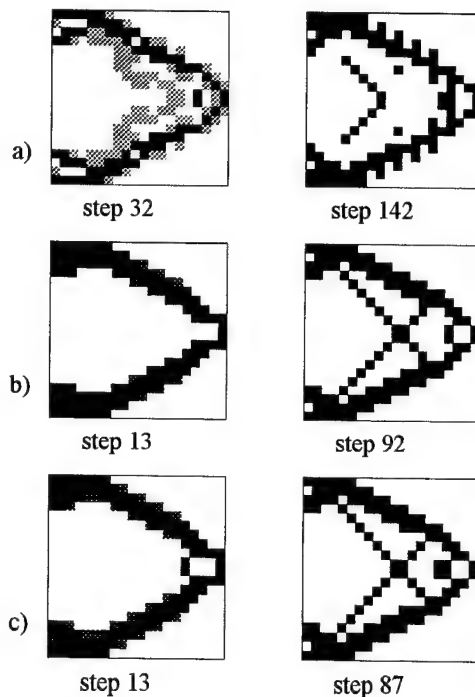


Fig. 2 Topologies for (5a) a) for $\varepsilon = 10^{-4}$,
b) $\varepsilon = 10^{-5}$, c) $\varepsilon = 10^{-7}$

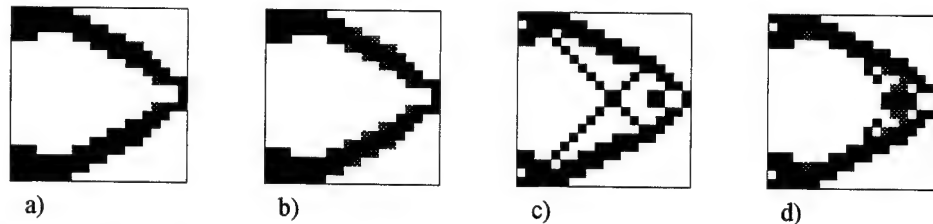


Fig. 4 Topologies for (2b) a) $\varepsilon = 10^{-4}/j$,
step 88, b) $\varepsilon = 10^{-3}/((\rho^0)^2 j^2)$, step 92

Fig. 5 Topologies for (5c) a) and c), for (5d) b) and d) - for (2a) a) and b), for (2b) c) and d)

similar and both pictures are for 12th step. For the same ε functions, but for (2b) threshold functions we have topologies in the Fig. 5c and 5d. Fig. 5c is made for 87th step and Fig. 5d for 81 step. The topologies showed here are made for final optimal step.

3. Conclusion

Most of presented definitions of the ε - relaxed functions let to obtain the optimal topology, in meaning of fulfilling optimality criteria for each one case separately.

4. References

1. CHENG, G.D., GUO, X.: ε - relaxed approach in structural topology optimization; *Structural Optimization*, 1997, 258-266
2. DUYSINX, P., BENDSOE M.P., Topology optimization of continuum structures with local stress constraints; *Int. J. Numer. Meth. Engng*, 1998, 1453-1478.
3. RAMM, E., BLETZINGER, K.-U., REITINGER, R., MAUTE K.: The challenge of structural optimization; *Advances in Structural Optimization* 1994, 27-52
4. KUTYŁOWSKI, R.: On an effective topology procedure; Accepted for publishing in *Structural Optimization* in 2000.

Address: RYSZARD KUTYŁOWSKI, Ph. D., Institute of Civil Engineering, I-14, Wrocław University of Technology, Wyb. Wyspiańskiego 27, PL-50-370 Wrocław, Poland, e - mail: kutyłows@i14odt.iil.pwr.wroc.pl,

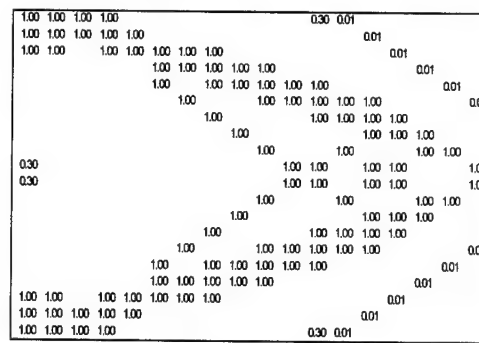


Fig. 3 Topology for $\varepsilon = 10^{-3}/j$ for (2b), step 98

The optimal topology for (5a) definition is presented in the Fig. 2, where on the left side we have the topologies for (2a) threshold function formulation and on the right side for (2b) threshold function (ε is here constant during the process). The best solution is at the

right side ($\varepsilon = 10^{-7}$, step number of the optimal topology is here equal to 87). In the Fig. 3 the topology for $\varepsilon = 10^{-3}/j$ and for (2b) threshold function is presented. In this case as we can see the convergence is not achieved. It is enough to change the power row to -4 and the solution is satisfied (Fig. 4a). If we change ε definition into (5c) we obtain the result as in the Fig. 4b. In the Fig. 5a and 5b we have the final topologies for (2a) threshold function formulation for (5c) and (5d) ε functions. Topologies are very

LINDEMANN, J., BECKER, W.

Optimization of Composite Laminates under Uniaxial Tension with Respect to the Free-Edge Effect

High interlaminar stresses in the vicinity of free edges of composite laminates can result in laminate failure by free-edge delamination. In the current work it is shown in which way the interlaminar normal stress component is reduced by means of structural optimization resulting in laminate configurations with a minor risk of delamination.

1. Introduction

The occurrence of high interlaminar stresses in the immediate vicinity of free edges of composite laminates is a well-known phenomenon which is not taken into account by the classical laminated plate theory (CLPT) [1,2,3]. This so-called 'free-edge effect' may result in a detrimental reduction of the laminate strength because the interlaminar stresses can cause laminate failure by free-edge delamination already before the strength limit predicted by the CLPT is reached. In the present work structural optimization methods are used to reduce the level of the interlaminar normal stress σ_z . For both the example of a quasi-isotropic $[0^\circ / \mp 60^\circ]_s$ - and a $[0^\circ / \pm \alpha / \pm \beta]_s$ -laminate under uniaxial tension a significant reduction of the interlaminar normal stress is achieved.

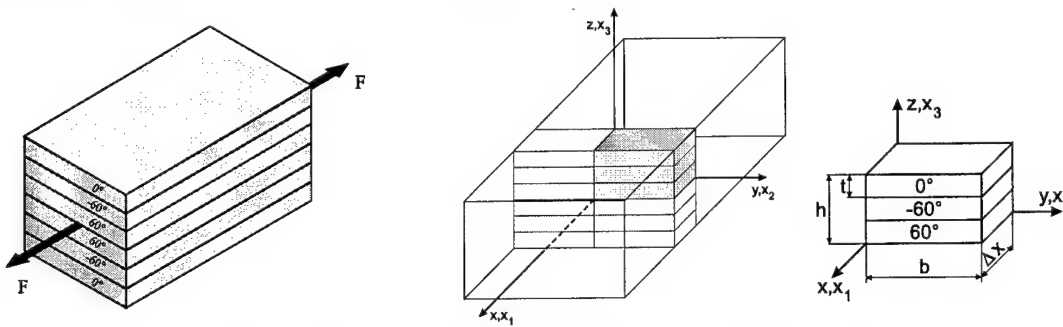


Figure 1: Laminate with considered characteristic quarter-slice

2. Optimization Problem

Subject of consideration are laminates with UD-fiber-reinforced layers under uniaxial tension (fig. 1). The geometry is given by a total laminate width of 50 mm and total height of 2 mm. The load is applied as uniform axial strain of $\varepsilon_x = 0.001$. The structural analyses are performed by three-dimensional finite element analyses with the commercial program MSC/NASTRAN whereby only a characteristic quarter-slice is considered because the field quantities like stresses and strains are independent of the x_1 -direction. Each layer is discretized with 12 layers of 36 20-noded volume elements (coarse mesh) and, for comparison, with 24 layers of 48 elements (fine mesh). The optimization is performed with two different optimization algorithms, a zero order method similar to the method of conjugate search directions and a generalized reduced gradient method. For the example of the quasi-isotropic laminate the orientation angle α of the whole laminate is chosen as design variable resulting in an effective $[0^\circ + \alpha / -60^\circ + \alpha / 60^\circ + \alpha]_s$ -layup. For the second example the design variables are the ply-angles α and β in the $[0^\circ / \pm \alpha / \pm \beta]_s$ -layup for which additionally the ratio of the laminate extensional stiffnesses A_{22} and A_{11} is constrained in order to avoid that all layers get the same orientation: $0.4 \leq A_{22}/A_{11} \leq 1.0$. The design objective in both cases is to minimize the level of the interlaminar normal stress σ_z in order to reduce the tendency to free-edge delamination:

$$f(\alpha) = \sigma_z^2 \rightarrow \min \quad \text{over all elements.} \quad (1)$$

The reason for choosing the square σ_z^2 as objective is that minimizing σ_z would result in a concentrated high compressive stress at the interfaces between two layers at the free edge but, furthermore, in an undesired high tensile stress nearby with a maximum of σ_z that could be detrimental inside the laminate at some distance from the free edge.

3. Optimization Results and Discussion

Algorithm	initial design		final design			
	α_{init}	$f(\alpha_{init})/\text{MPa}^2$	coarse mesh		fine mesh	
			α_{final}	$f(\alpha_{final})/\text{MPa}^2$	α_{final}	$f(\alpha_{final})/\text{MPa}^2$
zero order method	15°	177.725	0.17°	0.865	0.59°	0.916
	75°	376.254	60.02°	0.046	60.02°	0.055
	135°	286.843	120.25°	0.785	120.41°	1.048
generalized reduced gradient	15°	177.725	-1.71°	5.952	0.61°	0.910
	75°	376.254	60.03°	0.046	60.02°	0.055
	135°	286.843	120.12°	0.784	120.41°	1.048

Table 1: Optimization results for the quasi-isotropic laminate

For the case of the quasi-isotropic laminate the results are shown in table 1. In dependence of the initial value α_{init} of the orientation angle the determined optimal orientations are 0°, 60° and 120°, independent of the chosen optimization algorithm and the discretization effort. This indicates that a relatively coarse mesh is sufficient for the optimization whereas a detailed investigation of the stress distribution requires still a finer discretization. A comparison of the stress-results for the initial value of $\alpha = 15^\circ$ and the final design $\alpha = 0^\circ$ shows that the maximum of the interlaminar normal stress σ_z can be reduced by a factor of about 60.

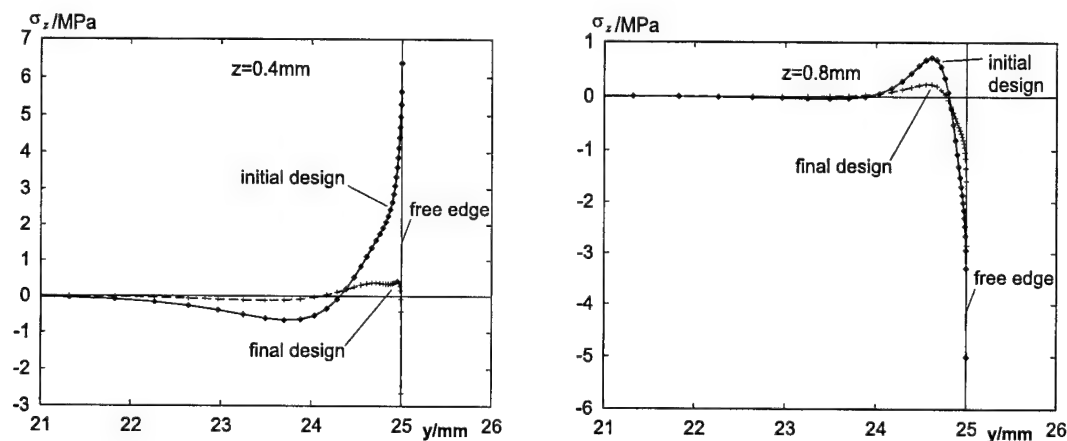


Figure 2: Interlaminar normal stress at the $+\beta/-\alpha$ - and $+\alpha/0^\circ$ -Interface for the initial and final design

In the second example of the symmetric $[0^\circ/\pm\alpha/\pm\beta]_s$ -laminate a quasi-isotropic $[0^\circ/\pm 36^\circ/\pm 72^\circ]_s$ -layup has been chosen as initial design. For the final design $[0^\circ/\pm 48^\circ/\pm 56^\circ]_s$ a significant reduction of the interlaminar normal stress has been achieved, too, as it can be seen e.g. for the interfaces at $z = 0.4\text{mm}$ and $z = 0.8\text{mm}$ (fig. 2).

Acknowledgements

This work has been performed under the financial support of 'Deutsche Forschungsgemeinschaft' under BE 1090/3-1 which is gratefully acknowledged.

4. References

- 1 PIPES, R. B., PAGANO, N. J.: Interlaminar stresses in composite laminates under uniform axial extension. *Journal of Composite Materials* 4 (1970), 538-548.
- 2 HERAKOVICH, C. T.: Free Edge Effects in Composite Laminates. In: *Handbook of Composites*, Vol. 2 - Structure and Design. Elsevier 1989.
- 3 STIFTINGER, M.: Semi-analytical finite element formulations for layered composite shells with consideration of edge effects; *Fortschritt-Berichte VDI Reihe 18*, Nr. 203, VDI-Verlag, Düsseldorf 1996.

Address: JAN LINDEMANN, WILFRIED BECKER, University of Siegen,
Institute of Mechanics and Control Engineering, Paul-Bonatz-Str. 9-11, D-57068 Siegen, Germany

MARTI, KURT

Robust Optimal Control of Robots by means of Stochastic Optimization

1. Robotic systems with random parameters

Modelling a robot through the *dynamic equation*

$$M(p_D, q(t)) \ddot{q}(t) + h(p_D, q(t), \dot{q}(t)) = u(t), \quad t_0 \leq t \leq t_f, \quad q(t_0) = q_0, \dot{q}(t_0) = \dot{q}_0 \quad (1)$$

for the robot coordinates $q(t)$ and the kinematic equation, a main problem is that the vectors p_D, p_K of dynamic, kinematic parameters, but also the vectors p_C, p_J of model parameters in the objective function and in the constraints are random.

2. Control of dynamic systems

In control of dynamic systems, the total input $u = u(t)$, $t_0 \leq t \leq t_f$, is represented by

$$u(t) = u^{(0)}(t) + \Delta u^{(0)}(t), \quad t_0 \leq t \leq t_f, \quad (2)$$

where $u^{(0)} = u^{(0)}(t)$, $t \geq t_0$, is a *feedforward control* based on a certain *reference trajectory* $q^{(0)} = q^{(0)}(t)$, $t \geq t_0$, and $\Delta u^{(0)}(t)$ denotes a *control correction* to compensate the deviation of the system from the reference trajectory.

In order to find an appropriate reference trajectory $q^{(0)} = q^{(0)}(t)$, $t \geq t_0$, and a feedforward control $u^{(0)} = u^{(0)}(t)$, $t \geq t_0$, in case of random model parameters, stochastic optimization methods are applied [1].

2.1 Transformation of the variable time interval onto a fixed s -parameter domain

The variable time interval $[t_0, t_f]$ is transformed first onto a fixed s -parameter interval $[s_0, s_f]$ by using a strictly monotoneous increasing function $s = s(t)$, $t_0 \leq t \leq t_f$, $s_0 \leq s \leq s_f$. The trajectory $q = q(t)$ is given then by

$$q(t) = q_e(s(t)), \quad t_0 \leq t \leq t_f, \quad (3a)$$

where $q_e = q_e(s)$, $s_0 \leq s \leq s_f$, is the **geometric path in configuration space**. Moreover, $s = s(t)$ is the solution of the initial value problem

$$\dot{s}(t) = \sqrt{\beta(s)}, \quad s(t_0) = s_0, \quad t \geq t_0, \quad (3b)$$

where $\beta = \beta(s)$, $s_0 \leq s \leq s_f$, is the **velocity profile**. Hence, the **unknowns** are the functions $q_e(\cdot), \beta(\cdot)$.

3. Optimal stochastic trajectory planning (OSTP)

Determine first an *optimal velocity profile* $\beta^{(0)}(s)$ and an *optimal geometric path* $q_e^{(0)}(s)$, $s_0 \leq s \leq s_f$, by solving a **variational problem** based on a deterministic substitute for the basic stochastic trajectory planning problem, see [1]:

$$\text{minimize}_{\beta(\cdot), q_e(\cdot)} \int_{s_0}^{s_f} E \left(f_0(p_J, s, q_e(s), q'_e(s), q''_e(s), \beta(s), \beta'(s)) | \mathcal{A}_{t_0} \right) ds \quad (4a)$$

s.t.

$$q_e(s_0) = \bar{q}_0^{(0)}, q'_e(s_0) \sqrt{\beta(s_0)} = \bar{q}_0^{(0)}, q_e(s_f) = \bar{q}_f^{(0)}, \beta(s_f) = \beta_f = 0 \quad (4b)$$

$$P \left(q^{\min}(p_C) \leq q_e(s) \leq q^{\max}(p_C) | \mathcal{A}_{t_0} \right) \geq \alpha_q, P \left(\dot{q}^{\min}(p_C) \leq q'_e(s) \sqrt{\beta(s)} \leq \dot{q}^{\max}(p_C) | \mathcal{A}_{t_0} \right) \geq \alpha_{\dot{q}} \quad (4c)$$

$$P \left(u^{\min}(p_C) \leq u_e(p_D, s; q_e(\cdot), \beta(\cdot)) \leq u^{\max}(p_C) | \mathcal{A}_{t_0} \right) \geq \alpha_u, \quad s_0 \leq s \leq s_f. \quad (4d)$$

Note. \mathcal{A}_t denotes the information set up to time $t > t_0$. The function u_e in (4d) is defined by $u_e = u_e(p_D, s; q_e(\cdot), \beta(\cdot)) := F(p_D, q_e(s), \frac{d}{dt}q_e(s), \frac{d^2}{dt^2}q_e(s))$, where $F = F(p_D, q, \dot{q}, \ddot{q})$ denotes the left hand side of the dynamic equation.

Having $\beta^{(0)}(s), q_e^{(0)}(s)$, $s_0 \leq s \leq s_f$, we solve (3b) with $\beta := \beta^{(0)}$ for $s = s^{(0)}(t)$. Define then the optimal reference trajectory $q^{(0)}(t) := q_e^{(0)}(s^{(0)}(t))$ and the optimal feedforward control $\mathbf{u}^{(0)} = \mathbf{u}^{(0)}(t)$, $t \geq t_0$, by "inverse dynamics":

$$u^{(0)}(t) := M(\bar{p}_D^{(0)}, q^{(0)}(t))\ddot{q}^{(0)}(t) + h(\bar{p}_D^{(0)}, q^{(0)}(t), \dot{q}^{(0)}(t)), \quad \bar{p}_D^{(0)} := E(p_D(\omega)|\mathcal{A}_{t_0}). \quad (5)$$

4. On-line control corrections

Due to random variations $\Delta p_D = p_D - \bar{p}_D^{(0)}$ of the model parameters, there is a remaining deviation between the actual trajectory $q(t)$ and the optimal reference trajectory $q^{(0)}(t)$. In order to define a **control correction** (feedback control law)

$$\Delta u(t) := u(t) - u^{(0)}(t) = \varphi(t, q(t) - q^{(0)}(t), \dot{q}(t) - \dot{q}^{(0)}(t)), \quad t \geq t_0, \quad (6)$$

with a function $\varphi = \varphi(t, \Delta q, \dot{\Delta}q)$ such that $\varphi(t, 0, 0) = 0$, $t \geq t_0$, the trajectories $q(t), q^{(0)}(t)$, $t \geq t_0$, are embedded into a one-parameter family (homotopy) $q = q(t, \epsilon)$, $t \geq t_0, 0 \leq \epsilon \leq 1$, of the trajectories, related to the **perturbed** vectors $p_D(\epsilon) := \bar{p}_D^{(0)} + \epsilon \Delta p_D$, $q_0(\epsilon) := \bar{q}_0 + \epsilon \Delta q_0$, $\dot{q}_0(\epsilon) := \bar{\dot{q}}_0 + \epsilon \dot{\Delta}q_0$, $0 \leq \epsilon \leq 1$, of model parameters and initial values, such that $q(t, 0) = q^{(0)}(t)$, $q(t, 1) = q(t)$, $t \geq t_0$. The tracking error

$$\Delta q(t) = q(t) - q^{(0)}(t) = \int_0^1 \frac{\partial q}{\partial \epsilon}(t, \epsilon) d\epsilon = \sum_{l=1}^{\nu=1} \frac{1}{l!} d^l q(t) + R_\nu(t), \quad \text{with } d^l q(t) := \frac{\partial^l q}{\partial \epsilon^l}(t, 0), \quad l \geq 1, \quad t \geq t_0, \quad (7)$$

can be computed by means of Taylor expansion of $q = q(t, \epsilon)$ with respect to ϵ at $\epsilon = 0$. Then, based on the expansion of $\Delta q(t)$, **with some stability requirements**, also the coefficients of the corresponding Taylor expansion

$$\varphi(t, \Delta q, \dot{\Delta}q) = \sum_{l=1}^{\infty} \frac{1}{l!} D_z^l \varphi(t, 0) \cdot (\Delta q, \dot{\Delta}q)^l \quad \left(\text{with } D_z^l \varphi(t, z) := \frac{\partial^l \varphi}{\partial z^l}(t, z) \right) \quad (8)$$

of the feedback control law $\varphi = \varphi(t, \Delta z)$ with respect to $\Delta z = (\Delta q, \dot{\Delta}q)$ at $\Delta z = 0$ can be determined [2].

5. Reduction of the on-line correction expenses by (OSTP)

Since $E(\Delta p_D(\omega)|\mathcal{A}_{t_0}) = 0$, for the 1st order error term $dz(t) = (dq, \dot{dq})$ we have, with a stability matrix A , see [2]:

Theorem 5.1. *First order stability in the mean.* $E(dz(t)|\mathcal{A}_{t_0}) = e^{A(t-t_0)} \Delta z_0 \rightarrow 0$, $t \rightarrow \infty$.

For the *mean absolute deviation* $\delta(dz(t)|\mathcal{A}_{t_0}) := E(\|dz(t) - E(dz(t)|\mathcal{A}_{t_0})\| | \mathcal{A}_{t_0})$ of $dz = dz(t)$ follows:

Theorem 5.2. $\delta(dz(t)|\mathcal{A}_{t_0}) \leq \int_{t_0}^t \|e^{A(t-\tau)}\| \cdot \|M^{(0)}(\tau)^{-1}\| \sigma_{u_e}(s^{(0)}(\tau)) d\tau$, where $\sigma_{u_e}(s^{(0)}(t))$ is the *generalized variance of the feed forward control* $u^{(0)}(t)$, and $M^{(0)}(t) := M(\bar{p}_D^{(0)}, q^{(0)}(t))$. Thus, according to the *minimality/boundedness of the 1st order expansion term of the tracking error*, the on-line correction expenses are reduced.

6. References

- 1 MARTI, K.: Path Planning for Robots under Stochastic Uncertainty. *Optimization* **45** (1999), 163–195.
- 2 MARTI, K.: Adaptive Optimal Stochastic Trajectory Planning and Control (AOSTPC) for Robots. UniBw München, 2000, to appear.

Addresses: PROF. DR. KURT MARTI, Federal Armed Forces University, Aero-Space Engineering and Technology, 85577 Neubiberg/Munich, Germany.

MECKBACH, S.; EHRENSTEIN, G.W.

Erweitertes Optimierungsverfahren für den Spritzgießprozess

Zur Prozessoptimierung beim Spritzgießen wird ein Betriebspunkt bestimmt, an dem vorgegebene Eigenschaften der Teile eingehalten werden und der Prozess unempfindlich gegen Störungen ist. Das vorgestellte Optimierungskonzept basiert auf Antwortflächen, welche durch Scattered Data Interpolation Methoden erzeugt werden. Probleme die im Zusammenhang mit der Wahl des geeigneten Interpolationsmodells auftreten werden diskutiert.

1. Einleitung

Zur Gewährleistung eines stabilen Herstellungsprozesses werden heute bereits im Vorfeld der Produktion qualitäts-sichernde Maßnahmen ergriffen. Eine wichtige Anforderung ist nicht nur die genaue Einhaltung der Formteilspezifikationen, sondern das genaue Einhalten der Zielgrößen mit einer möglichst geringen Streuung [1, 7]. Durch eine Offline-Prozessoptimierung wird vor Beginn der Produktion ein robuster Betriebspunkt bestimmt. Für diesen gilt, dass am Punkt selbst und in einem Bereich um diesen, dem sogenannten Betriebsfenster, die Streuung der Zielgrößen gering ist und gleichzeitig die Formteilspezifikationen eingehalten werden. Ein solches Betriebsfenster wird als robustes Betriebsfenster bezeichnet.

2. Prozessanalyse und -optimierung

Die vorgestellte Methode der Offline-Prozessoptimierung basiert auf Antwortflächen. Ausgehend von Versuchen an ausgewählten Stützstellen im Maschinenparameterbereich wird eine Funktion konstruiert, welche Auskunft über den potentiellen Wert der Qualitätsmerkmale an allen Parameterkombinationen gibt. Anstelle der bisher gängigen Regressionsmethoden werden die Antwortflächen mithilfe von Interpolationsmodellen basierend auf radialen Basisfunktionen [5] konstruiert. Aufgrund ihrer einfachen Darstellung und großen Variabilität werden Multiquadrics [3] bevorzugt. Sind $x_i \in \mathbb{R}^k, i = 1, \dots, N$, die Stützstellen im k -parametrischen Betriebsraum und soll an den Stützstellen x_i der Wert p_i angenommen werden, so wird mittels Multiquadrics die Antwortfläche analytisch durch eine Funktion der Gestalt

$$f(x) = \sum_{i=1}^N a_i \phi(\|x - x_i\|)$$

gegeben mit $\phi(r) = \sqrt{c^2 + r^2}, c \in \mathbb{R}$. Die Koeffizienten a_i bestimmen sich aus den Bedingungen $f(x_i) = p_i, i = 1, \dots, N$. Hierbei ist die reelle Zahl c geeignet zu wählen. Im Falle, dass durch die Interpolation eine bekannte Funktion angenähert werden soll, liefert [4] eine Methode zur Wahl des Parameters c . Im allgemeinen ist kein funktionaler Zusammenhang zwischen den Parameterkombinationen und der Ausprägung der Qualitätsmerkmale bekannt (beispielsweise bei der Standardabweichung). Daher ist zur Prozessoptimierung diejenige Interpolationsfunktion am besten geeignet, welche zwischen den Stützstellen möglichst direkt verläuft. Dies erfordert eine Methode zur Beurteilung der Welligkeit einer Fläche. Es zeigt sich, dass das Integral der mittleren Krümmung über den untersuchten Parameterbereich ein geeignetes Maß ist, welches aber im Falle von mehr als zwei Parametern recht aufwendig zu berechnen ist. Eine einfachere Möglichkeit liefert im Falle von zwei Parametern die Minimierung des Energiefunktional

$$E := \int \int \left[\left(\frac{\partial^2 f(x, y)}{\partial x^2} \right)^2 + 2 \left(\frac{\partial^2 f(x, y)}{\partial x \partial y} \right)^2 + \left(\frac{\partial^2 f(x, y)}{\partial y^2} \right)^2 \right] dx dy, \quad (1)$$

wobei auch hier das Integral über den untersuchten Parameterbereich gebildet wird. Das Energiefunktional lässt sich problemlos in den höherdimensionalen Raum verallgemeinern und wird dann als Rauheitsmaß bezeichnet [2]. Schwierigkeiten bereitet bei der Interpolation mit Multiquadrics, dass für zu hohe Werte von c numerische Instabilitäten auftreten. Diesen kann begegnet werden, indem man mithilfe des Integrals (1) prüft, für welche Werte von c die Interpolationsfläche eine geringe Welligkeit aufweist ohne dass der stabile Bereich verlassen wird. Die Abbildung 1 zeigt den Verlauf des Wertes des Integrals (1) in Abhängigkeit von c .

Zur Optimierung der Prozessrobustheit ist ein Betriebspunkt zu bestimmen, an dem vorgegebene Sollwerte und Toleranzen eingehalten werden, die Standardabweichungen möglichst gering bzw. die sogenannten SN-Kennzahlen

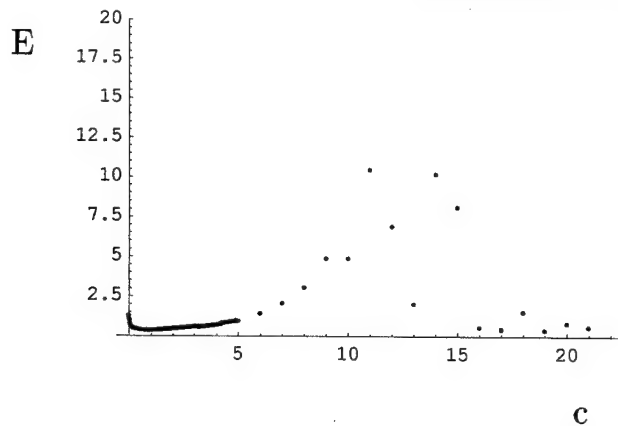


Abbildung 1: Werte des Integrals (1) in Abhängigkeit von c

[6] möglichst groß sind; zudem sollen diese Bedingungen auch in einem Betriebsfenster vorgegebener Größe um den Punkt erfüllt sein, damit Schwankungen der Maschinenparameter aufgefangen werden können. Anstatt dieses Problem wie bisher üblich durch Kombination der Zielfunktionen auf ein eindimensionales Optimierungsproblem zu reduzieren, setzen wir für die zu optimierenden Größen untere bzw. obere Schranken fest. Für die Parameterkombinationen, an denen keine Messwerte vorliegen, werden die durch Interpolation gewonnenen Näherungswerte als Grundlage gewählt. Das Optimierungsverfahren selbst verläuft so, dass die Schnittmenge aller Punkte festgestellt wird, in denen die Kriterien jeweils im ganzen Betriebsfenster um den Punkt erfüllt sind. Reduziert sich die Schnittmenge auf einen einzigen Punkt ist das Optimierungsverfahren erfolgreich abgeschlossen; der Punkt wird als robuster Betriebspunkt gewählt. Erfüllen mehrere Punkte alle Bedingungen, so kann man entweder durch Verschärfung der Kriterien und nochmaligem Durchlaufen des Optimierungsverfahrens zu einem einzigen robusten Punkt gelangen oder man wählt den Punkt mit dem größtmöglichen robusten Betriebsfenster. Findet sich kein robuster Punkt, so muss das Verfahren mit gelockerten Kriterien oder verkleinertem Betriebsfenster nochmals durchlaufen werden.

Für zwei und drei Parameter wurde das Verfahren in einem PC-lauffähigen Programm realisiert. Durch Darstellungen in farbigen Grafiken werden dem Benutzer Hilfestellungen bei der Verschärfung oder Lockerung der Kriterien gegeben.

Acknowledgements

Die Autoren danken der Deutschen Forschungsgemeinschaft (DFG) für die finanzielle Unterstützung der Arbeit.

3. References

- 1 BOURDON, R.: Zur Optimierung der Prozeßrobustheit. Dissertation, Universität Erlangen-Nürnberg (1994).
- 2 DYN, S.: Interpolation of scattered data by radial functions. In: Chui, C., Schumaker, L. Utreras, F. (eds.): Topics in Multivariate Approximation (1987), 47-61
- 3 HARDY, R.L.: Multiquadric equations of topography and other irregular surfaces. J. Geophysical Res. **76** (1971), 1905-1915
- 4 RIPPA, S.: An algorithm for selecting a good value for the parameter c in radial basis function interpolation. Advances in computational Mathematics. **11** (1999)2,3, 193-210
- 5 SCHABACK, R.: Multivariate Interpolation and Approximation by Translates of a Basis Funktion. In: Chui, C., Schumaker, L. (eds.): Approximation Theory VIII, Vol. 1: Approximation and Interpolation, World Scientific Publishing Co. (1995)
- 6 TAGUCHI, G.: Systems of Experimental Design (Vol. 1,2). American Supplier Institute, Dearborn/Michigan, USA (1987)
- 7 WORTBERG, J.: Qualitätssicherung in der Kunststoffverarbeitung. Carl Hanser Verlag, München, Wien (1996)

Addresses: DR. S. MECKBACH, PROF. DR.-ING., DR. H.C. G.W. EHRENSTEIN, Lehrstuhl für Kunststofftechnik, Am Weichselgarten 9, 91058 Erlangen-Tennenlohe

MIKULSKI, L.

Querschnittsoptimierung unter mehrfacher Belastung

Mit Hilfe des Maximumprinzips kann gezeigt werden, daß die Optimierung der durchlaufenden Träger, die simultan verschiedene Belastungsfälle aushalten, und dabei die maximale Spannung (Verschiebung) minimal halten, ein Mehrpunktrandwertproblem (MPRWP) ist. Die maximale Spannung (Verschiebung) soll unter verschiedenen Nebenbedingungen minimal sein $J(U) = \min_U \{ \max_x \sigma_x \}$. Als Steuervariablen wird die Höhe des rechteckigen Querschnitts und auch die Lage der Unterstützungspunkte gewählt. Durch die Einführung des Steuerungsparameter p kann das Zielfunktional auf das Mayerischesproblem zurückgeführt werden. Das erhaltene Mehrpunktrandwertproblem mit Dimension 161 kann mit Hilfe des Dircolprogramm gelöst werden.

1. Der durchlaufende Träger für verschiedene Belastungsfälle

In dieser Arbeit widmen wir uns der Gestaltoptimierung von durchlaufenden Trägern, die simultan verschiedene Belastungsfälle aushalten, und dabei die maximale Verschiebung b.z.w. die maximale Spannung minimal halten.

Wir betrachten einen durchlaufenden Träger, der an einem Ende eingespannt und am anderen frei drehbar ist. Außerdem besitzt er drei innere Unterstützungen ξ_{pi} . Wir betrachten zehn verschiedene Belastungsfälle [3]:

- Belastungsfall I: Der Träger ist durch sein Eigengewicht belastet, und die Felder von 0 bis l sind mit der konstanten Belastung q_0 versehen.
- Belastungsfall II: Der Träger ist durch sein Eigengewicht belastet, und das Feld von 0 bis ξ_{p1} ist mit der konstanten Belastung q_0 versehen.
- Belastungsfall III: Der Träger ist durch sein Eigengewicht belastet, und das Feld von ξ_{p1} bis ξ_{p2} ist mit der konstanten Belastung q_0 versehen.
- Belastungsfall IV: Der Träger ist durch sein Eigengewicht belastet, und das Feld von ξ_{p2} bis ξ_{p3} ist mit der konstanten Belastung q_0 versehen.
- Belastungsfall V: Der Träger ist durch sein Eigengewicht belastet, und das Feld von ξ_{p3} bis l ist mit der konstanten Belastung q_0 versehen.
- Belastungsfall VI: Der Träger ist durch sein Eigengewicht belastet, und die Felder von ξ_{p1} bis ξ_{p2} sowie ξ_{p3} bis l sind mit der konstanten Belastung q_0 versehen.
- Belastungsfall VII: Der Träger ist durch sein Eigengewicht belastet, und die Felder von 0 bis ξ_{p1} sowie ξ_{p2} bis ξ_{p3} sind mit der konstanten Belastung q_0 versehen.
- Belastungsfall VIII: Der Träger ist durch sein Eigengewicht belastet, und die Felder von 0 bis ξ_{p2} sowie ξ_{p3} bis l sind mit der konstanten Belastung q_0 versehen.
- Belastungsfall IX: Der Träger ist durch sein Eigengewicht belastet, und die Felder von ξ_{p1} bis ξ_{p3} sind mit der konstanten Belastung q_0 versehen.
- Belastungsfall X: Der Träger ist durch sein Eigengewicht belastet, und die Felder von 0 bis ξ_{p1} sowie ξ_{p2} bis l sind mit der konstanten Belastung q_0 versehen.

Jedem der zehn Belastungsfälle wird ein Satz von Zustandsdifferentialgleichungen zugeordnet mit Zuständen y_1, y_2, y_3, y_4 für den Belastungsfall I, mit Zuständen y_5, y_6, y_7, y_8 für den Belastungsfall II, mit den Zuständen $y_9, y_{10}, y_{11}, y_{12}$ für den Belastungsfall III, mit den Zuständen $y_{13}, y_{14}, y_{15}, y_{16}$ für den Belastungsfall IV, mit den Zuständen $y_{17}, y_{18}, y_{19}, y_{20}$ für den Belastungsfall V, mit den Zuständen $y_{21}, y_{22}, y_{23}, y_{24}$ für den Belastungsfall VI, mit den Zuständen $y_{25}, y_{26}, y_{27}, y_{28}$ für den Belastungsfall VII, mit den Zuständen $y_{29}, y_{30}, y_{31}, y_{32}$ für den Belastungsfall VIII, mit den Zuständen $y_{33}, y_{34}, y_{35}, y_{36}$ für den Belastungsfall IX, mit den Zuständen $y_{37}, y_{38}, y_{39}, y_{40}$ für den Belastungsfall X. Dabei repräsentieren $y_1, y_5, y_9, y_{13}, y_{17}, y_{21}, y_{25}, y_{29}, y_{33}, y_{37}$ die Verschiebungen, $y_2, y_6, y_{10}, y_{14}, y_{18}, y_{22}, y_{26}, y_{30}, y_{34}, y_{38}$ die Winkel $y_3, y_7, y_{11}, y_{15}, y_{19}, y_{23}, y_{27}, y_{31}, y_{35}, y_{39}$ die Biegemomente $y_4, y_8, y_{12}, y_{16}, y_{20}, y_{24}, y_{28}, y_{32}, y_{36}, y_{40}$ die Querkraften.

2. Das Mehrpunktrandwertproblem für den durchlaufenden Träger (MPRWP)

Als Steuerung betrachten wir die normierte Höhe des rechteckigen Trägers $U = \frac{h}{h_0}$. Die Steuervariable wird nun so

bestimmt, daß die maximale Verschiebung (Spannung) minimal wird [2]

$$J(U) = p = \{ \max_{\xi \in [0,1]} |y_1| + \max_{\xi \in [0,1]} |y_5| + \max_{\xi \in [0,1]} |y_9| + \max_{\xi \in [0,1]} |y_{13}| + \max_{\xi \in [0,1]} |y_{17}| + \max_{\xi \in [0,1]} |y_{21}| + \max_{\xi \in [0,1]} |y_{25}| + \max_{\xi \in [0,1]} |y_{29}| + \max_{\xi \in [0,1]} |y_{33}| + \max_{\xi \in [0,1]} |y_{37}| \}. \quad (1)$$

wobei zusätzliche Beschränkungen berücksichtigt werden. Die resultierende Optimierungsaufgabe hat die Form : $\min_U J(U)$ mit den Nebenbedingungen:

$$\begin{aligned} \text{Differentialgleichung} \quad & y'_i = f[y_i(\xi), U(\xi)] \quad i = 1 \dots 41, \\ \text{Vorgegebene Randwerte und innere Punktbedingungen} \\ & y_i(\xi_{pj}) = 0 \quad i = 1, 5, 9, 13, 17, 21, 25, 29, 33, 37 \quad j = 1, 2, 3, \\ & y_k(\xi_{pj}^+) = y_k(\xi_{pj}^-) + D_{j,k} \quad k = 4, 8, 12, 16, 20, 24, 28, 32, 26, 40, \\ \text{Steuerbeschränkungen} \quad & U_1 \leq U(\xi) \leq U_2 \quad , \quad \int_0^1 U(\xi) d\xi = V_0, \\ \text{Zustandsbeschränkungen} \quad & G(y_i, p) \geq 0. \end{aligned} \quad (2)$$

Die Theorie der optimalen Steuerung liefert notwendige Bedingungen [1], [4] für eine optimale Lösung des Problems. Es wird die Hamiltonfunktion H mit den adjungierten Variablen $\lambda_i(\xi)$ eingeführt. Die adjungierten Variablen genügen auf nicht-zustandsbeschränkten Bögen den Differentialgleichungen $\lambda'_i = -H_{y_i}$ und es gelten die natürlichen Randbedingungen. Die Steuerung wird aus dem Minimumprinzip bestimmt. Die freie Steuerung $U(\xi)$ bestimmt sich aus $H_U = 0$. Für Intervalle mit aktiver Steuerbeschränkung bestimmt sich die Randsteuerung $U(\xi)$ zu $G(y_i, p) = 0$. An einem Unterstützungspunkt ξ_{pi} sind die Gleichungen (3) erfüllt.

$$\begin{aligned} \lambda_j(\xi_{pi}^+) &= \lambda_j(\xi_{pi}^-) + B_j \quad j = 1, 5, 9, 13, 17, 21, 25, 29, 33, 37 \quad i = 1, 2, 3 \\ H(\xi_{pi}^+, y, \lambda, U) &= H(\xi_{pi}^-, y, \lambda, U) + \sigma_i \quad i = 1, 2, 3 \\ H(\xi_{pi}^+, y, \lambda, U) &= H(\xi_{pi}^-, y, \lambda, U) \quad (\text{die Lage der Unterstützungspunkte wird mitoptimiert}) \end{aligned} \quad (3)$$

Die Optimalsteuerungsaufgabe führt auf ein mehr-dimensionales Mehrpunkttrandwertproblem mit zusätzlichen Schaltpunkten ξ_i und vielen Sprüngen der Zustandsgrößen und der adjungierten Variablen. Diese Aufgabe wurde numerisch mit einer leistungsfähigen direkten Lösungsmethode dem Kollokationsverfahren DIRCOL [5] gelöst. Die Berechnungen entsprechen einem durchlaufenden Träger mit folgenden Ausmaßen: die Länge $l = 4 \cdot 7.2 = 28.8$ m, die Belastung $q_0 = 7.0 \frac{KN}{m^2}$, Elastizitätsmodul $E = 19200 \cdot 10^3$, von den Bodeneigenschaften abhängige Konstante $k = 50000.0 \frac{KN}{m^2}$. Für den durchlaufenden Träger mit drei inneren Unterstützungen $\xi_{p1}, \xi_{p2}, \xi_{p3}$ und zehn Belastungsfällen hat das Mehrpunkttrandwertproblem die Dimension 161 [3].

Tab. 1. MPRWP für den durchlaufenden Träger

Zustandsvariablen $y_i(\xi)$	Adjungiertenvariablen λ_i	$\mu(\xi)$	$D_{j,k}$	B_j	ξ_i	Zielfunktion	MPRWP
$y_i(\xi) \quad i = 1..41$	$\lambda_i(\xi) \quad i = 1..41$	1	30	30	18	$0.118355 \cdot 10^{-3}$	161

3. References

- 1 BULIRSCH, R.: Die Mehrzielmethode zur numerischen Lösung von nichtlinearen Randwertproblemen und Aufgaben der optimalen Steuerung, Report, Carl-Cranz Gesellschaft, 1971.
- 2 BULIRSCH, R., F. MONTRONE, H. J. PESCH: Abort Landing in the Presence of a Windshear as a Minimax Optimal Control Problem Part:1 Necessary Conditions. Journal of Optimization Theory and Applications 70 pp. 1-23 (1991 A).
- 3 MIKULSKI, L.: Optymalne kształtowanie sprężystych układów prętowych, Monografia PK 259, Kraków 1999, PL ISSN 0860-097X, 1-249.
- 4 PESCH, H. J.: A Practical Guide to the Solution of Real-Life Optimal Control Problems. Control and Cybernetics, 23, 1/2 (1994), 7-60.
- 5 STRYK, O. VON: User's Guide DIRCOL A Direct Collocation Method For The Numerical Solution Of Optimal Control Problems. Technische Universität München, Zentrum Mathematik, Version 2.1 November 1999.

Addresses: DR. -ING. LESZEK MIKULSKI, Technische Universität Krakau, Institut für Baumechanik PL-31-155 Kraków, Warszawska 24, email- mikul@optra.wil.pk.edu.pl.

RIJPKEMA, J.J.M.; SCHOOF, A.J.G.; ETMAN, L.F.P.

RSM Based Design Optimization

Response Surface Models (RSM) based on data from designed numerical experiments are useful as approximation models in Engineering Optimization. Their construction can be enhanced by the inclusion of design sensitivity data. In this short paper we discuss two strategies to accomplish this. We compare both strategies in a numerical example and draw some general conclusions regarding their practical value.

1. Introduction

Response Surface Models (RSM) can be constructed successfully from data generated by numerical models [4], though implicit statistical assumptions may be disputed with data from deterministic numerical models [3]. The RSM's obtained are useful as approximation models in Engineering Optimization. On a global scale they may identify promising regions in design space for optimal designs. Furthermore, polynomial functions, often used for RSM's, tend to average out non-smooth response behavior, preventing from premature convergence of optimization algorithms to local extremes. On a local- or mid-range scale RSM's may be too inflexible to capture detailed local functional behavior and a subsequently adapted approach should be considered. After an optimum has been found, RSM's build around the optimum can be used to investigate the effect of changes in the design variables without the need to rerun the full analysis. This is profitable with e.g. Multidisciplinary Optimization, MDO.

2. Strategies to augment RSM's with design sensitivities

Regression techniques for RSM-construction are well known [2]. They start from a postulated relation between the dependent variable, y , and the n independent variables, \mathbf{x} , which is linear in the k model parameters β for linear regression. To include design sensitivity information relations for partial derivatives can be added, resulting in:

$$y(\mathbf{x}) = \mathbf{f}^T(\mathbf{x}) \cdot \beta + \epsilon_1, \quad \frac{\partial y(\mathbf{x})}{\partial x_i} = \frac{\mathbf{f}^T(\mathbf{x})}{\partial x_i} \cdot \beta + \epsilon_{i+1} \quad i = 1, \dots, n, \quad (1)$$

with approximation errors ϵ_i . Relations (1) can be summarized as: $\mathbf{u}(\mathbf{x}) = \mathbf{F}^T(\mathbf{x}) \cdot \beta + \epsilon$.

To train the model an experimental design is determined, with points in design space for which (numerical) experiments have to be carried out. Principles from statistical Design of Experiments [1] may be used to limit the number of training sites, N . When all information has been collected, experimental data for response and sensitivities at all training sites are compared with their respective model predictions. Relations (1) for individual training sites, \mathbf{x}_j , may be combined into an overall matrix equation: $\tilde{\mathbf{u}} = \mathbf{G} \cdot \beta + \tilde{\epsilon}$, from which model parameters can be estimated. Matrix \mathbf{G} is the so called *design matrix*, which contains all model information.

As response quantities and their sensitivities have different (physical) dimensions, weighting factors must be used to express their relative importance. This can be achieved through a Weighted Least Squares approach (WLS) [2]. With an appropriate weighting matrix \mathbf{B} and a design matrix \mathbf{G} estimates for the model parameters follow from:

$$\hat{\beta} = (\mathbf{G}^T \cdot \mathbf{B} \cdot \mathbf{G})^{-1} \cdot \mathbf{G}^T \cdot \mathbf{B} \cdot \mathbf{y}. \quad (2)$$

A common choice for \mathbf{B} is the inverse of the covariance matrix of the experimental data. Assuming independent results between the N training sites and equal covariance matrices, \mathbf{V} , at individual training sites it reduces to:

$$\mathbf{B} = [\text{Cov}(\tilde{\mathbf{u}})]^{-1} = (\mathbf{I}_{N \times N} \otimes \mathbf{V}_{n+1 \times n+1})^{-1} = \mathbf{I}_{N \times N} \otimes \mathbf{V}_{n+1 \times n+1}^{-1}. \quad (3)$$

An estimate of the covariance matrix, \mathbf{V} , can be determined from the experimental data:

$$\hat{\mathbf{V}} = \frac{1}{N-k} \sum_{j=1}^N (\mathbf{u}(\mathbf{x}_j) - \mathbf{F}^T(\mathbf{x}_j) \cdot \beta) \cdot (\mathbf{u}(\mathbf{x}_j) - \mathbf{F}^T(\mathbf{x}_j) \cdot \beta)^T. \quad (4)$$

In this so called *covariance oriented* approach correlations between responses and sensitivities are taken into account. An alternative is the so called *variance oriented* approach, where \mathbf{V} is assumed to be diagonal. Elements follow

from corresponding diagonal elements in (4) and represent variances of the data considered. For both approaches an iterative procedure of estimation should be employed as model parameters both depend on and influence the weighting matrix through $\hat{\mathbf{V}}$. Once convergence has been reached the estimated model parameters can be used to predict both responses and sensitivities for other designs, \mathbf{x} .

3. Numerical example

To compare both methods, they are applied to a simple two-variable analytical test function:

$$f(\mathbf{x}) = 2 + 4x_1 + 4x_2 - x_1^2 - x_2^2 + a \cdot \sin(bx_1) \cdot \sin(bx_2) \quad 0.5 \leq x_1, x_2 \leq 3.5. \quad (5)$$

Parameter choices are restricted to three representative cases, namely $a = 0.5$; $b = 2$ (smooth behavior), $a = 2$; $b = 2$ (smoothly fluctuating behavior) and $a = 0.5$; $b = 10$ (strongly fluctuating behavior). For all three cases two training designs are used to train a full quadratic model: a 2^2 -classical design with factor levels $\{0.5, 3.5\}$ and a 3^2 -classical design with factor levels $\{0.5, 2, 3.5\}$. Once model parameters are estimated, they are used to generate model predictions for both responses and sensitivities on a regular 101×101 grid in the design space considered. The average squared difference between these model predictions and the exact values from the analytical test function (5) is used as an Empirical Integrated Squared Error criterion. These values are summarized in the following table, together with results for a standard Least Squares (LS) approach on response data.

Method	$a = 0.5; b = 2$		$a = 2; b = 2$		$a = 0.5; b = 10$	
	f	$\partial f / \partial x$	f	$\partial f / \partial x$	f	$\partial f / \partial x$
LS (3^2 -design)	$7.82 \cdot 10^{-2}$	$2.75 \cdot 10^{-1}$	1.25	4.39	$6.84 \cdot 10^{-2}$	6.26
WLS (variance; 2^2 -design)	$1.06 \cdot 10^{-1}$	$2.54 \cdot 10^{-1}$	1.67	4.06	3.74	7.73
WLS (variance; 3^2 -design)	$6.49 \cdot 10^{-2}$	$2.56 \cdot 10^{-1}$	1.04	4.10	$7.11 \cdot 10^{-2}$	6.26
WLS (covariance; 3^2 -design)	$6.20 \cdot 10^{-2}$	$2.50 \cdot 10^{-1}$	$9.92 \cdot 10^{-1}$	4.01	$6.56 \cdot 10^{-2}$	6.26

Comparing results for the 3^2 -designs indicates that inclusion of sensitivity information in the smooth and the smoothly fluctuating case leads to an improvement of the RSM-models for the response, f , with the covariance-oriented WLS-approach being slightly superior. However, in the smoothly fluctuating case a second order polynomial function seems inadequate to capture the real functional behavior. In the strongly fluctuating case gains are small or even absent. RSM-models for sensitivities, $\partial f / \partial x$, perform poorly in all but the smooth case. In fact, the second order polynomial function used is not capable to capture the real behavior of these sensitivities properly.

Including sensitivity information in the model training makes it possible to reduce the necessary number of training sites, improving the efficiency of model training. Its practical implication is illustrated by comparing results from the standard LS approach on a 3^2 -design with those from the variance oriented WLS approach on a 2^2 -design. Results show that a (substantial) reduction in training effort by including sensitivity information seems to pay off in the smooth and the smoothly fluctuating case, whereas it is inadequate in the strongly fluctuating case.

4. Conclusions

The efficiency of model training of Response Surface Models can be improved by including information on design sensitivities in the model training. This holds especially for those situations where design sensitivities are easily available, as is the case with e.g. Finite Element Models. However, if the response is non-smooth or contains discontinuities sensitivity data can disturb the global behavior of the response and should not be used. Furthermore, the proposed RSM-model should be flexible enough to capture the behavior of both responses and sensitivities properly. If sensitivity information can only be obtained numerically, through additional model analyses, there seems to be no clear advantage to spend additional effort on obtaining sensitivity information instead of using it directly for gathering response information from a larger training design.

5. References

- 1 MONTGOMERY, D.C.: Design and analysis of experiments, J.Wiley, New York 1997.
- 2 MYERS, R.H., MONTGOMERY, D.C.: Response surface methodology, J. Wiley, New York 1995.
- 3 SACKS, J., WELCH, W.J., MITCHELL, T.J., WYNN, H.P.: Design and analysis of computer experiments, Statistical Science 4 (1989), 409–435.
- 4 SCHOOF, A.J.G., KLINK, M.B.M., VAN CAMPEN, D.H.: Approximation of structural optimization problems by means of designed numerical experiments, Structural Optimization 4 (1992), 206–212.

Addresses: DR.J.J.M.RIJKEMA, DR.IR.A.J.G.SCHOOF, DR.IR.L.F.P.ETMAN,
Eindhoven University of Technology, Department of Mechanical Engineering, P.O.Box 513, 5600 MB
Eindhoven, The Netherlands. E-mail: j.j.m.rijpkema@tue.nl; a.j.g.schoofs@tue.nl; l.f.p.etman@tue.nl

ROTTLER, A. AND ESCHENAUER, H.A.

Optimal layouts of structural components considering fatigue strength

Designing complete systems or system components, it is of vital importance for the manufacturers nowadays to optimally fulfil the ever increasing demands pertaining to safety, durability, reduction of energy consumption, noise reduction, improvement of comfort, accuracy, etc. This, for instance, applies to all types of traffic and transportation systems like rail vehicles, automobiles, airplanes, and ships.

1. Problem definition

Increased demands on rail vehicles like high driving speeds, low stresses of railbeds, low life cycle costs, etc. require the application of computer-aided computation methods already at a very early stage of the design process. In the present paper, a proposal for modeling, simulation and optimization of rail vehicle systems and components (Fig. 1) is presented for two very important effects, namely the fulfilling of fatigue strength and durability requirements.

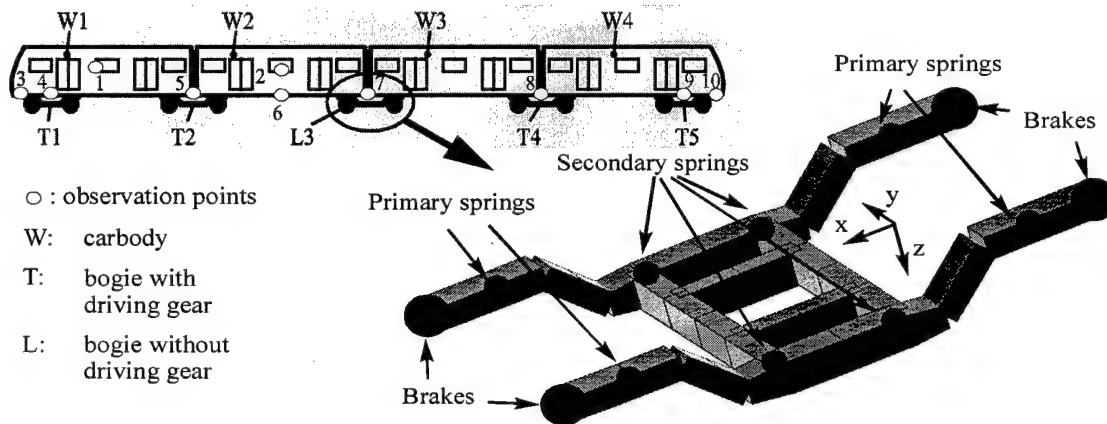


Fig. 1 Rail vehicle system and components.

2. Durability and Fatigue Strength

Durability and fatigue strength play a further important role for finding layouts of rail vehicle components. Bogie frames are such typical components within the global system "train". Currently, the layout of these frames with respect to durability is only carried out on the basis of substantially reduced load assumptions. The thus determined stress results reflect the real loads only very roughly and both over- and underdimensioning are possible. Using a more precise consideration of the states of operation, an improved layout is achieved with an optimal exploitation of the material properties. This concept is realized by calculating the forces acting on the bogie frame using dynamic MBS-simulations of the global system "train", by an FE-analysis of the bogie frame, and finally by evaluating the transient stresses by means of the rainflow counting procedure (see Fig. 2, [2,3]).

3. Optimization concept

The fatigue strength concept is integrated into the optimization procedure SAPOP (Structural Analysis Program and Optimization Procedure) [1,6], see optimization loop in Fig. 3. The objective function is the minimization of the bogie frame mass. Formulating constraints it is demanded that the estimated damage at each point is less than a critical damage. Using gradient methods to solve the optimization task, some difficulties occur. These difficulties are illustrated, existing problems are outlined, and solution approaches are described [4, 5].

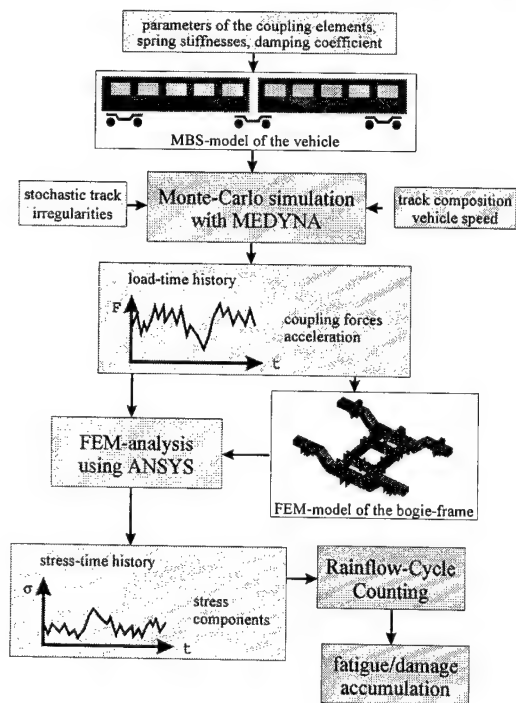


Fig. 2 Flow chart for the bogie frame layout with respect to fatigue strength.

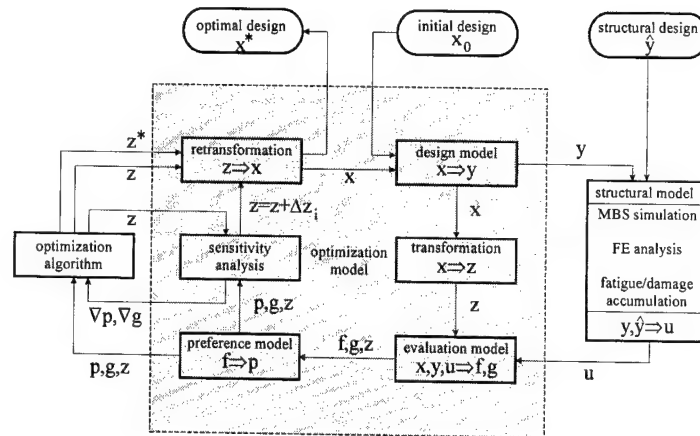


Fig. 3 Optimization loop in SAPOP

4. Results - Conclusions

The bogie frame is optimized by way of three different optimization models (thickness optimization, geometry optimization, as well as a simultaneous thickness and geometry optimization). The layout with respect to fatigue according to DS 952 is compared with a layout with respect to operational durability according to EUROCODE 3. This yields different optimum designs, owing to the different load assumptions and design limits of the respective codes. To achieve realistic data, the structural model has to be improved; long-term measurements are required to evaluate the calculations in order to verify the defined load assumptions and loadings.

Acknowledgement: The support of Adtranz, DaimlerChrysler Rail Systems, Siegen/Netphen, for this R&D-projekt is gratefully acknowledged

5. References

- [1] Eschenauer, H.A.; Koski, J.; Osycka, A. (1990): Multicriteria Design Optimization – Procedures and Applications. Springer, Heidelberg, New York
- [2] Dragos, R.; Eschenauer, H.A. (1998): Simulation and Optimization of the Dynamical Behavior of Rail Vehicle Systems. Proc. of the 1998 ASME Design Engineering Technical Conferences (CD-ROM), Sept. 13 – 16, 1998, Paper No. DAC-5573
- [3] Dragos, R. (2000): Methoden zur Optimierung des Systemverhaltens von Schienenfahrzeugen. Doctoral Thesis, FOMAAS, University of Siegen (to appear)
- [4] Rottler, A.; Eschenauer, H.A. (1998): Optimal Layout of Bogie Frames Considering Fatigue Strength. Proc. of the 1998 ASME Design Engineering Technical Conferences (CD-ROM), Sept. 13 – 16, 1998, Paper No. DAC-5574
- [5] Rottler, A. (2000): Optimale Auslegung von Bauteilkomponenten unter Berücksichtigung der Betriebsfestigkeit. Doctoral Thesis, FOMAAS, University of Siegen (to appear)
- [6] Eschenauer, H.A.; Geilen, J.; Wahl, H.J. (1993): SAPOP – An Optimization Procedure for Multicriteria Structural Design. In: Hörnlein, H.R.E.M.; Schittkowski, K. (eds.): Software Systems for Structural Optimization, Birkhäuser-Verlag, Basel, 207-227

Address: A. Rottler, H.A. Eschenauer, University of Siegen, FOMAAS, Am Herrengarten, D-57068 Siegen, GERMANY

SCHWARZ, ST.; KEMMLER, R.; RAMM, E.

Structural optimization in nonlinear mechanics

In the present study geometrically and materially nonlinear response is considered in topology and shape optimization in order to introduce more realism into the structural design. Typical objectives are to minimize the weight or to maximize the structural ductility or the critical load factor of a construction. The crucial point of the optimization procedure is the sensitivity analysis. In case of path-dependent problems, such as elastoplasticity the sensitivities are also path-dependent and have to be determined after each incremental step. With respect to the specific features of either topology or shape optimization different methods of sensitivity analysis are applied. The entire optimization procedure is verified by several design problems.

1. Structural analysis

The structural response based on an elastic and elastoplastic material model (Prandtl-Reuss) and a nonlinear kinematic relation is determined by an incremental, iterative solution procedure. The strains are restricted to be small. The critical points are evaluated using an augmented set of equations, namely the extended system (see [4]).

2. Sensitivity analysis

In the present study gradient based optimization procedures are used (SQP, OC). Therefore the sensitivities of the design criteria have to be determined. Depending on the number of optimization variables (n_v), the number of design criteria (n_c) and structural behavior a suitable method has to be chosen. For path-independent problems the main criteria for the choice is the ratio of n_v to n_c . Thus in topology optimization the adjoint method is preferred while for shape optimization problems the direct method is common. But for path-dependent problems the direct method is preferable in general; here the sensitivities have to be determined after each incremental step (see [2], [6]).

3. Numerical examples

Stiffness optimization with critical load constraint:

This example deals with the minimization of internal energy (which corresponds to the maximization of structural stiffness in elasticity) for prescribed mass. The structural situation and the material data are given in Fig. 1. Due to symmetry only one half of the structure is discretized by 800 eight-noded shell elements. First the optimum topology is generated based on linear kinematics (left side of Fig. 1). Afterwards a nonlinear kinematic relation is adopted. Additionally stability constraints ($\lambda_c \geq 1.4$) for the perfect as well as the imperfect structure are taken into account. The buckling mode of the lowest critical point is assumed as geometrical imperfection with a maximum amplitude of $0.075m$ (right side of Fig. 1). Because of the limited number of optimization variables (densities, SIMP-approach) the stability constraints could not be reached exactly. This problem can be overcome by using more variables. For further examples it is referred to [1], [3].

Minimization of weight of a Vierendeel girder:

The structural situation and the material data are given in Fig. 2. Due to symmetry only one half of the thin plate structure is shown, analyzed and optimized with respect to the shape of the holes. Here elastoplastic material without hardening is adopted (see also [3]).

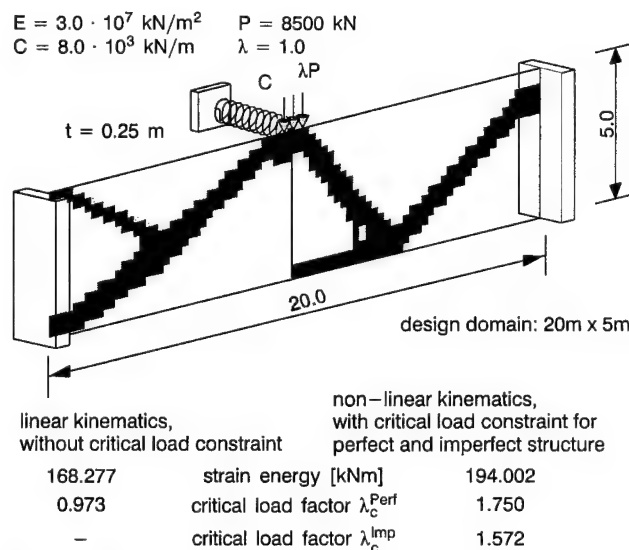


Figure 1: Results of the topology optimization with and without critical load constraints.

material data:

Young's modulus:	$E = 2.1 \cdot 10^8 \text{ kN/m}^2$
hardening modulus:	$E_T = 0.00001 \text{ kN/m}^2$
Poisson's ratio:	$\nu = 0.3$
density:	$\rho = 78.5 \text{ kN/m}^3$
yield stress:	$\sigma_y = 2.0 \cdot 10^5 \text{ kN/m}^2$
thickness:	$t = 0.044 \text{ m}$

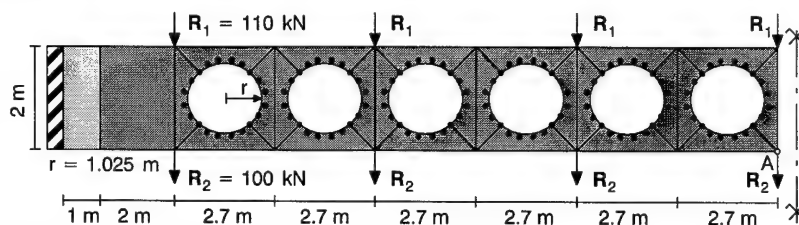


Figure 2: Discretization of the Vierendeel girder and material data.

The objective is to minimize the structural weight considering several constraints. The von Mises stresses along the edges are limited to $\sigma_v = 2.0 \cdot 10^5 \text{ kN/m}^2$ and the shear stresses between the holes are restricted to $\tau = 8.0 \cdot 10^4 \text{ kN/m}^2$. The maximum possible displacement in the center A of the girder is limited to $u_A = l/300 \approx 0.12 \text{ m}$. The optimization variables are the coordinates of the shape describing design-nodes. The nodes are allowed to move only to the center of the related hole. The optimization variables are linked to enforce symmetry to the longitudinal axis of the girder. For comparison the girder is optimized based on either an elastic or an elastoplastic material model. For the elastic

optimization based on elastic material behavior

optimization based on elastoplastic material behavior

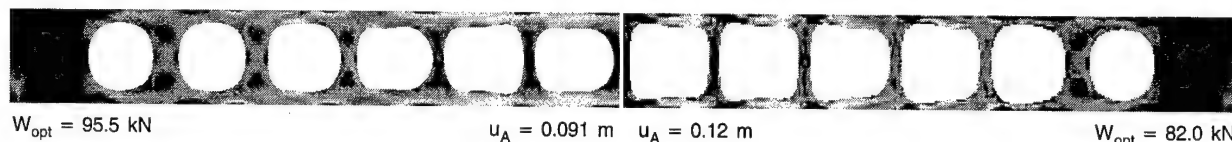


Figure 3: Example 2: Results of the shape optimization and related stresses.

material model all constraints are considered. The weight of the starting design ($W_0 = 105.7 \text{ kN}$) is reduced to the optimum weight of $W_{\text{opt}} = 95.5 \text{ kN}$ using the elastic material model (left side of Fig. 3). The optimization procedure is terminated by the von Mises stress constraint. For the optimization based on an elastoplastic material model the stress constraint is 'replaced' by the von Mises yield stress with $\sigma_y = \sigma_v = 2.0 \cdot 10^5 \text{ kN/m}^2$. The other constraints are furtheron considered. The optimization process stops, when the displacement constraint at point A becomes active. The structural weight can be reduced to $W_{\text{opt}} = 82.0 \text{ kN}$ (right side of Fig. 3). The reason for the additional reduction is that the elastoplastic material behavior allows a redistribution of stresses. This leads to a more balanced stress state. Further examples maximizing the structural ductility can be found in [3], [5].

Acknowledgements

This work is part of the Deutsche Forschungsgemeinschaft (DFG) research projects Ra 218/16-2 "Adaptive Methods in Topology Optimization" and Ra 218/11-3 "Algorithms, Adaptive methods, Elastoplasticity". The support is gratefully acknowledged. The first author thanks for the financial support provided by the Swiss foundation "Besinnung und Ordnung". The second author would like to acknowledge the financial support by the DFG within the graduate collegium "Modellierung und Diskretisierungsmethoden für Kontinua und Strömungen".

4. References

- 1 KEMMLER, R., SCHWARZ, S., RAMM, E.: Topology optimization including geometrically nonlinear response. Proceedings of the 3rd World Congress of Structural and Multidisciplinary Optimization, May, 17–21, 1999, Buffalo, USA.
- 2 KLEIBER, M., ANTÚNEZ, H., HIEN, T.D., KOWALCZYK, P.: Parameter sensitivity in nonlinear mechanics: Theory and finite element computations. Wiley & Sons, Chichester (1997).
- 3 RAMM, E., SCHWARZ, S., KEMMLER, R.: Advances in structural optimization including nonlinear mechanics. Proceedings of the European Congress on Computational Methods in Applied Sciences and Engineering (ECCOMAS 2000), Barcelona, Spain, September 11–14, 2000.
- 4 REITINGER, R., RAMM, E.: Buckling and imperfection sensitivity in the optimization of shell structures. Thin-Walled Structures 23 (1995), 159–177.
- 5 SCHWARZ, S., KEMMLER, R., RAMM, E.: Shape and topology optimization with nonlinear structural response. Proceedings of the European Conference on Computational Mechanics. August 31 – September 3 (1999), München, Germany.
- 6 VIDAL, C.A., HABER, R.B.: Design sensitivity analysis for rate-independent elastoplasticity. Comp. Meth. Appl. Mech. Eng. 107 (1993), 393–431.

Addresses: DIPL.-ING. STEFAN SCHWARZ, DIPL.-ING. ROMAN KEMMLER, PROF. DR.-ING. EKKEHARD RAMM, Institute of Structural Mechanics, University of Stuttgart, Pfaffenwaldring 7, D-70550 Stuttgart, Germany.

GERALD STÖCKL

Topology Optimization of Trusses under Stochastic Uncertainty

1. Topology Optimization

In case of topology optimization, the unknown optimal or satisfying structure is a (proper) substructure of an initial topology, called ground structure [1]. A ground structure is given by a set of nodal points, where at some of these nodes external loads apply and support conditions are defined, and n potential bars, connecting two of the nodal points. Different ground structures can be defined e.g. by connecting the direct neighbours only (Fig.3) or connecting nodes in a larger vicinity (Fig.4-6) up to connecting all nodes (Fig.7), without considering overlapping bars.

2. Foundations from Structural Mechanics

In collapse load analysis [2,4,5] and plastic, elastic design (synthesis) [2,4,5] of mechanical structures, e.g. trusses, structural survival is described by the following two basic conditions: The equilibrium equation $CF = R$, where C is the $m \times n$ equilibrium matrix with $\text{rank}(C) = m < n$, and R is the external load vector; The yield, strength or safety condition $F^L(\sigma^L, \sigma^U, X) \leq F \leq F^U(\sigma^L, \sigma^U, X)$ which is a linear approximation (yield polygon) of the actual convex yield, strength or safety conditions for the n -vector F of internal forces. The n -vector bounds F^U, F^L depend on the μ -vectors σ^U, σ^L of yield or allowable stresses in compression, in tension, resp., and a certain r -vector X of design variables. In the important special case of trusses [4,5] we have that $F^L := (\sigma_1^L A_1(X), \dots, \sigma_n^L A_n(X))' = \sigma_d^L A(X)$, $F^U := (\sigma_1^U A_1(X), \dots, \sigma_n^U A_n(X))' = \sigma_d^U A(X)$, where $A = A(X) := (A_1(X), \dots, A_n(X))'$ is the n -vector of cross-sectional areas of the elements (members) of the truss. Moreover, σ_d^L, σ_d^U denotes the $n \times n$ diagonal matrix having the diagonal elements $\sigma_j^L, \sigma_j^U, j = 1, \dots, n$, respectively. Since the m -vector R of external loads $R_i, i = 1, \dots, m$, and the μ -vectors σ^L, σ^U of yield or allowable stresses are not given, fixed quantities in practice, but must be modelled as random vectors $R = R(\omega), \sigma^L = \sigma^L(\omega), \sigma^U = \sigma^U(\omega), \omega \in (\Omega, A, P)$, on a certain probability space, (Ω, A, P) , the original structural optimization problem with random data must be replaced by an appropriate substitute problem, see [6,7].

3. Topology Optimization under Stochastic Uncertainty

For the topology optimization problem we select the 1st stage cost (weight or volume) function $G_0 = G_0(\omega, X)$, e.g. $G_0(\omega, X) := \sum_{k=1}^n \gamma_k(\omega) A_k(X) L_k$. Due to possible violations of the yield, strength or safety condition, we have then to take into account the 2nd stage costs $\Delta G := \Delta G(\omega, X, q^L(\omega), q^U(\omega))$ arising from the damage, maintenance or repair of the structure, where $q^L(\omega), q^U(\omega)$ denote certain vectors of cost factors. The total costs are given then by $G(\omega, X) := G_0(\omega, X) + \Delta G(\omega, X, q^L(\omega), q^U(\omega))$, where in the following we consider linear 2nd stage cost models $\Delta G(\omega, X, q^L(\omega), q^U(\omega)) = q^L(\omega)' \Delta F^L + q^U(\omega)' \Delta F^U$ with the second stage cost factors $q^L(\omega), q^U(\omega)$. In case of trusses, and assuming discrete probability distributions, e.g. after discretization of the probability distribution, the basic structural optimization problem with random data

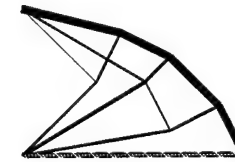
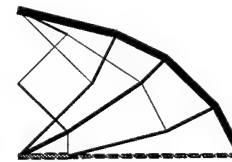
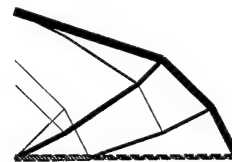
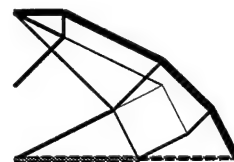
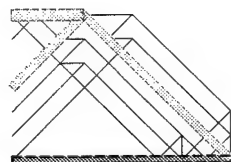
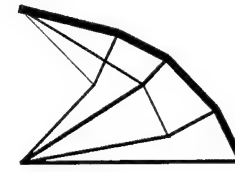
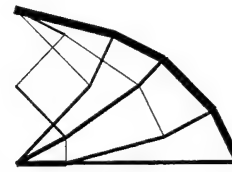
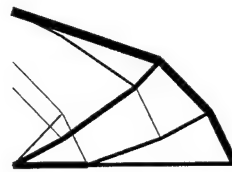
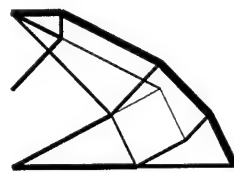
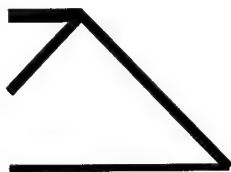
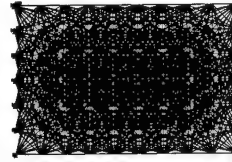
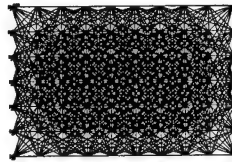
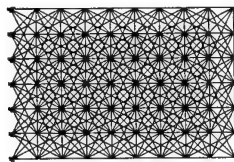
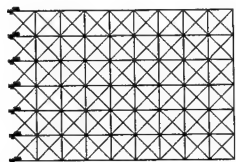
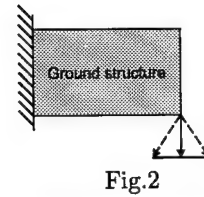
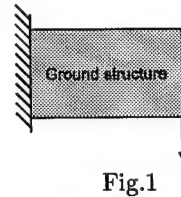
$$\min G_0 = G_0(\omega, X) \quad \text{s.t.} \quad CF = R(\omega), \quad F^L(\sigma^L, \sigma^U, X) \leq F \leq F^U(\sigma^L, \sigma^U, X), \quad X \in D_0,$$

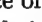
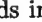
is replaced by a deterministic (large scale) LP with a dual decomposition data structure, details see [3,6,7],

$$\begin{aligned} \min \quad & \bar{G}_0(X) + [p_1 q(\omega_1)' y(\omega_1) + \dots + p_J q(\omega_J)' y(\omega_J)] \\ \text{s.t.} \quad & T(\omega_1, X) + W y(\omega_1) = h(\omega_1) \\ & \vdots \quad \quad \quad \ddots \quad \quad \quad \vdots \\ & T(\omega_J, X) + W y(\omega_J) = h(\omega_J) \\ & X \in D_0, y(\omega_j) \geq 0, j = 1, \dots, J. \end{aligned}$$

4. Numerical Examples

In the following we compare the optimal topologies obtained from the ground structures Fig.3-7 in case of a deterministic single load, cf. Fig.1, and for a random load with a uniform discrete distribution, cf. Fig.2.



Obviously, by taking into account random parameter variations by stochastic optimization methods, robust designs can be obtained: In comparison to the optimal solutions of the deterministic topology design problem, cf. Fig. 8-12, the corresponding optimal design obtained by using SLP techniques, cf. Fig.13-17, demands for additional bars and/or greater () /smaller () cross-sectional areas, with the maximum difference of 20% in this examples, for some bars in order to cope with stochastic variations of the model parameters (loads in this case). Moreover, the optimal topologies obtained from ground structures with a higher order vicinity (more directions available) tend to a Michell structure and have lower total costs.

5. References

- 1 ACHTZIGER, W.: Topology Optimization of Discrete Structures. In: G.I.N. Rozvany, Topology Optimization in Structural Mechanics, Springer-Verlag 1997, pp. 57-100.
- 2 HAFKA, R.T. ET AL.: Elements of structural optimization. Dordrecht-Boston-London, Kluwer 1990
- 3 KALL, P. AND MAYER, J.: On Solving Stochastic Linear Programming Problems. In: K. Marti, P. Kall (Eds.): Stochastic Programming - Numerical Techniques and Engineering Applications. LNEMS Vol. 458. Berlin-Heidelberg, Springer-Verlag 1998, pp. 329-344
- 4 KIRSCH, U.: Structural Optimization. Berlin-Heidelberg-New York, Springer-Verlag 1993
- 5 MARTI, K.: Approximation and derivatives of probabilities of survival in structural design. Structural Optimization 13, 1997, pp. 230-243
- 6 MARTI, K., STÖCKL, G.: Optimal Design of Trusses by Using Stochastic Linear Programming Techniques. ZAMM 79, Suppl. 1, 1999, S59-62
- 7 MARTI, K., STÖCKL, G.: Optimal (Topology) Design under Stochastic Uncertainty. In: Safety and Reliability (eds. Schueller, G.I., Kalka, P.), Vol. 2, Rotterdam-Brookfield: A.A. Balkema 1999, 1597-1602

Addresses: STÖCKL, G., Federal Armed Forces University Munich, Werner-Heisenberg-Weg 39, 85577 Neubiberg, Germany.

K. VERVENNE, H. DE BOER AND F. VAN KEULEN

Accuracy and implementation of refined second order semi-analytical design sensitivities

Accurate second order design sensitivities of finite element responses play an important role in the optimization process. The semi-analytical (SA) method is often used to compute these sensitivities. A disadvantage of the SA method is that severe inaccuracies may be observed for shape design variables. To improve the accuracy of the SA method a refined second order method has been proposed and implemented. The improvement has been based on the consistency conditions for rigid body modes and their derivatives. Both analytical and numerical examples indicate a considerable accuracy improvement of the refined method over the standard SA method.

1. Introduction

Computation of second order design sensitivities is often done by using the semi-analytical (SA) method. The governing finite element equations are

$$\mathbf{K}\mathbf{u} = \mathbf{f} \quad (1)$$

and second order displacement sensitivities are derived from the finite element equations by differentiating twice with respect to the design variables which gives

$$\mathbf{u}_{,ij} = \mathbf{K}^{-1} (\mathbf{f}_{,ij} - \mathbf{K}_{,ij}\mathbf{u} - \mathbf{K}_{,i}\mathbf{u}_{,j} - \mathbf{K}_{,j}\mathbf{u}_{,i}). \quad (2)$$

Here $\dots_{,i}$ denotes partial differentiation with respect to design variable i . For a SA formulation the derivatives $\mathbf{K}_{,i}$ and $\mathbf{K}_{,ij}$ are approximated using finite differences. Advantages of the semi-analytical method are the ease of implementation and its efficiency. An important disadvantage is that severe accuracy problems can occur, especially for shape design variables (see [1]).

2. Accuracy improvement of semi-analytical design sensitivities

Several methods to improve the accuracy of first order semi-analytical sensitivities have been proposed in [2-5]. To improve the accuracy of the second order semi-analytical sensitivities a similar approach as discussed in [4] can be used. For that purpose the element displacement vector is decomposed into a rigid body part and a deformational part

$$\mathbf{u}_e = \mathbf{u}_e^r + \sum_k \alpha_k \mathbf{r}_e^k \quad \text{with} \quad \alpha_k = \frac{\mathbf{u}_e \cdot \mathbf{r}_e^k}{\mathbf{r}_e^k \cdot \mathbf{r}_e^k}. \quad (3)$$

Here \mathbf{r}_e^k denotes the set of rigid body modes for a single element. Similarly, the element pseudo-load vector is decomposed into a self-equilibrating part and a non-self-equilibrating part

$$\mathbf{q}_e = \mathbf{q}_e^{SE} + \sum_k \beta_k \mathbf{r}_e^k \quad \text{with} \quad \beta_k = \frac{\mathbf{q}_e \cdot \mathbf{r}_e^k}{\mathbf{r}_e^k \cdot \mathbf{r}_e^k}. \quad (4)$$

Furthermore, for rigid body modes of a single element, it holds that

$$\mathbf{K}_e \mathbf{r}_e^k = \mathbf{0} \quad (5)$$

$$\mathbf{K}_{e,i} \mathbf{r}_e^k + \mathbf{K}_e \mathbf{r}_{e,i}^k = \mathbf{0} \quad (6)$$

$$\mathbf{K}_{e,ij} \mathbf{r}_e^k + \mathbf{K}_{e,i} \mathbf{r}_{e,j}^k + \mathbf{K}_{e,j} \mathbf{r}_{e,i}^k + \mathbf{K}_e \mathbf{r}_{e,ij}^k = \mathbf{0}. \quad (7)$$

These equations are referred to as consistency equations. As analytical derivatives of the rigid body modes are very easy to calculate, the consistency equations can be used together with (2), (3) and (4) to replace some of the

derivatives of \mathbf{K}_e by derivatives of \mathbf{r}_e^k . This results in an improved accuracy of the pseudo-load vector and therefore also of the design sensitivities. Possible errors in the self-equilibrating part of the pseudo-load vector do not have a large effect on the accuracy of the design sensitivities. This can be concluded from Saint Venant's principle: the effect of inaccuracies in self-equilibrating terms tends to damp out. The accuracy of the non-self-equilibrating part can be improved by using the consistency equations for rigid body modes and analytical differentiation of rigid body modes.

3. Example: plate problem

A rectangular strip, clamped at one end, and loaded by a bending moment at the other end, is studied. Second order design sensitivities of the tip displacement with respect to the length of the strip are computed for various choices of the relative perturbation, using both the semi-analytical method and the proposed refined semi-analytical method. From Fig. 1 it can be concluded that the refined semi-analytical method resulted in accurate second order sensitivities in a much larger range of relative perturbations, compared to the semi-analytical method.

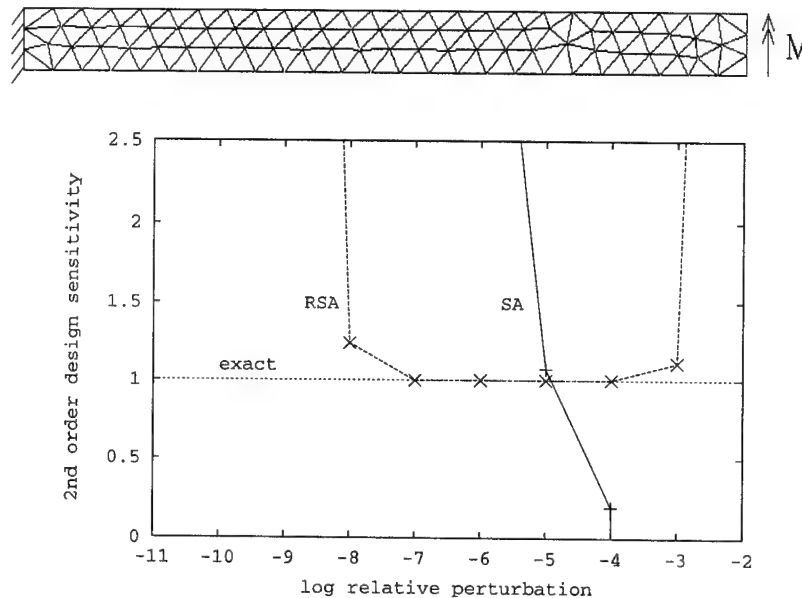


Figure 1: Second order design sensitivities of the tip displacement

4. Conclusions

It can be concluded that the use of refined semi-analytical design sensitivities gives a significant accuracy improvement of the traditional semi-analytical design sensitivities. Furthermore, the implementation is easy in an existing finite element code. Finally, the increase in computational cost is minor.

5. References

- 1 DE BOER, H.; VAN KEULEN, F.: Error Analysis of Refined Semi-Analytical Design Sensitivities. *Struct. Optim.* **14** 1997, 242–247.
- 2 OLHOFF, N.; RASMUSSEN, J.: Method of error elimination for a class of semi-analytical sensitivity analysis problems. *Lecture notes in Engineering* **63** 1991, 193–200.
- 3 MLEJNEK, H.P.: Accuracy of semi-analytical sensitivities and its improvement by the “natural method”. *Structural Optimization* **4** 1992, 128–131.
- 4 VAN KEULEN, F.; DE BOER, H.: Rigorous Improvement of Semi-Analytical Design Sensitivities by Exact Differentiation of Rigid Body Motions. *Int. J. Numer. Meth. Engng.* **42** 1998, 71–91.
- 5 HÖRNLEIN, H.R.E.M.: Effiziente semi-analytische Gradientenberechnung in der Strukturoptimierung. To be published in the proceedings of GAMM 2000.

Addresses: K. VERVENNE, H. DE BOER & F. VAN KEULEN

DELFT UNIVERSITY OF TECHNOLOGY, FACULTY FOR DESIGN, ENGINEERING AND PRODUCTION, P.O. Box 5033, 2600 GA DELFT, THE NETHERLANDS

VIETOR, THOMAS

Optimal design in automotive engineering with scattering design variables

The development of a passenger car is a multidisciplinary task. The vehicle has to fulfill demands out of different attributes like vehicle dynamics, driveability, acoustics, thermal and heat management, safety, durability, crash and economics. One main problem is the variability of mechanical quantities responsible for the performance and customer perception of a car. To overcome this, the extension of the conventional deterministic oriented development process to a process which includes stochastic quantities is necessary. In this paper the current deterministic approach is described briefly. It is not possible to perform the extension in a single step. In a first extended version of the process the variability of material parameters is included. In further steps the formulation and solution of stochastic optimization problems for sub-problems is necessary. Finally the complete approach should fully integrate the variability of stochastic quantities.

1. Development process

Vehicle system concepts (e.g. body structure, front- and rear suspension, powertrain mounting systems, etc.), which are selected in an early program phase, have significant influence on the attribute performance of the vehicle. It is almost impossible to solve attribute concerns resulting from selection of poor concepts in a later program phase. A good understanding of dynamics of the vehicle is needed to design and realize mounting systems that allow the company to reach its attribute leadership goals. The selection of the mounting concept and the design of the mounting system is a highly complex task which requires the involvement of all related areas. The process should be driven by CAE analyses, as there is no hardware available in an early development stage. The principle of the development process is shown in Fig. 1 [1,2].

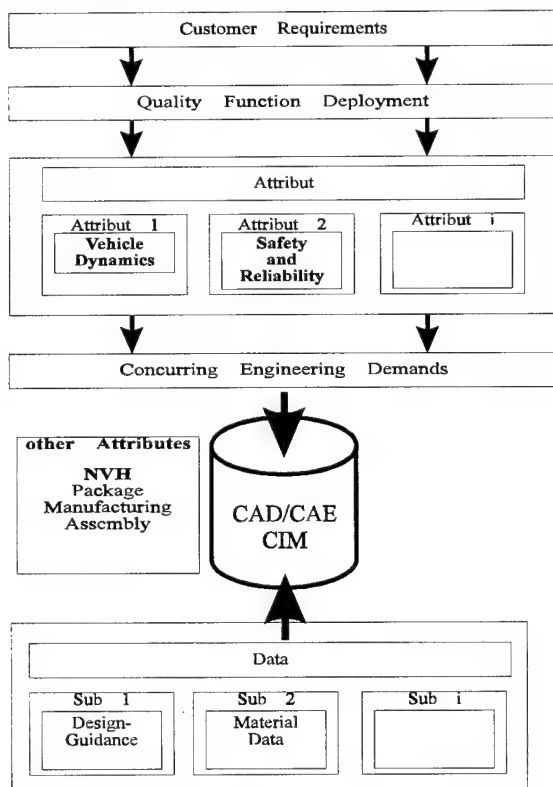


Fig. 1 Development Process in Automotive Engineering.

Concept development has become more and more part of the ongoing process. It is done by core and advanced groups of the car manufacturer. Proven concepts have to be available at the start of a new vehicle program. Otherwise, the program team would not be able to meet the restricted time schedule, which has been significantly reduced in recent years. CAE is used extensively for concept design evaluations. The advantage of analytical models is, that the engineer gets a better understanding of the system behavior. Sensitive areas of the design can be identified, which helps to guide the design. With the start of a new vehicle program, market research and benchmark studies are carried out. Vehicle targets are derived from subjective evaluation and from measurements of the base vehicle, which is to be replaced, and the main competitors. With respect to NVH, the vehicle targets are given for example by the interior noise level at specific drive conditions. The NVH requirements have a big impact on the vehicle development. In particular the structural design of the powertrain concepts and the body architecture is influenced by NVH. CAE studies are helpful when it comes to the system and component target setting. One important strategy for NVH is, to avoid coupling of system and

component resonances with other resonances or with primary excitation sources. That means, a proper alignment of modal frequencies and vehicle excitations is critical to meeting the overall vehicle targets. For example, the global body modes (e.g. torsion/bending) have to be separated from engine idle conditions. Targets are also set for the powertrain and suspensions modes. Following the system target setting the program team has the task, to select proper concepts, which have the potential to fulfill the overall targets. CAE is utilized to compare concept alternatives for the vehicle program and to support the decision process. The next step in the development process is the definition of components targets and the

hardware optimization. Generally, CAE is a very strong tool for component optimization. As hardware testing is not done in many cases due to time and budget restrictions, it is the only way to make an assessment of the design. In the late program phase the required NVH performance of the vehicle is confirmed with prototype vehicles. CAE is of minor importance as far as the NVH assessment is concerned. In case of NVH concerns being identified with prototypes the models are used to carry out root cause analyses and to identify measures in order to fix the problems.

2. Introduction of scattering design variables

In the development process a number of parameters and design variables are scattering. In conventional approaches they are assumed deterministic. With increasing importance of reliability the deterministic approach has to be extended and at least the most important parameters and variables have to be modelled stochastically. These most important quantities have to be identified with sensitivity methods. Only with the limitation to the most sensitive quantities the models can be handled. The key factors for the introduction of scattering design variables are:

- stochastic data like geometry, dimensions, thicknesses and statical and dynamical stiffnesses of different materials like rubber, foams, etc. [3]
- different stochastic models like gaussian, weibull, lognormal distributions
- objectives like sound pressure, vibrations, ride and handling, costs, manufacturing, assembly, package
- solution strategies like RSM, First Order Second Moment reliability methods (FOSM) and different methods of stochastic optimization like mean value Taylor methods [4]

3. Solution strategy for stochastic variables [4]

Fig. 2 shows the transformation of stochastic variables to standard normally distributed variables. This is the basis for the application of First Order Second Moment reliability methods. The magnitude β of vector \mathbf{y}^* is a measure for the probability of failure $P_f = \Phi(-\beta)$. This measure for failure can be introduced for each stochastic constraint. With this formulation the well known optimization procedure [5] can be extended [4]. Because of the very high numerical effort the stochastic optimization problem can be solved only after introducing simplified models for the structural analysis and the use only of the most important stochastic quantities. These examples show the big influence of the stochastic character to optimal results.

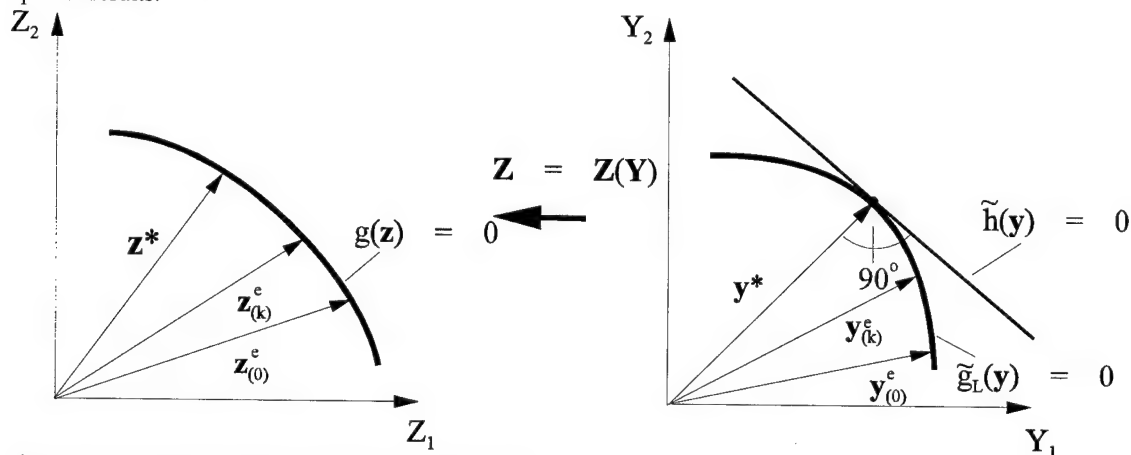


Fig. 2 Transformation to standard normally distributed variables.

5. References

- [1] Eichhorn, U., Sauerwein, D., Schmitz, T., de Vlugt, A., Teubner, H.-J.: Kundenorientierte Entwicklung am neuen Ford Fiesta, ATZ 97 (1995) 9, S. 522-531
- [2] The new Ford Focus, Special Edition ATZ, 1999
- [3] Vietor, T., Deges, R., Hampl N., Bürger, K.-H., :Robust Design of Elastic Mounting Systems, SAE Noise & Vibration Conference, Michigan, USA, 1997
- [4] Vietor, T.: Stochastic Optimization for Mechanical Structures. In: Marti, K. (ed.): Special Issue on Structural Reliability and Stochastic Structural Optimization. Mathematical Methods of Operations Research, Vol 46, Issue 3, 1997, Physica Verlag, Heidelberg, pp. 377-408.
- [5] Eschenauer, H.A.; Koski, J.; Osyczka, A.: Multicriteria Design Optimization. Springer-Verlag: Berlin, 1990.

Address: Thomas Vietor, Ford Motor Co., D-50725 Köln, GERMANY

VONDRÁK, V.; DOSTÁL, Z.; RASMUSSEN, J.

Duality based contact shape optimization

An implementation of semi-analytic method for the sensitivity analysis in contact shape optimization without friction is described. This method is then applied to the contact shape optimization.

1. Duality based solution of state problem

The finite element discretization of conditions of equilibrium of a system of elastic bodies in contact results in the quadratic programming problem

$$\min_{Nu \leq d} \frac{1}{2} u^T K u - u^T f, \quad (1)$$

where K is a stiffness matrix, f represents a load vector and inequality constraints $Nu \leq d$ describe contact conditions of non-interpenetration of the bodies. In design optimization, all these matrices and vectors may depend on the vector of design variables α . After introducing the Lagrange multipliers λ for the inequalities and elimination of the displacements u , we obtain dual formulation of the problem 1 in form

$$\min_{\lambda \geq 0} \frac{1}{2} \lambda^T N K^{-1} N - \lambda^T (N K^{-1} f - d). \quad (2)$$

The latter formulation is suitable for application of the efficient quadratic programming solvers. In particular, these methods can exploit rather well conditioned Hessian and bound constraints. After solving 1 for λ , we can evaluate the displacement vector u by the formula $u = K^{-1} (f - N^T \lambda)$.

2. Sensitivity Analysis

The goal of the sensitivity analysis is evaluation of the gradient of the solution of the state problem 1 with respect to the design variables. The most straightforward method for evaluation of these directional derivatives is so called overall finite difference method which is based on numerical approximation of derivatives by the finite differences $\partial u / \partial \alpha_i \approx \frac{1}{t} \{u(\alpha_1, \dots, \alpha_i + t e_i, \dots, \alpha_p) - u(\alpha_1, \dots, \alpha_p)\}$, where e_i denotes the vector with 1 in i^{th} position and zeros elsewhere, α_i is i^{th} design variable, and t is a sufficiently small perturbation parameter. Thus to carry out the sensitivity analysis, we should assemble and decompose the stiffness matrix $p + 1$ times.

A more sophisticated method for sensitivity analysis is so called semi-analytical method. Using the symbolic differentiation of Lagrangian of the state problem and analyzing all possible cases of interaction on the contact interface, we obtain the quadratic programming problem

$$\min_{z \in G(\alpha, e_i)} \frac{1}{2} z^T K(\alpha) z - z^T (f'(\alpha, e_i) - K'(\alpha, e_i) u(\alpha) - N'^T(\alpha, e_i) \lambda(\alpha)) \quad (3)$$

whose solution is formed by the directional derivatives in the design variables α_i . In this problem, symbols $f'(\alpha, e_i)$, $K'(\alpha, e_i)$, $N'(\alpha, e_i)$ denote the directional derivatives of the load vector, stiffness matrix and constraint matrix, respectively. They can be evaluated by direct computation. The vectors $u(\alpha)$, $\lambda(\alpha)$ are primal and dual solutions of the state problem. The set of constraints is defined as

$$G(\alpha, e_i) = \{z : N_j(\alpha) z \leq d'_j(\alpha, e_i) - N'_j(\alpha, e_i) u(\alpha), \forall j \in I_w; \\ N_k(\alpha) z = d'_k(\alpha, e_i) - N'_k(\alpha, e_i) u(\alpha), \forall k \in I_s\}. \quad (4)$$

The set I_w comprises indices i of the dual solution with $\lambda_i(\alpha) = 0$, and I_s those with $\lambda_i(\alpha) > 0$. Thus the semi-analytical method requires only one assembly and decomposition of the stiffness matrix. More details on the implementation of the solution of 3 and on the semi-analytical method may be found in papers 1 and 2, respectively.

In finishing this local procedure **step 4** gives the BB coefficient z_n (\square) as $z_n = \alpha_n a_{ni} + \beta_n a_{nj} + \gamma_n a_{nk}$. The obtained cubic C^1 spline s satisfies

$$s(P_i) = z_i, \quad \text{grad } s(P_i) = g_i, \quad P_i \text{ vertex of } \Delta, \quad \text{grad } s\left(\frac{P_i+P_j}{2}\right) n_{ij} = d_{ij}, \quad P_i P_j \text{ edge of } \Delta.$$

2. Nonnegative and range restricted C^1 interpolants

Of course, the above spline s is nonnegative on Ω if only the BB coefficients from the steps 1 and 2 are nonnegative. This, in turn, holds true if we set $g_i = 0$ for all vertices P_i of Δ , $d_{ij} = 0$ for all edges $P_i P_j$ of Δ and if we assume

$$(S_n - P_\mu)(P_\nu - P_\mu) > 0 \text{ for } \mu, \nu \in \{i, j, k\}, \mu \neq \nu, \Delta_n \in \Delta. \quad (1)$$

These relations require certain angles to be acute. For example, the inequalities (1) are satisfied if the S_n are chosen to be the incenters of the triangles Δ_n . Thus, we have proved the nonnegative C^1 interpolation to be always successful with cubic splines on Clough-Tocher refinements Δ_{CT} of the triangulation Δ which satisfy the condition (1).

The existence proof should be followed by a fairing step. A fairing functional, for example the thin plate functional is minimized with respect to the gradients g_i and the normal derivatives d_{ij} subject to the nonnegativity constraints $a_{\mu\nu} \geq 0$, $b_{\mu\nu} \geq 0$ for $\mu, \nu \in \{i, j, k\}$, $\mu \neq \nu$, $\Delta_n \in \Delta$.

More general, cubic C^1 splines on Clough-Tocher refinements Δ_{CT} with the property (1) are suitable in range restricted interpolation provided the obstacles are piecewise constant, i.e., if $L_n \leq s(P) \leq U_n$ for $P \in \Delta_n$, $\Delta_n \in \Delta$ is required. Of course, the prescribed obstacles L_n and U_n have to be compatible with the function values z_i , z_j , z_k on any triangle $\Delta_n \in \Delta$. We remark that this problem was shown to be solvable also by means of quadratic C^1 splines on Powell-Sabin refinements Δ_{PS} of Δ in [2].

To demonstrate the described procedure we have chosen the often used data set illustrated by Figure 2. The triangulation Δ is refined to Δ_{CT} by means of the incenters. We have constructed range restricted interpolants to the obstacles $L_n = 0$, $U_n = 1$, $\Delta_n \in \Delta$. Comparing the Figures 3 and 4, in this example and in others the spline obtained by minimizing the thin plate functional is visually much more pleasing than the spline used in showing the solvability of the problem of range restricted C^1 interpolation.

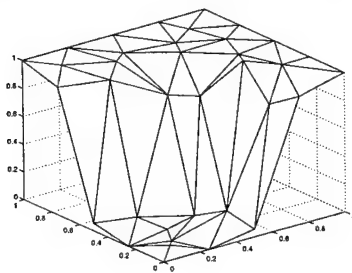


Figure 2: Data set and the piecewise linear interpolant on an admissible triangulation Δ .

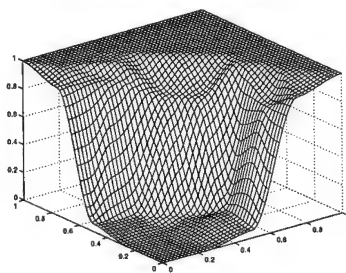


Figure 3: Range restricted interpolant used in the existence proof.

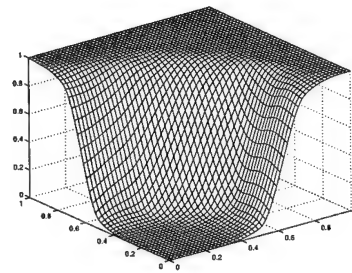


Figure 4: Range restricted thin plate interpolant.

3. References

- 1 COSTANTINI, P., MANNI, C.: A Parametric Cubic Element with Tension Properties; SIAM J. Numer. Anal. **36** (1999), 607–628.
- 2 HERRMANN, M., MULANSKY, B., SCHMIDT, J. W.: Scattered Data Interpolation Subject to Piecewise Quadratic Range Restrictions; J. Comput. Appl. Math. **73** (1996), 209–223.
- 3 MANN, S.: Cubic Precision Clough-Tocher Interpolation; Comput. Aided Geom. Des. **16** (1999), 85–88.
- 4 SCHMIDT, J.W.: Range Restricted Interpolation by Cubic C^1 -Splines on Clough-Tocher Splits; in: Advances in Multivariate Approximation, W. Haußmann, K. Jetter, and M. Reimer (eds.), Wiley-VCH, Berlin (1999), 253–267.
- 5 SCHMIDT, J.W., BASTIAN, M., MULANSKY, B.: Nonnegative Volume Matching by Cubic C^1 Splines on Double Clough-Tocher Splits; Technische Universität Dresden, Preprint MATH-NM-01-2000 (2000).

BENNER, P.

On a numerical method for the regularization of descriptor systems

We discuss a numerically stable algorithm, originally proposed in [3], that computes a regularizing output feedback for descriptor systems. In [3], the system is transformed to a condensed form via a sequence of singular value decompositions (SVDs). We show that the expensive SVDs can be replaced by reliable, more efficient orthogonal decompositions. Moreover, we demonstrate how the feedback is obtained from our slightly different condensed form.

1. Introduction

Consider the linear, time-invariant descriptor system

$$E\dot{x}(t) = Ax(t) + Bu(t), \quad x(0) = x^0, \quad y(t) = Cx(t), \quad A, E \in \mathbb{R}^{n \times n}, B \in \mathbb{R}^{n \times m}, C \in \mathbb{R}^{p \times n}, \quad (1)$$

where x , y , and u are the states, outputs, and inputs (controls), respectively, of the system.

The solution of optimal control problems with quadratic performance criterion for descriptor systems of the form (1) is considered, e.g., in [3,4]. In [3] it is shown that essentially, the classical theory from the linear-quadratic optimal control problem with E invertible carries over to the descriptor case (E singular) if the pencil $A - \lambda E$ is regular and has index at most 1. If the system is strongly stabilizable and strongly detectable it can then be shown (see [1,3]) that an output feedback $K \in \mathbb{R}^{m \times p}$ exists such that the matrix pencil $(A + BKC) - \lambda E$ has the required properties. As output feedback represents a generalized state-space transformation, the solution of the original problem is equivalent to the solution of the transformed system. Here we will discuss a stable numerical method for computing the required regularizing output feedback.

2. Output regularization

In [3] a numerically stable algorithm is given that computes an output feedback for a strongly stabilizable/detectable system such that the transformed system is regular and has index at most 1. A similar algorithm for systems with the more common properties of strong or complete controllability/observability is considered in [1]. As fewer generalized state-space transformations are required in the algorithm from [3], we demonstrate our ideas here for this algorithm due to space limitations. But the algorithm from [1] can be modified analogously.

In the algorithms in [1,3], SVDs are chosen for reducing the system to a condensed form as these reductions involve several critical rank decisions. Unfortunately, SVDs are quite expensive. We show here that cheaper orthogonal decompositions can be employed that also reveal the rank of a matrix reliably. A *rank revealing QR decomposition* (RRQR) of a matrix $A \in \mathbb{R}^{n \times m}$ is given by $A = URP^T = U \begin{bmatrix} R_1 & R_2 \\ 0 & R_3 \end{bmatrix} P^T$, where $U \in \mathbb{R}^{n \times n}$ is orthogonal, $P \in \mathbb{R}^{m \times m}$ is a permutation matrix, $R_1 \in \mathbb{R}^{k \times k}$ is upper triangular, and $\|R_3\|_2 < \text{tol} \cdot \sigma_{\max}(A)$, for a given tolerance threshold tol . The size $k \leq m$ of R_1 is the *numerical rank* of A . An RRQR is computed via a QR decomposition with column pivoting followed by some iterative post-processing in order to determine the rank correctly, see [2] and the references therein. A *UTV (decomposition)* is given by a factorization $A = UTV^T = U \begin{bmatrix} T_1 & T_2 \\ 0 & T_3 \end{bmatrix} V^T$, where $U \in \mathbb{R}^{n \times n}$, $V \in \mathbb{R}^{m \times m}$ are orthogonal, $T_1 \in \mathbb{R}^{k \times k}$ is a numerically non-singular, triangular matrix, tol is as above, and $\|T_j\|_2 < \text{tol} \cdot \sigma_{\max}(A)$, $j = 2, 3$. Again, the numerical rank of A is determined by the size k of T_1 . Stable algorithms for computing a UTV with T_1 upper or lower triangular have been proposed; see [2] and the references therein. The SVD is a special UTV with T_1 diagonal. Here we will use URVs, i.e., UTVs with T_1 upper triangular. The complexity of computing these decompositions and accumulating the orthogonal transformations (which is needed here) for a nonsingular $n \times n$ matrix is $21n^3$ flops for the SVD, $\frac{8}{3}n^3$ flops for the RRQR and the URV (the latter two decompositions being identical in this case). If the rank of the matrix is $r < n$, the cost of the SVD remains the same while the costs for RRQRs and URVs become $8r(n^2 - nr + \frac{1}{3}r^2)$ and $2r(6n^2 - 5nr + \frac{5}{3}r^2)$ flops, respectively. As we replace two of the four SVDs needed in the regularization method from [3] by RRQRs and the other two by URVs, it is clear that a significant acceleration will be obtained. Moreover, if the left and right orthogonal factors of such a decomposition have to be applied to other matrices (as is the case in the regularization procedure considered in the sequel), an RRQR is very advantageous as its right orthogonal factor is a permutation

matrix such that its application to other matrices can be performed without floating point operations.

Assume now a strongly stabilizable/detectable system as in (1) is given. The modified regularization method can then be formulated as follows.

1. Compute a URV of E : $U_E^T E V_E = \begin{bmatrix} R_E & 0 \\ 0 & 0 \end{bmatrix} =: E_1$, where $R_E \in \mathbb{R}^{n_E \times n_E}$. Apply U_E, V_E to A, B, C :

$$A_1 := U_E^T A V_E = \begin{bmatrix} A_{11} & A_{12} \\ A_{21} & A_{22} \end{bmatrix}, \quad B_1 := U_E^T B = \begin{bmatrix} B_{11} \\ B_{21} \end{bmatrix}, \quad C_1 := C V_E = \begin{bmatrix} C_{11} & C_{12} \end{bmatrix},$$

where the partitioning of A_1, B_1, C_1 is analogous to that of E_1 . If $n_E = n$, then we are done.

2. Compute an RRQR of B_{21} : $\hat{U}_B^T B_{21} P_B = \begin{bmatrix} R_B & B_{22} \\ 0 & 0 \end{bmatrix}$, where $R_B \in \mathbb{R}^{n_B \times n_B}$ and $B_{22} \in \mathbb{R}^{n_B \times (m-n_B)}$.

Let $U_B := \begin{bmatrix} I_{n_E} & 0 \\ 0 & \hat{U}_B \end{bmatrix}$ and set $E_2 := E_1, C_2 := C_1$,

$$B_2 := U_B^T B_1 P_B = \begin{bmatrix} B_{11} & B_{12} \\ R_B & B_{22} \\ 0 & 0 \end{bmatrix}, \quad A_2 := U_B^T A_1 = \begin{bmatrix} A_{11} & A_{12} \\ A_{21} & A_{22} \\ A_{31} & A_{32} \end{bmatrix}.$$

3. Compute a URV of A_{32} : $\hat{U}_A^T A_{32} \hat{V}_A = \begin{bmatrix} R_A & 0 \\ 0 & 0 \end{bmatrix}$, where $R_A \in \mathbb{R}^{n_A \times n_A}$.

Let $U_A := \begin{bmatrix} I_{n_E+n_B} & 0 \\ 0 & \hat{U}_A \end{bmatrix}$, $V_A := \begin{bmatrix} I_{n_E} & 0 \\ 0 & \hat{V}_A \end{bmatrix}$, and set $E_3 := E_2, C_3 := C_2 V_A = \begin{bmatrix} C_{11} & C_{12} & C_{13} \end{bmatrix}$,

$$A_3 := U_A^T A_2 V_A = \begin{bmatrix} A_{11} & A_{12} & A_{13} \\ A_{21} & A_{22} & A_{23} \\ A_{31} & R_A & 0 \\ A_{41} & 0 & 0 \end{bmatrix}, \quad B_3 := U_A^T B_2 = \begin{bmatrix} B_{11} & B_{12} \\ R_B & B_{22} \\ 0 & 0 \\ 0 & 0 \end{bmatrix}.$$

4. Compute an RRQR of C_{13} : $U_C^T C_{13} P_C = \begin{bmatrix} R_C & C_{14} \\ 0 & 0 \end{bmatrix}$, where $R_C \in \mathbb{R}^{n_C \times n_C}$, $C_{14} \in \mathbb{R}^{n_C \times (n-n_E-n_A-n_C)}$.

Let $V_C := \begin{bmatrix} I_{n_E+n_A} & 0 \\ 0 & P_C \end{bmatrix}$ and set $E_4 := E_3, B_4 := B_3$,

$$A_4 := A_3 V_C = \begin{bmatrix} A_{11} & A_{12} & A_{13} & A_{14} \\ A_{21} & A_{22} & A_{23} & A_{24} \\ A_{31} & R_A & 0 & 0 \\ A_{41} & 0 & 0 & 0 \end{bmatrix}, \quad C_4 := U_C^T C_3 V_C = \begin{bmatrix} C_{11} & C_{12} & R_C & C_{14} \\ C_{21} & C_{22} & 0 & 0 \end{bmatrix}.$$

The system (E_4, A_4, B_4, C_4) is strongly stabilizable/detectable as orthogonal changes of basis preserve these properties. Hence, $n_E + n_B + n_A = n = n_E + n_A + n_C$, which implies $n_B = n_C$. Thus, the new system has the form

$$E_4 := \begin{bmatrix} R_E & 0 & 0 \\ 0 & 0 & 0 \\ 0 & 0 & 0 \end{bmatrix}, \quad A_4 := \begin{bmatrix} A_{11} & A_{12} & A_{13} \\ A_{21} & A_{22} & A_{23} \\ A_{31} & R_A & 0 \end{bmatrix}, \quad B_4 := \begin{bmatrix} B_{11} & B_{12} \\ R_B & B_{22} \\ 0 & 0 \end{bmatrix}, \quad C_4 := \begin{bmatrix} C_{11} & C_{12} & R_C \\ C_{21} & C_{22} & 0 \end{bmatrix}.$$

5. Now let $\Sigma_A := \sigma_{\max}(R_A) I_{n_B}$. The output feedback is $K := \begin{bmatrix} K_{11} & K_{12} \\ 0 & 0 \end{bmatrix}$, where $K_{11} = R_B^{-1} (\Sigma_A - A_{23}) R_C^{-1}$ and $K_{12} = -R_B^{-1} (A_{22} + (\Sigma_A - A_{23}) R_C^{-1} C_{12}) C_{22}^+$. (Note that $\sigma_{\max}(R_A)$ is a by-product of the URV in Step 3.)

The regularized system is then given by $\hat{A} := A_4 + B_4 \hat{K} C_4 = \begin{bmatrix} A_{11} & A_{12} & A_{13} \\ A_{21} & (A_{22} + (\Sigma_A - A_{23}) R_C^{-1} C_{12} (I - C_{22}^+ C_{22})) & A_{23} \\ A_{31} & R_A & 0 \end{bmatrix}$, $\hat{E} := E_4$, $\hat{B} := B_4$, and $\hat{C} := C_4$. The system $(\hat{E}, \hat{A}, \hat{B}, \hat{C})$ has the desired properties, i.e., the matrix pencil $\hat{A} - \lambda \hat{E}$ is regular and has index at most 1 because R_E, R_A , and Σ_A are nonsingular. Moreover, the regularized system is still strongly stabilizable/detectable as output feedback is a generalized state-space transformation.

3. References

- 1 BUNSE-GERSTNER, A. MEHRMANN, V., NICHOLS, N.K.: Regularization of descriptor systems by output feedback; **170** (1994), IEEE Trans. Automat. Control **39** (1994), 1742–1748.
- 2 GOLUB, G.H., VAN LOAN, C.F.: Matrix Computations; Johns Hopkins University Press, Baltimore, 3rd edition, 1996.
- 3 MEHRMANN, V.: The Autonomous Linear Quadratic Control Problem, Theory and Numerical Solution; Springer-Verlag, Heidelberg, 1991.
- 4 MÜLLER, P.C.: Lineare optimale Regelung von kausalen und nichtkausalen Deskriptorsystemen; Z. Angew. Math. Mech. **78**, Suppl. 1 (1998), S35–S38.

Addresses: PETER BENNER, Universität Bremen, FB 3, Zentrum für Technomathematik, 28334 Bremen, FRG.

BOESE, F. G.

On the Distribution of the Zeros of Polynomials Related to the Daubechies Wavelets

To locate all zeros of the polynomials $q_n(z)$ from (1) as precise as possible is our aim. These polynomials are related to the sequence of Daubechies wavelets. Zero enclosures up to a separation of all zeros are communicated. The enclosing sets are conformal lemniscate rectangles.

1. Problem and Motivation

Consider for $n \in \mathbb{N}$ the rational function $P_n(z) := (1-z)^{-n}$ of the complex variable $z \in \mathbb{C} \setminus \{1\}$. Truncate its Taylor series expansion around the origin $z = 0$ after n terms to obtain the polynomials of the title,

$$q_n(z) := \sum_{k=0}^{n-1} \binom{n-1+k}{k} z^k = 1 + nz + \frac{n(n+1)}{2!} z^2 + \cdots + \frac{n(n+1) \cdots (2n-2)}{(n-1)!} z^{n-1}. \quad (1)$$

Our goal is to locate all $n-1$ zeros of $q_n(z)$ for all $n \in \mathbb{N}$ as precise as possible. For our purposes, it is convenient to consider besides the $q_n(z)$ the associated polynomials $p_n(z) := q_{n+1}(z/2)$. What is the interest in these zeros? As the title informs, our polynomials occur in a wavelet context and are related to the Daubechies wavelet sequence $\psi_n(t)$, $n \in \mathbb{N}$, see Daubechies [1] or Mallat [3]. The elementary operation to be carried out many times in a wavelet transform with a $\psi_n(t)$ is the convolution of two sequences. One of the sequences is a filter sequence. An explicit knowledge of the zeros of the $q_n(z)$ would lead to explicit coefficients h_0, \dots, h_{2n-1} in the filter transfer factor $H_n(z) := h_0 + h_1 z + \cdots + h_{2n-1} z^{2n-1}$. Fig. 1 shows the 100 zeros of $p_{100}(z)$. The striking feature in Fig. 1 is the regularity of the zeros which seem to lie on a smooth curve, cf. Lemma 2.2.

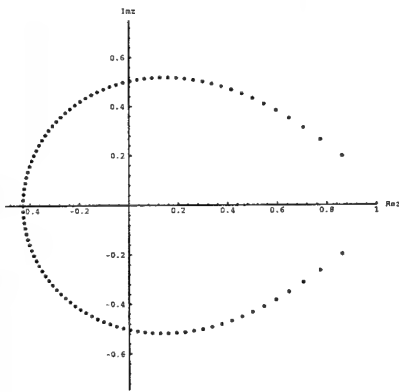


Figure 1: All 100 zeros of $p_{100}(z)$ in the complex z plane.

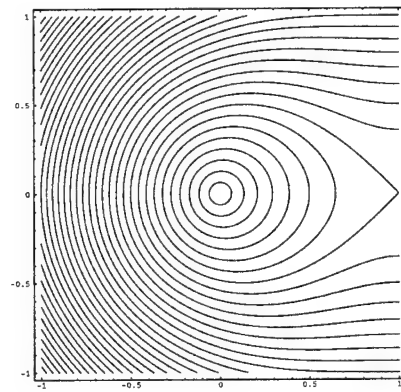


Figure 2: lemniscate strips $\Lambda(r_1, r_2)$ in the square $|\Re(z)|, |\Im(z)| \leq 1$.

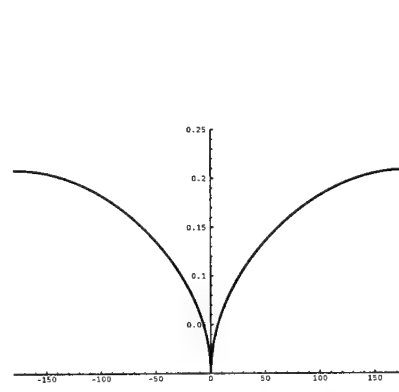


Figure 3: The limiting density $d_\Lambda(\alpha)$ from (9) for $-180 \leq \alpha \leq 180$.

2. First Enclosure and Polynom Representations

The coefficients of the $p_n(z)$ form a sequence of positive, non-decreasing coefficients. This fact allows a zero inclusion by a circular sector of the form $D(\alpha) := \{z \in \mathbb{C} : |z| < 1, |\arg(z)| > \alpha\}$.

Lemma 2.1. *The zeros of $p_n(z)$, $n > 1$, are simple and lie in the open circular sector $D(2\pi/(2n-1))$.*

More precise zero enclosures can be obtained by using appropriate representations for the $q_n(z)$,

$$q_n(z) = \frac{1}{(n-1)!} \left(\frac{d}{dz} \right)^{n-1} \frac{1-z^{2n-1}}{1-z}, \quad (2)$$

$$= \frac{1 - \beta_n \int_0^z [t(1-t)]^{n-1} dt}{(1-z)^n}, \quad \beta_n := \frac{\Gamma(2n)}{\Gamma^2(n)}, \quad (3)$$

$$= \frac{1}{(1-z)^n} - \binom{2n-1}{n} z^n \int_0^1 \frac{(1-t)^{n-1}}{(1-zt)^{2n}} dt, \quad (4)$$

$$= \frac{1}{(1-z)^n} - \frac{(4z)^n}{2\pi i} \int_{C(1/2)} \left(\frac{w^2}{2w-1} \right)^n \cdot \frac{dw}{w(1-2zw)}. \quad (5)$$

The positively oriented contour $C(1/2)$ in (5) surrounds the point $w = 1/2$. The next lemma explains the regularity of the zero distribution in terms of the incomplete Beta function $B(a, b; z) := \int_0^z t^{a-1}(1-t)^{b-1} dt$, $\Re(a), \Re(b) > 0$.

Lemma 2.2. *The $n-1$ zeros of $q_n(z)$, $n > 1$, lie at the intersection points of level curves and argument curves of the incomplete Beta function $B(n, n; z)$,*

$$|B(n, n; z)| = \frac{\Gamma^2(n)}{\Gamma(2n)}, \quad \arg[B(n, n; z)] = 2k\pi, \quad 1 \leq |k| \leq (n-1)/2. \quad (6)$$

3. A Lemniscate Strip Enclosure

We define the truncated lemniscate strip $\Lambda(r_1, r_2)$, the truncated lemniscate ray strip $\Lambda^\perp(\alpha_1, \alpha_2)$, and the lemniscate rectangles $\Lambda(r_1, r_2, \alpha_1, \alpha_2) := \Lambda(r_1, r_2) \cap \Lambda^\perp(\alpha_1, \alpha_2)$ by

$$\Lambda(r_1, r_2) := \{z \in \mathbb{C} : r_1 \leq |z(2-z)| \leq r_2, |z| \leq 1\}, \quad \Lambda^\perp(\alpha_1, \alpha_2) := \{z \in \mathbb{C} : \alpha_1 \leq \arg[z(2-z)] \leq \alpha_2, |z| \leq 1\}.$$

Fig. 2 shows 35 (not truncated) subsequent lemniscate strips $\Lambda(r_1, r_2)$ in the square $|\Re(z)|, |\Im(z)| \leq 1$.

Theorem 3.1. *All zeros of $p_n(z)$, $n > 1$, lie in the truncated lemniscate strip $\Lambda(r_1, r_2)$ with*

$$r_1 := 2^{1/n}, \quad r_2 := r_1 \cdot \left(\frac{2n-1}{2n-2} \cdot \sqrt{4\pi n \epsilon_n} \right)^{1/n}, \quad \epsilon_n := \frac{1}{n\pi} \cdot \left[\frac{4^n}{\binom{2n}{n}} \right]^2. \quad (7)$$

Theorem 3.2. *For $n > 1$, the lemniscate rectangle $\Lambda_k := \Lambda(r_1, r_2, \alpha_{1,k}, \alpha_{2,k})$, $1 \leq k \leq n/2$, with r_1, r_2 from (7) and*

$$\alpha_{1,k} := (2k-1)\pi/n, \quad \alpha_{2,k} := 2k\pi/n,$$

contains exactly one zero of $p_n(z)$.

4. The Limiting Density of the Zeros

By Theorem 3.1, the truncated lemniscate $\Lambda(1, 1)$ is the limiting ($n \rightarrow \infty$) set of the zeros. How are the zeros of $p_n(z)$ distributed along $\Lambda(1, 1)$ after the passage to the limit $n \rightarrow \infty$?

Theorem 4.1. *The limiting density of the distribution of the zeros of $p_n(z)$ for $n \rightarrow \infty$ along the truncated lemniscate $\Lambda(1, 1)$ at the point $z(\alpha)$ is $d_\Lambda(\alpha)$,*

$$z(\alpha) := 1 + e^{i[3\pi \operatorname{sgn}(\alpha) + \alpha]/4} \cdot \sqrt{2 \sin(|\alpha|/2)}, \quad 0 \leq |\alpha| \leq \pi, \quad (8)$$

$$d_\Lambda(\alpha) := \frac{\Gamma(5/4)}{2\sqrt{\pi}\Gamma(3/4)} \cdot \sqrt{\sin(|\alpha|/2)}. \quad (9)$$

Fig. 3 shows the density $d_\Lambda(\alpha)$ in the parameterization of (8) and (9), $\int_{-\pi}^{\pi} d_\Lambda(\alpha) d\alpha = 1$.

5. Discussion

The restricted printing space allows not to include the proofs (at least of the new results). Our problem was treated earlier by Shen and Strang [4]. In our notation, they achieved – among others – the inclusion by $\Lambda(2^{1/n}, 1)$ for the zeros of the $p_n(z)$, see Th. 2.3 in [4]. The goal in the work of Kateb and Lemarié-Rieusset [2] was more ambitious. A zero localization served to investigate the asymptotical ($n \rightarrow \infty$) behavior of the phase $\arg[H_n(z)]$, $|z| = 1$, and the high order asymptotics of the Daubechies wavelets. Szegő's problem [5] is connected to ours.

6. References

- 1 DAUBECHIES, I.: Ten Lectures on Wavelets, SIAM, Philadelphia, 1992.
- 2 KATEB, D. LEMARIÉ, P.: The Phase of Daubechies Filters, *Revista Matemática Iberoamericana* **13**(1997)2, 245-305.
- 3 MALLAT, S.: A Wavelet Tour of Signal Processing, Academic Press, San Diego, 1998.
- 4 SHEN, J., STRANG, G.: Asymptotic Analysis of Daubechies Polynomials, *Proc. Amer. Math. Soc.* **124**(1997)12, 3819-3833.
- 5 SZEGŐ, G.: Über eine Eigenschaft der Exponentialreihe, *Sitzungsberichte der Berliner Mathematischen Gesellschaft*, **23**(1924), 50-64.

Address: DR. F. G. BOESE, Max-Planck-Institut für extraterrestrische Physik, Postbox 1312, D-85741 Garching, gub@mpe.mpg.de

DETMERS, F.; HERZBERGER, J.

Enge Schranken für den Effektivzinssatz nach der PAngV bei einem Annuitätenproblem

Ein spezielles Problem stellt die Ermittlung des Effektivzinssatzes einer geänderten Annuität gegenüber der ursprünglichen Annuität dar. Daraus ergibt sich die Aufgabe, eine formelmäßige Abschätzung des Zusammenhangs zwischen den eindeutigen positiven Wurzeln zweier zugeordneter Polynome zu finden. In unserem Modell wird diese Aufgabe bei Anwendung der deutschen Preisangabeverordnung (PAngV) mathematisch gelöst.

Wir betrachten hier zunächst jährliche, einfache Annuitäten, wobei unter einer Annuität eine gewöhnliche Annuität mit fester Laufzeit von n Jahren verstanden wird (siehe [3] oder [5]). Bei einer solchen Annuität wird die Schuld S über einen Zeitraum von n Jahren mit festen Jahresraten A , welche die anfallenden Zinsen und einen Tilgungsanteil enthalten, in der Weise bedient, daß am Ende der Laufzeit die Schuld getilgt ist. Der vereinbarte Zinssatz sei i (in Dezimalschreibweise) und es bezeichne $q = 1 + i$. Die bestimmende Gleichung einer solchen Annuität ergibt sich nach dem Prinzip: "Summe der mit Zinseszins verzinsten Annuitätenraten (Wert der Annuität) ist am Ende der Laufzeit gleich der mit Zinseszins verzinsten Schuld (wobei beidemale der Zinssatz i sei)."

Mathematisch ergibt dies die Gleichung

$$S \cdot q^n = A \sum_{\nu=0}^{n-1} q^{n-1-\nu} \quad \text{oder} \quad p(q) = q^n - a \cdot \sum_{\nu=0}^{n-1} q^{n-1-\nu} = 0, \quad a = A/S. \quad (1)$$

Sind die Schuld S und die Annuitätenrate A , sowie die Laufzeit n bekannt, dann ergibt sich der Effektivzinssatz der Annuität i^* aus der nach der DESCARTESSchen Vorzeichenregel eindeutig existierenden positiven Wurzel q^* von p .

Polynomgleichungen der Art (1) wurden in der Numerik bereits im Zusammenhang mit der Berechnung der Konvergenzordnung iterativer Prozesse betrachtet, siehe dazu etwa TRAUB [7]. Eine neuere Arbeit von PETKOVIĆ & PETKOVIĆ [6] ergibt in diesem einfachen Fall z. B. die Unterschranke

$$q^* > (2 \cdot a + a \cdot (n-1) \cdot (n+2)) / (2 + a \cdot (n-1) \cdot n). \quad (2)$$

Von H. LICHTENBERG [4] wurde folgendes Problem mitgeteilt: "Bei gleicher Laufzeit, also n Jahren, soll die Ratenhöhe auf A/k ($k > 1$) gesenkt werden, aber gleichzeitig die Anzahl der Raten auf die k -fache angehoben werden (also auf $k \cdot n$). Wie hoch ist der Effektivzinssatz der so geänderten Annuität?"

Für den Fall der US-Methode zur Berechnung des Effektivzinssatzes (siehe [3]) wurde das Problem in [2] gelöst. Setzen wir die ursprüngliche Annuität mit jährlichen Raten an, dann fällt die geänderte Annuität in den unterjährlichen Bereich, und die (1) entsprechende Polynomgleichung nach der PAngV läßt sich nicht ohne weiteres niederschreiben. Bei jährlichen Zahlungen fallen US-Methode und PAngV-Methode zusammen. Da bei der PAngV die unterjährlichen Zahlungen als reine Tilgungen zu behandeln sind und linear proportional verzinst werden, müssen wir zunächst die jährliche Ersatzrate \bar{A} ausrechnen. Diese ergibt sich als $\bar{A} = (A/2k)((k+1) + (k-1) \cdot q)$.

Damit erhalten wir dann die (1) entsprechende Gleichung der geänderten Annuität als

$$p_k(q) = q^n - \bar{a} \cdot \sum_{\nu=1}^{n-1} q^{n-\nu} - \bar{b} = 0, \quad (3)$$

$$\text{mit } \bar{a} = (2 \cdot A \cdot k) / (2 \cdot k \cdot S - A \cdot (k-1)) \quad \text{und} \quad \bar{b} = A \cdot (k+1) / (2 \cdot k \cdot S - A \cdot (k-1)).$$

Beide Polynome sind bei uns von gleichem Grad (anders wie in [2]), aber besitzen verschieden aufgebaute Koeffizienten. Das mathematische Problem der von H. LICHTENBERG gestellten Aufgabe ist nun das folgende:

“Es ist für $k > 1$ ein formelmäßiger Zusammenhang zwischen den eindeutigen positiven Wurzeln der beiden Polynome

$$p(q) = q^n - a \cdot \sum_{\nu=0}^{n-1} q^{n-1-\nu} \quad \text{und} \quad p_k(q) = q^n - \bar{a} \cdot \sum_{\nu=1}^{n-1} q^{n-\nu} - \bar{b} \quad (\bar{a}, \bar{b} \text{ wie in (3)})$$

herzustellen.”

Bezeichnet i^* den (bekannten) Zinssatz der ursprünglichen Annuität und j^* denjenigen der geänderten, dann zeigen elementare Rechnungen

$$\lim_{n \rightarrow \infty} j^* = (2 \cdot k \cdot i^* / (2 \cdot k - i^*(k-1))) =: u.$$

Außerdem zeigen numerische Beispiele, daß stets $j^* > u$ gilt.

Diese beiden Beobachtungen führen uns auf die beiden ersten (groben) Schranken:

$$u = (2 \cdot k \cdot i^*) / (2 \cdot k - i^*(k-1)) < j^* < (2 \cdot A \cdot k) / (2 \cdot k \cdot S - A \cdot (k-1)) = o \quad (4)$$

Der Beweis erfolgt durch etwas längere technische Umformungen durch die Nachweise, daß stets $p_k(1+u) < 0$ und $p_k(1+o) > 0$ gelten. Diese Schranken sollen nun verbessert werden. Da das besagte Polynom p_k sich im betrachteten Intervall als konvex erweist, führt die explizite Anwendung eines Sekantenschrittes mit den beiden obigen Schranken als Näherungswerte auf die neue untere Schranke

$$j^* > \frac{2 \cdot k \cdot i^*}{2 \cdot k - i^*(k-1)} - \frac{\frac{2 \cdot k \cdot i^*}{2 \cdot k - i^*(k-1)} - \frac{2 \cdot A \cdot k}{2 \cdot k \cdot S - A(k-1)}}{1 - \frac{i^* S}{\left[\left(1 + \frac{2 \cdot k \cdot i^*}{2 \cdot k - i^*(k-1)} \right)^n (i^* S - A) \right] + A}} \quad (5)$$

Entsprechend liefert ein expliziter NEWTON-Schritt, ausgehend von der obigen groben Unterschranke, dann die verbesserte Oberschranke

$$j^* < t - \frac{(1+t)^n 2 \cdot (i^* k \cdot S - k \cdot A) + 2 \cdot A \cdot k}{i^* (2 \cdot k \cdot S - A(k-1))} ;$$

$$(1+t)^{n-1} \left[n - \frac{2 \cdot A \cdot k}{2 \cdot k \cdot S - A(k-1)} \cdot \frac{(n-1) \cdot (1+t) - n}{t^2} \right] - \frac{2 \cdot A \cdot k}{2 \cdot k \cdot S - A(k-1)} \cdot \frac{1}{t^2} \quad (6)$$

$$t = \frac{2 \cdot k \cdot i^*}{(2 \cdot k - i^*(k-1))}.$$

Als numerisches Beispiel betrachten wir die Daten: $n = 12$, $k = 2$, $i^* = 0.005$ und erhalten mit (5) und (6) das Intervall $0.0051128166954 < j^* < 0.0052031802759$ während der iterativ berechnete Wert $j^* = 0.0052028941$ ist.

Literaturverzeichnis

- 1 DETMERS, F.: Schranken für den Effektivzinssatz nach der PAngV bei einem speziellen Annuitätenproblem. Diplomarbeit, Universität Oldenburg 1998 (nicht erhältlich).
- 2 HERZBERGER, J.: Bounds for the positive root of certain polynomials with applications. BIT **39:2** (1999), 366–372.
- 3 HERZBERGER, J.: Einführung in die Finanzmathematik. R. Oldenbourg Verlag, München 1999.
- 4 LICHTENBERG, H.: Private Mitteilung, 1998.
- 5 LOCAREK, H.: Finanzmathematik. R. Oldenbourg Verlag, München 1991.
- 6 PETKOVIĆ, M.S.; PETKOVIĆ, L.D.: On the bounds of the R -order of some iteration methods. Z. Angew. Math. Mech. **69** (1989), 197–198.
- 7 TRAUB, J.F.: Iterative Methods for the Solution of Equations. Prentice-Hall Inc., Englewood-Cliffs, N. J. 1964.

Anschriften: FRANK DETMERS, Oldenburgische Landesbank AG, Organisationsabteilung, Stau 17, 26122 Oldenburg, Germany

PROF. DR. JÜRGEN HERZBERGER, Fachbereich Mathematik, Universität Oldenburg, 26111 Oldenburg, Germany.

DYLLONG, E.; LUTHER, W.

Flatness criteria for subdivision of rational Bézier curves and surfaces

Many of well-known algorithms in the context of Computer Aided Geometric Design are based on subdivision techniques. Unfortunately, termination criteria for subdivision mostly require a time-consuming computation of the maximum deviation between any given curve segment and its linear approximation at each subdivision step. We generalize results by Wang for Bézier curves [3] and present an approach which in advance specifies the number of necessary subdivision steps to obtain a piecewise linear approximation within an assumed accuracy for a given rational Bézier curve or surface.

1. Introduction

Computer Aided Geometric Design (CAGD) is concerned with algorithms to handle parametric curves and surfaces. Many algorithms for finding intersections or calculating the distance between two rational Bézier curves or surfaces, or for drawing and displaying a rational Bézier curve or surface are based on subdivision techniques, as they are especially suited for them. In this paper we deal with flatness criteria for subdivision, that means criteria which specify conditions for piecewise linear approximation of a rational Bézier curve or surface within a given tolerance ε and which are commonly used to terminate the subdivision process.

Let $C(u)$ be a rational Bézier curve of degree n defined by

$$C(u) = \frac{\sum_{i=0}^n \omega_i P_i B_{i,n}(\frac{u-a}{b-a})}{\sum_{i=0}^n \omega_i B_{i,n}(\frac{u-a}{b-a})}, \text{ for } a \leq u \leq b, \quad (1)$$

with control points $P_i = (x_i, y_i, z_i)$, Bernstein basis functions $B_{i,n}(\frac{u-a}{b-a}) = \binom{n}{i} \frac{(u-a)^i (b-u)^{n-i}}{(b-a)^n}$, and positive weights $\omega_i, i = 0, \dots, n$. In order to discuss under which condition a rational Bézier curve can be replaced by appropriate line segments within a given tolerance ε , we define the height of $C(u)$ as follows:

Let $C(u), a \leq u \leq b$, be a parametric curve and let $l_{C(\alpha), C(\beta)}$ be the line segment between $C(\alpha)$ and $C(\beta)$, $a \leq \alpha < \beta \leq b$. Then we call the maximum perpendicular distance $h_{C, \alpha, \beta}$ defined by

$$h_{C, \alpha, \beta} := \max_{\alpha \leq u \leq \beta} d(C(u), l_{C(\alpha), C(\beta)}) := \max_{\alpha \leq u \leq \beta} \{ \min_{0 \leq \xi \leq 1} \|C(u) - [\xi C(\alpha) + (1 - \xi) C(\beta)]\| \} \quad (2)$$

the height of $C(u)$ within the parameter interval $[\alpha, \beta], a \leq \alpha < \beta \leq b$.

Furthermore, for the sequence $X : (X_0, \dots, X_n)$ with $X_i \in \mathbb{R}^3$ we define $\Delta_X^0 := \max_{0 \leq i \leq n} \{\|X_i\|_\infty\}$, $\Delta_X^1 := \max_{0 \leq i \leq n-1} \{\|X_{i+1} - X_i\|_\infty\}$ and $\Delta_X^2 := \max_{0 \leq i \leq n-2} \{\|X_{i+2} - 2X_{i+1} + X_i\|_\infty\}$.

Subdivision of curve (1) into two rational Bézier curves with control points $P_{0,k}$ and $P_{1,k}, k = 0, \dots, n$, can be described using pseudo-code as follows:

```
for k := 0 to n do begin
  Pw[0][k] := Pw[0]; Pw[1][n-k] := Pw[n-k];
  for i := 0 to n-k-1 do Pw[i] := (Pw[i] + Pw[i+1])/2;
end.
```

Here $Pw[i]$ describes the control points of $C(u)$ in homogeneous coordinates $P_i^\omega = (\omega_i x_i, \omega_i y_i, \omega_i z_i, \omega_i)$, and $Pw[0][k], Pw[1][k]$ the control points $P_{0,k}^\omega, P_{1,k}^\omega$ of the two Bézier curves $C_0(u), C_1(u)$ after subdivision, respectively. The subdivision process is continued until a certain flatness criterium is fulfilled. In this case the subdivision technique can be used to replace a rational Bézier curve by line segments within a given tolerance.

2. Flatness criteria for subdivision of a rational Bézier curve

Flatness criteria for subdivision are based on a rough estimate of the height of curve segments. If the height is smaller than the given tolerance ε , then the subdivision can be stopped and the curve segment can be replaced by the corresponding line segment. These termination criteria for subdivision yield a piecewise linear approximation of curve (1). Wang and Xu give in [2] the following estimation for the height of curve (1):

Theorem 1. For the height of the rational curve (1) of degree n ($a = 0, b = 1$) is $h_{C,0,1} \leq \Phi(\omega_0, \dots, \omega_n) \cdot \max_{1 \leq i \leq n-1} d(P_i, l_{P_0, P_n})$, with $\Phi(\omega_0, \dots, \omega_n) := 1 - (1 + (2^{n-1} - 1) \cdot \max(\omega_0^{-1}, \omega_n^{-1}) \cdot (\max_{1 \leq i \leq n-1} \omega_i))^{-1}$.

The estimation in Theorem 1 has the advantage that the approximations are carried out in an adaptive manner and no redundant subdivisions have to be done. But its disadvantages are that the tests need to be made after each subdivision step and the maximal depth of subdivision is not known in advance. To know the maximal depth before starting the subdivision process is useful in many cases, e.g. choosing adequate distance algorithms etc. We have proved in [1] the following theorem for an a priori estimated upper bound for the depth of subdivision:

Theorem 2. Let $C(u)$ be a rational Bézier curve of degree n with $a \leq u \leq b$, control points $P_i = (x_i, y_i, z_i)$ and weights $\omega_i > 0$, $i = 0, \dots, n$. Moreover, let $R : (R_0, \dots, R_n)$ be a sequence with $R_i := (\omega_i x_i, \omega_i y_i, \omega_i z_i)$, $i = 0, \dots, n$, and $\omega : (\omega_0, \dots, \omega_n)$, as well as $\Delta := \min_{0 \leq i \leq n} \{\omega_i\}$. For a given $\varepsilon > 0$ we set $r := \log_4 ((\sqrt{3}nL)/(8\varepsilon))$ with $L := (n-1)\Delta_R^2/\Delta + ((n-1)\Delta_R^0\Delta_\omega^2 + 2n\Delta_R^1\Delta_\omega^1)/(\Delta)^2 + 2n\Delta_R^0(\Delta_\omega^1)^2/(\Delta)^3$. If $-\log_2((\beta-\alpha)/(b-a)) \geq r$ for $a \leq \alpha < \beta \leq b$, then the estimation $h_{C,\alpha,\beta} < \varepsilon$ is valid.

This theorem is an extension of Wang's Theorem [3] to the case of a rational Bézier curve. If $\omega_i = \text{const}$, the curve $C(u)$ describes a Bézier curve and L reduces to $L = (n-1)\Delta_P^2$.

The geometric meaning of Theorem 2 is that after r subdivisions we can replace the rational Bézier curve by line segments according to the r -th level of subdivision within the given tolerance ε .

Example 3. Let $C(u)$ be a rational cubic Bézier curve $C(u)$ with $P_0 = (1, -1, 0)$, $P_1 = (5, 6, 0.5)$, $P_2 = (8, 1, 0.6)$, $P_3 = (5.5, 1, 0)$ and $\omega_0 = 0.5$, $\omega_1 = 1$, $\omega_2 = 1.5$, $\omega_3 = 1$ (cf. Fig. 1). Then Theorem 2 yields $r = 13$ and we need 0.15 sec CPU time (AMD K6-2/333MHz) to compute a piecewise linear approximation of $C(u)$ within the tolerance $\varepsilon = 10^{-6}$ using pure subdivision technique. In comparison, using Theorem 1 we need 0.21 sec. But the a priori estimated upper bound for the depth of subdivision depends much more than the flatness criteria by Wang and Xu (Theorem 1) on the weights. If we set $\omega_1 = 1.5$, then Theorem 2 yields $r = 14$ and the CPU time doubles. For $\omega_1 = 0.2$ depth r increases to 16. The computing time using Theorem 1 is roughly the same in all cases.

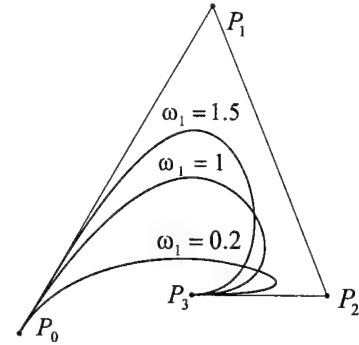


Figure 1: $C(u)$ with ω_1 varying

3. Subdivision bounds for rational Bézier surfaces

Let $S(u, v)$, $a \leq u \leq b$, $c \leq v \leq d$, be a rational Bézier surface defined as a tensor product of two rational Bézier curves of degree n and m , and let the height $h_{S,\alpha,\beta,\xi,\eta}$ of $S(u, v)$ be defined according to the height of $C(u)$. For a vector matrix $X : \{X_{i,j}\}_{\substack{0 \leq i \leq n-1 \\ 0 \leq j \leq m-1}}$ with $X_{i,j} \in \mathbb{R}^3$ we define the constants $\Delta_X^{0,0}$ etc. according to Δ_X^0 etc., e.g. $\Delta_X^{1,0} := \max_{\substack{0 \leq i \leq n-1 \\ 0 \leq j \leq m-1}} \{\|X_{i+1,j} - X_{i,j}\|\}$. Then the following a priori estimated upper bound for the depth of subdivision is valid: After $r := \lceil \log_4 ((\sqrt{3}L_S)/(8\varepsilon)) \rceil$ subdivision steps in u - and v -direction for $a \leq \alpha < \beta \leq b$, $c \leq \xi < \eta \leq d$ and $(\beta-\alpha)/(b-a) = (\eta-\xi)/(d-c) = 2^{-r}$ is $h_{S,\alpha,\beta,\xi,\eta} \leq \varepsilon$. Here denote $L_S := nL_{uu} + 2nmL_{uv} + mL_{vv}$ with

$$\begin{aligned} L_{uu} &:= (n-1)\Delta_R^{2,0}/\Delta + ((n-1)\Delta_R^{0,0}\Delta_\omega^{2,0} + 2n\Delta_R^{1,0}\Delta_\omega^{1,0})/(\Delta)^2 + 2n\Delta_R^{0,0}(\Delta_\omega^{1,0})^2/(\Delta)^3, \\ L_{uv} &:= \Delta_R^{1,1}/\Delta + (\Delta_R^{0,0}\Delta_\omega^{1,1} + \Delta_R^{0,1}\Delta_\omega^{1,0} + \Delta_R^{1,0}\Delta_\omega^{0,1})/(\Delta)^2 + 2\Delta_R^{0,0}\Delta_\omega^{1,0}\Delta_\omega^{0,1}/(\Delta)^3, \\ L_{vv} &:= (m-1)\Delta_R^{0,2}/\Delta + ((m-1)\Delta_R^{0,0}\Delta_\omega^{0,2} + 2m\Delta_R^{0,1}\Delta_\omega^{0,1})/(\Delta)^2 + 2m\Delta_R^{0,0}(\Delta_\omega^{0,1})^2/(\Delta)^3. \end{aligned}$$

and $R : \{R_{i,j}\}_{\substack{0 \leq i \leq n-1 \\ 0 \leq j \leq m-1}}$, $R_{i,j} := (\omega_{i,j}x_{i,j}, \omega_{i,j}y_{i,j}, \omega_{i,j}z_{i,j})$, and $\omega : \{\omega_{i,j}\}_{\substack{0 \leq i \leq n-1 \\ 0 \leq j \leq m-1}}$, $\Delta := \min_{\substack{0 \leq i \leq n-1 \\ 0 \leq j \leq m-1}} \{\omega_{i,j}\}$.

For the proof see [1]. This result has rather theoretical meaning because in this case of approximation, techniques based on triangulation are generally more efficient than those based on rectangular structures.

Acknowledgements

We thank the referee for valuable comments. This research was supported by Deutsche Forschungsgemeinschaft within the scope of Sonderforschungsbereich 291 "Elastic manipulation systems for heavy loads in complex environments".

4. References

- 1 DYLLONG, E.: A priori bestimmte obere Schranken für die Unterteilungstiefe rationaler Bézier-Kurven und -Flächen. Preprint: Schriftenreihe des Fachbereichs Mathematik der Universität Duisburg, SM-DU-474.
- 2 WANG, G.; XU, W.: The Termination Criterion for Subdivision of the Rational Bézier Curves. Graphical Models and Image Processing, Vol. 5, No. 1 (1991), 93–96.
- 3 WANG, G.: The Subdivision Method for Finding the Intersection between Two Bézier Curves or Surfaces. Zhejiang University Journal, Special Issue on Computational Geometry (in Chinese), 1984.

Addresses: EVA DYLLONG, WOLFRAM LUTHER, University of Duisburg, Department of Informatics, Lotharstr. 65, D-47057 Duisburg, Germany

EHRHARDT, K., BORCHARDT, J., GRUND, F., HORN, D.

Distributed Dynamic Process Simulation

In chemical process industry a heterogeneous simulation concept is required which distributes the solution of a dynamic overall model to a computer network such that the submodels of the global process flowsheet can be solved independently of each other on subsequent time intervals. To this end a iteration technique is used which estimates the vector of input variables of the submodels, calculates the corresponding time behaviour of the output variables concurrently, and matches then the profiles of the interconnecting variables of the overall process model iteratively. For the common case that the submodels do not provide input-output sensitivities a specific Broyden-type acceleration of this waveform iteration method is considered.

1. Process flowsheet definition of coupled processes

On the basis of a global process flowsheet an overall dynamic process model is usually assembled from p autarkic models of subprocesses by defining the appropriate interconnecting process variables. It is presumed that the submodels generate an output function $v_i(t)$ for each given input function $u_i(t)$ uniquely, i.e.

$$v_i(t) = G_i(u_i(t)), \quad i = 1, \dots, p \quad t \in [t_0, t_E]. \quad (1)$$

Here the submodel functions G_i are only given implicitly by applying a numerical solution procedure to the respective submodel equations. Frequently, the internal model of subprocess i is described by a large system of differential algebraic equations, cf. ([1]),

$$F_i(t, y_i(t), \dot{y}_i(t), u_i(t)) = 0, \quad y_i(t_0) = y_i^0, \quad (2)$$

with $y_i = (x_i, v_i)^T$. These internal submodel equations (2), the dimension of the resulting discretized model, and details of their numerical implementation are usually not known in detail during overall process model formulation.

The global process flowsheet definition allocates each component of the overall input vector $u(t) = (u_1, \dots, u_p)^T$ uniquely to one component of the overall output vector $v(t) = (v_1, \dots, v_p)^T$. Thus the system of equations describing the coupling between the submodels is defined by

$$f(u(t)) \equiv u(t) - PG(u(t)) = 0, \quad t \in [t_0, t_E], \quad (3)$$

where $P = ((p_{ij}))$, with $p_{ij} \in \{0, 1\}$, is a permutation matrix which defines this allocation of individual input and output variables of all subprocesses, and G represents all submodel functions G_i , cf. (1). The behaviour of the time-dependent system (3) is then mainly determined by the corresponding Jacobian $J = I - P \frac{\partial G}{\partial u}$, where $\partial G / \partial u$ denotes the overall block diagonal matrix of the dynamic input-output-sensitivities $\partial G_i / \partial u_i$ of the submodels. Unfortunately, these dynamic sensitivities are not provided by most of the simulation tools which are frequently used in chemical engineering. Even an initial estimation of the Jacobian at t_0 will be difficult to obtain with reasonable effort. Additionally, a heterogeneous process simulation approach requires to solve different submodels on various computer platforms and to retain tested software for submodel integration with its own internal step size and accuracy control. It is obvious that for the distributed simulation of coupled subprocesses an adapted waveform iteration method, cf. [4], can be used. The basic idea of waveform iteration is to solve submodels of an overall model independently of each other on subsequent time intervals, so called windows. To this end, on the actual window, the time behaviour of the vector of input variables of the submodels is estimated, the corresponding time behaviour of the output variables is computed concurrently for all submodels, and the interconnecting variables of the flowsheet are matched iteratively.

2. Iterative solution of coupling equations

Due to the need to simplify communication and synchronization between subprocess simulations, the time variable $t \in [t_0, t_E]$ is discretized within each window equidistantly. Keeping in use the same symbols for notational simplicity, now u_i , and v_i denote the vectors of all discretized input and output variables at all internal time points of the current window in an appropriate order, and u and v the related overall vectors $u = (u_1, \dots, u_p)^T$ and $v = (v_1, \dots, v_p)^T$,

respectively.

A quasi-Newton-type iteration, which solves (3) at the grid points of the current window, is given by

$$u^{k+1} = u^k - (B^k)^{-1} (u^k - PG(u^k)), \quad B^k \approx I - PG_u^k, \quad (4)$$

$$u^{k+1} = Pv^{k+1}, \quad (5)$$

where k denotes the iteration index. Obviously, the evaluation of (4) can be done in parallel for all subprocesses, followed by a common step (5) of allocating the output variables to the related inputs. In order to get continuous approximations of the inputs u_i in (4) in this paper a continuous piecewise linear interpolation is used. This avoids the permanent reinitialization of the integration procedure, as it has to be done in the case of piecewise constant inputs.

In (4), G_u^k represents a reasonable approximation of the overall block diagonal matrix of the dynamic input-output sensitivities of submodels at all internal time points of the current window. Again, a trusted estimation of G_u^k at the beginning of a window, even at t_0 , will be difficult to get. Therefore, we have been looking for an acceleration procedure in the case that no initial estimation is available, i.e. the iteration starts with $G_u^0 = 0$, as it is discussed in [3], or in the case that only some of the submodels can provide such information. To this end the conventional Broyden update is applied to the investigated waveform iteration technique by calculating an adjacent matrix in (4) which still satisfies the quasi-Newton condition with the most recent function values. Obviously, this update strategy can be applied to G_u^k directly to get

$$\begin{aligned} G_u^{k+1} &= G_u^k - \frac{(G_u^k \Delta u^k - \Delta v^k)(\Delta u^k)^T}{(\Delta u^k)^T \Delta u^k} \\ &= G_u^k \left(I - \frac{\Delta u^k (\Delta u^k)^T}{(\Delta u^k)^T \Delta u^k} \right) + \frac{\Delta v^k (\Delta u^k)^T}{(\Delta u^k)^T \Delta u^k}, \quad (\Delta u^k)^T \Delta u^k \neq 0 \end{aligned} \quad (6)$$

with

$$\Delta u^k \equiv u^{k+1} - u^k, \quad \Delta v^k \equiv v^{k+1} - v^k, \quad \Delta f^k \equiv f^{k+1} - f^k = \Delta u^k - P \Delta v^k. \quad (7)$$

3. Applications

The proposed update strategy has been implemented within the framework of the *Simulation Manager* software [2]. This tool allows to distribute the numerical solution of subprocess models to a computer network, handles the overall process flowsheet dependencies, and provides appropriate submodel communication software according to (5). Details of extensive numerical investigations will be reported elsewhere. One can summarise that the update strategy (6) improves the waveform iteration (4), (5) significantly even in the case $G_u^0 = 0$, especially in the case of large window length.

Acknowledgements

We thank Bayer AG, Leverkusen, for valuable support.

4. References

- 1 BORCHARDT, J., EHRHARDT, K., GRUND, F., HORN, D.: Parallel Modular Dynamic Process Simulation. In: Keil, F. et al. (eds.), *Scientific Computing in Chemical Engineering II, Simulation, Image Processing, Optimization and Control*, Springer, Berlin (1999) 152–159
- 2 BRÜLL, L.: Simulation manager: A software tool for process simulation in a heterogeneous hard- and software environment. *SPEEDUP Journal* 10 (1996) 51–53
- 3 KELLEY, C. T.: *Iterative Methods for Linear and Nonlinear Equations*. SIAM Series: Frontiers in Applied Mathematics 16, Philadelphia (1995)
- 4 LELARASMEE, E., RUEHLI, A.E., SANGIOVANNI-VINCENTELLI, A.L.: The Waveform Relaxation Method for Time-Domain Analysis of Large Scale Integrated Circuits. *IEEE Trans. on CAD of Integrated Circuits and Systems* 1 (1982) 131–145
- 5 SECCHI, A.R., MORARI, M., BISCAIA JR., E.C.: The Waveform Relaxation Method in the Concurrent Dynamic Process Simulation. *Comput. Chem. Engrg.* 17 (1993) 683–704

Addresses: PROF. DR. F. GRUND, Weierstrass Institute for Applied Analysis and Stochastics, Mohrenstrasse 39, 10117 Berlin, Germany. – grund@wias-berlin.de

FASSBENDER, H.; BENNER, P.

Computing roots of matrix products

The problem of computing a k th root of a matrix product $W = \prod_{i=1}^k A_i$ is considered. The explicit computation of W may produce a highly inaccurate result due to rounding errors, such that the computed root $\widehat{W}^{\frac{1}{k}}$ is far from the actual root $W^{\frac{1}{k}}$. An algorithm for computing the square root of W is presented which avoids the explicit computation of W by employing the periodic Schur decomposition and therefore yields better accuracy in the computed root $\widehat{W}^{\frac{1}{2}}$. In principle, the techniques are applicable to $k > 2$ as well but lead to solving 2×2 polynomial matrix equations which are difficult to treat. The case $k = 3$ is also addressed briefly.

1. Introduction

Computing the square root of the product of two matrices can be used in model reduction methods based on the cross-Gramians; see [1] and the references therein. This lead us to consider the more general problem of computing the k th root of a matrix product $W = A_1 A_2 \cdots A_{k-1} A_k$ where $A_i \in \mathbb{R}^{n \times n}$. That is, a matrix $W^{\frac{1}{k}}$ is sought such that $W = (W^{\frac{1}{k}})^k$. A k th root of a matrix may not exist. For example, it is easy to verify that the matrix $\begin{bmatrix} 0 & 1 \\ 0 & 0 \end{bmatrix}$ has no square root. Here we will not discuss existence results any further.

The direct approach for computing the k th root of W involves first the explicit computation of W followed by the computation of its k th root. Already the explicit computation of W may produce a highly inaccurate result due to rounding errors, such that the computed product \widehat{W} is far from the actual matrix W . Then one can not expect that the computed root $\widehat{W}^{\frac{1}{k}}$ is close to the actual root $W^{\frac{1}{k}}$. Hence explicitly forming the matrix W should be avoided if possible. The approach suggested here was inspired by the work in [2]. There a fast and stable method for computing the square root X of a given matrix A is developed. The method is based on the Schur factorization $A = QSQ^H$ and uses a fast recursion to compute the upper triangular square root U of S . Then $X = QUQ^H$ is the desired square root. The fast recursion is obtained by comparing coefficients in the equation $U^2 = S$.

The algorithm for computing the k th root of W sketched in the following avoids the explicit computation of W by employing the periodic Schur decomposition. That is, the real Schur factorization $W = Q_1 R Q_1^T$ will be computed implicitly by simultaneously reducing all but the first A_j to upper triangular matrices R_j , A_1 can only be reduced to a quasi-upper triangular matrix R_1 . Then the k th root of the product of the factors R_j is computed. Hence the computed root has the same quasi-upper triangular form as R_1 . This root is then transformed back to the root of W . But note that even in case a k th root of $Q_1^T W Q_1$ exists, it must not necessarily have the form of R_1 .

The process will be demonstrated for $k = 2$, the case $k = 3$ is briefly discussed. By avoiding to form the product W explicitly, this approach yields better accuracy in the computed root $\widehat{W}^{\frac{1}{k}}$ than the direct approach.

2. First step: The periodic Schur decomposition

In order to avoid explicitly computing the matrix W a two step approach for computing the k th root of W is proposed which implicitly computes the desired root without ever forming the explicit matrix product W . The first step of the algorithm consists of employing the periodic Schur decomposition.

Theorem 1. Let $A_j \in \mathbb{R}^{n \times n}$, $j = 1, \dots, k$. There exist orthogonal matrices Q_j , $j = 1, \dots, k$, such that

$$R_1 = Q_1 A_1 Q_2^T, \quad R_2 = Q_2 A_2 Q_3^T, \quad \dots, \quad R_{k-1} = Q_{k-1} A_{k-1} Q_k^T, \quad R_k = Q_k A_k Q_1^T,$$

where R_2, \dots, R_k are upper triangular and R_1 is in quasi-upper triangular form with 1×1 and 2×2 diagonal blocks. Moreover, Q_1 puts W into real Schur form, i.e. $Q_1^T W Q_1 = R_1 R_2 \cdots R_{k-1} R_k$ is quasi-upper triangular.

Constructive proofs and algorithms for computing the periodic Schur decomposition without explicitly forming the product W can be found in [3] and [4].

3. Second step: The k th root

Here we will assume $k = 2$. Using the periodic Schur decomposition the product $W = A_1 A_2$ is transformed to

$\widehat{W} = Q_1^T W Q_1 = (Q_1^T A_1 Q_2)(Q_2^T A_2 Q_1)$ such that $H = Q_1^T A_1 Q_2$ is quasi-upper triangular and $R = Q_2^T A_2 Q_1$ is upper triangular. \widehat{W} has the same quasi-triangular form as H . Comparing the coefficients in $\widehat{W} = X^2$ gives us formulae to compute the elements of the square root X of \widehat{W} . Then $W^{\frac{1}{2}} = Q_1 X Q_1^T$. In order to compute the elements of X we first have to consider the diagonal blocks. In case of a 1×1 block $h_{\ell\ell}$ with $h_{\ell+1,\ell} = h_{\ell,\ell+1} = 0$ we can directly read off $x_{\ell\ell} = \sqrt{h_{\ell\ell} r_{\ell\ell}}$. In case of a 2×2 block $\begin{bmatrix} h_{\ell\ell} & h_{\ell,\ell+1} \\ h_{\ell+1,\ell} & h_{\ell+1,\ell+1} \end{bmatrix}$ we follow the approach from [2]. First orthogonal matrices U, V are computed such that $\tilde{R} = V^T \begin{bmatrix} r_{\ell\ell} & r_{\ell,\ell+1} \\ 0 & r_{\ell+1,\ell+1} \end{bmatrix} U$ is upper triangular, $\tilde{H} = U^T \begin{bmatrix} h_{\ell\ell} & h_{\ell,\ell+1} \\ h_{\ell+1,\ell} & h_{\ell+1,\ell+1} \end{bmatrix} V$ and $\tilde{H}\tilde{R} = \begin{bmatrix} a & b \\ c & a \end{bmatrix}$ with $cb < 0$ (i.e., $\tilde{H}\tilde{R}$ is in standard real Schur form). Then

$$x_{\ell\ell} = x_{\ell+1,\ell+1} = \sqrt{\frac{1}{2}(a + \sqrt{a^2 - bc})}, \quad x_{\ell+1,\ell} = \frac{1}{2x_{\ell\ell}}c, \quad x_{\ell,\ell+1} = \frac{1}{2x_{\ell\ell}}b.$$

The transformation matrices U and V have to be applied to rows and columns $\ell, \ell+1$ of H, R and Q_1 in order to complete this part of the computation. Now the other elements of X can be computed one superdiagonal at a time. Four different cases have to be distinguished depending on the indices of $x_{j\ell}$:

1.: the indices j and ℓ are such that neither h_{jj} nor $h_{\ell\ell}$ belong to a 2×2 diagonal block, then

$$x_{j\ell} = \frac{\sum_{m=\max(1,j-1)}^{\ell} h_{jm} r_{m\ell} - \sum_{m=j+1}^{\ell-1} x_{jm} x_{m\ell}}{x_{jj} + x_{\ell\ell}}.$$

2.: index j is such that h_{jj} does not belong to a 2×2 diagonal block, while index ℓ is such that $h_{\ell\ell}$ belongs to a 2×2 diagonal block (assume w.l.o.g. that the 2×2 block is given by $\begin{bmatrix} h_{\ell\ell} & h_{\ell,\ell+1} \\ h_{\ell+1,\ell} & h_{\ell+1,\ell+1} \end{bmatrix}$), then we obtain a 2×2 system of linear equations for $x_{j\ell}$ and $x_{j,\ell+1}$ which yields with $s_p = \sum_{m=j}^p h_{jm} r_{mp} - \sum_{m=j+1}^{p-1} x_{jm} x_{mp}$

$$x_{j,\ell+1} = \frac{s_{\ell+1}(x_{jj} + x_{\ell\ell}) - s_{\ell} x_{\ell,\ell+1}}{(x_{jj} + x_{\ell\ell})(x_{jj} + x_{\ell+1,\ell+1}) - x_{\ell,\ell+1} x_{\ell+1,\ell}}, \quad x_{j\ell} = \frac{s_{\ell} - x_{j,\ell+1} x_{\ell+1,\ell}}{x_{jj} + x_{\ell\ell}}.$$

3.: index ℓ is such that $h_{\ell\ell}$ does not belong to a 2×2 diagonal block, while index j is such that h_{jj} belongs to a 2×2 diagonal block (assume w.l.o.g. that the 2×2 block is given by $\begin{bmatrix} h_{j-1,j-1} & h_{j-1,j} \\ h_{j,j-1} & h_{jj} \end{bmatrix}$), then we obtain a 2×2 system of linear equations for $x_{j\ell}$ and $x_{j-1,\ell}$ which yields with $s_p = \sum_{m=\max(1,j-1)}^{\ell} h_{pm} r_{m\ell} - \sum_{m=j+1}^{\ell-1} x_{pm} x_{m\ell}$

$$x_{j\ell} = \frac{s_j(x_{j-1,j-1} + x_{\ell\ell}) - x_{j-1,\ell} s_{j-1}}{(x_{jj} + x_{\ell\ell})(x_{j-1,j-1} + x_{\ell\ell}) - x_{j,j-1} x_{j-1,j}}, \quad x_{j-1,\ell} = \frac{s_{j-1} - x_{j-1,j} x_{j\ell}}{x_{j-1,j-1} + x_{\ell\ell}}.$$

4.: both indices j and ℓ are such that h_{jj} and $h_{\ell\ell}$ belong to 2×2 diagonal blocks (assume as before, that h_{jj} and $h_{\ell\ell}$ are the (2,2), resp. the (1,1) element of the respective 2×2 block), then the 4 elements of $X_{j\ell} = \begin{bmatrix} x_{j-1,\ell} & x_{j-1,\ell+1} \\ x_{j,\ell} & x_{j,\ell+1} \end{bmatrix}$ can be computed via solving a 2×2 Sylvester equation

$$\begin{bmatrix} x_{j-1,j-1} & x_{j-1,j} \\ x_{j,j-1} & x_{jj} \end{bmatrix} X_{j\ell} + X_{j\ell} \begin{bmatrix} x_{\ell\ell} & x_{\ell,\ell+1} \\ x_{\ell+1,\ell} & x_{\ell+1,\ell+1} \end{bmatrix} = C_{j\ell},$$

where $C_{j\ell} = H_{j-1,j-1,\ell+1} R_{1,\ell+1,\ell,\ell+1} - X_{j-1,j,j+1,\ell-1} X_{j+1,\ell-1,\ell,\ell+1}$ (employing standard MATLAB notation).

In case the square root does not exist as in the example described in the introduction, the above algorithm fails due to a zero denominator. Numerical examples show that the approach presented here for computing the square root of $W = A_1 A_2$ gives better accuracy than when applying the method proposed in [2] to the product W . In case $A_1 A_2$ is already in the form quasi-upper triangular/triangular, both algorithms behave similarly as 1.–4. are adapted from [2]. Similar to the approach above algorithms for computing the k th root of a product of k matrices can be derived. These formulae are much more involved, e.g., for a 3rd root, 2×2 equations of the form $A^2 X + A X B + X B^2 = C$ have to be solved. Stability issues and existence of k th roots also need further discussion.

4. References

- 1 ALDHAHERI, R.W.: Model order reduction via real Schur-form decomposition. *Int. J. Control* **53** (1991), 709–716.
- 2 BJÖRCK, A. AND HAMMARLING, S.: A Schur Method for the Square Root of a Matrix. *Lin. Alg. Appl.* **52/53** (1983), 127–140.
- 3 BOJANCZYK, A., GOLUB, G.H. AND VAN DOOREN, P.: The periodic Schur decomposition, algorithms and applications. In *Proc. SPIE Conf.*, **1770** (1992), 31–42.
- 4 HENCH, J.J. AND LAUB, A.J.: Numerical Solution of the Discrete-Time Periodic Riccati Equations. *IEEE Trans. Aut. Cont.* **39** (1994), 1197–1210.

Addresses: HEIKE FASSBENDER, Technische Universität München, Fakultät für Mathematik, 80290 München, FRG.
PETER BENNER, Universität Bremen, FB 3, Zentrum für Technomathematik, 28334 Bremen, FRG.

FLAJS, R.; SAJE, M.; ZAKRAJŠEK, E.

Global convergence of Newton's method to the solution of equations of Reissner's Elastica

The sufficient conditions under which the generalized solution of a planar elastic, Reissner's type cantilever beam if solely based on the rotation [5] loaded by conservative load, exists and is unique, are presented. Sufficient conditions for the global convergence of Newton's method and damped Newton's method with a short step are derived. The point load is also taken into account. The derived inequalities are sharp.

1. Existence and uniqueness of weak (generalized) solution

Reissner's model of an elastic beam was first presented in article [4] where the so called "Reissner's kinematical equations" were derived. The deformation of the cantilever is governed by the principle of minimum of an extended functional of the potential energy [5]. The generalized solution of the beam, $\phi \in \overset{\circ}{H}^1((0, L)) = \{u \in W^{1,2}((0, L)), u(L) = 0\}$, is obtained from the requirement that the functional

$$\begin{aligned} \Phi : \phi \mapsto & \int_0^L \left(\frac{\phi'^2}{2} + \frac{R_1}{EJ} (\cos \varphi_u - \cos \varphi) + \frac{R_2}{EJ} (\sin \varphi - \sin \varphi_u) \right. \\ & \left. - \frac{c(R_1^2 - R_2^2)}{EJ} (\cos(2\varphi_u) - \cos(2\varphi)) - \frac{cR_1R_2}{2EJ} (\sin(2\varphi) - \sin(2\varphi_u)) - \frac{m_y}{EJ} \phi \right) ds \end{aligned}$$

is minimal provided that the solution satisfies the prescribed boundary conditions $\phi'(0) = 0$ and $\phi(L) = 0$. We use abbreviations $c = \frac{1}{GA_s} - \frac{1}{EA}$ and $\phi = \varphi_u - \varphi$ where $\varphi, \varphi_u, m_y, L, EA, GA_s, EJ, R_1$ and R_2 designate the rotation of the cross-section, the rotation of the cross-section of the undeformed beam, the prescribed line moment, the length of the cantilever, the elastic axial, shear and bending stiffnesses and Lagrangian multipliers, respectively. Existence and uniqueness of the solution can be easily established by the following theorem [3].

Theorem 1. Let the functional Φ from the Hilbert space H to \mathbb{R} be twice differentiable in the Gâteaux sense. Let the second Gâteaux derivative at the point $u \in H$ be denoted by $D^2\Phi(u) : H \times H \ni (h, k) \mapsto D^2\Phi(u, h, k) \in \mathbb{R}$. Suppose that $u \mapsto D^2\Phi(u, h, k)$ is a continuous functional from H to \mathbb{R} for every fixed pair $h, k \in H$. Suppose further that the inequalities

$$\lambda \|h\|^2 \leq D^2\Phi(u, h, h) \leq \Lambda \|h\|^2, \quad \lambda > 0 \quad (1)$$

$$\text{hold and let } \bigcup_{n=1}^{\infty} H_n = H, \quad H_1 \subset H_2 \subset \dots, \quad \dim H_n = n.$$

Then there exists a unique minimizing sequence $\{u_n\} \in H_n$ and a unique minimizing $u \in H$ such that

$$\min_{v \in H_n} \Phi(v) = \Phi(u_n), \quad \min_{v \in H} \Phi(v) = \Phi(u), \quad \Phi(u_n) \rightarrow \Phi(u), \quad u_n \rightarrow u \quad \text{and} \quad \Phi(u_n) - \Phi(u) \geq \frac{\lambda}{2} \|u_n - u\|^2.$$

The convergence of discrete solutions, obtained, for example, by the conforming finite element method, to the exact solution can be seen from the theorem, too. Theorem 2 is an immediate consequence of Theorem 1.

Theorem 2. Let the external moment at the free end of the cantilever be zero. Let us further assume that the following relations hold: $\varphi_u \in \overset{\circ}{H}^1((0, L))$, $R_1 \in L_2((0, L))$, $R_2 \in L_2((0, L))$, $\int_0^L m_y(s) ds < \infty$. Then there exists a unique solution $\phi \in \overset{\circ}{H}^1((0, L))$ of the minimization problem whenever the inequality

$$\frac{1}{EJ} (\|R\|_{\infty} + c \|R\|_{\infty}^2) < \frac{\pi^2}{4L^2} \quad (2)$$

holds, where we have assumed $c > 0$, and denoted $R = \sqrt{R_1^2 + R_2^2}$ and $\|\cdot\|_\infty : u \mapsto \|u\|_\infty = \text{ess sup}_{s \in [0, L]} |u(s)|$.

The inequality in equation (2) is sharp, as it is easily seen from the straight cantilever loaded by an axial force at the free end.

2. Convergence of Newton's method and damped Newton's method with a short step

According to Nečas [4], we define the gradient $G(u)$ of the functional Φ and the Hessian linear operator $H(u)$ at the point $u \in H$ by equations $\langle G(u), h \rangle = D\Phi(u, h)$ and $\langle H(u)k, h \rangle = D^2\Phi(u, h, k)$. Assume that $H(u)$ is symmetric and positive definite. We construct the sequence $\{u_n\}$ by damped Newton's method using the equation

$$u_{n+1} = u_n - \rho H^{-1}(u_n) G(u_n), \quad n = 0, 1, \dots \quad (3)$$

By employing $\rho = 1$, Newton's method is obtained. Theorem 3 [3] ensures convergence of approximations, constructed by damped Newton's method, to the solution.

Theorem 3. *Let the hypotheses of Theorem 1 be satisfied. We construct the sequence $\{u_n\}$ by formula (3). Let $\rho \in (0, \frac{2\lambda}{\Lambda})$. Then*

$$\lambda^2 \|u_n - u\|^2 \leq \frac{\Lambda^2}{\rho \left(\lambda - \frac{\rho\Lambda}{2} \right)} (\Phi(u_n) - \Phi(u_{n+1})). \quad (4)$$

Thus, $u_n \rightarrow u$, where $G(u) = 0$. The function $\rho \mapsto \rho \left(\lambda - \frac{\rho\Lambda}{2} \right)$ attains its minimum at $\rho = \frac{\lambda}{\Lambda}$ and it gives

$$\|u_n - u\|^2 \leq \frac{2\Lambda^3}{\lambda^4} (\Phi(u_n) - \Phi(u_{n+1})).$$

The inequalities (1) of Theorem 1

$$D^2\Phi(u, h, h) \geq (1 - C^2 K) \int_0^L h'^2 dx = \lambda \int_0^L h'^2 dx = \lambda \|h\|^2, \quad (5)$$

$$D^2\Phi(u, h, h) \leq \int_0^L h'^2 dx + K \int_0^L h^2 dx \leq (1 + C^2 K) \int_0^L h'^2 dx = (1 + C^2 K) \|h\|^2 = \Lambda \|h\|^2 \quad (6)$$

are satisfied with the choice of constants $K = \frac{1}{EJ} (\|R\|_\infty + c \|R\|_\infty^2)$ and $C = \frac{2L}{\pi}$. According to Theorem 3, damped Newton's method (3) converges for all $\rho \in (0, \frac{2\lambda}{\Lambda})$. After considering estimates (5) and (6), the inequalities

$$2(1 - C^2 K) = 2\lambda > \rho\Lambda = \rho(1 + C^2 K) \quad \text{and} \quad (\|R\|_\infty + c \|R\|_\infty^2) < \frac{2 - \rho}{2 + \rho} \frac{\pi^2 EJ}{4L^2}$$

are derived. By making the constant ρ small enough, we could achieve the convergence under loads up to the critical load of the straight cantilever. In particular, the global convergence of Newton's method ($\rho = 1$) under load satisfying $(\|R\|_\infty + c \|R\|_\infty^2) < \frac{1}{3} \frac{\pi^2 EJ}{4L^2}$ is thus ensured. It is seen from the last inequality that the convergence of Newton's method under loads smaller than one third of the critical load of the straight cantilever is assured.

3. References

- 1 FLAJS, R.; ZAKRAJŠEK, E.; SAJE, M.: Existence and uniqueness of the solution of the equations of Reissner's model of an elastic cantilever (in Slovenian), Proc. Kuhelj's days 97, Mokrice, Slovenia, 1997, 1–8.
- 2 KANTOROVIČ, L. V.; AKILOV, G. P.: Functional analysis in normed spaces, Pergamon Press, Oxford, 1982.
- 3 NEČAS, J.: Introduction to the theory of nonlinear elliptic equations, John Wiley & Sons, Chichester, 1986.
- 4 REISSNER, E.: On one-dimensional finite-strain beam theory: the plane problem, J. Appl. Math. Phys. (ZAMP), **23**, 793–804, 1972.
- 5 SAJE, M.: Finite element formulation of finite planar deformation of curved elastic beams, Computers & Structures, **39**, 327–337, 1991.

Addresses: RADO FLAJS, rflajs@fgg.uni-lj.si, MIRAN SAJE, msaje@fgg.uni-lj.si,
EGON ZAKRAJŠEK, egon.zakrajsek@uni-lj.si, University of Ljubljana, Slovenia

BIRGIT HOFFEREK AND HEINRICH VOSS

Eigenvalue Reanalysis and Condensation with General Masters

In design optimization very often several changes of a structure are necessary to reach predetermined demands, and in each step very large eigenvalue problems have to be solved which are small modifications of each other. For large eigenvalue problems condensation methods are used to reduce the number of degrees of freedom to manageable size. In this note we take advantage of preceding computations by implementing eigenvectors of previous models as general masters into condensation.

1. Introduction

One purpose of a design process of a structure is to satisfy predetermined demands, such as given natural frequencies or dynamic responses. During this process the structure is modified a couple of times, and several eigenvalue problems appear which are small modifications of each other and which have similar eigenforms. Hence, reanalytical methods are welcome which take advantage of preceding calculations. A common way in reanalysis is to use Taylor expansions or Rayleigh quotient approximations or assumed mode approaches in a Rayleigh – Ritz method. In this note we consider condensation methods in eigenvalue reanalysis in two ways which are usually applied to reduce the number of degrees of freedom of large eigenvalue problems. First we demonstrate that the algebraic cost of condensation can be reduced substantially if the masters are chosen as interface degrees of freedom in a substructure decomposition of the underlying structure and only a few substructures are modified. Secondly the approximation properties of condensation are enhanced considerably if eigenmodes of previous models are used as general masters.

2. Substructuring and condensation

We consider the general eigenvalue problem

$$Kx = \lambda Mx \quad (1)$$

where $K \in \mathbb{R}^{(n,n)}$ and $M \in \mathbb{R}^{(n,n)}$ are symmetric and positive definite matrices which are usually the stiffness and mass matrix of a finite element model of a structure, respectively. To reduce the number of unknowns Irons and Guyan independently proposed nodal condensation, i.e. to choose a small number of degrees of freedom (called masters) which seem to be representative for the dynamic behaviour of the entire structure, and to eliminate the remaining unknowns (called slaves) neglecting inertia terms in some of the equations of (1).

It is well known that substructuring leads to data structures such that the proportions of the reduced matrices belonging to different substructures can be computed independently. To this end assume that the structure under consideration has been decomposed into r substructures and let the masters be chosen as interface degrees of freedom such that the substructures connect to each other through the master variables only. If the slave variables are numbered appropriately, then the stiffness matrix is given by

$$K = \begin{pmatrix} K_{mm} & K_{ms1} & K_{ms2} & \dots & K_{msr} \\ K_{sm1} & K_{ss1} & 0 & \dots & 0 \\ K_{sm2} & 0 & K_{ss2} & \dots & 0 \\ \vdots & \vdots & \vdots & \ddots & \vdots \\ K_{smr} & 0 & 0 & \dots & K_{ssr} \end{pmatrix}, \quad (2)$$

and the mass matrix M has the same block form. In this case it is easily seen that the condensed eigenvalue problem obtains the form

$$K_0 x_m = \lambda M_0 x_m \quad (3)$$

where the reduced stiffness and mass matrices K_0 and M_0 , respectively, are given by

$$K_0 = K_{mm} - \sum_{j=1}^r K_{mmj} := K_{mm} - \sum_{j=1}^r K_{msj} K_{ssj}^{-1} K_{smj}$$

and

$$M_0 = M_{mm} - \sum_{j=1}^r M_{mmj} =: M_{mm} - \sum_{j=1}^r K_{msj} K_{ssj}^{-1} M_{smj} - M_{msj} K_{ssj}^{-1} K_{smj} + K_{msj} K_{ssj}^{-1} M_{ssj} K_{ssj}^{-1} K_{smj}.$$

Obviously, these matrices can be updated at low cost if only a small number of substructures is modified in a reanalysis step since each of the terms in the sums depends only on data of a single substructure. Notice that this concept can be generalized to condensation methods in the presence of general masters. Details are given in [1].

3. Condensation with general masters

Nodal condensation has the disadvantage that it produces accurate results only for a small part of the lower end of the spectrum. The approximation properties can be improved substantially if general masters are considered. Let $z_1, \dots, z_m \in \mathbb{R}^n$ be independent vectors, and define $Z := (z_1, \dots, z_m) \in \mathbb{R}^{(n,m)}$. Then the projected eigenvalue problem

$$K_0 x_m := P^T K P x_m = \lambda P^T M P x_m =: \lambda M_0 x_m, \quad \text{where } P = K^{-1} Z (Z^T K^{-1} Z)^{-1} Z^T Z \quad (4)$$

is called condensed eigenvalue problem with general masters z_1, \dots, z_m . It is easily seen that this is exactly the reduced problem of nodal condensation if we choose z_1, \dots, z_m as unit vectors.

Since $(Z^T K^{-1} Z)^{-1} Z^T Z$ is a nonsingular matrix the condensed problem (4) is equivalent to the projection of problem (1) to the space spanned by the columns of $K^{-1} Z$. Hence, condensation is nothing else but one step of simultaneous inverse iteration with initial guess $X = M^{-1} Z \in \mathbb{R}^{(n,m)}$. Therefore, we can expect good approximation properties of condensation if we include general masters $z_j = M x_j$ where x_j are approximate eigenvectors of problem (1) corresponding to the desired eigenvalues. Hence, choosing approximate eigenvectors from previous design steps as general masters should improve the approximation properties.

4. A numerical example

To demonstrate the gain of accuracy by general masters we consider the free vibrations of a uniform thin clamped plate covering the rectangular region $\Omega := (0, 5) \times (0, 3)$. We discretized this problem by Bogner-Fox-Schmidt elements on a quadratic mesh with meshsize $h = 0.1$ and obtained a matrix eigenvalue problem of dimension $n = 5684$. Dividing Ω into 15 identical substructures each of them being a square of sidelength 1 and choosing all interface degrees of freedom as masters one obtains a reduced problem of dimension $m = 824$.

We modified the problem by doubling the mass in the rectangles $(2, 3) \times (0, 3)$ and $(4, 5) \times (0, 3)$, respectively. The following table contains the relative errors of the 12 smallest eigenvalues using nodal condensation (column 2 and 4) and of condensation if we complement the interface masters by 12 eigenvectors of the uniform plate as general masters (columns 3 and 5).

	(2, 3) × (0, 3)		(4, 5) × (0, 3)	
1	3.54e-3	1.19e-9	3.04e-3	2.63e-9
2	5.41e-3	3.15e-7	6.15e-3	7.99e-8
3	1.50e-2	1.70e-7	1.38e-2	1.67e-6
4	1.63e-2	1.19e-5	1.41e-2	1.84e-5
5	1.57e-2	1.18e-5	1.86e-2	5.58e-5
6	1.51e-2	9.46e-5	2.68e-2	2.76e-5
7	2.87e-2	9.78e-5	2.74e-2	2.30e-4
8	1.25e-1	3.85e-4	5.71e-2	5.26e-4
9	2.34e-2	3.93e-4	7.03e-2	1.63e-4
10	8.14e-2	4.23e-5	1.19e-1	6.18e-3
11	9.20e-2	1.62e-3	1.11e-1	2.09e-3
12	1.29e-1	8.48e-4	1.27e-1	7.93e-3

5. References

- 1 HOFFEREK, B.: Anwendung der Kondensation mit verallgemeinerten Mastern in der Eigenwert Reanalysis. In preparation
- 2 MACKENS, W., VOSS, H.: Nonnodal Condensation of Eigenvalue Problems. ZAMM 79 (1999), 243–255.

Addresses: BIRGIT HOFFEREK, HEINRICH VOSS, Arbeitsbereich Mathematik, Technische Universität Hamburg-Harburg, D – 21071 Hamburg, email: {hofferek, voss}@tu-harburg.de

KORELC, J.

Multi-language approach in automatic generation of numerical procedures

Practice shows that at the research stage of derivation of a new numerical software different languages and different platforms are the best means for assessment of performances and failures of the numerical model. By the classical approach, re-coding in different languages would be extremely time consuming and is never done. The paper presents the use of symbolic and algebraic systems for improved quality control of automatically generated numerical procedures. With the symbolic concepts the code is automatically generated for several languages and for several platforms from the same basic symbolic description.

1. Introduction

Finite element simulations are well established in several engineering fields and are becoming more frequently applied in biophysics, food production, pharmaceuticals and other sectors. However, only solutions of relatively simple process optimisation problems are available at present, so that considerable development efforts will be required to provide efficient analysis for multi-physics, multi-scale and multi-body problems. With the increasing complexity of phenomenon the reliability of numerical code and the procedures for a quality ensurance of the derived finite element code are more and more important. In this article the symbolic approach will be applied to enable a more general approach. Symbolic approach implemented in Symbolic Mechanics System (SMS) combines recent developments in computer science, in particular in computer symbolic algebra, automatic differentiation of numerical code, automatic code generation and theorem proving. More detailed description of the system can be found in Korelc [1].

2. Multi-language generation and multi-level testing of numerical codes

With the symbolic concepts the finite element code can be automatically generated for several languages and for several platforms from the same basic symbolic description, leading to the multi-level testing procedures. The basic tests which are performed on a single finite element or on a small patch of elements can be done most efficiently by using the general symbolic-numeric environments such as Mathematica, Maple, etc.

1. Mathematical description

$$u = \sum_{i=1}^3 N_i u_i$$

$$N_1 = \frac{x}{L}, \quad N_2 = 1 - \frac{x}{L}, \quad N_3 = \frac{x}{L} \left(1 - \frac{x}{L}\right)$$

$$f = u^2$$



2. Symbolic description in SMS

```
SMSInitialize["test", Language -> "C++"];
SMSModule["Test", Real[u$$[3], x$$, L$$, g$$[3]]];
{x, L} = {SMSReal[x$$], SMSReal[L$$]};
ui = Array[SMSReal[u$$[#]] &, 3];
Ni = {x/L, 1 - x/L, x/L (1 - x/L)};
u = Ni.ui; f = u^2;
g = SMSD[f, ui];
SMSEXPOT[g, g$$];
SMSWrite[];
```

3. Automatically generated code

FORTRAN

```
SUBROUTINE Test(v,u1,x,L,g)
REAL*8 v(500),u1(3),x,L,g(3)
v(6)=x/L
v(7)=1d0 - v(6)
v(8)=v(6)*v(7)
v(12)=2d0*(u(1)*v(6) +
- u(2)*v(7) + u(3)*v(8))
g(1)=v(12)*v(6)
g(2)=v(12)*v(7)
g(3)=v(12)*v(8)
END
```

C

```
void Test(double v[501],
double u1[3],double *x,
double *L,double g[3]){
v[6]=*x/*L;
v[7]=1e0 - v[6];
v[8]=v[6]*v[7];
v[12]=2e0*(u[0]*v[6] +
u[1]*v[7] + u[2]*v[8]);
g[0]=v[12]*v[6];
g[1]=v[12]*v[7];
g[2]=v[12]*v[8];}
```

MATHEMATICA

```
Test[]:=Module[{}],
$VV[6]=x$$/L$$;
$VV[7]=1 - $VV[6];
$VV[8]=$VV[6]*$VV[7];
$VV[12]=2*(u$$[1]*$VV[6] +
u$$[2]*$VV[7]+u$$[3]*$VV[8]);
g$$[1]=$VV[6]*$VV[12];
g$$[2]=$VV[7]*$VV[12];
g$$[3]=$VV[8]*$VV[12];
```

Figure 1: Multi-language generation of numerical codes

It is well known that many design flaws such as element instabilities or poor convergence characteristics can be easily identified if we are able to investigate element quantities on a symbolic level. Unfortunately, symbolic-numeric environments become very inefficient if we have a larger number of elements or if we have to perform iterative numerical procedures. In order to assess element performances under real conditions the easiest way is to perform tests on sequential machines with good debugging capabilities (typically personal computers and programs written in Fortran or C/C++ language). At the end, for real industrial simulations, large parallel machines have to be used. In Figure 1 a simple example is presented that illustrate standard SMS procedure for a multi-language generation of the numerical sub-program. The sub-program returns the gradient of a given function f with respect to the set of parameters u_i .

3. Example: strongly coupled magnetic-thermomechanic problem

In this section the simulation of induction heat treatment is presented (Figure 2a). Steel cylinder is encircled by one circular coil having a square cross section. Electromagnetic field produced by the current-carrying coil induces eddy currents in the workpiece. Eddy currents then produce heat sources throughout workpiece. The resulting strongly coupled, non-linear, transient, magnetic-thermomechanic problem was solved by the finite element method for unknown complex magnetic potential and temperature field. With the SMS the weak form of the coupled electromagnetic and heat conduction equations was consistently linearized leading to fully implicit, quadratically convergent numerical procedure. Derived finite element code was first verified on a symbolic level in Mathematica, then a C code for a general FE environment was generated. The results of the large scale simulation are presented in Figure 2b and 2c.

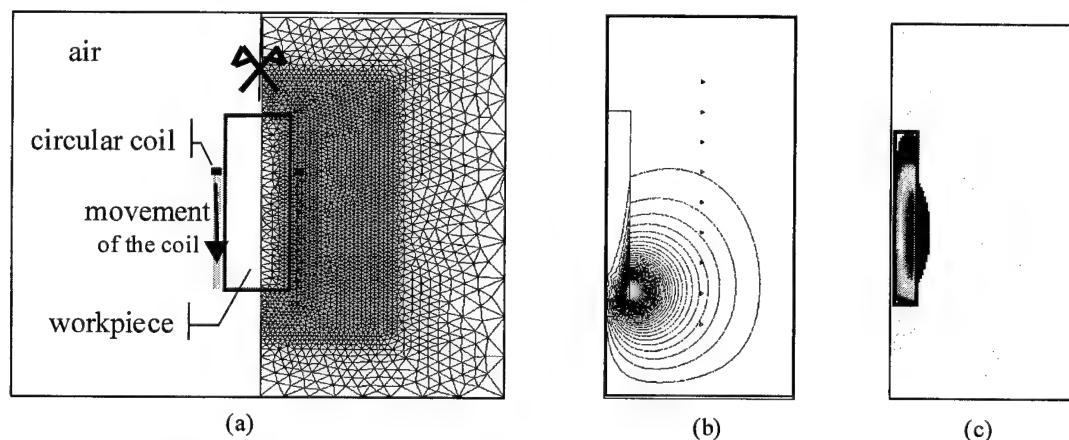


Figure 2: Description of the test example (a), absolute value of complex magnetic vector potential (b), and temperature distribution at the end of simulation (c)

Acknowledgements

Financial support from the Commission of European Communities, DG II, BRITE/EURAM project BE-3924 and Slovenian Ministry of Science and Technology, project J2-0935-0792-98 and is gratefully acknowledged.

4. References

- 1 KORELC, J.: Automatic generation of finite-element code by simultaneous optimization of expressions; *Theoretical Computer Science*, 187, (1997), 231-248.
- 2 KORELC, J., WRIGGERS, P.: Symbolic approach in computational mechanics, In *Computational Plasticity Fundamentals and Applications*, editor D.R.J. Owen, E. Onate and E. Hinton, pp. 286-304, CIMNE, Barcelona, (1997).
- 3 Wang, K.F., Chandrasekar, C., Yang, T.Y.: Finite element simulation of induction heat treatment, *Journal of Materials Engineering and Performance*, 1, (1992), 97-112.

Address: ASSIST. PROF. JOŽE KORELC, Faculty of Civil and Geodetic Engng., Jamova 2, SI-1000 Ljubljana, Slovenia, and Institut für Baumechanik und Numerische Mechanik; Universität Hannover, Germany
e-mail: jkorelc@fgg.uni-lj.si

LARS MÜLLER, GERT LUBE

A nonoverlapping DDM for the nonstationary Navier-Stokes problem

We consider the nonstationary incompressible Navier-Stokes problem in a bounded domain. A semidiscretization in time followed by a linearization procedure lead to Oseen type problems. For an efficient solution we take advantage of a nonoverlapping domain decomposition method (DDM) with interface conditions of Robin type. Strong convergence of the DDM-iterations to the Oseen solution can be proven. Furthermore we apply an a-posteriori estimate which controls the error on the subdomains in terms of the jumps of the velocity across the interface. This may serve as a stopping criterion and gives some information how to choose a free parameter appearing in the interface condition. A stabilized FEM is used to derive a discrete version of the DDM, and requires a modification of the method.

1. Time-discretization of the Navier-Stokes problem

We consider the Navier-Stokes problem in a bounded domain $\Omega \subset \mathbb{R}^d$ with Lipschitz continuous boundary $\partial\Omega$.

$$\partial_t u - \nu \Delta u + (u \cdot \nabla)u + \nabla p = f, \quad \nabla \cdot u = 0 \quad \text{in } (0, T] \times \Omega, \quad u = 0 \quad \text{on } (0, T] \times \partial\Omega, \quad u(0) = u_0 \quad \text{in } \Omega$$

Using $(\cdot, \cdot) = (\cdot, \cdot)_{L^2(\Omega)}$ and $a(w; u, v) := \nu(\nabla u, \nabla v) + ((w \cdot \nabla)u, v)$ the weak form reads: Find $u \in L^2(0, T; H_0^1(\text{div}; \Omega)) \cap L^\infty(0, T; L^2(\text{div}; \Omega))$ s.t. for all $v \in H_0^1(\text{div}; \Omega)$: $\partial_t(u, v) + a(u; u, v) = (f, v)$ in $\mathcal{D}'(0, T)$, $u(0) = u_0$.

Now we divide the time-interval $[0, T]$ into subintervals $J_n := (t_{n-1}, t_n]$, $0 = t_0 < t_1 < \dots < t_k = T$. With $\mathbf{V} \times \mathbf{Q} := (H_0^1(\Omega))^d \times L_0^2(\Omega)$, $\Pi_q := \{F : [0, T] \rightarrow \mathbf{V} \times \mathbf{Q} : F|_{J_n} = \sum_{i=0}^q \psi_i t^i, \psi_i \in \mathbf{V} \times \mathbf{Q}\}$ and $v_+^n := \lim_{t \rightarrow t_n+0} v(t)$, $v^n := v(t_n)$ the dg(q) method consists of finding $U = (u, p) \in \Pi_q$ s.t. for $n = 1, \dots, k$ and all $V = (v, q) \in \Pi_q$

$$\int_{J_n} \{(\partial_t u, v) + a(u; u, v) - (p, \nabla \cdot v) + (q, \nabla \cdot u)\} dt + (u_+^{n-1}, v_+^{n-1}) = (u^{n-1}, v_+^{n-1}) + \int_{J_n} (f, v) dt$$

In the following we consider dg(0). Then we must find $U^n = (u^n, p^n) \in V \times Q$ s.t. for all $V = (v, q) \in V \times Q$

$$a(u^n; u^n, v) - (p^n, \nabla \cdot v) + (q, \nabla \cdot u^n) + \frac{1}{k_n} (u^n, v) = \frac{1}{k_n} \left(\int_{J_n} f dt + u^{n-1}, v \right) =: (f^n, v).$$

We linearize with a simple iteration and with $A^n((u, p), (v, q)) := a(b; u, p) + \frac{1}{k_n} (u, v) - (p, \nabla \cdot v) + (q, \nabla \cdot u)$, $F^n((v, q)) := (f^n, v)$, $b = u^{n,i}$ we arrive at a stationary problem: $A^n((u^{n,i+1}, p^n), (v, q)) = F^n((v, q))$.

2. The Robin-Robin algorithm

In this section we describe the domain decomposition method for the linearized problem. First we do that on the continuous level in space. The proofs of the theorems can be found in [1]. We divide the domain into subdomains $\bar{\Omega} = \bigcup_{i=1}^M \bar{\Omega}_i$, $\Omega_i \cap \Omega_j = \emptyset$ for $i \neq j$ with the interface $\Gamma := \bigcup_{i \neq j} \Gamma_{ij}$, $\Gamma_{ij} := \partial\Omega_i \cap \partial\Omega_j$. Here we restrict ourselves to stripwise partitions, i.e. $\Gamma_{ij} \neq \Gamma_{kl} \Rightarrow \text{dist}(\Gamma_{ij}, \Gamma_{kl}) > 0$.

Theorem 1. (2-field-formulation) With $\mathbf{V}_i := \mathbf{V}|_{\Omega_i}$, $\mathbf{Q}_i := \mathbf{Q}|_{\Omega_i}$, $W_{ij} := \mathbf{V}|_{\Gamma_{ij}}$ and the restrictions $A_i^n(\cdot, \cdot)$ resp. $F_i^n(\cdot)$ of the bilinear- resp. linearform to Ω_i the weak Oseen-problem is equivalent to find $(u_i, p_i)_{i=1}^M \in \mathbf{X}_{i=1}^M(\mathbf{V}_i \times \mathbf{Q}_i)$ with $u_i = u_j$ in W_{ij} and $(\Lambda_{ij}) \in (W_{ij}^*)_{i \neq j}$ s.t. for $(v_i, q_i)_{i=1}^M \in \mathbf{X}_{i=1}^M(\mathbf{V}_i \times \mathbf{Q}_i)$, $\Phi \in W_{ij}$

$$A_i^n((u_i, p_i), (v_i, q_i)) - \langle \frac{1}{2} (b \cdot n_i) u_i - z_i \star u_i, v_i \rangle_{\Gamma_i} = F_i^n(v_i, q_i) + \sum_{j(\neq i)} \langle \Lambda_{ji}, v_i \rangle_{\Gamma_{ij}}, \quad (1)$$

$$\langle \Lambda_{ij} + \Lambda_{ji}, \Phi \rangle_{\Gamma_{ij}} = \langle (z_i + z_j) \star u_i, \Phi \rangle_{\Gamma_{ij}}. \quad (2)$$

The second equation corresponds to a Robin-type transmission condition. Dropping the constraint $u_i = u_j$ and decoupling of (1)-(2) leads to the following **Robin-Robin algorithm**.

Start with an initial guess $\Lambda_{0,ij} \in W_{ij}^*$ for $k \neq j$. Find $U_{m,i} = (u_{m,i}, p_{m,i}) \in \mathbf{V}_i \times Q_i$ s.t. for all $V_i = (v_i, q_i) \in \mathbf{V}_i \times Q_i$

$$A_i^n(U_{m,i}, V_i) + \langle (-\frac{1}{2}b \cdot n_i + z_i) \star U_{m,i}, V_i \rangle_{\Gamma_i} = F_i^n(V_i) + \sum_{j(\neq i)} \langle \Lambda_{m-1,ji}, v_i \rangle_{\Gamma_{ij}}.$$

Define a new functional $\Lambda_{m,ij} \in W_{ij}^*$ by $\langle \Lambda_{m,ij}, \phi \rangle := \langle (z_i + z_j) \star U_{m,i} - \Lambda_{m-1,ji}, \phi \rangle_{\Gamma_{ij}}$ for $\phi \in W_{ij}$.

Theorem 2. Assume that $z_i \in (L^\infty(\Gamma_i))^2$, $z_i = z_j$ on Γ_{ij} , $\inf_{x \in \Gamma_i} z_i(x) > 0$. Each subdomain problem has a unique solution $(u_{m,i}, p_{m,i})$. Moreover we have convergence to the restriction (u_i, p_i) of the global solution to Ω_i according to

$$\|u_{m,i} - u_i\|_{1,\Omega_i} \rightarrow 0, \quad \|\Pi_i(p_{m,i} - p_i)\|_{0,\Omega_i} \rightarrow 0, \quad \Pi_i q := q - \text{meas}(\Omega_i)^{-1}(q, 1)_{L^2(\Omega_i)}.$$

Theorem 3. In the case of two subdomains we have for the error $E_{m,i} := (e_i, \epsilon_i) := (u_{i,m} - u_i, p_{i,m} - p_i)$ ($i = 1, 2$)

$$M_i^{-1} \|\Pi_i \epsilon_i\| \leq \|E_{i,m+1}\| \leq K_j \|z_i - \frac{1}{2}(b \cdot n_i)\|_{\infty, \Gamma} \|u_{m+1,i} - u_{m,j}\|_{0,\Gamma} + L_j \|u_{m+1,i} - u_{m,j}\|_{H_{00}^{1/2}(\Gamma)}$$

with $\|(v, q)\|_i^2 := \nu |v|_{1,\Omega_i}^2 + \frac{1}{k_n} \|v\|_{0,\Omega_i}^2$ and constants K_j, L_j, M_j depending on problem data.

For the choice of the interface parameter we observe that in the limit case $\nu = 0$ no boundary condition should be imposed on the noninflow part $\Gamma_i^+ := \{x \in \Gamma_i : (b \cdot n_i)(x) \geq 0\}$. Thus we set $z_i = (\frac{1}{2}|b \cdot n_i| + R^1, \frac{1}{2}|b \cdot n_i| + R^2)$ with $\lim_{\nu \rightarrow 0} R^l = 0$, $l = 1, 2$. Balancing the constants L_j and K_j in the a-posteriori estimate gives

$$z_i^l = \frac{1}{2}|b \cdot n_i| + \max_{i=1,2} \frac{L_j}{K_j} \sim \frac{1}{2}|b \cdot n_i| + \max_{j=1,2} \frac{\nu}{H_j} \left(1 + \sqrt{\frac{1}{\nu k_n}} H_j + \|b\|_{\infty, \Omega_j} \min \left\{ \sqrt{\frac{k_n}{\nu}}, \frac{H_j}{\nu} \right\} \right).$$

To derive a *discrete DDM* we start from a (global) finite element spaces $\mathbf{V}_h \subset V$, $Q_h \subset Q$ and a SUPG-stabilization with bilinear- resp. linearforms $A_S^n(\cdot, \cdot)$ resp. $F_S^n(\cdot)$. We define local spaces $\mathbf{V}_{h,i} := \mathbf{V}_h|_{\Omega_i}$, $Q_{h,i} := Q_h|_{\Omega_i}$, $W_{h,ij} := V_h|_{\Gamma_{ij}}$ and the restrictions $A_{S,i}^n(\cdot, \cdot)$, $F_{S,i}^n(\cdot)$ to Ω_i . Now we need a two-field formulation of the discrete problem corresponding to Theorem 1. The proof uses the discontinuity of pressure. Thus we have two possibilities. The first one is to use pressure functions which are discontinuous (at least) across Γ . Then we must introduce pressure jump terms of the form $\sum_{E \subset \Gamma} \sigma_E([p]_E, [q]_E)_E$ in the stabilization. The other way is to introduce a Lagrangian multiplier for the pressure test functions. In both variants a decoupling of 2-field-formulation yields a modified Robin-Robin algorithm. With $\kappa = 1$ for continuous and $\kappa = 0$ for discontinuous pressure the method reads

$$\begin{aligned} & A_{S,i}^n(U_{m,i}, V_i) + \langle -\frac{1}{2}b \cdot n_i + z_i \star u_i, v_i \rangle_{\Gamma_i} + \kappa \langle \rho_i^p p_i, q_i \rangle_{\Gamma_i} + (1 - \kappa) \sum_{E \subset \Gamma_i} \sigma_E(p_{m,i}, q_i)_E \\ & = F_{S,i}^n(V_i) + \sum_{j(\neq i)} \langle \Lambda_{m-1,ji}^u, v_i \rangle_{\Gamma_{ij}} + \kappa \langle \Lambda_{m-1,ji}^p, q_i \rangle_{\Gamma_{ij}} + (1 - \kappa) \sum_{j(\neq i)} \sum_{E \subset \Gamma_{ij}} \sigma_E(p_{m-1,j}, q_i)_E. \\ & \langle \Lambda_{m,ij}^u, \phi^u \rangle := \langle (z_i + z_j) \star u_{m,i} - \Lambda_{m-1,ji}^u, \phi^u \rangle_{\Gamma_{ij}} \quad \text{for } \phi^u \in W_{h,ij}, \\ & \kappa \langle \Lambda_{m,ij}^p, \phi^p \rangle := \kappa \langle (\rho_i^p + \rho_j^p) p_{m,i} - \Lambda_{m-1,ji}^p, \phi^p \rangle_{\Gamma_{ij}} \quad \text{for } \phi^p \in R_{h,ij} := Q_h|_{\Gamma_{ij}}. \end{aligned}$$

The properties of the continuous method stated in Theorem 2 are also valid for the discrete method. We can prove the unique solvability of the subdomain problems and convergence of the discrete DDM-solutions to the global discrete solution with respect to a stabilized norm (see [2]). A result corresponding to Theorem 3 for the case of discontinuous pressure can be found in [3]. Numerical examples are included in these papers as well.

3. References

- 1 OTTO, F.-C. : A Non-Overlapping Domain Decomposition Method for Elliptic Equations, PhD Thesis, Institut für Numerical and Applied Mathematics, University of Göttingen 1999
- 2 LUBE, G., MÜLLER, L., MÜLLER, H.: A New Nonoverlapping DDM for Stabilized Finite Element Methods Applied to the Nonstationary Navier-Stokes Equations. Appears in : Numerical Linear Algebra with Applications, 2000.
- 3 LUBE, G., MÜLLER, L., AND OTTO, F.-C. : A Non-Overlapping Domain Decomposition Method for Stabilized Finite Element Approximations of the Oseen Equations. Appears in : Journal of Computational and Applied Mathematics, 2000.

Addresses: LARS MÜLLER, GERT LUBE, Universität Göttingen, Fakultät für Mathematik, D-37083 Göttingen

ANDREAS PELZER, BIRGIT HOFFEREK AND HEINRICH VOSS

Implementing Global Masters into Parallel Condensation

The dynamic analysis of structures leads to very large generalized eigenvalue problems. Their number of unknowns can be reduced to a manageable size by condensation methods which can be parallelized by combining it with substructuring. In this note we implement global masters into the parallel condensation process.

1. Condensation with general masters

In the analysis of the dynamic response of structures using finite element methods very often prohibitively many degrees of freedom are needed to model the behaviour of the system sufficiently accurate. Static condensation is frequently employed to economize the computation of a selected group of eigenvalues and eigenvectors. These methods choose from the degrees of freedom a small number of master variables. Neglecting inertia terms the remaining variables (termed slaves) are eliminated leaving a much smaller problem for the master variables only.

It has frequently been noted in the literature that the quality of the eigenvalue and eigenvector approximations produced by static condensation is satisfactory only for a very small part of the lower end of the spectrum. To improve the approximation properties of condensation Mackens and the third author [2] introduced general masters which allow to implement a priori information of the eigenmodes (such as eigenmodes of similar structures considered in reanalysis or prolongations of eigenvector approximations obtained on a coarser grid) into the condensation process.

We consider the general eigenvalue problem

$$Kx = \lambda Mx \quad (1)$$

where $K \in \mathbb{R}^{(n,n)}$ and $M \in \mathbb{R}^{(n,n)}$ are symmetric and positive definite matrices which are usually the stiffness and mass matrix of a finite element model of a structure, respectively. The dimension n is supposed to be very large.

To reduce the number of degrees of freedom we choose linear independent vectors $z_1, \dots, z_m \in \mathbb{R}^n$, and we define $Z := (z_1, \dots, z_m) \in \mathbb{R}^{(n,m)}$. Then the projected eigenvalue problem

$$K_0 x_m := P^T K P x_m = \lambda P^T M P x_m =: \lambda M_0 x_m, \quad \text{where } P = K^{-1} Z (Z^T K^{-1} Z)^{-1} Z^T Z \quad (2)$$

is called the condensed eigenvalue problem with general masters z_1, \dots, z_m . It is easily seen that this is exactly the reduced problem introduced by Irons and Guyan if we choose z_1, \dots, z_m as unit vectors. This special case is called nodal condensation.

Since $(Z^T K^{-1} Z)^{-1} Z^T Z$ is a nonsingular matrix the condensed problem (2) is equivalent to the projection of problem (1) to the space spanned by the columns of $K^{-1} Z$. Hence, condensation is nothing else but one step of simultaneous inverse iteration with initial guess $X = M^{-1} Z \in \mathbb{R}^{(n,m)}$. Therefore, we can expect good approximation properties of condensation if we include general masters $z_j = M x_j$ where x_j are approximate eigenvectors of problem (1) corresponding to the desired eigenvalues.

2. Parallel condensation

For nodal condensation the following strategy yields a coarse grained parallel algorithm developed in [4]. Suppose that the structure under consideration has been decomposed into r substructures and let the masters be chosen as interface degrees of freedom. Assume that the substructures connect to each other through the master variables only. If the slave variables are numbered appropriately, then the stiffness matrix is given by

$$K = \begin{pmatrix} K_{mm} & K_{ms1} & K_{ms2} & \dots & K_{msr} \\ K_{sm1} & K_{ss1} & 0 & \dots & 0 \\ K_{sm2} & 0 & K_{ss2} & \dots & 0 \\ \vdots & \vdots & \vdots & \ddots & \vdots \\ K_{smr} & 0 & 0 & \dots & K_{ssr} \end{pmatrix}, \quad (3)$$

and the mass matrix M has the same block form. In this case it is easily seen that the reduced matrices K_0 and M_0 in (2) are given by

$$K_0 = K_{mm} - \sum_{j=1}^r K_{mmj} := K_{mm} - \sum_{j=1}^r K_{msj} K_{ssj}^{-1} K_{smj}$$

and

$$M_0 = M_{mm} - \sum_{j=1}^r M_{mmj}, \text{ where } M_{mmj} := K_{msj} K_{ssj}^{-1} M_{smj} + M_{msj} K_{ssj}^{-1} K_{smj} - K_{msj} K_{ssj}^{-1} M_{ssj} K_{ssj}^{-1} K_{smj}.$$

It is obvious that they can be computed completely in parallel, and that the only communication consists of one fan in process. This approach can be generalized to general masters if each of them is contained in a single substructure (cf. [3]).

In Section 1 we pointed out that good approximation properties of condensation can be expected if general masters $z_j = Mx_j$ are in use where x_j are approximate eigenvectors of problem (1). In general these will have global support, and the block structure of K is destroyed. For this case we proposed a coarse grained parallelization concept the communication of which consists of two fan in processes and one broadcast to obtain the reduced matrices. Details are explained in [1].

3. Numerical experiments

We implemented the parallel algorithm in FORTRAN 90 using LAPACK 3 and BLAS routines for the linear algebra and MPI 1.05 for message passing. We tested the program on a heterogeneous workstation cluster consisting of one HP C3000, one HP J2240, and five HP 9000, 712/100 connected by fast-ethernet and on an HP N-Class parallel computer with 8 and 16 HP-PA 8500/440MHz processors organized as one and two clusters, respectively. The user can only assign each process to one of the clusters whereas the local scheduling is organized by the operating system. Moreover the computer is run in a multi-user environment. Hence we are not able to report on the load balancing of the processors.

Our test example was a finite element model of a container ship with 35262 degrees of freedom. We subdivided it into 10 substructures each of them consisting of between 1134 and 4792 unknowns, and obtained a reduced problem of dimension 2097. Besides the plain model of the ship which is called the dry model we took into account hydrodynamic masses. This model is usually called the wet model. The spectra of these two models differ quite a bit (cf. the first row of the following table which contains the relative distances). However, adding 12 dry eigenmodes corresponding to the smallest eigenvalues as general masters to the interface masters when computing the wet eigenmodes improves the eigenvalue approximations considerably (row 2 contains the relative errors of nodal condensation with interface degrees of freedom as masters only and row 3 the relative errors of condensation using 12 dry modes as general masters additionally).

rel.dist.	3.1e-1	1.5e-1	2.7e-1	7.5e-1	1.0e+0	8.9e-1	6.0e-1	6.7e-1	3.4e-1	4.4e-1	4.7e-1	7.5e-1
nod.cond.	4.9e-5	6.0e-5	2.4e-5	1.2e-4	3.9e-4	4.5e-4	6.4e-3	1.9e-2	2.1e-2	8.9e-2	1.0e-1	1.1e-1
gen.mast.	4.9e-7	7.5e-7	7.9e-7	1.7e-7	3.0e-8	1.4e-7	5.6e-7	1.0e-5	1.9e-5	1.7e-4	4.2e-3	1.2e-2

Acknowledgements

Thanks are due to Christian Cabos, Germanischer Lloyd, who provided us with the finite element model of the container ship. The first author gratefully acknowledges support by the Deutsche Forschungsgemeinschaft within the Graduiertenkolleg Meerestechnische Konstruktionen.

4. References

- 1 HOFFEREK, B., PELZER, A., VOSS, H.: Global masters in parallel condensation of eigenvalue problems. Submitted to Computers & Structures.
- 2 MACKENS, W., VOSS, H.: Nonnodal Condensation of Eigenvalue Problems. ZAMM 79 (1999), 243–255.
- 3 MACKENS, W., VOSS, H.: General Masters in Parallel Condensation of Eigenvalue Problems. Parallel Computing 25 (1999), 893–903.
- 4 ROTHE, K., VOSS, H.: A Fully Parallel Condensation Method for Generalized Eigenvalue Problems on Distributed Memory Computers. Parallel Computing 21 (1995), 907–921.

Addresses: BIRGIT HOFFEREK, ANDREAS PELZER, HEINRICH VOSS, Arbeitsbereich Mathematik, Technische Universität Hamburg-Harburg, D – 21071 Hamburg, email: {hofferek, pelzer, voss}@tu-harburg.de

M. SCHINNERL, U. LANGER, R. LERCH

Multigrid Simulation of Electromagnetic Actuators

A recently developed multigrid simulation scheme for coupled magneto-mechanical systems is presented. This scheme allows the efficient calculation of 3D dynamic motions of elastic ferromagnetic materials in a magnetic field. The 3D mechanical problem is discretized with nodal elements and the 3D magnetic problem with edge elements. Both meshes may be chosen independently and therefore, they can be adapted to the physical requirements of the mechanical and magnetic field. By applying fast multigrid solution techniques, very short solution times can be achieved even for large scale 3D problems. Using the developed scheme the transient behavior of a solenoid valve is calculated.

1. Introduction

Electromagnetic actuators convert electrical into mechanical energy by using nonlinear magnetic coupling effects. Therefore, the numerical simulation of these actuators must take into account the electrical, magnetical and mechanical fields and their interaction. This leads to very long simulation times, especially in the transient 3D case. In this paper a multigrid technique for the design of electromagnetical transducers, based on the finite element method (FEM) is presented. The application of geometrical multigrid solvers to the arising matrix-equation systems and the use of different grids for the magnetic and mechanical fields enables even for complex problems a fast solution process.

By using the developed scheme the nonlinear dynamical behavior of a solenoid valve is calculated and the simulation results are compared with measurements.

2. Theory

If displacement currents are neglected, which is possible for the considered class of actuators without restrictions to the accuracy, the magnetic field can be described by the parabolic partial differential equation

$$\nabla \times \left(\frac{1}{\mu} \nabla \times \vec{A} \right) = \vec{J}_e - \gamma \frac{\partial \vec{A}}{\partial t} - \gamma \nabla V + \gamma \frac{\partial \vec{d}}{\partial t} \times (\nabla \times \vec{A}). \quad (1)$$

In (1) μ denotes the permeability, γ the conductivity, \vec{A} the magnetic vector potential, V a known electric potential and \vec{J}_e an impressed source current density. For the mechanical displacement \vec{d} in a linear elastic medium the hyperbolic equation

$$\frac{E}{2(1-\nu)} \left((\nabla \cdot \nabla) \vec{d} + \frac{1}{1-2\nu} \nabla (\nabla \cdot \vec{d}) \right) + \vec{f}_V = \rho \frac{\partial^2 \vec{d}}{\partial t^2} \quad (2)$$

holds. Here E is the Young's modulus, ν the Poisson ratio and ρ the specific density of the material. The magnetic and the mechanical field are coupled by different effects like the Lorentz-force, surface forces at an interface between two materials with different permeability and the electro-motive-force. Additionally, in many cases the variation of the magnetic field caused by large mechanical displacements must be taken into account [1].

With the help of a nodal finite element (FE) discretization of (2) and an edge FE discretization of (1) a system of coupled ordinary differential equations is obtained. This system is solved by an efficient iterative coupling technique where multigrid solvers are applied to the arising matrix-equation systems [2]. For the case of 3D edge element discretization of the magnetic field a special multigrid technique, which is presented in [3], is used.

3. Simulation of a Solenoid Valve

As an application example the dynamical behavior of a magnetic solenoid valve is calculated (Fig. 1). It consists of a ferromagnetic pot-magnet with a copper coil and an armature which is fixed by a compression spring in its upper position. If the coil is loaded by a current pulse, produced by a capacitor discharge, the armature is attracted by the pot magnet. To avoid eddy currents, which causes high delay times between the current pulse and the magnetic force the pot magnet is sliced [4]. In Fig. 2 the coarse grid, which discretizes only a quarter of the valve, is shown.

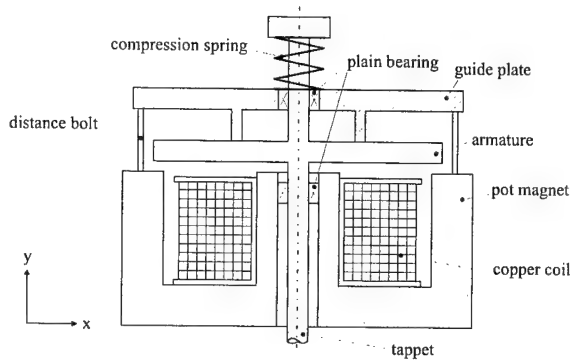


Figure 1: Principal setup of the magnetic solenoid valve

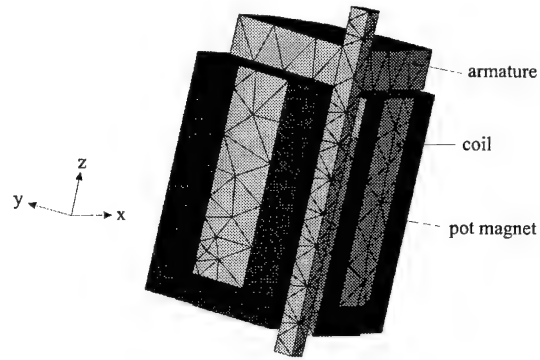


Figure 2: Coarse grid mesh of the solenoid valve (without air)

The mesh for the mechanical problem (12.000 nodes) and the much finer magnetic mesh (110.000 edges) are obtained by adaptive refinement of this coarse grid. The most time consuming part of the simulation process is the repeated solution of the matrix equation system arising by the edge element discretization of the magnetic problem. In Fig. 3 the convergence behavior of the used multigrid technique for this problem is compared to a standard approach. To reduce the residuum by a factor of 10^6 the MG solver needed 21 steps (320 s) and the PC-CG solver 108 steps (1266 s) (used Computer: SGI ORIGIN 300 MHz). The accumulated simulation time for the whole dynamical simulation, consisting of 40 time steps and approximately 6 nonlinear iterations per time step, was 14 hours. In Fig. 4 the measured and simulated magnetic force are compared. Thereby a good agreement is observed.

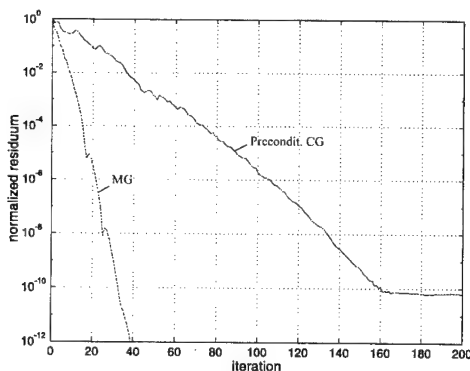


Figure 3: Convergence behavior of the multigrid method and a conventional solver

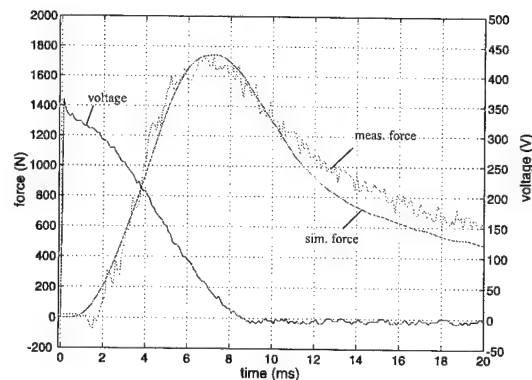


Figure 4: Comparison of measured and simulated magnetic force

Acknowledgements

This work has been supported by the Austrian Science Foundation - 'Fonds zur Förderung der wissenschaftlichen Forschung (FWF)' under project SFB F013 'Numerical and Symbolic Scientific Computing'

4. References

- 1 S. KURZ, J. FETZER, G. LEHNER: Threedimensional transient FEM-BEM coupled analysis of electrodynamic levitation problems, IEEE Trans. on Magnetics, **32**, No. 3, 1062-1065 (1996)
- 2 M. SCHINNERL, J. SCHÖBERL: Multigrid Methods for the 3D Simulation of Nonlinear Magneto-Mechanical Systems, SFB-Report 99-30, Linz (1999)
- 3 D. ARNOLD, R. FALK, R. WINTHER: Multigrid in $H(\text{div})$ and $H(\text{curl})$, Numer. Math.(2000), to appear
- 4 E. KALLENBACH, R. EICK, P. QUENDT: Elektromagnete, Stuttgart (1994)

Addresses: MICHAEL SCHINNERL, ULRICH LANGER, REINHARD LERCH, SFB013, Universität Linz, Altenbergerstr. 69, 4040 Linz, Austria

SCHWETLICK, H.; SCHNABEL, U.

An inverse subspace iteration for computing q smallest singular values of a matrix

Consider a matrix $A \in \mathbb{R}^{n \times n}$ with singular values $\sigma_1 \geq \sigma_2 \geq \dots \geq \sigma_p > \sigma_{p+1} \geq \dots \geq \sigma_{p+q}$, $p = n - q$. For computing the singular values $\Sigma_2 = \text{diag}(\sigma_{p+1}, \dots, \sigma_{p+q})$, i. e., for finding $U_2, V_2 \in \mathbb{R}^{n \times q}$ with $U_2^T U_2 = V_2^T V_2 = I_q$ and $AV_2 = U_2 \Sigma_2$, $A^T U_2 = V_2 \Sigma_2$, an iteration is proposed which requires per step to solve alternately a linear system with matrix $B_{2\ell} = B(Y_{2\ell}, X_{2\ell-1}, \Omega_{2\ell})$ or $B_{2\ell+1}^T = B(Y_{2\ell}, X_{2\ell+1}, \Omega_{2\ell+1})^T$, resp., $\ell \geq 0$, where

$$B(Y, X, \Omega) := \begin{bmatrix} A & Y \\ X^T & \Omega \end{bmatrix} \in \mathbb{R}^{(n+q) \times (n+q)}.$$

The B_k used have uniformly bounded condition numbers, and under weak assumptions the singular vector approximations extracted from $X_{2\ell-1}$ and $Y_{2\ell}$ converge linearly with factor $\kappa := \sigma_{p+1}/\sigma_p < 1$ whereas certain approximations to Σ_2 have the factor κ^2 . The theoretical results are confirmed by some numerical examples.

1. Problem

This paper is an extension of [3] where the case of $q = 1$ was considered. Let $A \in \mathbb{R}^{n \times n}$ be as above with $\text{rank}(A) \geq p$, $q := n - p \ll n$. In addition, suppose that also matrices $Y, X \in \mathbb{R}^{n \times q}$ with $Y^T Y = X^T X = I_q$ are given such that $\text{im } Y \approx \text{im } U_2$, $\text{im } X \approx \text{im } V_2$ in the sense that the angles

$$\eta := \angle(\text{im } Y, \text{im } U_2) := \max\{\min\{\angle(y, u) : u \in \text{im } U_2\} : y \in \text{im } Y\} \quad \text{and} \quad \xi := \angle(\text{im } X, \text{im } V_2)$$

– see [1] for this notion – are not too close to $\pi/2$. We want to find improved approximations $\text{im } Y^+$, $\text{im } X^+$ to $\text{im } U_2$, $\text{im } V_2$, defined by Y^+ , X^+ with $(X^+)^T X^+ = (Y^+)^T Y^+ = I_q$ such that the angles $\eta^+ := \angle(\text{im } Y^+, \text{im } U_2)$, $\xi^+ := \angle(\text{im } X^+, \text{im } V_2)$ are smaller than ξ , η . From these matrices Y^+ , X^+ we want to extract approximations to U_2 , V_2 , and Σ_2 .

2. Motivation from Singularity Theory

Consider a smooth map $F : \mathbb{R}^n \times \mathbb{R} \rightarrow \mathbb{R}^n$ and the related nonlinear system $F(z, \lambda) = 0$. Then (z^*, λ^*) is called a singular point of the solution manifold $\{(z, \lambda) : F(z, \lambda) = 0\}$ if $A(z^*, \lambda^*) := \partial_z F(z^*, \lambda^*)$ is singular. Under the assumption that $r := \text{rank } A(z, \lambda) \geq n - 1 \quad \forall (z, \lambda)$ in a neighborhood of (z^*, λ^*) there is a simple condition for $A(z, \lambda)$ being singular, cf. [2]:

Lemma 1. Define $(v, \mu) \in \mathbb{R}^n \times \mathbb{R}$ as function of (z, λ) by the linear system

$$\underbrace{\begin{bmatrix} A(z, \lambda) & y \\ x^T & 0 \end{bmatrix}}_{=: B(z, \lambda)} \begin{bmatrix} v \\ \mu \end{bmatrix} = \begin{bmatrix} 0 \\ 1 \end{bmatrix}$$

where y, x are chosen so that $B(z^*, \lambda^*)$ is nonsingular. Then we have

$$A(z, \lambda) \text{ singular} \iff \mu(z, \lambda) = 0 \quad \text{for all } (z, \lambda) \text{ close to } (z^*, \lambda^*).$$

If $\mu = 0$, then $Av = 0$, i.e., v is a right singular vector to $\sigma_n = 0$.

3. Generalization to the Case of Rank Drop $q \geq 1$

We choose Y, X, Ω such that $B(Y, X, \Omega) := \begin{bmatrix} A & Y \\ X^T & \Omega \end{bmatrix} \in \mathbb{R}^{(n+q) \times (n+q)}$ is nonsingular for the given matrix A . This holds true, for example, if $\Omega = 0$ and $(\sigma_{p+1}/\sigma_p) \tan \eta \tan \xi < 1$. Then we solve

$$AX^+ + YM^+ = 0, \quad X^T X^+ + \Omega M^+ = I_q$$

for (X^+, M^+) . It can be proved that $\text{rank } X^+ = q$ and $\tan \xi^+ \leq \kappa \tan \eta$ where $\kappa := \sigma_{p+1}/\sigma_p$. Moreover, we have $M^+ = 0$ if and only if $\text{rank } A = p$.

Remark 1. If B is replaced by B^T one obtains an analogous result for (Y^+, N^+) instead of (X^+, M^+) where $M^+ = (N^+)^T$.

4. Generalized Inverse Subspace Iteration (=GISI)

One double step of GISI ($k = 2\ell \rightarrow k+1 = 2\ell+1 \rightarrow k+2 = 2\ell+2$, $\ell = 0, 1, \dots$):

1. Compute $\begin{bmatrix} \tilde{X}_{2\ell+1} \\ \tilde{M}_{2\ell+1} \end{bmatrix}$ from $\begin{bmatrix} A & Y_{2\ell} \\ X_{2\ell-1}^T & N_{2\ell} \end{bmatrix} \begin{bmatrix} \tilde{X}_{2\ell+1} \\ \tilde{M}_{2\ell+1} \end{bmatrix} = \begin{bmatrix} 0 \\ I_q \end{bmatrix}$
2. Compute $[X_{2\ell+1}, R_{2\ell+1}]$ from the modified Gram-Schmidt-orthogonalization of $\tilde{X}_{2\ell+1}$, $M_{2\ell+1} := \tilde{M}_{2\ell+1} R_{2\ell+1}^{-1}$
3. Compute $\begin{bmatrix} \tilde{Y}_{2\ell+2} \\ \tilde{N}_{2\ell+2} \end{bmatrix}$ from $\begin{bmatrix} A^T & X_{2\ell+1} \\ Y_{2\ell}^T & M_{2\ell+1} \end{bmatrix} \begin{bmatrix} \tilde{Y}_{2\ell+2} \\ \tilde{N}_{2\ell+2} \end{bmatrix} = \begin{bmatrix} 0 \\ I_q \end{bmatrix}$
4. Compute $[Y_{2\ell+2}, R_{2\ell+2}]$ from the modified Gram-Schmidt-orthogonalization of $\tilde{Y}_{2\ell+2}$, $N_{2\ell+2} := \tilde{N}_{2\ell+2} R_{2\ell+2}^{-1}$

Theorem 1. Choose X_{-1}, Y_0, N_0 such that $B(Y_0, X_{-1}, N_0)$ is nonsingular. Then we have

1. All subsequent matrices $B_{2\ell} = B(Y_{2\ell}, X_{2\ell-1}, N_{2\ell})$, $B_{2\ell+1} = B(Y_{2\ell}, X_{2\ell+1}, M_{2\ell+1}^T)$ are nonsingular. Hence, the algorithm GISI is well defined.
2. The quality of $Y_{2\ell}, X_{2\ell+1}$ is characterized by $\tan \xi_{2\ell+1} \leq \kappa \tan \eta_{2\ell}$, $\tan \eta_{2\ell+2} \leq \kappa \tan \xi_{2\ell+1}$
3. The condition numbers of the matrices B_k are monotonically decreasing and asymptotically almost optimal:

$$\lim_{k \rightarrow \infty} \text{cond}(B_k) = \max \left\{ \sigma_1, \sqrt{1 + \sigma_{p+1}^2} \right\} / \min \left\{ \sigma_p, \sqrt{1 + \sigma_n^2} \right\}$$

From approximations Y and X with $\text{im } Y \approx \text{im } U_2$ and $\text{im } X \approx \text{im } V_2$ found by GISI we can obtain approximations $\tilde{U}_2, \tilde{V}_2, \tilde{\Sigma}_2$ to U_2, V_2, Σ_2 , resp., by the following generalized Rayleigh-Ritz-Procedure:

1. Form the projection $S := Y^T A X \in \mathbb{R}^{q \times q}$.
2. Compute the q -dimensional SVD $S := Y^T A X = \tilde{U}_2 \tilde{\Sigma}_2 \tilde{V}_2^T$.
3. Define $\tilde{U}_2 := Y \tilde{U}_2$, $\tilde{V}_2 := X \tilde{V}_2$.

Then we have $\tilde{U}_2^T A \tilde{V}_2 = \tilde{\Sigma}_2 = \text{diag}(\tilde{\sigma}_{p+1}, \dots, \tilde{\sigma}_n)$, $\tilde{U}_2^T \tilde{U}_2 = \tilde{V}_2^T \tilde{V}_2 = I_q$, and the Rayleigh-Ritz-approximations $\tilde{\Sigma}_2$ to Σ_2 satisfy $\|\tilde{\Sigma}_2 - \Sigma_2\|_F \leq C[\sin^2 \xi + \sin^2 \eta + \sin \xi \sin \eta]$ with a constant $C > 0$ provided that ξ, η are small enough.

Remark 2. If A is nonsingular then the algorithm is, in exact arithmetic, equivalent to classical inverse iteration with $A^T A$ for the X -iteration and $A A^T$ for the Y -iteration.

Let us remark that all results can be extended to rectangular matrices $A \in \mathbb{R}^{m \times n}$ with $m \leq n$.

5. Numerical Results

All computations with special almost singular matrices taken from singularity theory and randomly generated matrices confirm the expected linear convergence of the singular vector approximations and the better ("quadratic") convergence of the singular value approximations. Moreover, the speed depends on σ_{p+1}/σ_p and the condition of the matrices B_k is of order σ_1/σ_p independent of the size of $\sigma_{p+1}, \dots, \sigma_n$.

6. References

- 1 GOLUB, G. H., VAN LOAN, C. F.: Matrix Computations, Johns Hopkins University Press, Baltimore 1996.
- 2 GRIEWANK, A., REDDIEN, G. W.: Characterization and Computation of Generalized Turning Points. SIAM J. Numer. Anal. 21 (1984), 176–185.
- 3 SCHWETLICK, H., SCHNABEL, U.: Iterative Computation of the Smallest Singular Value and the Corresponding Singular Vectors of a Matrix. Preprint IOKOMO-06-97, TU Dresden (1997). Submitted for publication.

Addresses: PROF. DR. HUBERT SCHWETLICK, DIPL.-MATH. UWE SCHNABEL, Techn. Univ. Dresden, Inst. f. Numerische Mathematik, D-01062 Dresden, Germany

WIENERS, C.

The application of multigrid methods to plasticity at finite strains

We present a general method for the formulation of incremental plasticity at finite strains and the combination with multigrid methods. Therefore, the algorithms analyzed in [5], [6] for Prandtl-Reuß-plasticity are transferred to nonconvex energy functionals. The efficiency of the multigrid solver is demonstrated on a large scale numerical example in three space dimensions.

1. Plasticity at finite strains

We consider a quasi-static plasticity model which is determined by a deformation $\varphi: [0, T] \times \Omega \rightarrow \mathbb{R}^3$ of a reference configuration $\Omega \subset \mathbb{R}^3$ and the internal variable $C^{p-1}: [0, T] \times \Omega \rightarrow \mathbb{R}^6$ (describing the memory of the material) in the time interval $[0, T]$. Here, we consider a multiplicative decomposition of the deformation gradient $F = \nabla_x \varphi = F^e F^p$ in \mathbb{R}^9 , and the inverse of the plastic strain builds the internal variable $C^{p-1} = F^{p-1} F^{p-T}$; this defines the symmetric elastic Eulerian strain tensor by $b^e = F C^{p-1} F^T \in \mathbb{R}^6$.

Here, we assume that the model is determined by an isotropic stored free energy functional $\psi: \mathbb{R}^9 \times \mathbb{R}^6 \rightarrow \mathbb{R}$ of the form $\psi(F, C^{p-1}) = \hat{\psi}(F C^{p-1} F^T) = \hat{\psi}(b^e)$ (depending only on the elastic Eulerian strain) and a convex dissipation functional $\chi: \mathbb{R}^9 \rightarrow \mathbb{R}$ depending only on the symmetric Kirchhoff stress tensor $\tau = \partial_{b^e} \hat{\psi}(b^e) b^e$.

This defines for every material point the hyperelastic stress response (in the reference configuration)

$$P(F, C^{p-1}) = \partial_F \psi(F, C^{p-1}) = \tau F^{-T} \in \mathbb{R}^9 \quad (1)$$

and the plastic evolution (formulated via transformation by F into the current configuration)

$$F \dot{C}^{p-1} F^T \in -\partial_\tau \chi(\tau) F C^{p-1} F^T \subset \mathbb{R}^6. \quad (2)$$

Note that constitutive equations of this type leads to a consistent model [4, Chap. III], and the form of the evolution equation guarantees that the dissipation principle is not violated.

In addition to the evolution of the internal variables we prescribe boundary deformations on $\Gamma \subset \partial\Omega$, and (since we consider the quasi-static process) the momentum balance reduces to the equilibrium condition (for all $t \in [0, T]$)

$$\int_{\Omega} P(\nabla_x \varphi, C^{p-1}) \cdot \nabla_x \phi \, dx = L(t, \phi) \quad \text{for all } \phi: \Omega \rightarrow \mathbb{R}^3 \text{ with } \phi|_{\Gamma} = 0 \quad (3)$$

for a given load functional $L(t, \cdot)$ describing body forces and surface tractions. We start with $L(0, \cdot) = 0$.

2. A visco-plastic model

Following [4, Example 37.1, Model 1], we use the free energy functional

$$\hat{\psi}(b^e) = \frac{\mu}{2} \text{trace}(J^{-1/3} b^e - \mathbf{I}) + \frac{\kappa}{4} (J - 1 - \ln(J)), \quad J = \det(b^e) \quad (4)$$

and the (straightforward visco-plastic extension of the) dissipation functional

$$\chi(\tau) = \hat{\chi}(|\text{dev } \tau|), \quad \hat{\chi}(s) = \frac{K}{r+1} \left\langle \frac{s-k}{K} \right\rangle^{r+1}, \quad \langle s \rangle = \max\{0, s\} \quad (5)$$

depending only on the second invariant of the symmetric Eulerian stress tensor and material constants $r, K > 0$, $k \geq 0$. Note that for the limit case $r = \infty$ the model describes perfect plasticity with the elastic domain

$$\mathbf{E} = \text{dom } \hat{\chi} = \{\tau \in \mathbb{R}^9 \mid |\text{dev } \tau| \leq k + K\} \quad \text{for} \quad \hat{\chi}(s) = \begin{cases} 0 & |s| - k \leq K, \\ \infty & \text{else.} \end{cases} \quad (6)$$

3. Radial return

Let $t_0 = 0 < t_1 < \dots < t_N = T$ be a time series and $\Delta t_n = t_n - t_{n-1}$. For a given deformation gradient F_n and material history C^{p-1}_{n-1} , the radial return computes the update of the internal variables by solving

$$F_n \dot{C}^{p-1}(t) F_n^T \in -\partial_\tau \chi(\tau_n) F_n C^{p-1}(t) F_n^T, \quad \text{in } t \in [t_{n-1}, t_n] \text{ with } \tau_n = \mu \operatorname{dev}(\bar{b}_n^e) \quad (7)$$

subject to the initial condition $C^{p-1}(t_{n-1}) = C^{p-1}_{n-1}$ (and with $\bar{b}_n^e = \det(F_n)^{-2/3} F_n C^{p-1}(t_n) F_n^T$). This is solved by

$$\bar{b}_n^e = \exp \left(-\gamma_n \frac{\operatorname{dev}(\bar{b}_n^e)}{|\operatorname{dev}(\bar{b}_n^e)|} \right) \bar{b}_n^{e \text{ trial}}, \quad \bar{b}_n^{e \text{ trial}} = \det(F_n)^{-2/3} F_n C^{p-1}_{n-1} F_n^T \quad (8)$$

with $\gamma_n \in \Delta t_n \hat{\chi}'(\mu |\operatorname{dev}(\bar{b}_n^e)|)$, cf. [4, Section 47]. Implicitly, we define a function $\Gamma: \mathbb{R} \rightarrow \mathbb{R}^6$ by

$$\Gamma(\gamma_n) - \exp \left(-\gamma_n \frac{\operatorname{dev}(\Gamma(\gamma_n))}{|\operatorname{dev}(\Gamma(\gamma_n))|} \right) \bar{b}_n^{e \text{ trial}} = 0; \quad (9)$$

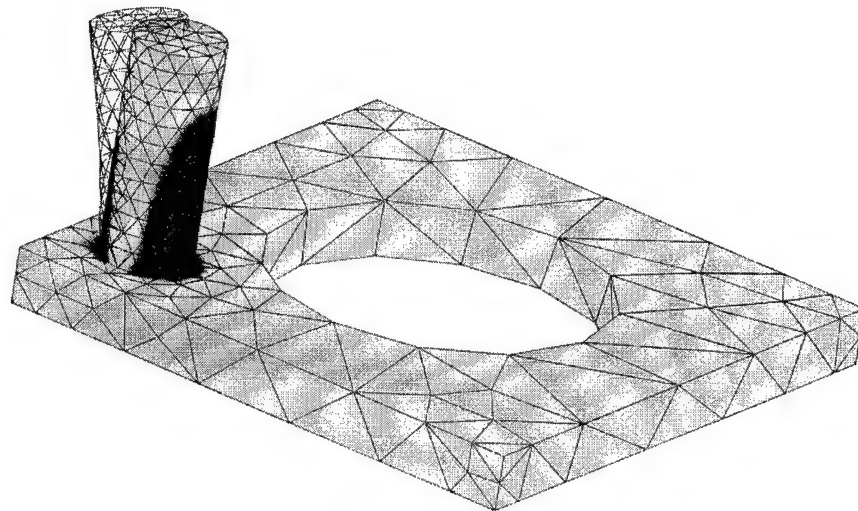
thus, the radial return is determined by the solution of the nonlinear problem (for $\mu |\operatorname{dev}(\bar{b}_n^{e \text{ trial}})| > k$)

$$\gamma_n = \Delta t_n \left(\frac{\mu |\operatorname{dev}(\Gamma(\gamma_n))| - k}{K} \right)^r. \quad (10)$$

In the implementation, (9) and (10) are evaluated by Newton methods, where the derivatives are approximated by difference quotients; in the same way, the consistent tangent operator is determined. The resulting linear system in every Newton step for the problem (3) is solved with a multigrid method.

4. Numerical experiment

The algorithm described above is realized in the finite element module of the software toolbox *UG* [1], which supports multigrid methods on unstructured meshes. We illustrate the plastic region and the deformation (visualization with scaled deformation by *GRAPE* [2]) for an example geometry with 57344 tetrahedra (mesh generation with *NETGEN* [3]). The result is obtained with the material parameters $\mu = 80193.8$, $\kappa = 164206.0$, $K = 293.94$, $k = 173.48$, $r = 5$, and $N = 16$ time steps.



5. References

- 1 BASTIAN, P., BIRKEN, K., JOHANNSEN, K., LANG, S., NEUSS, N., RENTZ-REICHERT, H., WIENERS, C.: *UG – a flexible software toolbox for solving partial differential equations*, Computing and Visualization in Science 1 (1997) 27-40.
- 2 RUMPF, M., WIRSE, A.: *Grape, eine objektorientierte Visualisierungs- und Numerikplattform*, Informatik Forschung und Entwicklung 7 (1992) 145-151.
- 3 SCHOEBERL, J.: *NETGEN – an advancing front 2D/3D-mesh generator based on abstract rules*, Computing and Visualization in Science 1 (1997) 40-52.
- 4 SIMO, J. C.: *Numerical Analysis and Simulation in Plasticity*, in: Handbook of Numerical Analysis VI, ed. P. G. Ciarlet and J. L. Lions (1998) 183-499.
- 5 WIENERS, C.: *Multigrid methods for Prandtl-Reuß-plasticity*, Numer. Lin. Alg. Appl. 6 (1999) 457-478.
- 6 WIENERS, C.: *Theorie und Numerik der Prandtl-Reuß-Plastizität*, Habilitationsschrift, Universität Heidelberg, submitted 1999.

Address: DR. CHRISTIAN WIENERS, Universität Heidelberg, IWR, Im Neuenheimer Feld 368, D-69120 Heidelberg, Germany

ARNOLD, M.

Constraint partitioning in dynamic iteration methods

Dynamic iteration (waveform relaxation) is a well approved approach to the numerical solution of coupled instationary differential equations that is based on a splitting into several subsystems. If the subsystems are coupled by constraints then there is no generic way to assign these constraints to the subsystems. In the present paper we consider three partitioning strategies for constraints that couple two differential-algebraic systems. An error analysis shows that the stability of the dynamic iteration method depends strongly on the partitioning of the constraints.

1. Introduction

In a modular approach to the modelling of coupled physical phenomena and coupled technical systems the overall problem is splitted into several subsystems that are in a first step modelled separately. In the second (and final) step these models for the subsystems are coupled to obtain a full model for the overall coupled problem. Typical coupling conditions are, e. g., balance equations, continuity conditions, and contact conditions [3].

The modular approach results in coupled systems of model equations. The special structure of such coupled systems may be exploited in the numerical solution [6]. As in the previous paper [1] we focus again on dynamic iteration methods for coupled differential-algebraic systems. Dynamic iteration (or waveform relaxation) methods have originally been introduced for the simulation of large scale electrical circuits [5]. Similar to the classical Picard iteration the dynamic iteration works in a function space, the iterates are continuous functions that approximate the solution of an initial or boundary value problem.

Dynamic iteration is a promising approach to the numerical solution of coupled differential equations since within each step of iteration the system is decoupled and the subsystems may be solved separately (*modular* time integration [4]). If the subsystems are coupled by constraints then each constraint has to be assigned to (at least) one of the subsystems. The partitioning of the overall coupled system into subsystems includes a partitioning of the constraints.

In the present paper we consider dynamic iteration methods with three different partitioning strategies for the constraints. Stability and convergence of these methods may be studied on the basis of the corresponding analysis for a special Gauss-Seidel type method that has been developed in detail in [1]. The error bounds indicate that the stability of the dynamic iteration depends strongly on the partitioning of the constraints.

The paper is organized as follows: In Section 2 we start with a more precise description of the coupled system. The class of dynamic iteration methods is defined in Section 3. In Section 4 stability and convergence of these methods are analysed. In the present paper we restrict ourselves to these theoretical investigations. A discussion of practical applications in mechanical engineering and results of numerical tests may be found in [1].

2. The problem class

As a typical but nevertheless simple problem class we consider the coupling of two differential-algebraic systems

$$\left. \begin{aligned} \dot{y}_1(t) &= f_1(y_1, y_2, z_1), & \dot{y}_2(t) &= f_2(y_1, y_2, z_2), \\ 0 &= h_1(y_1, y_2, z_1, u), & 0 &= h_2(y_1, y_2, z_2, u) \end{aligned} \right\} \quad (1a)$$

by n_u algebraic equations

$$0 = g(y_1, y_2, z_1, z_2). \quad (1b)$$

The i -th subsystem of (1a) consists of n_{y_i} differential equations $\dot{y}_i = f_i$ and n_{z_i} algebraic equations $0 = h_i$, ($i = 1, 2$). The subsystems are coupled by the arguments y_1, y_2 in the right hand sides of (1a) and by the constraints (1b). We assume that the initial value problem

$$y(0) = y_0, \quad z(0) = z_0, \quad u(0) = u_0 \quad (2)$$

for (1) has a unique solution $y = (y_1, y_2)^T : [0, T_e] \rightarrow \mathbb{R}^{n_y}$, $z = (z_1, z_2)^T : [0, T_e] \rightarrow \mathbb{R}^{n_z}$, $u : [0, T_e] \rightarrow \mathbb{R}^{n_u}$ on the

finite time interval $[0, T_e]$, $n_y = \sum n_{y_i}$, $n_z = \sum n_{z_i}$. In a neighbourhood of this solution the functions $f = (f_1, f_2)^T$, $h = (h_1, h_2)^T$, and g are supposed to be sufficiently often differentiable. Furthermore, it is supposed that the Jacobians

$$\begin{pmatrix} \frac{\partial h}{\partial z} & \frac{\partial h}{\partial u} \\ \frac{\partial g}{\partial z} & 0 \end{pmatrix}, \begin{pmatrix} \frac{\partial h_i}{\partial z_i} & \frac{\partial h_i}{\partial u} \\ \frac{\partial g}{\partial z_i} & 0 \end{pmatrix}, \frac{\partial h_i}{\partial z_i}, \quad (i = 1, 2) \quad (3)$$

are non-singular such that the coupled system (1) has index one [2]. Condition (3) guarantees that for $i = 1$ and $i = 2$ the equations $h_i(y_1, y_2, z_i, u) = 0$ are (locally) uniquely solvable w. r. t. z_i and the systems of equation

$$0 = h_i(y_1, y_2, z_i, u), \quad 0 = g(y_1, y_2, z_1, z_2)$$

are (locally) uniquely solvable w. r. t. z_i and u .

3. The class of dynamic iteration methods

In a dynamic iteration method the numerical solution of the initial value problem (2) for the coupled system (1) is composed of analytical solutions for initial value problems for the individual subsystems. Instead of considering the time integration for the subsystems in detail the convergence analysis for dynamic iteration focusses on the *coupling* between the subsystems.

Example 1. The iterates $(y_1^{(k)}, y_2^{(k)})$ of the classical Gauss-Seidel method for a system of two coupled ordinary differential equations (ODEs)

$$\dot{y}_1(t) = f_1(y_1, y_2), \quad \dot{y}_2(t) = f_2(y_1, y_2) \quad (4)$$

with initial values $y_i(0) = y_{i,0}$, ($i = 1, 2$) are defined as solutions of the initial value problems

$$\dot{y}_1^{(k)}(t) = f_1(y_1^{(k)}, y_2^{(k-1)}), \quad y_1^{(k)}(0) = y_{1,0}, \quad (5a)$$

$$\dot{y}_2^{(k)}(t) = f_2(y_1^{(k)}, y_2^{(k)}), \quad y_2^{(k)}(0) = y_{2,0}. \quad (5b)$$

The initial guesses $y_i^{(0)}$ may be set, e. g., to $y_i^{(0)}(t) := y_{i,0}$, ($t \in [0, T_e]$, $i = 1, 2$). If the right hand sides f_i satisfy a Lipschitz condition and the time interval of interest is bounded then (5) is convergent [7].

Dynamic iteration may suffer from very slow convergence on large time intervals. Therefore a practical implementation is based on a splitting of $[0, T_e]$ into *windows* $[T_n, T_{n+1}]$ with a discrete time grid $0 = T_0 < T_1 < \dots < T_N = T_e$. In each window an initial guess $y_{n,i}^{(0)} \in C([T_n, T_{n+1}], \mathbb{R}^{n_{y_i}})$ is obtained extrapolating the numerical solution \tilde{y}_i from $[0, T_n]$ to $[T_n, T_{n+1}]$. Then a finite number k_n of dynamic iteration steps is performed such that the numerical solution \tilde{y}_i is continued from $[0, T_n]$ to $[T_n, T_{n+1}]$ by

$$\tilde{y}_i|_{[T_n, T_{n+1}]} := y_{n,i}^{(k_n)}. \quad (6)$$

The coupled system (1) goes beyond the classical framework of Example 1 since the subsystems are coupled not only by the right hand sides in (1a) but additionally by constraints (1b). There is no generic way to consider these constraints in the dynamical iteration.

In [1] we generalized the Gauss-Seidel iteration (5) assigning all constraints (1b) to the second subsystem. In the first stage of the k -th Gauss-Seidel step the functions $y_{n,2}^{(k-1)}$ and $u_n^{(k-1)}$ are given and the initial value problem

$$\begin{aligned} \dot{y}_{n,1}^{(k)}(t) &= f_1(y_{n,1}^{(k)}, y_{n,2}^{(k-1)}, z_{n,1}^{(k)}), & y_{n,1}^{(k)}(T_n) &= \tilde{y}_1(T_n), \\ 0 &= h_1(y_{n,1}^{(k)}, y_{n,2}^{(k-1)}, z_{n,1}^{(k)}, u_n^{(k-1)}) \end{aligned} \quad (7a)$$

is solved w. r. t. $y_{n,1}^{(k)}$ and $z_{n,1}^{(k)}$. In the second stage these functions are inserted in the initial value problem

$$\begin{aligned} \dot{y}_{n,2}^{(k)}(t) &= f_2(y_{n,1}^{(k)}, y_{n,2}^{(k)}, z_{n,2}^{(k)}), & y_{n,2}^{(k)}(T_n) &= \tilde{y}_2(T_n), \\ 0 &= h_2(y_{n,1}^{(k)}, y_{n,2}^{(k)}, z_{n,2}^{(k)}, u_n^{(k)}), \\ 0 &= g(y_{n,1}^{(k)}, y_{n,2}^{(k)}, z_{n,1}^{(k)}, z_{n,2}^{(k)}) \end{aligned} \quad (7b)$$

that defines the remaining solution components $y_{n,2}^{(k)}$, $z_{n,2}^{(k)}$, and $u_n^{(k)}$.

On the other hand a Gauss–Seidel method for (1) may consider the constraints (1b) as well in the first subsystem:

$$\begin{aligned} \dot{y}_{n,1}^{(k)}(t) &= f_1(y_{n,1}^{(k)}, y_{n,2}^{(k-1)}, z_{n,1}^{(k)}), & y_{n,1}^{(k)}(T_n) &= \tilde{y}_1(T_n), \\ 0 &= h_1(y_{n,1}^{(k)}, y_{n,2}^{(k-1)}, z_{n,1}^{(k)}, u_n^{(k)}), \\ 0 &= g(y_{n,1}^{(k)}, y_{n,2}^{(k-1)}, z_{n,1}^{(k)}, z_{n,2}^{(k-1)}), \end{aligned} \quad (8a)$$

$$\begin{aligned} \dot{y}_{n,2}^{(k)}(t) &= f_2(y_{n,1}^{(k)}, y_{n,2}^{(k)}, z_{n,2}^{(k)}), & y_{n,2}^{(k)}(T_n) &= \tilde{y}_2(T_n), \\ 0 &= h_2(y_{n,1}^{(k)}, y_{n,2}^{(k)}, z_{n,2}^{(k)}, u_n^{(k)}). \end{aligned} \quad (8b)$$

Obviously, the approaches (7) and (8) may also be combined such that coupling conditions (1b) are considered in both subsystems. A typical method of this type is

$$\begin{aligned} \dot{y}_{n,1}^{(k)}(t) &= f_1(y_{n,1}^{(k)}, y_{n,2}^{(k-1)}, z_{n,1}^{(k)}), & y_{n,1}^{(k)}(T_n) &= \tilde{y}_1(T_n), \\ 0 &= h_1(y_{n,1}^{(k)}, y_{n,2}^{(k-1)}, z_{n,1}^{(k)}, U_1), \\ 0 &= g(y_{n,1}^{(k)}, y_{n,2}^{(k-1)}, z_{n,1}^{(k)}, z_{n,2}^{(k-1)}), \end{aligned} \quad (9a)$$

$$\begin{aligned} \dot{y}_{n,2}^{(k)}(t) &= f_2(y_{n,1}^{(k)}, y_{n,2}^{(k)}, Z_2), & y_{n,2}^{(k)}(T_n) &= \tilde{y}_2(T_n), \\ 0 &= h_2(y_{n,1}^{(k)}, y_{n,2}^{(k)}, Z_2, U_2), \\ 0 &= g(y_{n,1}^{(k)}, y_{n,2}^{(k)}, z_{n,1}^{(k)}, Z_2). \end{aligned} \quad (9b)$$

The functions $U_1(t)$, $U_2(t)$, $Z_2(t)$ are auxiliary functions that define the new iterates

$$z_{n,2}^{(k)}(t) := Z_2(t) + A(t)(U_2(t) - U_1(t)), \quad u_n^{(k)}(t) := U_2(t) + B(t)(U_2(t) - U_1(t)). \quad (9c)$$

The matrix valued functions $A : [0, T_e] \rightarrow \mathbb{R}^{n_z \times n_u}$, $B : [0, T_e] \rightarrow \mathbb{R}^{n_u \times n_u}$ are free parameters of method (9).

Assumption (3) guarantees that all three methods (7), (8), (9) are well defined since the subsystems (7a), (7b), ..., (9b) form differential-algebraic systems of index 1, see [2]. The initial values for the algebraic components $z_{n,i}^{(k)}$, $u_n^{(k)}$, Z_2 , and U_i are defined by the algebraic equations $h_i = 0$, $g = 0$.

4. Error estimates

Dynamic iteration methods for coupled ODEs define a contractive mapping in a scaled L^∞ -norm on $[0, T_e]$ such that convergence follows from the Fixed point Theorem [7]. If dynamic iteration is applied to coupled differential-algebraic systems then a *contractivity condition* has to be satisfied to guarantee also contractivity w. r. t. the algebraic solution components [5]. An additional contractivity condition is necessary for a stable error propagation from window to window [1].

The error is essentially influenced by the choice of the initial guesses $(y_n^{(0)}, z_n^{(0)}, u_n^{(0)})$ and by the number k_n of iteration steps in each window $[T_n, T_{n+1}]$. For simplicity of presentation we restrict ourselves to fixed window sizes $H := T_{n+1} - T_n$. It is supposed that the initial guesses for the differential components y and the algebraic components z and u are obtained extrapolating continuously from $(T_{n-1}, T_n]$ to $(T_n, T_{n+1}]$:

$$y_n^{(0)} := \Phi_n^{(d)}(\tilde{y}|_{(T_{n-1}, T_n]}), \quad (z_n^{(0)}, u_n^{(0)}) := \Phi_n^{(a)}((\tilde{z}, \tilde{u})|_{(T_{n-1}, T_n]}).$$

Here $(\tilde{y}, \tilde{z}, \tilde{u})$ is the result of the dynamic iteration method with a finite number of iteration steps, see (6). We assume that the extrapolation operators $\Phi_n^{(d)}$, $\Phi_n^{(a)}$ satisfy a Lipschitz condition

$$\|\Phi_n^{(d)}(\hat{Y}) - \Phi_n^{(d)}(Y)\| \leq L\|\hat{Y} - Y\|, \quad \|\Phi_n^{(a)}(\hat{Z}, \hat{U}) - \Phi_n^{(a)}(Z, U)\| \leq L(\|\hat{Z} - Z\| + \|\hat{U} - U\|)$$

with a Lipschitz constant L being independent of H ($\|\cdot\|$ denotes the L^∞ -norm).

The *extrapolation errors* are defined applying $\Phi_n^{(d)}$, $\Phi_n^{(a)}$ to the analytical solution of (1):

$$\delta_n^{(d)} := \Phi_n^{(d)}(y|_{(T_{n-1}, T_n]}) - y|_{(T_n, T_{n+1}]}, \quad \delta_n^{(a)} := \Phi_n^{(a)}((z, u)|_{(T_{n-1}, T_n]}) - \begin{pmatrix} z \\ u \end{pmatrix}|_{(T_n, T_{n+1}]}$$

With these assumptions the convergence result of Theorem 2.2 in [1] may be generalized to (7), (8), and (9):

Theorem 1. *If the contractivity conditions $\alpha \leq \bar{\alpha}$ and $L\alpha^{k_n} \leq \bar{\alpha}$ are satisfied for all $n \geq 0$ with $nH \leq T_N = T_e$ and a constant $\bar{\alpha} < 1$ then the dynamic iteration methods (7), (8) and (9) are convergent and there are constants $C_0, C^*, H_0 > 0$ such that for all $H \leq H_0$*

$$\|\tilde{y} - y\|_{[0, T_e]} + \|\tilde{z} - z\|_{[0, T_e]} + \|\tilde{u} - u\|_{[0, T_e]} \leq C^* \cdot \max_{0 \leq n < N} (\mu^{\max(0, k_n - 2)} \|\delta_n^{(d)}\| + \mu^{k_n - 1} \|\delta_n^{(a)}\|)$$

with a constant $\mu = \alpha + C_0 H / (\alpha + \sqrt{H})$. The constants C_0, C^* , and H_0 are independent of the contractivity constant α that is given

- by $\alpha := \max_{t \in [0, T_e]} \left\| \left[\left(\frac{\partial g}{\partial z_2} \left(\frac{\partial h_2}{\partial z_2} \right)^{-1} \frac{\partial h_2}{\partial u} \right)^{-1} \left(\frac{\partial g}{\partial z_1} \left(\frac{\partial h_1}{\partial z_1} \right)^{-1} \frac{\partial h_1}{\partial u} \right) \right] (y(t), z(t), u(t)) \right\|$ for Method (7),
 - by $\alpha := \max_{t \in [0, T_e]} \left\| \left[\left(\frac{\partial h_2}{\partial z_2} \right)^{-1} \frac{\partial h_2}{\partial u} \left(\frac{\partial g}{\partial z_1} \left(\frac{\partial h_1}{\partial z_1} \right)^{-1} \frac{\partial h_1}{\partial u} \right)^{-1} \frac{\partial g}{\partial z_2} \right] (y(t), z(t), u(t)) \right\|$ for Method (8), and
 - by $\alpha := \max_{t \in [0, T_e]} \left\| \left[\left(\frac{\partial h_2}{\partial z_2} \right)^{-1} \frac{\partial h_2}{\partial u} \left(\frac{\partial g}{\partial z_2} \left(\frac{\partial h_2}{\partial z_2} \right)^{-1} \frac{\partial h_2}{\partial u} \right)^{-1} \frac{\partial g}{\partial z_2} - A(t) R(t) \frac{\partial g}{\partial z_2} \right] (y(t), z(t), u(t)) \right\|$ for Method (9),
- $$R(t) := \left(\frac{\partial g}{\partial z_1} \left(\frac{\partial h_1}{\partial z_1} \right)^{-1} \frac{\partial h_1}{\partial u} \right)^{-1} + \left(\frac{\partial g}{\partial z_2} \left(\frac{\partial h_2}{\partial z_2} \right)^{-1} \frac{\partial h_2}{\partial u} \right)^{-1}.$$

Remark 1. a) If the contractivity conditions are violated and $\alpha > 1$ then the stability of the method may not be guaranteed. An exponential instability may be observed already in very simple model problems like (1) with scalar linear functions h_i and g .

b) The most important difference between (7), (8), and (9) is the way in that the constraints (1b) are assigned to the subsystems. Theorem 1 shows that this partitioning of the constraints has an essential influence on the stability of the dynamic iteration method.

c) In (9) constant α is independent of $B(t)$. For the most obvious choice $A(t) = 0$ constant α is given by the norm of a projector in $\mathbb{R}^{n_{z_2}}$ such that $\alpha \geq 1$ and the contractivity condition is always violated. However, stability and convergence may be achieved by an appropriate definition of $A(t)$. The optimal value $\alpha = 0$ is obtained for

$$A(t) := \left(\frac{\partial h_2}{\partial z_2} \right)^{-1} \frac{\partial h_2}{\partial u} \left(\left(\frac{\partial g}{\partial z_1} \left(\frac{\partial h_1}{\partial z_1} \right)^{-1} \frac{\partial h_1}{\partial u} \right) + \left(\frac{\partial g}{\partial z_2} \left(\frac{\partial h_2}{\partial z_2} \right)^{-1} \frac{\partial h_2}{\partial u} \right) \right)^{-1} \left(\frac{\partial g}{\partial z_1} \left(\frac{\partial h_1}{\partial z_1} \right)^{-1} \frac{\partial h_1}{\partial u} \right).$$

5. Summary

In a dynamic iteration method for coupled differential-algebraic systems the coupling conditions have to be assigned to one or more of the subsystems. Three different strategies for the partitioning of the constraints in a Gauss-Seidel type method have been analysed. The convergence analysis indicates that the constraints should be partitioned such that a problem and method dependent contractivity constant α is minimized.

6. References

- 1 ARNOLD, M., GÜNTHER, M.: Preconditioned dynamic iteration for coupled differential-algebraic systems. accepted for publication in BIT, 2000.
- 2 BRENNAN, K.E., CAMPBELL, S.L., PETZOLD, L.R.: Numerical solution of initial-value problems in differential-algebraic equations. SIAM, Philadelphia, 2nd edition, 1996.
- 3 HOSCHEK, M., RENTROP, P., WAGNER, Y.: Network approach and differential-algebraic systems in technical applications. Surveys on Math. in Industry 9 (1999), 49–75.
- 4 JACKSON, K.: A survey of parallel numerical methods for initial value problems for ordinary differential equations. IEEE Transactions on Magnetics 27 (1991), 3792–3797.
- 5 LELARSMEE, E., RUEHLI, A.E., SANGIOVANNI-VINCENTELLI, A.L.: The waveform relaxation method for time domain analysis of large scale integrated circuits. IEEE Trans. on CAD of IC and Syst. 1 (1982), 131–145.
- 6 LEWIS, R.W., BETTES, P., HINTON, E., EDITORS: Numerical methods in coupled systems. Wiley Series in Numerical Methods in Engineering. Wiley & Sons, Chichester, 1984.
- 7 MIEKKALA, U., NEVANLINNA, O.: Convergence of dynamic iteration methods for initial value problems. SIAM J. Sci. Stat. Comput. 8 (1987), 459–482.

Addresses: Martin Arnold, DLR German Aerospace Center, Institute of Aeroelasticity, P.O. Box 1116,
D - 82230 Wessling, Germany. email: martin.arnold@dlr.de

BARTEL, ANDREAS; GÜNTHER, MICHAEL

Developments in Multirating for Coupled Systems

In technologically computer-aided design, the demand for a refined modelling yields the numerical simulation of coupled systems. Often the dynamics of these systems can be described as initial value problems of ordinary differential equations, which are characterised by largely varying time constants. A natural approach is to use multirate integration schemes which integrate the subsystems by their inherent step size. The realisation of the couplings of these subsystems, however done, is the crucial point.

To begin, we give a short survey on multirate behaviour and its possible numerical exploitation in one-step-schemes. Based on the conception of generalised multirate, we classify multirate methods by the means, which compute the coupling terms for the internal stages: On one hand, extra/interpolation, on the other hand, the incremental formulation, which yields a genuine one-step-method. For the latter approach, we discuss the multirate W-method as an example and give finally test results for a multirate version of Prothero-Robinson's equation and the Inverter-Chain.

1. Survey on multirating

In various applications one has to investigate coupled systems. For instance, in electric circuits latent and active units are caused by signals passing through highly integrated circuits. Furthermore, in radio frequency cellular phones consist of analog and digital parts. In multibody dynamics Young's modulus might vary over some orders of magnitude as well as reaction speeds in chemical reaction dynamics. Thus, these systems are characterised by largely differing time constants. A naive integration of all components at a time with a single step size (in a single order, single method scheme) is conducted and limited by the behaviour of the fastest changing component. The idea of multirating is to use inherent step sizes for the units, while the administration cost and overhead due to couplings have to be taken into account. Thus the following analysis and tests are performed for two subsystems: slow and fast or latent and active, respectively.

1.1 Levels of latency exploitation. Normally, the term *multirating* is used for methods which split on the system levels in active and latent components. On this level we have *dynamic iteration* (waveform relaxation) [14] as indirect method, while *multi-step-sizes* (multirate), *multi-order* and *multi-method* are direct methods. Latency is not only found on system level, but also on equation level, here Schur-Complement-Techniques and Multi-Level-Newton methods are used for linear and nonlinear systems, see [7, 16].-

1.2 Multirate step size. Generally, the system is split in active and latent subsystems. The slow, latent part is integrated with the large *macro* step size H and the fast, active part m -times with the small *micro* step size h : $H = m h$. The realisation now depend not only on the underlying numerical scheme, but also (A) on which part is integrated first and, crucially, (B) how the coupling is done.

One origin of these method are the split Runge-Kutta schemes by Rice [18]. Investigating multirate BDF methods, Gear and Wells [6] addressed the question (A) which subsystem should be integrated first and introduced the notation of fastest- and slowest-first schemes. Later, G./Rentrop [9] designed multirate schemes based on Rosenbrock-Wanner methods. Similar to the previous approach, extra- and interpolation of the coupling variables are incorporated, which inevitably decompose the underlying one-step-method in a two-step procedure. Recently, a new answer to question (B), how to realise the coupling, was given by Kværnø/Rentrop [13] for explicit Runge-Kutta schemes: the internal stages are used to compute the coupling terms, too. Meanwhile, this so-called *generalised multirate* approach was extended to implicit schemes, e.g. ROW- and W-methods, to manage also stiff problems. We focus on this new type of method in section 2. Before going on with generalised multirate, we summarise some alternative ideas how to exploit multirate behaviour.

1.3 Multiorder. Here a single scheme method is used, but with different order for the subsystems. The methods [4, 5] by Engstler/Lubich are based either on Richardson's extrapolation or on high order RK-methods. According to the activity level in each time step, the order is automatically adapted to each variable. The schemes are explicit and well suited for astro-physical problems. However, the couplings are obtained by external procedures.

1.4 Multimethod. This approach uses different integration schemes for the subsystems. For example, it provides

the functionality to compute non-stiff components explicitly, while the stiff are computed implicitly. Multimethod schemes based on RK and RK/ROW methods and can be found by Hofer [10] and Rentrop [17]. The latter approach was generalised to linear implicit schemes by Weiner et al. [21]. An analogue idea is to split the iterative solution of the nonlinear system: functional iteration is used for the non stiff part, and a modified Newton approach for the stiff part.

1.5 Multirate PDE. Systems, driven by multitone signals with frequencies varying over some orders of magnitude, show obviously a multirate behaviour. A new idea introduced by Brachtendorf [3] is to rewrite the problem as a system of PDEs in all inherent time scales, which can be solved very efficiently in various ways [19]. Another approach, based on characteristics [15], can be regarded as multirate scheme applied to the underlying ODE.

2. Generalised Multirate

We start to give the outline of a somewhat generic generalised multirate one-step-method: the increments in Kronecker notation (as usual $\mathbf{k}_L^\top = (\mathbf{k}_{L,1}^\top, \dots, \mathbf{k}_{L,s}^\top)$ and $\mathbf{k}_A^\top = (\mathbf{k}_{A,1}^\top, \dots, \mathbf{k}_{A,s}^\top)$, similar for $\bar{\mathbf{Y}}_A$ and $\bar{\mathbf{Y}}_L$) read

$$\mathbf{k}_L = H \mathbf{f}_L(\mathbf{1}_s \otimes \mathbf{y}_{L,0} + (\tilde{\mathcal{A}} \otimes \mathcal{I}_L) \mathbf{k}_L, \boxed{\bar{\mathbf{Y}}_A}) + H \left(\tilde{\mathcal{G}} \otimes \frac{\partial \mathbf{f}_L}{\partial \mathbf{y}_L} \bigg|_{\mathbf{y}_0} \right) \mathbf{k}_L + m H \left(\tilde{\mathcal{N}} \otimes \frac{\partial \mathbf{f}_L}{\partial \mathbf{y}_A} \bigg|_{\mathbf{y}_0} \right) \mathbf{k}_A^0 \quad (1)$$

$$\mathbf{k}_A^\lambda = h \mathbf{f}_A(\boxed{\bar{\mathbf{Y}}_L^\lambda}, \mathbf{1}_s \otimes \mathbf{y}_{A,\lambda} + (\mathcal{A} \otimes \mathcal{I}_A) \mathbf{k}_A^\lambda) + h \left(\mathcal{G} \otimes \frac{\partial \mathbf{f}_A}{\partial \mathbf{y}_A} \bigg|_{\mathbf{y}_{0,\lambda}} \right) \mathbf{k}_A^\lambda + h/m \left(\mathcal{N} \otimes \frac{\partial \mathbf{f}_A}{\partial \mathbf{y}_L} \bigg|_{\mathbf{y}_{0,\lambda}} \right) \mathbf{k}_L \quad (2)$$

and the numerical solution is given by

$$\mathbf{y}_L^H(t_0 + H) = \mathbf{y}_{L,0} + (\tilde{\mathcal{B}}^\top \otimes \mathcal{I}_L) \mathbf{k}_L \quad \text{and} \quad \mathbf{y}_A^h(t_0 + (\lambda + 1)h) = \mathbf{y}_A^h(t_0 + \lambda h) + (\mathcal{B}^\top \otimes \mathcal{I}_A) \mathbf{k}_{A,i}^\lambda, \quad (3)$$

for $\lambda = 0, \dots, m-1$. Still, the coupling terms need to be defined, where we aim:

$$(\text{active to latent}) \quad \bar{\mathbf{Y}}_{A,i} \approx \mathbf{y}_A(t_0 + \tilde{\alpha}_i \cdot H) \quad \text{and} \quad (\text{latent to active}) \quad \bar{\mathbf{Y}}_{L,i}^\lambda \approx \mathbf{y}_L(t_0 + \lambda \cdot h + \alpha_i \cdot h).$$

with $\alpha_i := e_i \mathbf{A} \mathbf{1}_s$. Depending on the way coupling terms are computed, we get different types of multirate formulae:

1. **first type - MROW** [9]: The coupling terms are defined by the usage of rational extrapolations

$$(\text{active to latent}) \quad \boxed{\bar{\mathbf{Y}}_A} = \mathbf{y}_A^{\text{extra}}([t_0 + \tilde{\alpha}_i H]_i) \quad \text{and} \quad (\text{latent to active}) \quad \boxed{\bar{\mathbf{Y}}_L^\lambda} = \mathbf{y}_L^{\text{extra}}([t_0 + (\lambda + \alpha_i) h]_i);$$

furthermore $\mathcal{N} = \tilde{\mathcal{N}} = \mathbf{0}$, and both remaining coefficient matrices $(\mathcal{A}, \tilde{\mathcal{A}})$ are lower triangular. Last, the Jacobian is evaluated at: $\mathbf{y}_{0,\lambda}^\top = (\mathbf{y}_L^{\text{extra}}{}^\top(t_0 + \lambda h), \mathbf{y}_A^h{}^\top(t_0 + \lambda h))$, $\lambda = 0, \dots, m-1$. Thus the computation over each macro step is decoupled, a kind of weakened slowest first strategy [6].

2. **generalised multirate** [13]: the coupling terms are computed by their 'own' RK-like methods,

$$\boxed{\bar{\mathbf{Y}}_A} = \mathbf{1}_s \otimes \mathbf{y}_{A,0} + m(\tilde{\mathcal{D}} \otimes \mathcal{I}_A) \mathbf{k}_A^0, \quad \text{and} \quad \boxed{\bar{\mathbf{Y}}_L^\lambda} = \mathbf{1}_s \otimes \mathbf{y}_{L,0} + 1/m((\mathcal{D} + \mathcal{F}(\lambda)) \otimes \mathcal{I}_L) \mathbf{k}_L, \quad (4)$$

which gives us a genuine one-step-method. All coefficient matrices are lower triangular, except for $\mathcal{F}(\lambda)$, which is a matrix of polynomials, constant in each column. Fixing, where to evaluate the Jacobian and some finer structure of the coefficient matrices, yields different kinds of methods:

- **explicit Runge-Kutta** [13]: $\mathcal{G} = \mathcal{N} = \tilde{\mathcal{G}} = \tilde{\mathcal{N}} = \mathbf{0}$ - thus no Jacobian is coupled.
- **partitioned RK** [8]: $\mathcal{G} = \mathcal{N} = \tilde{\mathcal{N}} = \mathbf{0}$; $\tilde{\mathcal{G}}$ with non vanishing diagonal.
- **W-method** [2]: $\mathcal{G}, \tilde{\mathcal{G}}, \mathcal{N}$ and $\tilde{\mathcal{N}}$ have constant diagonals, which differ from zero at least for the first two matrices; in addition $\mathbf{y}_{0,\lambda} = \mathbf{y}_0$, i.e. the Jacobian is lagged over a single macro step in order to compute the micros.
- **ROW-method** [2]: conditions like W-method, plus evaluation of Jacobian on fine grid (specially).

The structure of system (1-4) yields a compound step of macro and first micro step, and decouples all later micro steps. By the linear implicitness, we may sequentially compute the increments $\mathbf{k}_i^\top = (\mathbf{k}_{L,i}^\top, \mathbf{k}_{A,i}^0{}^\top)$. If at least one diagonal of $\mathcal{N}, \tilde{\mathcal{N}}$ vanishes, a block triangular form of the system matrix for the increments is obtained, such that the increments may be computed in an interleaved mode: $\mathbf{k}_{L,1}, \mathbf{k}_{A,1}^0, \mathbf{k}_{L,2}, \mathbf{k}_{A,2}^0, \dots$. Furthermore, we have ROW-type coefficients, i.e. we need just one decomposition per time step.

The generalised multirate W-method over any whole macro step with $\mathbf{y}_{0,\lambda} = \mathbf{y}_0$ can be interpreted as a (generalised) partitioned ROW method (P-ROW). Therefore P-theory [11] can be applied to obtain the consistency equation for the this partitioned scheme. Furthermore, one demands dense output conditions restricted to the fine grid, since the multirate method has to be of the method order on the fine grid, too. Thus the order conditions of the P-ROW method might be transferred via technical proofs to the conditions for the W-method (including of course the RK variant). The consistency equations and a more thorough description is found in [2]. One can show, that the consistency equations are 'consistent' and coefficient sets can be exhibited.

3. Tests

Tests of a multirate W-scheme of order 2(3), which has been developed for circuit simulation, were executed within MatLab. Speed ups were measured for MatLab operations and for scalar function evaluations of the RHS, since the load part is most costly in circuit simulators.

3.1 Prothero-Robinson. This system was tailored to multirate systems by Kværnø [12]:

$$\mathbf{y}'(t) = \begin{pmatrix} \Upsilon & \varepsilon \\ \varepsilon & -1 \end{pmatrix} \begin{pmatrix} y_1(t) - \sin(t) \\ y_2(t) - \sin(\omega t) \end{pmatrix} - \begin{pmatrix} \cos(t) \\ \omega \cdot \cos(\omega t) \end{pmatrix}, \quad \mathbf{y}(0) = \begin{pmatrix} 0 \\ 0 \end{pmatrix}, \quad (5)$$

where Υ is the stiffness, ε the coupling and ω the activity level of the second component. Tests were performed using: $\Upsilon = -1000$, $\varepsilon = 10^{-1}$, $\omega = 100$. Using an extension of Shampine's coefficients for ode23s [20] to the multirate W-method one obtains:

mode	micros	macros	max error	cost [M ops]	$\Xi_{\text{ops}} = 4$ speed up	fct-evals	$\Xi_{\text{fct}} = 2$ ratio: evals
sr	1500 (300)		$2.5 \cdot 10^{-3}$	0.560	-	10200	-
mr/fix	1700(11)	17(11)	$5 \cdot 10^{-3}$	0.196	2.86	5195	1.96
mr/dyn	2090(56)	34(23)	$4.5 \cdot 10^{-3}$	0.285	1.96	6530	1.56

Legend: sr = single rate fix = fix multirate m fct-evals = number of scalar function evaluations
 mr = multirate dyn = dynamical adjusted m ratio-evals = (sr fct-evals) / (mr fct-evals)

Table 1: Synopsis of Prothero-Robinson Tests.

We notice, that multirating is achieved: firstly, the theoretical speed ups in MatLab operations $\Xi_{\text{ops}} \approx (n/n_A)^2$ (since $n - n_A \ll mn_A$; n number of unknowns, n_A number of active) and in scalar RHS-evaluations $\Xi_{\text{fct}} \approx (n/n_A)$ is almost obtained. Secondly, even more convincing, the number of micro steps reflects the number of steps in the single rate algorithm. It has to be noted, that the error scaling $\text{err} = 2(\mathcal{I} - h\gamma\mathbf{f}_y)^{-1}(\mathbf{y}^1 - \mathbf{y}^2)$ was necessarily used to obtain these results.

3.2 Inverter-Chain-Benchmark. This benchmark is well suited for multirate tests due to its regularity, scalability and stiffness control. The equations for n inverters are given by

$$\dot{u}_1 = U_{\text{op}} - u_1 - \Upsilon f(u_{\text{in}}, u_1, 0), \quad \dot{u}_k = U_{\text{op}} - u_k - \Upsilon f(u_{k-1}, u_k, 0) \quad \text{for } k = 2, \dots, n \quad (6)$$

where f is piecewise quadratic, and initial values consistent given. As input (u_{in}) serves a single pulse of length 12ns (modeled as a polyline), which is smoothened, delayed and of course inverted by each inverter. The parameter Υ controls stiffness. Furthermore, since activity is time dependent, a dynamic partitioning is necessary:

1. **Window strategy** (win) uses signal speed and width to define interval of active nodes
2. **Activation level** (act) uses node voltage to define activity (excitation from initial value)

We state some results for the non stiff case:

mode	error control	micros	macros	cost [M ops]	$\Xi_{\text{ops}} = 8.0$ speed up	fct-evals	$\Xi_{\text{fct}} = 2.9$ ratio: evals
sr		347(4)		111.8	-	52450	-
mr/win	no scal	564(56)	70(11)	25.6	4.4	42881	1.22
mr/act2	$h_{\text{max}} = 1$	565(67)	79(29)	34.4	3.3	46643	1.12

Table 2: Synopsis of multirate on the non stiff inverter chain.

In the non stiff case we detect speed ups as expected for MatLab operations, but a bit less for the function evaluations (up to 28 nodes were active of 50). In the stiff case, however were up to 77 of 100 nodes active, and speed ups in MatLab operations were found (factor 3). But, we observed, a dramatic increase of micro steps (about factor 4!), and no speed up in function evaluations was achieved for this rather unfavourable setting for multirating (up to 77 active / 33 latent). Furthermore, the above error scaling was not anymore favourable.

3.3 Conclusions. The generalised multirating seems to be very promising as the Prothero-Robinson example demonstrates. Still, the non stiff inverter chain performs well. The problem of the increased number of micros for the stiff inverter chain might be due to the lagged Jacobian, since (1) the Jacobian might change to much over one macro step, and (2) the error scaling bases on exact Jacobians. Thus to overcome these troubles, one might use a multirate-ROW method instead of the W-method.

Furthermore, the ratio of latent to active components is still very small: less than three in all cases. Therefore tests with a larger number of latent variables are necessary to reveal the hidden potential of multirating.

Acknowledgements

The first author's work was supported by Philips Electronics Eindhoven.

4. References

- 1 ARNOLD, M. AND GÜNTHER, M.: *Preconditioned dynamic iteration for coupled differential-algebraic systems*. Submitted to BIT.
- 2 BARTEL, A.: *Generalised Multirate — Two Row-type Versions for Circuit simulation*. Unclassified NatLab Report No. 2000/804. Philips Electronics (2000).
- 3 BRACHTENDORF, H.G., WELSCH, G., LAUR, R. AND BUNSE-GERSTNER, A.: *Numerical steady state analysis of electronic circuits driven by multi-tone signals*. Electrical Engineering **70** (1996), pp. 103–102.
- 4 ENGSTLER, CH. AND LUBICH, CH.: *Multirate extrapolation methods for differential equations with different time scales*. Computing **58** (1997), pp. 173–185.
- 5 ENGSTLER, CH. AND LUBICH, CH.: *MUR8: A Multirate Extension of the Eighth-order Dormand-Prince Method*. Appl. Numer. Math. **25** (1997), pp. 185–192, special issue Time Integrators.
- 6 GEAR, C.W. AND WELLS, D.R.: *Multirate Linear Multistep Methods*. BIT **24** (1984), pp. 484–502.
- 7 GRÄB, R., GÜNTHER, M., WEVER, U. AND ZHENG, Q.: *Optimization of Parallel Multilevel-Newton Algorithms on Workstation Clusters*. In: Euro-Par96 Parallel Processing. Eds.: L. Bouge et al. Berlin, Springer-Verlag, 91–96 (1996) (Lecture Notes in Computer Science 1124).
- 8 GÜNTHER, M., KVÆRNØ, A. AND RENTROP, P.: *Multirate Partitioned Runge-Kutta Methods*. Submitted to BIT.
- 9 GÜNTHER, M. AND RENTROP, P.: *Multirate ROW methods and latency of electric circuits*. Applied Numerical Mathematics **13** (1993), pp. 83–102.
- 10 HOFER, E.: *A partially implicit method for large stiff systems of ODEs with only few equations introducing small time constants*. SIAM J. Num. Anal. **13** (1976), pp. 645–663.
- 11 HAIRER, E.: *Order Conditions for Numerical Methods for Partitioned Ordinary Differential Equations*. Numerische Mathematik (1981) **36**, pp. 431–445.
- 12 KVÆRNØ, A.: *Multirate Runge-Kutta Schemes*. Norwegian University of Science and Technology, Trondheim.
- 13 KVÆRNØ, A. AND RENTROP, P.: *Low Order Multirate Runge-Kutta Methods in Electric Circuit Simulation*. Preprint Nr. 99/1, IWRMM, University of Karlsruhe.
- 14 MIEKKALA, U. AND NEVANLINNA, O.: *Convergence of dynamic iteration methods for initial value problems*. SIAM J.Sci.Stat.Comp. **8** (1987), pp. 459–482.
- 15 PULCH, R. AND GÜNTHER, M.: *A method of characteristics for solving MPDEs in radio frequency application*. In preparation.
- 16 RABBAT, N.B.G., SANGIOVANNI-VINCENTELLI A.L. AND HSIEH, H.Y.: *A multilevel Newton algorithm with macromodelling and latency for the analysis of large scale nonlinear circuits in the time domain*. IEEE Trans. CAS **26** (1979), pp. 733–741.
- 17 RENTROP, P.: *Partitioned Runge-Kutta methods with stiffness detection and step size control*. Numer. Math. **47** (1985), pp. 545–564.
- 18 RICE, J.R.: *Split Runge-Kutta methods for simultaneous equations*. J.Res.Natl.Buv.Stand. **64B** (1960), pp. 151–170.
- 19 ROYCHOWDHURY, J.: *Analysing circuits with widely-separated time scales using numerical PDE methods*. Manuscript TCAS98, Bell Labs, Murray Hill, 1998.
- 20 L.F. SHAMPINE AND M.W. REICHEL. *The MATLAB ode suite*. SIAM J. of Scient. Comp., **18** (1997), pp. 1–22.
- 21 WEINER, R., ARNOLD, M., RENTROP, P. AND STREHMEL, K.: *Partitioning strategies in Runge-Kutta type methods*. IMA J. Num. Anal. **13** (1993), pp. 303–319.

Addresses: ANDREAS BARTEL, DR. MICHAEL GÜNTHER, Universität Karlsruhe, Institut für Wissenschaftliches Rechnen und mathematische Modellbildung, Engesser Straße 6, D-76128 Karlsruhe, Deutschland.

CALLIES, R.

Multidimensional Stepsize Control

Optimization problems in technical simulation often lead to boundary value problems for systems of highly nonlinear ordinary differential equations with piecewise defined right hand sides and a large number of exceptional points with reduced differentiability. Classical integration schemes show a poor performance due to the large number of restarts of the integrator; integration intervals end before the stepsize control has stabilized. The new approach does not only use the information of the preceding integration step for stepsize control, but also information from the preceding iteration step, if the boundary value problem is solved by an iterative algorithm. Multistage search techniques improve the efficiency of the determination of the exceptional points. These new techniques are tightly coupled with the progress of the Newton process. The numerical solution of the boundary value problem is by the new multiple shooting code JANUS which fully exploits the new integration techniques.

1. Boundary Value Problem

A problem of optimal control and system optimization in technical simulation is transformed in a well-known manner into a multi-point boundary value problem (MPBVP, see e.g. [1]) for a system of highly nonlinear ordinary differential equations (ODE). The approximation of experimental data by e.g. Cardinal splines leads to a large number of exceptional points with reduced differentiability of the right hand side of the ODE system. The MPBVP is solved by the advanced multiple shooting method JANUS. A detailed description is given in [3], here only a short summary is presented. In JANUS the solution of the MPBVP is formally equivalent to the solution of a special system of nonlinear equations ($z := (y_0^+, t_{M+1}, y_1^+, t_1, \dots, y_M^+, t_M)^T$)

$$F(z) := (r_0(t_0, t_{M+1}, y_0^+, y(t_{M+1}^-)), r_1(t_1, y_1^+, y(t_1^-)), \dots, r_M(t_M, y_M^+, y(t_M^-)))^T = 0 \quad (1)$$

$y(t_{\nu+1}^-) := y(t_{\nu+1}; t_{\nu}, y_{\nu}^+)$, $\nu = 0, \dots, M$, is the solution at $t = t_{\nu+1}$ of the piecewise defined initial value problem

$$\begin{cases} \dot{y} = f_{\nu,\mu}(t, y), & t \in [t_{\nu,\mu}, t_{\nu,\mu+1}[, \quad \mu = 1, \dots, \kappa_{\nu} - 1, \\ r_{\nu,\mu}(t_{\nu,\mu}, y(t_{\nu,\mu}^+), y(t_{\nu,\mu}^-)) = 0, & \mu = 2, \dots, \kappa_{\nu} - 1, \\ y(t_{\nu}) = y_{\nu}^+ & \text{initial value, } t_{\nu} := t_{\nu,1}, \quad t_{\nu+1} := t_{\nu,\kappa_{\nu}}. \end{cases}$$

$f_{\nu,\mu} \in C^N(D_{\nu,\mu} \times \mathbb{R}^n, \mathbb{R}^n)$, $r_{\nu,\mu} : \mathbb{R} \times \mathbb{R}^n \times \mathbb{R}^n \rightarrow \mathbb{R}^{d_{\nu,\mu}}$ and $r_0 : \mathbb{R}^2 \times \mathbb{R}^n \times \mathbb{R}^n \rightarrow \mathbb{R}^{d_{M+1}}$ with $M, N, \kappa_{\nu}, d_{\nu,\mu}, d_0 \in \mathbb{N}$ and $D_{\nu,\mu} \supset [t_{\nu,\mu}, t_{\nu,\mu+1}]$ open; $y(t_{\nu,\mu}^-) := \lim_{t \rightarrow t_{\nu,\mu}^-} y(t; t_{\nu,\mu-1}, y_{\nu,\mu-1}^+)$. For the *micro discretisation* $\{t_{\nu,\mu}\}$ with $\nu = 0, \dots, M$, $\mu = 2, \dots, \kappa_{\nu} - 1$ only so-called "continuous design points" (CDP) are permitted. On the other hand, CDPs may also be part of the *macro discretisation* $t_0 < t_1 < \dots < t_{M+1} := t_F$.

DEFINITION 1: $t_{\nu,\mu}$ is called CDP $\iff y(t_{\nu,\mu}^-) = y(t_{\nu,\mu}^+)$.

The nonlinear system (1) is iteratively solved by a modified Newton method (iteration of the linearized system). The ξ -th iteration step reads $(DF(z^{(\xi)})) := \partial F(z)/\partial z|_{z=z^{(\xi)}}: z^{(\xi+1)} := z^{(\xi)} + \lambda \Delta F(z^{(\xi)})^{-1} F(z^{(\xi)})$ with $\Delta F(z^{(\xi)}) \approx DF(z^{(\xi)})$. An iteration step is accepted, if at least one of the following tests is valid:

$$\begin{aligned} \|F(z^{(\xi+1)})\| &\leq \|F(z^{(\xi)})\| && \text{(Test 1)} \\ \|(\Delta F(z^{(\xi)}))^{-1} F(z^{(\xi+1)})\| &\leq \|(\Delta F(z^{(\xi)}))^{-1} F(z^{(\xi)})\| && \text{(Test 2)} \end{aligned}$$

In addition we require that: $\|F(z^{(\xi+1)})\| < \|F(z^{(\xi-2)})\| \wedge \|(\Delta F(z^{(\xi)}))^{-1} F(z^{(\xi)})\| < \|(\Delta F(z^{(\xi-2)}))^{-1} F(z^{(\xi-2)})\|$.

The following (heuristic) assumption is motivated by the fact, that the assignment of design points to the macro or the micro discretisation is arbitrary (the assumption has to be validated separately in case of every application):

ASSUMPTION 2: For the t_{ν} and the $t_{\nu,\mu}$ similar convergence criteria are applicable, even if only the t_{ν} are directly modified by the Newton process.

2. Continuous Design Points: Detection by Multistage Techniques

Let $y(t)$ denote the exact and $\eta(t)$ the numerical solution. $\eta(\bar{t}_{i+1})$ is calculated by an unperturbed integration step $\bar{t}_i \rightarrow \bar{t}_{i+1} := \bar{t}_i + h_i$ of an integrator of p -th order with the right hand side $f_{\nu,\mu-1}(t, y(t))$ and step size h_i , for which $r_{\nu,\mu-1}(\bar{t}_i, \eta(\bar{t}_i)) \cdot r_{\nu,\mu-1}(\bar{t}_{i+1}, \eta(\bar{t}_{i+1})) < 0 \Rightarrow t_2 := t_{\nu,\mu} \in [\bar{t}_i, \bar{t}_{i+1}]$. In **Stage 1** dense output [5] of low order q_1 is calculated in $[\bar{t}_i, \bar{t}_{i+1}]$ without additional function evaluations (typical: $p = 7 \dots 9$, $q_1 = 3 \dots 5$ [3]) and a coarse estimate \hat{t}_2 for t_2 is determined from the dense output. In **Stage 2** $\eta(\hat{t}_2)$ is calculated (no step size control), then

another integration step is performed without step size control, but with dense output of order q_2 ($q_1 \leq q_2 < p$) and with a step size $h := 0.2 \cdot h_i^{p/q_2}$ (safety factor of 5) in direction of the solution. The local error $|y(\bar{t}_{i+1}) - \eta(\bar{t}_{i+1})|$ of the initial integration scheme and the local error of the dense output on a smaller subinterval with length h are of the same order. The algorithm solves the problem, that the dense output is mostly of lower order (and therefore of lower precision) than the underlying integrator. Only the critical integration step is reduced. Using Assumption 2 and applying the convergence criteria from Newton iteration, stage 1 in the ξ -th iteration step can be replaced by the following estimate (which is available at no extra cost):

$$t_{\nu,\mu}^{(\xi)} \in I_{t_{\nu,\mu}^{(\xi)}} := \left[t_{\nu,\mu}^{(\xi-1)} - 3|t_{\nu,\mu}^{(\xi-1)} - t_{\nu,\mu}^{(\xi-2)}|, t_{\nu,\mu}^{(\xi-1)} + 3|t_{\nu,\mu}^{(\xi-1)} - t_{\nu,\mu}^{(\xi-2)}| \right].$$

If Assumption 2 fails (which is rarely the case), only one additional integration step has to be performed.

3. Continuous Design Points: Additional Step Size Control

In case of one-step methods the additional information from the preceding iteration steps of the system (1) can be used to prevent a restart of the integrator. Fundamental for classical step size control of one-step methods is Gragg's theorem [4], which proves the existence of an asymptotic expansion of the global discretization error:

Let $f(t, y) \in C^{N+2}([t_0, t_f] \times \mathbb{R}^n, \mathbb{R}^n)$ and let the $(N+2)$ -th partial derivatives of f be bounded. Suppose that $\eta(t; t_0, y_0, h)$ is the numerical result of $\dot{y} = f(t, y)$, $y(t_0) = y_0$ computed by a one-step method of order $p \leq N$ with constant step size h . Rounding errors are neglected. For $\eta(t; t_0, y_0, h)$ an asymptotic expansion holds $\forall t \in [a, b]$, $\forall h = (t - t_0)/\nu$, $\nu = 1, 2, \dots$:

$$\eta(t; t_0, y_0, h) = y(t; t_0, y_0) + \sum_{i=p}^N d_i(t; t_0, y_0) h^i + h^{N+1} D_{N+1}(t; t_0, y_0, h), \quad |D_{N+1}(t; t_0, y_0, h)| < \infty \quad \forall h.$$

For a chosen stepsize h_i two approximations of order p and $p+1$ are computed [5] ($\sigma_i := \{t_i; t_{i-1}, \eta_{i-1}\}$):

$$\eta(\sigma_i, h_i) - \hat{\eta}(\sigma_i, h_i) = (d_{p+1}(\sigma_i) h_i^{p+1} + d_{p+2}(\sigma_i) h_i^{p+2} + \mathcal{O}(h_i^{p+3})) + (\hat{d}_{p+2}(\sigma_i) h_i^{p+2} + \mathcal{O}(h_i^{p+3}))$$

We obtain an estimate for the next integration step by the approximation (err_i average error, $\varepsilon_{i,j}$ tolerance):

$$\frac{1}{h_{i+1}^{p+1}} \geq \frac{err_{i+1}}{h_{i+1}^{p+1}} \simeq \sqrt{\frac{1}{n} \sum_{j=1}^n \left(\frac{|d_{p+1,j}(t_{i+1}; t_i, \eta_i)|}{\varepsilon_{i+1,j} \cdot h_{i+1}} \right)^2} \stackrel{(*)}{\simeq} \sqrt{\frac{1}{n} \sum_{j=1}^n \left(\frac{|d_{p+1,j}(t_i; t_{i-1}, \eta_{i-1})|}{\varepsilon_{i,j} \cdot h_{i+1}} \right)^2} \simeq \frac{err_i}{h_i^{p+1}} \cdot \frac{h_i}{h_{i+1}}$$

An approximation similar to that in $(*)$ is used to construct a second step size control specifically adapted to iteratively solved boundary value problems. Let $h_0(\nu, \mu)^{(\xi)}$ be the new integration step starting with $t_{\nu,\mu}^{(\xi)}$: $t_{\nu,\mu}^{(\xi)} \rightarrow t_{\nu,\mu}^{(\xi)} + h_0(\nu, \mu)^{(\xi)}$. The Newton iteration produces increasingly better approximations for $y(t)$ and $t_{\nu,\mu}$ and simultaneously improves the estimate for $h_0(\nu, \mu)$. Analogously to the classical step size control we obtain ($h_0 := h_0(\nu, \mu)$)

$$\frac{1}{(h_0^{(\xi+1)})^{p+1}} \geq \frac{err_0(\nu, \mu)^{(\xi+1)}}{(h_0^{(\xi+1)})^{p+1}} \simeq \left[\frac{1}{n} \sum_{j=1}^n \left(\frac{|d_{p+1,j}^{(\xi+1)}(t_{\nu,\mu}^{(\xi+1)} + h_0^{(\xi+1)}; t_{\nu,\mu}^{(\xi+1)}, \eta_{\nu,\mu}^{(\xi+1)})|}{\varepsilon_{i,j} \cdot h_0^{(\xi+1)}} \right)^2 \right]^{1/2} \simeq \frac{err_0(\nu, \mu)^{(\xi)}}{(h_0^{(\xi)})^{p+1}} \cdot \frac{h_0^{(\xi)}}{h_0^{(\xi+1)}}.$$

Now we choose: $h_0(\nu, \mu)^{(\xi+1)} := 0.9 h_0(\nu, \mu)^{(\xi)} \cdot [err_0(\nu, \mu)^{(\xi)}]^{-1/p} \cdot \min \left\{ |h_0(\nu, \mu)^{(\xi)}| / (20 \cdot |t_{\nu,\mu}^{(\xi)} - t_{\nu,\mu}^{(\xi+1)}|)^2, 1 \right\}$, if $|t_{\nu,\mu}^{(\xi)} - t_{\nu,\mu}^{(\xi+1)}| \ll h_0(\nu, \mu)^{(\xi)}$; otherwise $h_0(\nu, \mu)^{(\xi+1)}$ is determined as in case of the normal initial value problem. The more the estimate for $t_{\nu,\mu}$ alters between the ξ -th and $(\xi+1)$ -th step compared to $|h_0(\nu, \mu)^{(\xi)}|$, the more additional and hardly controllable effects play an important role in the determination of the initial step size $h_0(\nu, \mu)^{(\xi+1)}$: the safety factor is tightened. The numerical value of 20 and the quadratic weighting are due to numerical experiments.

4. Example Problem

As an example problem, the ascent optimization of a single-stage, suborbital hypersonic demonstrator system (HYD) is considered [2]. Experimental data for the aerodynamical model are approximated by Cardinal splines. This leads to a number of 122 exceptional points with reduced differentiability of the right hand side of the 17-dimensional system of nonlinear ODEs. The new technique allows a reduction of the number of function evaluations by 72 %.

5. Literaturverzeichnis

- 1 BRYSON, A. E. AND HO, Y.-C.: Applied Optimal Control, Revised Printing, Hemisphere Publ. Corp., Washington, 1975.
- 2 CALLIES, R. AND WIMMER, G.: Optimierung von Testflugbahnen, ZAMM 79 S3, 1999, pp. 929-931.
- 3 CALLIES, R.: Entwurfsoptimierung und optimale Steuerung. Differential-algebraische Systeme, Mehrgitter-Mehrzielansätze und numerische Realisierung, Habilitationsschrift, TU München, 2000.
- 4 STOER, J.: Numerische Mathematik 1, Springer Verlag, Berlin, Heidelberg, New York, 5 ed, 1989.
- 5 STREHMEL, K. AND WEINER, R.: Numerik gewöhnlicher Differentialgleichungen, B.G. Teubner Verlag, Stuttgart, 1995.

Anschrift: DR. RAINER CALLIES, Zentrum Mathematik, TU München, D-80290 München, Germany

LINSS, TORSTEN

Uniform pointwise convergence of finite difference schemes for quasilinear convection-diffusion problems

We study convergence properties of an upwind difference scheme on layer-adapted grids for the discretization of a class of singularly perturbed quasilinear two-point boundary value problems. We derive conditions that are sufficient for uniform convergence in the maximum norm, with respect to the perturbation parameter, of the method. These conditions are easy to check and enable one to immediately deduce the rate of uniform convergence.

1. Introduction

We consider the singularly perturbed quasilinear convection-diffusion problem

$$Tu := -\epsilon u'' - b(x, u(x))' + c(x, u) = 0 \quad \text{for } x \in (0, 1), \quad u(0) = u(1) = 0, \quad (1)$$

where $0 < \epsilon \ll 1$ is a small parameter. It is also assumed that $b_u(x, u) \geq \beta$ for $(x, u) \in (0, 1) \times \mathbb{R}$ with a positive constant β . The solution u generally has an exponential boundary layer at $x = 0$: it behaves as follows

$$|u^{(i)}(x)| \leq C(1 + \epsilon^{-i} \exp(-\beta x/\epsilon)) \quad \text{for all } x \in [0, 1] \text{ and } i = 0, \dots, q$$

for some fixed order $q \in \mathbb{N}$ that depends on the smoothness of the data, see [12]. Here and throughout C denotes a generic positive constant that is independent of the perturbation parameter ϵ .

It is well known that singularly perturbed differential equations require special numerical methods in order to obtain accuracy uniform in ϵ . One of the most attractive approaches is to use standard finite-difference schemes on a priori constructed nonequidistant meshes which are dense in the layer(s). A mesh of that kind was first introduced by Bakhvalov [2]. More recently, Shishkin [10] discovered that suitable piecewise equidistant meshes can also produce ϵ -uniform results. However, even though Shishkin meshes are simpler, they usually give numerical results which are inferior to Bakhvalov meshes. This prompted some work on improvements of the Shishkin meshes. In [11] a unified theory for Shishkin-type meshes is given. In that article the linear case of (1) is used as model problem.

2. Upwind discretization and mesh

Let $\Omega^N: 0 = x_0 < x_1 < \dots < x_N = 1$ be an arbitrary mesh with local mesh sizes $h_i := x_i - x_{i-1}$. For any mesh function $\{v_i\}_{i=0}^N$ defined on Ω^N we formally set $v_0 = v_N = 0$. We introduce the discrete norms

$$\|v\|_{d,\infty} := \max_{i=1,\dots,N-1} |v_i| \quad \text{and} \quad \|v\|_{d,1} := \sum_{i=1}^{N-1} h_{i+1} |v_i|.$$

We define a discrete first-order upwind operator T^u approximating the continuous operator T by

$$[T^u v]_i := -D^+ [\epsilon D^- v + b(\cdot, v)]_i + c(\cdot, v)_i,$$

where

$$[D^- v]_i := \frac{v_i - v_{i-1}}{h_i}, \quad [D^+ v]_i := \frac{v_{i+1} - v_i}{h_{i+1}} \quad \text{and} \quad g(\cdot, v)_i := g(x_i, v_i) \quad \text{for any function } g.$$

The discrete operator T^u enjoys the following stability properties

Theorem 1. *Let $\{v_i\}_{i=0}^N$ and $\{w_i\}_{i=0}^N$ be two arbitrary mesh functions. Then*

$$\|v - w\|_{d,\infty} \leq \beta^{-1} \|T^u v - T^u w\|_{d,1}.$$

Proof. See [9].

Theorem 2. Let $\{v_i\}_{i=0}^N$ and $\{w_i\}_{i=0}^N$ be two arbitrary mesh functions. Assume that the function c depends on x only, i.e., $c = c(x)$. Then

$$\|v - w\|_{d,\infty} \leq 2\beta^{-1} \left\| \sum_{j=0}^{N-1} h_{j+1} (T^u v_j - T^u w_j) \right\|_{d,\infty}.$$

Proof. A proof that is based on the fundamental works for linear problems in [1] is given in [4, Lemma 1].

For our discretization we use a mesh of the general type introduced in [11]. Let $N \geq 4$, our discretization parameter, be an even integer. Let $\lambda = 2\epsilon\beta^{-1} \ln N$ denote a mesh transition parameter. We shall consider a layer-adapted mesh which is equidistant in $[x_{N/2}, 1]$ but graded in $[0, x_{N/2}]$, where we choose the transition point $x_{N/2}$ in Shishkin's sense, i.e., $x_{N/2} = \lambda$. On $[0, x_{N/2}]$ let our mesh be given by a mesh generating function φ with $\varphi(0) = 0$ and $\varphi(1/2) = \ln N$ which is supposed to be continuous and monotonically increasing. Then our Shishkin-type mesh is

$$x_i = \begin{cases} 2\epsilon\beta^{-1}\varphi(i/N) & \text{for } i = 0, 1, \dots, N/2, \\ 1 - 2(1 - 2\epsilon\beta^{-1} \ln N)(N - i)/N & \text{for } i = N/2 + 1, \dots, N. \end{cases}$$

Let $\psi = \exp(-\varphi)$. We shall see that the crucial quantity determining the order of convergence is $\max_{t \in [0, 1/2]} |\psi'(t)|$.

Examples for the mesh characterizing function ψ are

$$\begin{array}{lll} \psi(t) = e^{-(\ln N)t} & \text{standard Shishkin mesh [10] with} & \max |\psi'| \leq C \ln N \quad \text{and} \\ \psi(t) = 1 - 2(1 - N^{-1})t & \text{Bakhvalov-Shishkin mesh [6, 8] with} & \max |\psi'| \leq C. \end{array}$$

Theorem 3. Assume that there exists a constant C such that the mesh characterizing function φ satisfies $\varphi'(t) \leq CN$ for $t \in [0, 1/2]$. Then the error of the upwind difference scheme $[T^u u^u]_i = 0$, $u_0^u = u_N^u = 0$ satisfies

$$\|u - u^u\|_{d,\infty} \leq CN^{-1} \max |\psi'|.$$

Proof. See [4, 9].

The numerical experiments in [4, 9] confirm that this error bound is sharp. The results of Theorems 1-3 can be extended to second-order upwind schemes [5,7] and to central difference approximations [3].

3. References

- 1 ANDREEV, V. B.; KOPTEVA, N. V.: On the convergence, uniform with respect to a small parameter, of monotone three-point difference approximations. *Diff. Equations* **34** (1998), 921-929.
- 2 BAKHVALOV, N. S.: Towards optimization of methods for solving boundary value problems in the presence of a boundary layer. *Zh. Vychisl. Math. Math. Fiz.* **9** (1969), 841-859, in Russian.
- 3 KOPTEVA, N. V.; LINSS, T.: Uniform second-order pointwise convergence of a central difference approximation for a quasilinear convection-diffusion problem. Preprint MATH-NM-13-99, TU Dresden, December 1999.
- 4 LINSS, T.: Uniform pointwise convergence of finite difference schemes using grid equidistribution. MATH-NM-11-99, TU Dresden, November 1999.
- 5 LINSS, T.: Uniform second order pointwise convergence of a finite difference approximation for a quasilinear convection-diffusion problem. Preprint MATH-NM-08-99, TU Dresden, June 1999.
- 6 LINSS, T.: An upwind difference scheme on a novel Shishkin-type mesh for a linear convection-diffusion problem. *J. Comput. Appl. Math.*, **110** (1999), 93-104.
- 7 LINSS, T.: Sufficient conditions for uniform convergence on layer-adapted grids. Preprint MATH-NM-08-99, TU Dresden, February 2000.
- 8 LINSS, T.: Analysis of a Galerkin finite element method on a Bakhvalov-Shishkin mesh for a linear convection-diffusion problem. *IMA J. Numer. Anal.*, to appear.
- 9 LINSS, T.; ROOS, H.-G.; VULANOVIĆ, R.: Uniform pointwise convergence on Shishkin-type meshes for quasilinear convection-diffusion problems. *SIAM J. Numer. Anal.*, to appear.
- 10 SHISHKIN, G. I.: A difference scheme for a singularly perturbed parabolic equation with a discontinuous boundary condition. *Zh. Vychisl. Math. Math. Fiz.* **28** (1988), 1679-1692, in Russian.
- 11 ROOS, H.-G.; LINSS, T.: Sufficient conditions for uniform convergence on layer adapted grids. *Computing* **63** (1999), 27-45.
- 12 VULANOVIĆ, R.: A uniform method for quasilinear singular perturbation problems without turning points. *Computing* **41** (1989), 97-106.

Addresses: DR. TORSTEN LINSS, Institut für Numerische Mathematik, TU Dresden, D-01062 Dresden, Germany.

NEHER, M.

Berechenbare Schranken von Taylorkoeffizienten analytischer Funktionen

Es werden Verfahren vorgestellt, um Schranken für Taylorkoeffizienten von auf dem Computer verfügbaren analytischen Standardfunktionen oder ihrer Verkettungen zu berechnen. Die Verfahren beruhen auf verschiedenen Modifikationen der Cauchy'schen Koeffizientenabschätzung. Bei praktischen Berechnungen auf dem Computer wird durch Intervallarithmetik sicher gestellt, dass alle auftretenden Diskretisierungs- und Rundungsfehler erfasst werden.

1. Cauchy'sche Koeffizientenabschätzung auf dem Computer

In dieser Arbeit werden verschiedene Verfahren vorgestellt, um mit Hilfe eines Computers garantierte Schranken von Taylorkoeffizienten analytischer Funktionen praktisch zu berechnen. Ein wesentliches Werkzeug hierzu ist die Intervallrechnung [1]. Dabei ist ein komplexes Intervall Z in dieser Arbeit stets durch ein Paar reeller Intervalle X und Y definiert: $Z = X + iY := \{z = x + iy : x \in X, y \in Y\}$, $i^2 = -1$.

Im Folgenden sei $r > 0$, B bezeichne die Kreisscheibe $\{z : |z| < r\}$ und C den Kreis $\{z : |z| = r\}$.

Eine bekannte Schranke für die Taylorkoeffizienten analytischer Funktionen ist die Cauchy'sche Koeffizientenabschätzung (im Folgenden kurz CK genannt): ist die Funktion $f(z)$ analytisch in B und beschränkt auf C , so besitzt sie eine Potenzreihenentwicklung $f(z) = \sum_{j=0}^{\infty} a_j z^j$, $|z| \leq r$, für die $|a_j| \leq \frac{M(r)}{r^j}$, $j \in \mathbb{N}_0$, gilt, wobei $M(r) := \max_{|z|=r} |f(z)|$.

Sei nun im Folgenden f eine analytische Verkettung rationaler Funktionen oder der üblichen auf dem Computer verfügbaren komplexen Standardfunktionen (wie e^z , $\sin z$, $\log z$, ...). In diesem Fall können Real- und Imaginärteil von f als Verkettungen reeller Standardfunktionen ausgedrückt werden. Solche Zerlegungen wurden in [2] zur Konstruktion komplexer Intervallstandardfunktionen benutzt, die in Programmiersprachen wie C-XSC [4] einfach implementiert werden können.

Zur praktischen Berechnung von $M(r)$ überdecken wir C mit komplexen Intervallen Z_k , $k = 1, \dots, k_{\max}$. Mit einer geeigneten Intervallerweiterung von f berechnen wir für jedes Z_k ein Intervall $[F_k, \bar{F}_k]$, das $|f(Z_k)|$, den Wertebereich von $|f|$ auf Z_k , einschließt. Das Maximum der Zahlen \bar{F}_k liefert dann eine verifizierte obere Schranke für $M(r)$.

Gute obere Schranken für $M(r)$ werden i. A. nur für hinreichend kleine Durchmesser der C überdeckenden Intervalle Z_k erhalten. Dies erreicht man durch adaptive Verfeinerung einer Anfangsüberdeckung mit Hilfe bekannter Methoden der verifizierenden globalen Optimierung [3]. Allerdings führt auch die präzise Berechnung von $M(r)$ nicht immer zu guten Schranken für die Taylorkoeffizienten von f , da die CK sehr pessimistisch sein kann. Zur Verbesserung der CK schlagen wir in den nächsten beiden Abschnitten zwei Modifikationen vor.

2. Schranken mit Hilfe von Polynomapproximationen

Satz 1. $f(z) = \sum_{j=0}^{\infty} a_j z^j$, $|z| \leq r$, $r > 0$, sei analytisch in $B = \{z : |z| < r\}$ und beschränkt auf $C = \{z : |z| = r\}$. $p_l(z)$ sei ein Polynom vom Grad l . Dann folgt durch Anwendung der CK auf $f - p_l$:

$$|a_j| \leq \frac{N(r, l)}{r^j} \quad \text{für } j > l, \quad \text{wobei } N(r, l) := \max_{|z|=r} |f(z) - p_l(z)|.$$

Falls p_l die Funktion f in der Maximumnorm gut approximiert, kann die auf dem Computer berechnete Schranke $N(r, l)$ erheblich kleiner sein als $M(r)$. In unseren praktischen Beispielen verwendeten wir als Approximationspolynom jeweils das Taylorpolynom T_l vom Grad l (mit Entwicklung um den Ursprung).

3. Schranken mit Hilfe von Ableitungen

Satz 2. $f(z) = \sum_{j=0}^{\infty} a_j z^j$, $|z| \leq r$, $r > 0$, sei analytisch in $B = \{z : |z| < r\}$ und die m -te Ableitung von f sei beschränkt auf $C = \{z : |z| = r\}$. Weiter sei $P(j, m) := (j+1) \cdots (j+m)$, $P(j, 0) := 1$ für $m \in \mathbb{N}$, $j \in \mathbb{N}_0$. Dann folgt durch Anwendung der CK auf $f^{(m)}$:

$$|a_j| \leq \frac{U(r, m)r^m}{P(j-m, m)r^j} \quad \text{für } j \geq m, \quad \text{wobei } U(r, m) := \max_{|z|=r} |f^{(m)}(z)|. \quad (1)$$

Die Abschätzung (1) ist eine wesentliche Verbesserung der CK, da $P(j-m, m)$ mit der Ordnung $O(j^m)$ gegen unendlich strebt.

Bemerkung 1. Die beiden zuletzt behandelten Abschätzungen lassen sich kombinieren, wenn bei der Berechnung von U zusätzlich eine Polynomapproximation von $f^{(m)}$ verwendet wird.

4. Numerische Beispiele

Die vorgeschlagenen Methoden wurden in der Programmiersprache C-XSC unter Linux auf einem PC mit einem Pentium II-Prozessor implementiert. Alle bei der Berechnung auftretenden Rundungsfehler wurden durch die in C-XSC vorhandene Intervallarithmetik erfasst.

Schranken für $f_1(z) = e^z$						Schranken für $f_2(z) = \frac{\cos z}{z^2 + 101}$					
r	l	m	$M/N/U$	a_{100}	a_{1000}	r	l	m	$M/N/U$	a_{100}	a_{1000}
1	—	—	2.8E+00	2.8E+00	2.8E+00	1	—	—	1.6E-02	1.6E-02	1.6E-02
1	8	—	4.3E-04	4.3E-04	4.3E-04	1	8	—	1.6E-06	1.6E-06	1.6E-06
1	—	50	2.8E+00	9.2E-94	9.8E-150	1	—	50	3.3E+18	1.1E-75	1.2E-131
10	—	—	2.7E+04	2.7E-96	2.7E-996	5	—	—	1.1E+00	1.4E-70	1.2E-699
10	25	—	4.1E+01	4.1E-99	4.1E-999	5	22	—	1.0E-03	1.3E-73	1.1E-702
10	—	50	2.7E+04	8.6E-140	9.2E-1096	5	—	50	1.1E+33	3.9E-96	3.5E-781
20	—	—	5.9E+08	4.7E-122	5.5E-1293	10	—	—	1.3E+04	1.3E-96	1.3E-996
20	—	50	5.9E+08	1.7E-150	2.2E-1377	10	—	50	1.1E+142	3.4E-02	3.6E-953

Die Tabelle zeigt die mit den verschiedenen Methoden erhaltenen Schranken für die Taylorkoeffizienten der beiden angegebenen Funktionen. N und U ergeben zum Teil wesentlich bessere Schranken als M . Allerdings wird eine gute Polynomapproximation von f durch T_l auf C bei großen Radien r nur durch Taylorpolynome hoher Ordnung erzielt, wodurch die Berechnung von N in diesem Fall sehr viel Rechenzeit erfordert.

f_2 besitzt eine Singularität bei $z = \sqrt{101}i$, der der Kreis mit Radius 10 sehr nahe kommt. Dennoch ist die Berechnung von M und U gut möglich, obwohl $U(10, m)$ mit wachsendem m schnell anwächst. Eine Verbesserung der CK erfolgt hier nur noch für Taylorkoeffizienten a_j mit hinreichend großem Index j .

Danksagung

Der Autor bedankt sich bei Herrn Ingo Eble für die Programmierung der numerischen Software.

5. References

- 1 ALEFELD, G., HERZBERGER, J.: Introduction to interval computations, Academic Press, New York, 1983.
- 2 BRAUNE, K., KRÄMER, W.: High-accuracy standard functions for real and complex intervals, in Computerarithmetic: Scientific computation and programming languages (Kaucher, E., Kulisch, U., Ullrich, Ch. Eds.), 81–114, Teubner, Stuttgart, 1987.
- 3 KEARFOTT, R. B.: Rigorous global search: Continuous problems, Kluwer, Dordrecht, 1996.
- 4 KLATTE, R., KULISCH, U., LAWO, CH., RAUCH, M., WIETHOFF, A.: C-XSC: A C++ class library for extended scientific computing, Springer, Berlin, 1993.

Anschrift: DR. MARKUS NEHER, Institut für Angewandte Mathematik, Universität Karlsruhe, D-76128 Karlsruhe, Germany

B.A. SCHMITT, R. WEINER, AND H. PODHAISKY

Parallel two-step W-methods

This paper deals with two-step W-methods for stiff initial value problems which allow the parallel solution of the stage equations. Special methods of order 3 and 4 are tested for both sequential and parallel implementations and compared with efficient sequential codes. The results show that the methods are already competitive in a sequential implementation and have a high level of parallelization especially in combination with Krylov solvers for linear equations of large dimensions.

1. Definition of the methods

There are various possibilities to exploit the facilities of parallel computers in the numerical solution of stiff initial value problems

$$y' = f(t, y), \quad y(t_0) = y_0,$$

see e.g. [1]. For computers with a relatively small number of processors two-step W-methods are an attractive class of methods. They combine the favourable properties of ROW-methods (e.g. [6], [4]) with a high potential of parallelization due to their use of external stages in a two-step fashion. These methods were introduced in [7] and are defined by

$$Y_{mi} = u_m + h_m \sum_{j=1}^s a_{ij} k_{m-1,j}, \quad (1)$$

$$(I - h_m \gamma T_m) k_{mi} = f(t_m + c_i h_m, Y_{mi}) + h_m T_m \sum_{j=1}^s \gamma_{ij} k_{m-1,j}, \quad (2)$$

$$u_{m+1} = u_m + h_m \sum_{i=1}^s (b_i k_{mi} + v_i k_{m-1,i}). \quad (3)$$

Here, T_m is an arbitrary matrix, usually an approximation to the Jacobian $f_y(t_m, u_m)$. Obviously, all stage increments k_{mi} can be computed in parallel with s processors.

In [7] the convergence properties of two-step W-methods are studied with the help of the simplifying conditions, where $\sigma = h_m/h_{m-1}$ is the current stepsize ratio,

$$C(q) : \quad \sum_{j=1}^s a_{ij} (c_j - 1)^{l-1} = \sigma^{l-1} \frac{c_i^l}{l}, \quad l = 1, \dots, q \quad (4)$$

$$\Gamma(q) : \quad \sum_{j=1}^s \gamma_{ij} (c_j - 1)^{l-1} = -\gamma \sigma^{l-1} c_i^{l-1}, \quad l = 1, \dots, q \quad (5)$$

$$B(r) : \quad \sum_{j=1}^s b_j \sigma^{l-1} c_j^{l-1} + \sum_{j=1}^s v_j (c_j - 1)^{l-1} = \frac{\sigma^{l-1}}{l}, \quad l = 1, \dots, r. \quad (6)$$

A standard analysis shows that with the conditions $C(q)$, $\Gamma(q)$ and $B(p)$ the methods are convergent of order $p^* = \min\{q+1, p\}$ for arbitrary matrices T_m under appropriate assumptions on the starting values k_{0j} .

When applied to the test equation of A-stability, $y' = \lambda y$ with $T_m = \lambda$ and with constant stepsize h , two-step

W-methods yield the recursion

$$\begin{pmatrix} hK_m \\ u_{m+1} \end{pmatrix} = M(z) \begin{pmatrix} hK_{m-1} \\ u_m \end{pmatrix}, \quad M(z) := \begin{pmatrix} w\beta & w\mathbb{1} \\ b^\top w\beta + v^\top & 1 + b^\top w\mathbb{1} \end{pmatrix}, \quad (7)$$

where $z = h\lambda$, $w := z/(1 - \gamma z)$, $K_m := (k_{mi})_{i=1}^s$, $\beta := A + \Gamma = (a_{ij} + \gamma_{ij})_{i,j=1}^s$ and $\mathbb{1} = (1, \dots, 1)^\top$.

Let $S \subseteq \mathbb{C}$ be the region where $\rho(M(z)) < 1$ holds. We call a method A -stable resp. $A(\alpha)$ -stable, if

$$\text{closure } S \supseteq \mathbb{C}^- \quad \text{resp.} \quad \text{closure } S \supseteq \{z \in \mathbb{C} : |\arg(z) - \pi| \leq \alpha\}.$$

For very stiff problems L -stability is a desirable property but its precise meaning has to be adapted to the form of the recursion (7). In [7] L -stability was defined by requiring A -stability and

$$\lim_{\operatorname{Re} z \rightarrow \infty} u_{m+1} = 0 \quad (8)$$

for arbitrary u_m , K_m . For two-step W-methods the property (8) can be ensured by the choice

$$c_s = 1, \quad b^\top = \gamma_s e_s^\top, \quad v^\top = e_s^\top \beta. \quad (9)$$

Methods satisfying (9) have been called *stiffly accurate* in [7].

With the help of the simplifying conditions special methods could be constructed which have order $p \geq s$, are stiffly accurate and at least $L(\alpha)$ -stable, see Table 1.

2. Numerical Experiments

The efficiency of parallel methods is determined by two aspects:

- The methods should be competitive with efficient sequential methods already in a sequential implementation.
- They have to show a good speed-up in parallel implementations.

In order to illustrate the promising properties of two-step W-methods we present two test problems where we compare three special $L(\alpha)$ -stable methods, described in Table 1, with efficient sequential codes. The first number in the names of the methods indicates the number of stages s , and the second number the order p .

Table 1: Parallel Two-Step W-methods

Name	$\rho(M(\infty))$	γ	c_1, \dots, c_s	defining conditions	$A(\alpha)$	order
PTSW23	0.65414	1.2	2.23809 1	$C(2), \Gamma(2)B(3), Eq.(9)$	90°	3
PTSW34	0.87852	0.84943	-1.71198 2.36572 1	$C(3), \Gamma(3), B(4), Eq.(9)$	89.7°	4
PTSW44	0	0.45645	-3.32526 -2.10534 -0.26604 1	$C(4), \Gamma(4), B(4), Eq.(9)$	68.4°	4

The computations were performed on a HP/Convex X-Class computer with shared memory. To reduce the number of matrix-vector products in the implementation, we rearrange the stage equations (2) into the form

$$(I - h_m \gamma T_{m,i})(k_{mi} + \sum_{j=1}^s \frac{\gamma_{ij}}{\gamma} k_{m-1,j}) = f(t_m + c_i h_m, Y_{mi}) + \sum_{j=1}^s \frac{\gamma_{ij}}{\gamma} k_{m-1,j}. \quad (10)$$

The methods were implemented with stepsize control by an embedded method. Since the methods have full order for arbitrary T_m it is computationally attractive to avoid frequent step size changes and to re-use old Jacobians and also the LR-decomposition of $(I - h_{m-1} \gamma T_{m-1})$ if $h_m = h_{m-1}$.

First, we consider the test problem PLATE of Hairer/Wanner [4]. The results in Figure 1 are from a sequential implementation and illustrate that the two-step W-methods are comparable for this problem with the well-known ROW-code RODAS [4].

Although all stages can be solved in parallel, the evaluation of the Jacobian and the LR-decomposition would restrict the speed-up considerably. We therefore see the main field of application of our methods in the class of large stiff problems, where the linear systems of equations are solved iteratively (e.g. by Krylov-methods) completely in parallel.

A special Krylov process is the full orthogonalization method which uses the Arnoldi algorithm to compute an orthogonal matrix $Q_i \in \mathbb{R}^{n \times \kappa}$ whose columns are basis vectors of the Krylov space $\mathcal{K}_i = \text{span}(r_i, Ar_i, \dots, A^{\kappa-1}r_i)$. The matrix A is the Jacobian $A = f_y$ and r_i is the right-hand-side of (10). The stage increments k_{mi} are approximated by solving a small linear system of size $\kappa \times \kappa$,

$$(I - h\gamma Q_i^T A Q_i)l_i = Q_i^T r_i, \quad k_{mi} = Q_i l_i - \sum_{j=1}^s \frac{\gamma_{ij}}{\gamma} k_{m-1,j}. \quad (11)$$

This method was applied in our second test equation, the two-dimensional Brusselator, see [5],

$$\begin{aligned} u_t &= \alpha(u_{xx} + u_{yy}) + 1 + u^2v - 4u \\ v_t &= \alpha(v_{xx} + v_{yy}) + 3u - u^2v \end{aligned}$$

with $\alpha = 0.02$ on a 100×100 grid. The dimensions of the Krylov spaces were restricted by $\kappa \leq 5$. Our code is compared with the Krylov multistep code VODPK [2] (using GMRES(5)) and with DOPRI5 [3], since this test problem is not too stiff. The results in Figure 2 show the efficiency of the two-step W-methods in the accuracy range of practical interest. The observed speedups are around 1.8, 2.6 and 3.2 for $s = 2, 3$ and 4 processors.

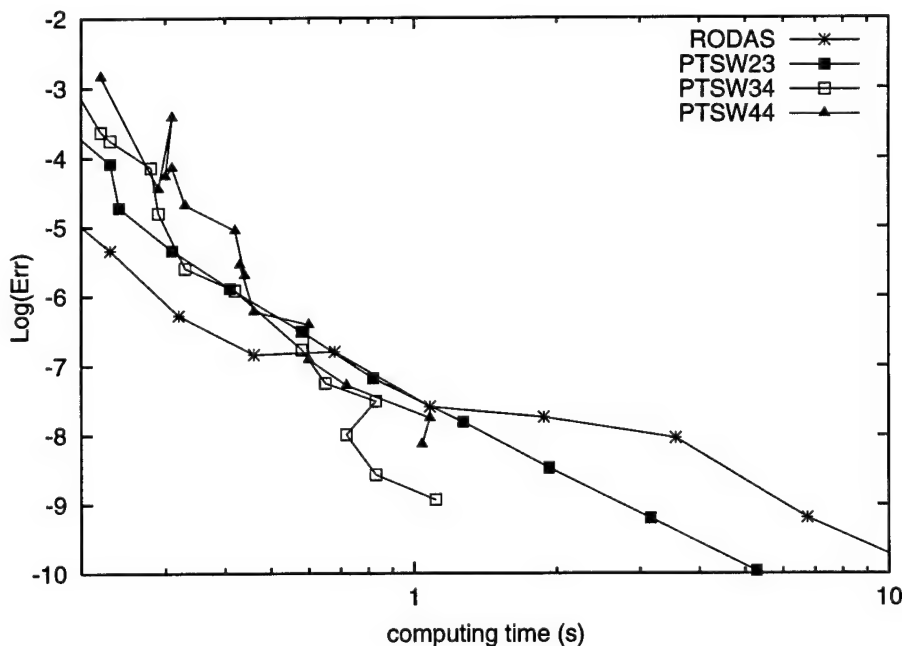


Figure 1: Results for Plate

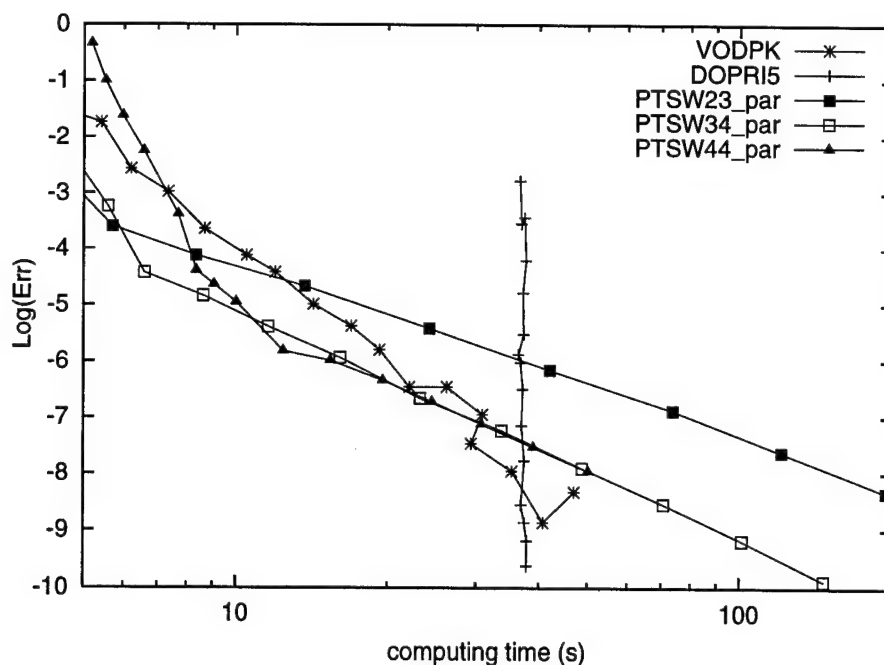


Figure 2: Results for Brusselator, PTW $_{sp}$ using s processors.

3. Conclusions

Two-step W-methods are a promising class for the solution of large stiff equations on parallel computers with few processors. In combination with Krylov techniques for the solution of the linear systems the s stages can be computed almost fully in parallel. First numerical tests show the potential of the methods. The tuning of coefficients, step-size control and of the Krylov process will be the topic of future work.

Acknowledgements

This work was supported by DFG.

4. References

- 1 BURRAGE, K.: Parallel and Sequential Methods for Ordinary Differential Equations, Oxford University Press, 1995
- 2 BYRNE, G.D.: Pragmatic experiments with Krylov methods in the stiff ODE setting, Clarendon Press, Oxford, 323–356, 1992
- 3 HAIRER, E., WANNER, G.: Solving Ordinary Differential Equations I, 2. ed., Springer-Verlag, 1993
- 4 HAIRER, E., WANNER, G.: Solving Ordinary Differential Equations II, 2. ed., Springer-Verlag, 1996
- 5 HOCHBRUCK M., LUBICH C.: Exponential integrators for large systems of differential equations, SIAM J. Sci. Comput., **19** (1998), 1552–1574
- 6 KAPS, P., RENTROP, P.: Generalized Runge-Kutta methods of order four with stepsize control for stiff ordinary differential equations, Numer. Math. **38**, 55–68, 1979
- 7 PODHAISKY, H., SCHMITT, B.A., WEINER, R.: Two-step W-methods with parallel stages, Report of the Inst. of Numerical Mathematics, University of Halle, No. 22, 1999

Addresses: B.A. SCHMITT, Universität Marburg, FB Mathematik, 35032 Marburg, Germany

e-mail: schmitt@mathematik.uni-marburg.de

R. WEINER, H. PODHAISKY, Universität Halle, FB Math./Inf., 06099 Halle, Germany

e-mail: {weiner,podhaisky}@mathematik.uni-halle.de

ADOLPH, T.; SCHÖNAUER, W.

The generation of high quality difference and error formulae of arbitrary order on 3-D unstructured grids

We generate difference and error formulae of arbitrary consistency order on 3-D unstructured grids for the finite difference method. Therefore we have to collect grid points so that we can determine the influence polynomials on which the generation of the formulae is based. The problem is to select the appropriate points so that we receive a well-structured system of equations of the finite difference method and a good error estimate. We present an algorithm for this selection that is controlled by two parameters. The high quality of the formulae is shown by an example.

1. Introduction

We have extended the FDM to arbitrary consistency order on an unstructured FEM grid with reliable error estimate [1, 2]. The corresponding generation of 2-D difference and error formulae has been given in [3]. The present paper describes the generation of the 3-D formulae.

To describe an unstructured FEM grid that is usually generated by a (commercial) mesh generator we have several tables: The coordinates of a grid point i are stored as $coord(i, j)$ where $j = 1, 2, 3$ denotes the x-, y- and z-coordinates. The nodes of an element e are stored as $nek(e, k)$ where $k = 1, \dots, 4$ is the local number of the node of a tetrahedron. From this information we want to generate high quality difference and error formulae of arbitrary consistency order q for each grid point.

2. Principle of the influence polynomials

FDM of order q means local approach of the solution by a 3-D polynomial of order q :

$$P_q(x, y, z) = a_0 + a_1x + a_2y + a_3z + a_4x^2 + a_5xy + a_6xz + \dots + a_{m-2}yz^{q-1} + a_{m-1}z^q \quad (1)$$

This polynomial has $m = (q+1) \cdot (q+2) \cdot (q+3)/6$ coefficients a_0 to a_{m-1} . Therefore we need m grid points to determine these coefficients. The form (1) is not suited for the generation of difference formulae, so in order to get explicit formulae we use the principle of the influence polynomials:

$$P_{q,i}(x, y, z) = \begin{cases} 1 & \text{for } (x_i, y_i, z_i) \\ 0 & \text{for } (x_j, y_j, z_j), j \neq i \end{cases}$$

Then the discretized solution u_d can be represented by

$$u_d := P_q(x, y, z) = \sum_{i=1}^m u(x_i, y_i, z_i) \cdot P_{q,i}(x, y, z) \quad (2)$$

By evaluating the influence polynomials for a grid point $x = x_i, y = y_i, z = z_i$ we get the coefficients of the interpolation polynomial. The coefficients of the corresponding difference formulae we obtain by differentiation of (2), e.g. $u_{x,d} := \partial P_q(x, y, z)/\partial x$, and evaluation at $x = x_i, y = y_i, z = z_i$.

For the determination of the m influence polynomials of a grid point i we use m surrounding grid points:

	influence polynomial	1	2	...	m	
pt.1:	$1 \cdot a_0 + x_1 \cdot a_1 + y_1 \cdot a_2 + z_1 \cdot a_3 + \dots + z_1^q \cdot a_{m-1}$	$= 1$	0	\dots	0	,
2:	$1 \cdot a_0 + x_2 \cdot a_1 + y_2 \cdot a_2 + z_2 \cdot a_3 + \dots + z_2^q \cdot a_{m-1}$	$= 0$	1	\dots	0	,
:		:	:		:	
m:	$1 \cdot a_0 + x_m \cdot a_1 + y_m \cdot a_2 + z_m \cdot a_3 + \dots + z_m^q \cdot a_{m-1}$	$= 0$	0	\dots	1	.

(3)

This can be written as $BX = I$, thus $X = B^{-1}$. The column k of the inverse B^{-1} yields the coefficients of the k -th influence polynomial.

We get the estimate of the discretization error by the difference of two difference formulae, that of control order $q+2$ and that of actual order q , e.g. for u_x we start from the relation $u_x = u_{x,d,q} + \bar{d}_{x,q} = u_{x,d,q+2} + \bar{d}_{x,q+2}$, and by neglecting the exact discretization error for the higher order $\bar{d}_{x,q+2}$ we get the error estimate $d_{x,q} := u_{x,d,q+2} - u_{x,d,q}$. This can be compared to the exact error $\bar{d}_{x,q} = u_x - u_{x,d,q}$. So we see that u_x has been replaced for the estimate by the higher order formula $u_{x,d,q+2}$. This type of error estimate needs an error control: the error must decrease with increasing order.

3. Selection of the m grid points

Now the problem is to select m appropriate surrounding grid points on an unstructured FEM grid, starting from the element list $nek(e, k)$. By indirect addressing we easily generate an inverted list $elem(node, i)$ where for each node the elements for $i = 1, \dots, i_{max}$ that contain this node are listed. We start at the central point of the difference formula and get the elements that contain this node from $elem(node, i)$. Then we get the neighboured nodes from the list $nek(e, k)$, and so we have got the first ring. For the next rings we do the same that we did for the central point for the points of the first ring and so on until we have sufficient grid points for order q . To avoid double counting of grid points we use two logical vectors for each grid point: one for the points found in previous rings and one for the neighbours of the outer ring. By logical composition of these two vectors we obtain the new outer ring.

For the solution of (3) we need m grid points. However, if these grid points do not contain sufficient x , y - and z -information the matrix B becomes singular. Therefore we collect points not only up to order q but up to a higher order $q + \Delta q$ so that we offer $m+r$ grid points to the Gauss-Jordan algorithm instead of only m . How to select the m "best" points on an unstructured grid that are as close as possible to the central point so that we receive a well-structured system of equations of the FDM and a good error estimate? We proceed as follows: 1. We move the central point to the origin and transform the other points to the unit cube. 2. We normalize the matrix B to absolute row sum equal to 1. 3. We prescribe a starting value for a pivot threshold ε_{pivot} . 4. We execute the Gauss-Jordan algorithm with row pivoting. We have subdivided the rows into groups that correspond to the number of points in a ring. Crossing a ring border is permitted only if $|pivot| < \varepsilon_{pivot}$. 5. If we have no success until the end we put $\varepsilon_{pivot} := \varepsilon_{pivot}/\sqrt{10}$ and restart at 4. until $\varepsilon_{pivot} < \varepsilon_{pivot,error} = 1.0 \cdot 10^{-18}$. It turned out that there is a complicated interplay of q , Δq and ε_{pivot} which is the key for the whole solution process of the PDEs.

4. An example

As an example we take a 64000-node unstructured cubic grid $Q_{64000} := [-1, 1] \times [-1, 1] \times [-1, 1]$ ($40 \times 40 \times 40$ nodes) which includes 296595 tetrahedrons. As test solution we take $u = \sin(\frac{\pi}{2} \cdot x) \cdot \cos(\frac{\pi}{2} \cdot y) \cdot \sin(\frac{\pi}{2} \cdot z)$. In Table 1 we present the results of the difference formulae and error estimates compared to the exact values for order $q = 4$, $\Delta q = 6$, $\varepsilon_{pivot} = 0.004$ for a typical grid point. We can see the high quality of the error estimates.

Table 1. Results for a typical grid point.

	derivative	difference formula	exact error	estimated error
u_x	$+ 0.139 \cdot 10^{-2}$	$+ 0.138 \cdot 10^{-2}$	$- 0.848 \cdot 10^{-5}$	$+ 0.610 \cdot 10^{-4}$
u_y	$- 0.149 \cdot 10^1$	$- 0.149 \cdot 10^1$	$- 0.137 \cdot 10^{-4}$	$- 0.148 \cdot 10^{-4}$
u_z	$- 0.396 \cdot 10^{-1}$	$- 0.396 \cdot 10^{-1}$	$+ 0.609 \cdot 10^{-6}$	$- 0.450 \cdot 10^{-5}$
u_{xx}	$- 0.772 \cdot 10^0$	$- 0.771 \cdot 10^0$	$+ 0.315 \cdot 10^{-3}$	$- 0.559 \cdot 10^{-2}$
u_{xy}	$- 0.507 \cdot 10^{-2}$	$- 0.658 \cdot 10^{-2}$	$- 0.151 \cdot 10^{-2}$	$- 0.147 \cdot 10^{-2}$
u_{xz}	$- 0.308 \cdot 10^{-3}$	$- 0.175 \cdot 10^{-3}$	$+ 0.133 \cdot 10^{-3}$	$+ 0.206 \cdot 10^{-3}$
u_{yy}	$- 0.771 \cdot 10^0$	$- 0.771 \cdot 10^0$	$- 0.164 \cdot 10^{-3}$	$- 0.174 \cdot 10^{-3}$
u_{yz}	$+ 0.189 \cdot 10^0$	$+ 0.188 \cdot 10^0$	$- 0.102 \cdot 10^{-2}$	$- 0.990 \cdot 10^{-3}$
u_{zz}	$- 0.772 \cdot 10^0$	$- 0.771 \cdot 10^0$	$+ 0.182 \cdot 10^{-4}$	$- 0.494 \cdot 10^{-4}$

5. References

- SCHÖNAUER, W.; ADOLPH, T.: How WE solve PDEs, to appear in J. of Computational and Applied Mathematics.
- SCHMAUDER, M.; ADOLPH, T.: Development of a black-box solver for nonlinear systems of elliptic and parabolic PDEs, to appear in Proc. ENUMATH'99.
- SCHÖNAUER, W.: Generation of difference and error formulae of arbitrary consistency order on an unstructured grid, in ZAMM 78, Supplement 3, 1998, pp. 1061–1062.

Addresses: TORSTEN ADOLPH, WILLI SCHÖNAUER, Rechenzentrum der Universität Karlsruhe, D-76128 Karlsruhe
E-mail: Torsten.Adolph@rz.uni-karlsruhe.de, schonauer@rz.uni-karlsruhe.de

ANGERMANN, L.; WANG, S.

A Conforming Exponentially Fitted Finite Element Scheme for the Semiconductor Continuity Equations in 3D

The paper presents an exponentially fitted tetrahedral finite element method for the decoupled continuity equations in the drift-diffusion model of semiconductor devices. This finite element method is based on a set of piecewise exponential basis functions constructed on a tetrahedral mesh. Error estimates for the approximate solution and its associated flux are given, where the error bounds depend on some first-order seminorms of the exact solution, the exact flux and the coefficient function of the convection terms.

1. The application of Gummel's [2] and Newton's methods to van Roosbroeck's drift-diffusion model [3] leads to a linear, decoupled system of partial differential equations, where the continuity equations are of the following form:

$$-\nabla \cdot \mathbf{f}(u) + Gu = F \quad \text{in } \Omega \quad (1)$$

$$\mathbf{f}(u) = \nabla u - \mathbf{a}u, \quad (2)$$

$$u|_{\partial\Omega_D} = 0, \quad \mathbf{f}(u) \cdot \mathbf{n}|_{\partial\Omega_N} = 0, \quad (3)$$

where $\Omega \subset \mathbb{R}^3$, $\partial\Omega = \partial\Omega_D \cup \partial\Omega_N$ is the boundary of Ω , $\partial\Omega_D \cap \partial\Omega_N = \emptyset$, $\partial\Omega_D$ is closed as a subset of $\partial\Omega$, and \mathbf{n} denotes the unit outward normal vector on $\partial\Omega$. If ψ denotes the electrostatic potential, the vector-valued function $\mathbf{a} \in (L^\infty(\Omega))^3$ equals $\nabla\psi$ and $-\nabla\psi$ respectively for the electron and hole concentrations, and the flux $\mathbf{f}(u)$ is the electron or hole current density. Furthermore, $G \in L^\infty(\Omega)$, $G \geq 0$ a.e. on Ω and $F \in L^2(\Omega)$.

It is well known that solutions to this kind of problems display sharp boundary layers so that conventional numerical methods often yield solutions with non-physical, spurious oscillations. To overcome this difficulty, several kinds of stabilized methods are used such as the streamline-diffusion method or upwind finite volume schemes. An alternative way of solving this problem is to use exponentially fitted finite element methods. Recently the second author proposed a set of new exponential basis functions and used them to formulate a Bubnov-Galerkin method based on a weighted inner product for the semiconductor device equations [4]. Here we describe an extension to the three-dimensional case.

Let $\{T_h\}_h$ be a regular sequence of meshes of the polyhedral domain Ω , each T_h consisting of tetrahedra having diameters less than or equal to h . Without loss of generality we assume that the (global) nodes of T_h are numbered such that $\{x_i\}_{i=1}^{N'}$ is the set of mesh nodes not on $\partial\Omega_D$.

If t is an arbitrary tetrahedron of a partition T_h with vertices $\{x_k\}_{k=1}^4$ (in a local notation), the nodal basis function $\phi_k : \bar{t} \rightarrow \mathbb{R}$ associated with the vertex x_k is defined as

$$\phi_k(x) = \frac{\lambda_k(x)B(-\mathbf{a}(x) \cdot (x - x_k))}{\sum_{m=1}^4 \lambda_m(x)B(\mathbf{a}(x) \cdot (x - x_m))}, \quad x \in \bar{t}, \quad m \in \{1, 2, 3, 4\},$$

where $\lambda_1(x), \dots, \lambda_4(x)$ denote the barycentric coordinates of $x \in t$ w.r.t. t .

Theorem 1. *Let $t \in T_h$. Then we have*

$$\begin{aligned} \phi_1(x_1) &= 1, & \phi_1(x) &= 0 \quad \forall x \in \Delta_{x_2x_3x_4}, & \phi_1(x) &> 0 \quad \forall x \in t, \\ \phi_1 + \phi_2 + \phi_3 + \phi_4 &= 1 \quad \forall x \in \bar{t}, \end{aligned}$$

where $\Delta_{x_2x_3x_4}$ denotes the triangular surface of t with vertices x_2, x_3 and x_4 .

Combining all the local functions associated with the (global) mesh node x_i we obtain a hat function ϕ_i defined on the union of all the tetrahedra sharing x_i , denoted by Ω_i . From Theorem 1 we see that this ϕ_i is unity at x_i and 0 on $\partial\Omega_i$. It can be shown that ϕ_i is continuous across inter-element boundaries and $\phi_i \in H^1(\Omega_i)$. Finally, we extend this hat function ϕ_i to $\bar{\Omega}$ by defining $\phi_i(x) = 0$ for all $x \in \bar{\Omega} \setminus \bar{\Omega}_i$, so that the resulting function becomes a

basis function defined globally on $\bar{\Omega}$. We remark that, when $\alpha \equiv 0$, the basis function ϕ_i reduces to the standard piecewise linear basis function with the support Ω_i .

We now put $S_h = \text{span}\{\phi_i\}_{i=1}^{N'}$. From the above discussion we see $S_h \subset C^0(\bar{\Omega}) \cap H_D^1(\Omega)$, where $H_D^1(\Omega) = \{v \in H^1(\Omega) : v|_{\partial\Omega_D} = 0\}$. Using the finite element space S_h and introducing the bilinear forms

$$(w, v)_\psi := (e^{-\psi} w, v),$$

$$A_\psi(u, v) := (\nabla u - \alpha u, \nabla v - \alpha v)_\psi + (Gu, v)_\psi,$$

we can formulate the following Bubnov-Galerkin problem:

Find $u_h \in S_h$ such that for all $v \in S_h$

$$A_\psi(u_h, v_h) = (F, v_h)_\psi. \quad (4)$$

It is not difficult to show that this problem has a unique solution.

We now consider the convergence of the finite element solution, where we will use the following weighted norms:

$$\|v\|_{0,\psi} := \sqrt{(v, v)_\psi},$$

$$\|v\|_{1,\psi} := \sqrt{A_\psi(v, v)},$$

$$|f|_{1,\infty,\psi,h} = \left\{ \sum_{t \in T_h} \int_t e^{-\psi} dx |f|_{1,\infty,t}^2 \right\}^{1/2} \quad (\text{seminorm}).$$

Theorem 2. Assume that the electro-static potential ψ is continuous and piecewise linear on the partition T_h of Ω .

Let u be the weak solution of (1) ... (3) and u_h be the solution of (4). Then there exists a constant $C > 0$, independent of h and u , such that

$$\|u - u_h\|_{1,\psi} \leq Ch(|f(u)|_{1,\infty,\psi,h} + \|u\|_{1,\infty}), \quad (5)$$

$$\|f(u) - f(u_h)\|_{0,\psi} \leq Ch(|f(u)|_{1,\infty,\psi,h} + \|u\|_{1,\infty}). \quad (6)$$

Theorem 2 shows that the solution of problem (4) and its associated flux converge to the exact ones with the convergence rate of order $O(h)$. The error bounds depend only on $\|u\|_{1,\infty}$ and the weighted first order seminorms of the exact flux and the coefficient function of the convection term. This is in contrast to the standard piecewise linear finite element method in which the error bound depends on $\|u\|_2$. Unlike most of the previous work the variable used in (5) is the electron or hole concentration rather than one of the Slotboom variables which are physically less interesting.

The method can be used to evaluate the terminal currents. It turns out that the computed terminal currents are convergent and conservative. Details are given in [1].

2. References

- 1 ANGERMANN, L., WANG, S.: An exponentially fitted conforming tetrahedral finite element method for the semiconductor continuity equations, Fakultät für Mathematik, Otto-von-Guericke-Universität Magdeburg, Preprint 10 (1999).
- 2 GUMMEL, H.K.: A Self-Consistent Iterative Scheme for One-Dimensional Steady State Transistor Calculation, IEEE Trans. Elec. Dev. **ED-11** (1964), 455-465.
- 3 VAN ROOSBROECK, W.V.: Theory of Flow of Electrons and Holes in Germanium and Other Semiconductors, Bell Syst. Tech. J., **29** (1950), 560-607.
- 4 WANG, S.: A new exponentially fitted triangular finite element method for the continuity equations in the drift-diffusion model of semiconductor devices, RAIRO Modél. Math. Anal. Numér., **33** (1999), 99-112.

Addresses: PROF. DR. LUTZ ANGERMANN, Institut für Analysis und Numerik, Otto-von-Guericke-Universität Magdeburg, PF 4120, D-39016 Magdeburg, DR. SONG WANG, Department of Mathematics and Statistics, University of Western Australia, Nedlands, Western Australia 6907, Australia.

CHAPKO, ROMAN

On the Numerical Solution of the Hyperbolic Evolution Problem on Closed Curve

We consider an evolution problem for a hyperbolic equation with the Dirichlet to Neumann operator. For the numerical solution we combine the Laguerre transformation with respect to the time variable and the boundary integral equation method. Then an infinite sequence of the integral equations of the second kind with a logarithmic singularity is obtained. The full discretization is realized by Nyström's method which is based on trigonometric quadrature rules.

1. Laguerre transformation and boundary integral equation method

Let $D \subset \mathbb{R}^2$ be a bounded and simply connected domain with the boundary Γ of the class C^2 and let $T > 0$ and $\beta > 0$. Let w be a solution of the Laplace equation $\Delta w = 0$ in D with the Dirichlet boundary condition $w = v$ on Γ . Now we introduce the Dirichlet to Neumann map as $Av = \frac{\partial w}{\partial \nu}$, where ν denotes the outward unit normal to the boundary Γ . We seek the bounded function u that satisfied the following problem

$$\frac{\partial^2 u}{\partial t^2} + (A + \beta I)u = f \quad \text{on } \Gamma \times (0, T], \quad u(\cdot, 0) = w_0, \quad \frac{\partial u}{\partial t}(\cdot, 0) = w_1 \quad \text{on } \Gamma. \quad (1)$$

Here f , w_0 and w_1 are the given functions. In [2] it is shown that for $f \in L^2(\Gamma \times (0, T))$, $w_0 \in H^{\frac{1}{2}}(\Gamma)$ and $w_1 \in L^2(\Gamma)$ the initial value problem (1) has the unique solution $u \in L^\infty(0, T; H^{\frac{1}{2}}(\Gamma)) \cap L^\infty(0, T; L^2(\Gamma))$. We propose for the solution of the problem (1) a combination of the classical Laguerre transformation and the boundary integral equation method. The Laguerre transformation is used for various non-stationary problems (see for example [1,3] and references therein). In this way the solution is expressed as Fourier-Laguerre series

$$u(x, t) = \kappa \sum_{n=0}^{\infty} u_n(x) L_n(\kappa t) \quad \text{with} \quad u_n(x) = \int_0^{\infty} u(x, t) \exp(-\kappa t) L_n(\kappa t) dt,$$

where $\kappa > 0$ is a some fixed parameter.

Theorem 1. *The Fourier-Laguerre series is the solution of the problem (1) if and only if the coefficients u_n satisfy the following system of operator equations*

$$(\gamma^2 I + A)u_n = g_n - \kappa^2 \sum_{m=0}^{n-1} \beta_{n-m} u_m \quad \text{on } \Gamma \quad (2)$$

for $n = 0, 1, \dots$ and where $\beta_n = n + 1$, $\gamma^2 = \kappa^2 + \beta$, $g_n = f_n + w_1 + \kappa(n + 1)w_0$ and $f_n(x) = \int_0^{\infty} f(x, t) \exp(-\kappa t) L_n(\kappa t) dt$.

Clearly, that the solution of the Dirichlet boundary value problem for the Laplace equation has an integral representation in the form of a single layer potential

$$U(x) = \frac{1}{2\pi} \int_{\Gamma} \mu(y) \Phi(x, y) ds(y).$$

Here $\Phi(x, y) = \ln|x - y|^{-1}$ is the fundamental solution and $\mu \in C(\Gamma)$ is the unknown density. Then from the properties of this potential [4] we have the following integral representation for the operator A

$$(Av)(x) = \frac{1}{2} \mu(x) + \frac{1}{2\pi} \int_{\Gamma} \mu(y) \frac{\partial}{\partial \nu(y)} \Phi(x, y) ds(y).$$

Thus the system of operator equation (2) equals to the system of integral equations of the second kind

$$\frac{1}{2} \mu_n(x) + \frac{1}{2\pi} \int_{\Gamma} \mu_n(y) [\gamma^2 \Phi(x, y) + \frac{\partial \Phi}{\partial \nu(x)}(x, y)] ds(y) = g_n(x) - \frac{\kappa^2}{2\pi} \sum_{m=0}^{n-1} \beta_{n-m} \int_{\Gamma} \mu_m(y) \Phi(x, y) ds(y), \quad (3)$$

where $x \in \Gamma$. By Riesz–Fredholm theory we can prove the well-posedness of integral equations (3) in $L^2(\Gamma)$.

2. Nyström method

We assume that the boundary curve Γ is given through a regular parametric representation $\Gamma = \{x(s) : 0 \leq s \leq 2\pi\}$. Then we transform (3) into the parametric form

$$q_n(s) + \frac{1}{2\pi} \int_0^{2\pi} q_n(\sigma) \{K_1(s, \sigma) - \gamma^2 [|x'(\sigma)| \ln \left(4 \sin^2 \frac{s-\sigma}{2} \right) - K_2(s, \sigma)]\} d\sigma = G_n(s), \quad 0 \leq s \leq 2\pi \quad (4)$$

with the right-hand sides

$$G_n(s) = 2g_n(x(s)) + \frac{\kappa^2}{2\pi} \sum_{m=0}^{n-1} \beta_{n-m} \int_0^{2\pi} q_m(\sigma) [|x'(\sigma)| \ln \left(4 \sin^2 \frac{s-\sigma}{2} \right) - K_2(s, \sigma)] d\sigma \quad (5)$$

for $n = 0, 1, 2, \dots$. Here $q_n(s) = \mu_n(x(s))$ and the kernels K_1 and K_2 have the form

$$K_1(s, \sigma) = 2|x'(\sigma)| \frac{(x(s) - x(\sigma)) \cdot \nu(x(s))}{|x(s) - x(\sigma)|^2} \quad \text{and} \quad K_2(s, \sigma) = |x'(\sigma)| \ln \frac{4 \sin^2 \frac{s-\sigma}{2}}{|x(s) - x(\sigma)|^2}.$$

Clearly, the smoothness of these kernels depends on the smoothness of the boundary Γ . Now using the trigonometric quadrature formulas for 2π -periodic functions [4] together with the collocation at the nodal points $s_k = k\pi/M$, $k = 0, \dots, 2M-1$, $M \in \mathbb{N}$ we get the following sequence of the system of linear equations

$$q_{n,k} + \sum_{i=0}^{2M-1} q_{n,i} \left\{ \gamma^2 \left[-|x'(s_i)| R_i(s_k) + \frac{1}{2M} K_2(s_k, s_i) \right] + \frac{1}{2M} K_1(s_k, s_i) \right\} = G_{n,M}(s_k),$$

where

$$G_{n,M}(s_k) = 2g_n(x(s_k)) - \kappa^2 \sum_{m=0}^{n-1} \beta_{n-m} \sum_{i=0}^{2M-1} q_{m,i} \left[-|x'(s_i)| R_i(s_k) + \frac{1}{2M} K_2(s_k, s_i) \right],$$

$k = 0, 1, \dots, 2M-1$, $n = 0, 1, \dots$ and R_k are the weight functions of the quadrature rule for the integral with logarithmic singularity. For a more detailed description of this Nyström method and an error and convergence analysis based on the theory of collectively compact operators we refer to [4]. The error analysis in a Sobolev space setting (see [4,5]) implies the following result for the numerical solution $\tilde{q}_{n,M}$ of (4).

Theorem 2. *Let Γ be analytic, the initial functions w_0, w_1 and the function f (with respect to the space variable) are $(p+1)$ -times continuously differentiable. Then $\|q_n - \tilde{q}_{n,M}\|_{\infty, \Gamma} \leq C_n M^{-p}$ with some constant $C_n > 0$.*

Thus the approximate solution of the hyperbolic initial value problem (1) has the following form

$$u_{N,M}(x(s), t) = \frac{\kappa}{2M} \sum_{n=0}^N \sum_{k=0}^{2M-1} q_{n,k} \left[-|x'(s_k)| R_k(s) + \frac{1}{2M} K_2(s, s_k) \right] L_n(\kappa t).$$

The numerical experiments show the fast convergence with respect to the number M of quadrature points for the numerical solution according to the theorem 2.

3. References

- 1 CHAPKO, R., KRESS, R.: On the numerical solution of initial boundary value problems by the Laguerre transformation and boundary integral equations; In: *Integral and Integro-differential Equations: Theory, Methods and Applications*. Series in Mathematical Analysis and Applications. Vol.2. (Agarwal, O'Regan eds.). Cordon and Breach Science Publishers. Amsterdam (2000), 55–69.
- 2 DAUTRAY, R., LIONS, J.-L.: *Mathematical Analysis and Numerical Methods for Science and Technologie*; Vol.1. Physical Origins and Classical Methods. Springer-Verlag, Berlin Heidelberg New York Berlin 1990.
- 3 GALAZYUK, V., CHAPKO, R.: The Chebyshev–Laguerre transformation and integral equations methods for initial boundary value problems for the telegraph equation; *Dokl. Akad. Nauk UkrSSR*. 8 (1990), 11–14 (in Russian).
- 4 KRESS, R.: *Linear Integral Equations*; 2nd. ed. Springer-Verlag, Berlin Heidelberg New York 1999.
- 5 KRESS, R., SLOAN, I.H.: On the numerical solution of a logarithmic integral equation of the first kind for the Helmholtz equation; *Numer. Math.* 66 (1993), 199–214.

Address: DR. ROMAN CHAPKO, Department of Applied Mathematics and Computer Science,
Lviv National University, 79000 Lviv, Ukraine

FISCHER, B., LUDWIG, M. AND MEISTER, A.

A finite volume method to compute the steady state temperature distribution in premature or newborn infants

A mathematical model is developed and used for a computer simulation of the thermoregulation of premature infants. We propose a finite volume technique for the solution of the associated partial differential equation on an unstructured grid. Emphasis is laid on the model and the validation of the numerical scheme. Beside various test runs using real life data, we present a discrete maximum principle for the steady state solution with respect to the non-convex computational domain. Keywords: Finite volume method, Thermoregulation, Maximum principle.

1. Governing Equation

We consider the integral form of the bio-heat equation (given in [1])

$$\frac{d}{dt} \int_{\sigma} T(\mathbf{x}, t) d\mathbf{x} = \int_{\partial\sigma} \lambda(\mathbf{x}) \nabla T^T(\mathbf{x}, t) \mathbf{n}(\mathbf{x}) ds + \int_{\sigma} f(\mathbf{x}, t) d\mathbf{x} \quad (1)$$

for all control volumes $\sigma \subset D$, where $T(\mathbf{x}, t)$ describes the temperature distribution in a two dimensional geometry $D \subset \mathbb{R}^2$ for the infant. Here, $\lambda(\mathbf{x})$ denotes the heat conductivity of the tissue. The source term is given by $f(\mathbf{x}, t) = Q_M(\mathbf{x}) + Q_B(\mathbf{x}, t)$, where Q_M is the rate of metabolic heat production and Q_B represents the heat transfer within the body due to the bloodstream. Actually, we are only interested in the steady state solution. To solve the integral equation (1) numerically, we supplement it by initial and Dirichlet boundary conditions.

2. Finite Volume Approximation

In order to solve equation (1) numerically by means of a finite volume method, we use a conforming triangulation of the domain \bar{D} as a primary grid (see [4]); the secondary mesh \mathcal{B}^h constructed hereupon is of box-type (see [3]).

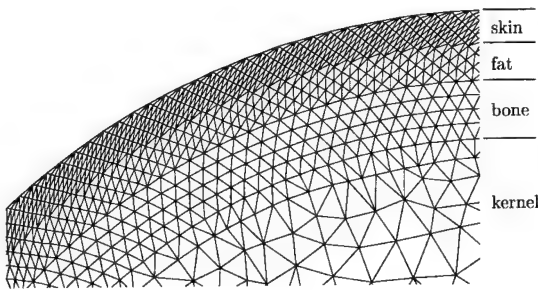


Figure 1: Tissue layers in the head region

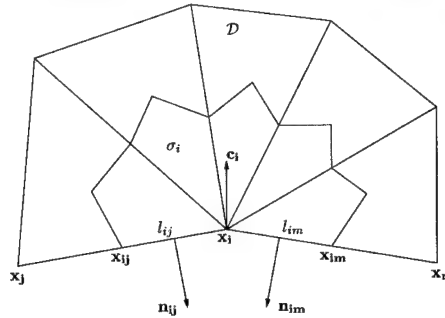


Figure 2: Boundary control volume

A finite volume method represents a discretization of the integral equation (1) for cell averages which are defined by means of the cell average operator $(\mathcal{M}_h T)(t)|_{\sigma} := \frac{1}{|\sigma|} \int_{\sigma} T(\mathbf{x}, t) d\mathbf{x}$, where $|\sigma|$ denotes the volume of the box σ . With regard to the secondary mesh \mathcal{B}^h we can rewrite the integral form of the heat equation as

$$\frac{d}{dt} (\mathcal{M}_h T)(t)|_{\sigma_i} = \int_{\partial\sigma_i} \lambda(\mathbf{x}) \nabla T^T(\mathbf{x}, t) \mathbf{n}(\mathbf{x}) ds + \int_{\sigma_i} f(\mathbf{x}, t) d\mathbf{x}, \quad \forall \sigma_i \in \mathcal{B}^h.$$

Taking account of the secondary mesh \mathcal{B}^h and using a unique linear distribution of T as well as the mean value of the heat coefficient λ_D on each triangle D of the primary grid lead directly to the formulation of a numerical flux function $H_{\nu}(T_i(t), T_j(t), T_m(t); \mathbf{n}_{ij}^k) = \lambda_D \nabla T_D^T(t) \mathbf{n}_{ij}^k$. Consequently, for each inner control volume we obtain

$$\int_{\partial\sigma_i} \lambda(\mathbf{x}) \nabla T^T(\mathbf{x}, t) \mathbf{n}(\mathbf{x}) ds = \frac{1}{|\sigma_i|} \sum_{j \in N(i)} \sum_{k=1}^2 H_{\nu}(T_i(t), T_j(t), T_m(t); \mathbf{n}_{ij}^k) |l_{ij}^k|.$$

A numerical approximation of the remaining boundary integral is required in order to ensure a discrete maximum principle in our numerical framework. Utilizing the notation introduced within figure 2 we define as an extended barycentre $\mathbf{c}_i = \mathbf{x}_i - \frac{\sqrt{3}\rho_i}{4\|\mathbf{n}_{ij} + \mathbf{n}_{im}\|_2} (\mathbf{n}_{ij} + \mathbf{n}_{im})$, with a certain weight ρ_i . Hence we get for the remaining boundary integral

$$\int_{\partial\sigma_i \cap \partial D} \lambda(\mathbf{x}) \nabla T^T(\mathbf{x}, t) \mathbf{n}(\mathbf{x}) ds = \sum_{\ell \in \{j, m\}} H_{\nu}(T_i(t), T_{i, \partial D}(\mathbf{x}_i), T_{i, \partial D}(\mathbf{x}_{i\ell}); \mathbf{n}_{i\ell}) |l_{i\ell}|,$$

A simple approximation of the source term yields $\frac{1}{|\sigma_i|} \int_{\sigma_i} f(\mathbf{x}, t) d\mathbf{x} = Q_M(\mathbf{x}_i) + Q_B(\mathbf{x}_i, t)$. We integrate the integral

form of the equation (1) from the time level t^n to the time level $t^{n+1} = t^n + \Delta t$. In order to use larger time steps we choose an implicit time discretization for the viscous part and an explicit approach for the source term. Thus we have to solve a linear system $\mathbf{A}\Delta\mathbf{T} = \mathbf{b}$, $\Delta\mathbf{T} = (\Delta T_1, \dots, \Delta T_N)^T$ where the matrix \mathbf{A} is large and sparse and the right hand side \mathbf{b} contains the explicit fluxes and source terms.

The following theorem and corollary show that the steady state solution achieved by the developed numerical method satisfies a discrete maximum principle if the source terms are neglected. The proofs are given in [2].

Theorem If our finite volume method has reached a steady state $\Delta\mathbf{T} = (\Delta T_1, \dots, \Delta T_N)^T = \mathbf{0}$ and if there is a control volume where a global maximum of the temperature is located, then the discrete temperature distribution is constant in \bar{D} .

Corollary If the finite volume method yields $\Delta\mathbf{T} = \mathbf{0}$, then the global minimum and maximum of the discrete temperature distribution are attained on the boundary ∂D .

3. Numerical Results

In this section we present some typical numerical results for the two-dimensional model. As remarked above, we employ an implicit time-marching procedure to reach the steady state solution. For the solution of the linear system we employ the BiCGSTAB method preconditioned by an incomplete LU-factorization. We present two test cases. They differ in the choice of the Dirichlet boundary conditions. Test case 1 was designed to reproduce the temperature distribution with respect to normal environmental conditions. In contrast, test case 2 models the attempt to lower the cerebral temperature by cooling the head. In the following figures the obtained temperature distributions are visualized. To verify the discrete maximum principle, stated in Theorem, we first treat test case 1 without any heat production or blood-flow, i.e., $f(\mathbf{x}, t) = 0$. As it is apparent from the top image in figure 3, the maximal and minimal temperature occurs at the boundary of D , as predicted by our theory.

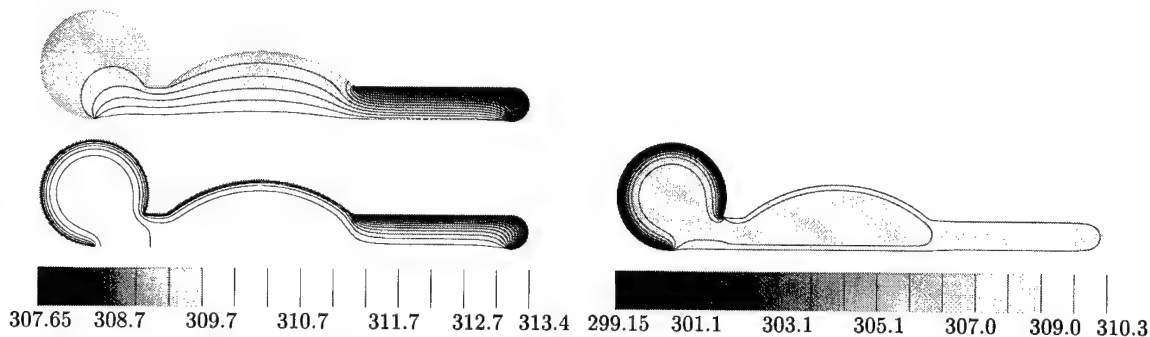


Figure 3: Temperature distribution for the test case 1 with $f = 0$ in the top figure.

Figure 4: Temperature distribution for the test case 2

Regarding temperature distributions with heat production and blood-flow, depicted in the bottom part of figure 3, we observe that our model resembles nicely the expected temperature distribution with respect to normal environmental conditions. Most interestingly, figure 4 shows that a selective cooling of the head only affects the skin of the head, a result, which triggered a controversy discussion within the medical community. It is worth noticing that recently Bußmann [1] obtained similar results in his computations.

4. Literatur

- 1 BUSSMANN, O.: *Modell der Thermoregulation des Früh- und Neugeborenen unter Einbeziehung der thermischen Reife*. Dissertation, Institute of Biomedical Engineering, Medical University of Lübeck, 2000.
- 2 FISCHER, B., LUDWIG, M. AND MEISTER, A.: An application of the finite volume method to the thermoregulation of infants. *Hamburger Beiträge zur Angewandten Mathematik, Reihe F, CFD and Data Analysis* 12, 2000.
- 3 FRIEDRICH, O.: A new method for generating inner points of triangulations in two dimensions. *Comp. Meth. Appl. Mech. and Eng.*, 104: 77–86, 1993.
- 4 SONAR, TH.: On the Construction of Essentially Non-Oscillatory Finite Volume Approximations to Hyperbolic Conservation Laws on General Trinagulations: Polynomial Recovery, Accuracy, and Stencil Selection. *Comp. Meth. Appl. Mech. Eng.*, 140: 157–181, 1997.

Adresse: PROF. DR. B. FISCHER, Institut für Mathematik, Medizinische Universität zu Lübeck.

DR. A. MEISTER, DIPL.-MATH. M. LUDWIG, Fachbereich Mathematik, Universität Hamburg.

FRÖHNER, A.; LINSS, T.; ROOS, H.-G.

The ε -Uniform Convergence of a Defect-Correction Method on a Shishkin Mesh

A defect correction method based on finite difference schemes is considered for a singularly perturbed boundary value problem on a Shishkin mesh. The method combines the stability of the upwind difference scheme and the higher-order accuracy of the central difference scheme. The almost second-order convergence of the scheme with respect to the discrete maximum norm, uniformly in the perturbation parameter ε , is proved. Numerical experiments support the theoretical results.

1. Foundation

We consider the model singularly perturbed linear convection-diffusion problem

$$Lu := -\varepsilon u'' - (b(x)u)' = f(x), \quad x \in (0, 1), \quad u(0) = u(1) = 0, \quad (1)$$

where $\varepsilon > 0$ is a small parameter, $b(x) \geq \beta > 0$ for all $x \in [0, 1]$ and f and b are sufficiently smooth functions. The solution u of (1) exhibits an exponential boundary layer at $x = 0$. The following estimate gives an useful bound for the solution u and its derivatives

$$|u^{(k)}(x)| \leq C \left(1 + \varepsilon^{-k} e^{-\beta x/\varepsilon} \right).$$

To solve differential equations with (boundary) layers approximately it is appropriate to use a priori chosen layer-adapted meshes. Our considerations are done on a piecewise uniform mesh as Shishkin introduced in the early 1990s. The mesh is generated as follows: one chooses a transition point $\lambda = \min(\frac{1}{2}, \frac{\lambda_0 \varepsilon}{\beta} \ln N)$ and places $N/2$ meshpoints in both $[0, \lambda]$ and $[\lambda, 1]$. Thus one has a very fine mesh with stepsize $h = O(\varepsilon N^{-1} \ln N)$ in the layer region and a relatively coarse mesh with stepsize $H = O(N^{-1})$ outside. All considerations made in the sequel can be extended to more general layer-adapted meshes as recently introduced by Linß and Roos [1]

Let us introduce some notation:

$$h_i = x_i - x_{i-1}, \quad \bar{h}_i = \frac{x_{i+1} - x_{i-1}}{2}, \quad \bar{f}_i = \frac{f_{i+1/2} + f_{i-1/2}}{2}, \quad [D^+ v]_i = \frac{v_{i+1} - v_i}{h_{i+1}}, \quad [D^o v]_i = \frac{v_{i+1} - v_{i-1}}{2h_i}.$$

We define the upwind difference scheme according to (1) to be

$$[L^u u^u]_i = -\frac{\varepsilon}{h_i} ([D^+ u^u]_i - [D^+ u^u]_{i-1}) - \frac{h_{i+1}}{\bar{h}_i} [D^+ (b u^u)]_i.$$

This scheme is stable but at best first-order convergent in the discrete maximum norm, with a convergence constant that is independent of ε , on a layer-adapted grid [3]. Furthermore we define the central difference scheme

$$[L^c u^c]_i = -\frac{\varepsilon}{\bar{h}_i} ([D^+ u^c]_i - [D^+ u^c]_{i-1}) - [D^o (b u^c)]_i$$

which is formally second order convergent but causes unphysical oscillations in domains where ε is small compared to the local step size.

2. Defect Correction Scheme

In the 1980s Hemker [2] proposed combining the advantages of both upwind and central difference methods — stability and higher-order accuracy — by means of a defect correction technique. In [4] the authors presented the probably first proof of a ε -uniform convergence of such a method for a model problem with constant coefficients. The defect correction scheme we investigate is:

$$\begin{array}{ll} \text{initial step:} & [L^u u^u]_i = f_i, \quad u_0^u = u_N^u = 0, \\ \text{defect:} & \tau_i = \bar{f}_i - [L^c u^u]_i \\ \text{correction:} & L^u \delta_i = \tau_i \\ & u^{dc} = u^u + \delta \end{array} \quad \Longleftrightarrow \quad \begin{array}{ll} [L^u u^u]_i = f_i, & u_0^u = u_N^u = 0, \\ [L^u u^{dc}]_i = \bar{f}_i + [(L^u - L^c) u^u]_i \end{array}$$

For this scheme we can prove the following convergence result in the discrete maximum norm $\|\cdot\|_\infty$:

Theorem Let $\lambda_0 \geq 2$. Then the error $\eta^{dc} := u^{dc} - u$ of the defect correction method satisfies

$$\|\eta^{dc}\|_\infty \leq C(N^{-1} \ln N)^2.$$

In the sequel we will point out the main ingredients of the proof: The consistency error of that scheme divides into two characteristic parts

$$L^u(u^{dc} - u) = ((L^u - L^c)(u^u - u)) + (\bar{f} - L^c u), \quad (2)$$

wherein the second addend represents the consistency error of the central difference scheme. The first addend is called the relative consistency error and extends to

$$[(L^u - L^c)(\eta^u)]_i = -\frac{(b\eta^u)_{i+1} - 2(b\eta^u)_i + (b\eta^u)_{i-1}}{2h_i},$$

wherein $\eta^u = u^u - u$. Classically, such higher order differences are analyzed by means of asymptotic error expansions. That turns out to be inappropriate for layer problems. Instead our convergence analysis is mainly based on the following stability property of L^u established by Andreyev and Kopteva [3]

$$\|v_i\|_\infty \leq \frac{2}{\beta} \left\| \sum_{j=1}^{N-1} h_j [L^u v]_j \right\| \text{ if } v_0 = v_N = 0.$$

Applying this inequality to (2) we estimate

$$\|\eta^{dc}\|_\infty \leq C(h\|\eta^u\|_\infty + \max_{i=1,\dots,N-1} h_{i+1} [D^+ \eta^u]_i + \left\| \sum_{j=1}^{N-1} h_j [\bar{f} - L^c u]_j \right\|).$$

All three terms can be bounded by $(N^{-1} \ln N)^2$ – as one shows in quite longish computations, see [5].

3. Numerical Results

We consider the test problem $-\varepsilon u''(x) + (1+x(1-x))u'(x) = f(x)$, $u(0) = u(1) = 0$, where the right hand side f is such that $u(x) = \frac{1-e^{(1-x)/\varepsilon}}{1-e^{-1/\varepsilon}} - \cos \frac{\pi}{2}x$. The numerical results are calculated using the perturbation parameter $\varepsilon = 10^{-8}$ and the grid parameter $\lambda_0 = \frac{1}{\beta}$

	coarse mesh		fine mesh	
N	max. error	conv. rate	max. error	conv. rate
256	8.7283e-05	2.0982	0.0003358	1.7316
512	2.0878e-05	2.0637	0.00010084	1.7355
1024	5.0784e-06	2.0396	2.9984e-05	1.7498
2048	1.2486e-06	2.024	8.6918e-06	1.7864

4. References

- 1 ROOS, H.-G., LINSS, T.: Sufficient conditions for uniform convergence on layer-adapted grids. Computing **63** (1999), 27–45
- 2 HEMKER, P.W.: The use of defect correction for the solution of a singularly perturbed o.d.e.. Report 139/82, afdeling numerieke wiskunde, Mathematisch Centrum Amsterdam (1982)
- 3 ANDREYEV, V.B., KOPTEVA, N.V.: Uniform with respect to a small parameter convergence of difference schemes for a convection-diffusion problem. Proceedings of the Workshop on the Analytical Solution and Computational Methods for Convection-Dominated and Singular Perturbed Problems, Lozenets, Bulgaria, August 1998
- 4 FRÖHNER, A., ROOS, H.-G.: The ε -uniform convergence of a defect-correction method on a Shishkin mesh. Appl. Num. Math., to appear
- 5 FRÖHNER, A., LINSS, T., ROOS, H.-G.: Defect correction on Shishkin-type meshes. in preparation

Addresses: DIPL.-MATH. ANJA FRÖHNER, DR. TORSTEN LINSS, PROF. DR. HANS-GÖRG ROOS, Institut für Numerische Mathematik, Technische Universität Dresden, D-01062 Dresden

H. HASCHKE, W. HEINRICHS

Splitting techniques for the Navier-Stokes equations

A pseudo spectral approximation for the Navier-Stokes equations is presented. After considering the unsteady Stokes equations we use the Uzawa algorithm to decouple the spectral system into Helmholtz equations for the velocity components and an equation with the Pseudo-Laplacian for the pressure. In order to avoid spurious modes the pressure is approximated with polynomials of one degree lower than the velocity on staggered grids. For the time discretization a high order backward differentiation scheme for the intermediate velocity is combined with a high order extrapolant for the pressure.

1. Time splitting scheme

We consider the unsteady Stokes equations

$$\frac{\partial u}{\partial t} - \nabla^2 u + \nabla p = f \text{ in } \Omega = (-1, 1)^2, \quad \nabla \cdot u = 0 \text{ in } \Omega, \quad u = 0 \text{ on } \partial\Omega, \quad (1)$$

where $u = (u_1, u_2)^t$ denotes the velocity and p the pressure. $f : \Omega \rightarrow \mathbb{R}^2$ is a given force. We impose the average pressure to be zero, i.e. $\int_{\Omega} p dx = 0$, as the pressure is only determined up to a constant. The BDF (see [2]) time discretization of (1) leads to the following scheme:

$$L_{t,k}^n u^{n+1} - \nabla^2 u^{n+1} + \nabla p^{n+1} = f^{n+1} \text{ in } \Omega, \quad \nabla \cdot u^{n+1} = 0 \text{ in } \Omega, \quad u^{n+1} = 0 \text{ on } \partial\Omega, \quad (2)$$

where Δt denotes the step size in t and the index $n+1$ indicates that the functions are evaluated at the time step $t_{n+1} = (n+1) \cdot \Delta t$. $L_{t,k}^n$ represents the backward differentiation scheme for the approximation of $\frac{\partial}{\partial t}$ and k is the order of the scheme. $L_{t,k}^n$ with suitable β_m can be written as: $L_{t,k}^n u^{n+1} = \frac{1}{\Delta t} \sum_{m=0}^k \beta_m u^{n+1-m}$.

To minimize the computational cost we introduce the following splitting scheme which was proposed by Maday, Patera and Rønquist [4]. We obtain:

$$L_{t,k}^n \tilde{u}^{n+1} - \nabla^2 \tilde{u}^{n+1} + \nabla \tilde{p}_l^{n+1} = f^{n+1} \text{ in } \Omega, \quad \tilde{u}^{n+1} = 0 \text{ on } \partial\Omega, \quad (3)$$

and

$$\beta_0 \frac{u^{n+1} - \tilde{u}^{n+1}}{\Delta t} + \nabla(p^{n+1} - \tilde{p}_l^{n+1}) = 0 \text{ in } \Omega, \quad \nabla \cdot u^{n+1} = 0 \text{ in } \Omega, \quad u^{n+1} \cdot \nu = 0 \text{ on } \partial\Omega. \quad (4)$$

Here ν denotes the outer unit normal, \tilde{u}^{n+1} an intermediate velocity and \tilde{p}_l^{n+1} an extrapolant for the pressure obtained from the previous l time steps. Obviously the order of convergence depends on the order k of the backward differentiation scheme and on the order l of the extrapolation where $\tilde{p}_l^{n+1} = \sum_{m=0}^{l-1} \gamma_m p^{n-m}$, with suitable coefficients γ_m , $m = 0, \dots, l-1$. Let $\tilde{f}^{n+1} = f^{n+1} - \frac{1}{\Delta t} \sum_{m=1}^k \beta_m u^{n+1-m} - \nabla \tilde{p}_l^{n+1}$. (3) is equivalent to the following Helmholtz problem:

$$\left(-\nabla^2 + \beta_0 \frac{1}{\Delta t} I \right) \tilde{u}^{n+1} = \tilde{f}^{n+1} \text{ in } \Omega, \quad \tilde{u}^{n+1} = 0 \text{ on } \partial\Omega. \quad (5)$$

The system (4) corresponds to:

$$\beta_0 \frac{1}{\Delta t} u^{n+1} + \nabla p^{n+1} = g^{n+1} \text{ in } \Omega, \quad \nabla \cdot u^{n+1} = 0 \text{ in } \Omega, \quad u^{n+1} \cdot \nu = 0 \text{ on } \partial\Omega, \quad (6)$$

where $g^{n+1} = \beta_0 \frac{1}{\Delta t} \tilde{u}^{n+1} + \nabla \tilde{p}_l^{n+1}$. By applying the divergence to the first equations of (6) and further using the

divergence-free condition (Uzawa decoupling) we finally obtain:

$$Bp^{n+1} = \nabla \cdot g^{n+1}. \quad (7)$$

The operator $B \in \mathbb{R}^{N^2, N^2}$ is called the *Pseudo-Laplacian* or *energy*. For the approximation we apply staggered grids where the velocity is defined at the Gauss-Lobatto nodes $(x_i, y_j) = (\cos \frac{i\pi}{N}, \cos \frac{j\pi}{N})$, $i, j = 0, \dots, N$, while the pressure is evaluated at the Gauss nodes $(z_i, w_j) = (\cos \frac{(2i-1)\pi}{2N}, \cos \frac{(2j-1)\pi}{2N})$, $i, j = 1, \dots, N$. We use the pseudo spectral Chebyshev discretization which can be found in [6]. In [3] we proved that the eigenvalues of the spectral Pseudo-Laplacian are real and negative. There we also present suitable preconditioners and we numerically show that a stable second order method in time for the velocity and at least first order for the pressure can be achieved.

2. The Navier-Stokes equations

We consider the unsteady Navier-Stokes equations for incompressible flows in velocity-pressure formulation:

$$\frac{\partial u}{\partial t} - \frac{1}{RE} \nabla^2 u + \nabla p + (u \cdot \nabla)u = f \quad \text{in } \Omega =]-1, 1[^2, \quad \nabla \cdot u = 0 \quad \text{in } \Omega =]-1, 1[^2, \quad (8)$$

$$u = h \quad \text{on } \partial\Omega, \quad u = u_0 \quad \text{for } t = 0, \quad \text{in } \Omega =]-1, 1[^2. \quad (9)$$

For the approximation of the convective term we use the Adams-Bashforth scheme of second order. So we can subtract this term from the right hand side and we are able to transfer our splitting to (8) - (9). We consider the driven-cavity problem with the following boundary conditions on the domain $\Omega = [0, 1]^2$: $u_1(\cdot, 1) = -1$, $u = 0$ else. The difficulty in the solution of this problem is the presence of singularities at the corners. At the two upper corners pressure and vorticity are not finite while at the two lower corners the singularities are much weaker since only the second derivative is unbounded. Therefore we have neglected these singularities. For the determination of u and p at the two upper corners we introduce the steady-state streamfunction ψ (such that $u_1 = \frac{\partial \psi}{\partial y}$, $u_2 = -\frac{\partial \psi}{\partial x}$) and we consider a local coordinate system $x = x_s + r \cdot \cos(\theta)$, $y = y_s + r \cdot \sin(\theta)$ (s belongs to the two upper corners). Then we yield the following asymptotic expansion in the neighbourhood of the singularity point (see [5]): $\psi^s = r f_1^s(\theta) + r^2 f_2^s(\theta, RE)$. The functions f_1^s and f_2^s are given in [1], along with the corresponding expression of the velocity and pressure. Then we have $u = \tilde{u} + \bar{u}$, $p = \tilde{p} + \bar{p}$, where \tilde{u} and \tilde{p} consist of the corresponding singular parts belonging to the two upper corners. Subtracting the terms with (\tilde{u}, \tilde{p}) from the right hand side of our system, we only have to solve the equations for the remaining smooth parts (\bar{u}, \bar{p}) . For the center of the cavity we obtain the following results shown in table 1. The corresponding values for the $N, N-2$ -method are given in [1]. A comparison between these two methods at the point $(0, 0.95)$ near the singularity is given in table 2.

Table 1: Comparison of the vorticity at the center of the cavity at $RE = 100$

N	stagg. grids	$N, N-2$ -method
16	1.17201	1.17351
24	1.17405	1.17438
32	1.17432	1.17441
48	1.17438	1.17441

Table 2: Convergence of the vorticity values at the point $(0, 0.95)$ near the upper left corner for $RE = 100$

N	stagg. grids	$N, N-2$ -method
16	-36.40664	-36.61642
24	-35.98513	-35.88211
32	-36.09436	-36.13314
48	-36.08085	-36.08094

3. References

- 1 O. BOTELLA, R. PEYRET, Benchmark Spectral Results on the Lid-Driven Cavity Flow, to appear in Computer & Fluids
- 2 P. DEUFLHARD AND F. BORNEMANN: Numerische Mathematik II, De Gruyter, Berlin, 1994
- 3 H. HASCHKE, W. HEINRICHS, Splitting techniques with staggered grids for the Navier-Stokes equations in the 2d case, submitted for publication
- 4 Y. MADAY, A.T. PATERA, E. RÖNQVIST: An operator-integration-factor splitting method for time-dependent problems: application to incompressible fluid flow, J. Sci. Comput., 5, 263-292, 1990
- 5 H.K. MOFFATT, Viscous and Resistive Eddies near a Sharp Corner, Journal of Fluid Mechanics, 18, 1-18, 1964
- 6 A. QUARTERONI, A. VALLI, Numerical Approximation of Partial Differential Equations, Springer-Verlag, Berlin, 1994

Addresses: HEIKE HASCHKE, WILHELM HEINRICHS, Universität GH Essen, Ingenieurmathematik, D-45141 Essen, Germany.

HEINRICHS, W. LOCH, B.

Spectral Schemes on Triangular Elements

First we consider the Poisson Problem with homogeneous Dirichlet boundary conditions on a triangle. The mapping between square and triangle is realized by mapping an edge of the square onto a corner of the triangle. Then standard Chebyshev collocation techniques can be applied. Numerical experiments demonstrate the expected high spectral accuracy. Further, it is shown that finite difference preconditioning can be successfully applied in order to construct an efficient iterative solver. Finally, a domain decomposition technique is applied to the patching of rectangular and triangular elements.

1. Introduction

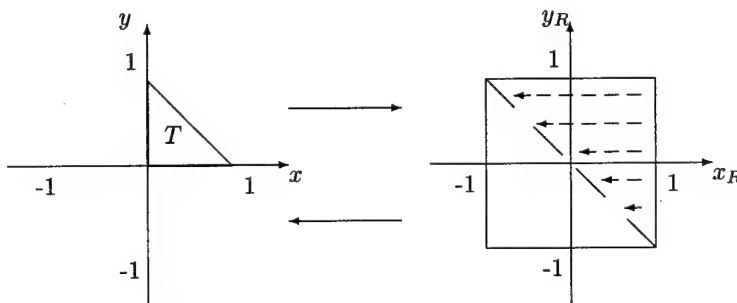
Pseudospectral collocation methods give good approximations to smooth solutions of elliptic partial differential equations. However, there is a huge disadvantage as these methods are confined to rectangles. Our aim is to find a suitable transformation between the standard square and the standard right triangle such that we can then apply spectral methods to (right) triangles, too. We present the numerical results received with our transformation for the Poisson problem as well as for domain decomposition problems and compare our results to those obtained in [3].

2. Transformation of the right triangle

The standard Chebyshev collocation scheme is defined for non-equally spaced Chebyshev-Gauss-Lobatto nodes $(s_i, t_j) = (\cos(\frac{i\pi}{N}), \cos(\frac{j\pi}{N}))$ on the square $[-1, 1]^2$. As we are interested in triangular domains we introduce the following transformation (see [4])

$$x = \frac{1}{4}(x_R + 1)(1 - y_R), \quad y = \frac{1}{2}(y_R + 1).$$

This transformation maps the right edge of a square onto the third edge of a triangle shifting all points to the left. It is no longer injective which however does not disturb the accuracy.



3. The Poisson Problem

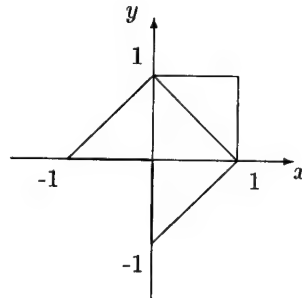
Numerous spectral algorithms for the numerical simulation of physical phenomena demand the approximative solution of one or more Poisson problems in a bounded domain. We consider the Poisson problem $\Delta u = f$ with homogeneous Dirichlet boundary conditions on our triangle. We apply the standard Chebyshev collocation scheme to a smooth exact solution and receive high exponential decay of the error. Our results are even better than those obtained in [3] using polar coordinate transformation. Next we consider a piecewise constant, discontinuous right hand side f . As expected, the error along the line of discontinuity is extremely large.

We are interested in a good condition number of our spectral operator which does not increase too fast such that efficient iterative solvers can be found. In this case, the maximum eigenvalue of the spectral Laplacian on the triangle scales as $O(N^8)$. By multiplying the operator by a certain factor we obtain $O(N^4)$. This result is typical for the square. In order to further improve the condition number we establish a finite difference preconditioner. Now the condition number scales as $O(N)$.

4. Domain Decomposition

Now that we can successfully apply spectral methods to triangular domains we are interested in domain decomposition problems. It may sometimes be more reasonable to decompose a domain in quadrilinear interior and triangular boundary elements instead of using only squares or rectangles. We use the iterative patching method with interface relaxation (see [2]). At interior nodes we solve the differential equation whereas at the interface we require continuity of the solution itself and its normal derivative. Again we consider the Poisson equation with Dirichlet boundary conditions. At the interface between two subdomains information is exchanged until continuity is reached. Into one direction we transfer Dirichlet and into the other direction Neumann information. At the Dirichlet side a weighted sum of subsolutions at the interface is handed over including a relaxation parameter which is chosen dynamically.

Numerical results for smooth solutions again show the high spectral accuracy while for less smooth solutions the results are of course somewhat worse. The number of iterations required to meet the continuity condition depends on the number of elements patched and not on N . The figure shows one of the domains we applied the method to. We have not considered time dependant problems. Experience shows that they cannot be treated efficiently using this method.



Summing up we can state that this spectral method is effective for time independent domain decomposition problems provided no cross points occur. If there are cross points, the number of iterations is quite large such that this method has to be improved in those cases.

5. The convection-diffusion equation

We also considered convection-diffusion problems. Lack of space forces us to leave out this chapter however the complete article has been submitted to the Journal of Computational Physics.

6. References

- 1 C. CANUTO, M. HUSSAINI, A. QUARTERONI, T. ZANG: Spectral Methods in Fluid Dynamics. Springer-Verlag, Berlin, 1988.
- 2 D. FUNARO, A. QUARTERONI, P. ZANOLLI: An iterative procedure with interface relaxation for domain decomposition methods. SIAM J. Num. Anal., 25, pp. 1213-1236 (1988)
- 3 W. HEINRICHS: Spectral collocation on triangular elements. J. Comp. Ph., 145, pp. 743-757 (1998)
- 4 S. SHERWIN, G. KARNIADAKIS: Triangular and tetrahedral spectral elements. ICOSAHOM'95, Proceedings of the third international conference on spectral and high order methods, 1996, Houston Journal of Mathematics

Addresses: WILHELM HEINRICHS, BIRGIT LOCH, Universitaet GH Essen, Fachbereich 10 bzw. 6, Arbeitsgruppe Ingenieurmathematik, Universitaetsstr. 3, 45117 Essen, Germany
 email: heinrich@ing-math.uni-essen.de, bloch@ing-math.uni-essen.de
 web: <http://www.uni-essen.de/ingmath>

T. KNOPP, G. LUBE, AND G. RAPIN

Stabilized FEM with shock-capturing for advection-diffusion problems

Stabilized FEM of streamline-diffusion type to advection-diffusion problems may exhibit local oscillations in crosswind direction(s). As a remedy, a shock-capturing variant is considered as an additional consistent (but nonlinear) stabilization. We present some preliminary results of the numerical analysis. The shock-capturing method has been applied within the numerical solution of the k/ϵ turbulence model of incompressible flow problems for the arising nonlinear advection-diffusion problems.

1. Stabilized finite element discretization with shock-capturing

Consider on a bounded polyhedral domain $\Omega \subset \mathbf{R}^d$ the linear advection-diffusion-reaction model

$$Lu = -\epsilon \Delta u + b \cdot \nabla u + cu = f \text{ in } \Omega, \quad u = 0 \text{ on } \partial\Omega \quad (1)$$

under the standard assumptions: $\epsilon > 0$, $b_i \in W^{1,\infty}(\Omega)$, $c \in L^\infty(\Omega)$ and $c - \frac{1}{2} \nabla \cdot b \geq 0$. The weak form of (1) on $V := H_0^1(\Omega)$ reads: Find $u \in V$ s.t. for all $v \in V$

$$a_G(u, v) := (\epsilon \nabla u, \nabla v)_\Omega + (b \cdot \nabla u + cu, v)_\Omega = l_G(v) := (f, v)_\Omega. \quad (2)$$

Let $\mathcal{T}_h = \{K\}$ be a shape-regular triangulation of Ω with $h_K = \text{diam}(K)$. A conforming Galerkin-FEM, which projects the solution of (2) to $V_h \subset V$, may suffer from nonphysical oscillations unless \mathcal{T}_h is fine enough. A standard approach is to use a stabilized FEM, e.g. the Galerkin/Least-squares method: Find $u_h \in V_h$ s.t. for all $v_h \in V_h$

$$a_{SG}(u_h, v_h) := a_G(u_h, v_h) + \sum_K \delta_K (Lu_h, Lv_h)_K = l_{SG}(v_h) := l_G(v_h) + \sum_K \delta_K (f, Lv_h)_K. \quad (3)$$

The analysis predicts the parameter choice $\delta_K = h_K(2b_K)^{-1} \min\{1, P_K\}$ with $P_K = h_K b_K \epsilon^{-1}$ and $b_K = \|b\|_{\infty, K}$.

The stabilized FEM (3) may exhibit local oscillations in crosswind direction(s). As a remedy, a shock-capturing variant is considered as an additional consistent (but nonlinear) stabilization: Find $U_h \in V_h$ s.t. for all $v_h \in V_h$

$$a_{SC}(U_h; U_h, v_h) := a_{SG}(U_h, v_h) + b_{SC}(U_h; U_h, v_h) = l_{SG}(v_h) \quad (4)$$

$$b_{SC}(w; u, v) := \sum_K \tau_K(w) (\nabla u, \nabla v)_K + \sum_K (\tau_K^{SL}(w) - \tau_K(w)) \left(\frac{b \cdot \nabla u}{\|b\|}, \frac{b \cdot \nabla v}{\|b\|} \right)_K.$$

Here we assume that $\|b\| > 0$ and $d = 2$. Scheme (4) is easy to implement (also in 3d) and guarantees a proper balance with the artificial diffusion from (3) acting in streamline direction. We rewrite the shock-capturing term as

$$b_{SC}(w; u, v) = \tau_K \left(\frac{b^\perp \cdot \nabla u}{\|b\|}, \frac{b^\perp \cdot \nabla v}{\|b\|} \right)_K + \tau_K^{SL} \left(\frac{b \cdot \nabla u}{\|b\|}, \frac{b \cdot \nabla v}{\|b\|} \right)_K \quad (5)$$

with splitting in crosswind and streamline directions b^\perp and b , respectively. Following [1], we set

$$\tau_K(w) = \epsilon \cdot S(P_K^*(w)), \quad S(P) = P \max\{0, \beta - P^{-1}\}; \quad P_K^*(w) = \frac{h_K R_K^*(w)}{2\epsilon},$$

$$R_K^*(w) = \frac{\|Lw - f\|_{0,K}}{1 + \|\nabla w\|_{0,K}}, \quad \tau_K^{SL}(w) = \max\{0, \tau_K(w) - \tau_K^{supg}\}, \quad \tau_K^{supg} = \frac{\delta_K}{\|b\|^2}$$

with a parameter $\beta > 0$. The local artificial viscosity of scheme (4) is always not smaller than $\tau_K(w)$. Only, if locally $\tau_K(w) \leq \tau_K^{supg}$, then we have a resulting artificial viscosity $\tau_K^{supg}(w) > \tau_K(w)$ in crosswind direction(s).

2. Numerical analysis of shock-capturing FEM

Here we neglect the effect of numerical integration. The first result states *consistency* and well-posedness.

L e m m a 1.

1. The stabilized FEM with shock-capturing (4) is consistent.
2. Scheme (4) has at least one solution U_h . The additional stabilization effect follows from the a-priori estimate

$$\|U_h\|_{SG}^2 + \sum_K \tau_K(U_h) \left\| \frac{b^\perp}{\|b\|} \cdot \nabla U_h \right\|_{0,K}^2 + \sum_K \tau_K^{SL}(U_h) \left\| \frac{b}{\|b\|} \cdot \nabla U_h \right\|_{0,K}^2 \leq C \|f\|_*$$

where $\|U\|_{SG}^2 = \epsilon \|\nabla U\|_0^2 + \|(c - \frac{1}{2} \nabla \cdot b)^{\frac{1}{2}} U\|_0^2 + \sum_K \delta_K \|LU\|_{0,K}^2$.

Proof. (1) For $u \in V$ of (1) with $Lu = f$ in $L^2(K)$ follows $\tau_K(u) = \tau_K^{SL}(u) = 0$. This implies consistency according to $a_{SC}(u; u, v) = a_G(u, v)$ for all $v \in V_h$.

(2) This follows via Brouwer's fixed point theorem using $a_{SC}(v; v, v) - l_{SG}(v) \geq a_{SG}(v, v) - l_{SG}(v)$.

A uniqueness result is still an open problem, whereas convergence follows from

Theorem 1. Let u resp. U_h be the solutions of (1) and of (4). Then we obtain: $\lim_{h \rightarrow 0} \|u - U_h\|_{1,\Omega} = 0$.

Proof. Split $u - u_h = (u - u_G) + (u_G - U_h)$ with Galerkin solution u_G . The proof follows using density arguments and the definition of the stabilization parameters.

The following result reflects that shock-capturing in (4) is only active where the weighted residual is too large.

Theorem 2. Let U_h and u_{SG} be the solutions of schemes (4) and (3) with and without shock-capturing, then

$$\|U_h - u_{SG}\|_{SG}^2 \leq \sum_K \tau_K^2(U_h) \|\nabla U_h\|_{0,K}^2 \sim \sum_K \frac{h_K^2}{4\epsilon} \|LU_h - f\|_{0,K}^2 \max \left\{ 0; \left(\beta - \frac{1}{P_K^*(U_h)} \right)^2 \right\} \quad (6)$$

Numerical simulations show indeed that the artificial shock-capturing viscosity acts only in (characteristic) layers and local oscillations in crosswind direction(s) are damped. Moreover, the (sharp) gradient from scheme (3) is preserved. Furthermore, note that the r.h.s. of (6) is computable and may serve as a-posteriori error indicator.

3. Linearization and applications

The nonlinear scheme (4) can be very efficiently solved via simple iteration

$$n \in \mathbb{N}_0 : \quad a_{SC}(U^n; U^{n+1}, v) = l_{SG}(v) \quad \forall v \in V_h. \quad (7)$$

L e m m a 2. The iteration procedure (7) generates a uniquely defined sequence of solutions $U^n \in V_h$.

Proof. This is a consequence of the Lax-Milgram Lemma together with $b_{SC}(w; v, v) \geq 0$ for all $w, v \in V_h$.

Iteration (7) is very robust and fast. A good initial guess is given by (3) using that $a_{SC}(0; U^1, v) \equiv a_{SG}(U^1, v) = l_{SG}(v)$. In our experience, one step is usually sufficient to remove crosswind oscillations from the initial guess (3).

We applied the shock-capturing variant of the stabilized scheme (3) as a proper discretization of nonlinear advection-diffusion-reaction equations arising within the k/ϵ turbulence model of incompressible flows following [2]. Local under- and overshoots of the very sensitive (nonnegative) turbulence quantities k and ϵ can be suppressed thus allowing a stable iteration scheme. In [3] we extended the approach to non-isothermal problems.

4. References

- 1 CODINA, R.: A discontinuity-capturing crosswind-dissipation for the finite element solution of the convection-diffusion equation, Comp. Meths. Appl. Mech. Engrg. 110 (1993), 325-342
- 2 CODINA, R., SOTO, O.: Finite element implementation of two-equation and algebraic stress turbulence models for steady incompressible flows, Intern. J. Numer. Meths. Fluids 90 (1999) 3, 309-343
- 3 KNOPP, T. ET.AL.: A non-overlapping DDM for the non-isothermal k/ϵ -turbulence model, submitted to Proc. Intern. Conf. Finite Element Methods 3D-Problems, Jyväskylä 2000

Addresses: University of Göttingen, Math. Departm., NAM, Lotzestraße 16-18, D-37083 Göttingen, Germany

CALLIES, R.; WIMMER, G.

Stabilisierte Hyperschallflugbahnen

Für ein Hyperschallflugzeug berechnet man optimale, dreidimensionale Flugbahnen unter neuartigen Stabilisierungsbeschränkungen. Dabei muß eine „gutmütige“ optimale Nominaltrajektorie in jedem Bahnpunkt genügend Spielraum bieten, um weitere Kriterien zu erfüllen. Ein Beispiel ist der Aufstieg eines Hyperschallflugsystems, wobei bei einem Triebwerksausfall ein Notlandeplatz erreichbar sein muß: Die Zusatzforderung verursacht starke Deformationen der ursprünglichen Flugbahn. Zu jedem Punkt der Nominalbahn ist ein sekundäres Optimalsteuerungsproblem zu lösen. Das Problem läßt sich als Randwertaufgabe für ein System hoch nichtlinearer Differentialgleichungen formulieren; die Stabilisierungsforderung wird adaptiv punktweise erfüllt. Die numerische Lösung erfolgt mit dem neuen Mehrzielverfahren Janus.

1. Modellsystem

Der Hyperschall-Erprobungsträger (HET) besitzt vergleichbare äußere Form wie der DC-XA Delta Clipper; seine Startmasse beträgt $m_0 = 2.1 \cdot 10^4$ kg und die Systemmasse $m_s = 7.4 \cdot 10^3$ kg.

Atmosphärenmodell: Für die Luftdichte ρ wird das folgende Modell verwendet (Bezugsluftdichte $\rho_0 = 1.225$ kg/m³, Skalierungshöhe $h_r = 12760$ m):

$$\rho(h) = \rho_0 e^{-h/h_r} \left[\frac{kg}{m^3} \right].$$

Schubmodell: Der Schub T wird durch zwei LOX/LH₂-Triebwerke mit einem spez. Vakuumimpuls $I_{sp,vac} = 404$ sec und einem max. Vakuumschub von je $T_{vac} = 311$ kN erzeugt. Für T gelte folgende Beziehung als Funktion des Drosselgrades δ :

$$T(\delta) = T_{vac} \cdot \delta.$$

Aerodynamisches Modell: Für den Auftrieb $L(v, h, C_L)$ und den Luftwiderstand $D(v, h, C_L)$ verwendet man das folgende Modell mit quadratischer Polare (Referenzfläche $S = 33$ m², Nullwiderstandsbeiwert $C_{D0} = 0.05$, Widerstandsbeiwert $C_{D1} = 1/0.7$).

$$D(v, h, C_L) = \frac{1}{2} \rho(h) v^2 S (C_{D0} + C_{D1} C_L^2), \quad L(v, h, C_L) = \frac{1}{2} \rho(h) v^2 S C_L.$$

2. Bewegungsgleichungen

Das mathematische Modell des einstufigen, raketentriebenen HET beschreibt die Bewegung einer Punktmasse über einer kugelförmigen rotierenden Erde [1]. Die Bewegungsgleichungen lauten ($x = (v, \gamma, \chi, h, \Lambda, m, \theta) : [t_0, t_f] \rightarrow \mathbb{R}^7$ Zustandsvektor, $u = (C_L, \varepsilon, \delta, \mu) : [t_0, t_f] \rightarrow \mathbb{R}^4$ Steuerungsvektor; t unabhängige Variable, hier die Zeit):

$$\begin{aligned} \dot{v} &= \{-D(v, h, C_L)/m - g(h) \sin \gamma\} + \omega^2 R \cos \Lambda (\sin \gamma \cos \Lambda - \cos \gamma \sin \chi \sin \Lambda) + A \cdot T(\delta) \cos \varepsilon / m \\ \dot{\gamma} &= \{L(v, h, C_L) \cos \mu / (mv) + (v/R - g(h)/v) \cos \gamma\} \\ &\quad + \omega^2 R \cos \Lambda (\sin \gamma \sin \chi \sin \Lambda + \cos \gamma \cos \Lambda) / v + 2\omega \cos \chi \cos \Lambda + A \cdot T(\delta) \sin \varepsilon \cos \mu / (mv) \\ \dot{\chi} &= \{L(v, h, C_L) \sin \mu / (mv \cos \gamma) - (v/R) \cos \gamma \cos \chi \tan \Lambda \\ &\quad + 2\omega (\sin \chi \cos \Lambda \tan \gamma - \sin \Lambda) - \omega^2 R \cos \Lambda \sin \Lambda \cos \chi / (v \cos \gamma) + A \cdot T(\delta) \sin \mu \sin \varepsilon / (mv \cos \gamma)\} \\ \dot{h} &= v \sin \gamma; \quad \dot{\Lambda} = v \cos \gamma \sin \chi / R; \quad \dot{m} = -A \cdot T_{vac} \cdot \delta / (g_0 I_{sp,vac}); \quad \dot{\theta} = v \cos \gamma \cos \chi / (R \cos \Lambda) \end{aligned}$$

mit den Abkürzungen $g(h) := g_0 R_0^2 / R^2$, $R := R_0 + h$ und der Schaltvariable A .

3. Optimalsteuerungsproblem

Die Nominalbahn $x(t)$ ergibt sich als Lösung des primären Optimalsteuerungsproblems (Aufstiegsbahn); jeder Punkt $x(t)$ der Nominalbahn ist Startpunkt eines sekundären Optimalsteuerungsproblems $y[x](t_{[x]})$ (Notflugbahn).

Primäres Optimalsteuerungsproblem (Nominalbahn):

Bewegungsgleichungen: $\dot{x} = f(x, u, t)$, $A = 1$, $t \in [t_0, t_f]$.
 Optimierungsaufgabe: Maximiere $v(t_i)$, bestimme $t_i \in]t_0, t_f[$, so daß $h(t_i) = h_T$ (h_T gegeben) und $\gamma(t_i) = 0$.
 Randbedingungen: $x(t_0)$ und $x(t_f)$ sind gegeben.
 Beschränkungen: $\delta \in 0 \cup [0.12, 1]$, $|C_L| \leq C_{L0}$, $|\varepsilon| \leq \varepsilon_0$ und $|\mu| \leq \mu_0$; $v^2 \varrho \leq S_0$ (Staudruckbeschr.).

Sekundäres Optimalsteuerungsproblem:

Bewegungsgleichungen: $\dot{y}[x] = \tilde{f}(y[x], u[x], t[x]) := f(y[x], u[x], t[x])|_{\delta=0}$, $A = 0$, $t[x] \in [t_{0[x]}, t_{f[x]}]$.
 Optimierungsaufgabe: Minimiere $t_{f[x]} - t_{0[x]}$.
 Randbedingungen: $y[x](t_{0[x]}) = x(t)$ (Kopplung von Nominal- und Sekundärbahn),
 $y[x](t_{f[x]})$ vorgegeben (Notlandeplatz für alle Sekundärbahnen gleich).
 Beschränkungen: $|C_L[x]| \leq C_{L0}$ und $|\mu[x]| \leq \mu_0$; $v^2 \varrho \leq S_0$.

Existiert zu gegebenem t eine Lösung für das Sekundärproblem, so erreicht das HET den Notlandeplatz P ; das Sekundärproblem wird unabhängig vom Primärproblem bearbeitet. Gibt es jedoch keine Lösung des sekundären Optimalsteuerungsproblems, so ist eine Kopplung zwischen Primär- und Sekundärproblem erforderlich, um die Nominaltrajektorie geeignet zu deformieren. Das Vorgehen wird für den Beispielfall einer sekundären Bahn aufgezeigt; die zur Nominal- bzw. Sekundärbahn gehörigen Größen sind mit N ($A = 1$) bzw. S ($A = 0$) gekennzeichnet.

Gekoppeltes Optimalsteuerungsproblem:

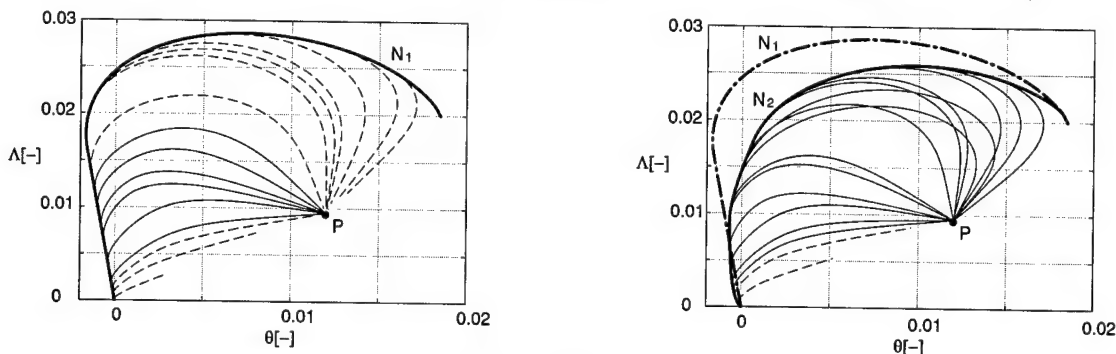
Nach Transformation auf ein festes Zeitintervall $\tau \in [0, 1]$ erhält man folgende Bewegungsgleichungen:

$$\left(\dot{x}^N - t_f^N \cdot f^N(x^N, u^N, \tau), \quad t_f^N, \quad \dot{x}^S - t_f^S \cdot f^S(x^S, u^S, \tau), \quad t_f^S \right)^T = 0$$

Mit dem Zielfunktional der Nominalbahn, den Randbedingungen und den Beschränkungen der Nominal- und Sekundärbahn ergibt sich das gekoppelte Optimalsteuerungsproblem, das gemäß dem Formalismus der optimalen Steuerung [2] in ein Mehrpunkt-Randwertproblem transformiert und mit dem Mehrzielverfahren JANUS gelöst wird. Die Kopplungsbedingung für die Nominal- und die Sekundärtrajektorie lautet: $x^N(\tau_i^+) - x^S(0) = 0$. Die Sprungbedingung für die zugehörigen adjungierten Variablen λ ($\dot{\lambda} = -H_x$, $H = \lambda^T f$) ergibt sich zu: $\lambda^N(\tau_i^+) - \lambda^N(\tau_i^-) + \lambda^S(0) = 0$. In der Praxis führt das skizzierte Vorgehen auf extrem große Differentialgleichungssysteme.

4. Numerische Lösung und Ergebnisse

Die linke Abbildung zeigt die ungestörte Nominalbahn N_1 mit Sekundärbahnen, die rechte Abbildung die stabilisierte Nominalbahn N_2 mit Sekundärbahnen (gestrichelt: P wird nicht erreicht; durchgezogen: P wird erreicht).



Für die ungestörte Bahn beträgt die maximale Geschwindigkeit 2798 m/s, für die stabilisierte Bahn 2755 m/s. Durch ein geringfügig kleineres Zielfunktional gewinnt die Nominalbahn ein hohes Sicherheitspotential.

Danksagung

Herrn Prof. Dr. Dr.h.c. R. Bulirsch danken wir für seine Unterstützung. Die Arbeit wurde teilweise von der DFG im Rahmen des SFB 255 (Transatmosphärische Flugsysteme) gefördert.

5. Literaturverzeichnis

- 1 CALLIES, R., BULIRSCH, R.: 3-D Trajectory Optimization of a Single-Stage VTVL System, AIAA-GNC 96-3903.
- 2 BRYSON, A.E., HO, Y.-C.: Applied Optimal Control, Rev. Printing, Hemisphere Publishing Corp., Washington D.C., 1975.

Anschrift: DR. RAINER CALLIES, GEORG WIMMER,

Zentrum Mathematik, Technische Universität München, D-80290 München, Germany

M. DINKELMANN, M. WÄCHTER, G. SACHS

Flugbahn-Optimalsteuerung für ein Hyperschall-Flugsystem zur Verringerung des instationären Wärmetransfers

Zur Reduzierung der hohen thermischen Belastung im Hyperschallflug wird ein Lösungsansatz vorgelegt, der den Zusammenhang von instationärem Wärmetransfer und Bewegung des Flugzeugs erfaßt und in einem Gesamt-Optimierungsprozeß behandelt. Bei der Beschreibung des instationären Wärmetransfers und der Dynamik des Flugsystems wird Wert auf eine realistische Betrachtungsweise gelegt. Dadurch gestaltet sich das mathematische Modell des Gesamtsystems sehr komplex. Die vorgelegten Ergebnisse zeigen, daß eine substantielle Reduzierung der thermischen Belastung durch eine geeignete, optimale Steuerung der Flugbahn erzielt werden kann.

1. Einleitung

Die hohe thermische Belastung von Hyperschall-Fluggeräten erfordert ein geeignetes Wärmeschutzsystem, um zu hohe Temperaturen zu verhindern oder die aufgenommene Wärmemenge zu begrenzen [2]. Die Form der Flugbahn beeinflusst die thermische Belastung, da die Aufheizung des Flugsystems vom Flugzustand abhängt. Daher kann durch eine geeignete Steuerung der Flugbahn die thermische Belastung verringert werden. In dieser Arbeit wird ein Lösungsansatz vorgelegt, der durch Kopplung von instationärem Wärmetransfer und Bewegung des Flugsystems in einer Gesamtoptimierung auf eine Reduzierung der thermischen Belastung im Hyperschallflug abzielt. Für realistische Ergebnisse sind wirklichkeitsgetreue Modellierungen zur Beschreibung der instationären Aufheizung und der Dynamik des Flugsystems erforderlich.

2. Modellierung

Zur Modellierung der instationären Aufheizvorgänge wird das Wärmeschutzsystem über ein Schichtenmodell nachgebildet [1]. Die einzelnen Schichten entsprechen hierbei dem Aufbau der Flugzeugwand, die aus unterschiedlichen Materialien besteht. Eine schematische Darstellung dieses Modells zeigt Abb. 1. Die Wärmeströme q_1, \dots, q_n durch die einzelnen Schichten können folgendermaßen beschrieben werden:

$$\begin{aligned} q_1 &= q_{air} - \varepsilon \sigma (T_1^4 - T_\infty^4), \\ q_i &= (T_{i-1} - T_i) \left(\frac{\lambda}{d} \right)_{i-1,i} + (T_{i-1}^4 - T_i^4) \varepsilon_{i-1,i} \sigma, \quad i = 2, \dots, n. \end{aligned} \quad (1)$$

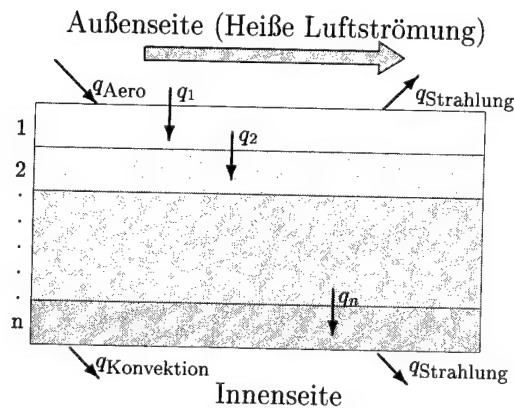


Abbildung 1: Aufheizungsmodell für die Rumpfunterseite

Der Temperaturverlauf ist durch die folgenden Differentialgleichungen bestimmt

$$\dot{T}_i = \frac{q_i - q_{i+1}}{\rho_i c_i d_i}, \quad \text{für } i = 1, \dots, n-1. \quad (2)$$

Im vorliegenden Fall wird der Bereich an der Rumpfunterseite unterhalb des Wasserstofftanks betrachtet. Für die

Temperatur der innersten Schicht (direkt unter dem Wasserstofftank) gilt $\dot{T}_n = 0$. Die Wärmetransfer in das Flugsystem hängt von der Außentemperatur T_1 , der Machzahl M , Flughöhe h und dem Anstellwinkel α ab. Um die insgesamt aufgenommene Wärmemenge in die innerste Schicht zu reduzieren, wird die folgende Zustandsbeschränkung eingeführt:

$$\int_0^{t_f} q_n dt \leq q_{n,limit} \quad (3)$$

Diese Beschränkungsbedingung führt zu einer Kopplung von instationärer Aufheizung und Dynamik des Flugsystems.

3. Ergebnisse

Im folgenden werden Ergebnisse zum Reichweitenflug eines Hyperschall-Flugsystems über 9000 km vorgestellt. Hierzu zeigt Abb. 2 die Temperaturverläufe in den einzelnen Schichten während des Flugs. Dabei werden zwei Fälle betrachtet, von denen der eine die Auswirkungen einer Beschränkung der aufgenommenen Wärmemenge und der andere eine unbeschränkte Referenzbahn betrifft. Abb. 2 zeigt, daß im beschränkten Fall die Temperaturen in den einzelnen Schichten höher sind. Dies ist auf die Verkürzung der Flugzeit infolge Erhöhung der Geschwindigkeit zurückzuführen. Weiter ist für beide Fälle bemerkenswert, daß die inneren Schichten ihr Temperaturmaximum deutlich später erreichen als die äußeren Schichten.

In Abb. 2 sind ferner die aufgenommenen Wärmemengen dargestellt. Der Vergleich der beiden betrachteten Fälle zeigt, daß eine signifikante Reduzierung der aufgenommenen Wärmemenge bei nur geringem Treibstoff-Mehrverbrauch möglich ist. Außerdem wird in Abb. 2 der Fall eines stationären Wärmetransfer-Modells betrachtet. Der Vergleich mit diesem Modell zeigt, daß die instationären Aufheizvorgänge eine bedeutsame Rolle spielen.

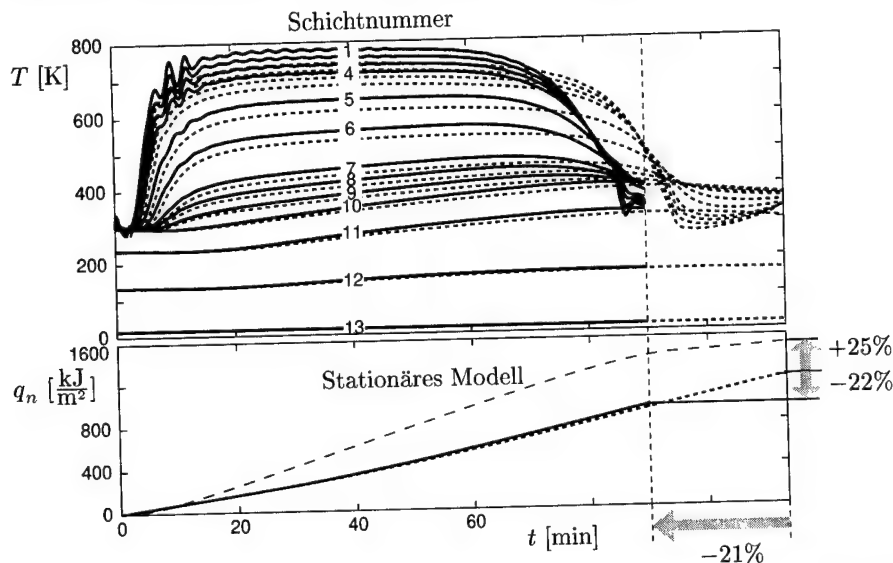


Abbildung 2: Temperaturverlauf der einzelnen Schichten und aufgenommene Wärmemenge in der innersten Schicht

----- ohne Beschränkung der Wärmemenge ($q_n = 1214 \text{ kJ/m}^2$, $m_B = 62654 \text{ kg}$, $t_f = 113.3 \text{ min}$)
 ——— mit Beschränkung der Wärmemenge ($q_n = 950 \text{ kJ/m}^2$, $m_B = 64459 \text{ kg}$, $t_f = 89.82 \text{ min}$)

4. Zusammenfassung

In der vorgelegten Arbeit wird dargelegt, daß die optimale Steuerung der Flugbahn eine signifikante Reduzierung der thermischen Belastung von Hyperschall-Flugsystemen bei nur geringem Treibstoff-Mehrverbrauch ermöglicht.

5. Literaturverzeichnis

- 1 DINKELMANN, M.: Reduzierung der thermischen Belastung eines Hyperschallflugzeugs durch optimale Bahnsteuerung, Dissertation, Technische Universität München. 1997.
- 2 WINDHORST, R., ARDEMA, M. D., BOWLES, J. V.: Minimum Heating Reentry Trajectories for Advanced Hypersonic Launch Vehicles. In AIAA Guidance, Navigation, and Control Conference, New Orleans, LA, AIAA-97-3535, August 1997.

Adressen: Dr.-Ing. Michael Dinkelmann, DaimlerChrysler Aerospace AG, 81663 München.

Prof. Dr.-Ing. Gottfried Sachs, Dipl.-Math. Markus Wächter, Technische Universität München, Lehrstuhl für Flugmechanik und Flugregelung, Boltzmannstraße 15, 85747 Garching.

N.N. FEDOROVA; I.A. FEDORCHENKO; E. SCHÜLEIN

Experimental and Numerical Investigation of the Oblique Shock Wave /Turbulent Boundary Layer Interaction at $M=5$

The results of the joint experimental investigations and numerical simulations of hypersonic separated flows are presented. The computed and experimental results are compared with respect to surface pressure, skin friction and Stanton numbers distributions as well as the integral boundary layer parameters and the mean gas-dynamic profiles.

The paper focuses on the problem of the mathematical modeling of Shock Wave / Turbulent Boundary Layer Interaction, which is of high importance for engineering applications. The case of the 2-D plane hypersonic flows ($M=5$) is selected for simulations, because it is closely related to the problems of the space transport systems. The configurations of the incident shock wave interacting with flat plate boundary layer is simple, but gives a rather good test of the turbulence model and computational ability to predict the turbulent boundary layer separation and recovery phenomena.

Three flow cases were studied with different shock generator angle α and hence, the different degree of flow separation, including the weak interaction case without separation (6° generator angle), the medium interaction case (10°) with small separation zone and the strongest (14°) interaction case. The experimental data include the flowfield shadowgraphs, the pressure distributions along the plate surface, profile measurements in the section before and after the interaction [1] as well as the optical skin friction and heat transfer measurements [2].

The computations were performed on the basis of the full unsteady 2-D Favre-averaged Navier-Stokes equations in strong conservation form closed by the Wilcox $k - \omega$ turbulence model [3]. The details of the method used in the computations can be found in [4].

Figure 1,a presents the experimental and computed pressure distributions along the plate surface for all three cases of generator angle and shows a good coincidence of the experimental (symbols) and computed (lines) distributions in the region of shock wave/ boundary layer interaction. In fig. 1,b the computed and experimental skin friction distributions are compared. Note, that the open markers are for the velocity profile data and closed markers are for the data obtained using oil-film interferometer technique. Figure 1 demonstrates that the computations predict the skin friction distributions well except for the strongest interaction case, where the level of skin friction after the interaction is underpredicted. Figure 2 presents the comparison of the experimental and computed Stanton numbers. It should be mentioned that for $\alpha = 6^\circ$ the computed results are in good agreement with the experiments but in the separated flow cases the computations overpredict the heat transfer level just after the reattachment point.

The comparison of experimental and computed profiles of mean velocity, density and temperature were also performed showing a good agreement for the weak and medium interaction intensity, but rather poor fitness for the strongest case. Possible reasons of this disagreement may be the turbulence model inability to describe properly the turbulence intensity growth after interaction with the strong shock wave. Another reason of this disagreement may be the fact that the computational model does not include all the factors of the real physical problem such as the acoustic perturbations coming to the region of interests from the boundary layer developing on the generator surface. The results of numerical simulations have shown the importance of taking into account the external level of turbulence which is of great importance for hypersonic flows, especially in the strongest interaction case.

Acknowledgements

The investigations were supported by the Russian Foundation for Basic Research grant No. 99-01-00565 and by the ESA Contract No. 11018/94/NL/FG/(SC).

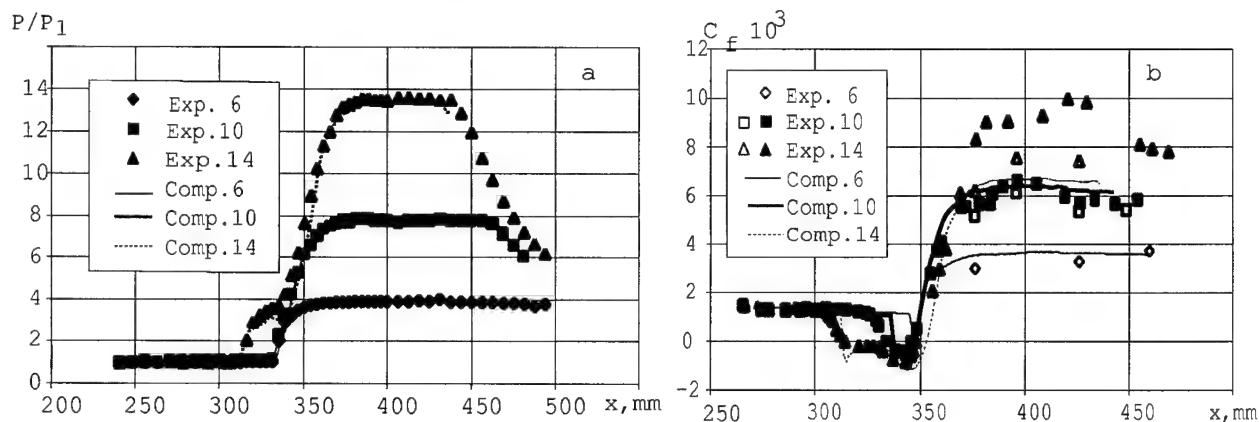


Figure 1: Experimental and computed surface pressure and skin friction distributions for $\alpha = 6^\circ, 10^\circ, 14^\circ$

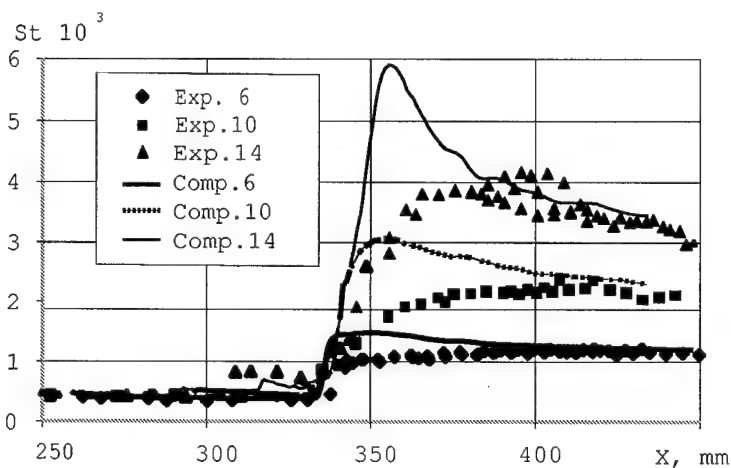


Figure 2: Experimental and computed Stanton number distributions for $\alpha = 6^\circ, 10^\circ, 14^\circ$

1. References

- 1 SCHÜLEIN, E., KROGMANN, P., STANEWSKY, E. : Documentation of Two-Dimensional Impinging Shock/Turbulent Boundary Layer Interaction Flow. DLR Forschungsbericht. IB 223 - 96 A 49 (1996) 69 pp.
- 2 SCHÜLEIN, E., KOCH, S., ROSEMAN, H.: Skin Friction Measurement and Transition Detection Techniques for the Ludwig Tubes at DLR. AGARD CP-601, AGARD FDP Symp. Advanced Aerodynamic Measurement Technology, Seattle, USA, September 22-25 (1997), 23-1 - 23-9.
- 3 ABID, R., MORRISON, J., GATSKI, T. AND SPEZIALE, C.: Prediction of Aerodynamical Flows with a New Explicit Algebraic Stress Model AIAA Journal, **34**(12) (1996) 2632-2635.
- 4 BORISOV, A.V., FEDOROVA, N.N.: Numerical Simulation of Turbulent Flows Near the Forward-facing Steps. Thermophysics and Aeromechanics, **3**, No. 1 (1996) 69-83.

Addresses: DR. NATALIE FEDOROVA, DIPL. ING. IRINA FEDORCHENKO,
ITAM SD RAS, Institutskaya, 4/1, Novosibirsk, 630090, Russia
DR. ERICH SCHÜLEIN,
DLR Institute of Fluid Mechanics, Bunsenstr. 10, 37073 Goettingen, Germany

SACHS, G. ; MAYRHOFER, M.

Reichweitensteigerung bei Hyperschall-Notflugbahnen durch Optimalsteuerung des Treibstoff-Ablaufvorgangs

Ein Missions-Abbruchszenario von zweistufigen Raumtransportsystemen betrifft antriebslose Notflugbahnen der Orbitalstufe nach Trennung von der Trägerstufe. Hierfür wird dargelegt, daß die optimale Steuerung des Treibstoff-Ablaufvorgangs eine Steigerung der erzielbaren Reichweite ermöglicht.

1. Einleitung

Bei zweistufigen Raumtransportsystemen [1] kann ein Notabstieg der Orbitalstufe nach der Separation von der Trägerstufe erforderlich sein, falls der Antrieb ausfällt oder ein anderer Systemfehler auftritt. Hierbei besteht die Forderung nach Erzielung einer möglichst großen Reichweite, um Not-Landeplätze erreichen zu können. Eine Steigerung der Reichweite ist durch optimale Steuerung des Treibstoff-Ablaufvorgangs möglich, der in geeigneter Weise im Verlauf der Flugbahn erfolgt (statt des üblichen Ablassens des Treibstoffs vor der Landung zur Reduzierung des Landegewichts). Zur Bestimmung dieser Reichweiten-Steigerung ist in der Optimierungsbetrachtung der Massenfluß beim Treibstoff-Ablassen als zusätzliche Steuergröße aufzunehmen.

2. Modellierung

Zur Berechnung der Flugbahn kann das Flugsystem auf Basis der Massenpunktdynamik modelliert werden, wobei die Erde als kugelförmig und rotierend angesetzt wird. Besonderer Wert wurde auf die realistische mathematische Beschreibung der Aerodynamik des Flugsystems und möglicher Flugbahn-Beschränkungen gelegt, um deren starken Einfluß auf die Flugleistungen erfassen zu können. Die Modellierung der Aerodynamik betrifft die Abhängigkeit der Beiwerte vom Anstellwinkel α , von der Machzahl M und von der Flughöhe h . Hinsichtlich der Flugbahn-Beschränkungen sind zulässige Grenzwerte in der Strukturbelastung, Wärmebelastung, Ruderwirksamkeit u.ä. zu berücksichtigen.

3. Ergebnisse

Im folgenden werden Ergebnisse zu einer Notflugbahn der Orbitalstufe eines zweistufigen Raumtransportsystems vorgestellt [2]. Hierzu zeigt Abb. 1 Werte einer optimalen Notabstiegsbahn nach einem Triebwerksdefekt bei halber Brennschlußzeit. Daraus geht hervor, daß das Treibstoff-Ablassen zu Beginn der Flugbahn erfolgt, d.h. in der Flugphase, in der die Fluggeschwindigkeit am höchsten ist. Damit kann die größte Reichweite erzielt werden.

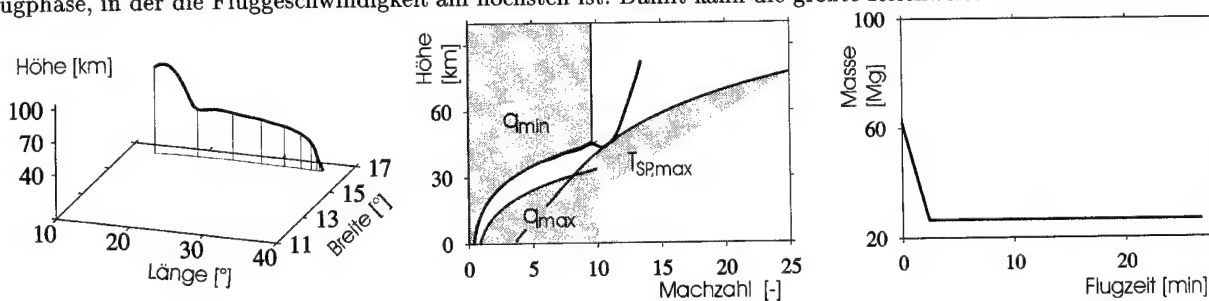


Abbildung 1: Notabstieg der Orbitalstufe eines zweistufigen Raumtransportsystems nach einem Triebwerksdefekt

4. Physikalische Deutung

Zur physikalischen Deutung des reichweitensteigernden Effektes kann man von folgender Beziehung ausgehen:

$$\Delta h \approx \int (\dot{m}_{TS}/m) h_{ref} dt \quad (1)$$

Diese Beziehung beschreibt den Höhengewinn, der durch Ablassen des Treibstoffs erzielt und zu einer Verlängerung des Gleitfluges genutzt werden kann.

Zur Bestimmung von h_{ref} werden die folgenden Relationen verwendet:

$$V = V^* = \sqrt{\frac{2m(t)g}{\rho(t)C_L^*(t)S}} \quad \text{Geschwindigkeit für Gleitflug maximaler Reichweite} \quad (2)$$

$$m \frac{V^2}{2} + mgh = \text{const.} \quad \text{konstante Gesamtenergie des Systems} \quad (3)$$

$$\rho = \rho_i e^{-b_i(h-h_i)} \quad \text{exponentielles Atmosphärenmodell} \quad (4)$$

$$m = m_{Anfang} - \dot{m}_{TS} t, \quad \dot{m}_{TS} = \text{const.} \quad \text{Treibstoffablassen} \quad (5)$$

Für den Auftriebsbeiwert C_A^* der Orbitalstufe gilt näherungsweise:

$$M < 0.8 : C_A^* \approx 0.165 \quad M > 1.2 : C_A^* \approx \frac{0.285}{\sqrt{M^2 - 0.218}} + 0.0664 \quad (6)$$

Mit den Gln. (2) bis (6) kann die folgende Beziehung für h_{ref} hergeleitet werden.

$$h_{ref} = \left[\frac{g}{c^2} \left(\frac{2}{M^2} + \frac{1}{MC_A^*} \frac{dC_A^*}{dM} \right) + b_i \right]^{-1} \quad (7)$$

Eine Auswertung hierzu zeigt Abb. 2.

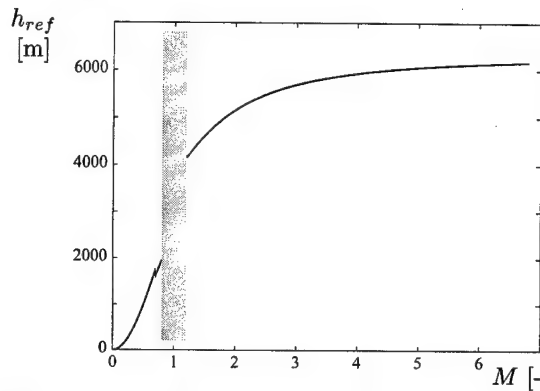


Abbildung 2: Auswertung von Gl. (7) für die untersuchte Orbitalstufe

Aus Abb. 2 ist ersichtlich, daß h_{ref} mit der Machzahl ansteigt. Dies bedeutet, daß ein maximaler Höhengewinn erzielt werden kann, wenn der Treibstoff bereits bei hohen Machzahlen abgelassen wird. Für Machzahlen $M > 5$ kann man h_{ref} für das betrachtete Fluggerät näherungsweise als konstant ansetzen.

Der betrachtete Höhengewinn kann zu einer Verlängerung des Gleitflugwegs genutzt werden. Dies kann bei dem größtmöglichen Verhältnis von C_A/C_W erfolgen, das normalerweise im Unterschall erreicht wird. Damit gilt für die Steigerung der Reichweite:

$$\Delta s \approx (C_A/C_W)_{\max, \text{sub}} \cdot \frac{0.95}{b_{\text{strato}}} \cdot \ln \frac{m_{\text{Anfang}}}{m_{\text{Ende}}} \quad (8)$$

5. Schlußfolgerung

Die Reichweite eines aerodynamisch getragenen Fluggeräts kann mittels Massenreduktion während des Fluges gesteigert werden. Hierbei kann der größte Reichweitengewinn erzielt werden, wenn die Masse bei möglichst hoher Fluggeschwindigkeit verringert wird.

6. Literaturverzeichnis

- 1 N.N.: SÄNGER-Entwurfsüberprüfung, Zwischenpräsentation, System-Definitionsstudie, DASA, Ottobrunn, Jan. 1989.
- 2 MAYRHOFER, M.; SACHS, G.: Notflugbahnen für einen Triebwerksausfall beim Orbitalstufen-Aufstieg, Seminar des Sonderforschungsbereichs 255 "Transatmosphärische Flugsysteme", Lehrstuhl für Flugmechanik und Flugregelung, Technische Universität München, Tagungsband, 2000.

Adresse: PROF. DR.-ING. GOTTFRIED SACHS, DIPL.-ING. MICHAEL MAYRHOFER, Technische Universität München, Lehrstuhl für Flugmechanik und Flugregelung, Boltzmannstr. 15, 85747 Garching, Deutschland.

TING, C.-C.

Visualization of Supersonic Flow past EOS^a

^aElliptic Aerodynamic Configuration ELAC 1's Orbital Stage [1]

The visualization of supersonic flow around EOS [1] involves analyzing shock wave positions and vortices at large angles of attack. The applied experimental methods include color Schlieren, oil film and vapor screen techniques. Depending on the Mach number and the angle of attack various vortex structures are observed on the leeward side.

1 Introduction

Heat transfer to surfaces and flight stability will always be two of the most important topics in the research of a space transportation system. The nonlinear shock waves, their interactions and the separation of flow on the transportation system are the important features for studying these problems. The high speed gas molecules pass through the shock wave and will be heavily decelerated across the shock wave. The kinetic energy of the gas molecules will be converted to internal energy and transferred to the model. The shock-shock interaction on EOS takes place between the fuselage shock, fin shock and delta wing shock. Special research into this problem can be found, for example, in reference [3]. The flow will separate along the delta wing at large angles of attack and this will generate vortices on the leeward side [4]. The shock-vortex interaction appears on EOS between the fin shock and the vortex on the cylindrical body.

2 Shock Wave in the EOS Nose Region

The supersonic flow passes through the compression wave and undergoes a strong increase in temperature, density and pressure before it partially impinges onto the model. This has the effect of causing considerable heat flux to the body due to the extremely high kinetic energy being converted to internal energy in a short period of time that is transferred to the surface of the model. This relatively high temperature can damage the surface of the model. The nose of EOS absorbs most energy, transported through the small shock stand-off distance.

To show the exact shock location various optical methods have been applied in the experiments. The experimental results have been compared with the theoretical findings based on Billig's equation (1967)[2] developed for supersonic and hypersonic flows across sphere-cone and cylinder-wedge models. The general equation reads

$$\frac{x}{R} = -1 - \frac{\Delta}{R} + \frac{R_c}{R} \cot^2 \theta \left[\left(1 + \frac{\left(\frac{y}{R} \right)^2 \tan^2 \theta}{\left(\frac{R_c}{R} \right)^2} \right)^{\frac{1}{2}} - 1 \right]$$

Here, the quantity θ is the shock angle and R_c represents the curvature of the shock on the symmetry axis (Fig. 1). For a sphere-cone model the ratios Δ/R and R_c/R are given by:

$$\begin{aligned} \frac{\Delta}{R} &= 0.143 \exp\left(\frac{3.24}{Ma^2}\right) \\ \frac{R_c}{R} &= 1.143 \exp\left(\frac{0.54}{(Ma-1)^{1.2}}\right) \end{aligned}$$

Fig. 1 shows the comparison of computed and measured results. Especially in the $Ma=1.5$ and $Ma=2.5$ cases the shock-wave positions in the EOS nose region are almost identical.

3 Topography of Vortices

The EOS model has a double delta wing with sweep angles of 80° and 65° . At large angles of attack the flow separates along the delta wing and reattaches on the fuselage separating into two vortex systems. The direction of the vortex axes of the primary wing and body vortices is almost alike. In the streamwise direction the vortex diameter grows approximately linearly resulting in two quasi-conical vortices.

Peake (1980)[4] introduced five topology rules using skin-friction lines and streamlines to classify the flow field

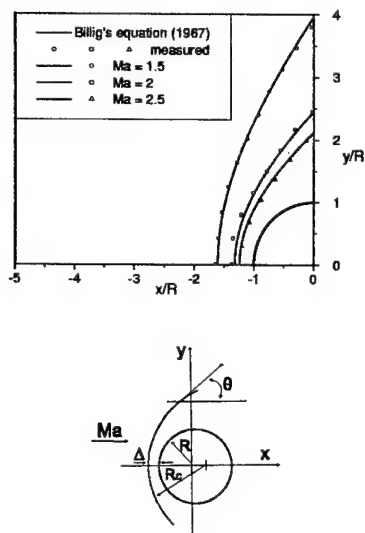


Fig 1: Comparison of measured and computed shock wave positions near the nose. The experimental results are based on the color Schlieren technique.

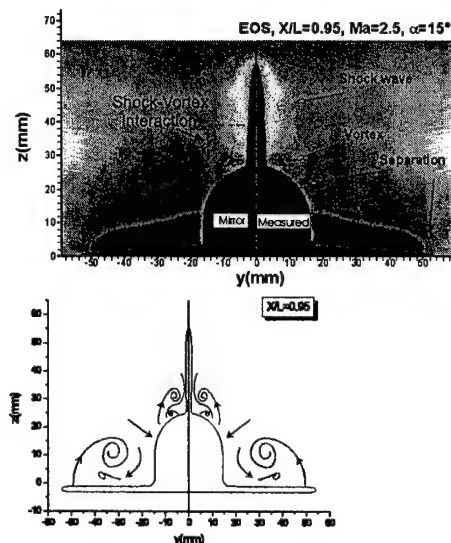


Fig 2: Description of topography on EOS at position $X/L=0.74$ compared with experimental results. The experimental result is based on the vapor screen technique.

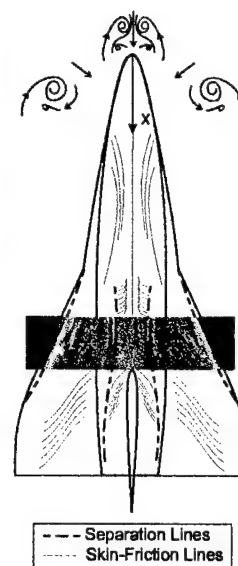


Fig 3: Description of skin-friction lines on EOS compared with experimental results from oil film photography.

in the vicinity of a model. Based on the streamlines on a two-dimensional plane cutting a three-dimensional body the topography is given by:

$$\left(\sum_N + \frac{1}{2} \sum_{N'} \right) - \left(\sum_S + \frac{1}{2} \sum_{S'} \right) = -1$$

where, N , S , N' and S' are node, saddle, half node and half saddle points, respectively. The vortices significantly influence the flight stability due to the induced pressure variations. In Fig. 2 a cross section of EOS at position $X/L=0.95$ and the flow field on the leeward side are illustrated. To better understand the flow structure a schematic of the vortices is also given. Fig. 3 shows a part of an oil film photography to evidence the separation lines on the delta wing and the fuselage. The skin-friction lines illustrate the flow direction in the vicinity of the surface.

4 Conclusion and Summary

At low Mach numbers the shock stand-off distances and the shapes of the bow shock of EOS are well identified using Billig's sphere-cone equation. The shock direction deviates at the cylinder body because of the acceleration of the supersonic flow across the expansion. The visualization of the structure of EOS vortices is limited by the low humidity of the vortex kernel in supersonic flow using the vapor screen technique. The interaction of the wing shock and the fin shock can only occur at low Mach numbers. At high Mach numbers the wing shock angle is so small that there is no interaction with the fin shock.

Acknowledgements

This work is supported by DFG's Graduiertenkolleg "Processes of Transportation in Hypersonic Flow" in Germany and is carried out at AIA.

References

- 1 Grundlagen des Entwurfs von Raumflugzeugen, Sonderforschungsbereich 253, (1995), Arbeits- und Ergebnisbericht.
- 2 BILLIG, F. S.: Shock-Wave Shapes around Spherical and Cylindrical-Nosed Bodies J. SPACECRAFT, Vol.4, No.6 (1967), 822-823.
- 3 EDNEY, B.: Anomalous Heat Transfer and Pressure Distributions on Blunt Bodies at Hypersonic Speeds in the Presence of an Impinging Shock, Aeronautical Research Institute of Sweden, FFA Report, No.115 (1968).
- 4 PEAKE, D. J. AND TOBAK, M.: Three-dimensional interactions and vortical flows with emphasis on high speeds, Tech. Report AGARD-AG-252, Advisory Group for Aerospace Research & Development, (1980).

Addresses: TING, C.-C., Aerodynamisches Institut RWTH Aachen, Wüllnerstr. zw. 5 u. 7, D-52062 Aachen

S. ALBENSOEDER, H. C. KUHLMANN AND H. J. RATH

The lid-driven cavity revisited: Stability of two-dimensional flow

The lid-driven cavity has been studied quite extensively both experimentally and numerically. Today it is the most wide-spread benchmark problem in CFD. Despite this fact, the linear stability of the steady two-dimensional flow has hardly been considered, not even for the square cavity. In the present study we revisit this classical problem and calculate the linear stability of the two-dimensional flow with respect to three-dimensional perturbations for various aspect ratios. The structure of the critical modes as well as the instability mechanism are addressed.

1. Introduction

Despite a number of investigations the linear stability of the two-dimensional one-sided lid-driven cavity flow (fig. 1a) is still an open problem. The first attempt to calculate the linear stability was due to Ramanan and Homsy [1]. For unit aspect ratio they predicted a critical mode with a wave number $k \approx 2$. This result was questioned by Kuhlmann *et al.* [4] who have shown that the mode predicted by Ramanan and Homsy is significantly stabilized for higher numerical grid resolutions. Ding and Kawahara [2, 3] confirmed the result of Kuhlmann *et al.* and found a new oscillatory mode with $k = 7.4$ to be supposedly critical. In this work we also solve the linear stability problem and show, in particular, that the mode found by Ding and Kawahara [3] is not the most dangerous mode.

The base flow (\vec{u}_0, p_0) is calculated by solving the steady incompressible Navier-Stokes equations for a viscous fluid with kinematic viscosity ν . A finite-volume technique in primitive variables on a staggered grid with refinement near the boundaries is used. The resulting nonlinear equations are solved by Newton-Raphson iteration. To calculate the three-dimensional linear stability we consider the normal modes $(\vec{u}, p) = (\vec{u}_0, p_0) + (\vec{u}(x, y), \hat{p}(x, y))e^{\sigma t + i(kz - \omega t)}$. The resulting general eigenvalue problem is solved by inverse iteration. While the typical grid resolution is 141×141 , convergence test were made by comparison with 71×71 grid points. Lengths, velocities, pressure, and time are scaled by h , ν/h , $\rho\nu^2/h^2$ and h^2/ν , respectively, where h is the height of the square cavity and ν the kinematic viscosity of the fluid. The non-dimensional parameters of the problem are the Reynolds number $Re = Vh/\nu$ and the aspect ratio $\Gamma = d/h$ with V being the lid velocity and d the width of the cavity.

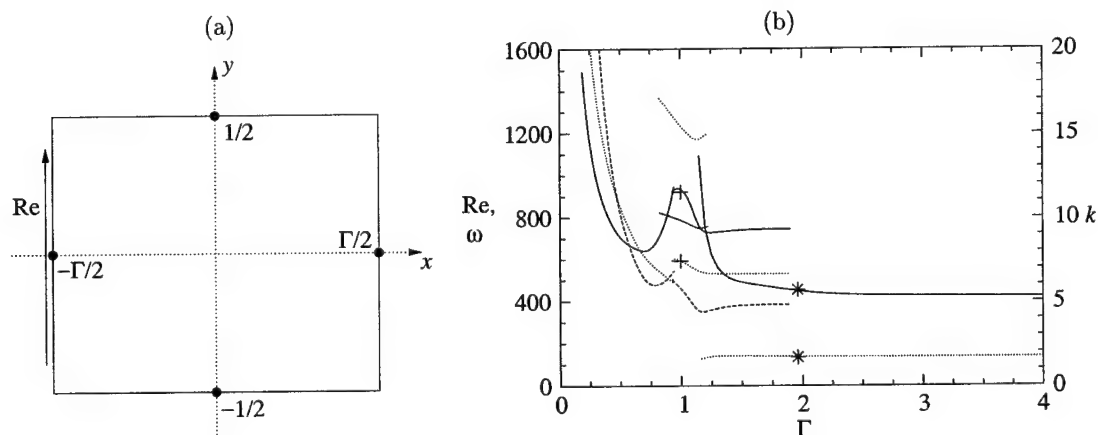


Figure 1: (a) Geometry of the lid-driven cavity. (b) Neutral Reynolds numbers Re_n (solid lines) as functions of the aspect ratio Γ . The dotted and dashed lines denote the wave number k and the oscillation frequency ω of the neutral mode, respectively. Previous results of [3] and [4] are indicated by (+) and (*), respectively.

2. Results

Calculated neutral Reynolds numbers are plotted in fig. 1b as a function of Γ . Additionally, the wave number k and the oscillation frequency ω are shown. Depending on Γ , four different instabilities are possible.

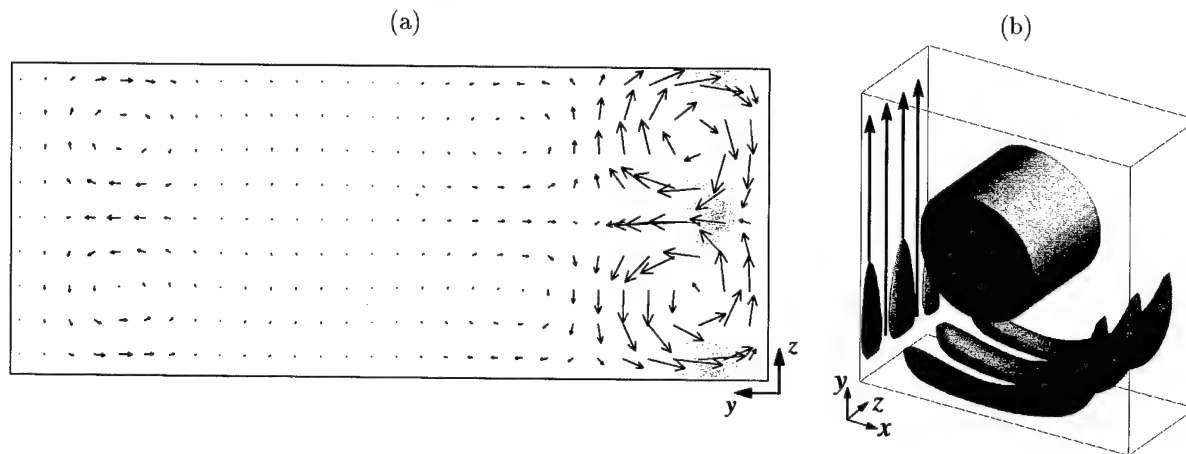


Figure 2: (a) Critical mode for $\Gamma = 1.00$ at $Re_c = 786.3$ in the $x = 0$ plane parallel to the lid. (b) Maximum energy transfer by transverse transport of longitudinal momentum. The solid arrows indicate the moving lid.

In the interval $\Gamma = [0; 0.888]$ the critical mode is oscillatory ($\omega \neq 0$). The critical parameters behave asymptotically for $\Gamma \rightarrow 0$ with $Re_c^* = \Gamma Re_c(\Gamma \rightarrow 0) \approx 275$, $k_c^* = \Gamma k_c(\Gamma \rightarrow 0) \approx 5.1$ and $\omega_c^* = \Gamma^2 \omega_c(\Gamma \rightarrow 0) \approx 124$, where Re_c^* , k_c^* , and ω_c^* represents quantities scaled with the width d instead of the height h . The analysis shows that the instability is caused by a centrifugal effect on the strong basic-state eddy that develops near the downstream cavity end.

For $0.888 < \Gamma < 1.163$ a steady short-wave-length mode is the critical one. This includes the classical aspect ratio $\Gamma = 1.00$ where the steady mode has a wave number $k_c = 15.43$. The critical Reynolds number is $Re_c = 786.3$. This value is about 16% lower than the neutral Reynolds number found by Ding and Kawahara, who only considered the restricted range $k = [0; 10]$. The continuation of the neutral mode of Ding and Kawahara becomes critical only in the small interval $\Gamma = [1.163; 1.207]$. Here the critical mode is oscillatory.

Finally, for $\Gamma > 1.207$, the critical mode is steady with a long wavelength. The critical parameters are asymptotic to $Re_c(\Gamma \rightarrow \infty) \approx 420$ and $k_c(\Gamma \rightarrow \infty) \approx 1.685$. This shows that the instability in deep cavities grows on the primary vortex near the lid. The secondary vortices are viscous and their intensity decays exponentially from the lid. Hence, they cannot support any instability.

By an energy-transfer analysis one can show [6] that all instabilities are caused by centrifugal effects. As an example, the base-state vortex core (center) and the regions of maximum amplification by transverse transport of longitudinal base-state momentum are shown in fig. 2b for $\Gamma = 1$ (high transfer is indicated by a dark shading). The latter coincide with the region in which the neutral mode is strongest (fig. 2a). Since the mode is caused by centrifugal effects and arises in a thin layer parallel to the basic streamlines, it may be called a Taylor-Görtler mode.

Acknowledgements

We gratefully acknowledge support by Deutsche Forschungsgemeinschaft under grant number Ku 896/8-1.

3. References

- 1 RAMANAN, N.; HOMSY, G. M.: Linear stability of lid-driven cavity flow. *Phys. Fluids* **8** (1994), 2690–2701.
- 2 DING, Y.; KAWAHARA, M.: Linear stability of incompressible fluid flow in a cavity using finite element method. *Int. J. Numer. Meth. Fluids* **27** (1998), 139–157.
- 3 DING, Y.; KAWAHARA, M.: Three-dimensional linear stability analysis of incompressible viscous flows using finite element method. *Int. J. Numer. Meth. Fluids* **31** (1999), 451–479.
- 4 KUHLMANN, H. C.; WANSCHURA, M.; RATH, H. J.: Flow in two-sided lid-driven cavities: Non-uniqueness, instabilities, and cellular structures. *J. Fluid Mech.* **336** (1997), 267–299.
- 5 KUHLMANN, H. C.; WANSCHURA, M.; RATH, H. J.: Elliptic instability in two-sided lid-driven cavity flow. *Eur. J. Mech. B/Fluids* **17** (1998), 561–569.
- 6 ALBENSOEDER, S.; KUHLMANN, H. C.; RATH, H. J.: Three-dimensional centrifugal-flow instabilities in the lid-driven-cavity problem. *Phys. Fluids* (submitted).

Addresses: STEFAN ALBENSOEDER, DR. HENDRIK C. KUHLMANN, PROF. DR. HANS J. RATH, ZARM – University of Bremen, Am Fallturm, 28359 Bremen, Germany, e-mail: salben@zarm.uni-bremen.de

BLOHM, C.; ALBENSOEDER, S.; KUHLMANN, H. C.; BRODA, M.; RATH, H. J.

The Two-Sided Lid-Driven Cavity: Aspect-Ratio Dependence of the Flow Stability

The transition from two-dimensional (2D) steady to three-dimensional (3D) flow is investigated experimentally in a two-sided lid-driven cavity for anti-parallel motion of two facing walls. Both wall speeds (Reynolds numbers) have the same absolute value. We present critical Reynolds numbers at the onset of steady three-dimensional flow as a function of the cross-sectional aspect ratio. The critical curve is composed of different neutral branches belonging to different instability modes. Comparison with numerical results enables insight into the corresponding mechanisms.

1. Introduction

Owing to its simplicity, the flow in lid-driven cavities has been investigated in the past as a fundamental model for interior vortex flows. Examples for applications are drying processes or different coating techniques like, e.g., the blade-coating [1]. A generalization of the well-known rectangular one-sided lid-driven cavity is obtained by introducing a second lid on the opposite side of the first one which moves with the same speed. In a such modified system vortex flows with improved symmetry can be generated and new hydrodynamic instabilities appear.

A sketch of the experimental setup is shown in fig. 1a, the geometry and coordinate system is given in fig. 1b. The dimensions of the cavity in x , y and z directions are $d = 39.5$ mm, 17.17 mm $\leq h \leq 131.67$ mm and $l = 660$ mm, respectively. Using the length scale h , we define $0.3 \leq \Gamma = d/h \leq 2.3$ as the aspect ratio in x direction and $5.01 \leq \Lambda = l/h \leq 38.44$ as the aspect ratio in z direction, thus $\Lambda = l/\Gamma d$. The Reynolds numbers at $x = \pm \Gamma/2$ are defined by $Re = Uh/\nu$, where ν is the kinematic viscosity and U is the velocity of the side walls, realized as steel belts. The belts move always in the same sense, thus the lids adjacent to the cavity move in opposite directions. The plates at $y = \pm 1/2$ and at $z = \pm \Lambda/2$ are fixed. As working fluid we use Baysilone M20 silicone oil with a kinematic viscosity $\nu = 22.2$ mm²/s and a density $\rho = 0.96$ g/cc at 20°C. To visualize the flow, a halogen light sheet and aluminum flakes suspended into the silicone oil were applied.

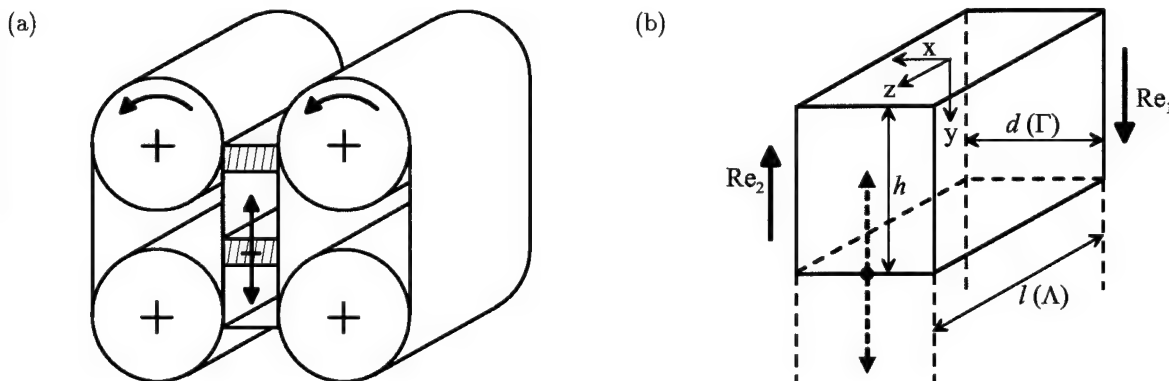


Figure 1: Sketch of the experimental setup (a); geometry and coordinate system of the cavity (b).

2. Results

For low Reynolds numbers the flow in the two-sided lid-driven cavity is nearly two-dimensional. Small three-dimensional disturbances are only present close to the stationary boundaries at $z = \pm \Lambda/2$. Using large cylinders as moving walls, Kuhlmann, Wanschura & Rath [2] found for $\Gamma = 1.96$ that the basic 2D flow consists of two co-rotating vortices. By increasing Re quasi-statically at a rate of $Re = 1/2$ min⁻¹ they observed a jump transition to the quasi 2D merged-vortex flow (mv) at $Re_{mv} = 232$ in which the former two discrete vortices partly merge. By reducing Re the flow switches back to the two-vortex flow (tv) at $Re_{tv} = 224$, so that hysteresis is present in the

flow. Using belts instead of cylinders in the present experiment confirms their results. For the transition points we find $Re_{mv} = 238 \pm 3\%$ and $Re_{tv} = 221 \pm 3\%$, shown as (o) in fig. 2b.

Further increase of Re for $\Gamma = 1.96$ leads to a 3D flow through an elliptical instability [3], which bifurcates via a pitchfork bifurcation at $Re_c = 275$ [4]. In the present experimental setup the critical point for the onset of the 3D flow has been observed at $Re_c = 269 \pm 3\%$, marked by (\square) in fig. 2b.

The 2D flow becomes 3D via an elliptical instability for aspect ratios $0.16 \leq \Gamma \lesssim 0.75$ and $1.05 \lesssim \Gamma \lesssim 1.96$. The transition points are marked by (\square) in fig. 2a. The results of a linear stability analysis are given by the full line in fig. 2a and show a good agreement with the experimental data (see also [2]). For $0.75 \lesssim \Gamma \lesssim 1.05$ and $2 \lesssim \Gamma \lesssim 2.5$ we found that the flow undergoes a centrifugal instability. For $0.75 \lesssim \Gamma \lesssim 1.05$ the 2D flow consists of a single vortex which becomes a 3D Taylor-Görtler-like oscillatory flow with spanwise propagating spiral waves. The critical points (\bullet) for the onset of the Taylor-Görtler-like oscillatory flow show a qualitatively good agreement to the results of the linear stability analysis (---). For $\Gamma = 1$, as an example, experimental and theoretical critical Reynolds and wave numbers $k = 2\pi/\lambda$ are $Re_c^{exp} = 700$, $k_c^{exp} = 13.9$, $Re_c^{num} = 669$, $k_c^{num} = 14.6$, respectively. For aspect ratios $\Gamma \gtrsim 2$ the 2D flow consists of two well separated vortices, which become 3D in the experiment at (+). The data qualitatively agrees with the linear stability analysis, shown as (---) in fig. 2b. In the supercritical stationary 3D state the vortices grow and shrink alternatingly in their diameters along the z direction.

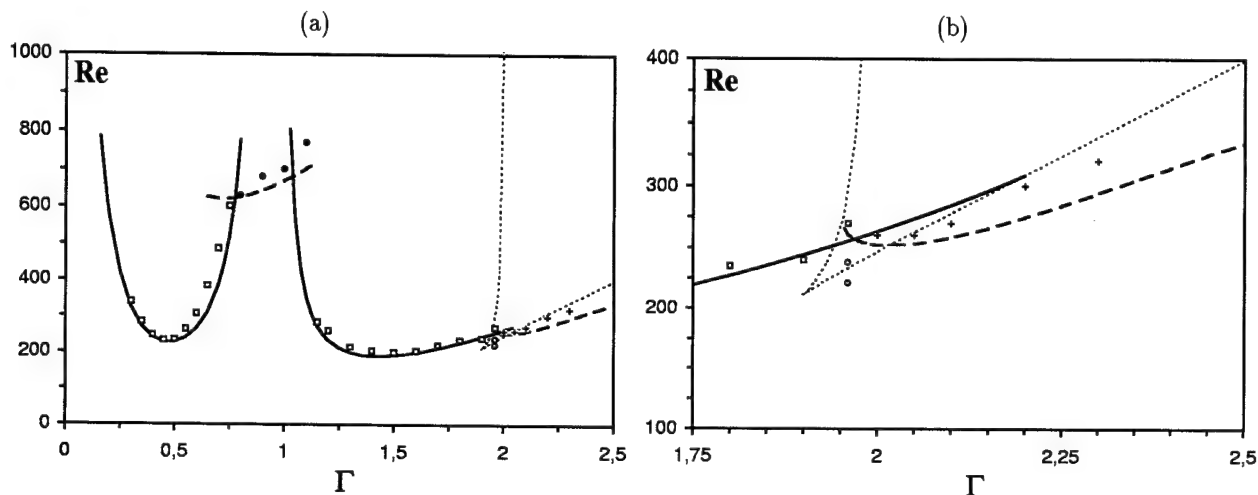


Figure 2: Onset of the 3D flow in the experiment (symbols) and the linear stability analysis (lines) as function of Γ (a); (b) shows an enlargement for $1.75 \leq \Gamma \leq 2.5$.

Acknowledgements

This work was supported by Deutsche Forschungsgemeinschaft under grant numbers Ku 896/5-2 and Ku 896/8-1.

3. References

- 1 AIDUN, C. K.; TRIANTAFILLOPOULOS, N. G.: High-speed blade coating. In: Liquid film coating. Kistler, S. F.; Schweizer, P. M. (eds.). Chapman and Hall (1997), 637-672.
- 2 KUHLMANN, H. C., WANSCHURA, M. & RATH, H. J.: Flow in two-sided lid-driven cavities: Non-uniqueness, instabilities, and cellular structures. J. Fluid Mech. **336** (1997), 267-299.
- 3 KUHLMANN, H. C., WANSCHURA, M. & RATH, H. J.: Elliptic instability in two-sided lid-driven cavity flow. Eur. J. Mech. B/Fluids **17**(4) (1998), 561-569.
- 4 BLOHM, C., KUHLMANN, H. C. & RATH, H. J.: Instabilities of two- and three-dimensional vortex flows in two-sided lid-driven cavities. In: ECS Advances in Coating and Drying of Thin Films. Durst, F.; Raszillier, H. (eds.). Shaker (1999), 399-404.

Addresses: CHRISTIAN BLOHM, STEFAN ALBENSOEDER, DR. HENDRIK C. KUHLMANN, MICHAEL BRODA AND PROF. DR. HANS J. RATH, ZARM - University of Bremen, Am Fallturm, 28359 Bremen, Germany, e-mail: blohm@zarm.uni-bremen.de

CLASS, A. G.

Rotating polyhedral flames

By systematically changing the mixture composition of a flame on a Bunsen burner the conical shape of the flame can suddenly be transformed into triangular cells forming a polyhedron. Often the polyhedron rotates rapidly about its vertical axis. We present a weakly nonlinear analysis which results in a Kuramoto-Sivashinsky equation describing cellular flames, which is coupled to a heat equation modeling the temperature of the burner rim. Numerical computations of the coupled set of equations exhibit rapidly rotating polyhedral patterns, which show the typical saw-toothed shape of the corrugations of the flame. In contrast to earlier considerations of this problem, where the rotation is explained as a result of mode interactions, we find a primary bifurcation to a rotating state, which may explain the high speeds of revolution.

1. Introduction

Polyhedral flames are a curiosity in flame experiments which have already been reported in the middle of the 19th century. A conical premixed flame is established at the mouth of a tube burner. For certain mixtures the circular symmetry of the flame is broken and the shape of the flame edge near the burner mouth forms a polygon with 3 to 20 sides. The corners of this polygon are connected to the tip of the flame by ridges, so that the flame shape corresponds to a polyhedron. Depending on the mixture composition and the burner properties, the flame may either be stationary or time dependent, where the simplest dynamics is a ridged rotation of the flame (not the gas). It is common understanding that the diffusional-thermal instability, which is present in mixtures with distinct heat and fuel-mass diffusivities, is associated with polyhedral flames. A first attempt to explain the patterns, i.e. the number of faces of the polyhedron and also the rotating dynamics was undertaken by Buckmaster [1] who studied a heuristic one-dimensional model for the flame edge in form of a modified Kuramoto-Sivashinsky equation (KS) [5], that accounted for the heat losses to the burner by a damping term. A similar damping term was derived from first principles by Class et al. [3] for a porous plug burner. Buckmaster [1] explains the rotating dynamics of the polyhedral flames by the interaction of two bistable modes with a distinct number of faces. Recently experiments have been reported by Gorman et al. [4] where cellular flames have been established on a circular porous-plug burner, that also show a stationary state or a rotating dynamics.

2. Model

The burner geometry considered here, is related to the experimental configuration employed by Gorman [4] where a premixed cellular flame is established above a circular porous plug burner. A mixture of fuel and oxidizer emerges from a cooled porous plug and reacts in a thin laminar flame to form the burnt products.

The main tasks of the burner are to uniformly deliver the fresh mixture and to stabilize the flame at a fixed location. If the porous plug is homogeneous, then the flow rate is constant and the most simple flame configuration corresponds to a stationary planar flame. If the porosity is larger or the thickness of the porous plug is smaller in the center of the porous plug, then the flow velocity is larger in the center than at the edge. The most simple flame configuration now corresponds to a bunsen cone type flame.

The burner consists of a porous plate which is cooled by an embedded cooling channel. In contrast to the model of Buckmaster [2] where the burner surface temperature is assumed to be constant, we assume that the temperature of the coolant is fixed. Therefore, small temperature variations along the burner surface may arise. By assuming a high heat capacity, and very small temperature variations of the burner surface temperature, we find an observable effect; the transition of the primary instability from stationary to oscillatory.

In the present consideration we analyze polyhedral flames, using a weakly nonlinear theory. The flame is assumed to be planar to a first order of approximation. Now the flame is displaced by an amount ϕ from its basic state and a solvability condition for ϕ is sought. In the derivation we allow for general perturbations of the boundary conditions and of the physical properties of the burner.

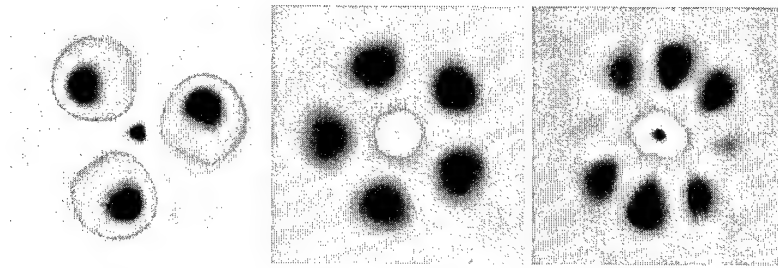


Figure 1: Simulations of polyhedral flames, the color coding visualizes ϕ .

In suitable nondimensional variables, the equations for the displacement ϕ and the burner surface temperature T are,

$$\partial_t \phi + \nabla^4 \phi + 2\nabla^2 \phi + (\nabla \phi)^2 + \mathbf{v}_t \cdot \nabla \phi + T = v_a, \quad (1)$$

$$a \partial_t T - b \nabla^2 T + T - c \phi = 0, \quad (2)$$

where \mathbf{v}_t is the tangential component of the velocity field along the flame and v_a deviation of the axial component of the flow from some reference value, which we typically take at the burner edge. For a bunsen type flame \mathbf{v}_t vanishes in the center of the burner and \mathbf{v}_t points towards the center otherwise. The axial velocity v_a is largest at the burner center. As a simple model of a bunsen flame we take a Gaussian profile for the axial velocity and a Gaussian times the radius for the tangential velocity.

In the heat equation for the burner, a is proportional to the inverse of the Fourier-number, b is proportional to the heat conductivity of the burner and c is a measure of the stand-off distance of the flame. Here $c = 0$ corresponds to a freely propagating flame which is not influenced by the burner, and $c > 0$ stands for a flame which is stabilized by heatlosses to the burner. For a burner with constant surface temperature, $B = 0$, and a constant flow velocity $\mathbf{v}_t = v_a = 0$ the equations reduces to a damped Kuramoto-Sivashinsky equation, $\partial_t \phi + \nabla^4 \phi + 2\nabla^2 \phi + (\nabla \phi)^2 + c\phi = 0$, which is known to exhibit cellular patterns for $c < 1$.

A linear stability analysis of flat flames, when $\mathbf{v}_t = v_a = 0$ shows that due to the heat capacity of the burner the primary bifurcation may be to an oscillatory state, thus explaining the fast rotating states observed in the experiments of Gorman [4]. Here large values of a are destabilizing and the diffusivity b is stabilizing.

3. Simulations

In the figure numerical simulations of bunsen type flames using a high resolution spectral collocation method are shown. The tangential flow along the flame is responsible for the formation of the typical ridges. The flame instability originates at the burner rim where the tangential flow is weak. The flame in figure 1a is a rotating polyhedral flame and the flames in figures 1b and 1c are oscillating polyhedral flames with five and eight sides respectively. These simulation results are in good agreement with the experimental observations.

4. References

- 1 BUCKMASTER, J.: Stability of the porous plug burner flame. *SIAM J. Appl. Math.*, **43** (1983), 1335-1349.
- 2 BUCKMASTER, J.: Polyhedral flames - An exercise in bimodal bifurcation analysis. *SIAM J. Appl. Math.* **44** (1984), 40.
- 3 CLASS, A. G., BAYLISS, A., AND MATKOWSKY, B. J.: Localized flickering flames. *SIAM J. Appl. Math.*, **59**(3), (1999), 942.
- 4 GORMAN M., HAMILL, C. F., EL HAMDI, M., AND ROBBINS, K. A.: Rotating and modulated rotating states of cellular flames. *Comb. Sci. and Tech.*, **98** (1994), 25.
- 5 SIVASHINSKY, G. I., Diffusional-thermal theory of cellular flames, *Combust. Sci. and Tech.*, **15** (1977), 137.

Addresses: DR. CLASS ANDREAS G., Forschungszentrum Karlsruhe,
Institut für Nuclear and Energy Technologies,
Postfach 3640, D-76021 Karlsruhe, Germany.

LEYPOLDT, J.; KUHLMANN, H.C.; RATH, H.J.

Stability of hydrothermal-wave states

The half-zone model is investigated for unit aspect ratio, zero gravity, and Prandtl numbers $Pr = 1.5 \dots 7$ by numerical simulations. For thermocapillary Reynolds numbers $Re > Re_c$, the 2D stationary flow is unstable to 3D travelling waves. In the simulations, standing waves can be generated slightly above Re_c . It is found, that these states are unstable and decay into either a clock- or a counter-clockwise propagating wave. Amplitude equations are used to quantitatively describe the instability of the standing wave states and to estimate the range of Pr within which only travelling waves are stable.

1. Introduction

We consider a cylindrical volume of liquid held between two circular disks of radius R and separated by a distance $d = R$. The Prandtl number of the fluid is defined as $Pr = \nu/\kappa$, where ν is the kinematic viscosity of the fluid and κ its thermal diffusivity. The temperature difference applied between the top (hot) and the bottom (cold) plate is ΔT . For our simulations we use the Navier-Stokes equations under zero gravity conditions and we assume thermal insulation at $r = R$, i.e. $\partial_r T = 0$ (see [2] for details).

2. Numerical procedure

The parameters of the model are the Prandtl number and $Re = |\partial\sigma/\partial T|\Delta T d/\rho\nu^2$ as a measure of the driving thermocapillary surface forces (σ = surface tension, ρ = density of the fluid). Beyond a critical value Re_c , finite-amplitude waves propagating azimuthally are stable. The azimuthal wave number is $m = 2$ in all cases presented here. If $\epsilon := Re/Re_c - 1 \ll 1$, the wave amplitudes and their nonlinear coupling is weak and may be described by a system of coupled equations. If we write $A_{L,R}e^{im\varphi \pm i\omega t \pm i\alpha_0} + \text{c.c.}$ for the left- and right-travelling waves, where $A_L(t) = L(t)e^{i\alpha_L(t)}$ and $A_R(t) = R(t)e^{i\alpha_R(t)}$, the system can be written as

$$\tau_0 \partial_t L = \epsilon L - g_s L^3 - g_c R^2 L, \quad \tau_0 \partial_t \alpha_L = c_0 \epsilon - c_2 g_s L^2 - c_3 g_c R^2, \quad (1)$$

$$\tau_0 \partial_t R = \epsilon R - g_s R^3 - g_c L^2 R, \quad \tau_0 \partial_t \alpha_R = c_0 \epsilon - c_2 g_s R^2 - c_3 g_c L^2. \quad (2)$$

Stable solutions exist for $g_s > -1$. These are travelling waves (TW) if $g_c/g_s =: \tilde{g}_c > 1$ and standing waves (SW) if $|\tilde{g}_c| < 1$ (see [1] for example):



From (1,2) we obtain $\tilde{g}_c = (A_{TW}/A_{SW})^2 - 1$, where A_{TW} and A_{SW} are the stationary amplitudes of the travelling and the standing wave state, respectively. In order to determine \tilde{g}_c for each Pr , 2D flows were computed for several $Re > Re_c$. Then standing waves were induced using a temperature perturbation $T_p \propto \sin m\varphi$. Once saturated, A_{SW} was calculated by means of a Fourier transform of the data from one oscillation period. For the investigated Pr the standing waves finally decayed into travelling waves, and the amplitudes of the latter were determined in the same way.

3. Results and conclusions

We are interested in \tilde{g}_c as a function of Pr , in order to find the value Pr^* where $\tilde{g}_c = 1$, see (3). It turns out that, due to corrections of higher order in ϵ not taken into account in the above amplitude equations, \tilde{g}_c depends on r , z , and ϵ (fig. 1(a)). The dependence on r and z vanishes if $\epsilon \rightarrow 0$. For each $\epsilon > 0$ the average over r and z of \tilde{g}_c is determined. To be consistent with the assumption of a weakly nonlinear coupling these values are extrapolated to $\epsilon = 0$ (fig. 1(b)). From fig. 2 one obtains $Pr^* = 7.8 \pm 0.1$.

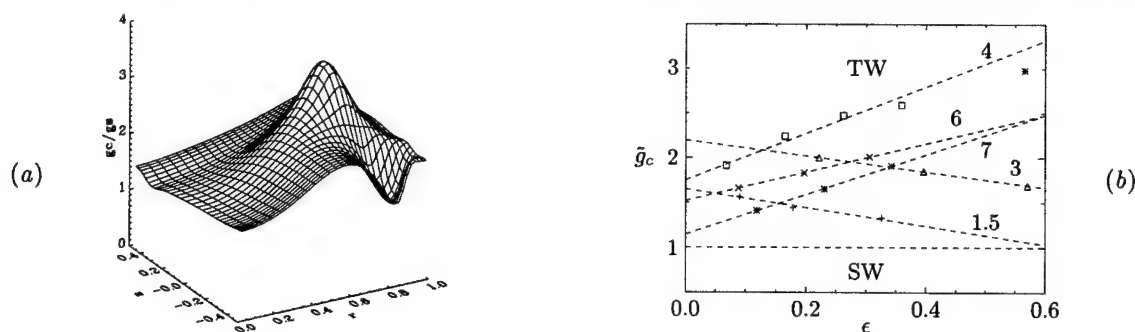


FIGURE 1: (a) Surface plot of $\tilde{g}_c(r, z)$ for $Pr = 4$, $\epsilon = 0.165$. Here we obtain $\tilde{g}_c = 1.99 \pm 0.43$. (b) Average values $\tilde{g}_c(\epsilon)$, computed from the oscillation amplitude of the azimuthal velocity v , for $Pr = 1.5$ (+), 3 (Δ), 4 (\square), 6 (\times) and 7 (*). The respective domains of stable travelling and stable standing waves are indicated by TW and SW. Using the oscillation amplitudes of the temperature field T , similar results are obtained (c.f. fig. 2).

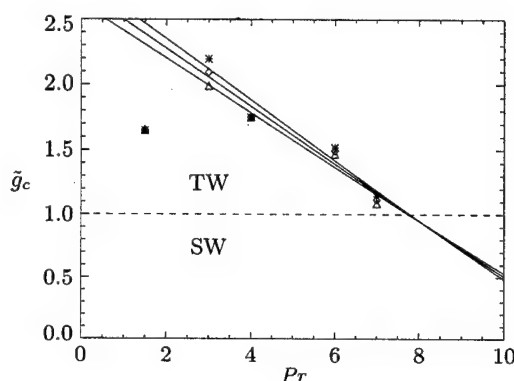


FIGURE 2: Extrapolation of $\tilde{g}_c(Pr, \epsilon = 0)$ to $\tilde{g}_c = 1$ from T (*), v (Δ), and the average of both (\diamond).

It can be concluded that for $Pr < Pr^*$ travelling waves are the stable solutions for small-amplitude 3D flows. On the other hand, for $Pr > Pr^*$ within a certain range the nonlinear coupling of small-amplitude hydrothermal waves will lead to stable standing waves. This is summarized in fig. 3.

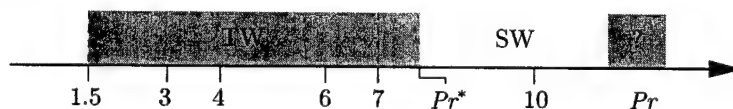


FIGURE 3: Type of the small-amplitude hydrothermal-wave states as a function of Pr .

The above prediction was confirmed by a simulation for $Pr = 10$ and $Re = 900$. Starting from a mixed state with $|A_L| = 1$ and $|A_R| = 0.25$ at $t = 0$, the amplitudes equilibrated as time proceeded, and the flow finally evolved into a standing wave state.

Acknowledgements

Financial support by DLR under grant number 50 WM 9901 is gratefully acknowledged.

4. References

- 1 CRAWFORD, J. D.; KNOBLOCH, E.: Symmetry and symmetry-breaking bifurcations in fluid dynamics. *Annu. Rev. Fluid Mech.* **23** (1991), 341–387.
- 2 LEYPOLDT, J.; KUHLMANN, H. C.; RATH, H. J.: Three-dimensional numerical simulation of thermocapillary flows in cylindrical liquid bridges. *J. Fluid Mech.* **414** (2000), 285–314.

Addresses: J. LEYPOLDT, H.C. KUHLMANN, H.J. RATH, ZARM, University of Bremen, Am Fallturm, D-28359 Bremen

LUTZ, TH.

Airfoil Design and Optimization

The aerodynamic efficiency of mildly swept wings is mainly influenced by the characteristics of the airfoil sections. The specific design of airfoils is therefore one of the classical tasks of aerodynamics. Since the airfoil characteristics are directly dependent on the inviscid pressure distribution the application of inverse calculation methods is obvious. The direct numerical airfoil optimization offers an alternative to the manual design and attracts increasing interest.

1. Inverse Subsonic Airfoil Design

In order to find a proper airfoil shape for a specific aerodynamic application different approaches may be used. In former times, when no theoretical methods were available, relevant geometric parameters were varied systematically and the effect on the aerodynamic characteristics was measured in a series of wind-tunnel tests. The first extensive experimental investigations in this sense were performed at the AVA after completion of the Göttinger low-speed wind-tunnel in 1917/1918.

After L. Prandtl developed the boundary-layer theory it became obvious that the outer-flow velocity distribution along the airfoil surface determines the airfoil performance. This gave reason to develop inverse methods which enable the calculation of the airfoil contour from a given velocity distribution. First methods for the approximate inverse solution of the Laplace equation were developed in the late twenties and the thirties. Exact solutions based on a conformal mapping procedure were proposed by Mangler (1938) and Lighthill (1945).

When inverse methods were available, knowledge was established how to shape the velocity distribution in order to obtain favourable airfoil characteristics, e. g. with respect to minimum drag or maximum lift. A milestone represent the well-known NACA laminar flow airfoils designed in the late thirties. As further examples the investigations of Eppler, Stratford and Wortmann should be mentioned.

A significant progress in airfoil design was achieved in the fifties by coupling the potential-flow methods with integral boundary-layer procedures to consider viscous effects. Since then, a large number of subsonic airfoil design tools were developed, for example the Eppler/Somers code or the methods of Drela. In the hands of experienced users such methods enable a carefully directed design and the adaption of the airfoil characteristics to specific applications. A good example in this respect is documented in the progress achieved in the aerodynamic performance of modern sailplanes. A significant portion of the improvements can be attributed to the successful design of low-drag laminar flow airfoils (e. g. DU, E, FX or HQ airfoils).

Another significant amount of investigations on inverse methods for the regime of transonic flows were performed in the seventies after the discovery of the supercritical airfoils. Due to the availability of supercomputers it is nowadays possible to handle semi-inverse solutions of the Euler equation, the coupled Euler boundary-layer equations or even for the Reynolds-averaged Navier-Stokes (RANS) equations.

2. Direct Numerical Airfoil Optimization

An alternative to the inverse or semi-inverse procedure is offered by direct numerical optimization. With this approach an automated search for an optimal solution with respect to a user-specified objective function, e. g. minimization of drag, is performed. This is done by means of an iterative variation of the chosen design variables. To parameterize the airfoil contour mostly geometric shape functions are applied with the respective coefficients representing the design variables. The choice of a proper optimization algorithm strongly depends on the topology of the considered objective function, the airfoil parameterization, the number of design variables and finally on the efficiency of the aerodynamic model. In general, gradient methods converge fast for simple topologies of the objective function but one may be trapped in a local optimum if a multimodal objective function is considered. Stochastic algorithms offer a greater chance to avoid this problem and can also cope with complex topologies but usually require much more iterations. The combination of stochastic optimizers with costly high-accuracy flow-solvers, e. g. based on the solution of the RANS equations, is therefore still limited to a relatively small number of design variables.

Numerical optimizations of subsonic airfoils featuring a detailed representation of the complete contour are hardly known. To reduce the computational effort, potential-flow methods coupled with integral boundary-layer procedures are preferred for the aerodynamic analysis, the number of optimization cycles is limited and a moderate number of design variables (usually below 10 ~ 15) is considered. Actually, most of the numerically optimized subsonic airfoils published so far show a great similarity to the initial shape.

3. Example on Numerical Shape Optimization of Subsonic NLF Airfoils

The objective of numerical optimizations performed by the present author was to design natural laminar flow (NLF) airfoils which show minimized average drag for a user-specified design lift region [1], [2]. In order to enable a detailed airfoil representation a large number of 34 design variables was considered. Contrary to the usual approach the airfoil was not parameterized by geometric shape functions. Instead, an inverse conformal mapping procedure according to Eppler was applied to generate the airfoil contour. The input parameters of this method directly control the local outer-flow velocity gradient and finally the boundary-layer development. A spline representation of the critical leading-edge region is avoided with this approach.

The potential-flow method was coupled with an integral boundary-layer procedure utilizing closure relations according to Eppler for laminar flow. The method proposed by Drela with a new shape-factor relation is used to calculate turbulent boundary-layers. To predict the laminar to turbulent transition location, an e^n database method based on spatial stability analysis for Falkner-Skan self-similar profiles was implemented. The effect of 'short' transitional separation bubbles is considered by means of a new efficient bubble model. The complete aerodynamic model was coupled with a commercial hybrid optimizer which consists of a combination of genetic algorithm, downhill simplex and a gradient method.

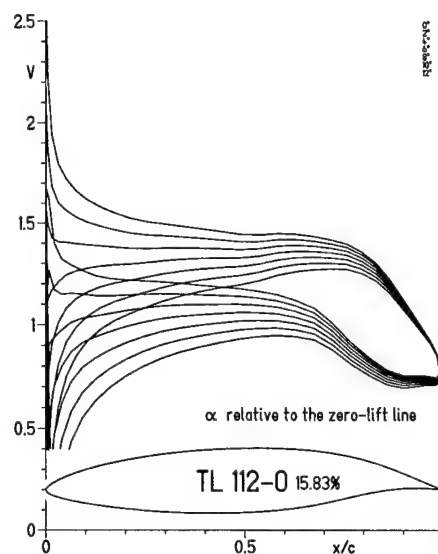


Figure 1: Inviscid velocity distribution for the optimized airfoil

One optimization result is depicted in Figs. 1 and 2. The objective was to minimize the average drag coefficient for angles of attack $\alpha_{design} = [2^\circ, 3^\circ, \dots, 8^\circ]$ relative to the zero-lift line. Two Reynolds numbers were considered, namely $Re_{design} = 3 \cdot 10^6$ and $9 \cdot 10^6$. In order to prevent a breakdown in lift at off-design conditions and to enhance the stall characteristics, the curvature of the lift curve was limited for $\alpha = [2^\circ, 3^\circ, \dots, 15^\circ]$. The resulting airfoil shows features which are well-known from manual airfoil design such as smooth transition ramps or a Stratford-like turbulent pressure recovery on the lower side (see Fig. 1).

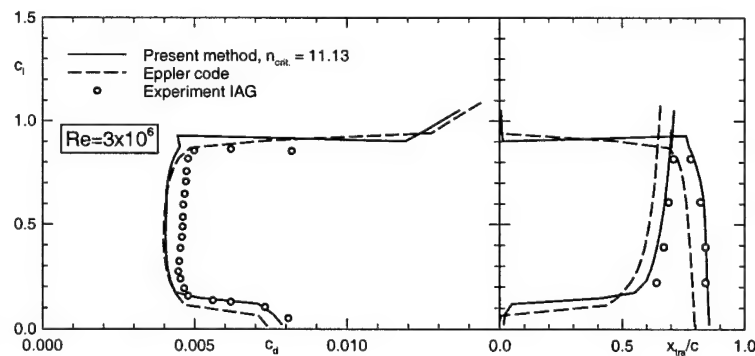


Figure 2: Predicted and measured drag polar for the optimized airfoil

Wind-tunnel tests for the optimized airfoil showed very low drag coefficients inside the laminar bucket which exactly coincides with the design lift region, see Fig. 2. The optimization method has furthermore been applied to design of airfoils which show minimized trailing-edge noise or minimal derivation to a user-specified drag polar.

4. References

- 1 LUTZ, TH.: Berechnung und Optimierung subsonisch umströmter Profile und Rotationskörper. VDI Fortschritt-Berichte, Reihe 7: Strömungstechnik, Nr. 378, ISBN 3-18-337807-8.
- 2 LUTZ, TH. AND WAGNER, S.: Numerical Shape Optimization of Subsonic Airfoil Sections. Proc. ECCOMAS 2000: European Congress on Computational Methods in Applied Sciences and Engineering, Barcelona, September 11-14, 2000.

Addresses: THORSTEN LUTZ, Institute for Aerodynamics and Gas Dynamics, University of Stuttgart (IAG), Pfaffenwaldring 21, D-70550 Stuttgart, email: lutz@iag.uni-stuttgart.de

B. SCHULTE-WERNING, C. HEINE AND G. MATSCHKE

Slipstream Development and Wake Flow Characteristics of modern High-Speed trains

The tendency to increased cruising velocity of high-speed trains is unbroken, although stabilising the level already reached is dominant [1]. In parallel the weight of the end coaches in the future train sets is decreased because of replacing the power car concept by the distributed traction concept and because of axle load limitations in the trans-European interoperability rules. This allows both for a less overall weight of the train with its reduced energy consumption effect and for an end car equipped with passenger seats, thus increasing the transport capacity of the train.

As higher speed means higher aerodynamic forces which then act on vehicles with lower mass, the vehicle reaction onto unsteady air force excitation, e.g. of the end car in trailing position, have come into the view of the railway operators. In the BriteEuram-funded research project RAPIDE (Railway Aerodynamics of Passing and Interaction with Dynamic Effects) the railway undertakings Deutsche Bahn AG (DB), the French SNCF and the Italian FS, joined their forces to investigate, among other examinations, the boundary layer flow of a modern high-speed train and the wake flow characteristics by means of currently available off-the-shelf CFD-codes. Full scale measurements both with a multi-pressure probe device and a LDA-system were performed for validation purposes up to train velocities of 280 km/h ([2]).

When the thick turbulent boundary layer separates at the end of the train the points of separation on the train surface may shift periodically in time, thereby causing aerodynamic excitation of oscillations of the last coach around the longitudinal axis; a phenomenon first detected by the Japanese railways some years ago ([3], [4]). The oscillation frequency with its related amplitude may cause discomfort to passengers in the rear coach because of its "nausea" effect. Confirmation of this effect has been given by Japanese measurements on the STAR21 [3] experimental train with speeds up to 315 km/h, showing these lateral oscillations to be at several Hertz as a peak value. As the lateral oscillations in a tunnel were found to be 10 times higher than in the open air because of the asymmetric flow expansion at the tail, the Japanese RTRI presented an initial CFD study of the train wake [4] in which they suggested an improved tail shape blunter than the original head geometry, to reduce drastically the oscillations in tunnels. Although the suggested tail shape reduces the lateral oscillations in the tunnel to a value only 2 times higher compared to the value for open air conditions, a blunter head shape clearly contradicts the efforts concerning the reduction of the micro-pressure wave emission ("sonic boom" effect) at the tunnel exit.

To feed the numerical calculations of the flow around the trailing car with the correct inflow conditions, the structure of the turbulent boundary layer was measured under full scale conditions with $Re=12 \cdot 10^6$ based on the equivalent diameter. Figure 1 shows the test arrangement and the data obtained in a log-log scaling. Approximated by a power law, for this highly turbulent flow the measured variation of the velocity with the distance to the train surface can be well represented by a power factor of 1/10, this factor is also supported by [5].

To come to a clear understanding of the train wake flow phenomena, the analysis methods of flow topology are used (see e.g. [6]). The surface flow field structure is represented due to its skeleton via the detection of the "singular points" in which in the wall plane the skin friction vector vanish identically. These singular points can be of the so-called nodal, saddle and focus type. Once having located these points on the train surface and the separating streamlines connecting them following the rules of flow topology, the visualisation of closed separation bubbles, separating and reattaching shear layers reaching into mid-air as well as vortical flow structures, leads to a clear portrait of the wake flow situation. Figure 2 exhibits a first comparison between a 1:7 model scale test of the ICE trailing car and the related numerical simulation using the commercial Navier-Stokes code FLUENT with a standard $k-\epsilon$ turbulence model. Concerning the overall flow separation on the trailer shoulders there is a quite resemblance between the experimental "oil flow visualisation" and the computational skin friction lines, although the details of this separation process were not resolved in the experiment.

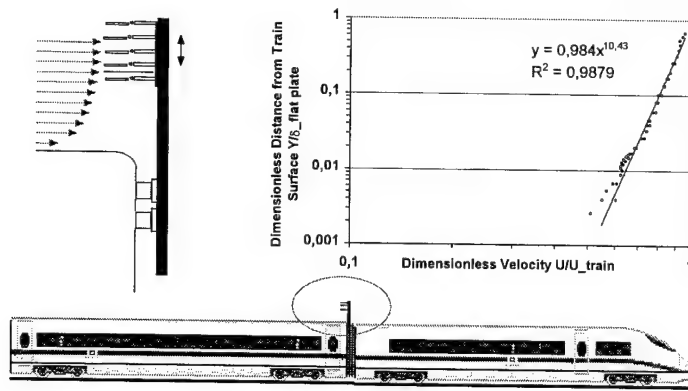


Figure 1: Test arrangement and measured data in log-log scaling near the surface of an ICE trailing car with $Re=12 \cdot 10^6$

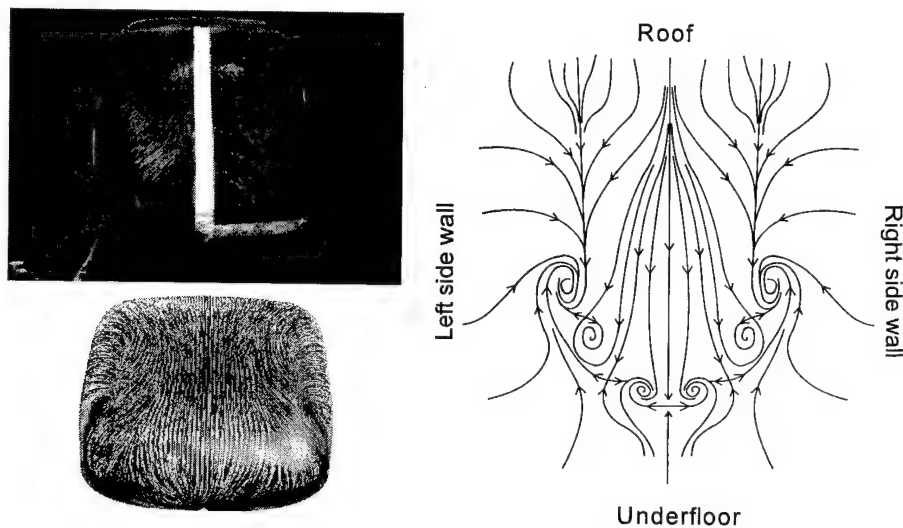


Figure 2: Wall flow pattern on the surface of the ICE trailing car (Top: wind tunnel test scale 1:7 with $Re=2 \cdot 10^6$, Bottom: numerical simulation of 1:1 scale test with $Re = 12 \cdot 10^6$, Right: topological structure at rear part with onflow from roof, side walls and underfloor)

The skin friction computation shows clearly the two vortices spiralling out of wall focus points on each of the nose shoulders and a vortex starting at the trailing "tip". All these vortices, on each side with the same sense of rotation, will combine in the wake to a complex overall left-right vortex system now subject to the classical rules of vortex dynamics. It can be expected that due to the induction law of vortex motion these vortices stay close together while slowly coming down to the ground, i.e. the track, where they then separate promptly for leaving the train's near wake to the left and right hand remaining close to the ground. This effect amplifies the slipstream velocity in the train wake basically created by the boundary layer thickening along the train and causes the massive train induced velocity increase in the slipstream after the complete train has passed, this is directly felt e.g. by passengers on the platform or maintenance workers near the tracks.

References

- 1 C. Taylor: *Quantity not quality, as high-speed operators mark time*; Railway Gazette Int., October 1999
- 2 RAPIDE Project Programme: Annex 1 to BriteEuRamIII-Contract BRPR CT97-0603 (1998)
- 3 Kohama Y, Koshikawa T & Okude: *Wake Characteristics of a High Speed Train in Relation to TailCoach Oscillations*, Vehicle Aerodynamics Conference, Loughbrough University, UK (1994)
- 4 Suzuki M, Maeda T & Arai N: *Numerical Simulation of Flow Around Train*, IMACS-COST Conference on 3D Complex Flows, Lausanne, Switzerland (1995)
- 5 Wiegardt K: *Theoretische Strömungslehre*, LAMM 4, B. G. Teubner, Stuttgart (1974)
- 6 Peake D.J. and Toback M., *Three Dimensional Interaction and Vortical Flows with Emphasis on High Speeds*, AGARDograph No. 252, (1980)

Adresses: DR. B. SCHULTE-WERNING, DR. C. HEINE AND G. MATSCHKE Deutsche Bahn AG, Forschungs-und Technologie-Zentrum, Völckerstr. 5, D-80939 München

MICHAEL HINZE

A remark on second order methods in control of fluid flow

We present the functional analytic framework for a tracking-type control problem of the instationary Navier-Stokes equations. As solution methods for the control problem we comparatively discuss Newton's method as an example of the black box approach, and the SQP-method as one of the all-at-once methods. It is argued that black box approaches in general outperform all-at-once methods since the numerical effort necessary to numerically solve linearizations of the instationary Navier-Stokes equations compares to that of the nonlinear Navier-Stokes system. We report a numerical comparison which illustrates our argumentation. For both approaches local convergence results are cited.

1. The optimal control problem

We consider the optimal control problem

$$\left. \begin{aligned} \min_{(y,u) \in W \times U} J(y,u) &:= \frac{1}{2} \int_{Q_o} |y - z|^2 dx dt + \frac{\alpha}{2} \int_{Q_c} |u|^2 dx dt \\ \text{subject to} \\ \frac{\partial y}{\partial t} + (y \cdot \nabla) y - \nu \Delta y + \nabla p &= Bu & \text{in } Q = (0, T) \times \Omega, \\ \operatorname{div} y &= 0 & \text{in } Q, \\ y(t, \cdot) &= 0 & \text{on } \Sigma = (0, T) \times \partial\Omega, \\ y(0, \cdot) &= y_0 & \text{in } \Omega. \end{aligned} \right\} \iff e(y,u) = 0 \text{ in } Z^*. \quad (1)$$

Here $Q_c := \Omega_c \times (0, T)$ and $Q_o := \Omega_o \times (0, T)$, with Ω_c and Ω_o subsets of $\Omega = (0, 1)^2$ denoting control and observation volumes, respectively. The first term in the cost functional values the control gain which here is to track the state z , and the second term measures the control cost, where $\alpha > 0$ denotes a weighting factor. In this form solving (1) appears at first to be a standard task. However, the formidable size of (1) and the goal of analyzing second order methods necessitate an independent analysis. One of the few contributions focusing on second order methods for optimal control of fluids are given by Ghattas *et al* [2] and Heinkenschloss [3]. These works are restricted to stationary problems, however. Among other things analytical investigations on second order methods are given by Kunisch and the author [5], where also further references can be found.

To define the spaces and operators required for the investigation of (1) we introduce the solenoidal spaces $H = \{v \in C_0^\infty(\Omega)^2: \operatorname{div} v = 0\}^{-1,1}_{L^2}$, $V = \{v \in C_0^\infty(\Omega)^2: \operatorname{div} v = 0\}^{-1,1}_{H^1}$, with the superscripts denoting closures in the respective norms. Further we define $W = \{v \in L^2(V): v_t \in L^2(V^*)\}$ and $Z := L^2(V) \times H$, where W is endowed with the norm $|v|_W = (|v|_{L^2(V)}^2 + |v_t|_{L^2(V^*)}^2)^{1/2}$, and set $\langle \cdot, \cdot \rangle := \langle \cdot, \cdot \rangle_{L^2(V^*), L^2(V)}$, with V^* denoting the dual space of V . Here $L^2(V)$ is an abbreviation for $L^2(0, T; V)$ and similarly $L^2(V^*) = L^2(0, T; V^*)$. In (1) further $U = L^2(Q_c)$ denotes the Hilbert space of controls which is identified with its dual U^* . The state z is assumed to an element of $L^2(H)$. It is not hard to show that the cost functional $J: L^2(H) \times U \rightarrow \mathbb{R}$ is bounded from below, weakly lower semi-continuous, twice Fréchet differentiable with locally Lipschitzian second derivative, and radially unbounded in u , i.e. $J(y, u) \rightarrow \infty$ as $|u|_U \rightarrow \infty$, for every $y \in W$. It is well known that the nonlinear mapping $e: W \times U \rightarrow Z^*$, $e(y, u) = (\frac{\partial y}{\partial t} + (y \cdot \nabla) y - \nu \Delta y - Bu, y(0) - y_0)$ is onto [1]. Here, $Bu(t, \cdot)$ denotes the Leray-projection of the extension by zero of $u(t, \cdot)$ to the whole of Ω and $y_0 \in H$. Therefore, with respect to existence (1) can equivalently be rewritten as $\min \hat{J}(u) = J(y(u), u)$ subject to $u \in U$, where $y(u) \in W$ satisfies $e(y(u), u) = 0$. It is proved in [1] that this problem admits a solution $x^* = (y^*, u^*) \in W \times U =: X$.

We distinguish two numerical approaches for the numerical solution of (1): In the *black-box* approach Newton's method is applied to the equation $\nabla \hat{J}(u) = 0$ in U . For a given control iterate $u = u^0$ the Newton step amounts to the solution of one Navier-Stokes system for $y(u)$, the solution of one adjoint system for $\lambda(u)$, and the solution of the Newton system $H((y(u), u), \lambda(u)) \delta u = -\nabla \hat{J}(u)$, see [5]. In the *all-at-once* approach the SQP-method is applied to solve (1). This is equivalent to apply Newton's method to solve $\nabla L(x, \lambda) = 0$, where $L: X \times Z \rightarrow \mathbb{R}$, $L(x, \lambda) = J(x) + \langle e(x), \lambda \rangle_{Z^*, Z}$ denotes the Lagrangian corresponding to problem (1). For a given iterate (x, λ) the numerical amount in every iteration step of this approach consists in solving one linearized Navier-Stokes system (with solution b1), and two adjoint-like linear systems (with solutions b2 and b3, respectively) to provide the right-

hand-side r in the reduced system $H(y, u, \lambda)\delta u = r$, and of the solution of the reduced system for δu . The increments δy and $\delta \lambda$ can then be obtained from δu , b1, b2 and b3 [5]. In both approaches $H(x, \lambda) = T^*(x)L_{xx}(x, \lambda)T(x)$ denotes the reduced Hessian, where $T(x) := [-e_y^{-1}(x)e_u(x), Id_U]^t$ with $x = (y, u)$. It is worth noting that due to the structure of the reduced Hessian these systems themselves have to be solved iteratively. For the numerical example presented in Tab. 1 we utilized the cg-algorithm. Proofs of local convergence with expected rates for both methods are given in [5] for a wide range of control problems. In [3] it is claimed that *all-at-once* approaches in general numerically outperform *black-box* approaches, since in the latter ones nonlinear systems have to be solved iteratively, whereas in the *all-at-once* approaches only linear system solves are required. Arguing in this way seems not to be correct for control problems for fluid flow since the numerical effort necessary to numerically solve linearizations of the instationary Navier-Stokes equations compares to that of the nonlinear Navier-Stokes system [5].

In Tab. 1 we present a numerical comparison of Newton's method and the SQP-approach to the control of a cavity flow at Reynolds number $1/\nu = \text{Re}=400$. We chose $\Omega_c = \Omega_o = (0, 1)^2$ and $\alpha = 10^{-2}$. As initial guess for the SQP-algorithm we utilized the tuple (x^0, λ^0) where $x^0 = (y^0, u^0)$ is obtained from applying one step of Newton's method with initial control equal to zero to the numerical solution of $\nabla \hat{J}(u) = 0$, i.e. with u^0 computed by Newton's method y^0 denotes the solution of the Navier-Stokes equations in (1) with $u = u^0$. Finally, the initial guess for the Lagrange multiplier is set to $\lambda^0 = -e_y(x^0)J_y(x^0)$. Newton's method is initialized with $u^0 = 0$. The numerical details can be found in [4,6]. The SQP-method takes 10 iterations and approximately 3 hours cpu to calculate a numerical solution, whereas Newton's method takes only 4 iterations at 1.3 hours cpu. As is expected due the inexact solution of the reduced systems both methods only converge super-linearly. All computations were performed on a ORIGINTM 200.

Table 1: Performance of the SQP- method (left) versus Newton's Method (right)

It	CG-It	$\frac{ L'(x, \lambda) }{ L'(x^0, \lambda^0) }$	$\frac{ \delta(x^k, \lambda^k) }{ \delta(x^{k+1}, \lambda^{k+1}) }$	$J(x^k)$	CG-It	$\frac{ J'(u^k) }{ J'(u^0) }$	$\frac{ \delta u^k }{ \delta u^{k-1} }$	$\hat{J}(u^k)$
0	-	-	-	1.188772e-2	-	1.e0	-	1.188772e-2
1	11	1.e0	1.	3.216904e-3	13	3.343476e-1	1.	3.216904e-3
2	3	2.342777e-1	0.456	1.661840e-3	11	5.032540e-2	0.489	1.618184e-3
3	16	5.846246e-1	1.110	2.041436e-3	18	8.839902e-3	0.428	1.479364e-3
4	5	1.574504e-1	0.959	1.548152e-3	16	1.126838e-4	0.079	1.477881e-3
5	14	2.718657e-2	0.554	1.683024e-3	-	-	-	-
6	23	6.744024e-2	0.914	1.485434e-3	-	-	-	-
7	18	8.005254e-2	0.874	1.521882e-3	-	-	-	-
8	18	1.852064e-2	0.197	1.480751e-3	-	-	-	-
9	23	1.343532e-3	0.146	1.479234e-3	-	-	-	-
10	26	1.698641e-4	0.127	1.479219e-3	-	-	-	-

Acknowledgements

This work was supported by the Sonderforschungsbereich 557 Beeinflussung komplexer turbulenter Scherströmungen, sponsored by the Deutsche Forschungsgemeinschaft.

2. References

- 1 ABERGEL, F., TEMAM, R.: On some Control Problems in Fluid Mechanics. *Comput. Fluid Dynamics* 1 (1990), 303–325.
- 2 GHATTAS, O., BARK, J.J.: Optimal control of two- and three-dimensional incompressible Navier-Stokes flows. *Journal of Computational Physics* 136 (1997), 231–244.
- 3 HEINKENSCHLOSS, M.: Formulation and Analysis of a Sequential Quadratic Programming method for the Optimal Dirichlet Boundary Control of Navier-Stokes Flow. In *Optimal Control, Theory, Algorithms, and Applications*. Kluwer Academic Publishers B.V. (1998)
- 4 HINZE, M.: The SQP-method for tracking-type control of the instationary Navier-Stokes equations, Fachbereich Mathematik, Technische Universität Berlin (2000)
- 5 HINZE, M., KUNISCH, K.: Second order methods for optimal control of time-dependent fluid flow. Karl-Franzens Universität Graz, Institut für Mathematik, Spezialforschungsbereich F003, Bericht 165 (1999)
- 6 HINZE, M., KUNISCH, K.: Newton's method for tracking-type control of the instationary Navier-Stokes equations. To appear in *ENUMATH99*, Eds. P. Neittaanmäki et al., Jyväskylä, Finland (1999)

Addresses: PROF. DR. MICHAEL HINZE, TU Dresden, Fakultät für Mathematik, Zellescher Weg 12-14, D-01069 Dresden.

THOMAS SLAWIG

Domain Optimization for the Navier-Stokes Equations by an Embedding Domain Technique

A class of domain optimization problems for the two-dimensional stationary Navier-Stokes equations is studied. An embedding domain technique provides an equivalent formulation of the problem on a fixed domain, a reduction of the computational effort for the solution of the state equations, and moreover a simply computable formula for the derivative of the cost functional with respect to the domain. Existence of a solution to the class of domain optimization problems is proved. Numerical examples show the reliability of the derivative formula.

1. A Class of Domain Optimization Problems

We consider domains $\Omega_\gamma \subset \mathbb{R}^2$ where the control parameter $\gamma : I \rightarrow \Gamma_\gamma$ is a function whose graph is a part of $\partial\Omega_\gamma$, whereas the remaining part Γ is fixed. E.g., Ω_γ may be the unit square with Γ consisting of three of its sides, and $I := (0, 1)$. For the embedding domain technique and the explicit formula of the derivative we need a combination of C^2 and convex polygonal boundary. Thus the set of admissible functions γ is defined as

$$\mathcal{S} := \{\gamma \in H^3(I) : \|\gamma\|_{H^3(I)} \leq c_S, \gamma(0) = \gamma(1) = 0, c_0 \leq \gamma(x) \leq c_1, x \in (\delta, 1 - \delta), \gamma'|_{(0, \delta)} = c^0, \gamma'|_{(1 - \delta, 1)} = c^1\}$$

with $c_0, c_1 \in (0, 1)$, $\delta \in (0, \frac{1}{2})$, $c_S, c^0 \in \mathbb{R}^+$, $c^1 \in \mathbb{R}^-$ fixed. For an observation region $\Omega_C \subset \Omega_\gamma$ with $\text{dist}(\Gamma_\gamma, \Omega_C) > 0$ for all $\gamma \in \mathcal{S}$, $\mathcal{A} \in \mathcal{L}(H^1(\Omega_\gamma)^2, L^2(\Omega_C)^k)$, and $\mathbf{u}_d \in L^2(\Omega_C)^k$ with k appropriately chosen, we study the problem

$$\min_{\gamma \in \mathcal{S}} \mathcal{J}(\gamma) := \frac{1}{2} \|\mathcal{A}\mathbf{u}_\gamma - \mathbf{u}_d\|_{L^2(\Omega_C)^k}^2 \quad (1)$$

where $\mathbf{u}_\gamma \in H^2(\Omega_\gamma)^2$ together with $p_\gamma \in H^1(\Omega_\gamma) \cap L_0^2(\Omega_\gamma)$ is a variational solution of the Navier-Stokes equations

$$\begin{aligned} -\nu \Delta \mathbf{u}_\gamma + \mathbf{u}_\gamma \cdot \nabla \mathbf{u}_\gamma + \nabla p_\gamma &= \mathbf{f}_\gamma & \text{in } \Omega_\gamma \\ \nabla \cdot \mathbf{u}_\gamma &= 0 & \text{in } \Omega_\gamma \\ \mathbf{u}_\gamma &= \Phi & \text{on } \Gamma \\ \mathbf{u}_\gamma &= \mathbf{0} & \text{on } \Gamma_\gamma. \end{aligned} \quad (2)$$

The stated regularity is guaranteed by the choice of \mathcal{S} , $\mathbf{f}_\gamma \in L^2(\Omega_\gamma)^2$, and $\Phi \in L^2(\Gamma)^2$ with a divergence-free extension onto $H^2(\Omega_\gamma)^2$, see e.g. [1]. Problem (1) includes cost functionals as tracking type or drag studied e.g. in [2], [3].

2. The Embedding Domain Technique

We choose $\hat{\Omega}$ with $\Omega_\gamma \subset \hat{\Omega}$ for all $\gamma \in \mathcal{S}$, see the left figure below, and compute $(\hat{\mathbf{u}}_\gamma, \hat{p}_\gamma, g_\gamma) \in H^1(\hat{\Omega})^2 \times L_0^2(\hat{\Omega}) \times H_\gamma^*$ such that

$$\begin{aligned} -\nu \Delta \hat{\mathbf{u}}_\gamma + \hat{\mathbf{u}}_\gamma \cdot \nabla \hat{\mathbf{u}}_\gamma + \nabla \hat{p}_\gamma - \tau_\gamma^* g_\gamma &= \tilde{\mathbf{f}}_\gamma & \text{in } H^{-1}(\hat{\Omega})^2 \\ \nabla \cdot \hat{\mathbf{u}}_\gamma &= 0 & \text{in } L_0^2(\hat{\Omega}) \\ \tau_\gamma \hat{\mathbf{u}}_\gamma &= \mathbf{0} & \text{in } H_\gamma. \end{aligned} \quad (3)$$

where τ_γ denotes the trace operator onto Γ_γ and $H_\gamma := H_{00}^{1/2}(\Gamma_\gamma)^2$ is defined in [4, VII. §2 Sec. 2.1 Rmk. 1]. Problems (2) and (3) are equivalent in the following sense:

Theorem 1. Let $\gamma \in \mathcal{S}$ and \mathbf{f}_γ, Φ as described at the end of the last section. Then $(\hat{\mathbf{u}}_\gamma, \hat{p}_\gamma, g_\gamma)$ is a solution of (3) if and only if $(\mathbf{u}_\gamma, p_\gamma) := (\hat{\mathbf{u}}_\gamma, \hat{p}_\gamma)|_{\Omega_\gamma}$ solves (2), $(\hat{\mathbf{u}}_\gamma, \hat{p}_\gamma)|_{\Omega_\gamma^c} = (\mathbf{0}, 0)$, and $g_\gamma = \tau_\gamma(\nu \frac{\partial \hat{\mathbf{u}}_\gamma}{\partial \mathbf{n}_\gamma} - p_\gamma \mathbf{n}_\gamma)$ in $H^{1/2}(\Gamma_\gamma)^2$. Here $\Omega_\gamma^c := \hat{\Omega} \setminus \bar{\Omega}_\gamma$ and \mathbf{n}_γ denotes the outer (with respect to Ω_γ) normal on Γ_γ .

Proof. The result is proved by testing the weak form of (2) with functions that vanish on Ω_γ^c , applying a uniqueness result for the homogeneous Navier-Stokes equations and Green's formula. See [5, Th. 3.5].

3. Differentiability and Derivative Formula

With the assumption on \mathcal{S} we can show continuous dependence of the solution of (3) with respect to variations in γ and the existence of a solution to problem (1), see [5, Ths. 3.7, 3.8]. Moreover the dependence of the velocity vector is even Lipschitz. This fact is used to proof the following result on differentiability. In the derivative formula presented below the solutions $(\hat{\lambda}_\gamma, \hat{\mu}_\gamma, \chi_\gamma) \in H_0^1(\hat{\Omega})^2 \times L_0^2(\hat{\Omega}) \times H_\gamma^*$ of the adjoint problem on the fictitious domain, i.e.

$$\begin{aligned} -\nu \Delta \hat{\lambda}_\gamma + \nabla \hat{\mu}_\gamma \cdot \hat{\lambda}_\gamma - \hat{\mathbf{u}}_\gamma \cdot \nabla \hat{\lambda}_\gamma + \nabla \hat{\mu}_\gamma - \tau_\gamma^* \chi_\gamma &= -D_u \mathcal{J}(\gamma) \quad \text{in } H^{-1}(\hat{\Omega})^2 \\ \nabla \cdot \hat{\lambda}_\gamma &= 0 \quad \text{in } L_0^2(\hat{\Omega}) \\ \hat{\lambda}_\gamma &= 0 \quad \text{in } H_\gamma \end{aligned}$$

are used. Here we have to restrict the parameter ν . For more details and the proof of this result see [5, Th. 3.10].

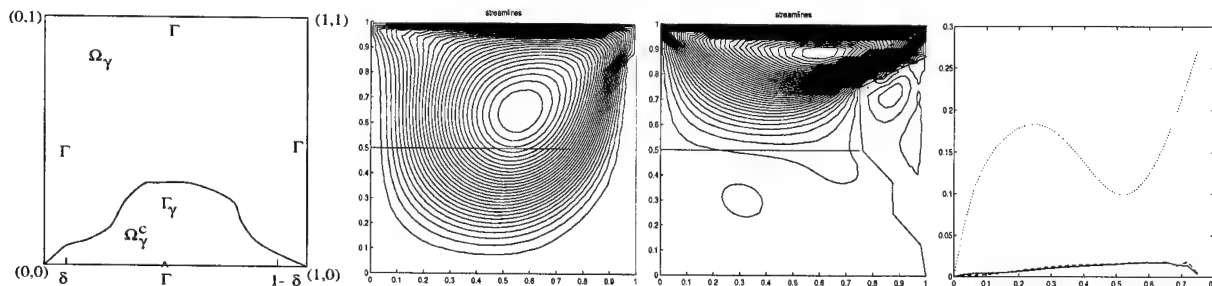
Theorem 2. Let $\gamma \in \text{int } \mathcal{S}$, $\mathbf{f} \in L^\infty(\hat{\Omega})^2$, $\mathbf{f}_\gamma := \mathbf{f}|_{\Omega_\gamma}$, and $\nu > \nu_1$. Then \mathcal{J} is Fréchet differentiable with respect to γ and the derivative in γ in direction $\bar{\gamma} \in \mathcal{S}' := \{\bar{\gamma} \in H^3(I) : \bar{\gamma}|_{[0,\delta] \cup [1-\delta,1]} = 0\}$ satisfies

$$D_\gamma \mathcal{J}(\gamma) \bar{\gamma} = \frac{1}{\nu} \int_I [g_\gamma(x, \gamma(x)) \cdot \chi_\gamma(x, \gamma(x)) - p_\gamma(x, \gamma(x)) \mu_\gamma(x, \gamma(x))] \bar{\gamma}(x) dx.$$

Evaluating this formula only requires computation of a one-dimensional integral that can be performed – e.g. for FE discretizations as used below – exactly by simple quadrature rules. No normal derivatives have to be computed.

4. Numerical Example

Aim was to move the vortex arising in a standard driven cavity flow at $Re = \frac{1}{\nu} = 500$ over the line $\Omega_C := [0, 0.75] \times \{0.5\}$. We used $\mathcal{J}(\gamma) := \int_{\Omega_C} \|\mathbf{u}_\gamma\|_2^2 dx$ and controlled by variation of the right wall in $[0.75, 1] \times [0.125, 0.75]$. Starting at a straight line at $x = 0.99$ (2nd picture) an SQP optimization method using the derivative formula above reaches a geometry (3rd picture) with a reduction of \mathcal{J} to one percent in just seven iterations. For the velocity norm along Ω_C see the 4th picture. Dotted: starting curve, solid: solution, dashed: comparison with Γ_γ being a straight line at $x = 0.75$. Compared to this the value of \mathcal{J} for the geometry obtained by the optimization algorithm is even 10 percent lower. In this sense we regard the solution as “optimal”.



Acknowledgements

The author would like to thank Max Gunzburger for the invitation to the Special Session on Flow Control at GAMM 2000.

5. References

- 1 GUNZBURGER M.D., H. KIM, Existence of an optimal solution of a shape control problem for the stationary Navier-Stokes equations, SIAM J. Control Optim. **36**, No. 3 (1998), 895-909.
- 2 GALDI, G.P.: An Introduction to the Mathematical Theory of the Navier-Stokes Equations, Vol.1, Springer New York 1994.
- 3 KELLOGGS, R.B., J.E. OSBORN: A Regularity Result for the Stokes Problem in a Convex Polygon, Journal on Functional Analysis, **21** (1976), 397-431.
- 4 DAUTRAY R., J.-L. LIONS, Mathematical Analysis and Numerical Methods for Science and Technology, Vol. 2, Springer Berlin 1988.
- 5 SLAWIG, T., Domain Optimization for the stationary Stokes and Navier-Stokes Equations by an Embedding Domain Technique, Shaker Aachen 1998.

Addresses: T. S., Potsdam Institute of Climate Impact Research, P.O. Box 601203, 14412 Potsdam, Germany.

Author Index

- Adolph, T. 753
 Aksel, N. 487, 493
 Albensoeder, S. 779, 781
 Angermann, L. 755
 Antes, H. 589
 Arnold, M. 735
 Aurnhammer, A. 653
 Avsec, J. 505, 515

 Ballmann, J. 457
 Bartel, A. 739
 Bastian, M. 705
 Baumbach, V. 517
 Becker, W. 663, 667, 683
 Beckert, K. 511
 Bednarik, M. 587
 Beg, D. 679
 Benner, P. 707, 717
 Berger, A. 611, 623
 Bielert, U. 519
 Bittner, L. 655
 Blachut, J. 657
 Blohm, C. 781
 Blome, P. 523
 Bockhorn, H. 529, 531
 Boese, F. G. 709
 Böhme, G. 459
 Borchardt, J. 715
 Breitung, W. 519
 Breuer, M. 461
 Broda, M. 781
 Burgeth, B. 519
 Burgmair, R. 659
 Bushe, W. K. 563

 Callies, M. 613
 Callies, R. 613, 743, 769
 Cervenka, M. 587
 Chapko, R. 757
 Chelminski, K. 595
 Chen, J.-Y. 541
 Cheng, A. H.-D. 591
 Chernigovski, S. 447
 Chun, Ch.-H. 503
 Ciglaric, I. 661
 Class, A. G. 783

 Darabiha, N. 567
 De Boer, H. 699
 Delfs, J. 583
 Demuth, R. 469
 Detmers, F. 711
 Diebels, S. 521
 Dillmann, A. 449
 Dinkelmann, M. 771
 Dobes, J. 451
 Dostal, Z. 703

 Dreizler, A. 527
 Dreyer, M. 517, 577
 Dyllong, E. 713
 Dziecielak, R. 585

 Ehlers, W. 521, 523
 Ehrenstein, G. W. 687
 Ehrhardt, K. 715
 Engels, H. 663
 Eschenauer, H. A. 693
 Etman, L. F. P. 691
 Exner, A. 463

 Farge, M. 465, 485
 Faßbender, H. 717
 Favier, V. 525
 Fedorchenko, I. A. 773
 Fedorova, N. N. 773
 Fischer, B. 759
 Flajs, R. 719
 Fokin, D. 453
 Forkel, H. 541
 Fort, J. 451
 Frank, W. 467
 Franke, J. 467
 Fricke, K. J. 447
 Fröhner, A. 761
 Fürst, J. 451

 Gasser, I. 597
 Geiß, S. 527
 Gerlinger, W. 529, 531
 Gicquel, O. 567
 Gittler, P. 473
 Glatzel, W. 447
 Glocker, C. 665
 Göppert, St. 507
 Grogger, H. 583
 Grund, F. 715
 Günther, M. 739
 Gutheil, E. 533
 Gwiazda, P. 599

 Halama, J. 451
 Hansel, W. 667
 Haschke, H. 763
 Heiken, S. 469
 Heiler, M. 575
 Heine, C. 789
 Heinrichs, W. 763, 765
 Heinz, S. 471
 Henselowsky, C. 497
 Herwig, H. 507, 511
 Herzberger, J. 711
 Hinze, M. 791
 Hirschler, T. 455
 Hofferek, B. 721, 727

 Horn, D. 715
 Hörnlein, H. R. E. M. 669
 Hozejowska, S. 499
 Hozejowski, L. 499
 Hribersek, M. 501
 Huld, T. 537

 Idenbirken, M. 539
 Istratie, V. 671

 Janicka, J. 483, 527, 541
 Jankovic, S. 625

 Kegl, M. 673
 Kemmler, R. 695
 Kempf, A. 541
 Kiriazov, P. 675
 Kluwick, A. 463, 473, 475
 Knobloch, S. 601
 Knopp, T. 767
 Kohout, M. 615
 Kolesnik, A. D. 637
 Konicek, P. 587
 Konickova, J. 677
 Korelc, J. 723
 Kotchourko, A. 519
 Kozel, K. 451
 Krajnc, A. 679
 Krasna, S. 661
 Kronberger, R. 475
 Krumbein, A. 477
 Kubicek, M. 615
 Kucaba-Pietal, A. 617
 Kuhlmann, H. C. 497, 503, 509, 779, 781, 785
 Kunze, M. 603
 Kutylowski, R. 681

 Lamanna, G. 569
 Lange, M. 543
 Langemann, D. 619
 Langer, S. 589
 Langer, U. 729
 Lauke, Th. 583
 Laurien, E. 469, 555, 559
 Lee, Y.-S. 503
 Lerch, R. 729
 Leypoldt, J. 785
 Lindemann, J. 683
 Linß, T. 745, 761
 Loch, B. 765
 Lübcke, H. 481
 Lube, G. 725, 767
 Ludwig, M. 759
 Lummer, M. 583
 Lunter, G. 627
 Luo, K. 545

- Luther, W. 713
 Lutz, Th. 787
 Machu, G. 547, 549
 Maltsev, A. 483, 527
 Mang, J. 479
 Marcic, M. 505, 515
 Markert, B. 521
 Marti, K. 653, 685
 Matschke, G. 789
 Mayrhofer, M. 775
 Mazur-Sniady, K. 639
 Meckbach, S. 687
 Meile, W. 547, 549
 Meinköhn, D. 551
 Meironke, H. 553
 Meister, A. 759
 Mikulski, L. 689
 Mocikat, H. 507
 Müller, L. 725
 Neff, P. 607
 Neher, M. 747
 Niemann, J. 555
 Nienhäuser, Ch. 509
 Nitsche, L. 547
 Pellegrino, G. 465
 Pelzer, A. 727
 Pfeiffer, F. 659
 Podhaisky, H. 749
 Prast, B. 569
 Prazak, J. 507
 Prebil, I. 661
 Raguz, A. 609
 Ramm, E. 695
 Rapin, G. 767
 Rasmussen, J. 703
 Rath, H. J. 497, 503, 509, 517, 577, 779, 781, 785
 Richter, M. 641
 Rieder, A. 621
 Rijpkema, J. J. M. 691
 Rogg, B. 557
 Roos, H.-G. 761
 Rottler, A. 693
 Rumberg, O. 557
 Rung, T. 481
 Sachs, G. 771, 775
 Sadiki, A. 483, 527, 541
 Saje, M. 719
 Saptoadi, D. 559
 Sauer, J. 561
 Schaflinger, U. 479
 Schaflinger, U. 547, 549, 565
 Schagerl, M. 623
 Schanz, M. 591
 Schinnerl, M. 729
 Schmidt, J. W. 705
 Schmitt, B. A. 749
 Schnabel, U. 731
 Schneider, K. 465, 485, 529, 531
 Schnerr, G. H. 561
 Schnerr, G. H. 573, 575, 579, 581
 Scholle, M. 487, 493
 Schönauer, W. 753
 Schoofs, A. J. G. 691
 Schreiber, I. 615
 Schüle, E. 773
 Schulte-Werning, B. 789
 Schwarz, St. 695
 Schwetlick, H. 731
 Seiler, W. M. 629
 Severin, J. 511
 Sieniawska, R. 643, 645
 Slawig, T. 793
 Sniady, P. 639, 645
 Socha, L. 647
 Sokala, M. 499
 Soong, C. Y. 489
 Starkloff, H.-J. 641, 649, 651
 Steiner, H. 563
 Steinrück, H. 513
 Stöckl, G. 697
 Strauß, K. 539
 Szymczyk, J. A. 553
 Teppner, R. 565
 Thevenin, D. 567
 Thiele, F. 481
 Ting, C.-C. 777
 Tuliszka-Sznitko, E. 489
 Ungarisch, M. 479
 van Dongen, M. E. H. 569
 van Keuk, J. 457
 van Keulen, F. 699
 Vervenne, K. 699
 Vervisch, L. 525
 Vietor, Th. 701
 vom Scheidt, J. 641, 649, 651
 Vondrak, V. 703
 Vortmann, C. 573
 Voss, H. 721, 727
 Vrdoljak, M. 625
 Wächter, M. 771
 Wagner, C. 491
 Wagner, S. 453
 Wang, S. 755
 Warnatz, J. 543
 Weiner, R. 749
 Wichmann, T. 633
 Wieners, C. 733
 Wierschem, A. 487, 493
 Wilkening, H. 537
 Wimmer, G. 769
 Winkler, G. 575
 Wölk, G. 577
 Wunderlich, R. 649, 651
 Wunsch, O. 459
 Wursthorn, S. 579
 Wysocka, A. 643
 Yin, J. 583
 Yuan, W. 581
 Zakrajsek, E. 719
 Zerz, E. 635
 Zgonik, M. 505
 Ziegler, F. 593
 Zlatanovski, T. 495
 Zukowski, S. 643, 645

Great News in 2002 - Price Reduction of ZAMM!

It is a great pleasure for Wiley-VCH to announce several fundamental changes in 2002 of

ZAMM Zeitschrift für angewandte Mathematik und Mechanik Journal of Applied Mathematics and Mechanics

1. Price reduction of more than 650 DM!

Starting from 2002 the full price for institutional subscribers will be reduced from actual € 1628 to € 1300 p.a., which means you save € 328 (app. 650 DM) per year! Of course the number of articles in their usual high quality will not change.

2. Free access to the Electronic Publication of "Proceedings in Applied Mathematics and Mechanics"!

The proceedings of the GAMM-Conferences (starting with the Zurich 2001 GAMM-Conference) will be published in a new electronic journal "Proceedings in Applied Mathematics and Mechanics" which will be free of charge for GAMM members and subscribers of *ZAMM - Journal for Applied Mathematics and Mechanics*.

The *Proceedings in Applied Mathematics and Mechanics* will be part of Wiley InterScience (www.interscience.wiley.com) and available on CD-ROM.

3. Save time by Early View!

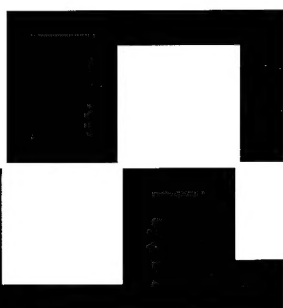
Articles of the electronic publication are available up to 75 days earlier than the printed version

For further information please contact us:

WILEY-VCH Reader Service
P.O. Box 10 11 61
D-69451 Weinheim, Germany

Phone +49 (0) 6201 / 606 147
Fax +49 (0) 6201 / 606 117
E-mail subservice@wiley-vch.de

<http://www.wiley-vch.de/berlin>



Contents:

- The Conjugate Operator Method.
Applications to Dirac Operators and to Stratified Media
- Singular Interaction Problems of Parabolic Type with Distribution and Hyperfunction Data
- Asymptotic Laplace Transforms and Evolution Equations
- Local Operator Methods and Time Dependent Parabolic Equations on Non-cylindrical Domains
- Feshbach Resonances in the Semi-classical Limit
- Elliptic Complexes of Pseudodifferential Operators on Manifolds with Edges

Demuth, Michael et al. (ed.)

Evolution Equations, Feshbach Resonances, Singular Hodge Theory Advances in Partial Differential Equations

Series: Mathematical Topics (Volume 16)

1999, 432 pages with 14 figures. Hardcover.
DM 198.-/€ 101,24/sFr 176.-. ISBN 3-527-40233-0

Evolution equations describe many processes in science and engineering, and they form a central topic in mathematics. The first three contributions to this volume address parabolic evolutionary problems: The opening paper treats asymptotic solutions to singular parabolic problems with distribution and hyperfunction data. The theory of the asymptotic Laplace transform is developed in the second paper and is applied to semigroups generated by operators with large growth of the resolvent. An article follows on solutions by local operator methods of time-dependent singular problems in non-cylindrical domains.

The next contribution addresses spectral properties of systems of pseudodifferential operators when the characteristic variety has a conical intersection. Bohr-Sommerfeld quantization rules and first order exponential asymptotics of the resonance widths are established under various semiclassical regimes.

In the following article, the limiting absorption principle is proven for certain self-adjoint operators. Applications include Hamiltonians with magnetic fields, Dirac Hamiltonians, and the propagation of waves in inhomogeneous media. The final topic develops Hodge theory on manifolds with edges; its authors introduce a concept of elliptic complexes, prove a Hodge decomposition theorem, and study the asymptotics of harmonic forms.



PA0399

WILEY-VCH • P.O. Box 10 11 61 • 69451 Weinheim, Germany
Fax: +49 (0) 62 01-60 61 84 • e-mail: sales-books@wiley-vch.de •
<http://www.wiley-vch.de/>



Contents

Preface	S437
Table of Contents	S439
Sections 9–25	S447
Author Index	S795